CONTENTS

S.NO	Name of the teacher	Title of the book/chapters published	Title of the paper	Page No
		Calendar Year 2022		
1	Dr. G. Ramalakshmi		Bandwidth enhancement of a Hybrid Minkowski Koch fractal Bowtie antenna using Wilkinson Power divider for X band and Ku band applications	4-8
2	M. SRAVANI		Performance Analysis of Dual Band Circularly Polarized Hybrid Dielectric Resonator Antenna	9-11
3	Dr. R. Sridevi	Internet of Things		12-17
4	Anand Gondesi	Implementation of IT-SMC for fault rectification in a grid-connected PV system for Maximum power point tracking		18-45
5	Anand Gondesi	A Comparative Study in the Design of an Ann-Based Controller		46-62
6	Anand Gondesi	Fuzzy System-Based Load Frequency Control of Hydro-Thermal- Thermal Interconnected Power System		63-74
7	Dr. K. Anuradha	Network Security		75-77
8	Dr. K. Anuradha		Nomenclature of Diverse Feature Selection in Sentiment Analysis using Machine Learning Techniques: A Comparative Study	78-82
9	Dr. G. Vamsi Krishna		Prediction Of Chronic Kidney Disease with Various Machine Learning Techniques: A Comparative Study"	83-88

10	P. Rajyalakshmi	QCM sensor-based alcohol classification using an Ensembled stacking model		89-104
11	P. RajyaLakshmi	Identification of Heart Failure in early stages using SMOTE-Integrated Adaboost Framework		105-120
12	D. Karun Kumar Reddy	A Fog-Based Intelligent Secured IoMT Framework for Early Diabetes Prediction		121
13	Dr. D. Raja Kishor	Fuzzy Perceptron Learning for Non-Linearly Separable Patterns		122-139
14	Dr. K. Anuradha		Implementation of a Smart Intelligent Digital Home Lightning Control System	140-146
Calendar Year 2021				
1	Arunima M		GIS Approach in Demarcating Groundwater Potential Zones—A Case Study in Visakhapatnam District, A.P.	147-154
2	Dr. G. Vamsi Krishna	Data Communications and Computer Networking,		155-157
3	D. Karun Kumar Reddy	Advanced Machine Learning and Nature-inspired Optimization in Heart Failure Clinical Records Dataset		158
4	D. Karun Kumar Reddy	Deep Neural Network-based security model for IoT Device Network		159
Calendar Year 2020				
1	D. Deenabandhu		Laser applications for the optical exploration of the Dy3+ doped Li2O-CaF2 - Al2O3-B2O3-SiO2 glasses	160-169
2	D. Deenabandhu		First-principles study of structural, elastic, electronic, and optical properties of cubic perovskite LiMgF3 for novel applications	170-178
3	Dr. D. Raja Kishor	Segmenting Images Using Hybridization of K-Means and Fuzzy C-Means Algorithms		179-205

4	Srikanth Dasari	Classification of BrainTumors Using Deep Learning-Based Neural Networks		206-218
5	J. Vankara	Classification of BrainTumors Using Deep Learning-Based Neural Networks		206-218
6	Muddada Murali Krishna	Classification of BrainTumors Using Deep Learning-Based Neural Networks		206-218
Calendar Year 2019				
1	Dr. R. Sridevi		Reduction of PAPR in OFDM Signals Using Grey Wolf Optimization combined with SLM"	219-228
2	Deepak Chowdary Duvvada	Brain Storm Optimization Algorithms: Concepts, Principles and Applications		229-261
3	M. Amareswari Reddy	Theory of machines-I Kinematics of machinery		262
4	Arunima M		Real-Time Flood Forecast for Vamsadhara River Basin Through Unsteady Flow Simulation"	263-275
5	Dr. D. Madhavi		Medical Image Classification Through Deep Learning"	276-284
6	Dr. D. Madhavi		A Q learning Approach for sales prediction in Heterogeneous Information networks	285-294
Calendar Year 2018				
1	Deepak Chowdary Duvvada	Critical Developments and Applications of Swarm Intelligence		295-309
2	S. Siva Jyothi		Elemental analysis of Indian natural Chrysoberyl gemstones by PIXE technique-	310-315
3	Dr. K. Anuradha		A High-Speed Two-Step Flash ADC	316-326
4	Dr. K. Anuradha		A 10-bit High-Speed Pipelined ADC	327-332
5	Dr. K. Anuradha		A 6-bit Low Power SAR ADC	333-343
6	Dr. D. Madhavi	k-NN based Approach Using MapReduce for Meta path Classification in Heterogeneous Information Networks		344-351

Bandwidth Enhancement Of A Hybrid Minkowski Koch Fractal Bowtie Antenna Using Wilkinson Power Divider for X And Ku Band Applications

Dr.G. Ramalakshmi
Department Of ECE
Dr.L.B.College of Engineering
Visakhapatnam, India
gr.laxmi12@gmail.com

Abstract— This paper presents a Hybrid Minkowski Koch Fractal Bowtie antenna designed using FR-4 epoxy material with a dielectric constant value of 4.4 and thickness of 1.6mm. The size of the proposed antenna is 50x50x1.6mm^3. A special feed network is being introduced in this paper named as Wilkinson power divide network, which divides the power equally into the two ports. The antenna design is explained using three design stages. In the initial stage of design a simple Bowtie antenna, fed with a simple strip line feed. Further modifications done on this stage-1 by employing the Minkowski and Koch fractal shapes on the bow tie arms which is mentioned as stage-2 of the proposed design. The performance of the stage-2 is further improved by employing a Wilkinson power driver in the stage-3. ANSYS HFSS tool is used to simulate the structures over the frequency sweep of (10-16GHz). The bandwidth and gain values are observed to be improved from stage-1 to stage-3. The proposed antenna possesses two bands with a BW of 2.0GHz in X, Ku band and 1.5GHz in Ku band. The gain values are improved to 10.98 dB, 5.4dB respectively for the two operating bands of stage-3 proposed antenna.

Keywords— Bowtie antenna, Koch Fractal, Minkowski fractal, Wilkinson divider

I. INTRODUCTION

The modern wireless communication systems require antennas with wide operating frequency bands. It is being a complex task to design an antenna which serves several communication systems with multiple frequency bands as there should be a compromise between antenna's size, cost and frequency. In recent years the planar patch antennas are becoming the attractive source for antenna design engineers. The bandwidth enhancement of wide variety antennas are reported using slots of different shapes and fractals too [1-4]. However the conventional patch antennas resonates about half wave length which increases the size. Due to this reason Slot antennas are not suitable for many applications. On the other hand slot antennas possess limited bandwidth. A Bowtie antenna is the popular source for obtaining wideband characteristics [2][12]. A coaxial fed slotted Bowtie antenna designed for multiband applications like GSM,LTE and GPS applications [5].The studies reveal that high data rates are required for video transmission services involved in satellite communication systems [6]. A multiband antenna is designed for X and Ku band applications with a minimum value of return loss -22.75 dB [5]. A microstrip antenna with two parasitic patches is designed for obtaining wider Bandwidth [8]. A simple Bowtie antenna designed with slots for trainband applications [7]. Fractal geometry plays a vital role in antenna design due to its self similar structure and compactness[11] [13].A Koch fractal antenna designed for Wi-Fi /WiMAX, WLAN with an impedance bandwidth of 9.8%. A Minkowski fractal antenna have been designed with a SRR on the ground plane leads two resonances with a gain of 1.52dB and 3.45dB respectively. Different feeding techniques like quarter wave feed , Coaxial feed , SIW feed mechanism and Wilkinson power divider are the most commonly used feeding mechanisms for antennas, mixer circuits, modulators and other communication systems to reduce the transmission loss [14].

In this paper a Bowtie antenna is proposed with both Koch and Minkowski Fractal slots and a Wilkinson Power divider network is designed to feed the proposed antenna.

II. DESIGN METHODOLOGY

In the view of performance enhancement the proposed Hybrid Minkowski Koch Fractal Bowtie antenna using Wilkinson power divider is designed in three consecutive stages named as stage-1, stage-2 and stage-3 shown in Fig.1. The basic antenna dimensions for all the 3 stages are shown in Table-1.

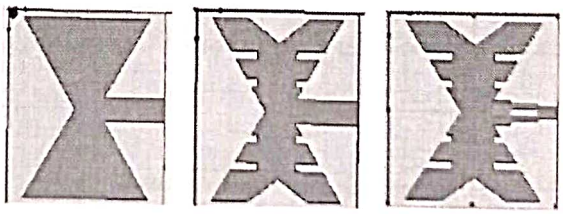

(a) Stage-1 (b)) Stage-1 (c) Stage- 3

Fig. 1. Stages of proposed Hybrid Minkowski Koch Fractal Bowtie antenna

Table:1 Geometrical parameters of proposed antenna

Parameter	Dimensions

Substrate Length	50mm
Substrate Width	50mm
Ground Length	50mm
Ground Width	50mm
patch Length	40mm
patch Width	46mm
Dielectric constant	4.4
Height of the substrate	1.6mm
Feed length	20mm
Feed width	6mm

A. Design methodology of Stage-1

A rectangular patch of dimension 28mmx40mm is designed on the substrate of 50x50mm^2. The patch dimensions are considered as 40x46mm^2 in order to create two triangular arms of Bowtie. The arms of Bowtie are formed by subtracting triangles from the rectangular structure. A simple strip line feed of dimension 20mmx6mm is united with the patch structure shown in Fig.1(a).

B. Design methodology of Stage-2

Two types of Fractal structures are accommodated on the stage-1 design namely Minkowski and Koch in order to increase the electrical path volume by the creation of more number of radiation edges as shown in Fig.2 (a) and (b). The Koch and Minkowski Fractal structures are carved on the bowtie patch arms to enhance the radiation standards.

The fractal dimension of any fractal geometry is given by

$$D = \frac{\log(N)}{\log(S)}. \qquad (1)$$

Where N is the self similar replicas and S is the scale factor. The standard D value for Koch and Minkowski fractals are 1.28 and 1.465 respectively. The optimum dimensions of fractal slots are shown in Fig.2(c).

C. Design methodology of Stage-3

The proposed model is presented in stage-3 with a special feeding mechanism. The Wilkinson power driver consists of a strip line, which is divided into some specific number of lines, each of length λ/4.There are 3 ports. Port-1 is 50Ω port and Port-2, port-3 are 100Ω ports which are isolated from each other by providing high RF resistance between them. The characteristic impedance of output port is Z_0. The impedance of each quarter wave line is $\sqrt{2Z_0}$ .This power divide network will increase the % BW and gain of antenna. The feed dimensions are mentioned in Fig.3.

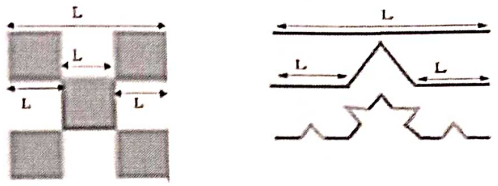

(a) The 0th iteration of fractal Minkowski Fractal (b) The 2nd iteration of Koch

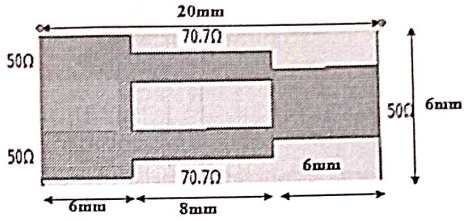

(c) Dimensions of Wilkinson power divider feed network

Fig.2. Wilkinson power driver feed and fractal geometries

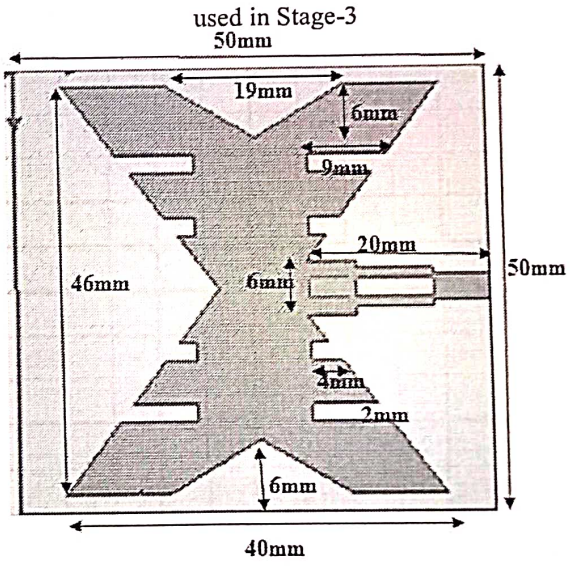

Fig.3 proposed Hybrid Minkowski Koch Fractal Bowtie antenna with Wilkinson power divider

III. Results and Discussions

The simulation results for stage-1, stage-2 and stage-3 antennas are analyzed using HFSS tool over the frequency range (10-16GHz). Different radiation parameters like Return loss, VSWR, BW and gain are reported and compared. The return loss vs. Frequency plot of stage-1

antenna has 3 operating bands shown in Fig.4 with considerable VSWR values.

Stage-2 enhances the radiation edges so the return loss vs. frequency plot has 6 operating bans reported in the Table.2. The optimum value of S_{11} dB is -28.35 at 14.0 GHz. The maximum gain value is 5.07 dB at 15.7GHz.

The return loss vs. Frequency plot and the VSWR vs. Frequency plot of stage-3 proposed antenna are shown in Fig.5 and Fig.6 respectively. The operating bands are (10.3-13.3GHZ) and (14.5-16.0GHz) with return loss values -46.73 dB and -32.0dB respectively. The VSWR values are below 2 for these operating bands. The % BW values are also good 26.1% and 9.86%. The gain values are also reasonable with 10.98 dB and 5.42 dB over these resonating bands.

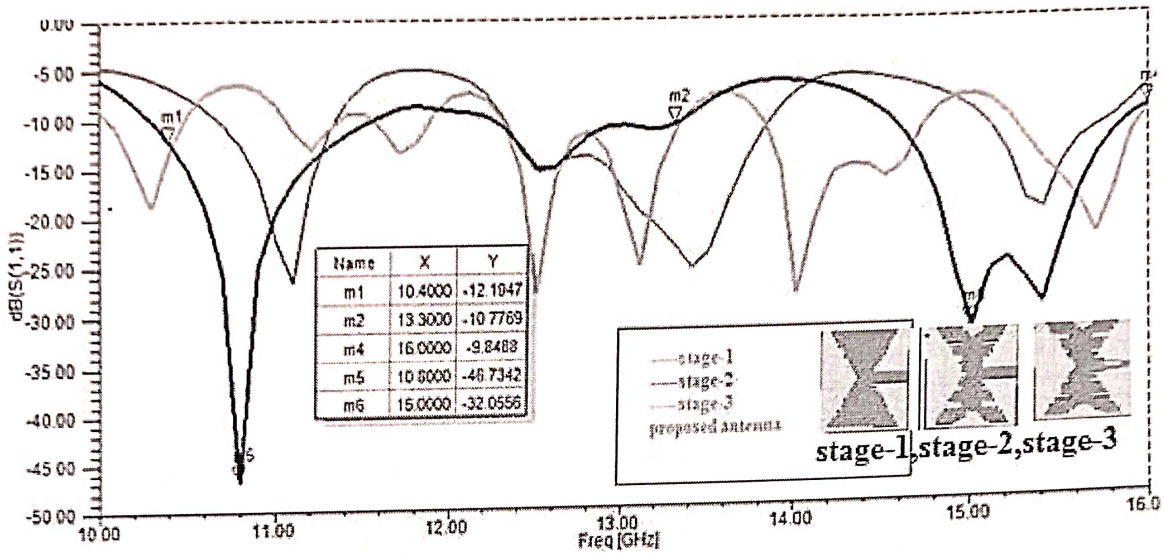

Fig.4. Return loss vs. Frequency plot for Stage-1 , stage-2 and stage-3 of proposed Hybrid Minkowski Koch Fractal Bowtie antenna.

Table2: Comparison of simulation results of stage-2 and stage-3 (proposed) antenna

S.No	f_r(GHz)	Return loss (S11)dB	Bandwidth (f_1-f_2)GHz	BW(GHz)	%BW	Gain (dB)
Stage-2 With strip line feed	10.3	-18.85	10.05-1048	0.43	4.1	1.276
	11.2	-13.02	11.04-11.36	0.32	2.85	2.83
	11.7	-13.45	11.53-11.88	0.35	2.99	3.89
	12.5	-27.74	12.3-13.35	1.05	3.78	3.57
	14.0	-28.35	13.8-14.70	0.9	6.42	3.66
	15.7	-23.12	15.2-16.00	0.8	5.09	5.07
Proposed Stage-3 with Wilkinson power divider	10.8	-46.73	10.3-13.3	2.0	26.1	10.98
	15.0	-32.0	14.5-16.0	1.5	9.86	5.42

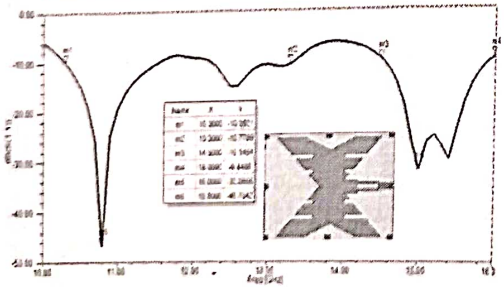

Fig.5. Return loss vs. Frequency plot for stage-3 of proposed Hybrid Minkowski Koch Fractal Bowtie antenna

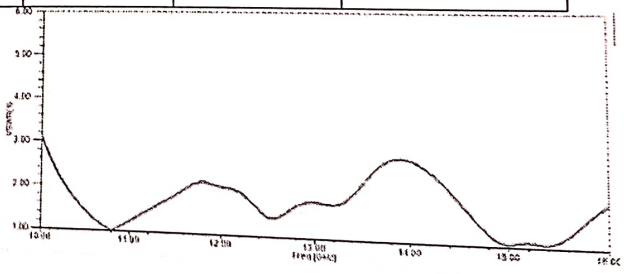

Fig.6 VSWR vs. Frequency plot for stage-3 of proposed Hybrid Minkowski Koch Fractal Bowtie antenna

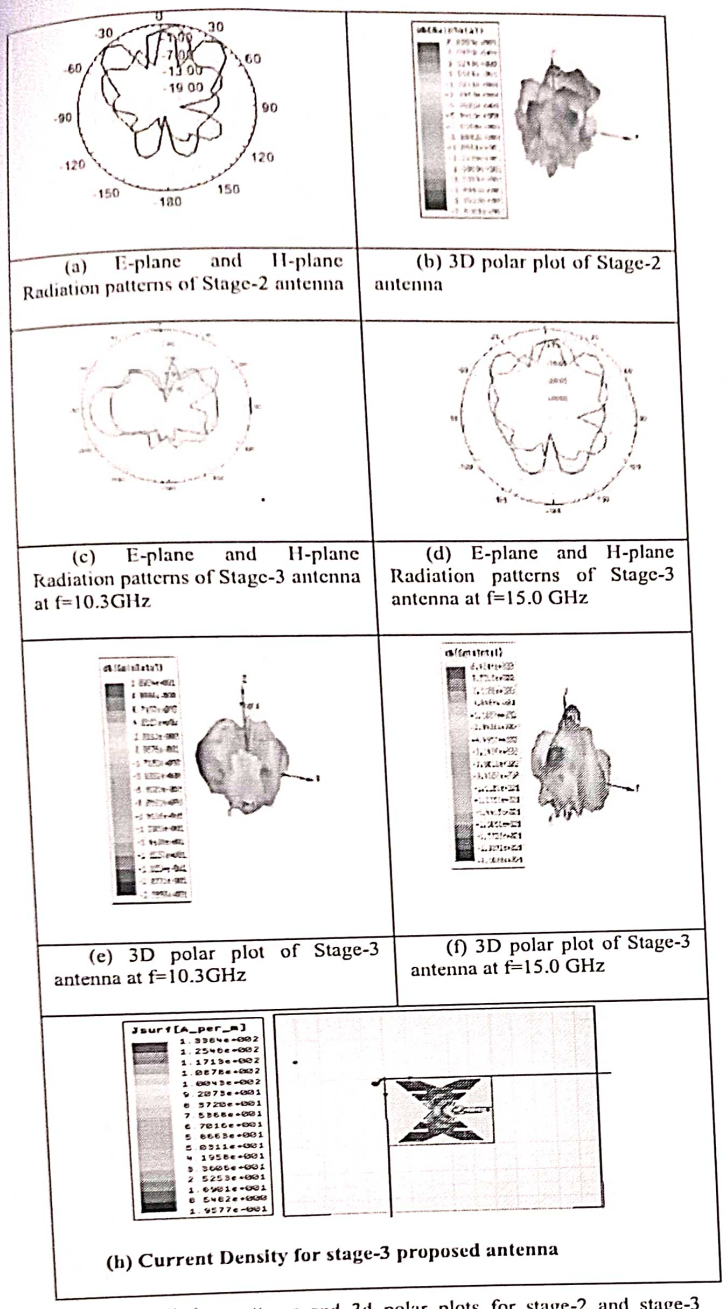

(a) E-plane and H-plane Radiation patterns of Stage-2 antenna

(b) 3D polar plot of Stage-2 antenna

(c) E-plane and H-plane Radiation patterns of Stage-3 antenna at f=10.3GHz

(d) E-plane and H-plane Radiation patterns of Stage-3 antenna at f=15.0 GHz

(e) 3D polar plot of Stage-3 antenna at f=10.3GHz

(f) 3D polar plot of Stage-3 antenna at f=15.0 GHz

(h) Current Density for stage-3 proposed antenna

Fig.7. radiation patterns and 3d polar plots for stage-2 and stage-3 antennas

IV. CONCLUSION

Fractal geometries along with Wilkinson power driver are proved responsible for the Bandwidth and Gain enhancement of proposed Hybrid Minkowski Koch Fractal Bowtie antenna. The fractal slots are etched from the patch area to support miniaturization. The Wilkinson power divider network provides better impedance matching between the feed and antenna element. The first operating band (10.3-13.3GHZ) covers almost 50% of the X band. The second band covers (14.5-16.0GHz) covers a part of the Ku band. The proposed antenna is suitable for satellite and defense communications as it can serve with a high gain about 10.98dB at 10.3GHz with a maximum percentage of 26.1%. Further Bandwidth enhancement for the proposed antenna can be obtained by employing different CSRR structures on the ground plane.

REFERENCES

[1] W. Liu, Y. Yin, W. Xu and S. Zuo, "Compact Open-Slot Antenna With Bandwidth Enhancement," in *IEEE Antennas and Wireless Propagation Letters*, vol. 10, pp. 850-853, 2011, doi: 10.1109/LAWP.2011.2165197. J. Clerk Maxwell, A Treatise on Electricity and Magnetism, 3rd ed., vol. 2. Oxford: Clarendon, 1892, pp.68–73.

[2] S. Liu, F. Xu, L. Cao and K. Wu, "Bow-tie slot antenna based on circular substrate integrated waveguide cavity," *2017 Sixth Asia-Pacific Conference on Antennas and Propagation (APCAP)*, 2017, pp. 1-3, doi: 10.1109/APCAP.2017.8420976. K. Elissa, "Title of paper if known," unpublished.

[3] W. Li, Z. Xia, B. You, Y. Liu and Q. H. Liu, "Dual-Polarized H-Shaped Printed Slot Antenna," in *IEEE Antennas and Wireless Propagation Letters*, vol. 16, pp. 1484-1487, 2017, doi: 10.1109/LAWP.2016.2646805

[4] S. T. Fan, Y. Z. Yin, B. Lee, W. Hu and X. Yang, "Bandwidth Enhancement of a Printed Slot Antenna With a Pair of Parasitic Patches," in *IEEE Antennas and Wireless Propagation Letters*, vol. 11, pp. 1230-1233, 2012, doi: 10.1109/LAWP.2012.2224311.

[5] M. A. Motin, M. I. Hasan and M. S. Islam, "Design and simulation of a low cost three band microstrip patch antenna for the X-band, Ku-band and K- band applications," *2012 7th International Conference on Electrical and Computer Engineering*, 2012, pp. 397-400, doi: 10.1109/ICECE.2012.6471571.

[6] W. Ata and M. I. Jawadeh, "Double-Slotted Multiband Bowtie Antenna," *2019 International Symposium on Advanced Electrical and Communication Technologies (ISAECT)*, 2019, pp. 1-6, doi: 10.1109/ISAECT47714.2019.9069692.

[7] H. Liu, H. Jiang, X. Guan, J. Lei and S. Li, "Single-Feed Slotted Bowtie Antenna for Triband Applications," in *IEEE Antennas and Wireless Propagation Letters*, vol. 12, pp. 1658-1661, 2013, doi: 10.1109/LAWP.2013.2294751

[8] S. E. Muthumani, Vallikannu R and H. R. Patnam, "Compact slot loaded Koch fractal microstrip patch antenna," *2013 IEEE Applied Electromagnetics Conference (AEMC)*, 2013, pp. 1-2, doi: 10.1109/AEMC.2013.7045102.

[9] C. B. Nsir, J. -M. Ribero, C. Boussetta and A. Gharsallah, "A Wide Band Transparent Koch Snowflake Fractal Antenna Design for Telecommunication Applications," *2019 IEEE 19th Mediterranean Microwave Symposium (MMS)*, 2019, pp. 1-3, doi: 10.1109/MMS48040.2019.9157327

[10] J. Li, "Novel Design of Wilkinson Power Dividers With Arbitrary Power Division Ratios", IEEE Transactions on Industrial Electronics, vol. 58, no. 6, pp. 2541-2546, 2011

[11] B. H. Ahmad and H. Nornikman, "Fractal microstrip antenna with Minkowski Island split ring resonator for broadband application," *2013 IEEE International RF and Microwave Conference (RFM)*, 2013, pp. 214-218, doi: 10.1109/RFM.2013.6757252

[12] S. N. Shafie, I. Adam and P. J. Soh, "Design and Simulation of a Modified Minkowski Fractal Antenna for Tri-Band Application," *2010 Fourth Asia International Conference on Mathematical/Analytical Modelling and Computer Simulation*, 2010, pp. 567-570, doi: 10.1109/AMS.2010.114.

[13] V. S. Bhaskar, E. L. Tan and L. K. H. Holden, "Design of Wideband Bowtie Slot Antenna Using Sectorially Modified Gielis Curves," in *IEEE Antennas and Wireless Propagation Letters*, vol. 17, no. 12, pp. 2237-2240, Dec. 2018, doi: 10.1109/LAWP.2018.2872009

[14] N. Najib, K. Y. You, C. Y. Lee, M. N. Dimon and N. H. Khamis, "Compact and wideband modified wilkinson power dividers," *2017 IEEE 4th International Conference on Smart Instrumentation, Measurement and Application (ICSIMA)*, 2017, pp. 1-4, doi: 10.1109/ICSIMA.2017.8311977

AICTE SPONSORED
INTERNATIONAL CONFERENCE ON
ADVANCEMENT IN ELECTRONIC SYSTEMS AND COMMUNICATION TECHNOLOGIES
(ICAESCT 2022)
4TH & 5TH NOVEMBER, 2022

PRAGNANAM BRAHMA
ANITS

CERTIFICATE

OF **PARTICIPATION** PRESENTED TO

AICTE
All India Council for Technical Education

Dr.G. Ramalakshmi

from DR.L.B.COLLEGE OF ENGINEEING has presented a paper titled *"Bandwidth Enhancement Of A Hybrid Minkowski Koch Fractal Bowtie Antenna Using Wilkinson Power Divider for X And Ku Band Applications"* in International Conference on Advancement in Electronic Systems and Communication Technologies (ICAESCT 2022) on 4th & 5th November 2022. Organized by Department of Electronics and Communication Engineering, Anil Neerukonda Institute of Technology and Sciences.

Dr. V. Rajya Lakshmi	**Dr. B. Jagadeesh**	**Dr. K. Sri Rama Krishna**
Convener, ICAESCT 2022	**HOD, ECE**	**Principal**

2022 International Conference on Breakthrough in Heuristics And Reciprocation of Advanced Technologies (BHARAT) | 978-1-6654-3625-0/22/$31.00 ©2022 IEEE | DOI: 10.1109/BHARAT53139.2022.00018

Performance Analysis of Dual Band Circularly Polarized Hybrid Dielectric Resonator Antenna

M. Sravani
Department of EECE
GITAM School of Technology
GITAM Deemed to be University
Visakhapatnam, INDIA
smaliset@gitam.in

S. Neeraja
Department of EECE
GITAM School of Technology
GITAM Deemed to be University
Visakhapatnam, INDIA
nsajja@gitam.edu

***Abstract*—The performance analysis of asymmetrical slot-based hybrid Dielectric Resonator Antenna (DRA) is presented in this paper. The volume of proposed DRA is 60mm x 60mm x 1mm and the DR material used is Alumina ceramic with dielectric constant of 9.8 various parameters studied. The proposed DRA possesses two resonances at 2.65GHz with a bandwidth of 900 MHz and 3.47 GHz with a bandwidth of 800 MHz. The Axial ratio is observed as 2.5dB at the bandwidth of 200MHz. The maximum gain obtained is 4.99 dBi. The suggested DRA meets the Wi-Max and basic 5G applications.**

Keywords—Asymmetric Slot, Dual-band, Dielectric Resonator Antenna.

I. INTRODUCTION

Most of all the Circular Polarization antennas cannot be used in Ultra-Wide Band (UWB) applications due to their limited circular polarization (3-dB Axial Ratio) and bandwidth of impedance. The printed Circular Polarization Slot Antenna is appealing for wireless communications due to its broadband characteristics. Polarizations are considered orientation of electric fields, to minimize the power loss occurred due to multipath and Faraday effects. Circular Polarization antennas are selected to differentiate the line of sight signal from other reflected signals with reverse polarization. Asymmetrical feeding line is applied to achieve dual orthogonal modes to present Circular Polarization radiation [1-2].

Circular Polarization waves are normally excited by dual orthogonal linearly polarized element with a phase difference of 90^0 and similar amplitude. The practical outline for the antenna with Circular Polarization involves single-fed method with structural perturbation, structural rotation of numerous linearly polarized components and dual-fed technique. Bidirectional Circular Polarization (Bi-CP) is essential in different applications in modern wireless communications like radio frequency identification system, microcellular base station. Dielectric Resonator Antennas (DRAs) are in demand due to inherent advantages like light weight, low profile, wide bandwidth, absence of conduction losses in the resonator and high radiation efficiency. In applications like satellite and modern wireless communication, spacing of transmitter and receiver antenna is critical. In such cases, CP DRAs are chosen because they are insensitive to the alignment. DRAs are made up of various materials with wide range of permittivity [3-4].

Massive Multiple Input Multiple Output (MIMO) technology is required for achieving 5G, as it is able to give multi-gigabit per-second data throughput, multiplexing and through large-scale diversity. The pattern of CP DRAs is focused in the literature using single or multiple feeds. In contrary, with linearly polarized systems, CP systems are less affected by the propagation effects and misalignment of antenna [5].

The flexibility of DRA in feeding techniques and shape provide to select the specific characteristics such as wideband, multiband, circular polarization, linearly polarization, monopole and omni directional radiation patterns. Antenna weight reduces when slots are initiated, polarization can be reversed by varying ratio of slot dimensions or orientation of slots. Initially, the dimensions of DRA can be adjusted to acquire the desired operating frequency, subsequently by changing the stub and slot lengths for impedance matching [6]. For most of the communication systems, it is suggested to operate in the CP mode, where the trajectory of the tip of the vector rotates about the propagation axis as a time function [7].

Broadside Circular Polarization DRA's can be excited by annular slots. E_φ *and* E_θ are same in amplitude and 90° phase difference then omnidirectional CP fields are achieved [8].

In this paper, Hybrid DRA performance analysis can be carried out by using asymmetric slot which is proposed for dual band applications.

II. PROPOSED HYBRID DRA CONFIGURATION

The proposed Asymmetrical slot-based Hybrid DRA has been introduced as a candidate for low-profile application. The rectangular DR has taken with relative permittivity, ε_r is 9.8 for Alumina ceramic material and it is placed on the C shaped feed line with a rectangular asymmetrical slot. Here the substrate is taken on FR4 Epoxy (ε_r = 4.4). Substrate length, width and height can be considered as 60mm x 60mm x 1mm. The C shaped feed line is the combination of different stubs with dissimilar widths and lengths. To obtain the circular polarization, asymmetrical slots are considered in the proposed configuration of antenna which is shown in Fig. 1. The dimensions of design parameters of proposed Hybrid DRA are shown in Table I.

For the C-Shaped feed line along with asymmetrical rectangular slot plays the major role for the generation of orthogonal modes of TE^x_{11} and TE^y_{11} which are responsible to getting circular polarization from the proposed Hybrid DRA. Effective dielectric constant of the substrate and impedance is calculated by using equation (1) and (2) respectively

.

$$\epsilon_{eff} = \left(\frac{\epsilon_r+1}{2}\right) + \frac{\epsilon_r-1}{2}\left[\left(1+12\frac{Sh}{Ws}\right)\right]^{-0.} \quad (1)$$

$$Z = \frac{120\pi}{\sqrt{\epsilon_{eff}}}\left[\frac{Ws}{Sh} + 1.393 + 0.677ln\left(\frac{Ws}{Sh} + 1.444\right)\right]^{-1} \quad (2)$$

978-1-6654-3625-0/22/$31.00 ©2022 IEEE
DOI 10.1109/BHARAT53139.2022.00018

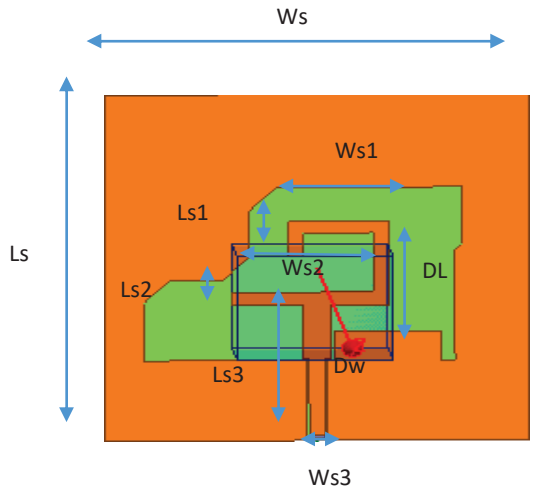

(i) Top View

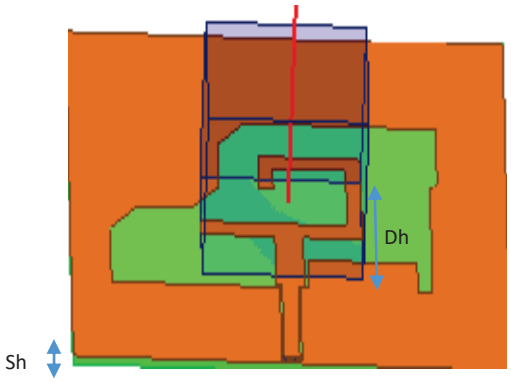

(ii) Side View

Fig. 1. Proposed Hybrid Dielectric Resonator Antenna

TABLE I. THE DIMENSIONS OF DESIGN PARAMETERS OF HYBRID DRA

S.No	Parameter	Value
1	Substrate height Sh	1mm
2	Substrate length L_s	60mm
3	Substrate width Ws	60mm
4	Ground length $Ls = l_g$	60mm
5	Ground width $Ws = w_g$	60mm
6	Ground height h_g	0.035mm
7	DR height Dh	19mm
8	DR length DL	18mm
9	DR width Dw	20mm
10	Length of stubs (Ls1, Ls2, Ls3)	3.9mm, 2,2mm, 2.3mm
11	Width of stubs (Ws1, Ws2, Ws3)	11.5mm, 14.2mm, 2.2mm

Initially, the proposed antenna contains DRA and symmetrical rectangular slot by using coplanar waveguide feed technique to achieve the linear polarization. To obtain the circular polarization and also improvement for impedance bandwidth purpose rectangular slot changes to asymmetrical slot, then the orthogonal modes with approximate equal magnitudes can be generated in rectangular Hybrid DRA. To enhance the bandwidth purpose some more stubs considered in the slot structure and also feed line technique can be changed to C shaped.

III. RESULTS & DISCUSSION

The reflection coefficient of proposed DRA is -19dB which is shown in Fig. 2. Dual frequencies are observed in the graph one is circular polarization and another one is linear polarization. The CP is observed at 2.65 GHz frequency with 900 MHz (2.1GHz - 3 GHz) bandwidth and also the linear polarization is obtained at 3.47GHz frequency with 800 MHz (3GHz – 3.8GHz) bandwidth.

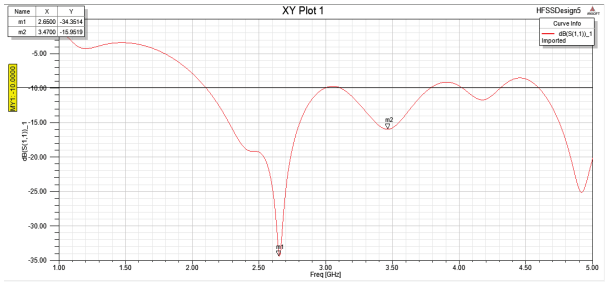

Fig. 2. Reflection Coefficient

Fig. 3 represents the Axial ratio at 2.5dB of bandwidth is observed at 200MHz (2GHz - 2.2GHz). The Axial ratio is observed for the recommended antenna at < 3 dB.

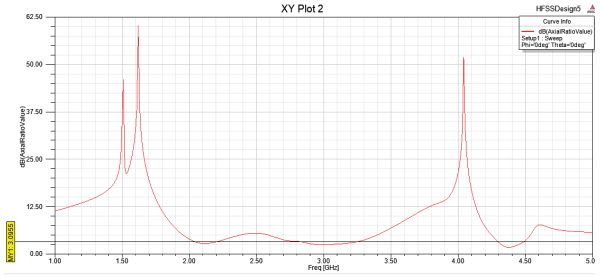

Fig. 3. Axial Ratio

The proposed gain of this antenna is obtained at 4.99 dBi is shown in Fig. 4. The radiation efficiency and average gain in the backside direction are similar to the broad side direction.

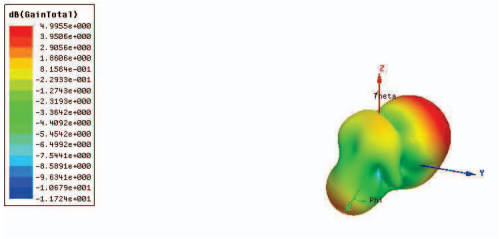

Fig. 4. Gain plot

Fig. 5. represents the radiation pattern and also it clearly indicates that left hand circularly polarization.

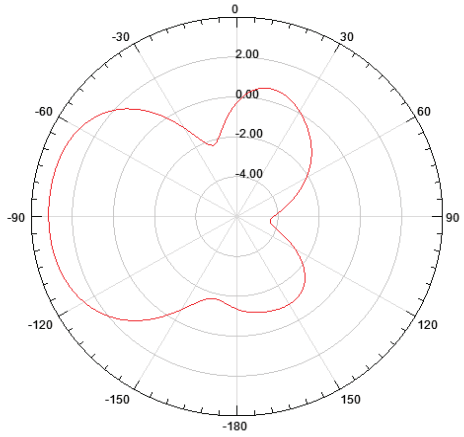

Fig. 5. Radiation pattern

IV. Conclusion

In this paper, Dual band asymmetrical slot Hybrid Dielectric Resonator Antenna (DRA) is proposed. The proposed DRA has a ground plane of 60mm x 60mm with DR height of 19mm and dielectric constant of DR is 9.8. The performance of the DRA is estimated based on various parameters using CST simulator. The dual-band DRA operates at 2.65GHz with bandwidth of 900 MHz and 3.47 GHz with a bandwidth of 800MHz. The axial ratio of 2.5dB for bandwidth 200MHz, the maximum gain obtained is 4.99dBi. The proposed DRA is suitable for Wi-Max and basic 5G applications.

References

[1] Nasimuddin ZNC, Qing X. Symmetric-aperture antenna for broadband circular polarization. IEEE Trans Antennas and Propag. 2011, vol. 59, pp: 3932-3936.

[2] Shen J, Lu C, Cao W, Yang J, Li M. A novel bidirectional antenna with broadband circularly polarized radiation in X-band. IEEE Antennas Wireless Propag Lett. 2014, vol. 13, pp. 7-10.

[3] Petosa A. Dielectric resonator antenna handbook. Norwood, MA: Artech House, 2007.

[4] Patel P, Mukherjee B, Mukherjee J. Wideband circularly polarized rectangular dielectric resonator antennas using square shaped slots. IEEE Antennas Wireless Propag Lett. 2016, vol. 15, pp. 1309-1312.

[5] Fakhte S, Oraizi H, Karimian R, Fakhte R. A new wideband circularly polarized stair-shaped dielectric resonator antenna. IEEE Trans Antennas and Propag. 2015, vol. 63, pp. 1828-1832.

[6] Pan Y, Leung KW. Wideband circularly polarized trapezoidal dielectric resonator antenna. IEEE Antennas Wireless Propagation Letter, 2010, vol. 9, pp. 588-591.

[7] Kumar R, Chaudhary RK. A new modified CPW-fed wideband circularly polarized half–split cylindrical dielectric resonator antenna with different permittivity of two layers in radial direction. Int J RF Microwave Computer-Aided Engineering 2017, vol. 27, pp. 1-9. https://doi.org /10.1002/ mmce.21068.

[8] Yang N, Leung KW, Lu K, Wu N. Omnidirectional circularly polarized dielectric resonator antenna with logarithmic spiral slots in the ground. IEEE Trans Antennas and Propag. 2017, vol. 65, pp. 839-844.

INTERNET OF THINGS

First Edition

About this Book:

This Internet of Things (IOT) Book in general illustrates the various aspects of IOT Technology. The chapters are arranged in systematic order explain the basic information regarding IOT and gradually focused on advanced topics covering almost all aspects of IOT technology. Saying about IOT, it is a modern digital technology which is used to interface wide variety of physical things in and around through internet for remote communication. Here sensors and embedded circuit plays a vital role. This IOT technology currently emerging in various applications and different sectors based on its merits and its demerits. All these detailed and associated information's are arranged systematically as various chapters.

TECHNO PUBLISHERS

amazon books

BookDeal

To Contact for Copies:
Techno Publishers,
Chennai.
Ph: 8939613196
Email: technopublishersmail@gmail.com
Website: www.technopublishers.com

ISBN 978-81-955080-0-6

Price: Rs. 369

INTERNET OF THINGS First Edition

First Edition

INTERNET OF THINGS

Dr.Santhosh Kumar Sahoo
Reddi Sri Devi
K.Ashok Kumar
Vanga Karunakaran Reddy

TECHNO PUBLISHERS

First Edition

Internet of Things

Dr. Santosh Kumar Sahoo

Dr. R. Sridevi

Dr. K. Ashok Kumar

Vanga Karunakar Reddy

Techno Publishers, Chennai
www.technopublishers.com
technopublishersmail@gmail.com
Ph: 8939613196

ISBN 978-81-955080-0-6

Internet of Things

First Edition

Authors:

Dr. Santosh Kumar Sahoo, Dr. R. Sridevi, Dr. K. Ashok Kumar, Vanga Karunakar Reddy

Printed on acid-free paper

International Standard Book Number-13: 978-8-1955-0800-6 (Hardback)

Published by:

Techno Publishers, Chennai.
www.technopublishers.com
technopublishersmail@gmail.com
Ph: 8939613196

Price: Rs. 369

TECHNO PUBLISHERS

ISBN 978-81-955080-0-6
9 788195 508006

Preface

This Internet of Things (IoT) Book in general illustrates the various aspects of IoT Technology. The chapters are arranged in sequential order explaining the basic information regarding IoT and gradually focused on advanced topics covering almost all aspects of IoT technology. Saying about IoT, it is a modern digital technology which is used to interface wide variety of physical things in and around through internet for remote communication. Here sensors and embedded circuit plays a vital role. This IoT technology currently emerging in various applications as well as different sectors based on its merits and its demerits. All these detailed and associated information are arranged as following chapters in this book.

Chapter 1: Introduction of IoT

Chapter 2: Historical Development of IoT

Chapter 3: Architecture of IoT

Chapter 4: Technologies used in IoT

Chapter 5: Merits and Demerits of IoT

Chapter 6: Applications of IoT

I wish to express my profound thanks to all those who helped in making this book a reality. I wish to thank the publisher and the entire team of Techno Publishers to made this book to print. Any suggestion for the improvement will be acknowledged and well appreciated.

Editor
(Dr. M. R. Arun)

CONTENTS

1) INTRODUCTION OF IOT

   a) Definition
   b) System Components
   c) Need
   d) Benefits
   e) Building Blocks

2) HISTORICAL DEVELOPMENTS OF IOT

   a) Milestones in Evolution

3) ARCHITECTURE OF IOT

   a) Sensors
   b) Actuators
   c) Communication Protocol
   d) Router
   e) Protocol Layers
   f) End Devices
   g) Gateway

4) WORKING OF IOT

   a) Device Management
   b) Device Security
   c) Device Networking
   d) Power Management

e) Energy Utilization

f) Networking

5) TECHNOLOGIES USED IN IOT

a) Access Technology

b) Network Topology

c) Enabling Technologies

d) 5G Technology

e) Big Data Analytics

f) Cloud Computing

g) Edge Technology

5) MERITS AND DEMERITS OF IOT

a) Advantages

b) Disadvantages

6) APPLICATIONS OF IOT

a) Medical Domain

b) Business Field

c) Automotive Domain

d) Agriculture Domain

e) Industrial Filed

ADVANCES IN ELECTRICAL ENGINEERING

VOLUME - 5

Chief Editor

Dr. G. Durgadevi
Professor, Department of ECE, New Prince Shri Bhavani College of Engineering and Technology, Chennai, Tamil Nadu, India

Co-Editor

Dr. A.V. Sudhakara Reddy
Associate Professor, Malla Reddy Engineering College (Autonomous), Maisammaguda, Hyderabad, Telangana, India

AkiNik Publications
New Delhi

Published By: AkiNik Publications

AkiNik Publications
169, C-11, Sector - 3,
Rohini, Delhi-110085, India
Toll Free (India) – 18001234070
Phone No. – 9711224068, 9911215212
Email – akinikbooks@gmail.com

Chief Editor: Dr. G. Durgadevi
Co-Editor: Dr. A.V. Sudhakara Reddy

Publications Year: 2022

Pages: 112

ISBN:

Book DOI: https://doi.org/

Price: ₹ 653/-

Contents

Chapters **Page No.**

1. Uncertainty Management in Electrical Power System 01-18
   (Dr. Muhammad Shahzad, Muhammad Abbas Raza and Amir Raza)

2. A Comparative Study in the Design of an Ann Based Controller 19-36
   (Dr. Ch. Varaha Narasimha Raja and Dr. G. Anand)

3. Study of Energy Capture with Photovoltaic Cell in Zinc Tile 37-53
   (Dr. A. Manjula, R Niraimathi, S. Chitra Devi and Dr. S. Lakshmi Kanthan Bharathi)

4. Implementation of IT-SMC for Fault Rectification in a Grid-Connected PV System for Maximum Power Point Tracking 55-80
   (Dr. Ch. Varaha Narasimha Raja, M. Vijaya Kumari, R. Jayank Maanas, M. Bhavan, Dr. G. Anand and Dr. I.E. Sanyasi Naidu)

5. Analysis of the Floating Junction in the Area of the Rear Boron Diffuser in Bifacial Pert Solar Cells 81-99
   (Raja Reddy Duvvuru, R. Sireesha and V. Lakshmi Devi)

6. A New Algorithm for the Order Reduction of High Order Uncertain Systems 101-112
   (Dr. T. Narasimhulu, Dr. S. Srikanth and Dr. G. Raja Rao)

Chapter - 4

Implementation of IT-SMC for Fault Rectification in a Grid-Connected PV System for Maximum Power Point Tracking

Dr. Ch. Varaha Narasimha Raja, M. Vijaya Kumari, R. Jayank Maanas, M. Bhavan, Dr. G. Anand and Dr. I.E. Sanyasi Naidu

Abstract

PV systems are becoming increasingly popular as a sustainable energy source. However, in the control community, establishing control systems that enable maximum power extraction for grid-connected PV arrays while adequately mitigating grid faults is still a difficult task. An integral terminal sliding mode control (ITSMC) method for grid-connected PV arrays is proposed in this study. The method tries to maximise power extraction while reducing the effects of irradiance changes and bulk voltage oscillations. The proposed approach's favourable aspects include effective voltage drag removal and maximum power point tracking. A simulation analysis comprising numerous operating circumstances and various malfunctioning situations was used to examine the efficiency of the proposed approach. In this paper the fault will be mitigated by controller and the maximum power extracted by irradiance fluctuations and oscillations in the voltage. Elimination of fluctuations, disturbances and maximum power can be tracked among the proposed approach by considering various scenarios based on the concepts of Irradiance and temperature.

Keywords: Photovoltaic, MPPT, integral terminal sliding mode control, electric power quality

1. Introduction

Photovoltaic plants are becoming a more popular source of energy. While individual PV panels are quite robust still failures tend to happen Due to arrangement of interconnection of PV panels in an array and if failure of single panel can impact the whole array [1]. The PV are known for efficiency of up to 30% which provides small output power compared to the input it takes. To maximize the efficiency and to reduce installation cost MPPT

trackers are used with the system. The output power of a solar PV depends upon on solar irradiance level, temperature and load current which lead to nonlinear operation of the system [2, 27]. The implementation of a boost converter for a PV cell which will help us to get maximum power which is obtained by using MPPT algorithms such as perturb and observe algorithm and observe and understand the performance of PV system which is subjected to irradiance [3]. By integrating a lower cost highly efficient MPPT tracker to be integrated into a PV cell which can result in 25% energy enhancement compared to standard PV cell while still performing with better voltage regulation. MPPT, an affordable solution for small PV energy systems is used which results in better efficiency and helps in transfer of more energy to the load [4]. The photovoltaic (PV) generation are extensively increasing, since it is considered as an essentially inexhaustible and broadly available energy resource. The output power generated in the photovoltaic modules is dependent on solar radiation and temperature of the solar cells. Hence using MPPT is done by using ITSMC controller which helps in enhancement energy conversion efficiency of the PV system [5].

Now a day's application like water pumping is becoming popular using inverter powered by photovoltaic arrays [7]. A Current-fed parallel resonant push-pull inverter and PV cells are used for important applications in rural areas such as water pumping system. [8]. The focus is the model of photovoltaic cell for energy harvest application (EHV). This model facilitates to specify the optimal conditions for operating the PV cell and define the maximum power point (MPPT) [9, 27]. The excellent cell characterisation achieved at low illumination density increase the benefit of solar power supply compared to standard solar cell. Pilot line production by fabricating high efficiency solar cell are used in small high efficiency modules integrated proto type of solar powered portable device like cell phones, hand held computer etc. [10].

A DC-DC converter is used between the solar cell and the load as an interface. The duty cycle is changed so that the impedance matching between the cell output and the load is obtained, by tracking the maximum power point of the cell [11]. The DC bus voltage of the system is held constant through the DC link voltage proportional-integral (PI) controller. The output of DC link voltage PI controller and the PV array feed forward term are used to generate reference speed command [12]. The operating point (I, V) corresponds to a point on the power-voltage (P-V) curve at maximum point is called the maximum power point tracking PV system can extract maximum power point tracking system to get the best performance from

solar PV panels [13]. PI based controllers are most commonly used controllers for the power production. MPPT device is charge control devices which are more efficient that allows a panel array to be of higher voltage than the battery bank. To implement MPPT, sense the voltage and current and implement the MPPT, from that obtained reference voltage as output it is compared with the actual PV voltage to find the error. This error is then fed to the PI controller. The output of PI controller will give the required duty ratio for PWM generator and this value is compared with the carrier signal and given to the MOSFET.A distributed MPPT pattern can be used for PV system, which permits the control of each DC-link voltage [14]. It gives better MPPT tracking performance since it has a closed loop control mechanism. It is a technique used with variable power sources to maximize energy extraction as conditions vary. To enhance the efficiency of the solar device, a maximum power point tracking algorithm is essential. There are methods for MPPT such as fractional open circuit voltage, fractional short circuit current. The nonlinear characteristics of PV cells were simulated for MPPT by using a sliding mode control method based on fuzzy exponential approach rate (SMC-FEAR) [15].

In this display paper proposes a novel ITSMC control plot for grid-connected PV arrays subject to vulnerabilities and irradiance changes. The most commitments of this paper is to plan of an unused necessarily terminal sliding mode control (ITSMC) for a grid-connected PV frameworks, Usage of a modern ITSMC-based MPPT plot for stand-alone PV control frameworks. The rest of the paper is organized as follows. The framework associated PV control era framework is talked about in section II. Section III gives the vital subtle elements for the plan of the proposed ITSMC approach for the framework associated PV. Section IV, simulation results are provided in sections IV to demonstrate the effectiveness of the proposed control strategy in achieving maximum power under various disturbances.

2. System model

a) PV CELL modeling

When photons of light strike's a solar cell technically a semiconductor p-n junction. They get absorbed in solar cell thus resulting in breaking the bond of outer electrons in the semiconductor. These electrons are emitted when energy of photon is greater than the band gap energy. Thus, a semiconductor device which converts light into electrical energy by photovoltaic effect. The process of generation of voltage or electric current in a photovoltaic cell when exposed to sun light is recognized as

photovoltaic cell or photo electric cell [18]. The whole phenomena involves absorption of solar rays, ejection or generation of electrons and collection of these free charged at the end of a PV system.

The Shockley diode equation of a single diode PV cell [19]

$$I_D = I_o \left[\exp\left(\frac{qV_{PV}}{AKT}\right) - 1\right] \quad (1)$$

The output PV current with output PV voltage Vpv is defined

$$I_{PV} = I_{SC} - I_o \left[\exp\left(\frac{qV_{PV}}{AKT}\right) - 1\right] \quad (2)$$

Here the variation of the reverse saturation current Io of a PV cell is given by

$$I_o = I_{or}\left[\frac{T}{T_R}\right]^3 exp\left(\frac{qE_g}{K\alpha}\left[\frac{1}{T_R} - \frac{1}{T}\right]\right) \quad (3)$$

b) Grid Connected PV array

The diagrammatic representation of a grid connected PV array is depicted in the figure 1.The PV array is attached to the DC-DC converter and then to the DC-AC inverter that is ultimately connected to the grid. The two parameters Ipv and Vpv are approximated from the PV array which is given to the Perturb and Observe Algorithm [20]. It yields the reference voltage at the maximum power. The ITSMC controller receives the reference voltage so that it can keep the output voltage in track with the reference voltage. It is obtained by controlling and modifying the duty cycle.

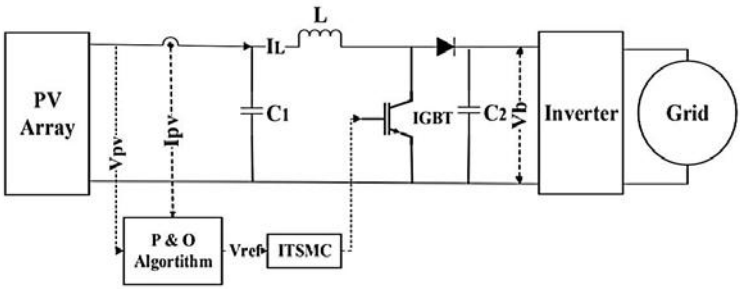

Fig 1: Topology of a grid connected PV array

In fig 1, a fundamental DC-DC converter circuit is also known as boost converter can be observed. A single-pole double-throw (SPDT) switch is connected to the DC input voltage as shown. IGBT has improved power gain than usual bipolar type transistors mainly because they combine the higher voltage operation of the bipolar type transistor and lower input losses of MOSFET [21]. So, IGBT's are preferred over BJT or MOSFET.

A DC-DC boost converter is to control the output voltage of the PV array (V_{PV}) and achieve maximum solar power generation. The capacitor current is given by [22]

$$I_{C1} = C_1 \frac{dV_{pv}}{dt} = I_{PV} - I_L \quad (4)$$

Where, I_L is the current through the inductor.

The voltage across the inductor L is found out as:

$$V_L = L\frac{dIL}{dt} = V_{PV} - V_b(1 - t) \quad (5)$$

Where, t is the duty cycle fed to the IGBT switch and V_b is the bulk voltage across the capacitor C_2.

c) MPP searching

The main features of a PV cell are the short circuit current and open circuit voltage. The current obtained from the PV cell at zero load resistance is known as the short circuit current. When the load resistance is infinity, the current is zero and the open circuit voltage becomes maximum. Maximum power is achieved when there is a blend of best voltage and current as shown in fig 2.

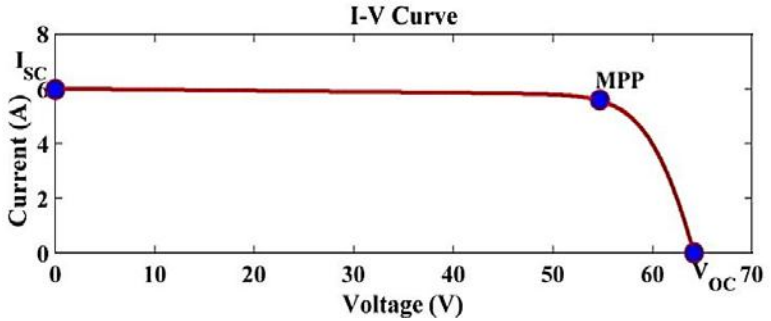

Fig 2: I-V characteristic curve showing crucial points

Maximum Power Point Tracking algorithm is essential to improve the efficiency of the solar device. There are various methods for MPPT, such as fractional short circuit current, Perturb and observer, fractional open circuit voltage, fuzzy control and neural control [23]. Perturb and Observe Algorithm is opted due to its simplicity and popularity for less implementation cost [24]. Perturb and observe technique has simple implementation, optimum MPP tracking time and is economical.

Fig 3. Depicts general flowchart for perturb and observe algorithm that tracks the maximum power point by altering the PV voltage in line with the

reference voltage given by the algorithm. The change in the PV voltage depends on the PV power. The reference voltage is also varied. For Example, during a rise in power, the perturbation should be in the same direction. When power is reduced, the perturbation will progress in the reverse direction. The whole process repeats until the MPP is obtained.

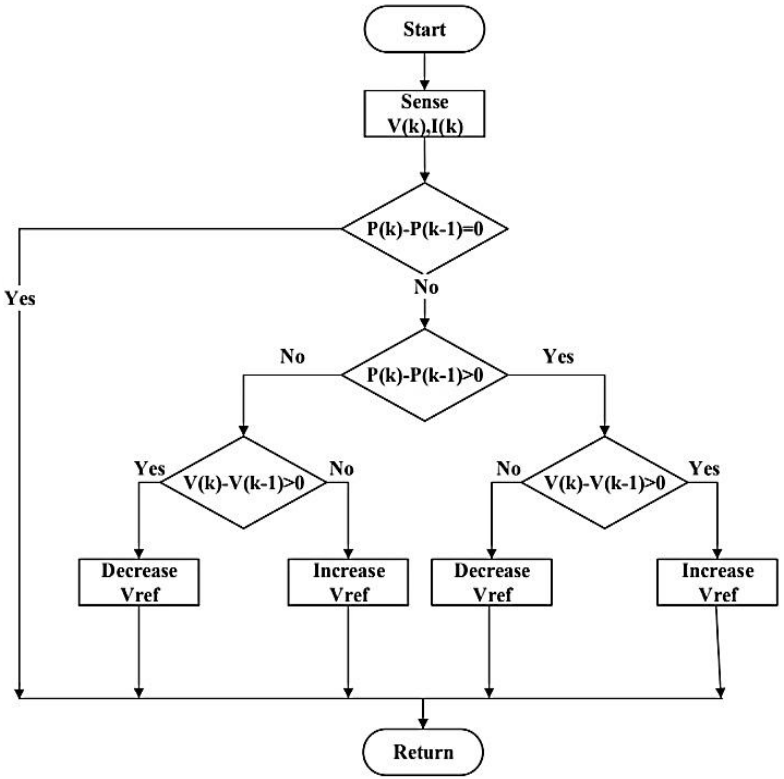

Fig 3: MPPT flowchart of proposed approach

3. Control scheme

Due to the unhinged instantaneous dc input and ac output powers, voltage ripples often occur on the dc link voltage at the output of the boost converter in grid connected PV systems. This ripple leads to fluctuations in the PV output voltage, as well as sudden variations in the input voltage of the boost converter [26]. This will lead to power losses due to the resulting improper MPP operations. Hence, the proposed approach ITSMC is designed for the proper MPPT control under uncertain conditions. The aim of the ITSMC is to hold the system error on an integral terminal sliding surface and then unite this error to the origin in finite time [27].

Consider the following switching variable for a grid connected PV device:

$s=e(t)+\alpha e_i(t)$ (6)

Where $e(t) = V_{PV} — V_{ref}$ refers to the error between the output PV voltage V_{PV} and the reference voltage V_{ref} and $e_i(t)$ is the integral term added to the original error ($\ddot{e}_7(t)$=sign(e(t))). Also, α is a constant coefficient which is greater than zero.

Consider the following sliding manifold σ:

$$\sigma = \dot{e}(t) + \alpha \dot{e}_i(t) \quad (7)$$

The control signal is obtained when $\dot{\sigma}=0$. Thus,

$$\sigma = \dot{e}(t) + \alpha \dot{e}_i(t) \quad (8)$$

Equation (8) leads to:

$$\ddot{V}_{PV} - \ddot{V}_{ref} + \alpha \ddot{e}_i(t) = 0 \quad (9)$$

Equation (4) provides the expression of $\ddot{V}_{PV}$, which when substituted in equation (9) leads to,

$$\frac{1}{C_1}[I_{PV} - \dot{I}_L] - \dot{V}_{ref} + \alpha \ddot{e}_i(t) = 0 \quad (10)$$

Substituting equation (5) in equation (10) yields:

$$u = \frac{1}{V_b}\left[L\dot{I}_{PV} + LC_1\alpha\ddot{e}_i(t) - LC_1\ddot{V}_{ref} - V_{PV} + V_b - ksign(s)\right] \quad (11)$$

Consider the following Lyapunov function:

$$V = \frac{1}{2}\sigma^2 \quad (12)$$

$\dot{V}=\sigma\dot{\sigma}<0$ (13)

Substituting equation (8) in equation (13) we get,

$\dot{V} = \sigma\{\ddot{e}(t)+\alpha\ddot{e}_i(t)\}$ (14)

$$\dot{V} = \sigma\{e(t) + \ddot{\alpha e}_{i(t)}\}$$

$$\dot{V} = \sigma\{\frac{1}{C_1}[I_{PV} - I_L] - V_{ref+}\alpha\ddot{e}_i(t)\}$$

$$= \sigma\{\frac{1}{C_1} I_{PV-} \frac{\dot{1}}{LC1} V_{PV} + \frac{1}{LC_1} V_b (1-u) - \ddot{V}ref + \alpha e_l(\ddot{t})\}$$

$$= ||\alpha||\{\left|\left|\frac{I_{PV}}{C1} I_{PV}\right|\right| - ||\frac{V_{PV}}{LC_1}|| + \left|\left|\frac{V_b}{LC_1}\right|\right| - \left|\left|\frac{V_B}{LC_1}\right|\right| - \left|\left|\frac{V_b}{LC_1}\right|\right| u - ||\ddot{V_{ref}}|| + \alpha||\ddot{e_l}(t)||\} \quad (15)$$

Substituting *u* in the above equation yields:

$$\dot{V} \leq ||\sigma||\{—||\frac{Vb/}{}LC1||k\} \quad (16)$$

$$\dot{V} \leq —||\sigma||\{||V_b/LC_1||k\} \quad (17)$$

It is obvious that if eq. (17) holds then the exponential convergence of *e* to zero is guaranteed.

4. Simulation results

In this section, conducted a series of computer simulation under various operating conditions to evaluate the performance of the proposed control scheme. The solar panel Sun Power SPR-305E-WHT-D with 96 cells per module is considered in the simulation. The array consists of 66 panel strings and 5 series-connected modules of string. The capacitor C1 value is taken to be 100F and an inductor L with a value of 5mH is used. A diode with a length of 0.1m is connected to the capacitor C2.which is given as 24mF In ITSMC, k is set to 5,and is 0.5is the voltage source's switching frequency. The frequency converter is 60 hertz, and the frequency of the PWM is 5000 hertz. The initial duty cycle value is assumed to be 0.5. Ideally, the PV array should be capable of delivering a maximum of 100 W/m2. at the number 1000 Irradiance of W/m2 with a total of 330 sun power modules. The scenarios below demonstrate the controller and the performance under varying irradiance conditions were evaluated.

Case-1: Now consider the irradiance and the temperature to be varying as shown in Fig.4. The transformer's output voltage and the boost converter's output voltage and power are then impacted and the duty cycle is as shown in fig. 5

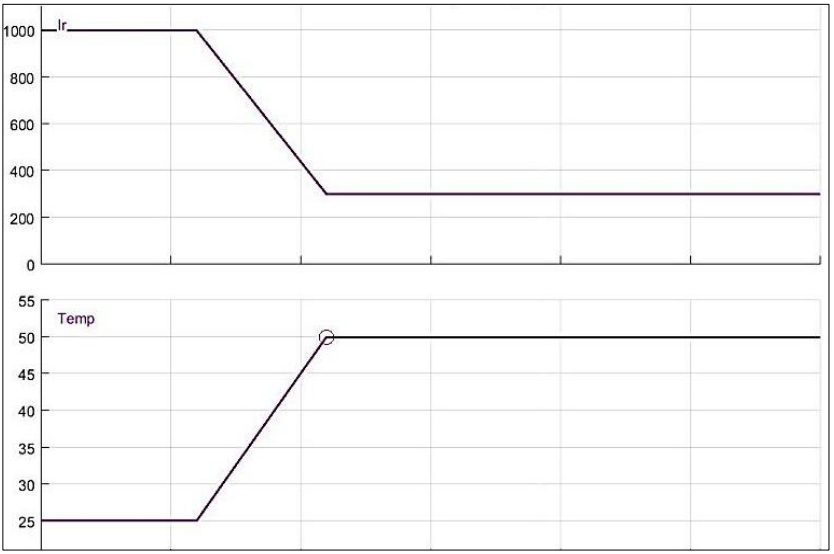

Fig 4: Irradiance and temperature for Case-1

From fig. 4, the voltage changes in response to changes in temperature and irradiance; initially, the voltage drops, but it quickly settles and returns to normal. A large voltage spike may be noticed in relation to the fault, but it returns to normal. Later, we can observe there is a slight increase in voltage than the normal.

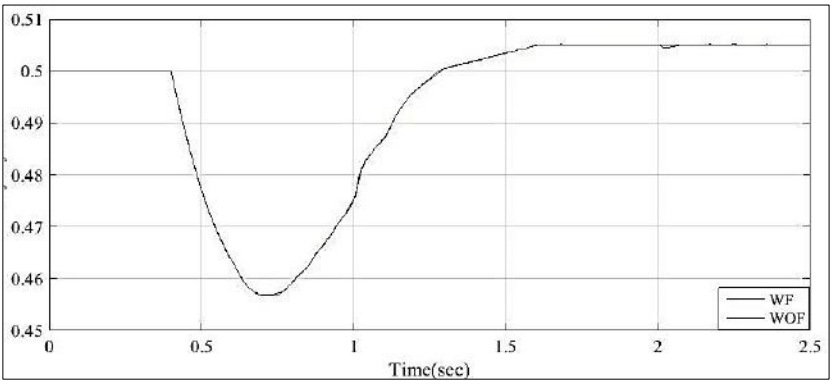

Fig 5: Duty cycle for Case-1

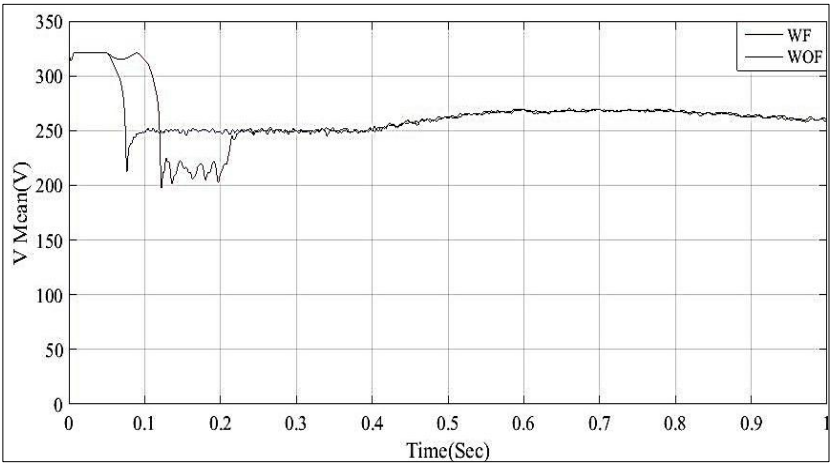

Fig 6: Output voltage of Boost Converter for Case-1

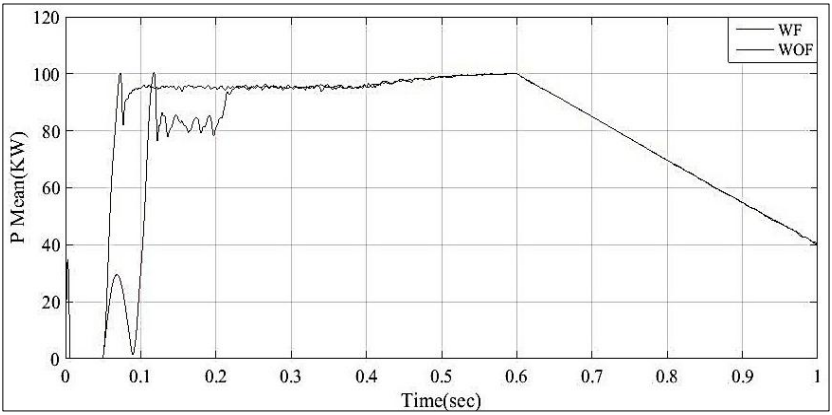

Fig 7: Output power of Boost Converter for Case-1

From fig. 5 to fig. 7, the power increases slowly irrespective of change in temperature and irradiance. When a fault occurs we can observe that there are fluctuations initially and then slowly adjusts itself to the desired value and then remains constant later there is a steep decline in the power irrespective to fault.

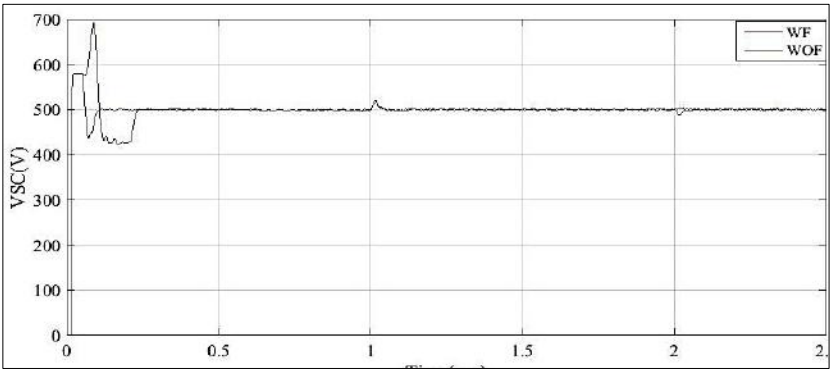

Fig 8: Output Voltage of Transformer for case-1

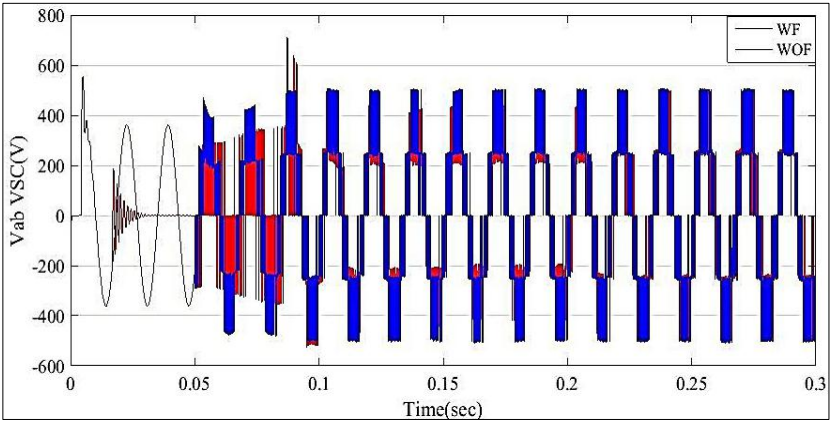

Fig 9: Output Voltage of One of the three phases of FITSMC

From fig. 8, deduce from the preceding figure that when the temperature and irradiance fluctuate, so does the transformer voltage, but it eventually returns to the desired range. When there is aproblem, however, it lowers below the required level before returning to normal. The accompanying illustration shows that it is practically ripple-free. From fig. 9, the output from FITSMC is continuous and distortion-free.

Case-2: Now consider the irradiance and the temperature to be varying as shown in fig. 10.The transformer's output voltage and the boost converter's output voltage and power are then impacted and the duty cycle is as shown in fig. 11.

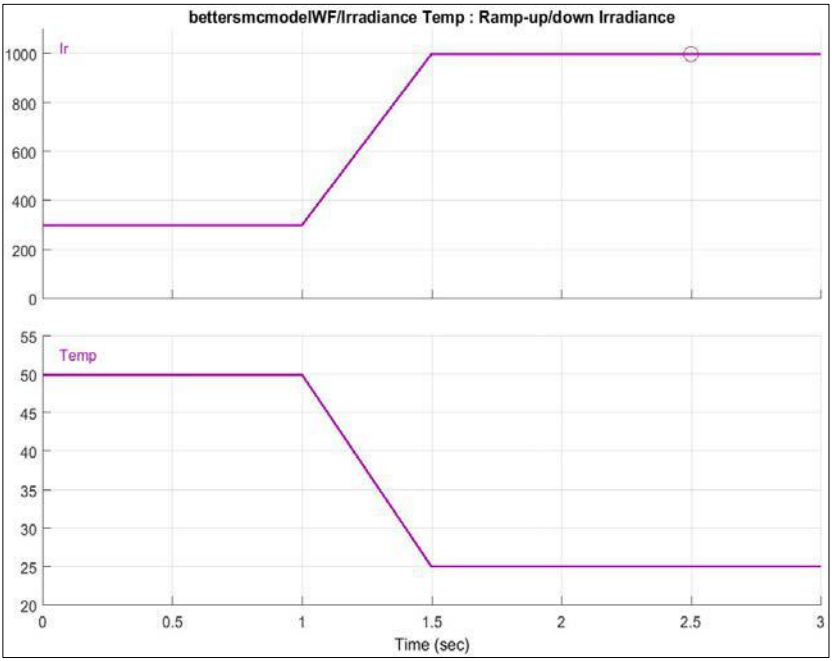

Fig 10: Irradiance and temperature input to PV module in case-2

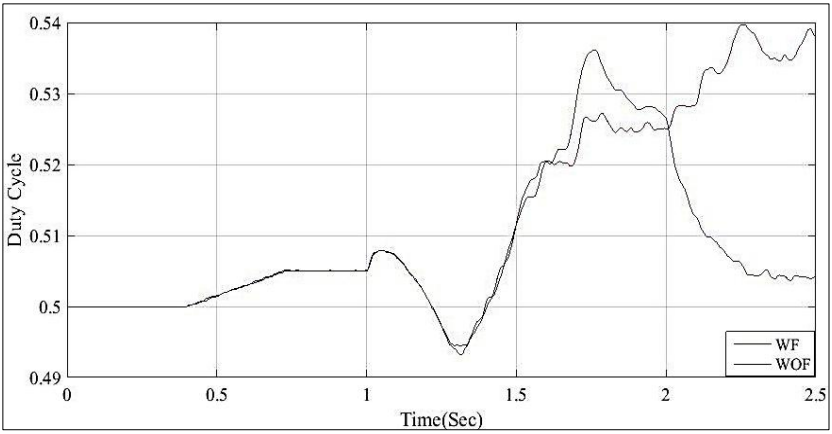

Fig 11: Duty Cycle Case-2

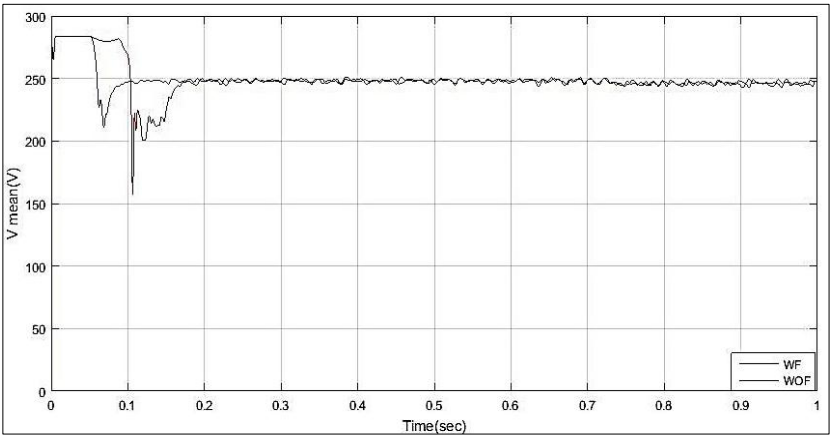

Fig 12: Boost converter output voltage for case-2

From fig. 9 to fig.12, the voltage responds to temperature and irradiance variations; at first, the voltage lowers, but it quickly settles and returns to normal. The fault may cause a high voltage surge, but it quickly returns to normal. Hence, the voltage is slightly higher than normal condition.

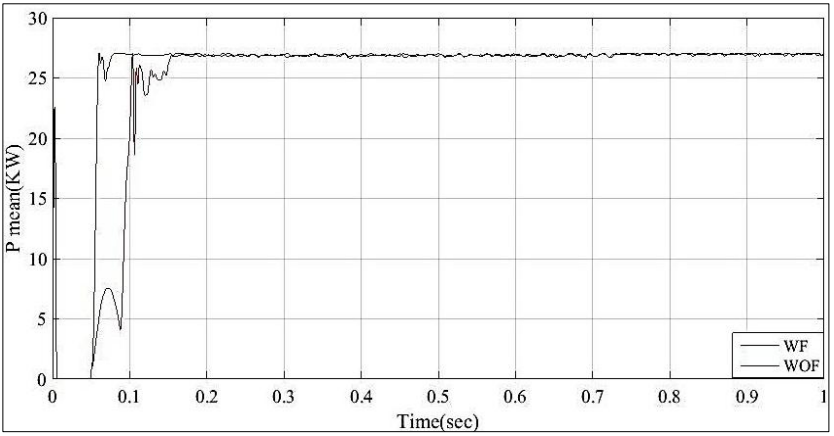

Fig 13: Boost converter output Power for case-2

From fig. 13, the power increases slowly regardless of temperature or irradiance changes. When a fault occurs, fluctuations can be noticed at first, then the power gradually adjusts to the desired value and ultimately remains constant. There is a fast fall in power regardless of fault.

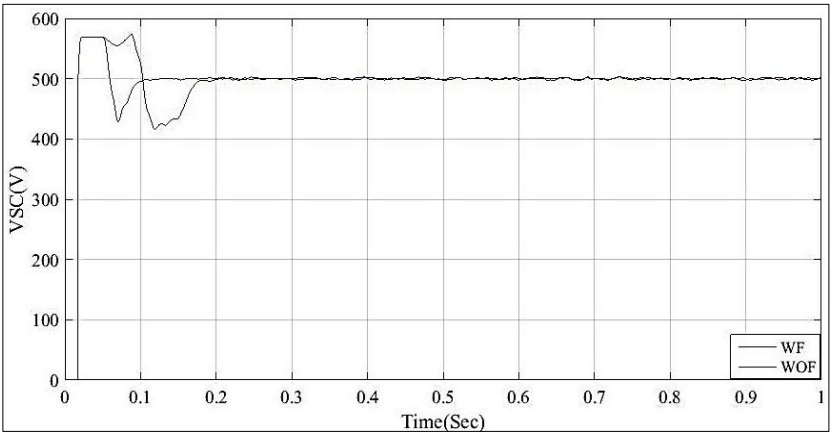

Fig 14: Output Voltage of Transformer for case 2

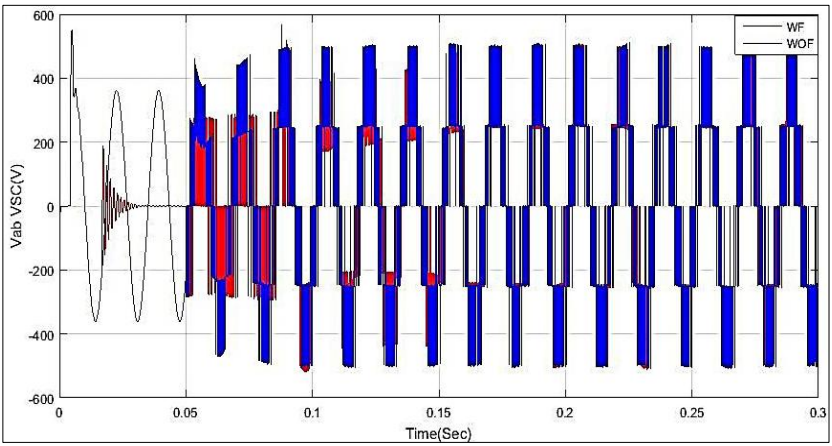

Fig 15: Output Voltage of One of three phases of FITSMC

From fig. 14, the transformer voltage fluctuates with temperature and irradiance, but it finally returns to the correct range. However, when there is a problem, it drops below the needed level before returning to normal and it is nearly ripple-free. From fig. 15, the output from FITSMC is continuous and distortion-free.

Case 3: Consider temperature to be constant at 25 °C and irradiance to be varying as shown in fig 16. The output voltage of inverter and the boost converter's output voltage and power are then impacted and are shown.

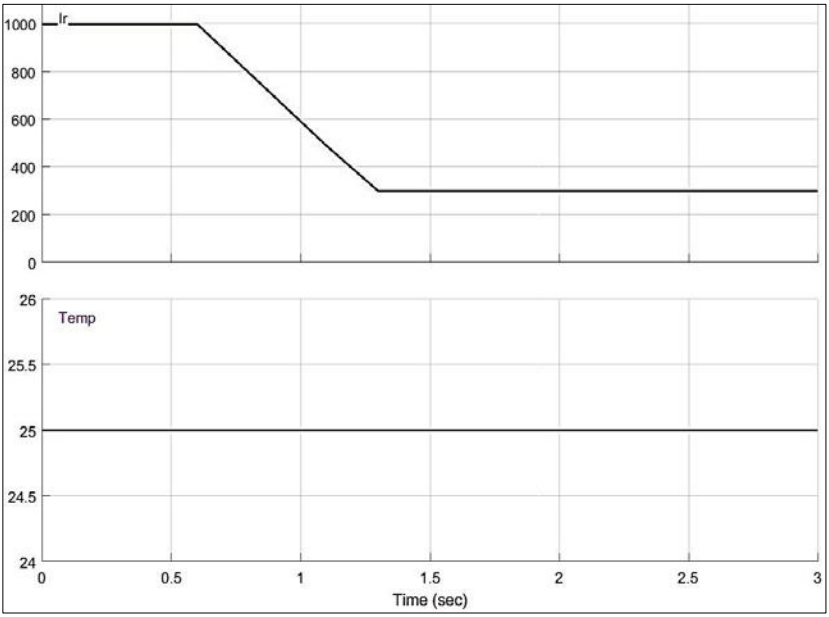

Fig 16: Irradiance and temperature for case-3

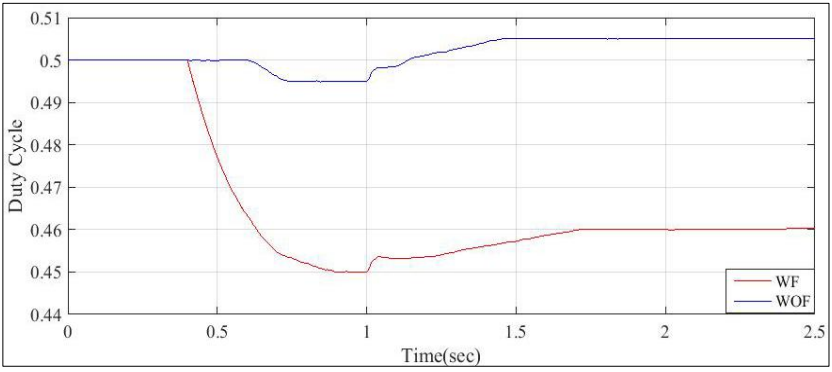

Fig 17: Duty cycle for case-3

MPPT controller generates duty cycle in order to create switching signals for the converter. The switching signal allows the boost converter to operate the PV system at optimum voltage and current so that maximum power extraction is possible. Fig. 17 shows us the duty cycle for case-3 with and without fault conditions.

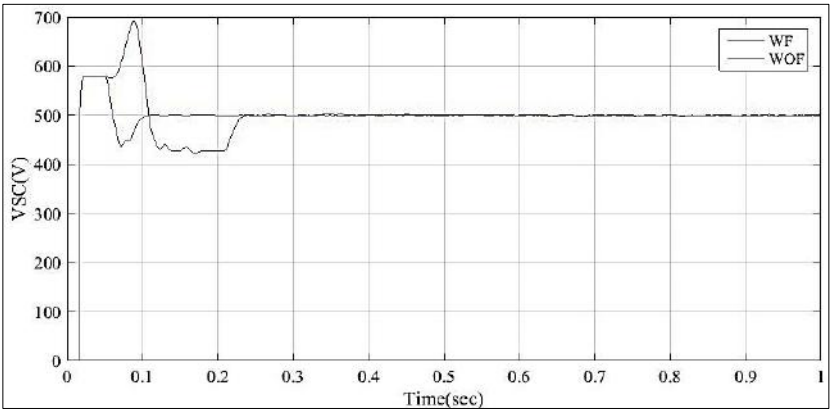

Fig 18: Output voltage of boost converter for case-3

From fig. 18, when the irradiance decreases there is also a fall in transformer voltage but it sets back into the desired range. But when there is a fault, before settling back it further drops below the required and then settles back. From the above fig. 18, there are less distortions in the graph of with fault but they are ripple free in without fault condition.

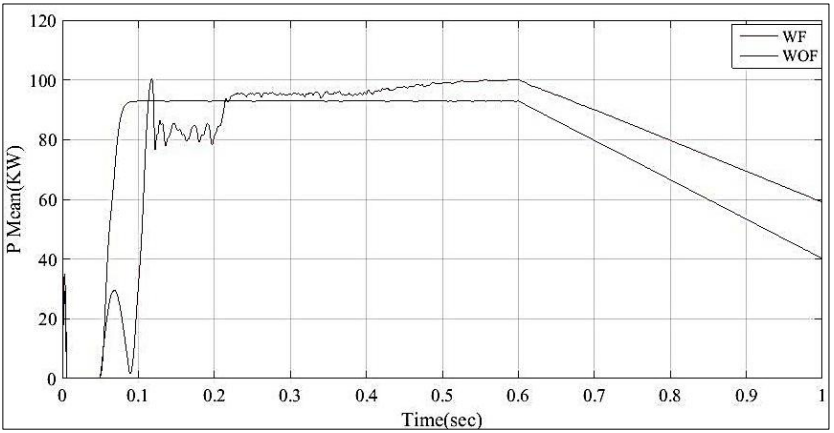

Fig 19: Boost converter output power for case-3

From the fig. 19, when the irradiance is constant at 1000 W/m^2 the power remains constant in without fault condition but in with fault condition the power remains constant but with distortions and slightly increases and as the irradiance decreases from 1000 W/m^2 to 300 W/m^2 the power also reduces from 95KW to 25KW. The power remains constant at constant irradiance and constant temperature.

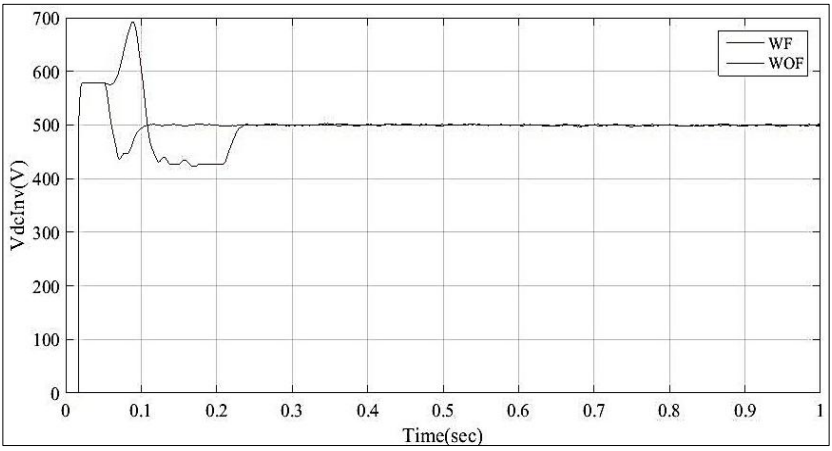

Fig 20: Output voltage of inverter for case-3

From fig. 21, with constant irradiance at 1000 W/m^2 there are small distortions in the voltage for with fault condition the voltage increases and decreases in small duration and remains constant, Same is the case with without fault condition as voltage falls and gets back to constant level irrespective of the irradiance and temperature levels.

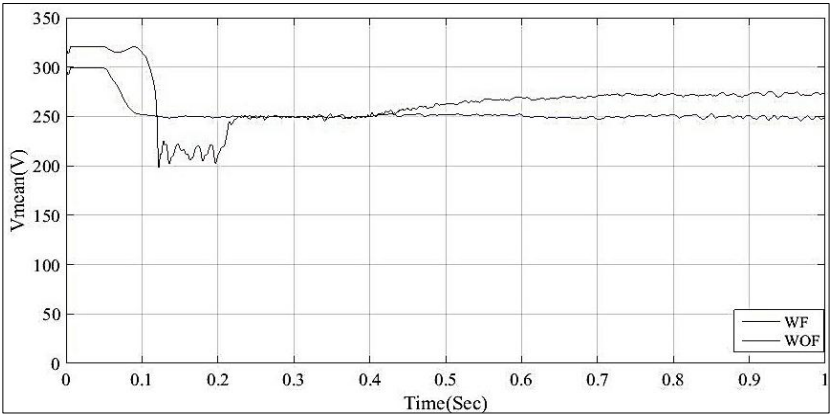

Fig 21: Output voltage of transformer for case-3

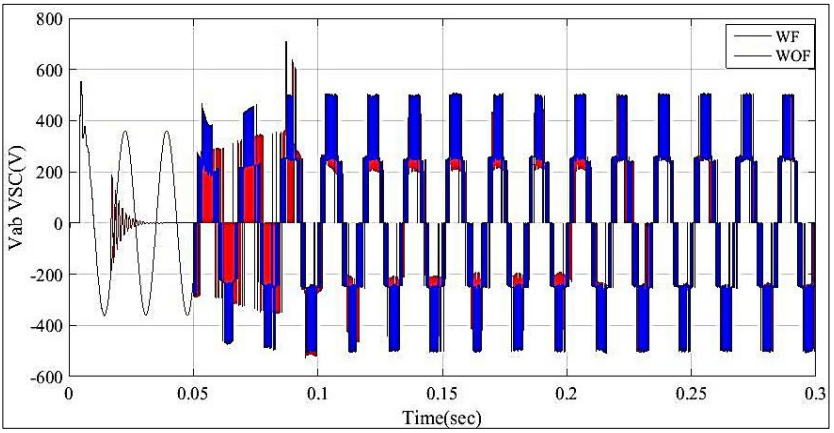

Fig 22: Output voltage of one of three phases of FITSMC

From fig. 21, At starting there are small distortions in the voltage level at 1000 W/m^2, after with respective to decrease in the irradiance levels the voltage level remains constant without any distortions in the voltage at constant temperature level. From fig. 22, the output through FITSMC is constant and is distortion free.

Case-4: Now consider the irradiance and the temperature to be varied as shown in fig 23.

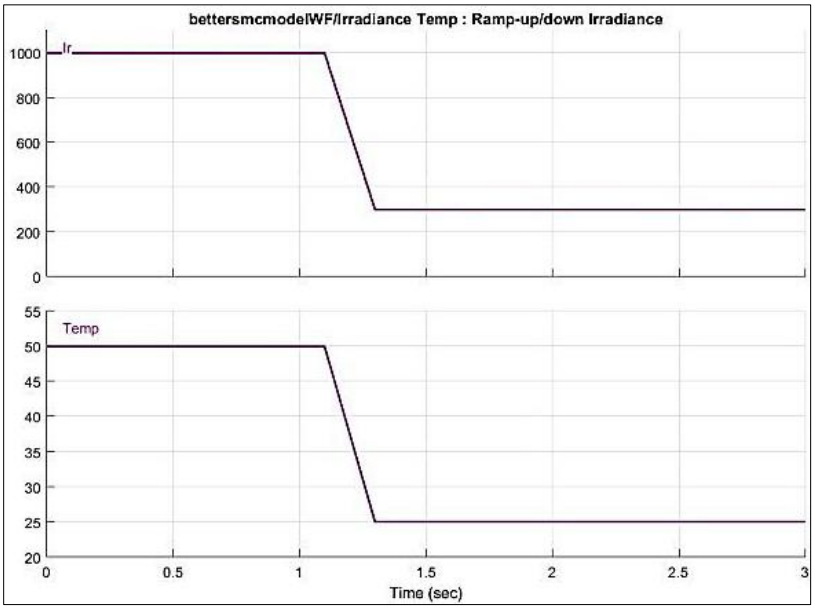

Fig 23: Irradiance and temperature input given to PV module Case – 4

Irradiance and Temperature Parameters are initially constant and then they decrease respectively with again reaching the state of constant.

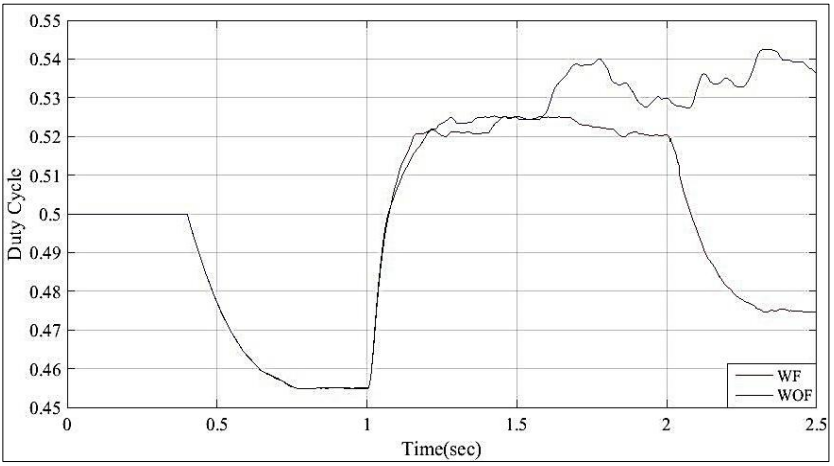

Fig 24: Duty cycle for case-4

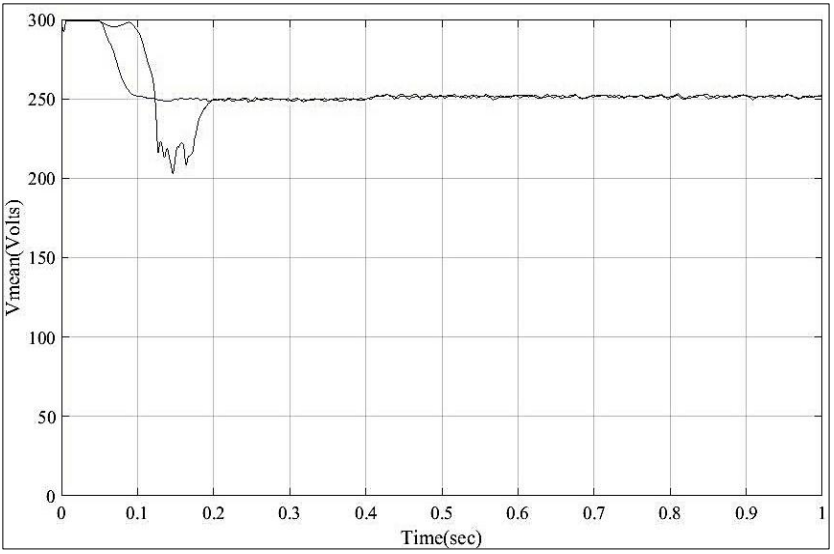

Fig 25: Output voltage of boost converter for case-4

From fig. 24 and fig. 25, initially, there are small distortions in the voltage level at 1000 W/m^2, after with respective to decrease in the irradiance levels the voltage level remains constant without any distortions in the voltage at constant temperature level.

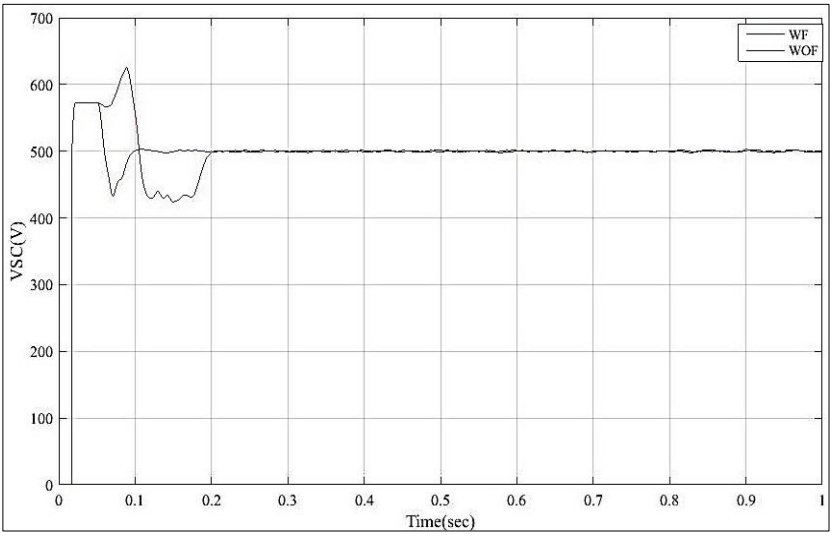

Fig 26: Output voltage of boost converter for case-4

From fig. 26, when the irradiance decreases there is also a fall in transformer voltage but it sets back into the desired range. But when there is a fault, before settling back it further drops below the required and then settles back. And also from the above figure, there are less distortions in the graph of with fault but they are ripple free in without fault condition.

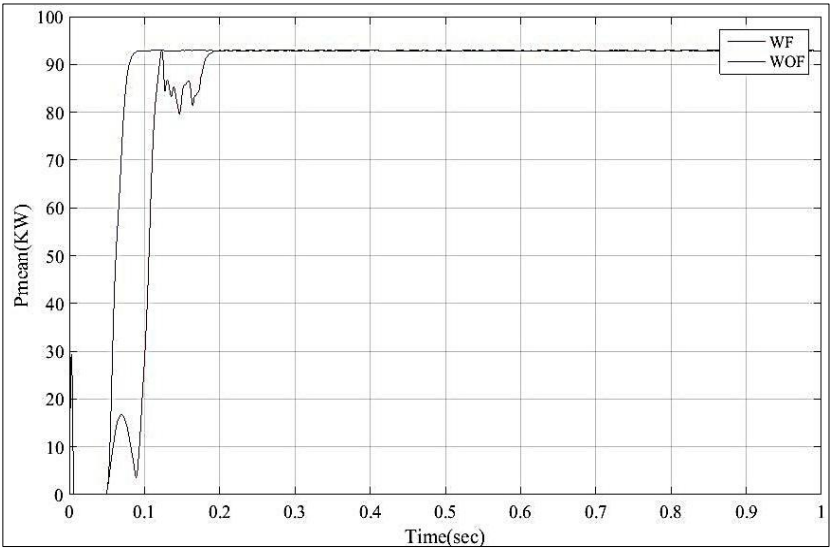

Fig 27: Boost converter output power for case-4

From fig. 27, the power increases slowly regardless of temperature or irradiance changes and also when a fault occurs, fluctuations at first, then the power gradually adjusts to the desired value and ultimately remains constant. There is a fast fall in power regardless of fault.

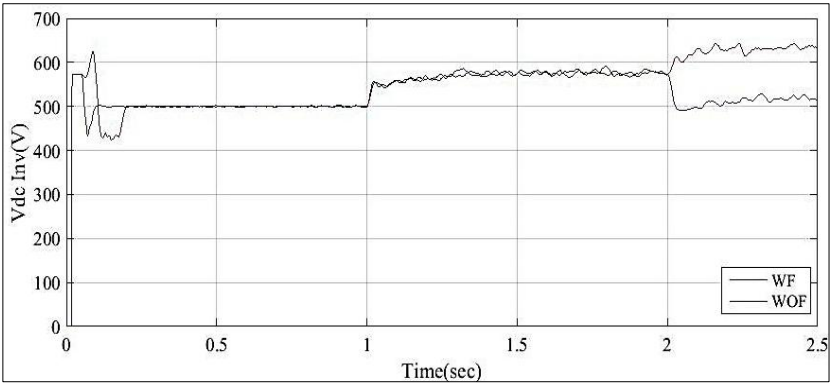

Fig 28: Output voltage of inverter for case-4

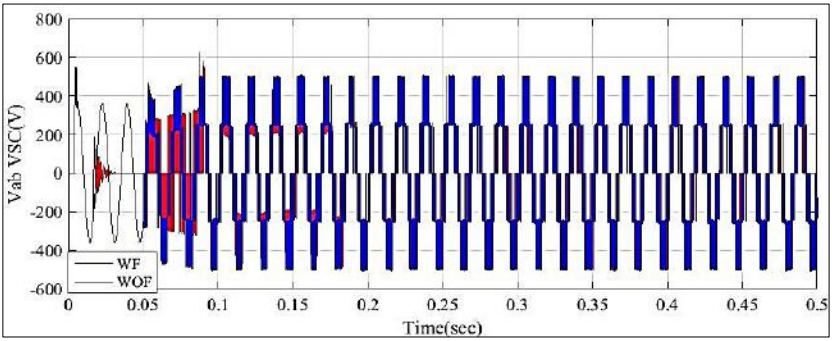

Fig 29: Output voltage of one of three phases of FITSMC

From fig. 29, the constant irradiance at 1000 W/m^2 there are small distortions in the voltage for with fault condition the voltage increases and decreases in small duration and remains constant, Same is the case with without fault condition as voltage falls and gets back to constant level irrespective of the irradiance and temperature levels.From fig. 29, the output through FITSMC is constant and is distortion free.

5. Conclusion

This study designed an integral terminal sliding mode control system for a grid-connected PV array under various operating conditions. The sliding mode idea aimed to enhance power extraction while reducing the effects of irradiance variations and bulk voltage oscillations. The reference for

maximum power point tracking was established using the perturb and observe method. Because it required minimal driving power and a simple drive circuit, an IGBT switch was used in the design. From the simulation results, the proposed ITSMC controller successfully decreases faults under various initial scenarios. The proposed ITSMC features excellent maximum power point tracking and voltage sag minimization.

References

1 Pillai DS, Rajasekar N. " An MPPT-Based Sensor less Line–Line and Line–Ground Fault DetectionTechnique for PV Systems, " in IEEE Transactions on Power Electronics. 2019;34(9):8646-8659.

2 Ibrahim O, Yahaya NZ, Saad N, Umar MW. Matlab/Simulink model of solar PV array with perturb and observe MPPT for maximising PV array efficiency, 2015 IEEE Conference on Energy Conversion (CENCON), 2015, 254-258.

3 Enslin JHR, Wolf MS, Snyman DB, Swiegers W. Integrated photovoltaic maximum power point tracking converter, in IEEE Transactions on Industrial Electronics. 1997;44(6):769-773.

4 Orkisz M. "Estimating Effects of Individual PV Panel Failures on PV Array Output," in IEEE Transactionson Industry Applications. 2018;54(5):4825-4832. doi: 10.1109/TIA.2018.2841818.M. Orkisz.et al [2018]

5 Kottas TL, Boutalis YS, Karlis AD. New maximum power point tracker for PV arrays using fuzzy controller in close cooperation with fuzzy cognitive networks, in IEEE Transactions on Energy Conversion. 2006;21(3):793-803.

6 Aloulou R *et al*. Improved circuit model of photovoltaic cell for energy harvesting application, MELECON 2014 - 2014 17th IEEE Mediterranean Electrotechnical Conference, 2014, 548-552.

7 Taha MS, Suresh K. Maximum power point tracking inverter for photovoltaic source pumping applications," Proceedings of International Conference on Power Electronics, Drives and Energy Systems for Industrial Growth. 1996;2:883-886.

8 Martins DC, Mezaroba M, Ruther R, Barbi I. Water pumping from photovoltaic cells using a current-fed parallel resonant push-pull inverter, Conference Record of the Twenty-Eighth IEEE Photovoltaic Specialists Conference - 2000 (Cat. No.00CH37036), 2000, 1529-1532.

9 Prakash G, Pradeepa S. Design and Modeling of MPPT for Solar Based Power Source, 2018 4th International Conference on Electrical Energy Systems (ICEES), 2018, 624-629.

10 Glunz SW *et al*. High-efficiency silicon solar cells for low-illumination applications, Conference Record of the Twenty-Ninth IEEE Photovoltaic Specialists Conference, 2002, 450-453.

11 Zanotti JW, Martins DC. Input characteristic impedance technique of power converters circuits applied to the maximum power point tracker of photovoltaic panels, 2014 IEEE Asia Pacific Conference on Circuits and Systems (APCCAS), 2014, 292-295.

12 Kashif M, Murshid S, Singh B. Standalone solar PV array fed SMC based PMSM driven water pumping system, 2018 IEEMA Engineer Infinite Conference (eTechNxT), 2018, 1-6

13 Verma R, Ansari MA. Photovoltaic Power Efficient Adjustment using Maximum Power Point Tracking and Boost Converter, 2021 4th International Conference on Recent Developments in Control, Automation & Power Engineering (RDCAPE), 2021, 43-46.

14 Dehedkar MN, Vitthalrao Murkute S. Optimization of PV System using Distributed MPPT Control, 2018 International Conference on System Modeling& Advancement in Research Trends (SMART), 2018, 216-220.

15 Tian J, Chen G, Luo L. Sliding Mode MPPT Control Based on Fuzzy Exponential Approach Rate for PV Cells, IEEE 4th Conference on Energy Internet and Energy System Integration (EI2), 2020, 623-626.

16 Shahida LR, George TM. Implementation of sliding mode control for a buck converter in a photovoltaic system, 2014 International Conference on Advances in Green Energy (ICAGE), 2014, 245-250.

17 Pandey S, Dwivedi B, Tripathi A. Performance analysis of SMC controlled PV fed boost converter, 2016 7th India International Conference on Power Electronics (IICPE), 2016, 1-4

18 Villalva MG, Gazoli JR, Filho ER. Comprehensive Approach to Modeling and Simulation of Photovoltaic Arrays IEEE transactions on power electronics, 2009, 24(5).

19 Rauschenbach HS. Solar Cell Array Design Handbook. New York: Van Nostrand Reinhold, 1980.

20 Liu X, Lopez LAC. An improved perturbation and observation

maximum power point tracking algorithm for PV arrays, Proc. of IEEE Power Electronics Specialists Conf., 2004.

21 Choe HJ, Chung YC, Sung CH, Yun JJ, Kang B. Passive Snubber for Reducing Switching-Power Losses of an IGBT in a DC–DC Boost Converter" IEEE transactions on power electronics, 2014, 29(12).

22 Montoya DG, Ramos-Paja CA, Giral R. Improved Design of Sliding-Mode Controllers Based on the Requirements of MPPT Techniques IEEE transactions on Power Electronics. 2016;31(1):235-247.

23 Esram T, Chapman PL. Comparison of photovoltaic array maximum power point tracking techniques, IEEE Trans. Energy Convers. 2007;22(2):439-449.

24 Femia N, Petrone G, Spagnuolo G, Vitelli M. Optimization of perturb and observe maximum power point tracking method, IEEE Trans. Power Electron. 2005;20(4):963-973.

25 Salem M, Atia Y. Control scheme towards enhancing power quality and operational efficiency of single-phase two-stage grid-connected photovoltaic systems J. of Electrical Systems and Information Technology. 2015;2(3):314-327.

26 Chiu C, Shen C. Finite-time control of DC-DC buck convertersvia integral terminal sliding modes, International Journal of Electronics. 2012;99(5):643-655,.

27 Ch. Raja VN, Sai Vamsi P, Sowjanya K, Hari Vardhan M, Rajeev P. Necessity to Design a Controller for PV Module, International Journal of Innovative Technology and Exploring Engineering (IJITEE). 2020;9(3):1932-1937.

ADVANCES IN ELECTRICAL ENGINEERING

VOLUME - 5

Chief Editor

Dr. G. Durgadevi
Professor, Department of ECE, New Prince Shri Bhavani College of Engineering and Technology, Chennai, Tamil Nadu, India

Co-Editor

Dr. A.V. Sudhakara Reddy
Associate Professor, Malla Reddy Engineering College (Autonomous), Maisammaguda, Hyderabad, Telangana, India

AkiNik Publications
New Delhi

Published By: AkiNik Publications

AkiNik Publications
169, C-11, Sector - 3,
Rohini, Delhi-110085, India
Toll Free (India) – 18001234070
Phone No. – 9711224068, 9911215212
Email – akinikbooks@gmail.com

Chief Editor: Dr. G. Durgadevi
Co-Editor: Dr. A.V. Sudhakara Reddy

Publications Year: 2022

Pages: 112

ISBN:

Book DOI: https://doi.org/

Price: ₹ 653/-

Contents

Chapters **Page No.**

1. Uncertainty Management in Electrical Power System 01-18
   (Dr. Muhammad Shahzad, Muhammad Abbas Raza and Amir Raza)

2. A Comparative Study in the Design of an Ann Based Controller 19-36
   (Dr. Ch. Varaha Narasimha Raja and Dr. G. Anand)

3. Study of Energy Capture with Photovoltaic Cell in Zinc Tile 37-53
   (Dr. A. Manjula, R Niraimathi, S. Chitra Devi and Dr. S. Lakshmi Kanthan Bharathi)

4. Implementation of IT-SMC for Fault Rectification in a Grid-Connected PV System for Maximum Power Point Tracking 55-80
   (Dr. Ch. Varaha Narasimha Raja, M. Vijaya Kumari, R. Jayank Maanas, M. Bhavan, Dr. G. Anand and Dr. I.E. Sanyasi Naidu)

5. Analysis of the Floating Junction in the Area of the Rear Boron Diffuser in Bifacial Pert Solar Cells 81-99
   (Raja Reddy Duvvuru, R. Sireesha and V. Lakshmi Devi)

6. A New Algorithm for the Order Reduction of High Order Uncertain Systems 101-112
   (Dr. T. Narasimhulu, Dr. S. Srikanth and Dr. G. Raja Rao)

Chapter - 2

A Comparative Study in the Design of an Ann Based Controller

Dr. Ch. Varaha Narasimha Raja and Dr. G. Anand

Abstract

The power system stabilizer is based on artificial neural networks and is designed to cope with changing operational circumstances in real-world applications. The parameters of a conventional or supplementary power system stabilizer are generated with changing operating circumstances using a Multi-layer feed-forward with back propagation (MLP) Artificial neural network in this paper. As a result, the power system stabilizer's utility becomes more stable. Many researchers included this artificial neural network in their designs; however, information on network creation functions, hidden layer size, non-linear (active) functions employed in output and hidden layers, and back propagation training functions were not studied in detail. In this paper a study is carried out on these aspects to explore the effect of these aspects on the functionality of power system stabilizers.

Keywords: Artificial neural network, Multi-layer back propagation, Single Machine Infinite Bus, Eigen value Placement technique

a) Introduction

An Artificial Neural Network (ANN) is an information [8] processing paradigm that is inspired by the way biological nervous systems, such as the brain, process information. The key element of this paradigm is the novel structure of the information processing system. It is composed of a large number of highly interconnected processing elements (neurons) working in unison to solve specific problems. ANNs, like people, learn by example. An ANN is configured for a specific application, such as pattern recognition or data classification, through a learning process. Learning in biological systems involves adjustments to the synaptic connections that exist between the neurons. This is true of ANNs as well. Two reasons are put forward for using ANN. First, since an ANN is based on parallel processing, it can provide extremely fast processing facility. The second reason for the high level of interest is the ability of ANN to realize complicated nonlinear mapping from the input space to the output space.

A popular type of Artificial neural network, the Multi-layer feed-forward with back propagation (MLP) training method [3, 9], is employed. Till now, so many authors utilized this method for solving complex systems, however information on network creating functions, size of the hidden layer, non-linear (active) functions employed in output and hidden layers, training functions of back propagation were not clearly discussed. In this paper, these aspects are explored in the design of power system stabilizer for single machine infinite bus system. ANN is an imitated network of neurons which interact with each other to process and transfer information [8]. It is a network of inter connected elements and these elements were inspired from the studies of biological nervous systems. In other words, neural network are an attempt at creating machines that work in a similar way to the human brain by building these machines using components that behave like biological neurons [9]. The basic ANN model has an input layer with any number of neurons, a number of hidden layers can be there with any number of neurons supported by the system for a particular operation and then there is an output layer which takes the weighted sum of all the hidden layer neurons and give a certain output [8]. The ability of ANN to model complex relationships makes them superior to conventional controller system. Conventional controllers require a good knowledge about mathematical model of controlled system, which may not be available. Most ANN controllers on the other hand do not need such requirements and can handle complex systems efficiently. They learn to map input-output relationships by training process. The ANN are trained to identify a process either off-line or on-line during the real time operation of the system [9-11]. ANN can easily handle complicated problems and can identify and learn correlated patterns between sets of input data and corresponding target values. After training, these networks can be used to predict the outcome from new input data. Being universal function approximates, they are capable of approximating any continuous nonlinear function to arbitrary accuracy [9]. From advance adaptive neural network have a built-in capability to adapt their synaptic weights to changes in the surrounding environment in particular, a neural network trained to operate in a specific environment can be easily retrained to deal with minor changes in the operating environmental conditions. Moreover, when it is operating in a non-stationary environment a neural network can be designed to change its synaptic weight in real time. The neural architecture of a neural network for pattern classification, signal processing and control applications, coupled with adaptive capability of the network, makes it an ideal tool for use in adaptive pattern classification, adaptive signal processing and adaptive control [12].

In the present paper, Section II: various techniques of improving the damping characteristics of a synchronous machine infinite bus system [1, 5, 14] with simulation results have been discussed and Section III: Artificial neural network based power system stabilizers with some special aspects like network creating functions, size of the hidden layer, non-linear (active) functions employed in output and hidden layers, training functions of back propagation have been discussed and finally.

b) Single Machine connected to Infinite Bus

An infinite bus is a source of constant frequency and voltage either in magnitude and angle. A schematic representation of this system is shown in fig 1.

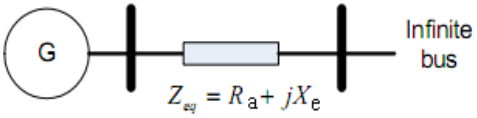

Fig 1: Single Machine Connected to a large system through transmission line [4]

In order to analyze the small signal stability of the system with synchronous machine, DeMello and Concordia [1] has come with an approach by developing the expression for the elements of the state matrix as explicit functions of system parameter.

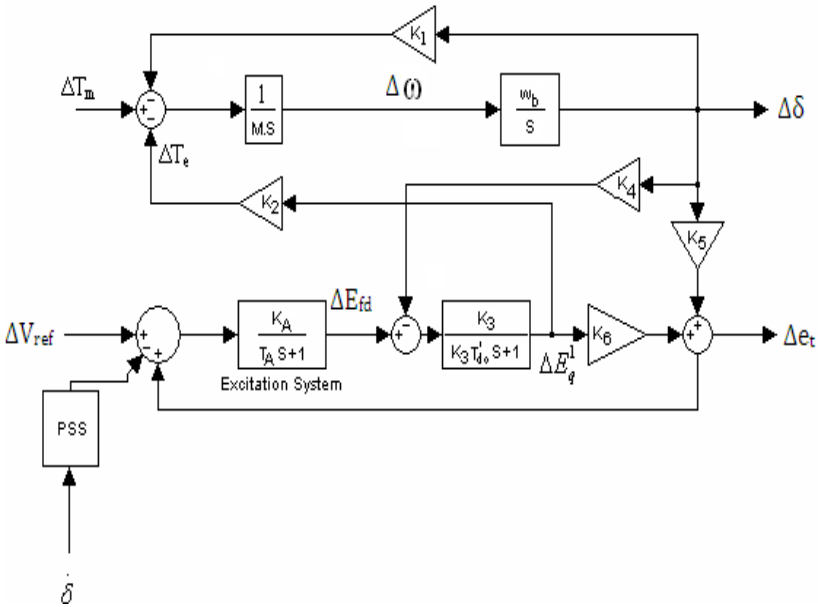

Fig 2: Block diagram representation of SMIB [6]

c) Controlling Techniques

a) Conventional Lead-Lag PSS (CPSS):

Electromechanical oscillations of generator are damped by compensator that one type of it is shown in fig 3.

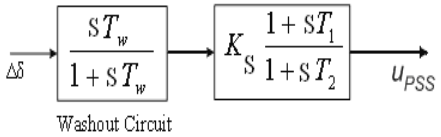

Fig 3: Block diagram of Conventional PSS

Where K_S is the stabilization gain,

T_W is the washout time constant,

T_1 is the transient time constant and

T_2 is the steady state time constant

Generally, we take T_w=2 and T_2=0.05

The main disadvantage of this method is improper operation for electromechanical oscillation when system parameters varied.

b) State Variable feedback Technique [2]

The system equations should be written in the state variable form

$$\dot{X} = AX+bU \qquad (1)$$

Where X is the n-dimentional state vector, A-is a nxn constant matrix, b-is a constant n-vector and U-is the supplementary control input.

The simple way to select state variables is to take them as the outputs after first order blocks in the diagram of fig.2, loading to

$$X = \left[\Delta\delta \quad \Delta\omega \quad \Delta E_q^1 \quad \Delta E_{FD}\right]^T \qquad (2)$$

The corresponding A and B matrices are given in the Appendix.

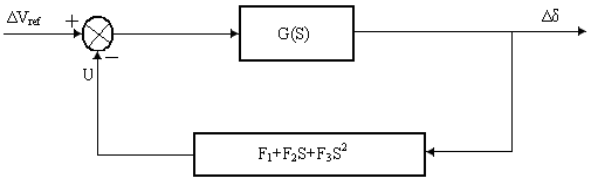

Fig 4: Block diagram of system with phase variable feedback controller

The effect of phase variable feedback is seen to be equivalent to the introduction of a feedback compensator with zeros given by

$$F_1+F_2S+F_3S^2=0 \quad (3)$$

It may be noted from (3) if the zeros are chosen as $-3.0 \pm j5.2$; two of the eigenvalues can be expected to be near these.

3. ANN Applied to power system stabilizers

For on-line adaptation of PSS parameters, the ANN design is such that the nodes in the input layer receive input signals from the outside world and directly pass the signals to the nodes in the next layer. In the present work, the multilayer feed forward neural network is employed to adapt PSS parameters according to generator loading conditions.

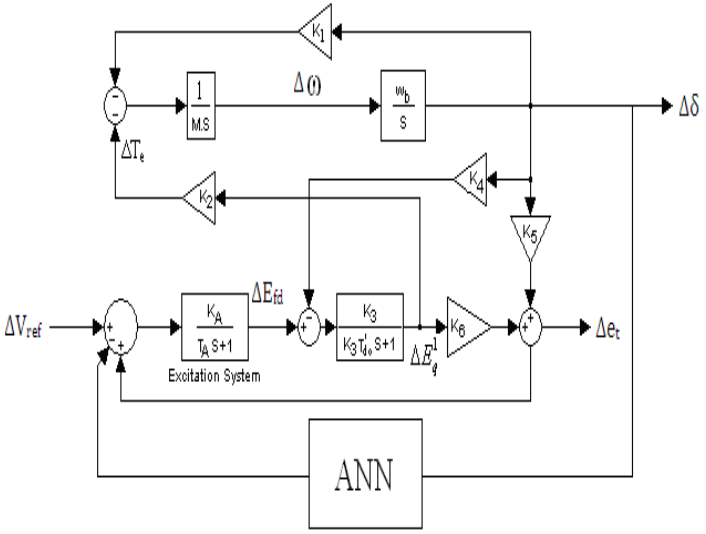

Fig 5: Block diagram of SMIB with Artificial neural network

A set of 80 training patterns are first generated. Each training pattern contains generator real power (P) and reactive power (Q), which serve as the inputs to the ANN, and the desired PSS parameters (K_{STAB} and T1 in the case of CPSS and F1, F2 and F3 in the case of Eigen value placement technique) which is the desired output (target) signals of the ANN. When the ANN has been trained using these training patterns, it can be employed to yield the desired PSS controlling parameters for any monitored loading condition (Real power (P) and reactive power (Q)). Thus, the PSS parameters can be adapted in real-time based on online measured generator operating condition.

4. Result

In this section the dynamic performance of the system with self-tuning ANNPSS is evaluated for nominal operating condition and then observe the dynamic performances for operating points other than nominal. Following three typical loading conditions spread over the entire domain of operation for which the ANN was trained are chosen for assessing the robustness of the self tuning ANNPSS

1. P = 1.0 pu Q = 0.0 pu
2. P = 1.0 pu Q = 0.5 pu
3. P = 0.5 pu Q = 0.0 pu

Fig 6 and Fig. 7 shows the schematic block diagram used for simulating the dynamic performance of the system with Self-Tuning ANNPSS and Fig 8 shows the schematic block diagram used for simulating the performance of the system with Self-tuning of various ANN's PSS (Test System data is given in APPENDIX). A sampling period of 10msec is assumed. The sampled values of P, Q of the synchronous generator are applied to ANN. The ANN computes the optimum values of PSS parameters (K_{STAB} and T1 in the case of CPSS and F_1, F_2 and F_3 in the case of Eigen value placement technique). The stabilizing signal, ΔV_s is computed by the PSS using the PSS parameters. During the sampling period, the stabilizing signal so computed remains constant.

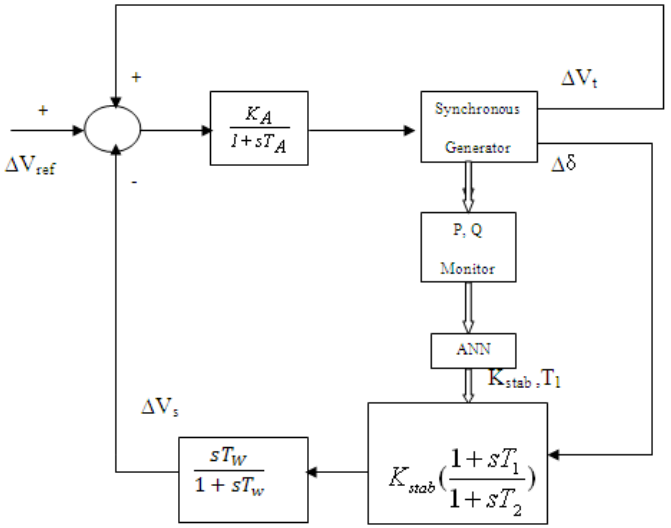

Fig 6: Schematic diagram of a synchronous generator with ST-ANN CPSS.

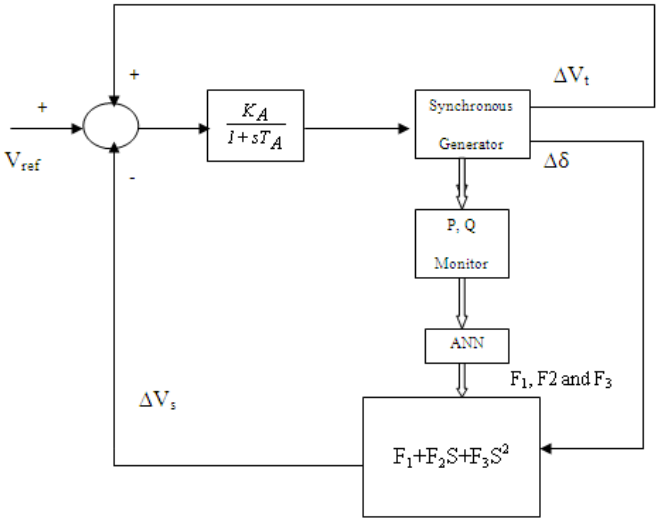

Fig 7: Schematic diagram of a synchronous generator with ST-ANN EVP PSS

Case 1: Responses of Power system stabilizers using *newff* creating function:

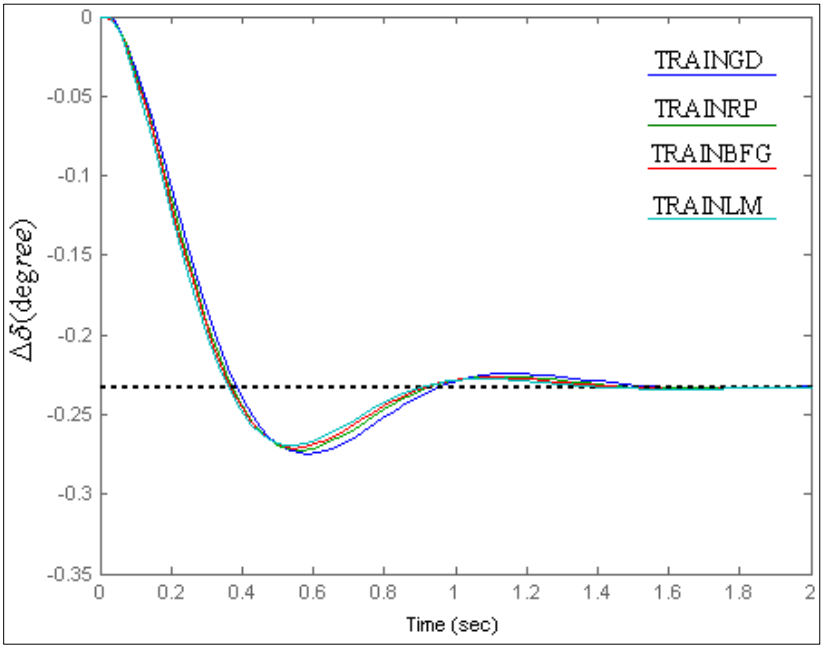

Fig 8: Single Hidden layer with various Back Propagation training function

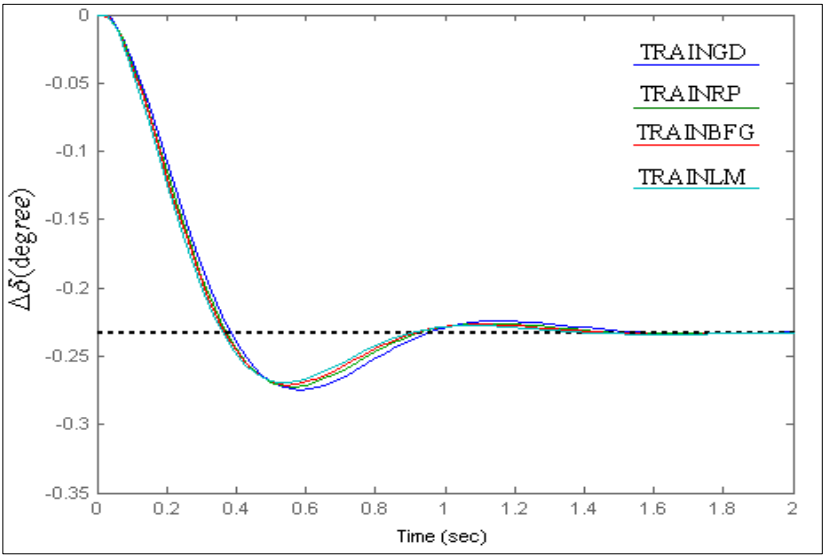

Fig 9: Two Hidden layer with various Back Propagation training function

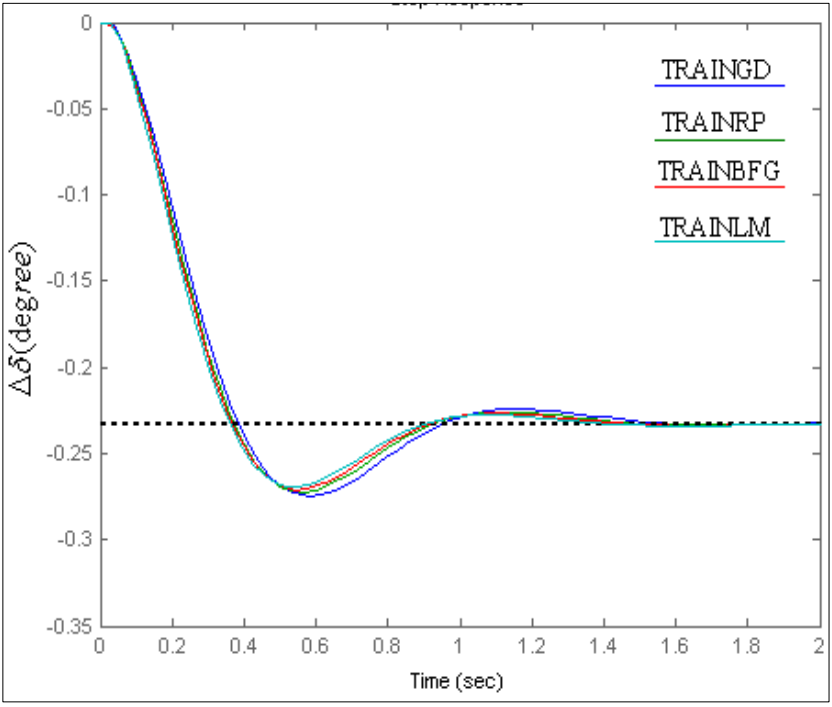

Fig 10: Three Hidden layer with various Back Propagation training function

From figure 8 to figure 10, the BPT function TRAINLM is very fast, but it requires a lot of memory to run. The BPT function TRAINBFG, which is slower but undersized efficient than TRAINLM. The BPT function TRAINRP, which is slower but undersized efficient than TRAINBFG. The BPT function TRAINGD, which is slower but undersized efficient than TRAINRP. By increasing the number of hidden layers, we may get low training error but it requires a lot of time to run. Therefore, for training the linear model systems single hidden layer and trainlm back propagation training function is sufficient for creation of neural network.

Case 2: Responses of Power system stabilizers using *newcf* creating function

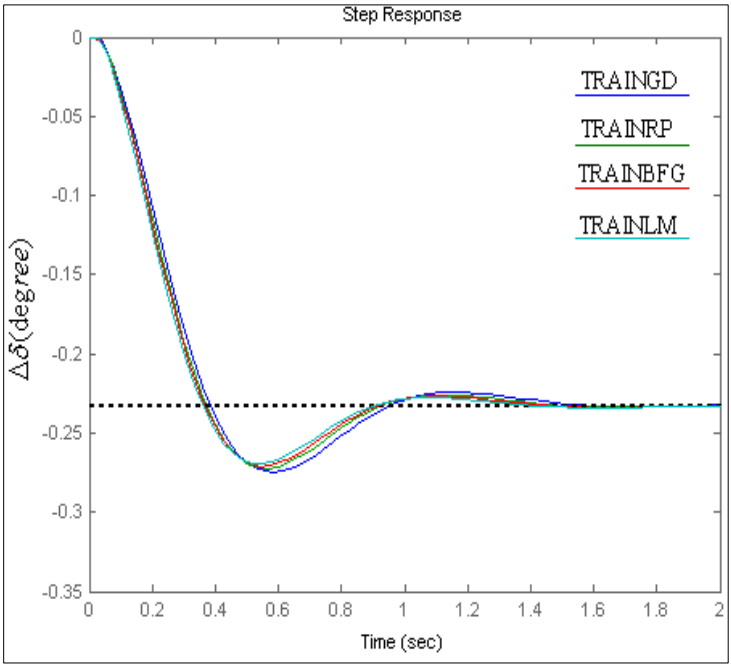

Fig 11: Single Hidden layer with various Back Propagation training function

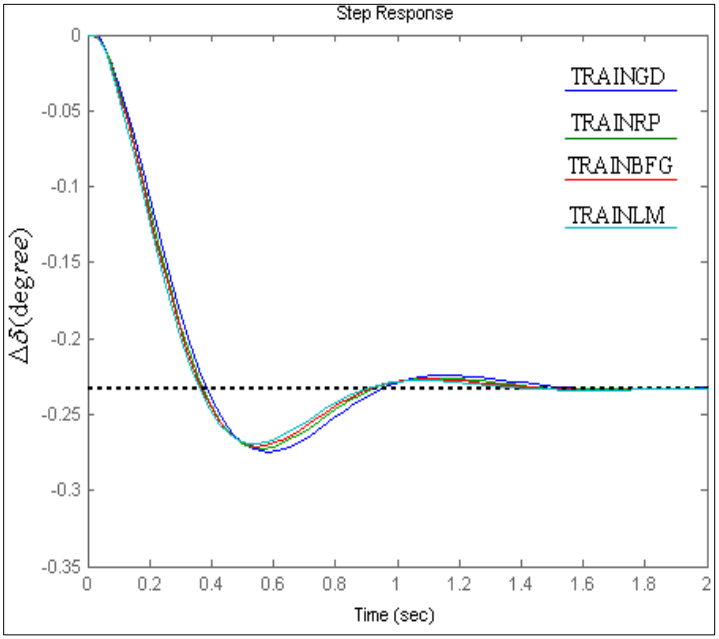

Fig 12: Two Hidden layer with various Back Propagation training function

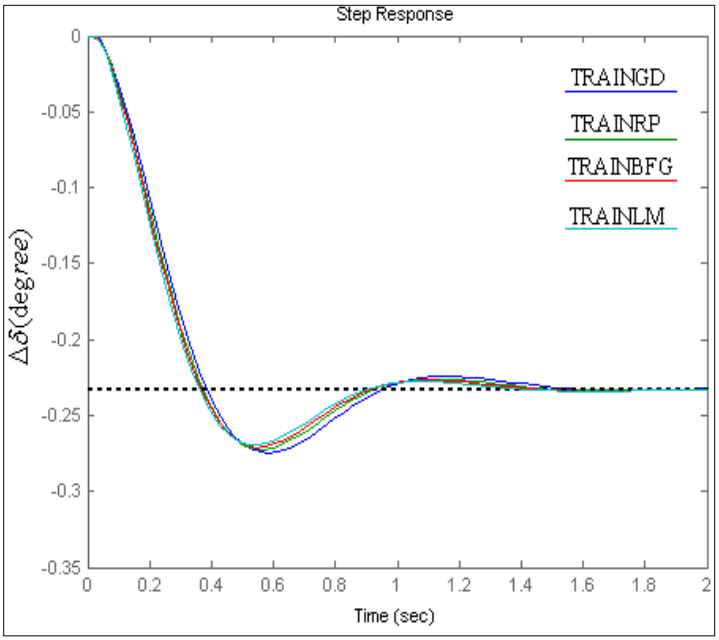

Fig 13: Three Hidden layer with various Back Propagation training function

From figure 11 to figure 13: The BPT function TRAINLM is very fast, but it requires a lot of memory to run. The BPT function TRAINBFG, which is slower but undersized efficient than TRAINLM. The BPT function TRAINRP, which is slower but undersized efficient than TRAINBFG. The BPT function TRAINGD, which is slower but undersized efficient than TRAINRP. By increasing the number of hidden layers, we may get low training error but it requires a lot of time to run. Therefore, for training the linear model systems single hidden layer and trainlm back propagation training function is sufficient for creation of neural network.

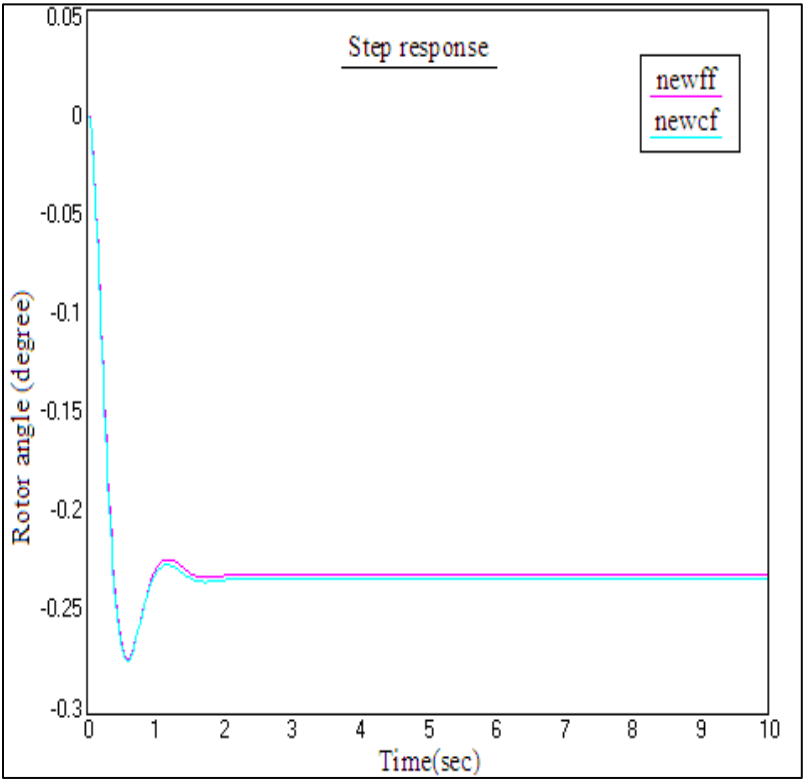

Fig 14: Comparing responses of various network creating functions (newff & newcf)

From fig. 14, for training the power system stabilizer system single hidden layer, trainlm back propagation training function and newff network creating function is sufficient.

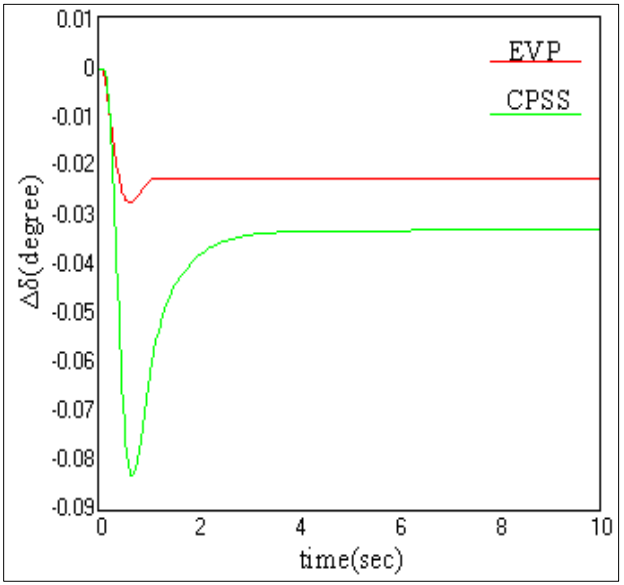

Fig 15: Comparing response of Conventional and EVP Technique using ANN at P=1.0 pu Q= 0.5 pu

Table I and Table II shows the PSS parameters computed using trained ANN and those obtained by off-line computations, for five typical test operating conditions. It is clearly seen that the PSS parameters computed using ANN match very closely with the corresponding off-line computed values.

Table I: PSS parameters (K_{stab},T_1) computed using trained ANN for few operating points.

Operating condition in pu		**PSS parameters Computed using ANN**		**PSS parameter computed through off-line studies**	
P	Q	K_{stab}	T_1	K_{stab}	T_1
1.0	0.0	0.2426	0.0027	0.2425	0.0027
1.0	0.5	0.2853	0.0615	0.2850	0.0615
1.0	-0.5	0.3433	0.0810	0.3430	0.0809
0.5	0.0	0.1174	0.2891	0.1174	0.2883
0.1	0.0	0.0960	2.4633	0.0958	2.4633

Table II: Eigenvalues computed using trained ANN for few test operating points.

S. No.	**Operating Point**	**Eigenvalues Computed using ANN**	**Eigenvalues computed through off-line studies**
1	1.0+j0.0	-7.3717±j57.782 -2.8601±j5.4616	-7.3714±j57.779 -2.8601±j5.4616
2	1.0+j0.5	-7.4410±j53.989 -2.7906±j5.5468	-7.4409±j53.985 -2.7906±j5.5468

3	1.0-j0.5	-7.2800±j59.875 -2.9517±j5.4649	-7.2797±j59.872 -2.9517±j5.4649
4	0.5+j0.0	-7.27800±j59.875 -2.9517±j5.4649	-7.2797±j59.872 -2.9517±j5.4649
5	0.1+j0.0	-7.3581±j82.879 -2.8732±j5.2047	-7.3583±j82.878 -2.8732±j5.2047

5. Conclusions

In this paper. A brief introduction about artificial neural network, architecture of artificial neural network, network creating functions, back propagation training functions, non-linear (active) functions and hidden layers is given in second section. In section III analysis of the conventional and supplementary power system stabilizer is carried out with changing operating conditions, simulations are also carried out with stabilizers under parameter changes and it is shown that the dynamic output stabilizer is more effective in stabilizing the system. However in the implementation of these stabilizers the tuning of the parameters of the stabilizers is to be carried out manually with changing operating conditions. This is not possible in online real time applications. So a compromise solution is to design a stabilizer using trail and error method so that it is robust under varying operating conditions. The simulations show that this approach is not fusible in the present conditions. Finally, section IV an artificial neural network based power system stabilizer is designed for online and real time applications. While designing this power system stabilizer effect of certain aspects of Multi layer feed-forward with back propagation (MLP) are studied in the simulations. The network creating function in MLP method automatically initialized the weights and biased the network, the increase in hidden layers reduced the training error; the nonlinear (active) functions which were employed reduced the output from reaching a large value and paralyzed the output for better training of neural network. These aspects ultimately helped in designing an accurate controller for ANN based power system stabilizer controller.

6. Appendix

Data used for test system [15]

f_b	H	R_a	x_e	T_{d0}^1
60	5	0	0.4	6.0
x_d	x_d^1	x_q	K_A	T_A
1.6	0.32	1.55	200	0.05

Phase Variable Model [13], [15]

$$A=\begin{bmatrix}0 & 1 & 0 & 0\\ 0 & 0 & 1 & 0\\ 0 & 0 & 0 & 1\\ a_0 & a_1 & a_2 & a_3\end{bmatrix} \qquad b=\begin{bmatrix}0\\ 0\\ 0\\ \dfrac{-377K_AK_2K_3}{MK_3T_{d0}^1T_A}\end{bmatrix}$$

Open loop transfer function is

$$G(S)=\frac{-377K_AK_2K_3 \Big/ MK_3T_{d0}^1T_A}{S^4+a_3S^3+a_2S^2+a_1S+a_0}$$ Where

$$a_0=377[(K_1-K_2K_3K_4)+K_AK_3(K_1K_6-K_2K_5)] \Big/ MK_3T_{d0}^1T_A$$

$$a_1=377[K_1K_3T_{d0}^1+T_A(K_1-K_2K_3K_4)] \Big/ MK_3T_{d0}^1T_A$$

$$a_2=[M(1+K_AK_3K_6)+377T_AK_1K_3T_{dO}^1] \Big/ MK_3T_{d0}^1T_A$$

References

1. Wang Y, Wen FS, Yang SF. A power system transient stability analysis based on MATLAB, 2014 IEEE PES Asia-Pacific Power and Energy Engineering Conference, 2014, pp. 1-4,
2. Hadidi R, Jeyasurya B. Reinforcement learning based real-time wide-area stabilizing control agents to enhance power system stability, IEEE Trans. Smart Grid. 2013;4(1):489-497.
3. Gupta P, Pal A, Vittal V. Coordinated Wide-Area Damping Control Using Deep Neural Networks and Reinforcement Learning, in IEEE Transactions on Power Systems. 2022;37(1):365-376.
4. Du W, Dong W, Wang Y, Wang H. A Method to Design Power System Stabilizers in a Multi-Machine Power System Based on Single-Machine Infinite-Bus System Model, in IEEE Transactions on Power Systems. 2021;36(4):3475-3486.
5. Aribowo W, Muslim S, Munoto Suprianto B, Kartini UT, Asto Buditjahjanto IGP. Tuning of Power System Stabilizer Using Cascade Forward Backpropagation, 2020 Third International Conference on Vocational Education and Electrical Engineering (ICVEE), 2020, pp. 1-5.
6. Peter Sauer W, Pai MA. Power System Dynamics and Stability, Prentice Hall Inc., New-Jersey, USA, 1998.

7. Anderson PM, Foud AA. Power system control and stability IOWA state university press, 1980.
8. Sourav K. Multiple System Artificial Neural Network Model, International Journal of Scientific & Engineering Research, 2013, 4(6). ISSN: 2229-5518.
9. Unar. Ship Steering Using Feedforward Neural Networks, Ph.D. Thesis, University of Glasgow, Glasgow, Scotland, U.K., 1999. [10] Fausett, L, Fundamentals of Neural Networks, Architectures, Algorithms and Applications, 2nd edition, Prentice Hall, 1994.
10. Memon AP, Uqaili MA, Memon Z. Design of FFNN AVR for Enhancement of Power System Stability Using Matlab/Simulink, Mehran University Research Journal of Engineering and Technology, 2012, 31(3).
11. Pagariya R, Bartere M. Review Paper on Artificial Neural Network, International Journal of Advanced Research in Computer Science, 2013, 4(6).
12. Ch. Raja VN. Generation of a SMIB controlling parameters using Artificial neural networks proceedings of NSER-2011, Anna University of Technology, Tiruchirappalli.
13. Kumbhar SV, Mohale VP. Comparative Study of the Effect of Power System Stabilizer on a Single Machine Infinite Bus, 2020 International Conference on Smart Electronics and Communication, 2020, pp. 1288-1292.
14. Ch. Raja VN. Two Parameter Controller for a Single Machine Infinite Bus System, Bulletin of Electrical Engineering and Informatics. 2014;3(1):45-50.

Fuzzy System Based Load Frequency Control of Hydro-Thermal -Thermal Interconnected Power System

Dr. Anand Gondesi
Assistant Professor
Department of EEE
Dr. Lankapalli Bullayya College of Engineering
&
Dr. Varaha Narasimha Raja. Ch
Assistant Professor
Department of EEE
Anil Neerukonda Institute of Technology & Sciences (A)
Visakhapatnam, Andhra Pradesh, India

Abstract

Today, in power systems the Load Frequency Control (LFC) problem plays a vital role in an interconnected power system, wherein it maintains the system frequency and tie line flow at their scheduled values during normal period. It is due to frequency of power system, which changes over time with respect to continuous load variation. The present chapter proposes a new methodology to study the Load Frequency Control (LFC) problem of a three area inter-connected system using R Fuzzy system (FS) approach. Moreover, this technique is applied to control the systems which include three areas considering a non-linearity Generation Rate constraint (GRC) having two steam turbines and one hydro-turbine tied together. The main advantage of this controller is its high insensitivity to large load changes and plant parameter variations even in the presence of non-linearity. Furthermore, it is tested on a three-area power system to illustrate its robust performance. The results obtained by using Rule Based Fuzzy PID controller explicitly show that the performance of this proposed controller is superior to conventional controller in terms of several parameters like overshoot, settling time and robustness.

Keywords: Load Frequency Control, Reliability, Fuzzy Controller, Power System.

Introduction

Today, due to rise in the demand for electric power, electric power system is becoming more and more complicated. The power system operates in normal state, which is characterized by constant frequency and voltage profile with certain system reliability. Therefore, the supply of electric power with stability and high

ISBN: 978-81-942938-7-3
DOI: 10.47059/CIIR/BP20002/14

reliability is required. Under dynamic operation of power system, decentralization of control action to individual areas is important. Load Frequency Control (LFC) is a very important issue in power system operation control for supplying sufficient and reliable electric power with good quality. An interconnected power system is a combination of different control areas, in which two areas are connected together with a transmission line called tie-line. In each control area, all generators are assumed to form a coherent group. The power system is subjected to local variations of random magnitude and duration. Moreover, the satisfactory operation of a power system, the frequency and tie-line deviations should be maintained within the specified tolerance. The frequency of a system depends on active power balance. As frequency is a common factor throughout the system, a change in active power demand at one point is reflected throughout the system.

Objectives

- To develop mathematical models for multi-area power system
- To devise and implement PID and fuzzy Load Frequency controllers for multi area interconnected power systems

Literature Survey

The coherent areas are interconnected through tie lines which are used for contractual energy exchange between areas and provide inter-area support during abnormal operations (Talaq & Al-Basri, 1998) Automatic Generation Control (AGC) or Load Frequency Control (Chaturvedi, Satsangi & Kalra, 1999; Chown & Hartman, 1998) is a very important issue in power system operation and control for supplying sufficient and reliable electric power with good quality. In large interconnected power system, thermal, hydro, nuclear and gas power units generate large amount of power. The gas power plants, tidal power plants, nuclear power plants, etc. produces a very small percentage of total system generation. Hence, such plants do not play a significant role LFC of large power system and gas plants are used to meet peak demands only. Thus, the natural choice for LFC falls on either thermal or hydro units. Also, it is observed that most of the earlier works in the area of LFC pertain to interconnected thermal systems and relatively lesser attention has been devoted to the LFC of an interconnected hydro-thermal system (Sudha & Santhi, 2012) involving thermal and hydro subsystem of widely different characteristics. Concordia and Kirchmayer have given the LFC of a hydro-thermal system (Sudha, Raju & Sekhar, 2012) considering non-reheat type thermal system neglecting non-linearity like generation rate constraints. This has been observed by Nanda, Kothari and Satsangi in 1983, wherein they presented the comprehensive analysis of AGC (Khamsum et al. 2006) of an interconnected hydrothermal system in continuous-discrete mode with classical controllers. Usually, the hydro system uses a mechanical governor and the thermal system uses reheat turbine in an interconnected hydro-thermal system. It is over decades, intelligent controllers like

ISBN: 978-81-942938-7-3
DOI: 10.47059/CIIR/BP20002/14

Fuzzy Logic Controllers (FLCs) have been successfully developed for analysis and control of nonlinear systems (Indulkar & Raj, 1995; Shayeghi, Jalili & Shayanfar, 2005). The major advantage of this fuzzy reasoning approach is motivated to handle ambiguous information, like uncertainties in available knowledge (Chang & Fu, 1997; Indulkar & Raj 1995; Gayadhar, Sidhartha & Ardil, 2009) proposed different fuzzy scheduling schemes for conventional PI and/or PID controllers. These methods provide good performances under steady state but the system transient and dynamic responses are relatively. Moreover, the main objective of this research is to determine Load Frequency Control problem for a multi area power system, wherein taking into consideration the uncertainties in the parameters of power system. Thus, to solve this problem, many researchers have proposed basic fuzzy logic-based controllers to power systems (Mendel, 2000; Nanda & Sakkaram, 2003) and termed as classical or Type-1 fuzzy.

Problem Identification

The main goals of Load Frequency Control (LFC) are to maintain frequency and to control change in tie-line power between control areas. In furtherance, the conventional controllers do not take into consideration due to inherent nonlinearities of different power system components. They also failed to adapt the controller gains with change in operating points.

Methodology

A power system is made up of several sub-systems, which are used to deliver electricity from generation to consumption. It is important to see that frequency of all areas in a steady state remains identical. The LFC is a control method that ensures all areas in steady state have zero change in frequency and tie-line power deviations. Moreover, in this present research study work fuzzy logic controllers are implemented for large scale power systems which are distributed into for LFC problem.

Modeling of Power System & Problem Formulation

Usually, a large-scale power system consists of different complicated nonlinear models. It constitutes of number of inter-connected control areas, which are linked by tie-lines power, but to design LFC, a simplified and linearized model is employed. The detailed block structure consisting of two steam turbines and one hydro -turbine tied together through power lines of multi area power system including Generation Rate Constraint (GRC) for load frequency control has been investigated in this chapter as shown in fig.1 with Area Control Error (ACE) and its derivatives are given as the inputs to controllers.

ISBN: 978-81-942938-7-3
DOI: 10.47059/CIIR/BP20002/14

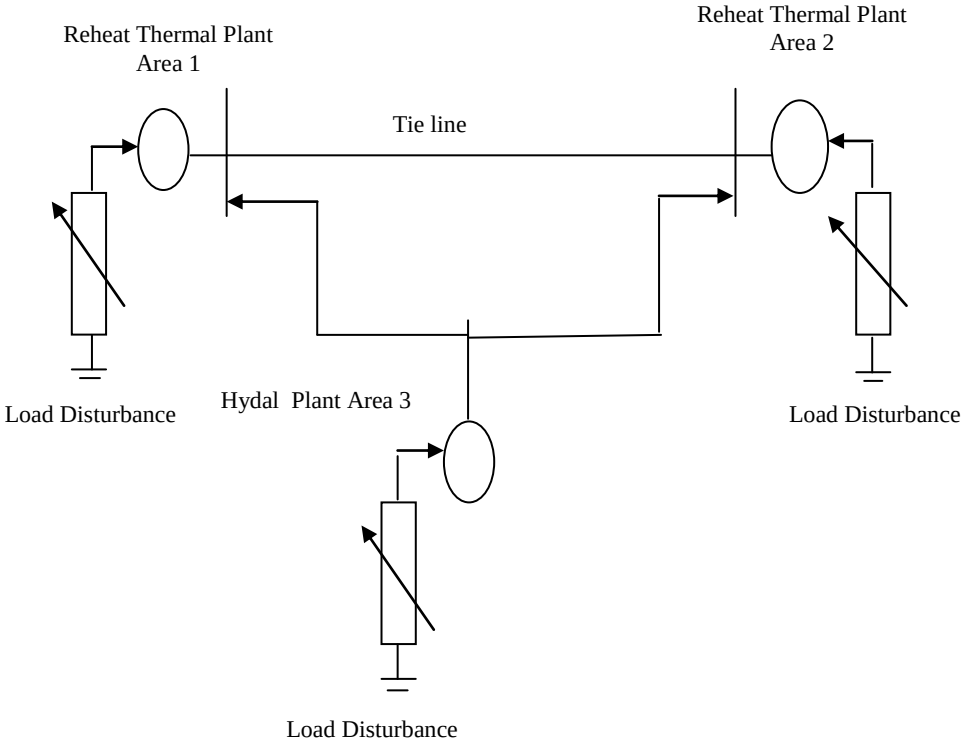

Fig. 1: Three - Area Interconnected Power System

The detailed block diagram of interconnected power system model is shown in figure 2, wherein the parameters of three areas are given in Appendix (Surya Prakash & Sinha, 2011). Also, the modeling of speed governors and turbines are discussed in (Kothari, Kauld & Nanda, 1980). The power generation can change only at a specified maximum rate for steam plants. Hence, in order to restrict the generation rate for steam plants, limiters are added to the governors. A typical value of Generation Rate Constraint (GRC) for thermal units of 3 percent / min is considered. The two limiters, bounded by ± 0.0005 are used within the LFC to prevent the excessive control action. The generation rate constraints for all the areas are taken into account by adding limiters to the turbines.

ISBN: 978-81-942938-7-3
DOI: 10.47059/CIIR/BP20002/14

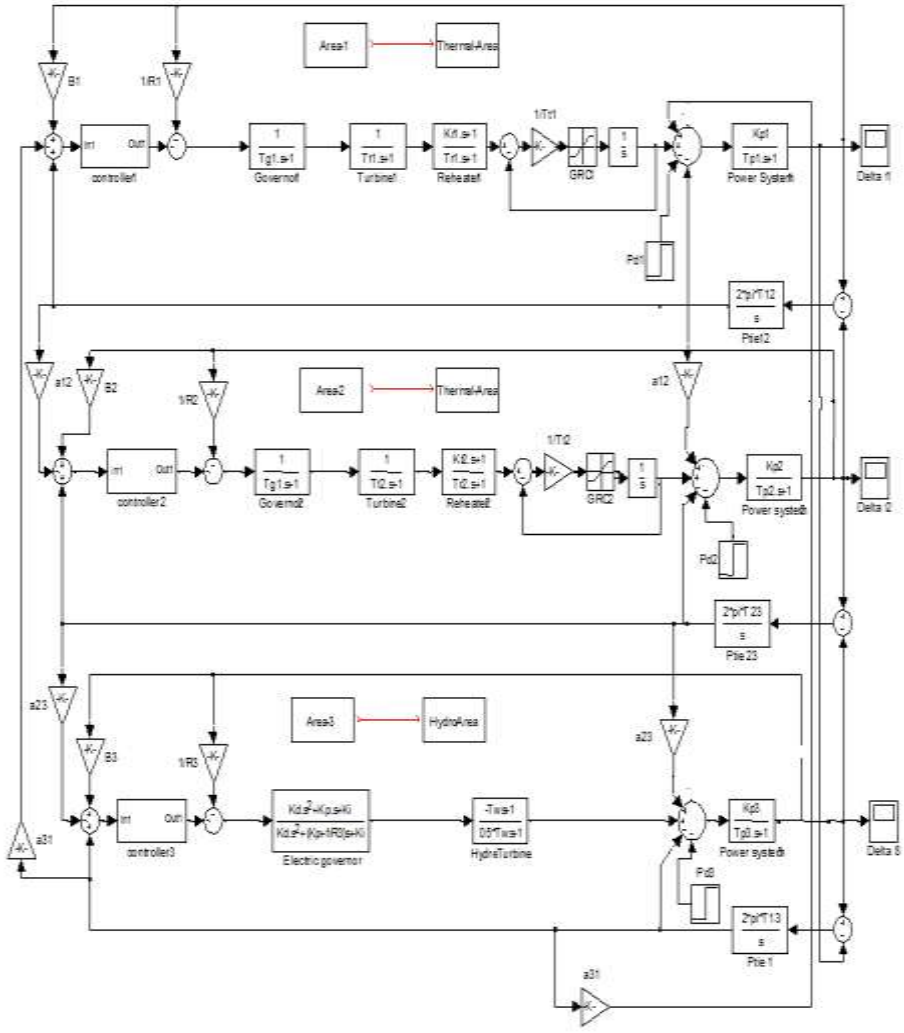

Fig. 2: Block Diagram of Three Area Interconnected system

Fuzzy Logic controllers

Fuzzy logic controllers have no fixed structure like conventional PI, PD and PID controllers because there is still no well-defined criteria for deciding on the shape of MF's, the number of linguistic values, the standard rule base, the most appropriate inference mechanism and defuzzification strategy. This is probably due to these aforementioned reasons with regard difficulties in designing an FLC analytically (Sudha & Santhi, 2012). The structure of a Fuzzy PI controller preserves the basic properties and merits of general PI controller. It has four simple fuzzy IF-THEN rules. The basic characteristics of proposed design may differ from other fuzzy or non-fuzzy PID-type controllers, which include the following aspects:

ISBN: 978-81-942938-7-3
DOI: 10.47059/CIIR/BP20002/14

1. It has the same linear structure as the conventional PI controller, but has variable gains; the proportional and integral gains are non- linear functions of the input signals.

2. The controller is designed based on the precise mathematical model of a discrete PI controller, from which the fuzzy control law is derived.

3. Membership functions are simple symmetric trapezoidal and asymmetrical trapezoidal, which use only four fuzzy logic IF-THEN rules with two membership functions in each input and use eight fuzzy logic IF-THEN rules with three membership functions in each input.

4. The Fuzzification, control-rule execution and defuzzification steps are all embedded in the final product of fuzzy control law, which is an explicit conventional formula, so that the fuzzification-rules-defuzzification routine is not needed for all the process control steps.

The performance of conventional PID controller is considered to be quite adequate for linear first order system with the small-time delay. However, its performance for a system with large time delay and also for a nonlinear system may be very poor due to large overshooting and excessive oscillation (Sudha & Santhi, 2012). To improve the performance of a conventional PID controller, engineers have tried to use fuzzy PID controller instead of classical ones. Ying has developed the fuzzy PID controller (Castillo, Urias & Mellin, 2007). He also suggested that the improvement is actually due to the nonlinearity of fuzzy PID controller (Sudha & Santhi, 2012). The present work is an attempt to analyze in detail the derivation of analytical structure of fuzzy controllers using Trapezoidal MFs (Symmetrical and asymmetrical). To show the effectiveness of fuzzy controllers over conventional controllers' time delay systems and nonlinear systems are considered for simulations. As a case study of dc motor along with saturation non-linearity, an aircraft attitude-control system and high-speed steel-rolling mill are considered and simulations are carried out to demonstrate the superiority of Fuzzy PID controllers over the conventional PID controller have done by using symmetric and asymmetrical Trapezoidal membership sets in input and output.

ISBN: 978-81-942938-7-3
DOI: 10.47059/CIIR/BP20002/14

Table 1: Control Rules for Fuzzy Controller

Rule-1	If $x(\dot{\delta})$ is P and $x(\delta)$ is P and $x(\ddot{\delta})$ is P then output is NB
Rule-2	If $x(\dot{\delta})$ is P and $x(\delta)$ is P and $x(\ddot{\delta})$ is N then output is NS
Rule-3	If $x(\dot{\delta})$ is P and $x(\delta)$ is P and $x(\ddot{\delta})$ is Z then output is NM
Rule-4	If $x(\dot{\delta})$ is P and $x(\delta)$ is N and $x(\ddot{\delta})$ is P then output is NM
Rule-5	If $x(\dot{\delta})$ is P and $x(\delta)$ is N and $x(\ddot{\delta})$ is Z then output is Z
Rule-6	If $x(\dot{\delta})$ is P and $x(\delta)$ is N and $x(\ddot{\delta})$ is N then output is NS
Rule-7	If $x(\dot{\delta})$ is P and $x(\delta)$ is Z and $x(\ddot{\delta})$ is P then output is NM
Rule-8	If $x(\dot{\delta})$ is P and $x(\delta)$ is Z and $x(\ddot{\delta})$ is Z then output is NS
Rule-9	If $x(\dot{\delta})$ is P and $x(\delta)$ is Z and $x(\ddot{\delta})$ is N then output is Z
Rule-10	If $x(\dot{\delta})$ is N and $x(\delta)$ is P and $x(\ddot{\delta})$ is P then output is NS
Rule-11	If $x(\dot{\delta})$ is N and $x(\delta)$ is P and $x(\ddot{\delta})$ is Z then output is Z
Rule-12	If $x(\dot{\delta})$ is N and $x(\delta)$ is P and $x(\ddot{\delta})$ is N then output is PS
Rule-13	If $x(\dot{\delta})$ is N and $x(\delta)$ is N and $x(\ddot{\delta})$ is P then output is PS
Rule-14	If $x(\dot{\delta})$ is N and $x(\delta)$ is N and $x(\ddot{\delta})$ is N then output is PB
Rule-15	If $x(\dot{\delta})$ is N and $x(\delta)$ is N and $x(\ddot{\delta})$ is Z then output is PM
Rule-16	If x($\dot{\delta}$) is N and x(δ) is Z and x($\ddot{\delta}$) is P then output is Z
Rule-17	If $x(\dot{\delta})$ is N and $x(\delta)$ is Z and $x(\ddot{\delta})$ is Z then output is PS
Rule-18	If $x(\dot{\delta})$ is N and $x(\delta)$ is Z and $x(\ddot{\delta})$ is N then output is PM
Rule-19	If $x(\dot{\delta})$ is Z and $x(\delta)$ is P and $x(\ddot{\delta})$ is P then output is NM
Rule-20	If $x(\dot{\delta})$ is Z and $x(\delta)$ is P and $x(\ddot{\delta})$ is N then output is Z
Rule-21	If $x(\dot{\delta})$ is Z and $x(\delta)$ is P and $x(\ddot{\delta})$ is Z then output is NS
Rule-22	If $x(\dot{\delta})$ is Z and $x(\delta)$ is N and $x(\ddot{\delta})$ is P then output is Z
Rule-23	If $x(\dot{\delta})$ is Z and $x(\delta)$ is N and $x(\ddot{\delta})$ is N then output is PM
Rule-24	If $x(\dot{\delta})$ is Z and $x(\delta)$ is N and $x(\ddot{\delta})$ is Z then output is PS
Rule-25	If $x(\dot{\delta})$ is Z and $x(\delta)$ is Z and $x(\ddot{\delta})$ is P then output is NS
Rule-26	If $x(\dot{\delta})$ is Z and $x(\delta)$ is Z and $x(\ddot{\delta})$ is Z then output is Z
Rule-27	If $x(\dot{\delta})$ is Z and $x(\delta)$ is Z and $x(\ddot{\delta})$ is N then output is PS

Simulation Results

The frequency deviation of the first area, Δf_1, the frequency deviation of the second area, Δf_2 and the frequency deviation of the third area, Δf_3 signals of the closed-loop system are shown in figures 3 to 5. Using proposed method, the frequency deviations and inter area tie power is quickly driven back to zero and the controller designed using Type-1fuzzy controller has the best performance in control and damping of frequency and tie-power in all responses when compared with conventional PID Controller.

ISBN: 978-81-942938-7-3
DOI: 10.47059/CIIR/BP20002/14

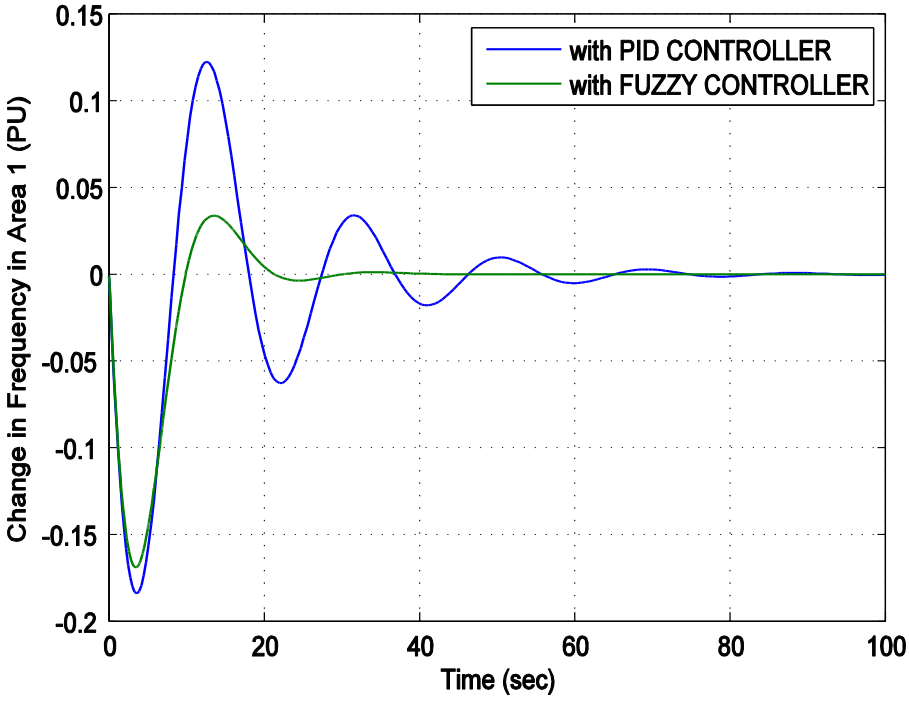

Fig.3: Change in Frequency Deviation in Area 1

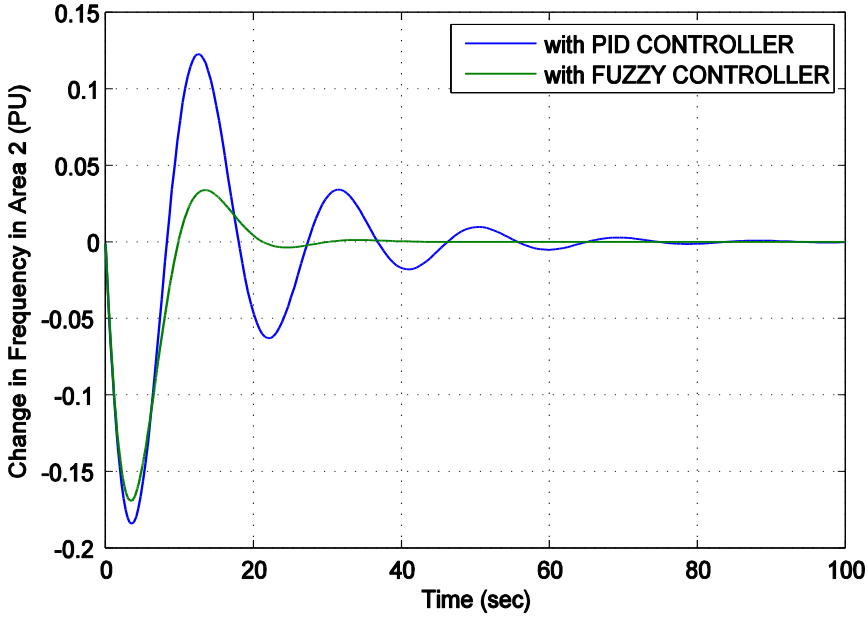

Fig.4: Change in Frequency Deviation in Area 2

ISBN: 978-81-942938-7-3
DOI: 10.47059/CIIR/BP20002/14

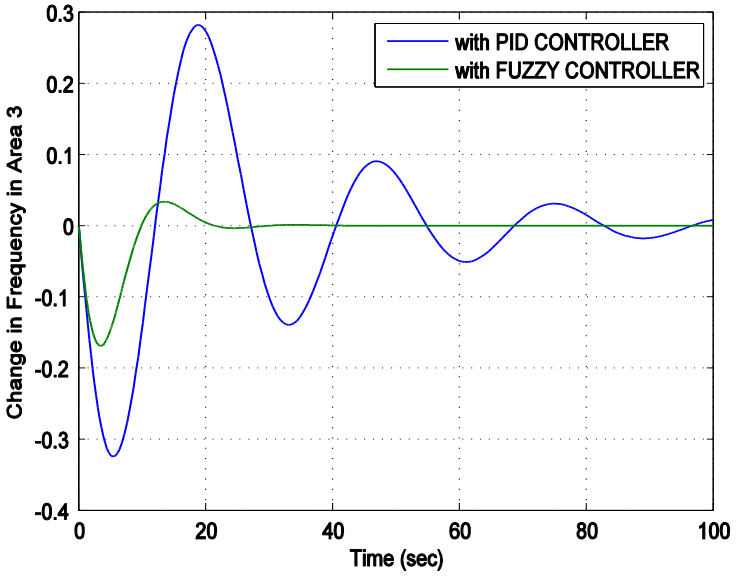

Fig.6: Change in Frequency Deviation in Area 3

Table 2: Frequency response in various control strategies

Frequency	Controller	Peak Overshoot	Peak Undershoot	Settling Time (Sec)
Change in frequency in Area 1	PID	0.12	-0.18	76.54
	Type 1 Fuzzy	0.033	-0.16	37.9
Change in frequency in Area 2	PID	0.12	-0.18	72.85
	Type 1 Fuzzy	0.034	-0.17	34.58
Change in frequency in Area 3	PID	0.28	-0.32	>100
	Type 1 Fuzzy	0.033	-0.17	30.11

Suggestion

Fuzzy PID controller is designed and acted as controller for solving LFC problem for multi area power system, wherein future researchers may focus on designing an optimization-based design methodology using Genetic Algorithm-Fuzzy controllers or Honey Bee Mating optimization algorithm for tuning Fuzzy PI/PID controllers. The LFC design can also be done using certain techniques like Active Disturbance rejection control for Fuzzy system. The present research work may be extended with drawing extra degree of freedom framing as Type-2 Fuzzy.

ISBN: 978-81-942938-7-3
DOI: 10.47059/CIIR/BP20002/14

Conclusions

The present research proposed a new method for Load Frequency Control using fuzzy controller including Generation Rate Constraint (GRC) with system uncertainty parametric and various loads conditions. The simulation results proved that designed controller guarantees the robust performance such as precise reference frequency tracking and disturbance attenuation under a wide range of parameter uncertainty and area load conditions. Also, upon reducing the rule base, it has been proved that the output of reduced rule base follows the outputs of full rule base. Moreover, the Settling Time, Maximum Overshoot and Undershoot indicated the robustness of proposed Fuzzy controller has better performance as compared to conventional PID controller.

References

Castillo, O., Urias, J. & Mellin, P. (2007). A Method for Response Integration in Modular Neural Networks Using Interval Fuzzy Logic, Proceedings IEEE FUZZ Conference, pp.247-252.

Chang, C. S. & Fu, W. (1997). Area Load-Frequency Control Using Gain Scheduling of PI Controllers, International Journal of Electric Power & Energy Systems, Vol.42, No.2, pp.145-152.

Chaturvedi, D. K., Satsangi, P. S. & Kalra, P. K. (1999). Load Frequency Control: A Generalized Neural Network Approach, International Journal of Electric Power & Energy Systems, Vol.21, No.6, pp.405-415.

Chown, G. A. & Hartman, R. C. (1998). Design and Experiment with a Fuzzy Controller for Automatic Generation Control (AGC), IEEE Transactions on Power Systems, Vol.13, No.3, pp.965-970.

Concordia, C. & Kirchmayer, L. K. (1954). Tie-Line Power and Frequency Control of Electric Power System, AIEE Transaction, Vol.73, Part-III-A, pp.133-146.

Gayadhar, P., Sidhartha, P. & Ardil, C. (2009). Hybrid Neuro Fuzzy Approach for Automatic Generation Control of Two-Area Interconnected Power System, International Journal of Computational Intelligence, Vol.5, No.1, pp.80-84.

Khamsum, C., Pothiya S., Taowklang, C. & Sangiamvibool, W. (2006). Design of Optimal PID Controller using Improved Genetic Algorithm for AGC including SMES Units, In Proceedings: International Conference on Sustainable Development: Issues and Prospects for GMS, December 6-7.

ISBN: 978-81-942938-7-3
DOI: 10.47059/CIIR/BP20002/14

Kothari, M. L., Kaul, B. L. & Nanda, J. (1980). Automatic Generation Control of Hydro-Thermal System, Journal of Institute of Engineers (India), Vo1.61, pt EL2, pp.85-91.

Indulkar, C. S. & Raj, B. (1995). Application of Fuzzy Controller to Automatic Generation Control, Electrical Machines and Power Systems, Vol.23, No.2, pp.209-220.

Mendel, J. M. (2000). Uncertain Rule-Based Fuzzy Logic Systems: Introduction and New Directions (Eds.), Prentice Hall, USA, 576p.

Nanda, J., Kothari, M. L. & Satsangi, P. S. (1983). Automatic Generation Control of an Interconnected Hydrothermal System in Continuous and Discrete Modes Considering Generation Rate Constraints, IEEE Proceedings, Vol.130, pt D, No.1, pp.455-460.

Nanda, J. & Sakkaram, J. S. (2003). Automatic Generation Control with Fuzzy Logic Controller Considering Generation Rate Constraint, Proceedings of 6th International Conference on Advances in Power System Control, Operation and Management, APSCOM 2003, Hong Kong, pp.770-775.

Shayeghi, H., Jalili, A. & Shayanfar, H. A. (2005). Fuzzy PI Type Controller for Load Frequency Control Problem in Interconnected Power System, 9th World Multi Conference on Systemic Cybernetics and Information, Orlando, Florida, USA, July 10-13, pp.24-29.

Sudha, K. R. & Santhi, R. V. (2012). Load Frequency Control of an Interconnected Reheat Thermal System Using Type-2 Fuzzy System Including SMES Units, International Journal of Electrical Power & Energy Systems, Vol.43, No.1, pp.1383-1392.

Sudha, K. R., Raju, Y. B. & Sekhar, A. C. (2012). Fuzzy C-Means Clustering for Robust Decentralized Load Frequency Control of Interconnected Power System with Generation Rate Constraint, International Journal of Electrical Power & Energy Systems, Vol.37, No.1, pp.58-66.

Surya Prakash & Sinha, S. K. (2011). Load Frequency Control of Three Area Interconnected Hydro-Thermal Reheat Power System Using Artificial Intelligence and PI Controllers, International Journal of Engineering Science and Technology Vol.4, No.1, pp.23-37.

Talaq, J. & Al-Basri, F. (1999). Adaptive Fuzzy Gain Scheduling for Load Frequency Control, IEEE Transactions on Power Systems, Vol.14, No.1, pp.145-150.

ISBN: 978-81-942938-7-3
DOI: 10.47059/CIIR/BP20002/14

Tripathy, S. C., Balasubramanian, R. & Chandramohanan Nair, P. S. (1992). Effect of Superconducting Magnetic Energy Storage on Automatic Generation Control Considering Governor Deadband and Boiler Dynamics, IEEE Transactions on Power Systems, Vol.7, No.3, pp.1266-1273.

Yesil, E., Guzelkaya, M. & Eksin, I. (2004). Self-Tuning Fuzzy PID Type Load and Frequency Controller, Energy Conversion and Management, Vol.45, No.3, pp.377-390.

ISBN: 978-81-942938-7-3
DOI: 10.47059/CIIR/BP20002/14

Network Security

Author's Name:
Dr. M. Vamsi Krishna
Dr.K.Anuradha

Published by:

BH INTERNATIONAL PUBLICATIONS, Hyderabad.

Publisher's Address:
302, Ranga Sai Nilayam, Addagutta, KPHB, Hyderabad - 500072,
Telangana, India. editor@bhpublications.in, www.bhpublications.in

Printer Details:
BH INTERNATIONAL PUBLICATIONS, Hyderabad.

Edition Detail : 1
ISBN : 978-81-949705-9-0

Network Security

Dr. M. Vamsi Krishna
M.Sc., M.Tech.,PhD.,

Dr. M. Vamsi Krishna MCA, M.Tech, Ph.D, MISTE is working as an Associate Professor in the department of Computer Science and Engineering in Aditya Engineering College, Surampalem, India. He is having a total of 20 Years of Experience in this teaching profession. He obtained his Masters in Computer Applications from Indira Gandhi Open University (IGNOU), New Delhi in 2004, Master of Engineering & Technology (M.Tech) Degree in Computer Science and Engineering with Specialization in Artificial Intelligence and Robotics, from Andhra University, in 2008. He obtained his PhD in Computer Science and Engineering from Centurion University, Odisha in 2016. He is having Supervisorship in the Faculty of Computer Science and Engineering in Centurion University, Odisha for guiding Ph.D candidate. 10 Research scholars have been awarded Ph.D under his supervision. A total of 5 more scholars are pursuing Research under his supervision. He has more than 50 articles in Scopus/SCI indexed Journals/Conferences to his credit. His Research Interest includes Machine Learning, Deep Learning and Data Science. His roles include as Reviewer of reputed journals globally like Springer, Elsevier, Taylor & Francis, IGI Global. He is also an Editor – in – Chief for one of the Journals which is listed under UGC Care Group – II.

Dr. K. Anuradha
M.Sc., M.Tech.,PhD

Dr. K. Anuradha has obtained M.Sc in Applied Statistics from SVU Tirupathi in 1999. She obtained her Ph.D in Statistics in 2009 from Sri Venkateswara University Tirupathi. She obtained her Master of Technology in Computer Science and Engineering From Andhra University College of Engineering, Visakhapatnam in 2010.

Dr. K.Anuradha has almost 20 years of Experience in Teaching and Research. Dr. K.Anuradha has started teaching in 2000at N.P.S.GovernmentDegreeCollegeforWomen,Chittoor and she joined in Dr.L.Bullayya group of colleges in 2006. Presently working as Assistant Professor at Dr.L.Bullayya college of Engineering, Visakhapatnam,Andhra Pradesh, India.

Dr. K.Anuradha published 1 patent and published almost 25 research articles in different national and International Journals and conferences.Dr. K.Anuradha is pursuing her Ph.D in Computer Science and Engineering with Network Security is her field of interest.Dr. K.Anuradha research interest includes computer application such as neural networks, machine learning, sentimental analysis and speech recognition.

BHIP

₹275/-

BH INTERNATIONAL PUBLICATIONS
Email : editor@bhpublications.in,
www.bhpublications.in

ISBN 978-81-947705-9-0

CONTENTS

UNIT – 1 SECURITY TRENDS AND ATTACKS	2 - 18
UNIT – 2 SECURITY SERVICES AND MECHANISMS	19 - 29
UNIT – 3 CLASSICAL ENCRYPTION - PART I	30 - 49
UNIT – 4 CLASSICAL ENCRYPTION - PART II	50-59
UNIT – 5 BLOCK CIPHER PRINCIPLES	61-73
UNIT – 6 DES - DATA ENCRYPTION STANDARD	74-88
UNIT – 7 ATTACKS ON DES AND MULTIPLE ENCRYPTIONS	89-98
UNIT – 8 STREAM CIPHERS	99-110
UNIT – 9 ESSENTIAL MATHEMATICS FOR ASYMMETRIC ENCRYPTION	112-123
UNIT – 10 PRINCIPLES OF PUBLIC KEY SYSTEMS	124 - 135
UNIT – 11 ASYMMETRIC ENCRYPTION - RSA	136-146
UNIT –12 KEY EXCHANGE AND AUTHENTICATION	147 – 171
UNIT – 13 E-MAIL SECURITY	73 - 187
UNIT – 14 IP AND WEB SECURITY	188-196
UNIT – 15 INTRUDER DETECTION AND PASSWORD MANGEMENT	197-211
UNIT – 16 MALICIOUS SOFTWARE AND FIREWALLS	212 -232

Nomenclature of Diverse Feature Selection in Sentiment Analysis using Machine Learning Techniques: A Comparative Study

Dr.K.Anuradha1
Research Scholar,
Centurion University of Technology & Management,
Odisha

Dr.M.Vamsi Krishna[2]
nya InPrincipal,
Chaitastitute of Science & Technology,
Kakinada

Dr.Banitamani Mallik[3]
Associate Professor,
Centurion University of Technology & Management,
Odisha

***Abstract* - Sentiment analysis has gained in importance in recent decades as the amount of digital text documents has increased in tandem with the advent of IT. The goal of sentiment analysis in the field of natural language processing (NLP) is to extract positive or negative polarity from social media text. Feature Selection (FS) is important based on critical analysis and efficiently identifying the necessary information for better segregation. The purpose of this research is to assess and compare the performance of several sentiment analysis FS techniques. Several Feature Selection (FS) procedures are studied in order to select the optimal Selection of features from a feature set. Various Machine Learning techniques such as Decision Tree (DT), Naive Bayes (NB), Support Vector Machines (SVM), K-Nearest Neighbour (KNN) and Logistic Regression (LR) are used to train the selected features on the Online Movie Reviews Dataset. According to the findings of the experiments, the proposed system decreases data dimensionality, picks efficient aspects for better analysis**

Keywords: Sentiment Analysis (SA); Machine Learning; Feature Selection(FS); Online Reviews; Text Classification;

I. INTRODUCTION

Text mining is becoming more important as the volume of digitised text documents increases due to rapid improvements in information technology. SA, sometimes called as opinion mining, is a text categorization method that involves classifying emotive messages as positive or negative. Document-level, sentence-level, and aspect-level SA are the three granularities that can be applied. [1]. To retrieve data from this textual content, text mining techniques are used [2]. SA is used to collect subjective knowledge and opinion from internet material, codify it and evaluate it for specific applications [3].Feature selection is a technique for improving the analysis of machine learning algorithms and implementations by clearing irrelevant data set [4].

The FS process [4] can be used to overcome this problem by tackling the the efficiency of ML techniques [5]. Because the feature set used to accomplish classification is the most important component of data for a learning algorithm, identifying the best set that accurately reflects the entire data set is vital. Thus, FS must focus on variables that accurately reflect input data while considering irrelevant, redundant data and guaranteeing good classifier performance. This is still a topic of discussion among scientists [6].

Traditional FS methodologies are employed in this research. Various ML approaches, such as K-Nearest Neighbour (KNN), Naive Bayes (NB), Decision Tree (DT), Support Vector Machines (SVM) and Logistic Regression (LR) are employed to investigate the classification evaluation of the FS approaches. This study used an online movie review dataset collected from Pang and Lee [7], which comprised movie reviews from the Internet Movie Database (IMDb).

II. RELATED WORKS

Sentiment classification is becoming increasingly important as the use of digital text data expands [1]. The following table summarises all the studies in the and investigations in public's feelings, opinions, attitudes, and emotions about diverse components such as subjects, products or services, people, or organisations.

Author	*Objective*	*Method*	*Outcome*
Tang, H., et al. (2009)[8]	Sentiment Detection of Reviews	Survey of all methods	Multi-parametric output of document, sentence, and feature level
Singh N. K., et al. (2020) [9]	SA in Social Media	Comparative analysis of various methods	Processing a large text takes significant time and space
Kim K. (2018) [10]	Improvement by Feature Weighting	Semi-supervised dimensionality reduction	Social media data suffers from the curse of dimension
Xu F., et al. (2020) [11]	E-Commerce Product Review SA	NB Continuous Learning Method	Dimension reduction resulting in reducing computing costs
Li B., et al. (2007) [12]	Blog clustering using author comments	FS Approach	Cut processing costs and remove irrelevant information
Yousefpour. A et al. (2017) [13]	Ordinal & Frequency based Integration	FS Approach	High-quality minimum feature subset can be obtained by SA
Liu Y., et al. (2017) [14]	Experimental Multi Class Sentiment Classification	FS Approach and ML	Dimension reduction in sentiment classification using particle swarm optimisation (PSO)
Akthar, M.S., et al. (2017) [15]	Feature Selection & ensemble construction	Two-step method for aspect based SA	GR and SVM fared the best.

Zheng L., et al. (2018) [16]	Effects of FS on SA on Chinese internet reviews	FS Approach	Chi-Square (CS2) method is utilised to determine the data analysis
Omar N., et al. (2014) [17]	Comparative study on Arabic sentiment	Multiple approach including NB, SVM & KNN	SVM classifier outperformed the other classifiers for all FS approaches
Agarwal B., et al. (2016) [18]	Prominent feature for English Movie reviews	SVM & multinomial NB	NB surpasses the stated vector machine .
Wu et al. (2015) [19]	Improvement in Text feature selection	Expected Cross Entropy Method	FS strategy distinct classes is needed for enhancing the overall performance

The proposed technique identifies properties that are shared by all classes. Classifiers which includes advanced machine learning methods and tools that are used to evaluate the classification accuracy of the proposed FS approach.

III. Proposed Methodology

This section describes the SA method used in this paper. The review papers were collected and preprocessed using common NLP techniques such as Tokenisation, Stop Word Removal, and Stemming. The remaining tokens were classified by the frequency with which they appeared across the entire collection of papers. Using various FS procedures, the top n-ranked distinguishing features were then chosen in addressing the SA task performance.

A. Preprocessing

1) Tokenisation

Tokenisation can be accomplished during the preprocessing stage by dividing texts into a collection of words. After reviewing the reviews to extract tokens, which comprise both words and numbers, the files are made accessible for further analysis. [20].

2) Stop Words (SW) Removal

The SW elimination method reduces the dimensionality of data sets, allowing effective feature extraction methods to quickly discover the remaining essential words in the review collection [20].

3) Stemming

Stemming is a key preprocessing step in the new collations process. Porter's stemmer is a popular method for stemming in the English language [20].

B. Feature Selection

The features are assigned scores depending on which they are accepted or rejected [21]. The two basic types of FS strategies are filters and wrappers.

1) Filter based Selection

Filter-based measures are simple to implement, rapid to compute, and can be used for a wide range of classifiers [1]. Some of the most commonly used filter-based FS metrics in the literature include the Chi-Square Gain Ratio, Information Gain, and ReliefF.

a) Chi-Square (CS2)

The CS2 indicates that the linked class relies on the specified attribute more [22]. As a result, a low-scoring feature is no longer necessary and should be removed [23]. For feature p and k, a 2-by-2 contingency table could be used,.

$$C_s^2\ (\pi, \nu) = \frac{X(IL-KJ)^2}{(I+K)(J+L)(I+J)(K+L)} \quad ----(1)$$

As demonstrated below, CS2 is then integrated over all classes to provide the scores for each feature.

$$C_s^2\ (\pi) = \sum_{n=1}^{W} F(k_n) C_s^2\ (\mathrm{p}, k_n) \quad ----(2)$$

The CHI2 technique has one disadvantage in that it can contribute to better scores for infrequent traits if they are still employed for one class. This is surprising given that irregular features are rarely used in text and so have little impact on text classification. It isn't a big concern for SA because so many sentiment-expressing elements were rarely used inside a single comment [22].

b) Information Gain (IG)

Commonly, FS tactics for SA is information gain [22, 23, 24], which specifies the related features. Entropy, which often indicates the uncertainty can be used to compute information content. Given an m number of classes, the entropy can be calculated by using the following: K = $\{k_1, k_2, \ldots, k_i\}$:

$$\mathrm{P(K)} = \sum_{n=1}^{W} F(k_n)\ log_2(k_n) \quad ----(3)$$

where $F(k_n)$ is the frequency that there would be documents in the class (k_n).

$$\mathrm{P(K|I)} = \sum_{q=1}^{W} \left(-F(i_q)\ \sum_{n=1}^{W} F\left(k_n|i_q\right) log_2(k_n|i_q)\right) \quad --(4)$$

Where $F(i_q)$ is the risk that a document possesses the attribute value i_q, and $F\left(k_n|i_q\right)$ is the possibility that a document of class k_n includes the attribute value i_q. According to the definitions above, the entropy values before and after the attribute.:

$$\mathrm{G(I) = R(K) - R\ (K|I)} \quad ----(5)$$

As a result, by locating keywords with high information gain scores, it may be possible to minimise the amount of features in a comparable pattern. [22].

c) ReliefF Algorithm

Relief-F randomly selects feature occurrences, calculates their immediate surroundings, and applies a final feature weighting vector [2]. The modification favours characteristics that distinguish the instance document from its peers in other classes. From the probabilities presented below, it assists in establishing the optimum estimate of Wf for feature f:

R_p = E (difference value of p| closest features from various class) – E (difference value of p| closest features from similar class) ----(6)

d) Gain Ratio (GR)

By balancing the categorisation choice GR improves IG [2]. This can be mathematically expressed as:

$$\Sigma \mathrm{I}\ (\Gamma) = \sum_{n=1}^{r} \frac{|G_p|}{|G|} * \lambda o \gamma \frac{|G_n|}{|G|} \quad ----(7)$$

2) Wrapper Based Selection

Wrapper techniques wrap the FS phase around the framework of the learning algorithm to examine the feature space. This FS is made with the help of a classifier and search algorithms that hunt for and assess acceptable traits [21]. Several alternative search algorithm approaches were employed to create wrapper feature choices. [21].

C. Classification Techniques

1) Logistic Regression (LR)

It estimates the probability using the sigmoid on the linear product. If the likelihood is greater than 0.5, the label 1 is assigned; otherwise, the label 0 is assigned. The LR [25] is the basic structure of a Multilayer Perceptron.

$$F(b=1|i) = g_\alpha(i) = \frac{1}{1+n^{-\alpha R}{}_i} \quad \text{----(8)}$$

The following is the cost function for training LR:

$$L(\alpha) = \frac{-1}{n}\sum b \log g_x(i) + (1\text{-}b) \log (1\text{-}g_\alpha(i)) \quad \text{----(9)}$$

2) Support Vector Machine (SVM)

SVM is extensively used in image and text categorisation. For non-linear data, the Radial Basis Function kernel is utilised. Use the following cost function to train an SVM:

$$\Sigma(\chi, \psi) = min_{c,y}\ \frac{1}{2}\ ||c||^2 \quad \text{-----(10)}$$

$$g^{(n)}(c^j\ a^{(n)} + y) \geq 1,\ n = 1,2,\ldots,z \quad \text{----(11)}$$

3) K-Nearest Neighbour (KNN)

It classifies the test document using the class labels of training data that are similar to the test dataset [2]. As a result, it lacks a declarative form for the class k_n [26]. If k = 1, the instance is allocated to the class of its nearest neighbour.

The weighted total is stated as follows in KNN classification:

$$\text{Score}(x, k_n) - \sum_{k_n \in N(x)} Sim(x, x_b).\gamma(x_b, k_n) \quad \text{----(12)}$$

The document set of KNN of document d is referred to as KNN(x). If x_b is a member of k_n, $(x_b, k_n) = 1$, else 0. [2].

4) Decision Tree (DT)

Iteratively categorising the document feature vector space into parts yields decision trees [2]. Decision trees are straightforward to learn and train since the tree structure can be readily depicted, and we may follow branches down the tree based on input variables. The J48 classifier, which implements the C4.5 decision tree learning algorithm, is described in this paper [27].

5) Naïve Bayes (NB) Classifier

The Bayes' rule is used to forecast the probability of a class n given a document t in the following manner.

$$N^* = avg.max_n z(n|t) \quad \text{-----(13)}$$

Bayes' rule is used by the Nave Bayes (NB) classifier:

$$Z(n|t) = (z(n)\ z(t|n))/z(t) \quad \text{----(14)}$$

z(t) has no impact on the Selection of N*. Nave Bayes decays the phrase z(n|t) to evaluate it by considering conditional probabilities of features b_x's given t's class:

$$z(n|t) = \frac{z(n)\sum_{x-1}^{n} z(b_x|n)^{x_a(t)}}{z(t)} \quad \text{----(15)}$$

z(n) and $z(b_x|n)$ the number of occurrences is estimated by add-one filtering in the training method. Although the assumption of independence of the Nave Classification algorithm is simply incorrect in real-world circumstances, it nevertheless functions excellently in sentiment categorisation [28].

IV. Experimental Results

When compared to all other classifiers, CS2 achieved the highest classification accuracy among all FS techniques. As a result, CS2 appears to be a viable FS strategy for SA.

TABLE I. Comparison of FS Method using Machine Learning

Methods	LR	SVM	KNN	DT	NB
CS2	67.43	91.25	75.31	74.82	89.35
IG	64.91	90.13	69.28	70.51	87.39
Relief-F	63.45	82.19	63.49	67.49	80.43
GR	66.74	89.46	73.48	73.17	91.54

As illustrated in Figure 1, the biggest disadvantage of GR identified was its sensitivity to the amount of parameters chosen. As can be shown, IG is a preferred outcome when we require consistent results and don't like to experiment with the number of characteristics to choose. This finding is also in line with recent research [24] that compared IG to CHI, GR, and Chi-Square-based FS techniques.

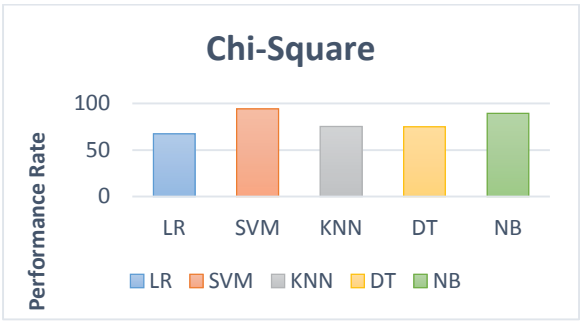

Fig. 1. Evaluation Using Chi-Square based FS

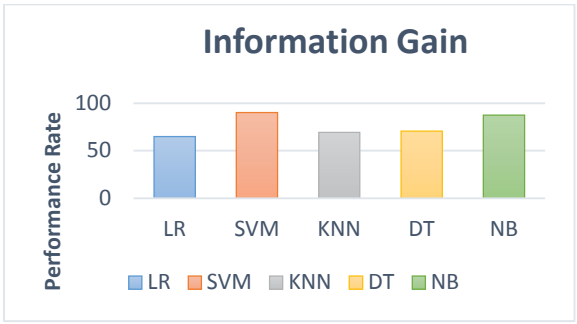

Fig. 2. Evaluation Using Information Gain (GA) based FS

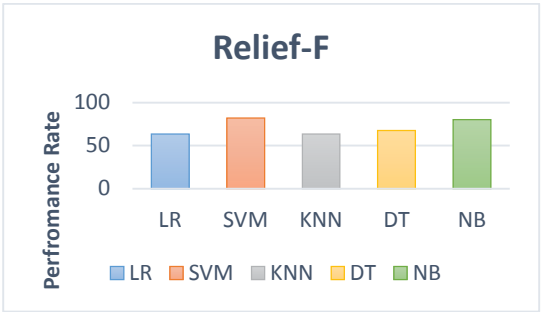

Fig. 3. Evaluation Using Relief-F based FS

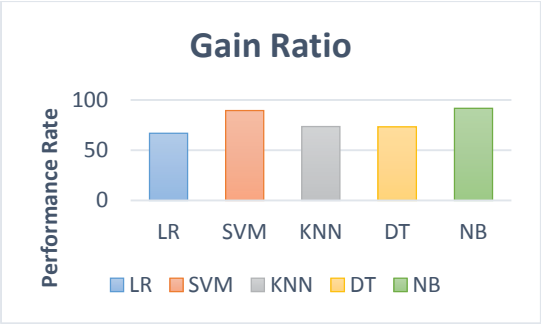

Fig. 4. Evaluation Using Gain Ration (GR) based FS

The criteria Accuracy are used to measure the effectiveness of the FS methods. Metrics were used to assess the performance of the FS techniques. It is defined as

$$\text{Accuracy} = \frac{TP+TN}{(TP+FP+FN+TN)} \quad \text{----(16)}$$

To put it another way, the higher the TPR, the fewer positive data points will be overlooked.

$$\text{TPR/Sensitivity} = \frac{TP}{TP+FN} \quad \text{----(17)}$$

The higher the FPR, the more negative data will be misclassified.

$$\text{Fallout/FPR} = \frac{FP}{FP+TN} \quad \text{----(18)}$$

The ratio of genuine negatives to total negatives in the data is known as specificity.

$$\text{Specificity} = \frac{TN}{(TN+FP)} \quad \text{----(19)}$$

The performance results of various machine learning techniques for SA are shown in Table 2.

TABLE II. PERFORMANCE RESULTS OF MACHINE LEARNING TECHNIQUES FOR SA

Metrics/ Methods	LR	SVM	KNN	DT	NB
Accuracy	78.27	94.59	93.21	80.9	81.5
Sensitivity	45.46	71.23	68.94	74.53	48.5
Specificity	58.13	84.15	80.91	63.04	83.49
Fall-Out	30.04	54.93	49.81	38.41	34.18

While NB is a common evaluation approach owing to its efficiency, the significant assumption of independence does not work in applications like SA.

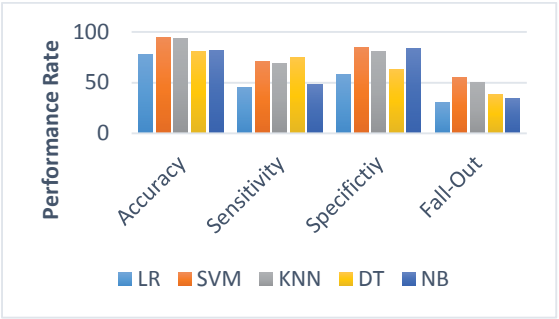

Fig. 5. Graphical Representation of Comparison of performance Evaluation of Machine Learning Techniques

When experimenting with several FS approaches, it was determined that SVM and KNN are extremely sensitive to the number of features picked. When Ada-boost and Winnow were used with different FS approaches, the results were found to be inconsistent. As a result, the weighted term frequency representations and FS approaches cannot be effectively used by these algorithms.

V. CONCLUSION

Sentiment analysis is difficult domain in which NLP is used. The key significance is an examination of the accuracy of various FS and ML approaches. The results reveal that CS2 based FS outperforms all other sentiment FS methods, and SVM outperforms all other sentiment classification methods, whereas Nave Bayes and K-Nearest Neighbour classifiers perform better with fewer features.

REFERENCES

[1] Gokalp, O., Tasci, E., & Ugur, A. (2020). A novel wrapper feature selection algorithm based on iterated greedy metaheuristic for sentiment classification. *Expert Systems with Applications*, *146*, 113176.

[2] Sharma, A., & Dey, S. (2012, October). A comparative study of feature selection and machine learning techniques for sentiment analysis. In *Proceedings of the 2012 ACM research in applied computation symposium* (pp. 1-7).

[3] Liu, B. (2010). Sentiment analysis and subjectivity. *Handbook of natural language processing*, *2*(2010), 627-666.

[4] Omuya, E. O., Okeyo, G. O., & Kimwele, M. W. (2021). Feature selection for classification using principal component analysis and information gain. *Expert Systems with Applications*, *174*, 114765.

[5] Nguyen, T. H., Shirai, K., & Velcin, J. (2015). Sentiment analysis on social media for stock movement prediction. *Expert Systems with Applications*, *42*(24), 9603-9611.

[6] Powers, D. M. (2020). Evaluation: from precision, recall and F-measure to ROC, informedness, markedness and correlation. *arXiv preprint arXiv:2010.16061*.

[7] Pang, B., & Lee, L. (2005). Seeing stars: Exploiting class relationships for sentiment categorisation with respect to rating scales. *arXiv preprint cs/0506075*.

[8] Tang, H., Tan, S., & Cheng, X. (2009). A survey on sentiment detection of reviews. *Expert Systems with Applications*, *36*(7), 10760-10773.

[9] Singh, N. K., Tomar, D. S., & Sangaiah, A. K. (2020). Sentiment analysis: a review and comparative analysis over social media. *Journal of Ambient Intelligence and Humanized Computing*, *11*(1), 97-117.

[10] Kim, K. (2018). An improved semi-supervised dimensionality reduction using feature weighting: application to sentiment analysis. *Expert Systems with Applications*, *109*, 49-65.

[11] Xu, F., Pan, Z., & Xia, R. (2020). E-commerce product review sentiment classification based on a naïve Bayes continuous learning framework. *Information Processing & Management*, *57*(5), 102221.

[12] Li, B., Xu, S., & Zhang, J. (2007, March). Enhancing clustering blog documents by utilising author/reader comments. In *Proceedings of the 45th annual southeast regional conference* (pp. 94-99).

[13] Yousefpour, A., Ibrahim, R., & Hamed, H. N. A. (2017). Ordinal-based and frequency-based integration of feature selection methods for sentiment analysis. *Expert Systems with Applications*, *75*, 80-93.

[14] Liu, Y., Bi, J. W., & Fan, Z. P. (2017). Multi-class sentiment classification: The experimental comparisons of feature selection and machine learning algorithms. *Expert Systems with Applications*, *80*, 323-339.

[15] Akhtar, M. S., Gupta, D., Ekbal, A., & Bhattacharyya, P. (2017). Feature selection and ensemble construction: A two-step method for aspect based sentiment analysis. *Knowledge-Based Systems*, *125*, 116-135.

[16] Zheng, L., Wang, H., & Gao, S. (2018). Sentimental feature selection for sentiment analysis of Chinese online reviews. *International journal of machine learning and cybernetics*, *9*(1), 75-84.

[17] Omar, N., Albared, M., Al-Moslmi, T., & Al-Shabi, A. (2014, December). A comparative study of feature selection and machine learning algorithms for Arabic sentiment classification. In *Asia information retrieval symposium* (pp. 429-443). Springer, Cham.

[18] Agarwal, B., & Mittal, N. (2016). Prominent feature extraction for review analysis: an empirical study. *Journal of Experimental & Theoretical Artificial Intelligence*, *28*(3), 485-498.

[19] Wu, G., Wang, L., Zhao, N., & Lin, H. (2015, October). Improved expected cross entropy method for text feature selection. In *2015 International Conference on Computer Science and Mechanical Automation (CSMA)* (pp. 49-54). IEEE.

[20] Ghosh, M., & Sanyal, G. (2017). Preprocessing and feature selection approach for efficient sentiment analysis on product reviews. In *Proceedings of the 5th International Conference on Frontiers in Intelligent Computing: Theory and Applications* (pp. 721-730). Springer, Singapore.

[21] Hung, L. P., Alfred, R., & Ahmad Hijazi, M. H. (2015). A review on feature selection methods for sentiment analysis. *Advanced Science Letters*, *21*(10), 2952-2956.

[22] Parlar, T., Özel, S. A., & Song, F. (2018). QER: a new feature selection method for sentiment analysis. *Human-centric Computing and Information Sciences*, *8*(1), 1-19.

[23] Parlar, T., & Özel, S. A. (2016, August). A new feature selection method for sentiment analysis of Turkish reviews. In *2016 International Symposium on INnovations in Intelligent SysTems and Applications (INISTA)* (pp. 1-6). IEEE.

[24] Zhao, X., Li, D., Yang, B., Chen, H., Yang, X., Yu, C., & Liu, S. (2015). A two-stage feature selection method with its application. *Computers & Electrical Engineering*, *47*, 114-125.

[25] Madasu, A., & Elango, S. (2020). Efficient feature selection techniques for sentiment analysis. *Multimedia Tools and Applications*, *79*(9), 6313-6335.

[26] Tan, S., & Zhang, J. (2008). An empirical study of sentiment analysis for chinese documents. *Expert Systems with applications*, *34*(4), 2622-2629.

[27] Annett, M., & Kondrak, G. (2008, May). A comparison of sentiment analysis techniques: Polarizing movie blogs. In *Conference of the Canadian Society for Computational Studies of Intelligence* (pp. 25-35). Springer, Berlin, Heidelberg.

[28] Kang, H., Yoo, S. J., & Han, D. (2012). Senti-lexicon and improved Naïve Bayes algorithms for sentiment analysis of restaurant reviews. *Expert Systems with Applications*, *39*(5), 6000-6010.

Prediction of Chronic Kidney Disease with Various Machine Learning Techniques: A Comparative Study

K. Swathi and G. Vamsi Krishna

Abstract Chronic kidney disease is one of the serious health care issues faced by people across the globe. It is majorly resulting in kidney failure or sometimes leads to cardiovascular disease, or sometimes leads to the death of a person. So, the detection of this disease in the early stages plays a significant role which helps in treating and controlling the disease. In this paper, various machine learning algorithms are demonstrated that disclose and extract hidden information from clinical and laboratory patient data, which can aid clinicians in maximizing accuracy for illness severity stage assessment. Several machine learning algorithms like KNN, RF, AdaBoost, gradient boost, and a voting classifier were considered, and a comparative study was done. These comparisons were made by taking the CKD dataset available in the UCI repository. The models employed for the study provide much accuracy, greater than prior research, suggesting that they are more trustworthy than the previous models.

Keywords Classification · Machine learning · Chronic kidney disease

1 Introduction

Chronic kidney disease (CKD) is a long-lasting disease that affects the kidney that may further lead to end-stage renal failure, which will stop the entire kidney from functioning and not be able to perform the waste removal or excess water or any chemicals from your body may cause disparity [1]. The renal failure might expose cardiac arrest and various artery failures and lead to death. CKD affects various people worldwide and ranges between 7 and 15%. Globally, in 2007, around 1.21

K. Swathi (✉)
Department of Computer Science and Engineering, Vignan's Institute of Information Technology (A), Visakhapatnam, AP, India
e-mail: swathi.kalam@gmail.com

G. Vamsi Krishna
Department of Computer Science and Engineering, Dr. Lankapalli Bullayya College of Engineering, Visakhapatnam, AP, India

K. A. Ogudo et al. (eds.), *Smart Technologies in Data Science and Communication*,
Lecture Notes in Networks and Systems 558,
https://doi.org/10.1007/978-981-19-6880-8_27

million people were found dead because of this CKD, and the mortality rate increased in the next years [2].

Early detection of kidney damage can help with treatment, which is not always possible. To avoid serious injury, we need to comprehend a few renal illness indications better. The major motive of this examination is to anticipate kidney sickness by undergoing a deep analysis of data from the observed indices, using various machine learning classification algorithms to prognosticate the ill health, and then predicting it by selecting the best technique that gives a better accuracy estimate [3].

The main objective of this work is to undertake a comparative examination of multiple machine learning algorithms to predict renal illness. The accuracy percentage for most of the studies was above 90%, which was regarded as excellent. This paper is unique because it employs a variety of algorithms and achieves above 97% accuracy rate, which is greater than in the previous studies.

2 Literature Review

Many researchers are working on the prediction of CKD using a variety of classification algorithms. They evaluate the algorithms, namely random forest and the back propagation approach, and found that back propagation, a supervised learning model called a feedforward neural network, produces the best results [4]. Finally, for the system, the random forest implementation method is selected [5]. W.H.S. D Gunarathne et al. [6] made the comparison to find out the solution from different machine learning models. Out of all algorithms, they finally found that the multiclass decision forest technique performs best compared with earlier techniques, with a higher accuracy rate of 99%. However, this algorithm works well when the smaller dataset is taken, and they take only 14 attributes. Ramya et al. [4] employed multiple machine learning classification algorithms to minimize the diagnostic meter and to upgrade diagnostic accuracy rate. Reddy et al. [7] tested 12 different classification algorithms on a CKD dataset of 400 records and 24 attributes. They assessed the accuracy of prediction findings by comparing computed to actual results. As evaluation criteria, accuracy which will tell how well a model works, sensitivity tells how good a model can identify true positive instances, precision, and specificity were used. The decision tree approach has an accuracy of up to 98.6%, a sensitivity of 0.9720, a precision of one, and a specificity of one. Arif-Ul-Islam et al. suggested a method that uses boosting classifiers and J48 decision tree to forecast sickness. This present work aims to identify the CKD by examining the boosting algorithm performance. They also derive the regulations that illustrate correlations between CKD features. The model's accuracy will be based on the prediction of outputs and will be affected by missing values in the dataset. They found a solution to this problem by recalculating CKD stages, which resulted in uncertain results. To fill up the gaps, they computed missing data and use a machine learning paperback method to detect CKD. They get their data from a 400-record dataset with 25 factors that indicate

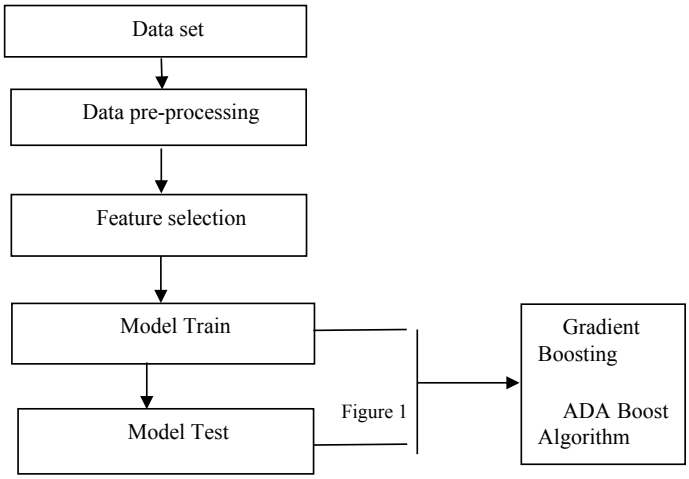

Fig. 1 Block diagram

whether or not a patient has CKD. They use K-nearest neighbors, neural networks, and random forest to arrive at their conclusions.

3 Materials and Method

This section provides block diagrams, flow diagrams, evaluation matrices, and the study's approach and methodology, as well as a description of the dataset.

The suggested system is represented in Fig. 1 by a block diagram. The CKD prediction dataset is used by the framework. Gradient boosting, KNN, AdaBoost algorithm, and random forest algorithms have all been employed after pre-processing and feature selection. In the next subsections, we will go over each of the diagram's components in detail.

Dataset: The CKD dataset was used for this study. This data collection consists of 400 rows and 20 columns. A value of "1" or "0" appears in the output column "class."

Feature Selection: It is a method of selection of only the necessary features that are needed for our model training.

4 Results and Discussion

1. Gradient Boosting: It is one of a kind of ensemble technique and the most powerful algorithm to deal with tabular data. We can even find from the complex

problems. Usually, the complex problems do have non-linearity and that can be used predicted using the non-linear activation function like ReLU, Sigmoid, etc. This algorithm will also help you to deal with missing values. We can achieve better performance by combining together multiple models which are weak. It can have one or more functions as illustrated by the gradient function. And this also cut down the loss functions by continuously repeating the function over a data point again and again. This works on improvement of loss function, and it is determined as a weak learner. It performs randomized sampling of data. It can reduce overfitting of data so the model performance can be increased. It uses sequential classifier because it is a boosting technique. When applied on the dataset using gradient boost, the accuracy achieved is 97.8% and is shown with the help of ROC curve.

2. AdaBoost Algorithm: Versatile helping likewise know as AdaBoost takes additional duplicates of a base classifier continuously on the equivalent dataset. Choice stumps are utilized as feeble students. Choice stumps are only trees which have just a single split. More weight is given to hard to characterize occasions though lesser weight is given simple to arrange perceptions. A normal of the weighted yield from every one of the singular students gives the eventual outcome. Using this AdaBoost algorithm, the accuracy obtained on the dataset is 95.6% and the ROC curve as follows (Figs. 2 and 3):

3. K-nearest Neighbor
   K-nearest neighbor is the semi-parametric artificial intelligence estimations considering the controlled learning strategy's NN computation, and it uses the immediacy to exhibit the classifications determining how the grouping of similar objects. The KNN can be used to work with classification as well as regression problems. In view of classification of different classes is based on majority of

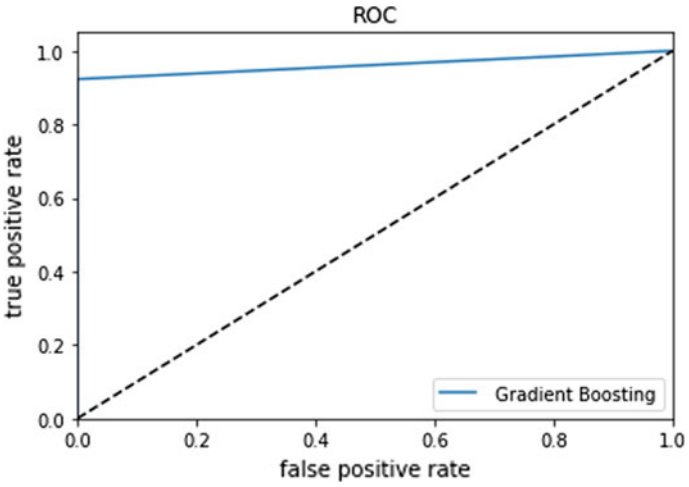

Fig. 2 ROC curve for test data using gradient boosting algorithm

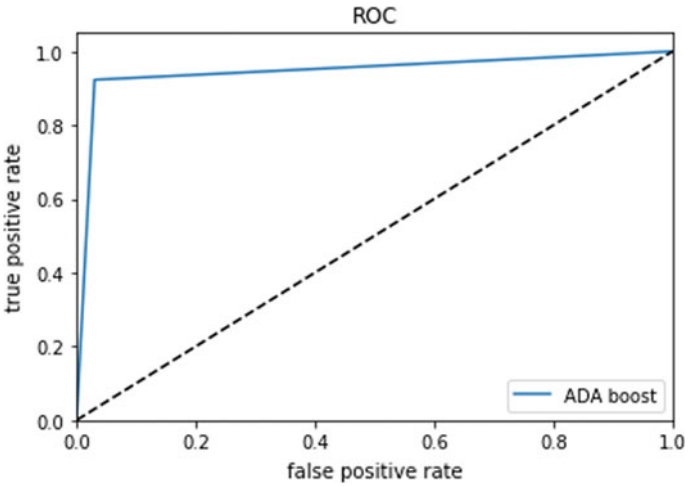

Fig. 3 ROC curve for test data using AdaBoost algorithm

votes. And the regression is based on calculating Euclidean distance, which is used to find out the distance between two nearest data points, and the objects are clustered which are of nearest distance. The KNN algorithm is regarded as a lazy because it can only have the capability to store the training data, and whenever any classification is made it creates over head on the memory pool where the training data is residing. While storing the data in memory, it will not perform any sort of calculations. It always tries to find out the points to determine to which cluster that particular data point refers. And it is a simple way to classify the data. If any newly discovered data comes into the account, the classifier will classify that data into a cluster to where it should belong to the kidney dataset uses KNN algorithm which results in 91.3% accuracy, and ROC is shown as Fig. 4:

5 Conclusion

This research aims to observe and examine the outcomes obtained by employing various AI computations to predict chronic kidney failure in the clinical area. This paper presented an expectation computation to predict CKD in its early stages. The dataset includes input limitations gathered from CKD patients, and the models are ready and authorized for the specified data limitations. Gradient boosting, AdaBoost, KNN, and random forest learning models are used to complete CKD. The models' performance is evaluated in terms of assumption accuracy. The assessment findings revealed that the gradient supporting model better predicts CKD in conjunction with AdaBoost, random forests, and KNN. The comparison should also be conceivable based on the execution time, including setting the decision as to the act of spontaneity of this investigation. A combination of classifiers is also implemented as part of voting

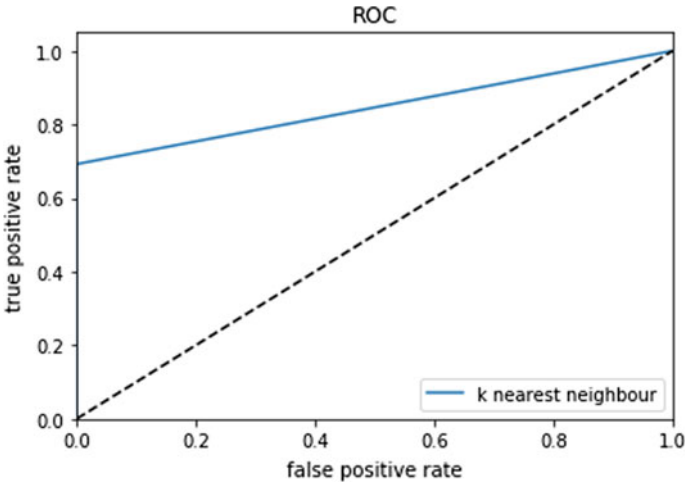

Fig. 4 ROC curve for test data using K-nearest neighbor algorithm

classifiers, where voting classifier 1 uses RF, KNN, and gradient boost, resulting in the highest accuracy equal to the gradient boost algorithm, whereas voting classifier 2 uses RF and KNN, resulting in lower accuracy of 95.6% when compared to voting classifier 1 (GB versus KNN versus RF).

References

1. Hooi LS, Ong LM, Ahmad G, Bavanandan S, Ahmad NA, Naidu BM et al (2013) A population-based study measuring the prevalence of chronic kidney disease among adults in West Malaysia. Kidney Int 84(5):1034–1040. pmid:23760287
2. Chandra Sekhar, P., Thirupathi Rao, N., Bhattacharyya, D., & Kim, T. -. (2021). Segmentation of natural images with k-means and hierarchical algorithm based on mixture of pearson distributions. Journal of Scientific and Industrial Research, 80(8), 707–715. Retrieved from www.scopus.com
3. Gao S, Manns BJ, Culleton BF, Tonelli M, Quan H, Crowshoe L et al (2007) Prevalence of chronic kidney disease and survival among aboriginal people. J Am Soc Nephrol 18(11):2953–9. pmid:17942955
4. Eali SNJ, Bhattacharyya D, Nakka TR, Hong S (2022) A novel approach in bio-medical image segmentation for analyzing brain cancer images with U-NET semantic segmentation and TPLD models using SVM. Traitement Du Signal 39(2):419–430. https://doi.org/10.18280/ts.390203
5. Bhattacharyya D, Doppala BP, Thirupathi Rao N (2020) Prediction and forecasting of persistent kidney problems using machine learning algorithms. Int J Curr Res Rev 12(20):134–139. https://doi.org/10.31782/IJCRR.2020.122031
6. Doppala BP, Raj SNM, Joshua ESN, Rao NT (2021) Automatic determination of harassment in social network using machine learning. https://doi.org/10.1007/978-981-16-1773-7_20 Retrieved from www.scopus.com
7. Reddy DKK, Behera HS, Nayak J, Routray AR, Kumar PS, Ghosh U (2022) A fog-based intelligent secured IoMT framework for early diabetes prediction, 199–218

QCM Sensor-Based Alcohol Classification Using Ensembled Stacking Model

Pemmada Suresh Kumar, Rajyalaxmi Pedada, Janmenjoy Nayak, H. S. Behera, G. M. Sai Pratyusha, and Vanaja Velugula

Abstract Alcohol consumption is the global yoke of injury and disease attributable as per the early study. The excessive intake of alcohol is coupled with unconstructive consequences and jeopardizing future prospects. This paper presents an ensemble model made of an array of five chemical compounds of quartz crystal microbalance (QCM) sensors to find the corresponding compositions of a gas mixture. This study makes use of QCM sensor responses to determine the gas compositions. These physical device sensors are used to sense the resonance frequency change of gas sensors by classifying the chemical compounds and recognizing their harmful effects. The main focus of the study is to determine the reaction of QCM sensors to five different alcohols, such as 1-octanol, 1-propanol, 2-butanol, 2-propanol, and 1-isobutanol, and to determine the effective sensor type in the classification of these compounds. The experiment is conducted to classify and identify the constituent component amount through an ensemble classifier to progress the efficiency of the QCM sensors. The results of 125 different scenarios illustrated that various alcohols could be classified effectively using a stacking classifier from the QCM sensor data.

Keywords QCM sensor · Alcohol · Machine learning · Stacking · Ensemble learning

P. Suresh Kumar
Department of Computer Science and Engineering, Aditya Institute of Technology and Management (AITAM), Tekkali, India

H. S. Behera
Department of Information Technology, Veer Surendra Sai University of Technology, Burla 768018, India

R. Pedada · G. M. Sai Pratyusha · V. Velugula
Department of Computer Science and Engineering, Dr. Lankapalli Bullayya College of Engineering, Visakhapatnam 530013, India

J. Nayak (✉)
Department of Computer Science, Maharaja Sriram Chandra BhanjaDeo (MSCB) University, Baripada, Odisha 757003, India

J. Nayak et al. (eds.), *Computational Intelligence in Data Mining*, Smart Innovation, Systems and Technologies 281, https://doi.org/10.1007/978-981-16-9447-9_49

1 Introduction

Nowadays, the detection of chemical compounds and their effects plays an important role. The alcohols have adverse effects when used in high quantities. Generally, alcohols like ethanol, propanol, and methanol are using in many skincare products, medicine, drugs, and cleansers. Some food items will also have alcohol for the long durability of the item unintentionally consuming by the human. In order to reduce the effects caused by alcohol, there must be some intelligent computing techniques that detect alcohol. Now, the pattern classification with gas sensors is best suited for recognition, detection, and classification. For the classification of alcohol, a highly selective sensor is required. Hence, QCM is a promising technology in detecting alcohols. QCM is an acoustic sensor having an array of gas sensors. The fact behind its sensor ability is that it detects the mass deposited on its crystal surface by estimating the change in its resonance frequency (f). QCM is an e-nose sensor that resembles the human nose to detect alcohols through its odor since different alcohols have different aromas.

Many industries strive for technologies that inexpensively detect chemical compounds. QCM is a sensor with high sensitivity, stability, low cost, low power requirements, small size, and low weight. By its thin layer, it can be used in gas absorption studies [1]. The alcohols would place on a thin layer of QCM and are identified by changing their fundamental oscillation frequency, as shown in Eq. 1.

$$\Delta f = \frac{C_f f_0^2}{A} \Delta m \tag{1}$$

where

A is the area of sensitive layers,
C_f is the mass sensitivity constant of the quartz crystal,
f_0 fundamental resonance of the quartz crystals,
Δm mass change.

The array of gas sensors is used as a detecting system to measure the alcohol mixtures. The sensors would produce a signal when the mass is placed on its thin layer. The signals from the sensors are preprocessed and taken as a dataset by using preprocessing algorithms. Machine learning algorithms train the dataset to find the corresponding composition of alcohols [2].

Machine learning is more accessible with information as it can process, analyze, and generate data from existing data, and this process can be automated. Machine learning can have a continuous upgrade as we can add new information without changing the historical data such that we can add new features to the model and improve the algorithm for better accurate results. Sometimes machine learning models have time constraints with fewer data, and more training to the system is required while classifying to make the predictions and decisions easily. The algorithms must be a promising technique to verify the data [3].

Artificial neural network (ANN) is one of the most used machine learning techniques for alcohol classification [4]. Classification results are used for different approaches like effects of alcohol in cosmetics and hygiene products, predicting flavors in Chinese liquors [5], estimating anesthesia dose [6], and many. Palaniappan et al. [7] addressed the problem of alcohol classification and proposed an array of operational amplifiers. Because of its prediction and decision, many classification models in machine learning are used to find the type of alcohol placed on QCM. Connor et al. [8] combined clinical experiences with machine learning algorithms such as decision trees, which promise a better understanding of complex relationships. Ordukaya and Karlik [9] analyzed the raw data is collected from fruit juice and alcohol mixture, fruit juice halal authentication, and alcohol mixture with e-nose by using KNN, support vector machines are used in most of the studies. Also, hybrid models such as Kanna et al. [10] utilized multilayer perceptron using the backpropagation algorithm to classify the alcohol abusers on the features extracted from gamma brand spectral power of the multichannel visual evoked potential signal in the time domain. The ensemble learning technique is a machine learning technique that produces the best predictive output from the base models. So that it deals with the pros of machine learning by ignoring its cons, we can choose the best technique to apply to data and predict the best outcome.

The significant contribution of this research includes:

(a) A stacking classifier is proposed to classify the different types of alcohol
(b) Classification of alcohol experimentation is done by using the dataset from the UCI repository proposed by Fatih et al. [11]
(c) Compare the performance of the proposed stacking classifier with several machine learning methods such as stochastic gradient descent (SGD), Gaussian naive Bayes (GNB), quadratic discriminant analysis (QDA), multilayer perceptron (MLP), linear discriminant analysis (LDA), linear regression (LR), decision trees (DT), K-nearest neighbor (KNN), gradient boosting (GB), AdaBoost. From the results, it is evident that the proposed method outperformed well.

The remaining paper is organized into five sections: Sect. 2 presents the literature study on alcohol classification using QCM sensors. Section 3 describes the methodology used, including the proposed method, performance measures, and experimental setup. Section 4 explains the environment setup and result analysis of various machine learning and ensemble learning algorithms on alcohol classification using QCM sensors have been discussed in Sect. 5. Section 6 concludes the paper.

2 Literature Study

Adak et al. [12] developed a model to classify the alcohols obtained by QCM sensors with different characteristics using ant bee colony-based neural network. Optimization is achieved by an artificial bee colony that is based on nectar searching behavior. The performance of the proposed model is evaluated using mean absolute percentage

error and mean square error. Based on the evaluation results of 300 scenarios, the proposed method successfully classified the alcohols.

Katardjiev et al. [13] applied support vector machine, random forest, decision trees, and K-nearest neighbor algorithms on clinical trial data of alcohol addicted patients by a Uppsala-based company for alcohol relapse forecasting. K-nearest neighbor predictor fitted with a radial basis function (RBF) kernel to model the data, it predicts the best results for explained variance and root mean square error. Hence, it is evident that ML-based models help predict addicted patients.

Li et al. [5] proposed a random forest technique that is optimized by reversing the number of decision trees used to predict the flavors of Chinese liquors. The proposed random forest classifier is compared with various machine learning classifiers such as linear discriminant analysis, backpropagation artificial neural network (BP-ANN), and support vector machine. Modified random forest outperformed well in terms of accuracy than other models.

Some more literature on alcohol classification in QCM sensors using different machine learning algorithms has been presented in Table 1.

Table 1 Literature of alcohol classification in QCM sensor using machine learning

S. No.	Author	Year	Intelligent method	Dataset	Evolution factors	Reference
1	Triyana et al.	2018	Chisten-based QCM	Ethanol, n-propanol, isoamyl alcohol, and n-amyl alcohol	Resonance frequency, molecular weight, vapor pressure, boiling point, sensitivity	[14]
2	Pisutaporn et al.	2018	Decision tree, random forest	Dataset of Portuguese students	Precision, recall, accuracy	[15]
3	Zhu et al.	2018	Random forest	Forty-six controls and 46 short-term abstinent patients	Accuracy, precision	[16]
4	Palaniappan et al	2017	MLP	Student alcohol consumption dataset	Accuracy, squared error, and root mean squared error	[7]
5	Ordukaya and Karlik	2016	Naïve Bayesian, KNN, LDA, DT, ANN, and SVM classifiers	Halal authentication of fruit juice–alcohol mixture set	Sensitivity, specificity, precision, accuracy, error rates	[9]

3 Proposed Methodology

Stacking is a supervised machine learning method that provides an optimal amalgamation of predictions that support binary classification, multi-classification, and regression. Stacking is also called a stacked regression [17] or superlearner [18] developed in the year of 1992 [19]. Though it was introduced many years ago, bagging and boosting are utilized widely compared to stacking, which is challenging to examine theoretically. The working principle of stacking is different compared to bagging and boosting, as both use different base learners while stacking uses the same type of base learner. It involves second-level training called meta-learner that will find optimal prediction from the combination of base learners. Base-level learners are generated by applying various learning algorithms to a stated dataset [20].

Algorithm: Ensembled Stacking Classifier
Input: Data for training $DS = \{x_i, y_i\}_{i=1}^{m}$
Output: Ensemble classifier H
Level 1: Learning algorithm at the base level classifier
for $l = 1$ to L **do**
learn h_l based on DS
end for
Level 2: Creating various datasets for predictions
for $i = 1$ to m **do**
$DS_h = \{x_i', y_i\}$, where, $x_i' = \{h_1(x_i), \ldots, h_L(x_i)\}$
end for
Level 3: meta-classifier learning
learn H based on DS_h
return H

Considered features $X = \{x_i \in R^m\}$, set of class labels $Y = \{y_i \in N\}$ and data for training are given as $\mathrm{DS} = \{x_i, y_i\}_{i=1}^{m}$, here the learning model is M on the training data DS. In the first level, learning is performed on the original training dataset with distributed weights, and learning parameters are tuned on the base classifier. New datasets are created and predicted; the labels from the output of first-level classifiers are considered new features. In place of using predicted labels, we can use probability estimators of the said first-level classifiers.

The proposed stacking approach utilizes three base classifiers: K-nearest neighbor, random forest, and Gaussian naive Bayes to predict alcohol type, and logistic regression is used as a meta-classifier in the proposed method. Integration of independent methods of the proposed model and overall systematic process structure is represented in Fig. 1.

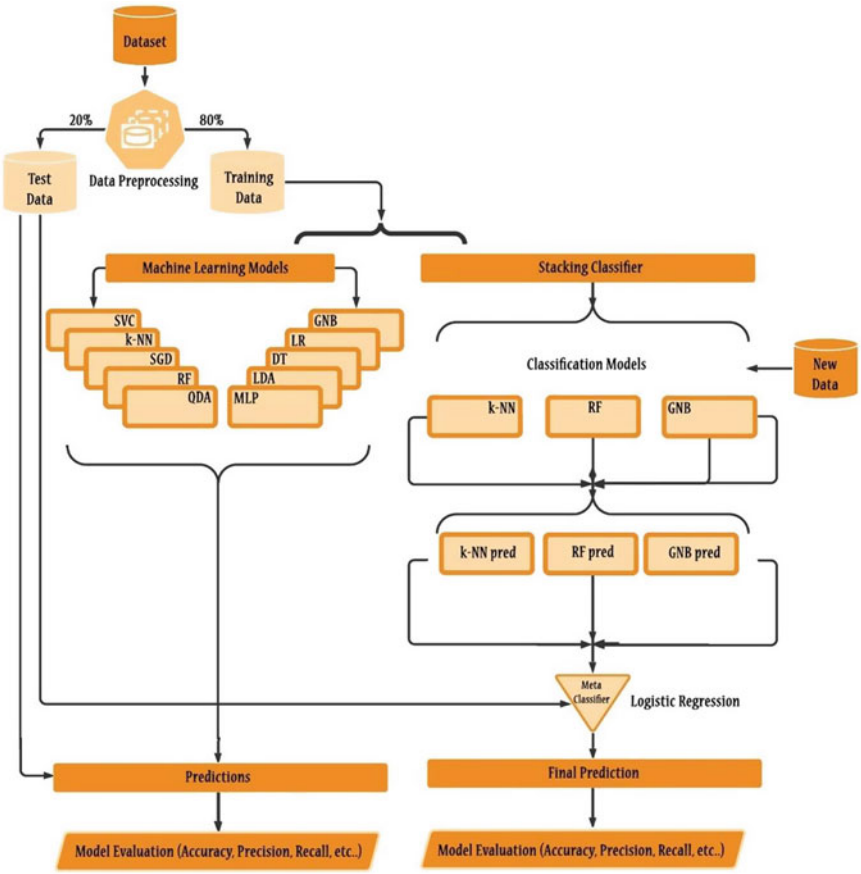

Fig. 1 Framework of the proposed stacking classifier

4 Environment Setup

In this section, we have discussed the dataset we have used for experimentation, performance measures considered to evaluate the models, and finally, explained the simulation environment and parameter setting of various models. Data preprocessing is applied to the dataset through data cleaning methods and then transforms into structured vectors. These vectors are divided into an 80:20 ratio for training and testing. We used the Intel i5 processor with 6 GB RAM on Windows 10 operating system. The proposed method and various machine learning algorithms are implemented using Scikit-learn, which is an open-source machine learning library based on python.

4.1 Empirical Data

Alcohol QCM sensor data is considered in this experiment and is available openly at the UCI machine learning repository [11]. Five different gas sensors are used for classification with various gas measurements such as 1-octanol, 1-propanol, 2-butanol, 2-propanol, and 1-isobutanol [12]. The feature distribution helps determine the dataset's characteristics. From the feature distribution, we can identify the data's possible temporal range and recurrence of occurrences. In comparison with partially skewed and fully skewed features, ordinarily, normally distributed characteristics are highly useful in obtaining good accuracy. Feature distribution of the alcohol dataset is shown in Fig. 2.

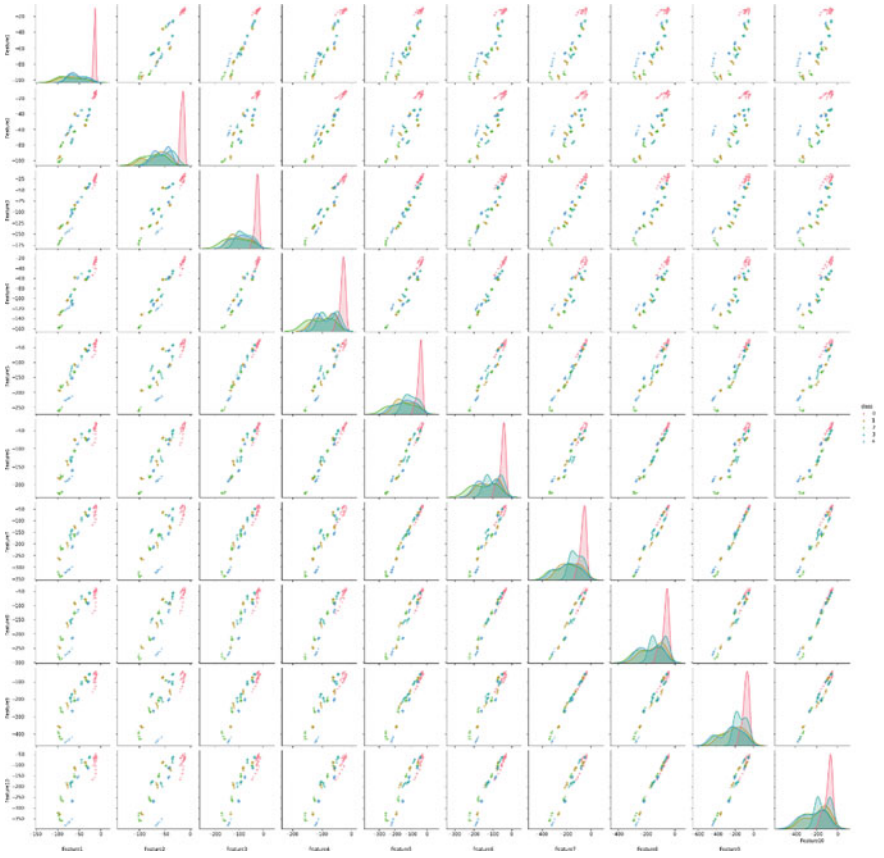

Fig. 2 Feature distribution of alcohol QCM sensor data

4.2 Performance Measure

The dataset is analyzed, and the performance has been evaluated by various evaluation metrics like True Positive (TP), False Positive (FP), True Negative (TN), False Negative (FN), True Negative Rate (TNR), False Negative Rate (FNR), and accuracy, recall, precision [21].

4.3 Experimental Setup

The experimentation was carried on the alcohol dataset obtained by the QCM sensor available in the UCI machine learning repository. Other competitive ML-based algorithms are simulated on the QCM sensor alcohol dataset along with the stacking classifier to obtain effective performance. The proposed method is compared with various machine learning techniques such as K-nearest neighbor, decision trees, stochastic gradient descent, Gaussian naive Bayes, logistic regression, linear discriminant analysis, multilayer perceptron, quadratic discriminant analysis, and some more ensemble methods such as AdaBoost, and gradient boosting. The parameter setting for the proposed method and other compared methods is shown in Table 2.

5 Result Analysis

This study shows the performance of ensemble stacking classifier for the various machine learning models which are presented in Table 3. The SGD and GNB classifiers deliver an enormous misclassification rate performance for all the classes. The accuracy of SGD and GNB is 0.37 and 0.44.

The classifiers QDA and MLP were classified precisely with the same results. Class 1-octanol is categorized accurately. The 1-propanol class classifies 12 instances correctly, and the remaining 8 instances are misclassified as 2-butanol, 2-propanol, and 1-isobutanol. The 2-butanol class classifies 9 instances correctly, and the remaining 11 instances are misclassified as 1-propanol, 2-propanol, and 1-isobutanol. The 2-propanol class shows that 17 of them are classified correctly, and the remaining 6 of 1-propanol and 2-butanol classes are misclassified as 2-propanol. The 1-isobutanol class classifies overall 20 instances correctly, but 3 instances of 1-propanol and 2-butanol are misclassified as 1-isobutanol. The overall accuracy of these is 0.77, whereas the individual accuracy of 100% is achieved for the 1-octanol class. The false positive, false negative, and FPR give 0 and recall, $F1$-score, precision give 1 for 1-octanol class compared to other classes.

The LDA classification classifies the classes 1-octanol and 1-isobutanol precisely, i.e., the individual accuracy of these classes is 100%. The 1-propanol class shows that 15 of them are classified correctly, and the remaining 5 are misclassified as

Table 2 Parameter setting of various models with 'Alcohol using QCM sensor'

Technique	Parameter setting
K-nearest neighbor	n_neighbors = 5, weights = 'uniform', algorithm = 'auto'
Decision tree	criterion = 'gini', splitter = 'best', max_depth = none,
Stochastic gradient descent	Solver = 'hinge' max_iter = 1000
Gaussian Naive Bayes	var_smoothing = 1e-09
Logistic regression	random_state = 1, solver = 'newton-cg'
Linear discriminant analysis	solver = 'svd'
Multilayer perceptron	activation = 'logistic', batch_size = 10, random_state = 2, solver = 'adam'
Quadratic discriminant analysis	reg_param = 0.0, store_covariance = False, tol = 0.0001
AdaBoost	base_estimator = DecisionTreeClassifier(max_depth = 5), n_estimators = 50, learning_rate = 1.0
Bagging	base_estimator = DecisionTreeClassifier(), n_estimators = 10, max_samples = 1.0 max_features = 1.0,
Gradient boosting	n_estimators = 40, random_state = 1
Stacking	classifiers = [KNN, RF, GNB], meta_classifier = LogisticRegression(), use_probas = True, use_clones = False

2-butanol and 2-propanol. The 2-butanol class shows that 14 of them are classified correctly, and the remaining 6 are misclassified as 1-propanol and 2-propanol. The 2-propanol class shows that 14 of them are classified correctly, and the remaining 7 are misclassified 1-propanol and 2-butanol. The individual accuracy of 1-propanol, 2-butanol, and 2-propanol classes is 0.92, 0.87, and 0.87. The LDA gives an overall accuracy of 0.83.

The result analysis of the LR classifier in the case of 1-octanol and 1-isobutanol class is classified precisely; therefore, the TPR, $F1$-score, precision, and accuracy of these classes are 100%. The 1-propanol class shows that 16 of them are classified correctly, and the remaining 4 are misclassified as 2-butanol and 2-propanol. The 2-butanol class shows that 16 of them are classified correctly, and the remaining 4

Table 3 Result analysis of proposed method and various classifiers

Class label	Model	TP	TN	FP	FN	TPR	FPR	$F1$-score	Precision	Accuracy	Over all accuracy
1-octanol	SGD	4	77	3	15	0.21	0.04	0.31	0.57	0.81	0.37
	GNB	17	80	0	2	0.89	0.00	0.94	1.00	0.97	0.44
	QDA	19	80	0	0	1.00	0.00	1.00	1.00	1.00	0.77
	MLP	19	80	0	0	1.00	0.00	1.00	1.00	1.00	0.77
	LDA	19	80	0	0	1.00	0.00	1.00	1.00	1.00	0.83
	LR	19	80	0	0	1.00	0.00	1.00	1.00	1.00	0.9
	DT	19	80	0	0	1.00	0.00	1.00	1.00	1.00	0.94
	GB	19	80	0	0	1.00	0.00	1.00	1.00	1.00	0.95
	KNN	16	80	0	3	0.84	0.00	0.91	1.00	0.96	0.97
	AdaBoost	19	80	0	0	1.00	0.00	1.00	1.00	1.00	0.98
	Stacking	19	80	0	0	1.00	0.00	1.00	1.00	1.00	0.99
1-propanol	SGD	4	75	4	16	0.20	0.05	0.29	0.50	0.79	
	GNB	5	71	8	15	0.25	0.10	0.30	0.38	0.76	
	QDA	12	72	7	8	0.60	0.09	0.62	0.63	0.84	
	MLP	12	72	7	8	0.60	0.09	0.62	0.63	0.84	
	LDA	15	76	3	5	0.75	0.04	0.79	0.83	0.92	
	LR	16	75	4	4	0.80	0.05	0.80	0.80	0.92	
	DT	18	79	0	2	0.90	0.00	0.94	1.00	0.97	
	GB	18	76	3	2	0.90	0.04	0.88	0.86	0.95	
	KNN	20	78	1	0	1.00	0.01	0.98	0.95	0.98	
	AdaBoost	19	78	1	1	0.95	0.01	0.95	0.95	0.98	
	Stacking	20	78	1	0	1.00	0.01	0.98	0.95	0.98	
2-butanol	SGD	9	59	20	11	0.45	0.25	0.37	0.31	0.68	
	GNB	10	65	14	10	0.50	0.18	0.45	0.42	0.75	
	QDA	9	73	6	11	0.45	0.08	0.51	0.60	0.82	
	MLP	9	73	6	11	0.45	0.08	0.51	0.60	0.82	
	LDA	14	72	7	6	0.70	0.09	0.68	0.67	0.87	
	LR	16	75	4	4	0.80	0.05	0.80	0.80	0.92	
	DT	20	76	3	0	1.00	0.03	0.93	0.86	0.96	
	GB	20	78	1	0	1.00	0.01	0.98	0.95	0.99	
	KNN	20	79	0	0	1.00	0.00	1.00	1.00	1.00	
	AdaBoost	20	78	1	0	1.00	0.01	0.98	0.95	0.98	
	Stacking	20	79	0	0	1.00	0.00	1.00	1.00	1.00	
2-propanol	SGD	10	61	18	10	0.50	0.23	0.42	0.36	0.71	
	GNB	11	47	32	9	0.55	0.41	0.35	0.26	0.58	

(continued)

Table 3 (continued)

Class label	Model	TP	TN	FP	FN	TPR	FPR	$F1$-score	Precision	Accuracy	Over all accuracy
	QDA	17	73	6	3	0.85	0.08	0.79	0.74	0.90	
	MLP	17	73	6	3	0.85	0.08	0.79	0.74	0.90	
	LDA	14	72	7	6	0.70	0.09	0.68	0.67	0.87	
	LR	18	77	2	2	0.90	0.03	0.90	0.90	0.96	
	DT	19	78	1	1	0.95	0.01	0.95	0.95	0.97	
	GB	18	78	1	2	0.90	0.01	0.92	0.95	0.97	
	KNN	20	79	0	0	1.00	0.00	1.00	1.00	1.00	
	AdaBoost	20	79	0	0	1.00	0.00	1.00	1.00	1.00	
	Stacking	20	79	0	0	1.00	0.00	1.00	1.00	1.00	
1-isobutanol	SGD	10	62	17	10	0.50	0.22	0.43	0.37	0.72	
	GNB	1	78	1	19	0.05	0.01	0.09	0.50	0.79	
	QDA	20	76	3	0	1.00	0.04	0.93	0.87	0.96	
	MLP	20	76	3	0	1.00	0.04	0.93	0.87	0.96	
	LDA	20	79	0	0	1.00	0.00	1.00	1.00	1.00	
	LR	20	79	0	0	1.00	0.00	1.00	1.00	1.00	
	DT	18	78	1	2	0.90	0.01	0.92	0.94	0.96	
	GB	19	79	0	1	0.95	0.00	0.97	1.00	0.99	
	KNN	20	77	2	0	1.00	0.03	0.95	0.91	0.97	
	AdaBoost	19	79	0	1	0.95	0.00	0.97	1.00	0.98	
	Stacking	19	79	0	1	0.95	0.00	0.97	1.00	0.98	

are misclassified as 1-propanol and 2-propanol. The 2-propanol class shows that 18 of them are classified correctly, and the remaining 2 are misclassified as 1-propanol and 2-butanol each. The LR classifier achieves an overall accuracy of 0.90.

The DT Classifier in the 1-octanol class is classified precisely; therefore, these classes' TPR, $F1$-score, precision, and accuracy are 1. The 1-propanol class shows that 18 instances are classified correctly, and 2 instances are misclassified as 2-butanol and 2-propanol. The 2-butanol class shows that 20 of them are classified correctly, and 3 instances of 1-propanol and 1-isobutanol are misclassified into 2-butanol. The 2-propanol class shows that 19 instances are classified correctly, and 1 instance is wrongly predicted as 1-isobutanol. The 1-isobutanol class shows that 18 instances are classified correctly, and 2 instances are misclassified as 2-butanol. The DT Classifier classifies each class approximately and achieved an overall accuracy of 0.94. The class 1-octanol achieves an individual accuracy of 1.00, as 1-propanol has a false negative of 2 and 2-butanol has a false positive of 3 that gives an individual accuracy of 0.97 and 0.96. The classes' 2-propanol and 1-isobutanol attained the individual accuracy of 0.97 and 0.96.

The GB Classifier predicts the 1-octanol class precisely; therefore, the TPR, $F1$-score, precision, and accuracy of these classes are 1. The 1-isobutanol shows that 19

instances are classified correctly, and the single remaining instance is misclassified as 1-propanol. The 1-propanol class shows that 18 instances are classified correctly, and the remaining 2 instances are misclassified as 2-butanol and 2-propanol. The 2-butanol class shows that 20 of them are classified correctly, and one instance of 1-propanol is wrongly predicted as 2-butanol. The 2-propanol class shows that 18 are classified correctly, and only 2 are wrongly predicted as 1-propanol. The class 1-octanol achieves an individual accuracy of 1.00, as 2-butanol and 1-isobutanol achieve an individual accuracy of 0.99, 2-propanol, and 1-propanol with an individual accuracy 0.97 and 0.95. The FPR for 2-butanol and 2-propanol gives a value of 0.01; i.e., one instance is misclassified for each and achieved an overall accuracy of 0.94.

The KNN Classifier classifies the classes' 2-butanol and 2-propanol precisely. The 1-octanol shows that 16 instances are classified correctly, and the two instances are misclassified as 1-isobutanol. The 1-propanol class shows that 20 of them are classified correctly, where one instance of 1-octanol is misclassified as 1-propanol. The1-isobutanol class shows that 20 instances are classified correctly, where two instances of 1-octanol are misclassified as 1-isobutanol. The FPR for 1-propanol and 1-isobutanol is 0.01 and 0.03 and for other classes is 0. The precision for 1-octanol, 2-butanol, and 2-propanol is 1.00, 1-propanol is 0.95, and 1-isobutanol is 0.91. The KNN Classifier achieves an overall accuracy of 0.97.

The AdaBoost classifier classifies the classes' 1-octanol and 2-propanol precisely. The class1-propanol shows that 19 of them are classified correctly, and one instance is wrongly classified as 2-butanol. The class 2-butanol shows that 20 of them are classified correctly, and one instance of 1-propanol is improperly classified as 2-butanol. The table shows that only two instances are wrongly classified, i.e., 1-propanol is misclassified as 2-butanol, and 1-isobutanol is misclassified as 1-propanol, with an overall accuracy of 0.98.

The stacking classifier precisely classifies all the classes except 1-propanol and 1-isobutanol. The 1-propanol class shows that 20 of them are classified correctly, and one instance of 1-isobutanol is wrongly classified as 1-propanol. Where the false positive of all classes that are 0 except 1-propanol is 1. The $F1$-score and precision for 1-octanol, 2-butanol, and 2-propanol are 1. The proposed method gives an overall accuracy of 0.99.

Figure 3 shows the ROC curve of all the proposed models, and finally, Fig. 4 represents the various graph plots for TPR, FPR, $F1$-score, precision, accuracy, and overall accuracies of the models for the dataset classes.

Figure 4 illustrates that TPR and $F1$-score of all the models with the target feature, where the GNB evaluates the lowest value for 1-isobutanol and SGD evaluate for 1-propanol and 1-octanol. Figure 4 shows that GNB and SGD evaluate the highest FPR for classes' 2-propanol and 2-butanol compared to other classes with various models. Figure 4 shows that $F1$-score to 1 for the 1-isobutanol class with LDA and LR models. The QDA, MLP, LR, LDA, DT, GBC models show the value of $F1$-score to 1 for the 1-octonal class. Similarly, STK, ADB, KNN evaluate the $F1$-score to 1 for the 2-proponal class. Figure 4 shows that all the models evaluate precision value to 1 for the class 1-octanol except for the model SGD. Similarly, LDA, LR, DT, GBC, ADB, and STK evaluate precision value to 1 for the 1-isobutanol class.

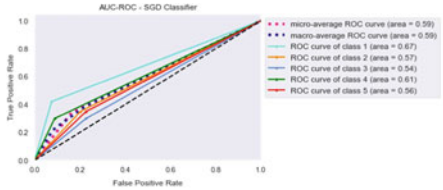

A: ROC curve of SGD

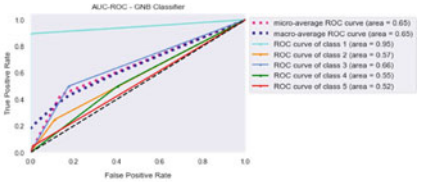

B: ROC curve of GNB

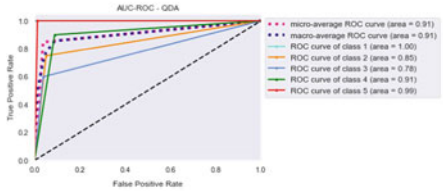

C: ROC curve of QDA

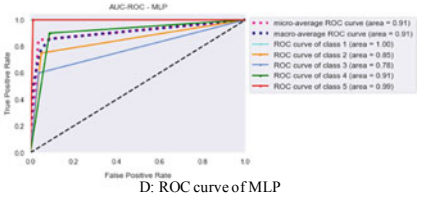

D: ROC curve of MLP

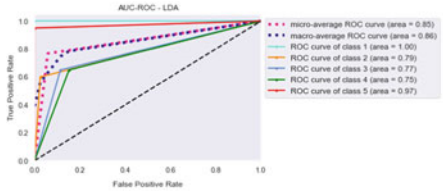

E: ROC curve of LDA

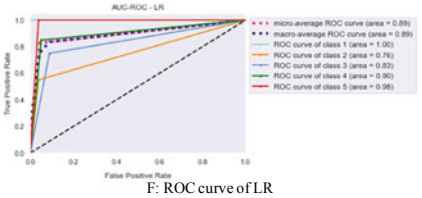

F: ROC curve of LR

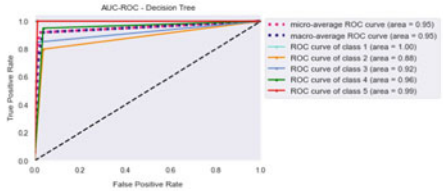

G: ROC curve of DT

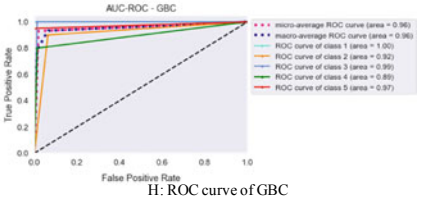

H: ROC curve of GBC

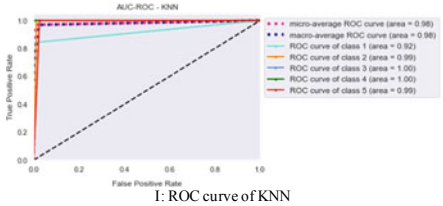

I: ROC curve of KNN

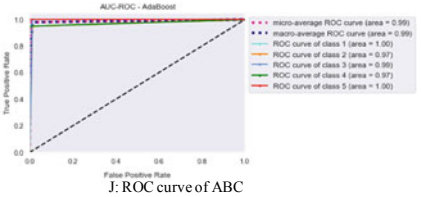

J: ROC curve of ABC

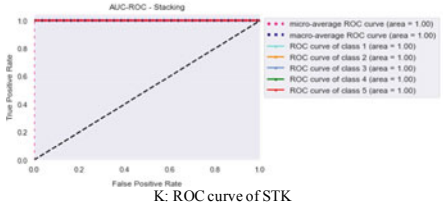

K: ROC curve of STK

Fig. 3 ROC curves of all models

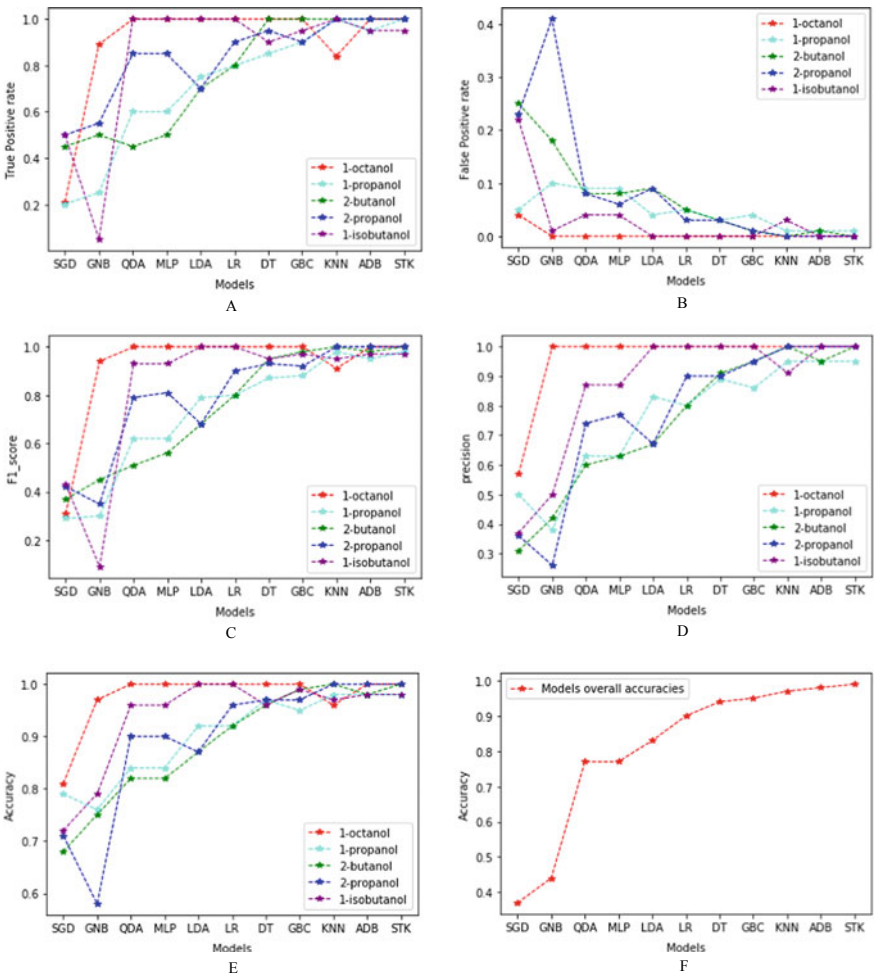

Fig. 4 **a** TPR versus models, **b** FPR versus models, **c** $F1$-score versus models, **d** precision versus models, **e** accuracy versus models, **f** accuracies of models

Figure 4 represents the individual class accuracies of all the models. Compared to other classes, 1-octanol and 1-isobutanol classes give good accuracy for all the models, except for k-Ninth ADB. STK has classified all the classes accurately (100%) except for 1-propanol and 1-isobutanol with 98%. Figure 4 clearly shows that the proposed model produces better accuracy than other models in identifying target classes.

6 Conclusion

This study proposed a classifier based on an ensemble model for determining the reaction of QCM sensors to five different alcohols such as 1-octanol, 1-propanol, 2-butanol, 2-propanol, and 1-isobutanol and classifying the sensors. Also, various ML algorithms are considered for effective analysis of the performances for classifying the accurateness. The classifiers QDA and MLP have driven the same results with an accuracy of 0.77 and performed well in categorizing the 1-octanol class. The LDA and LR performed well in classifying the classes' 1-octanol and 1-isobutanol, where LDA gives an accuracy of 0.83 and LR with an accuracy of 0.90. The DT and GB classifiers perform well in predominantly categorizing the 1-octanol class and other classes. The KNN performs well in classifying the classes 2-butanol and 2-propanol, but the 1-octanol class is misclassified to 1-propanol and 1-isobutanol. The AdaBoost performs well in categorizing the classes 1-octanol and 2-propanol. However, the proposed model shows that the classes 1-octanol, 2-butanol, and 2-propanol are categorized correctly. The class 1-isobutanol is misclassified as 1-propanol and gives an accuracy of 0.99. From this study, it is clear that all the models can classify 1-octanol class precisely except KNN. The QDA, DT, MLP, and GB can classify the 1-octanol class precisely. The LDA and LR classifiers are also able to classify 1-octanol and 1-isobutanol classes. AdaBoost is also able to classify the classes 1-octanol and 2-propanol. The overall results show that 1-octanol, 2-butanol, 2-propanol, and 1-isobutanol classes are categorized except the class1-propanol. Among all these models, the proposed method signifies its performance to a larger extent by correctly classifying the alcohol classes. In the future, a deep study may be conducted on other properties of alcohol by using deep learning methods for various practical applications.

References

1. X. Zeng, X. Jin, Y. Huang, A. Mason, Multichannel monolithic quartz crystal microbalance gas sensor array. Anal. Chem. **81**(2), 595–603 (2009). https://doi.org/10.1021/ac8018697
2. A. Özmen, F. Tekce, M.A. Ebeoğlu, C. Taşaltin, Z.Z. Öztürk, Finding the composition of gas mixtures by a phthalocyanine-coated QCM sensor array and an artificial neural network. Sens. Actuators, B Chem. **115**(1), 450–454 (2006). https://doi.org/10.1016/j.snb.2005.10.007
3. B.K. Rao, P.S. Kumar, D.K.K. Reddy, J. Nayak, B. Naik, QCM sensor-based alcohol classification by advance machine learning approach. pp. 305–320 (2021). https://doi.org/10.1007/978-981-15-8439-8_25
4. Y.C. Leung, D.H.F. Yip, W.W.H. Yu, An analogue ANN for classification of alcohol, in *1997 IEEE International Conference on Systems, Man, and Cybernetics. Computational Cybernetics and Simulation*, vol. 4(852), pp. 4010–4015 (1997). https://doi.org/10.1109/ICSMC.1997.633299
5. Q. Li, Y. Gu, N. Wang, Application of random forest classifier by means of a QCM-based E-nose in the identification of Chinese liquor flavors. IEEE Sens. J. **17**(6), 1788–1794 (2017). https://doi.org/10.1109/JSEN.2017.2657653

6. H.M. Saraoğlu, B. Edin, E-nose system for anesthetic dose level detection using artificial neural network. J. Med. Syst. **31**(6), 475–482 (2007). https://doi.org/10.1007/s10916-007-9087-7
7. S. Palaniappan, N.A. Hameed, A. Mustapha, N.A. Samsudin, Classification of alcohol consumption among secondary school students. JOIV Int. J. Inf. Vis. **1**(4–2), 224 (2017). https://doi.org/10.30630/joiv.1.4-2.64
8. J.P. Connor, M. Symons, G.F.X. Feeney, R.M. Young, J. Wiles, The application of machine learning techniques as an adjunct to clinical decision making in alcohol dependence treatment. Subst. Use Misuse **42**(14), 2193–2206 (2007). https://doi.org/10.1080/10826080701658125
9. E. Ordukaya, B. Karlik, Fruit juice–alcohol mixture analysis using machine learning and electronic nose. IEEJ Trans. Electr. Electron. Eng. **11**, S171–S176 (2016). https://doi.org/10.1002/tee.22250
10. P.S. Kanna, R. Palaniappan, K.V.R. Ravi, Classification of alcohol abusers: an intelligent approach, in *Third International Conference on Information Technology and Applications (ICITA'05)*, vol. 1, pp. 470–474 (2005). https://doi.org/10.1109/ICITA.2005.95
11. A. Fatih, P. Lieberzeit, P. Jarujamrus, N. Yumusak, UCI machine learning repository: alcohol QCM sensor dataset data set (n.d.). Retrieved April 17, 2020, from http://archive.ics.uci.edu/ml/datasets/Alcohol+QCM+Sensor+Dataset
12. M.F. Adak, P. Lieberzeit, P. Jarujamrus, N. Yumusak, Classification of alcohols obtained by QCM sensors with different characteristics using ABC based neural network. Eng. Sci. Technol. Int. J. **23**(3) (2019). https://doi.org/10.1016/j.jestch.2019.06.011
13. N. Katardjiev, S. Mckeever, A. Hamfelt, A machine learning-based approach to forecasting alcoholic relapses (2019)
14. Triyana et al., Chitosan-based quartz crystal microbalance for alcohol sensing. Electronics **7**(9), 1–11 (2018). https://doi.org/10.3390/electronics7090181
15. A. Pisutaporn, B. Chonvirachkul, D. Sutivong, Relevant factors and classification of student alcohol consumption, in *2018 IEEE International Conference on Innovative Research and Development (ICIRD)*, pp. 1–6 (2018). https://doi.org/10.1109/ICIRD.2018.8376297
16. X. Zhu, X. Du, M. Kerich, F.W. Lohoff, R. Momenan, Random forest based classification of alcohol dependence patients and healthy controls using resting state MRI. Neurosci. Lett. **676**, 27–33 (2018). https://doi.org/10.1016/j.neulet.2018.04.007
17. L. Breiman, Stacked regressions. Mach. Learn. **24**(1), 49–64 (1996). https://doi.org/10.1007/BF00117832
18. M.J. van der Laan, E.C. Polley, A.E. Hubbard, Super learner. Stat. Appl. Genet. Mol. Biol. **6**(1) (2007). https://doi.org/10.2202/1544-6115.1309
19. D.H. Wolpert, Stacked generalization. Neural Netw. **5**(2), 241–259 (1992). https://doi.org/10.1016/S0893-6080(05)80023-1
20. G. Wang, J. Hao, J. Ma, H. Jiang, A comparative assessment of ensemble learning for credit scoring. Expert Syst. Appl. **38**(1), 223–230 (2011). https://doi.org/10.1016/j.eswa.2010.06.048
21. P. Suresh Kumar, H.S. Behera, J. Nayak, B. Naik, Bootstrap aggregation ensemble learning-based reliable approach for software defect prediction by using characterized code feature. Innov. Syst. Softw. Eng. 1–22 (2021). https://doi.org/10.1007/s11334-021-00399-2

Identification of Heart Failure in Early Stages Using SMOTE-Integrated AdaBoost Framework

B. Kameswara Rao, U. D. Prasan, Mokka. Jagannadha Rao, Rajyalaxmi Pedada, and Pemmada Suresh Kumar

Abstract Heart disease, often known as Cardiovascular disease is one of the most lethal yet silent killers of humans, resulting in a rise in the mortality rate of sufferers per year. Every year, it kills nearly 17 million people worldwide in myocardial infarctions and cardiac attacks. Heart failure (HF) occurs when the heart cannot produce enough blood to satisfy the body's needs. On the other hand, current risk prediction techniques are moderately effective because statistical analytic approaches fail to capture prognostic information in big data sets with multi-dimensional interactions.The research investigates the proposed AdaBoost ensemble technique with Synthetic Minority Oversampling Technique (SMOTE) on the medical reports of 299 heart failure patients obtained during their follow-up period at Faisalabad Institute of Cardiology (Punjab) and Allied Hospital Faisalabad (Pakistan), during April–December, 2015. The proposed approach builds on ensemble learning techniques such as adaptive boosting. It provides a decision support mechanism for medical practitioners to identify and forecast heart diseases in humans based on risk factors for heart disease. The efficacy of the proposed method validates by comparing various machine learning algorithms, and it is evident that the proposed method performs better with an accuracy of 96.34.

Keywords Heart failure prediction · SMOTE · Adaptive boosting · Machine learning · Ensemble learning

B. Kameswara Rao · U. D. Prasan · P. S. Kumar (✉)
Department of Computer Science and Engineering, Aditya Institute of Technology and Management (AITAM), Tekkali, India

Mokka. Jagannadha Rao
Department of Geology, Andhra University, Visakhapatnam, AP, India

R. Pedada
Department of Computer Science and Engineering, Dr Lankapalli Bullayya College of Engineering, Visakhapatnam 530013, India

J. Nayak et al. (eds.), *Computational Intelligence in Data Mining*, Smart Innovation, Systems and Technologies 281, https://doi.org/10.1007/978-981-16-9447-9_41

1 Introduction

Heart issues are currently a major source of worry in the medical community. The heart plays a vital role in the human body's organs. The lack of blood circulation to the human body leads to the heartbeat disability and causes death in minutes. Major risk factors of heart disease are unhealthy blood cholesterols, usage of tobacco, alcohol, diabetes mellitus, obesity, eating high saturated fats, age, family history, lack of physical exercise, and poor diet [1]. As per the World Health Organization (WHO) reports, due to coronary artery disease (CAD), nearly, 17.5 million people are losing their life [2]. Various types of heart diseases are arrhythmia (occurs due to heartbeat abnormality), atherosclerosis (this condition leads to limits of oxygen flow to the organs, which causes heart stroke), hypertensive heart disease (leads to a thickness of heart muscles and heart failure), coronary artery disease (also called as ischemic heart disease), congenital heart defects, pulmonary valve stenosis (this condition arises before birth), heart infections (bacteria or viruses cause this condition). Some of the symptoms of heart disease problems are chest pain, breathlessness, fatigue, stomach pain, sweating, irregular heartbeat, arm or leg pain, depression, and swollen ankles [3–5].

In recent times, providing the best quality services and effective diagnosis is challenging in the medical field. The severity of heart disease is the leading cause, which may lead to sudden death. Heart disease, however, can be efficiently detected in its early stages and treated, controlled, and managed. An electrocardiogram (ECG) is a tool that examines the heartbeat rate and shows the possible functioning and irregularities of the heartbeat. Several clinicians are still unable to address the precise needs of heart disease patients. However, it is essential to define an accurate diagnosis system to avoid problems of heart disease. Therefore, it is necessary to develop a diagnostic plan based on ECG data and machine learning methods to classify heart diseases and detect the problems in the cardiovascular system. Machine learning is mainly used in the medical field to effectively diagnose, detect, and predict various diseases. Machine learning (ML) is progressively used to predict various heart diseases, and it is a subset of artificial intelligence (AI). Nowadays, it is critical to be able to sense the input data and decide the given task in the absence of human intervention. Machine learning works based on the models by receiving input data and applying mathematical or statistical models to predict the outputs. Various ML algorithms are utilized for daily actives in different domains, especially in the healthcare domain; more research is being conducted to forecast the severity level of the disease [6–9]. The ensemble learning model provides better accuracy by addressing the issues that machine learning algorithms face, such as time-consuming data collecting, error-prone methods, and selecting the correct algorithm. Individual machine learning algorithms are combined to form an ensemble learning model. The ensemble learning model provides high accuracy and addresses the issues faced on machine learning algorithms, such as time-consuming data collecting, error-prone methods, and selecting the correct algorithm.

The major contributions in the article include:

- Ensemble learning method adaptive boosting has been proposed for the identification of the heart disease in the early stages.
- The class imbalance issue in the data has been addressed by the oversampling technique SMOTE.
- The proposed method performance is compared with the different ensemble and ML models such as bagging, stacking, K-nearest neighbor (KNN), multi-layer perceptron (MLP), linear discriminant analysis (LDA), quadratic discriminant analysis (QDA), decision tree (DT), logistic regression (LR), and Gaussian Naive Bayes (GNB).

The remainder of the paper is divided into five sections. Section 2 discusses the literature study on the prediction of heart disease; Sect. 3 describes the proposed approach of the paper. Section 4 depicts the experimental setup for the proposed technique, which includes empirical data, data preprocessing, simulation environment, and parameter setting, as well as compared methodologies and performance measurements, are taken into consideration to validate the suggested method; Sect. 5 results are analyzed, and at last, but not least in Sect. 6 concludes the paper.

2 Literature Study

The diagnosis of cardiac disease in a patient is difficult for healthcare professionals since it necessitates various facts from multiple sources, such as laboratory test reports and equipment. Literature on heart disease prediction is presented here.

Singh and Kumar [6] investigated several machine learning algorithms to predict cardiac disorders using the dataset with 14 features of the patient from the UCI ML repository. Performance of the K-nearest neighbor algorithm is significantly better than decision tree, support vector machine, and linear regression with an accuracy of 87%. Apurb Rajdhan et al. [9] analyzed various data mining techniques along with the random forest. Experimentation has been done with the Cleveland dataset with 14 attributes which is collected from the UCI ML repository. Random forest obtained a better accuracy of 90.16%, which is better than the different techniques such as Naive Bayes, logistic regression, and decision tree methods. Masetic and Subasi [10] examined various ML techniques such as decision tree, k-nearest neighbor, support vector machine (SVM), random forest, and artificial neural networks to classify whether a patient had congestive heart failure or not. Feature extraction has been done using the auto-regression Burg method. Performance has been measured using different statistical metrics such as accuracy, specificity, sensitivity, f-measure, and ROC curve. Random forest performed well among various comparative methods with an accuracy of 100%. Literature on heart disease using various machine learning algorithms has been presented in Table 1.

Table 1 Literature on heart failure disease

S. No.	Data set (source)	Method	Performance	Evolution factor	References
1	Allied Hospital in Faisalabad (Punjab, Pakistan), and Faisalabad Institute of Cardiology, during April–December, 2015	Random forests, decision tree, linear regression, gradient boosting, artificial neural network, one rule, SVM radial, Naïve Bayes, K-nearest neighbor, SVM linear	Random forest—0.740 (accuracy)	Accuracy, $f1$-score, precision, AUC, TP rate, ROC-AUC, TN rate	[11]
2	Random clinical data	Supervised learning, unsupervised learning, deep learning	Random forest—0.963 (accuracy)	Accuracy, sensitivity, specificity, ROC-AUC	[12]
3	Clinical records from UCI repository	Random forest, support vector machine, K-nearest neighbor, decision tree, artificial neural network, Naïve Bayes	Random forest—94.31 (accuracy)	Accuracy, TP rate, PCR area, ROC area	[13]
4	Random clinical data	A stretch-driven growth model, hierarchical modeling, Bayesian inference, Gaussian process regression, logistic regression, support vector machine	A stretch-driven growth model—52.7% (average)	Average	[14]
5	UCI heart disease dataset	Random forest, decision tree, Naïve Bayes	Decision tree—93.19, Naïve Bayes—87.27, random forest—89.14, support vector machine—92.30, logistic regression—87.36 (accuracy)	Accuracy	[15]
6	Random clinical data	Machine learning assessment of risk and early mortality in heart failure (MARKER-HF) risk model, boosted decision tree algorithm	MARKER-HF-0.88 (AUC), 95% (CI)	AUC, TPR, CI, TNR	[16]

(continued)

Table 1 (continued)

S. No.	Data set (source)	Method	Performance	Evolution factor	References
7	Enterprise data warehouse, research patient data repository	Logistic regression, gradient boosting, max out networks, deep unified networks, cost-saving evaluation—connected cardiac care program (CCCP)	Deep unified networks—76.4% (accuracy)	Accuracy	[17]
8	1106 heart failure patients records, (MADIT-CRT)	Multiple kernel learning, K-means clustering	Multiple kernel learning—95%, K-means clustering—95% (CI)	CI, hazard ratio (HR)	[18]
9	Allied Hospital Faisalabad-Pakistan and Institute of Cardiology Apr–Dec, 2015 data	Cox regression, Kaplan Meier plot, Martingale residuals, bootstrapping	Cox regression—81% (discrimination ability)	Calibration slope, ROC curve, discrimination ability	[19]
10	Random clinical data	Multistep modeling strategy, EMR-wide predictive model	EMR-wide predictive model—0.78 (AUC), 83.19% (accuracy)	AUC, accuracy	[20]

3 Proposed Method

Freund et al. [21] presented an ensemble learning technique called adaptive boosting (AdaBoost). Base learner classifiers have been built based on the distribution of the dataset weights, where previous base learners' predictions determine the weights of the instances on the dataset. If a prediction on an instance causes misclassification, the instance weight increased in the next model; otherwise, the weight will remain unchanged. The weighted vote makes the final decision of the base learners and the weights basing on the models' misclassification rates. Usually, decision trees use as base learners in AdaBoost, where the model with a high prediction accuracy will have high weights, and a model with a low prediction accuracy will have low weights.

AdaBoost Algorithm	
1:	Initialize weights $w = \frac{1}{p}$, where p is instances in the data
2:	While $q < Q$ do: where Q is the number of models that need to be grown
	2.1 A model is constructed for all the data points, and the hypothesis is, $H_q(x_p)$, where x_p corresponds to the dataset and, y_p corresponding labels

(continued)

(continued)

AdaBoost Algorithm	
	2.2 Compute the error e for the training set, which sums over all data points x_p using Eq. 1 $e_q = \frac{\sum_{p=1}^{S} w_p^{(q)} * G(y_p \neq H_q(x_p))}{\sum_{p=1}^{S} w_p^{(q)}}$ (1) if G(condition) is valid returns 1 else and 0
	2.3 Compute ψ_q as shown in Eq. 2 $\psi_q = \log\left(\frac{1-e_q}{e_q}\right)$ (2)
	2.4 Update the weights for training S in the following $(q+1)$ model as shown in Eq. 3: $w_p^{(q+1)} = w_p^{(q)} * \exp(\mathbf{\Phi}_m * G(y_p \neq H_q(x_p)))$ (3)
3:	Continue Q iterations and compute the functional output by using Eq. 4: $f(x) = \text{sign}\left(\sum_{q}^{Q} \mathbf{\Phi}_q * H_q(x_p)\right)$ (4)

4 Experimental Setup

This section addresses the dataset, data processing followed in the experiment, simulation environment, parameter setting of the proposed method, and various classifiers, and performance measures to verify the proposed method performance with the comparable techniques.

4.1 Empirical Data

The clinical heart dataset considers for experimentation, and it comprises 299 patient's heart clinical medical history collected from Allied Hospital in Faisalabad (Punjab, Pakistan) and Faisalabad Institute of Cardiology during April–December, 2015 [11]. Out of 299 patients, 105 are women, and 194 are men ranging from 40 to 95 years. The dataset has 13 attributes that refer to essential features, clinical features, body features, and lifestyle features for each patient, including the detailed features, type, and description of each feature of the dataset is presented in Table 2. The dataset consists of Boolean features such as high blood pressure, anemia, diabetes, smoking, and sex. 'Creatinine phosphokinase' (CPK) reflects the level of CPK enzyme in the blood. When muscle tissue is damaged, CPK is released into the bloodstream, when tissues are damaged. CPK levels that are too high in a patient's blood can lead to heart failure. The 'ejection fraction' indicates how much blood the left ventricle pumps out as a proportion of each contraction. 'Platelets' are the count of platelets in the

Table 2 Type and meanings of each feature of the dataset

Attribute	Type	Description
Age	Numeric	Age of a patient
Anemia	Boolean	Red blood cell or hemoglobin deficiency
Creatinine phosphokinase	Numeric	CPK enzyme levels in the blood
Diabetes	Boolean	Whether or not the patient is diabetic
Platelets	Numeric	Platelets that are in the blood
High blood pressure	Boolean	If hypertension is found in a patient
Sex	Boolean	1—man, 0—woman
Serum creatinine	Numeric	In the blood, the creatinine level
Serum sodium	Numeric	In the blood, the sodium level
Ejection fraction	Numeric	The percentage of blood leaving the heart at each contraction
Time	Numeric	Follow-up period
Smoking	Boolean	Patient smokes or not
DEATH_EVENT	Boolean	1—live, 0—dead

blood. When a muscle breaks down, creatine produces 'serum creatinine', which is a waste product. Doctors use serum creatinine in the blood to monitor the functioning of the kidneys. Sodium is a mineral that helps nerves and muscles function correctly. The 'serum sodium' test is a common blood test that determines if a patient's blood sodium levels are normal or not. The goal attribute in the proposed work is 'Death event', which indicates whether the patient died or survived before the conclusion of the follow-up period, which is on average 130 days.

4.2 Data Preprocessing

Data preprocessing is a critical activity that will increase the quality of raw experimental data. It is a preliminary stage that takes all the data, sorts it, organizes it, and merges it. Data preprocessing can also significantly impact the efficiency of the generalization of a supervised machine learning algorithm. Null values in the dataset are verified, and there are no missing or null values. The dependent variable 'death_event' is highly imbalanced with '0': 203 and '1': 96, presented in Fig. 1. Synthetic minority oversampling technique (SMOTE) is used in the experimentation to resolve the class imbalance. SMOTE is implemented using over-sampling the minority class or under-sampling the majority class. In the article, oversampling of minority classes uses to address the class imbalance. Before feeding the data to the classification model, SMOTE was applied to obtain better accuracy. It is done simply by duplicating instances from the minority class example in the dataset until

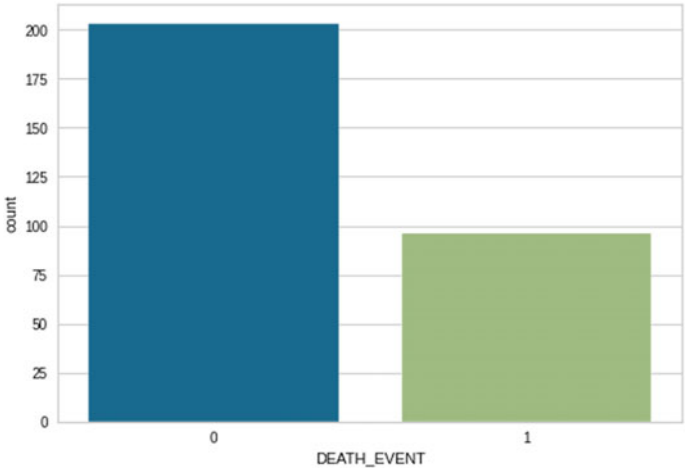

Fig. 1 Death_Event class before SMOTE

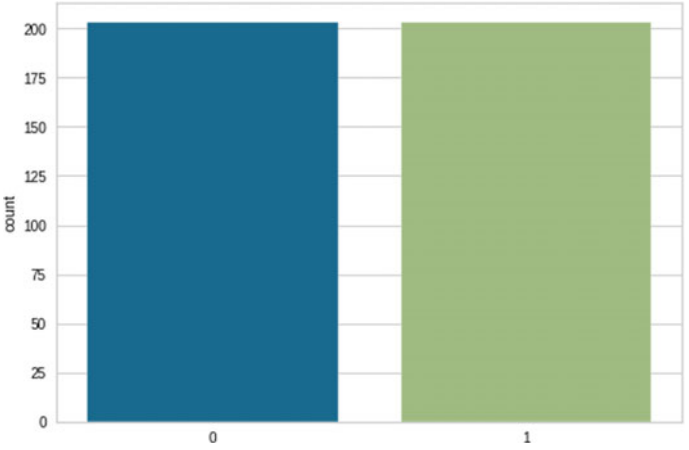

Fig. 2 Death_Event class after SMOTE

a model fit. After using SMOTE, the 'death_event' class consists of '0': 203 and '1': 203 presented in Fig. 2.

4.3 Simulation Environment and Parameter Setting

The experimentation performs on Windows 10 Pro, Intel(R) Core(TM) i5-6300U CPU @ 2.40 GHz, 64-bit operating system, ~2.5 GHz processor, and 8 GB RAM.

Table 3 Various classifiers parameter setting

Technique	Parameter setting
AdaBoost	base_estimator = DecisionTreeClassifier(criterion = 'gini', splitter = 'best', random_state = 4, max_depth = 5) n_estimators = 50; algorithm = 'SAMME.R'; learning_rate = 1.0
Stacking	Estimators = [RandomForestClassifier(random_state = 2, criterion = 'gini'), DecisionTreeClassifier(criterion = 'gini', splitter = 'best', random_state = 3)]; meta_classifier = LogisticRegression()
Bagging	base_estimator = DecisionTreeClassifier(); bootstrap = true; n_estimators = 100; random_state = 1
KNN	algorithm = 'kd_tree'; weights = 'distance'; n_neighbors = 3
MLP	hidden_layer_sizes = 15; activation = 'relu'; batch_size = 10; random_state = 2; max_iter = 1300
LDA	solver = 'svd'; tol: 0.0001
QDA	tol = 0.0002
LR	random_state = 1; solver = 'newton-cg'
GNB	var_smoothing = 1e−09
Random forest	random_state = 2; criterion = 'gini'
Decision tree	criterion = 'gini'; splitter = 'best'; random_state = 3
Stochastic gradient descent (SGD)	random_state = 100; penalty = 'l1'

Python programming frameworks such as sklearn use to perform data preprocessing tasks and various classification techniques such as machine learning and ensemble learning algorithms. Data analysis tasks were carried out by Numpy and Pandas framework. Functions based on data visualization done using Matplotlib and seaborn framework. Pycm module uses to deal with performance measures in the multiclass classification. The class imbalance problem solves by the technique called random oversampling using imblearn. Different methods and their parameters have presented in Table 3.

4.4 Performance Measures

The proposed adaptive boosting classifiers predict the survival of heart disease from the clinical records of several patients. For validating the performance, the proposed method compares with various machine learning and ensemble learning algorithms different performance metrics such as confusion matrix, true-positive rate, false-positive rate, precision, $f1$-score, accuracy, and ROC-AUC (Area under the receiver operating characteristic curve) [22].

5 Result Analysis

The survival of heart failure prediction using the AdaBoost ensemble technique and validated the proposed method with various ensemble learning techniques and machine learning is described in this section. The experimental results of the measures mentioned above, such as true positive (TP), true negative (TN), false positive (FP), false negative (FN), precision, true-positive rate (TPR), $F1$, ROC-AUC, and false-positive rate (FPR), are presented in Table 4. Compared to other techniques such as stacking, bagging, logistic regression, decision tree, linear discriminant analysis, quadratic discriminant analysis, multi-layer perceptron, K-nearest neighbor, and Gaussian Naive Bayes, the results obtained by the proposed AdaBoost technique are utterly better. Among all, k-nearest neighbor performs the worst in relative efficiency, while Ada-Boost performs the best.

From the assessment of the findings, ensemble learning methods obtained an accuracy between 96 and 90%, and machine learning algorithms achieved between 89 and 63%. In detail, the AdaBoost classifier achieved better accuracy of 96.34, followed by stacking and bagging, with 93.9% and 90.24%, respectively. Decision tree with 89.02%, logistic regression, and linear discriminant analysis obtained the same accuracy 86.59%; quadratic discriminant analysis, Gaussian Naïve Bayes, multi-layer perceptron produce 82.93%, 81.71%, 70.73% accuracies, respectively, and finally, k-nearest neighbor obtained 63.4% accuracy. True positive and true negative signifies the correctly classified instances. False positive and false negative represent incorrectly classified instances. In the proposed AdaBoost classifier, TP and TN are 36 and 43, indicating that 36 patients are healthy and predicted as healthy, and 43 patients are unwell and anticipated as sick. FP and FN are 0 and 3, signifying that all identified sick patients are predicted as unhealthy, and 3 patients are ill but predicted as healthy. In the case of a recall, stacking and decision tree produced the highest value with 0.95, followed by AdaBoost and multi-layer perceptron obtained 0.92; bagging achieved 0.87; LDA and LR got 0.85, Gaussian Naïve Bayes and QDA with 0.79, and k-nearest neighbor attained a value of 0.67. In the case of FPR value, AdaBoost obtained 0, followed by bagging, stacking, LDA, LR, QDA, DT, GNB, KNN, and MLP have 0.07, 0.07, 0.12, 0.12, 0.14, 0.16, 0.16, 0.40, 0.49, respectively. For precision, AdaBoost delivers a value of 1.00, followed by bagging, stacking, LDA, LR, DT, QDA, GNB, MLP, KNN produce 0.93, 0.92, 0.87, 0.87, 0.84, 0.84, 0.82, 0.63, 0.60 values, respectively. AdaBoost obtained the highest ROC-AUC value 0.96, then bagging, stacking, decision tree produced 0.94, 0.90, 0.89, LR, LDA, QDA, GNB, MLP, KNN obtained the values 0.86, 0.86, 0.83, 0.82, 0.72, and 0.64, respectively. The proposed method outperformed compared to various ensemble learning and machine learning models by considering all the results.

Figure 3a–j presents the precision-recall curves for machine learning techniques, proposed AdaBoost classifier, and other ensemble learning techniques. AdaBoost and stacking obtained the highest average precision value of 0.99, followed by bagging with 0.98, LDA, LR, GNB, MLP, DT, and KNN obtained average precision 0.93, 0.92,

Table 4 Performance evaluation of proposed and comparative methods

Intelligent technique	Accuracy	TP	FP	TN	FN	TPR (recall)	FPR	Precision	TNR	$F1$	ROC-AUC
AdaBoost	96.34	36.00	0.00	43.00	3.00	0.92	0.00	1.00	1.00	0.96	0.96
Stacking	93.90	37.00	3.00	40.00	2.00	0.95	0.07	0.93	0.93	0.94	0.94
Bagging	90.24	34.00	3.00	40.00	5.00	0.87	0.07	0.92	0.93	0.89	0.90
Decision tree	89.02	37.00	7.00	36.00	2.00	0.95	0.16	0.84	0.84	0.89	0.89
Logistic regression	86.59	33.00	5.00	38.00	6.00	0.85	0.12	0.87	0.88	0.86	0.86
Linear discriminant analysis	86.59	33.00	5.00	38.00	6.00	0.85	0.12	0.87	0.88	0.86	0.86
Quadratic discriminant analysis	82.93	31.00	6.00	37.00	8.00	0.79	0.14	0.84	0.86	0.82	0.83
Gaussian Naïve Bayes	81.71	31.00	7.00	36.00	8.00	0.79	0.16	0.82	0.84	0.81	0.82
Multi-layer perceptron	70.73	36.00	21.00	22.00	3.00	0.92	0.49	0.63	0.51	0.75	0.72
K-nearest neighbor	63.41	26.00	17.00	26.00	13.00	0.67	0.40	0.60	0.60	0.63	0.64

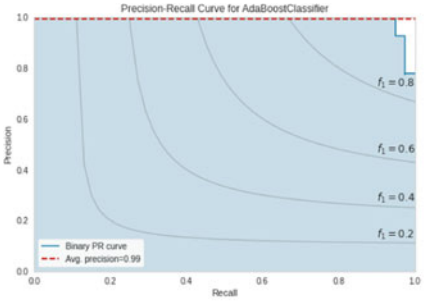

A: AdaBoost Precision-Recall curve

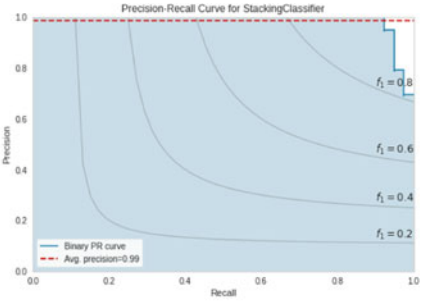

B: Stacking Precision-Recall curve

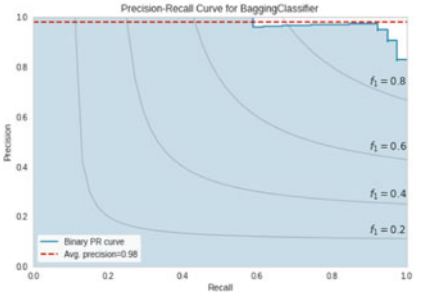

C: Bagging Precision-Recall curve

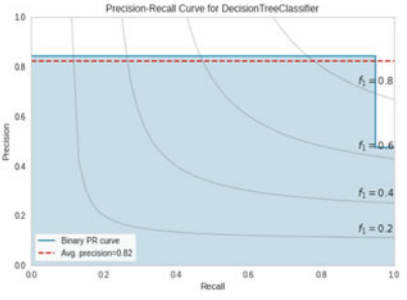

D: Decision Tree Precision-Recall curve

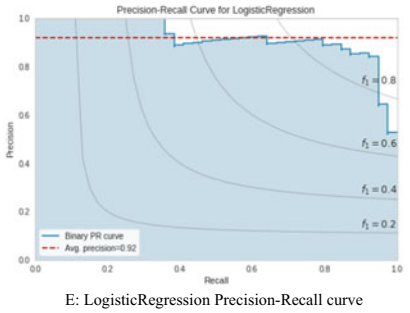

E: LogisticRegression Precision-Recall curve

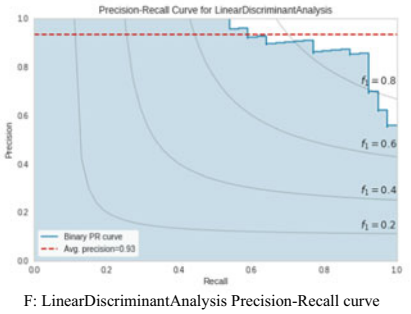

F: LinearDiscriminantAnalysis Precision-Recall curve

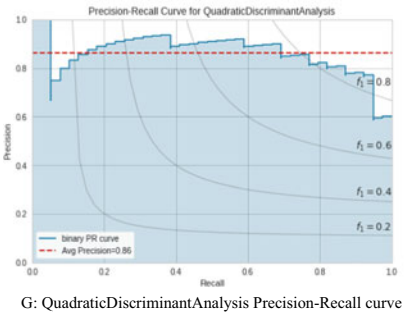

G: QuadraticDiscriminantAnalysis Precision-Recall curve

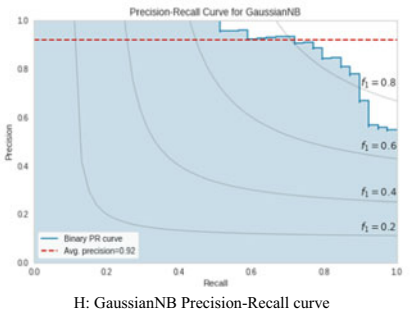

H: GaussianNB Precision-Recall curve

Fig. 3 Precision-recall curves of **a** AdaBoost, **b** stacking, **c** bagging, **d** DT, **e** LR, **f** LDA, **g** QDA, **h** GNB, **i** MLP, **j** KNN

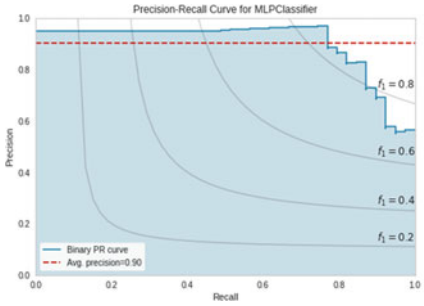

I: MLP Precision-Recall curve

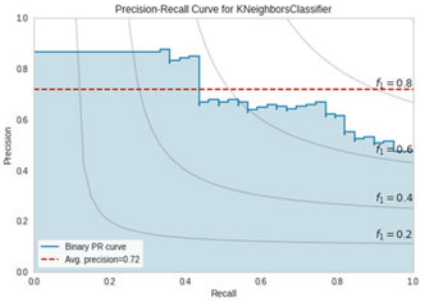

J: K-Nearest Neighbor Precision-Recall curve

Fig. 3 (continued)

0.92, 0.90, 0.82, and 0.72, respectively. The results show that AdaBoost performs very well in terms of average precision.

The prediction error is defined as the variation between predicted and actual values. In the proposed method, the 3 instances from class '0' predicted as class '1' are incorrectly classified instances in the test data in the proposed technique. The class prediction error for the proposed technique, other machine learning techniques, and ensemble learning techniques is shown in Fig. 4.

The accuracy of the proposed technique and various comparative models is presented in Fig. 5. The proposed adaptive boosting performed better than all methods.

6 Conclusion

In this article, we presented intelligent methods to strengthen assistance for heart failure-affected patients. The paper proposed a classification strategy to classify the survival of heart failure patients using the AdaBoost ensemble system. The proposed method validates by comparing various techniques such as stacking, bagging, GNB, LR, DT, LDA, QDA, MLP, and KNN. The efficiency of the classification model improved by solving the class imbalance problem by applying SMOTE to the data. Before comparing the models, every technique has been tested with different parameters to achieve the highest accuracy. The findings show that the AdaBoost outperformed the other machine learning algorithms in terms of different performance metrics in predicting the survival of heart failure students. In the future. The reported better classification performance in predicting heart failures comes from AdaBoost's extremely appealing properties, which we describe here. AdaBoost lowers the classification error on training data to zero as the number of training steps grows, based on the modest assumption that a weak learner obtains a lower error rate. AdaBoost also successfully optimizes the margin of the resultant ensemble classifier, in addition to reducing a given cost function. In the future, we will enhance the data with more

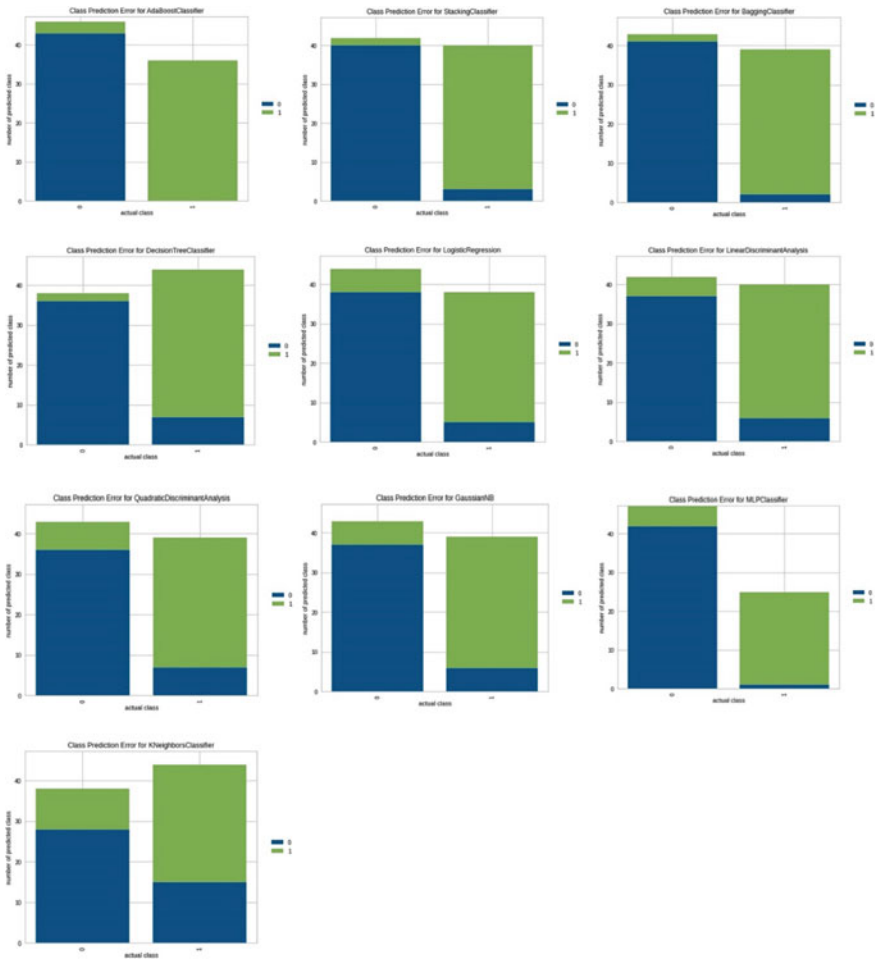

Fig. 4 Class prediction error for the various comparative methods and the proposed technique

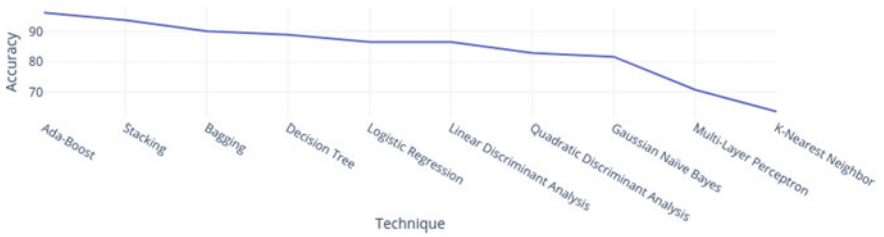

Fig. 5 Accuracy of the various comparative methods and the proposed method

number of patient records and extend the work using sophisticated deep learning techniques on the image data.

References

1. Y. Xing, J. Wang, Z. Zhao, Y. Gao, Combination data mining methods with new medical data to predicting outcome of coronary heart disease (2008), pp. 868–872. https://doi.org/10.1109/iccit.2007.204
2. J. Mackey, G. Mensah, WHO 2004_atlas oh heart disease and stroke.pdf (2004), p. 9
3. A.A. Ariyo et al., Depressive symptoms and risks of coronary heart disease and mortality in elderly Americans. Circulation **102**(15), 1773–1779 (2000). https://doi.org/10.1161/01.CIR.102.15.1773
4. M.A. Whooley et al., Depressive symptoms, health behaviors, and risk of cardiovascular events in patients with coronary heart disease. JAMA J. Am. Med. Assoc. **300**(20), 2379–2388 (2008). https://doi.org/10.1001/jama.2008.711
5. L.R. Wulsin, J.C. Evans, R.S. Vasan, J.M. Murabito, M. Kelly-Hayes, E.J. Benjamin, Depressive symptoms, coronary heart disease, and overall mortality in the Framingham Heart Study. Psychosom. Med. **67**(5), 697–702 (2005). https://doi.org/10.1097/01.psy.0000181274.56785.28
6. A. Singh, R. Kumar, Heart disease prediction using machine learning algorithms, in *2020 International Conference on Electrical and Electronics Engineering (ICE3)*, Feb 2020, pp. 452–457. https://doi.org/10.1109/ICE348803.2020.9122958
7. D. Shah, S. Patel, S.K. Bharti, Heart disease prediction using machine learning techniques. SN Comput. Sci. **1**(6), 345 (2020). https://doi.org/10.1007/s42979-020-00365-y
8. R. Katarya, P. Srinivas, Predicting heart disease at early stages using machine learning: a survey, in *Proceedings of the International Conference on Electronics and Sustainable Communication Systems, ICESC 2020* (2020), pp. 302–305. https://doi.org/10.1109/ICESC48915.2020.9155586
9. D.P.G. Apurb Rajdhan, M. Sai, A. Agarwal, D. Ravi, Heart disease prediction using machine learning. *Lect. Notes Electr. Eng.* **9**(04) (2020)
10. Z. Masetic, A. Subasi, Congestive heart failure detection using random forest classifier. Comput. Methods Programs Biomed. **130**, 54–64 (2016). https://doi.org/10.1016/j.cmpb.2016.03.020
11. D. Chicco, G. Jurman, Machine learning can predict survival of patients with heart failure from serum creatinine and ejection fraction alone. BMC Med. Inform. Decis. Mak. **20**(1), 1–16 (2020). https://doi.org/10.1186/s12911-020-1023-5
12. C.R. Olsen, R.J. Mentz, K.J. Anstrom, D. Page, P.A. Patel, Clinical applications of machine learning in the diagnosis, classification, and prediction of heart failure: machine learning in heart failure. Am. Heart J. **229**, 1–17 (2020). https://doi.org/10.1016/j.ahj.2020.07.009
13. S. Rahayu, J. Jaya Purnama, A. Baroqah Pohan, F. Septia Nugraha, S. Nurdiani, S. Hadianti, Prediction of survival of heart failure patients using random forest. *J. Pilar Nusa Mandiri* **16**(2), 255–260 (2020). [Online]. Available: www.ubsi.ac.id
14. M. Peirlinck et al., Using machine learning to characterize heart failure across the scales. Biomech. Model. Mechanobiol. **18**(6), 1987–2001 (2019). https://doi.org/10.1007/s10237-019-01190-w
15. F.S. Alotaibi, Implementation of machine learning model to predict heart failure disease. Int. J. Adv. Comput. Sci. Appl. **10**(6), 261–268 (2019). https://doi.org/10.14569/ijacsa.2019.0100637
16. E.D. Adler et al., Improving risk prediction in heart failure using machine learning. Eur. J. Heart Fail. **22**(1), 139–147 (2020). https://doi.org/10.1002/ejhf.1628
17. S.B. Golas et al., A machine learning model to predict the risk of 30-day readmissions in patients with heart failure: a retrospective analysis of electronic medical records data. BMC Med. Inform. Decis. Mak. **18**(1), 1–17 (2018). https://doi.org/10.1186/s12911-018-0620-z

18. M. Cikes et al., Machine learning-based phenogrouping in heart failure to identify responders to cardiac resynchronization therapy. Eur. J. Heart Fail. **21**(1), 74–85 (2019). https://doi.org/10.1002/ejhf.1333
19. T. Ahmad, A. Munir, S.H. Bhatti, M. Aftab, M.A. Raza, Survival analysis of heart failure patients: a case study. PLoS ONE **12**(7), 1–8 (2017). https://doi.org/10.1371/journal.pone.0181001
20. K. Shameer et al., Predictive modeling of hospital readmission rates using electronic medical record-wide machine learning: a case-study using Mount Sinai heart failure cohort, in *Pacific Symposium on Biocomputing 2017* (2017), pp. 276–287
21. Y. Freund, R.E. Schapire, M. Hill, Experiments with a new boosting algorithm rooms f 2B-428, 2A-424 g (1996)
22. B.K. Rao, P.S. Kumar, D.K.K. Reddy, J. Nayak, B. Naik, *QCM Sensor-Based Alcohol Classification by Advance Machine Learning Approach* (Springer, Singapore, 2021), pp. 305–320

A Fog-Based Intelligent Secured IoMT Framework for Early Diabetes Prediction

Dukka Karun Kumar Reddy, H. S. Behera, Janmenjoy Nayak, Ashanta Ranjan Routray, Pemmada Suresh Kumar, and Uttam Ghosh

1 Introduction

One of the chronic metabolic disorders swiftly mounting health catastrophes of this period, irrespective to the context of the ethnic, racial, and geographic situation, is diabetes mellitus. The metabolic disease is characterized by exalted levels of blood sugar (or blood glucose), which leads over time to serious mutilation to the blood vessels, nerves, eyes, heart, and kidneys. In general, diabetes is categorized into three types, called type 1, type 2, and gestational diabetes. Type 1 (is also described as insulin-dependent) occurs where the pancreas produces no insulin or little by itself due to the pancreatic beta cells which have been attacked by the immune system mistakenly. The most common type 1 diabetes symptoms are sudden weight loss, polyphagia, polydipsia, and polyuria. The type 2 diabetes develops when

D. K. K. Reddy
Department of CSE, Dr. Lankapalli Bullayya College of Engineering, Visakhapatnam, AP, India

H. S. Behera
Department of Information Technology, Veer Surendra Sai University of Technology, Burla, India

J. Nayak (✉)
Department of Computer Science and Engineering, Aditya Institute of Technology and Management (AITAM), Kotturu, AP, India

A. R. Routray
Department of I & CT, Fakir Mohan University, Balasore, Odisha, India

P. S. Kumar
Department of CSE, Aditya Institute of Technology and Management (AITAM), Kotturu, AP, India

U. Ghosh
Department of Electrical Engineering and Computer Science, Vanderbilt University, Nashville, TN, USA
e-mail: uttam.ghosh@vanderbilt.edu

U. Ghosh et al. (eds.), *Intelligent Internet of Things for Healthcare and Industry*, Internet of Things, https://doi.org/10.1007/978-3-030-81473-1_10

Chapter

Fuzzy Perceptron Learning for Non-Linearly Separable Patterns

Raja Kishor Duggirala

Abstract

Perceptron learning has its wide applications in identifying interesting patterns in the large data repositories. While iterating through their learning process perceptrons update the weights, which are associated with the input data objects or data vectors. Though perceptrons exhibit their robustness in learning about interesting patterns, they perform well in identifying the linearly separable patterns only. In the real world, however, we can find overlapping patterns, where objects may associate with multiple patterns. In such situations, a clear-cut identification of patterns is not possible in a linearly separable manner. On the other hand, fuzzy-based learning has its wide applications in identifying non-linearly separable patterns. The present work attempts to experiment with the algorithms for fuzzy perceptron learning, where perceptron learning and fuzzy-based learning techniques are implemented in an interfusion manner.

Keywords: perceptron learning, fuzzy-based learning, fuzzy C-means, interfusion, weighted distances, pattern recognition, sum of squared errors, clustering fitness

1. Introduction

A learning system could be thought as a collection of methods that are brought together in order to create an environment to facilitate different learning processes. The learning systems will provide various types of learning resources and descriptions of procedures for obtaining quality results [1]. The learning systems find their applications in the areas like, image recognition, speech recognition, traffic prediction, e-mail spam and malware filtering, automatic language translation, medical diagnosis, etc. [2].

As the data increases in large volumes in the digital repositories, it has become essential to look for alternative approaches to yield better results in extracting interesting patterns from the repositories. Intelligent learning systems are gaining attention from a wide range of researchers in the recent years in extracting patterns from the data repositories. The learning systems have three kinds of approaches. They are supervised, unsupervised, and semi-supervised learning approaches [3].

The concept of perceptron learning plays a critical role in pattern recognition, which has become a challenging problem in the data science research. In the recent years, perceptron learning algorithms are exhibiting their robust performance in identifying interesting patterns from large data repositories when compared to the traditional supervised learning approaches [4]. A perceptron can be thought as a computational prototype of a neuron. As a supervised learning approach, perceptron

learning is used for linear classification of patterns. This learning approach uses the already available labelled data to classify the future data by predicting the class labels.

In the literature, it is studied that many researchers experimented with perceptron learning for identifying interesting patterns from the data. A novel autonomous perceptron model (APM) was proposed to address the issues of complexity of traditional perceptron architectures [4]. APM is a nonlinear supervised learning model, which has the architecture using the computational power of the quantum bits (qubits). The researchers [5], using biophysical perceptron (BP), tried to simulate the pyramidal cells in the brain with a wide variety of active dendritic channels. The BP, here, explores the ability of real neurons with extended non-linear dendritic trees to effectively perform the classification task in identifying interesting patterns from the data. Many researchers have experimented with perceptron learning in a wide variety of ways. However, the perceptron learning suffers several limitations. It works well for linearly separable patterns. Though some researchers experimented for identifying non-linearly separable patterns, the perceptron learning produced best results for binary separation of patterns only [5]. Also that perceptron learning suffers poor performance in case of overlapping patterns, that is, when patterns are not having sharp boundaries.

Fuzzy-based learning, on the other hand, is found to show its ability in performing well for overlapping patterns [6]. As a fuzzy-based learning approach, fuzzy C-means (FCM) is widely used by researchers for pattern recognition. A weighted local fuzzy regression model showed a better efficiency than the least squares regression for non-linear and high-dimensional pattern recognition of transport system in China [7]. The new kernelized fuzzy C-means clustering algorithm [8] uses a kernel-induced distance function as a similarity measure showed improved performance in identifying the patterns when compared to the conventional fuzzy C-means technique. In many research findings, it is observed that the fuzzy-based learning approach was used in a wide variety of ways to achieve better results in extracting non-linear and overlapping patterns.

The present work attempts to experiment with fuzzy perceptron learning, which implements the perceptron learning and fuzzy-based learning techniques in an interfusion manner. In the research literature, we can find a good amount of work related to the combination of fuzzy logic with perceptron learning. The fuzzy neural network (FNN) was proposed for pattern classification, which uses supervised fuzzy clustering and pruning algorithm to determine the precise number of clusters with proper centroids representing the patterns to be recognised [9]. In the fuzzy neural integrated networks [10], the researchers attempted to integrate the concept of fuzzy sets and neural networks to deal with pattern recognition problems. In an enhanced algorithm for fuzzy lattice reasoning (FLR) classifier, a new nonlinear positive valuation function was defined to produce better results for pattern classification [11]. Along with these, however, many other research experiments of fuzzy perceptron learning are supervised learning approaches only. Therefore, the present work focuses on experimenting with effective implementation of some techniques involved in the perceptron and fuzzy-based learning systems for unsupervised learning to identify interesting patterns in large datasets. As part of the present work, five algorithms are developed, two of which are related to perceptron learning, one is the standard fuzzy C-means (FCM) algorithm. The remaining two algorithms are proposed by the present work, which implement the perceptron learning and fuzzy-based learning in an interfusion manner using weights and weighted distances respectively. All the algorithms are implemented using three benchmark datasets. The CPU time, clustering fitness (CF), and sum of squared errors (SSE) are taken into consideration for performance evaluation of the algorithms.

2. Perceptron learning

Nowadays, the perceptron learning model can be thought as a more general computational model in identifying interesting patterns in a dataset. It takes an input, aggregates it along with the weights and produces the result. A perceptron is used to learn patterns and relationships in data. Patterns help us knowing about the interesting features around which objects may be grouped in a given population of data.

A perceptron may be configured for a specific application, such as pattern recognition and data classification through some learning process [12]. Perceptrons are information processing devices, which are built from interconnected elementary processing units. These units are called neurons. The perceptrons are robust in exhibiting their ability in distributed representation and computation, learning, generalisation, adaptivity, inherent contextual information processing, and fault tolerance [13].

The perceptron learning uses an iterative weight adjustment for the enhanced retrieval of patterns from a dataset. The iterative process converges to the weights, which produce the patterns that represent the different groups of data objects in the dataset uniquely. While operating for learning on patterns, the perceptrons use weights in connection to every input vector. A weight represents the information used by the perceptron to solve a problem [14].

The perceptron with multiple neurons is shown in **Figure 1**.

In **Figure 1**, $X_1, X_2, \ldots, X_n$ are the n input vectors and $Y_1, Y_2, \ldots, Y_m$ are the m neurons. The input vector X_1 is connected to neurons $Y_1, Y_2, \ldots, Y_m$ with weights W_{11}, $W_{12}, \ldots, W_{1m}$, respectively, the input vector X_2 is connected to the neurons with weights $W_{21}, W_{22}, \ldots, W_{2m}$, respectively so on and the input vector X_n is connected to the neurons with the weights $W_{n1}, W_{n2}, \ldots, W_{nm}$, respectively. The weights of all input vectors for all neurons will be formulated as the weight matrix as shown below.

$$\begin{bmatrix} W_{11} & W_{12} & \ldots & \ldots & W_{1m} \\ W_{21} & W_{22} & \ldots & \ldots & W_{2m} \\ \ldots & \ldots & \ldots & \ldots & \ldots \\ \ldots & \ldots & \ldots & \ldots & \ldots \\ \ldots & \ldots & \ldots & \ldots & \ldots \\ W_{n1} & W_{n2} & \ldots & \ldots & W_{nm} \end{bmatrix}$$

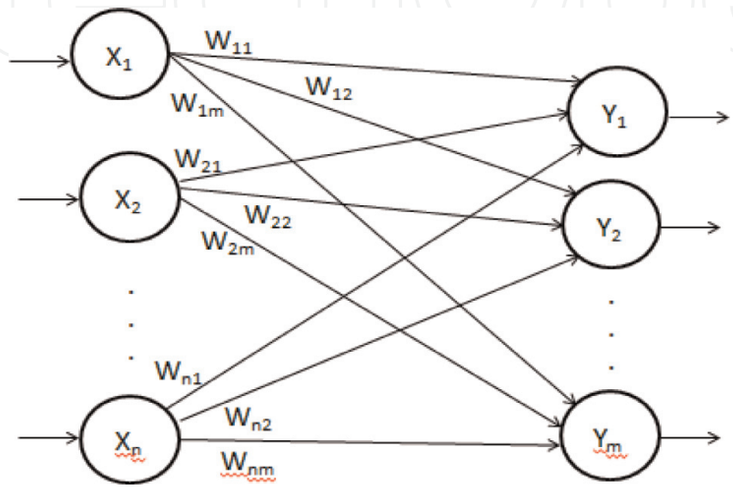

Figure 1.
A perceptron with a multiple neurons.

Though the perceptron learning exhibits its robustness in identifying the patterns in the data repositories, it works well for linearly separable patterns, that is, the patterns with sharp boundaries only. However, in the real time world, we may find overlapping patterns, that is, non-linearity in pattern associativity, where data objects may associate with multiple patterns. In such situations, the perceptron learning approach may suffer in identifying the patterns clearly. On the other hand, fuzzy-based learning has its wide applications in identifying patterns in the overlapping scenario. In the present work, two algorithms are implemented for perceptron learning. They are discussed in the following sub-sessions.

2.1 Perceptron learning using weights (PLW)

This algorithm implements the perceptron learning using weights [12]. With each input data vector, a weight is associated corresponding to each pattern. To generate the initial weights, one iteration of K-means algorithm is performed. The results of K-means iteration are used to compute the weight matrix. This weight matrix will be repeatedly updated in the subsequent iterations. For each input data vector weights are computed corresponding to every pattern. The input data vector is associated with the pattern corresponding to which the weight is maximum. This process is repeated for every iteration. The algorithm terminates when there is no change in the association of data vectors to the patterns. The algorithm for perceptron learning using weights is given below.

2.1.1 Algorithm PLW

Step 1: Determine the number of patterns, k, to be recognised from the dataset.

Step 2: Select k points randomly from the dataset and set them as cluster seeds to correspond the patterns to be recognised.

Step 3: Perform one iteration of K-means algorithm.

Step 4: Using the results of K-means iteration, compute cluster wise initial weights.

Step 5: Repeat steps 6–8 until the stopping condition.

Step 6: Generate weight matrix, where each element W_{ij} is computed as:

$$W_{ij}(i+1) = W_{ij}(i) + lr * \left(\|X_i\| - W_{ij}(i)\right) \quad (1)$$

Here, $W_{ij}(i+1)$ is the weight of ith data point X_i for jth cluster for the iteration $(i+1)$, $W_{ij}(i)$ is the weight of ith data point for jth cluster for the iteration i, $\|X_i\|$ is the norm of data point X_i, and lr is the learning rate. The lr may assume a value ranging between 0 and 1. To avoid possible biasedness in the computations, lr is assumed to be 0.5.

Step 7: Assign points to clusters using weights.

Step 8: Update cluster means, that is, refine patterns.

[End of step 5 loop]

Step 9: [End of algorithm]

2.2 Perceptron learning using weighted distances (PLWD)

This algorithm implements the perceptron learning using weighted distances [15]. With each input data vector, a weighted distance is associated corresponding to each pattern. To generate the initial weighted distances, one iteration of K-means algorithm

is performed. Using the results of K-means the weight matrix is computed. This weight matrix is used to compute the weighted distances for each input data vector. The data vector is associated with the pattern corresponding to which the weighted distance is minimum. This weight matrix will be repeatedly updated in the subsequent iterations to compute the new weighted distances. This process repeats for every iteration. The algorithm terminates when there is no change in the association of data vectors to the patterns. The algorithm for perceptron learning using weighted distances is given below.

2.2.1 Algorithm PLWD

Step 1: Determine the number of patterns, k, to be recognised from the dataset.

Step 2: Select k points randomly from the dataset and set them as cluster seeds μ_j ($j = 1, 2, \ldots, m$) to correspond the patterns to be recognised.

Step 3: Perform one iteration of K-means algorithm.

Step 4: Using the results of K-means iteration, compute cluster wise initial weights.

Step 5: Repeat steps 6–10 until the stopping condition.

Step 6: Generate weight matrix W using Eq. (1).

Step 7: For each data point X_i, compute the Euclidean distance $d(X_i, \mu_j)$ as follows:

$$d\left(X_i, \mu_j\right) = \sqrt{\sum_{l=1}^{d} \left(x_{il} - \mu_{jl}\right)^2} \tag{2}$$

Here, X_i is the ith data point, μ_j is the mean vector of the cluster j.

Step 8: For each data point compute the weighted distances as follows:

$$Wd_j = W_{ij}(i+1) \cdot d\left(X_i, \mu_j\right) \tag{3}$$

Step 9: Assign points to clusters using weights.

Step 10: Update cluster means, that is, refine patterns.

[End of step 5 loop]

Step 11: [End of algorithm]

Though the perceptron learning algorithms are experimented widely by many researchers, they exhibit their robustness in identifying linearly separable patterns only.

3. Fuzzy-based learning

Fuzzy-based learning is used to handle the concept of partial truth, where the truth value may range between completely true and completely false [16]. It is an approach that allows for multiple possible truth values to be processed through the same data object. In fuzzy-based learning, the data objects are assumed being associated with multiple patterns. For each data object, the degree of association is measured in membership. This membership value may range between 0 and 1 (1 being high similarity and 0 being no similarity with the pattern).

Fuzzy-based learning techniques focus on modelling uncertain and vague information that is found in the real world situations. These techniques deal with the

patterns whose boundaries cannot be defined sharply [17, 18]. By fuzzy-based learning, one can know if data objects fully or partially associate with the patterns that are under consideration based on their memberships of association [19]. Among the techniques of fuzzy-based learning, fuzzy C-means (FCM) is the most well-known one as it has the advantage of robustness for obscure information about the patterns [20, 21]. FCM is widely studied and applied in geological shape analysis [22], medical diagnosis [23], automatic target recognition [24], meteorological data [20], pattern recognition, image analysis, image segmentation and image clustering [25–27], agricultural engineering, astronomy, chemistry [28], detection of polluted sites [29], etc. The following section presents a brief discussion of FCM algorithm.

3.1 Fuzzy C-means (FCM)

The fuzzy C-means (FCM) is a technique that uses degree of membership for natural interpretation of patterns recognised [30]. The FCM associates the data vectors among k patterns. Each data vector may associate with each pattern with a membership degree. The membership of a data vector towards a pattern can range between 0 and 1.

The FCM algorithm is given below [31]. Here, U is the $k \times N$ membership matrix. While computing the cluster means and updating the membership matrix at each iteration, the FCM uses the fuzzifier factor, m. For most cases, m ranging between 1.5 and 3.0 gives good results [32]. In the present work, in all the experiments, m is set to 1.5.

3.1.1 Algorithm FCM

Step 1: Determine the number of patterns, k, to be recognised from the dataset.

Step 2: Select k points randomly from the dataset and set them as cluster seeds μ_j ($j = 1, 2, \ldots, m$) to correspond the patterns to be recognised.

Step 3: Perform one iteration of K-means algorithm. Set $t = 0$.

Step 4: Using the results of K-means iteration, compute membership matrix $U^{(0)}_{k \text{ X } N}$.

Step 5: Repeat steps 6–9 until the stopping condition.

Step 6: [Refine patterns] Update the mean of jth cluster μ_j as follows:

$$\mu_j = \frac{\sum_{i=1}^{N} (u_{ij})^m X_i}{\sum_{i=1}^{N} (u_{ij})^m} \tag{4}$$

Here, u_{ij} is the membership degree of the data point X_i w.r.t. jth pattern and m is the fuzzifier factor.

Step 7: Compute the new membership matrix using:

$$u_{ij}{}^{t+1} = \left[\sum_{l=1}^{k} \left(\frac{\left\| X_i - \mu_j{}^t \right\|^2}{\| X_i - \mu_l{}^t \|^2} \right)^{1/m-1} \right]^{-1} \tag{5}$$

Step 9: Assign points to clusters using membership degrees. Set $t = t + 1$.

[End of step 5 loop]

Step 10: [End of algorithm]

4. Fuzzy perceptron learning

The fuzzy perceptron learning works in an interfusion manner, where the fuzzy logic is combined with perceptron learning for identifying non-linear and overlapping patterns. Much research work may be found in the literation where fuzzy perceptron learning is experimented in different applications [33, 34]. However, those experiments are confined to supervised learning only. The present work attempts to experiment with fuzzy perceptron learning for unsupervised cases. The present work proposes two algorithms, one is for fuzzy perceptron learning using weights and the other is for fuzzy perceptron learning using weighted distances.

4.1 Fuzzy perceptron learning using weights (FPLW)

This algorithm implements the perceptron learning using weights and FCM techniques in an interfusion manner. These techniques are performed in alternative iterations until the termination condition. Initially, one iteration of K-means algorithm is performed. Using the results of K-means, initial weights are computed as mentioned in the Section 2.1. Using these weights, weight matrix is generated to perform one iteration of perceptron learning algorithm to associate the input data vectors to the patterns. Using the results of perceptron learning step, membership matrix is computed to perform one iteration of FCM algorithm as mentioned in Section 3.1. The results of FCM step are used to update weight matrix to perform perceptron learning step. In this way the perceptron learning and FCM algorithms are repeated in alternative iterations until termination condition. The algorithm for fuzzy perceptron learning using weights (FPLW) is given below.

4.1.1 Algorithm FPLW

Step 1: Determine the number of patterns, k, to be recognised from the dataset.
Step 2: Select k points randomly from the dataset and set them as cluster seeds μ_j $(j = 1, 2, \ldots, m)$ to correspond the patterns to be recognised.
Step 3: Perform one iteration of K-means algorithm.
Step 4: Using the results of K-means iteration, compute cluster wise initial weights.
Step-5: Update cluster means μ_j $(j = 1, 2, \ldots, m)$.
Step 6: Repeat steps 7–13 until the stopping condition.
Step 7: Compute the weight matrix using Eq. (1).
Step 8: Assign points to clusters using weights.
Step 9: If there is no change in cluster assignment then go to step 14.
Step 10: Update cluster means using Eq. (4).
Step 11: Generate membership matrix $U^{(0)}_{k \text{ X } N}$ using Eq. (5).
Step 12: Assign points to clusters using membership matrix.
Step 13: If there is no change in cluster assignment then go to step 14.
[End of Step 6 loop]
Step 14: [End of Algorithm]

4.2 Fuzzy perceptron learning using weighted distances (FPLWD)

This algorithm implements the perceptron learning using weighted distances and FCM techniques in an interfusion manner. These techniques are performed in alternative iterations until the termination condition. Initially, one iteration of K-means

technique is performed. Using the results of K-means, initial weights are computed as mentioned in the Section 2.2. Now, one iteration of perceptron learning algorithm is performed where the weight matrix is generated using the initial weights. Using this weight matrix, weighted distances are computed for every input vector X_i with respect to each pattern using the Eq. (3). The weighted distances are used to associate the input vectors to the patterns. Using the results of perceptron learning step, membership matrix is computed to perform one iteration of FCM algorithm as mentioned in Section 3.1. The results of FCM step are used to compute weight matrix for perceptron learning step. In this way the perceptron learning and FCM steps are repeated in alternative iterations until termination condition. The algorithm for fuzzy perceptron learning using weighted distances (FPLWD) is given below.

4.2.1 Algorithm FPLWD

Step 1: Determine the number of patterns, k, to be recognised from the dataset.
Step 2: Select k points randomly from the dataset and set them as cluster seeds μ_j (j = 1, 2, … , m) to correspond the patterns to be recognised.
Step 3: Perform one iteration of K-means algorithm.
Step 4: Using the results of K-means iteration, compute cluster wise initial weights.
Step-5: Update cluster means μ_j (j = 1, 2, … , m).
Step 6: Repeat steps 7–15 until the stopping condition.
Step 7: Compute the weight matrix using Eq. (1).
Step 8: For each data point compute the Euclidean distance using Eq. (2).
Step 9: For each data point compute weighted distances using Eq. (3).
Step 10: Assign points to clusters using weighted distances.
Step 11: If there is no change in cluster assignment then go to step 16.
Step 12: Update cluster means using Eq. (4).
Step 13: Generate membership matrix $U^{(0)}_{k \text{ X } N}$ using Eq. (5).
Step 14: Assign points to clusters using membership matrix.
Step 15: If there is no change in cluster assignment then go to step 16.
[End of Step 6 loop]
Step 16: [End of Algorithm]

5. Performance evaluation

For performance evaluation of algorithms, CPU time in seconds, sum of squared errors [35] and clustering fitness (CF) [36] are taken into consideration and are calculated for all the algorithms.

5.1 Sum of squared errors

The objective of pattern learning is to minimise the intra-cluster sum of squared errors (SSE). The lesser the SSE, the better the goodness of fit is. The SSE for the results of each algorithm is computed using Eq. (6).

$$SSE = \sum_{j=1}^{k} \sum_{X_i \in C_j} \left(X_i - \mu_j \right)^2 \tag{6}$$

Here, X_i is the ith data point in the dataset, μ_j $(j = 1, \ldots, k)$ is the mean of the cluster C_j, and k is the number of patterns to be recognised.

5.2 Cluster fitness

While achieving high intra-cluster similarity, it is also important to achieve well separation of patterns.

So, it is also important to consider inter-cluster similarity while evaluating the performance of the algorithms. For this, the present work, computes the clustering fitness (CF) as a performance criterion, which requires the calculation of both intra-cluster similarity and inter-cluster similarity. The computation of CF also requires the experiential knowledge, λ. The computation of CF results in higher value when the inter-cluster similarity is low and results in lower value for when the inter-cluster similarity is high. Also that to make the computation of CF unbiased, the value of λ is taken as 0.5 [36].

5.2.1 Intra-cluster similarity for the cluster C_j

It can be quantified via a function of the reciprocals of intra-cluster radii within each of the resulting clusters. The intra-cluster similarity of a cluster C_j $(1 = j = k)$, denoted as $S_{tra}(C_j)$ [36], is defined by:

$$S_{tra}(C_j) = \frac{1+n}{1+\sum_1^n dist(I_l, Centroid)} \tag{7}$$

Here, n is the number of items in cluster C_j, I_j $(1 = j = n)$ is the jth item in cluster C_j, and dist(I_j, *Centroid*) calculates the distance between I_j and the centroid of C_j, which is the intra-cluster radius of C_j. To smooth the value of $S_{tra}(C_j)$ and allow for possible singleton clusters, 1 is added to the denominator and numerator.

5.2.2 Intra-cluster similarity for one clustering result C

It is denoted as $S_{tra}(C)$ [36]. It is defined by:

$$S_{tra}(C) = \frac{\sum_1^k S_{tra}(C_j)}{k} \tag{8}$$

Here, k is the number of resulting clusters in C and $S_{tra}(C_j)$ is the intra-cluster similarity for the cluster C_j.

5.2.3 Inter-cluster similarity

It can be quantified via a function of the reciprocals of inter-cluster radii of the clustering centroids. The inter-cluster similarity for one of the possible clustering results C, denoted as $S_{ter}(C)$ [36] is defined by:

$$S_{ter}(C) = \frac{1+k}{1+\sum_1^k dist\left(Centroid_j, Centroid^2\right)} \tag{9}$$

Here, k is the number of resulting clusters in C, $1 = j = k$, $Centroid_j$ is the centroid of the jth cluster in C, $Centroid^2$ is the centroid of all centroids of clusters in C. We compute inter-cluster radius of $Centroid_j$ by calculating dist($Centroid_j$, $Centroid^2$), which is distance between $Centroid_j$, and $Centroid^2$. To smooth the value of $S_{ter}(C)$ and allow for possible all-inclusive clustering result, 1 is added to the denominator and the numerator.

5.2.4 Clustering fitness

The clustering fitness for one of the possible clustering results C, denoted as CF [36], is defined by:

$$CF = \lambda \text{ x } S_{tra}(C) + \frac{1-\lambda}{S_{ter}(C)} \tag{10}$$

Here, λ $(0 < \lambda < 1)$ is an experiential weight, $S_{tra}(C)$ is the intra-cluster similarity for the clustering result C and $S_{ter}(C)$ is the inter-cluster similarity for the clustering result C.

6. Experiments and results

Experimental work has been carried out on the system with Intel(R) Core(TM) i3-5005 U CPU@2.00GHz processor speed, 4GB RAM, Windows 7 OS (64-bit) and using JDK1.7.0_45. Separate modules are written for each of the above discussed methods to observe the CPU time for clustering any dataset by keeping the cluster seeds same for all methods. I/O operations are eliminated and the CPU time observed is strictly for clustering of the data.

Along with the proposed algorithms FPLW and FPLWD for fuzzy perceptron learning, experiments are also conducted with the algorithms PLW, PLWD and FCM for performance comparison. All the algorithms are executed using the benchmark datasets with varying number of patterns to be recognised. In the present work, Magic Gamma, Letter Recognition and Intrusion datasets are used from UCI ML data repository [37]. All the developed algorithms, PLW, PLWD, FCM, FPLW and FPLWD, are executed using these datasets for varying number of patterns to be recognised (k = 10, 11, 12, 13, 14, 15).

All the algorithms operate in an iterative manner and terminate when a stopping condition is met. The stopping condition is when there is no change in the pattern associativity of the data vectors. The termination condition is the same for all the algorithms.

Details of the datasets are available in **Table 1**.

S. No.	Dataset	No. of points	No. of dimensions
1	Magic Gamma data	19,020	10
2	Letter Recognition data	20,000	16
3	Intrusion data	4,94,019	35

Table 1.
Details of datasets.

6.1 Observations with Magic Gamma dataset

The results of all algorithms, using Magic Gamma dataset, with respect to CPU time in seconds, clustering fitness and sum of squared errors are shown in **Figures 2–4**, respectively.

6.2 Observations with Letter Recognition dataset

The results of all algorithms, using Letter Recognition dataset, with respect to CPU time in seconds, clustering fitness and sum of squared errors are shown in **Figures 5–7**, respectively.

6.3 Observations with Intrusion dataset

The results of all algorithms, using Intrusion dataset, with respect to CPU time in seconds, clustering fitness and sum of squared errors are shown in **Figures 8–10**, respectively.

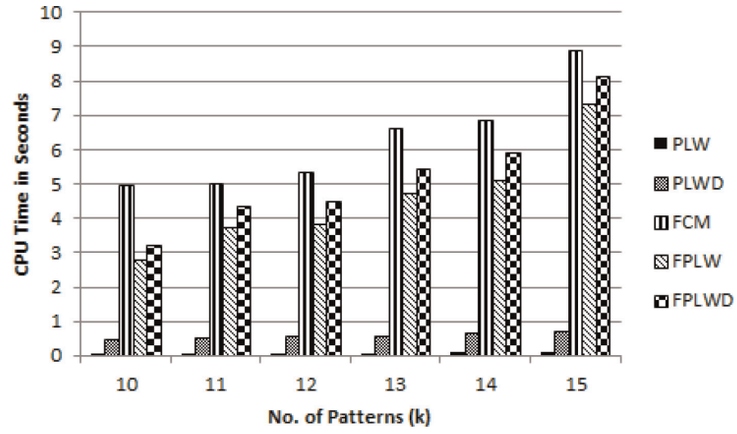

Figure 2.
CPU time of each clustering method (Magic Gamma dataset).

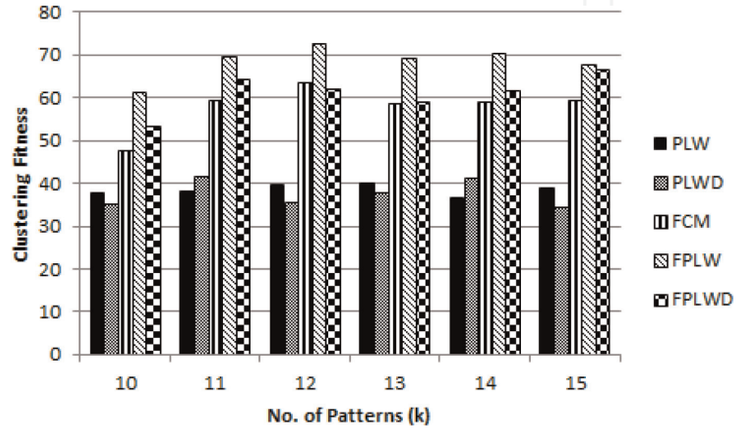

Figure 3.
Clustering fitness of each clustering method (Magic Gamma dataset).

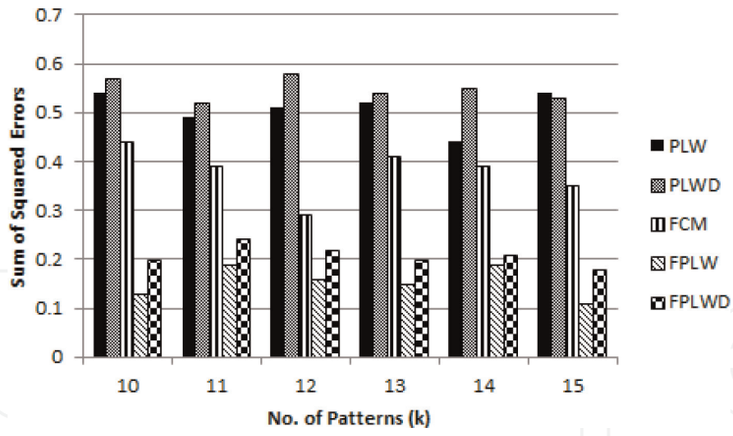

Figure 4.
SSE of each clustering method (Magic Gamma dataset).

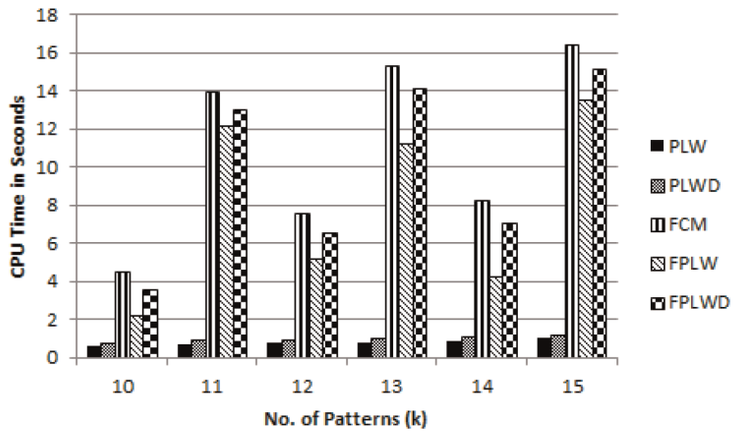

Figure 5.
CPU time of each clustering method (Letter Recognition dataset).

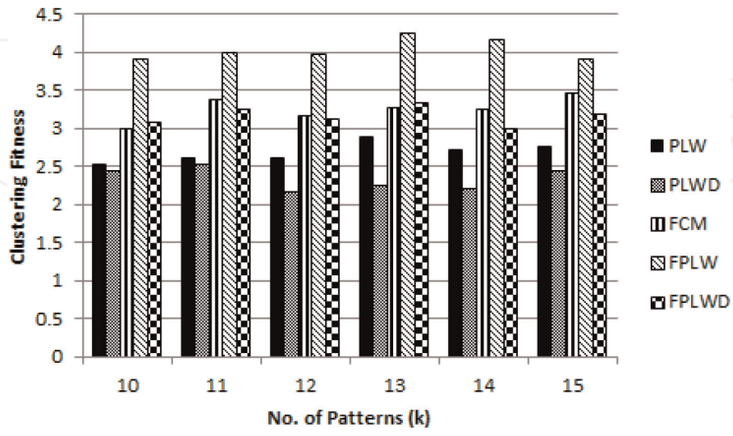

Figure 6.
Clustering fitness of each clustering method (Letter Recognition dataset).

In all the experiments, it is observed that the algorithm FPLW, which implements the perceptron learning using weights and the FCM techniques in an interfusion manner, is showing consistently better performance in terms of clustering fitness (CF) and SSE than the other algorithms.

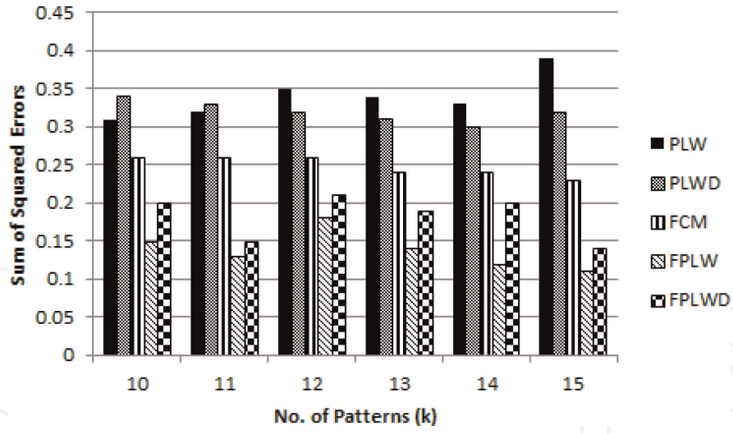

Figure 7.
SSE of each clustering method (Letter Recognition dataset).

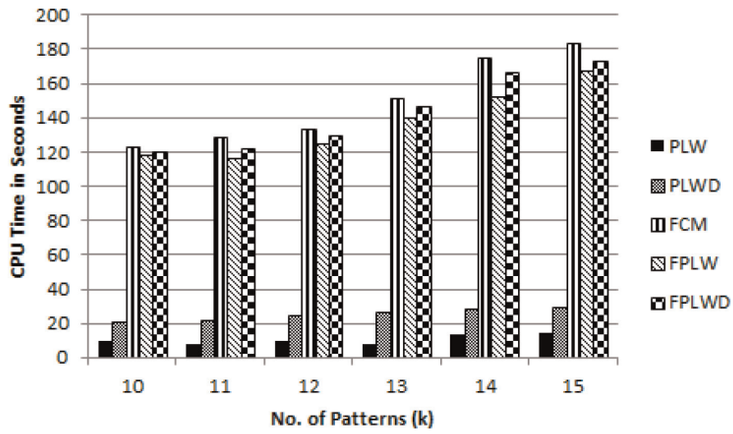

Figure 8.
CPU time of each clustering method (Intrusion dataset).

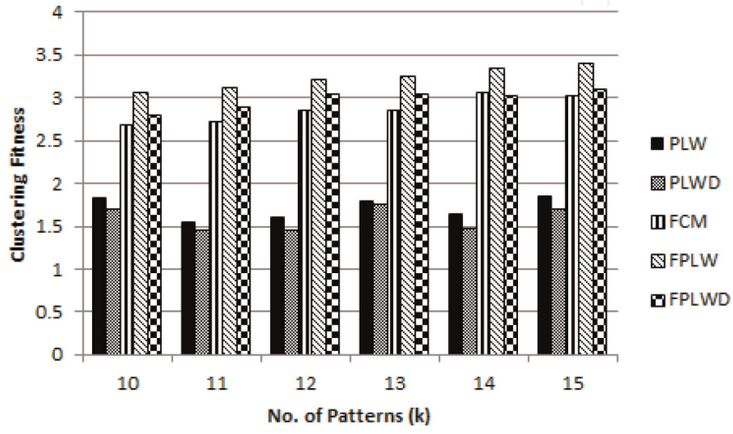

Figure 9.
Clustering fitness of each clustering method (Intrusion dataset).

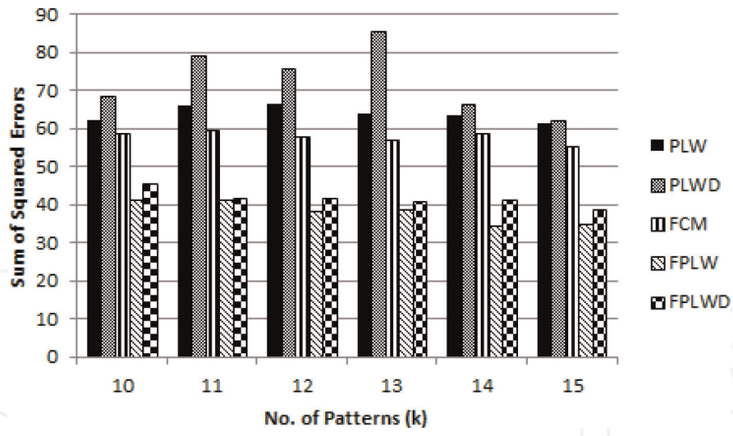

Figure 10.
SSE of each clustering method (Intrusion dataset).

7. Conclusion

The present experiment mainly focuses on the study fuzzy perceptron learning for recognising non-linear patterns in the datasets. Many researchers contributed greatly towards fuzzy perceptron learning. However, their experiments are confined to supervised learning only. So, the present work experimented with the fuzzy perceptron learning approaches for unsupervised learning. The work proposes two new algorithms, that is, FPLW and FPLWD. These algorithms are implemented using three benchmark datasets. Along with these algorithms, the algorithms for standard FCM and perceptron learning using weights and weighted distances are also implemented for performance comparison. For all the algorithms the CPU time in seconds, clustering fitness (CF) and sum of squared errors (SSE) are taken into consideration for performance evaluation. All the developed algorithms are experimented with varying number of patterns (k) to be recognised.

In all the experiments, it is observed that the proposed algorithm for fuzzy perceptron learning using weights (FPLW) is consistently showing better performance with respect to clustering fitness and SSE. Of course, the algorithm FPLW is taking a little more time for its execution than the other algorithms. However, it could be negligible, as the main concern is for clearly recognising the non-linear patterns in the datasets.

Author details

Raja Kishor Duggirala
Department of Computer Science Engineering, Dr. Lankapalli Bullayya College of Engineering, Visakhapatnam, Andhra Pradesh, India

*Address all correspondence to: rajakishor@gmail.com

References

[1] Satapathy SK et al. EEG Brain Signal Classification for Epileptic Seizure Disorder Detection, ScienceDirect, 2019, ISBN 978-0-12-817426-5, DOI: https://doi.org/10.1016/C2018-0-01888-5

[2] Benton WC, Hat R, Raleigh. Machine learning systems and intelligent applications. IEEE Software. 2020;**37**: 43-49. DOI: 10.1109/MS.2020.2985224

[3] Krendzelak M. Machine Learning and Its Applications in e-Learning Systems. Stary Smokovec, Slovakia: IEEE, 2014 IEEE 12th IEEE International Conference on Emerging eLearning Technologies and Applications (ICETA); 2014. pp. 267-269. DOI:10.1109/ICETA.2014.7107596

[4] Sagheer A, Zidan M, Abdelsamea MM. A novel autonomous perceptron model for pattern classification applications. Entropy. 2019;**21**(8):763. DOI: 10.3390/e21080763

[5] Moldwin T, Segev I. Perceptron learning and classification in a modeled cortical pyramidal cell. Frontiers in Computational Neuroscience. 2020. DOI: 10.3389/fncom.2020.00033. https://www.frontiersin.org/articles/10.3389/fncom.2020.00033/full

[6] Leoni Sharmila S, Dharuman C, Venkatesan P. A fuzzy based classification—An experimental analysis, International Journal of Innovative Technology and Exploring Engineering. 2019;**8**(10):4634-4638

[7] Tan Y, Chen S. Pattern recognition based on weighted fuzzy C-means clustering. In: 6th International Congress on Image and Signal Processing (CISP). 2013. pp. 1061-1065. DOI: 10.1109/*CISP*.2013.6745213

[8] Das S, Baruah H. A new kernelized fuzzy C-means clustering algorithm with enhanced performance. Semantic Scholar; 2014. Corpus ID: 212563388

[9] Kulkarni A, Kulkarni N. Fuzzy neural networks for pattern recognition. Procedia Computer Science. 2020;**167**:2606-2616. DOI: 10.1016/j.procs.2020.03.321

[10] Baraldi A, Blonda P, Petrosino A. Fuzzy neural networks for pattern recognition. In: Marinaro M, Tagliaferri R, editors. Neural Nets WIRN VIETRI-97. Perspectives in Neural Computing. London: Springer; 1998. DOI: 10.1007/978-1-4471-1520-5_2

[11] Jamshidi Khezeli YJ, Nezamabadi-pour H. Fuzzy lattice reasoning for pattern classification using a new positive valuation function. Advances in Fuzzy Systems. 2012;**2012**:206121. DOI: 10.1155/2012/206121

[12] Sivanandam SN, Sumathi S, Deepa SN. Introduction to Neural Networks Using Matlab 6.0. India: Tata McGraw Hill; 2008

[13] Nadal J-P, Parga N. Information processing by a perceptron in an unsupervised learning task. Network: Computation in Neural Systems. 1993; **4**(3):295-312. DOI: 10.1088/0954-898X_4_3_004

[14] Haykin S. Neural Networks: A Comprehensive Foundation. 2nd ed. New Delhi, India: Pearson Education; 2007

[15] Nalaie K, Ghiasi-Shirazi K, Akbarzadeh-T M. Efficient implementation of a generalized convolutional neural networks based on weighted Euclidean distance. In: 2017 7th International Conference on Computer and Knowledge Engineering (ICCKE). 2017. pp. 211-216. DOI: 10.1109/*ICCKE*.2017.8167877

[16] Novák V, Perfilieva I, Močkoř J. Mathematical Principles of Fuzzy Logic. Dordrecht: Kluwer Academic; 1999

[17] Zadeh LA. Fuzzy sets. Information and Control. 1965;**8**(3):338-353

[18] Lemiare J. Fuzzy insurance. ASTIN Bulletin. 1990;**20**(1):33-55

[19] Das S. Pattern recognition using fuzzy C-means technique. International Journal of Energy Information and Communications. 2013;**4**(1):1-14

[20] Lu Y, Ma T, Yin C, Xie X, Tian W, Zhong SM. Implementation of the fuzzy C-means clustering algorithm in meteorological data. International Journal of Database Theory and Application. 2013;**6**(6):1-18

[21] Kaltri K, Mahjoub M. Image segmentation by Gaussian mixture models and modified FCM algorithm. The International Arab Journal of Information Technology. 2014;**11**(1):11-18

[22] Bezdek JC, Trivedi M, Ehrlich R, Full WE. Fuzzy clustering: A new approach for geostatistical analysis. International Journal of System Measurement and Decision. 1981;**1**:13-23

[23] Bezdek JC. Feature selection for binary data-medical diagnosis with fuzzy sets. In: Proc. Nat. Comput. Conf. AFIPS Press; 1972. pp. 1057-1068

[24] Cannon RL, Dave JV, Bezdek JC. Efficient implementation of fuzzy C-means clustering algorithm. IEEE Transactions on Pattern Analysis and Machine Intelligence. 1986;**8**(2):248-255

[25] Cannon RL, Jacobs C. Multispectral pixel classification with fuzzy objective functions. Technical Report CAR-TR-51. College Park: Center for Automation Research, University of Maryland; 1984

[26] Gong M, Liang Y, Ma W, Ma J. Fuzzy C-means clustering with local information and kernel metric for image segmentation. IEEE Transactions on Image Processing. 2013;**22**(2):573-584

[27] Krinidis S, Krinidis M, Chatzis V. Fast and robust fuzzy active contours. IEEE Transactions on Image Processing. 2010;**19**(5):1328-1337

[28] Yong Y, Chongxun Z, Pan L. A novel fuzzy C-means clustering algorithm for image thresholding. Measurement Science Review. 2004;**4**(1):11-19

[29] Hanesch M, Scholger R, Dekkers MJ. The application of fuzzy C-means cluster analysis and non-linear mapping to a soil data set for the detection of polluted sites. Physics and Chemistry of the Earth, Part A. 2001;**26**(11–12):885-891

[30] Ghosh S, Dubey SK. Comparative analysis of K-means and fuzzy C-means algorithms. International Journal of Advanced Computer Science and Applications. 2013;**4**(4):35-39

[31] Klir GJ, Yuan B. Fuzzy Sets and Fuzzy Logic: Theory and Applications. India: Prentice Hall of India Private Limited; 2005

[32] Bezdek JC, Ehrlich R, Full W. FCM: The fuzzy C-means clustering algorithm. Computers and Geosciences. 1984;**10**(2–3):191-203

[33] Auephanwiriyakul S, Dhompongsa S. An investigation of a linguistic perceptron in a nonlinear decision boundary problem. In: 2006 IEEE International Conference on Fuzzy Systems. 2006. pp. 1240-1246

[34] Yang J, Wu W, Shao Z. A new training algorithm for a fuzzy perceptron and its convergence. In: Advances in Neural Networks—ISNN 2005, Second

International Symposium on Neural Networks, Chongqing, China; May 30–June 1 2005

[35] Han J, Kamber M. Data Mining Concepts and Techniques. 2nd ed. San Francisco, CA: Morgan Kaufmann Publishers, An Imprint of Elsevier; 2007

[36] Han X, Zhao T. Auto-K dynamic clustering algorithm. Journal of Animal and Veterinary Advances. 2005;**4**(5): 535-539

[37] Lichman M. UCI Machine Learning Repository. 2013. Available from: http://archive.ics.uci.edu/ml

Paper Id: 1154

Implementation of a Smart Intelligent Digital Home Lightning Control System

B.D. Sireesha[1] & K. Anuradha[2]

[1] Department of ECE, SVCET, Chittoor, A.P., India.

[2] Department of CSE, L.B.College of Engineering, Vishakhapatnam, AP, India.

Abstract: This paper introduces the digital home lighting control system (DHLS), with a low cost Smart building power management Architecture to suit diverse Indian market. A review on Smart Home automation research and market has been presented. Further low cost energy meters to update the customers about the billing and usage the system is developed through ARM micro-processor and wireless communication technology and network technology is proposed. In this proposed system, a more efficient home energy management system is introduced to reduce power consumption in home. The room has power outlets, a light, and ZigBee transceivers. The ZigBee hubs in each room communicate with the home server and report the power consumption information to the home server. According to the control commands, the home can be controlled automatically from the home server. Load sharing information can also be displayed on the home server.

Keywords: DHLS, ARMProcessor, Zigbee Wireless Communication, Home Server, Load Sharing.

I. INTRODUCTION

In India, Smart Power management/ Home automation is perceived to be a necessary. Thus for serving over 1.2 billion public low cost oriented should be the main aim. The entire system cost for smart power management faces a barrier for the large scale deployment by distribution utilities in India. In order to avoid this, in the Indian Smart Grid Task Force is working on developing a low-cost basic smart Power Management meter. This paper presents one such effort and paves a way for further research. As more and more home appliances and consumer electronics are deployed, power consumption in home area tends to grow. Although advanced integrated circuit (IC)chipset and hardware technology enhances the power efficiency of home appliances and consumer electronics, the current energy crisis and green house effect require more efficient energy management in all areas. In this proposed system, we have designed architecture with effective power management in the home section, which can be controlled by a home server.

In this paper, we propose more efficient DHLS based on ZigBee communication and ARM processor. To implement the automatic standby power cut-off outlet with power measurement function. The home server is designed to collect the information from the control section and at the same time the consumed power will be displayed in the control section itself. In this architecture, we proposed a clear management system, which is having an priority based control system. This is nothing but, when the server sends the command signal then the unit will go to the particular priority mode. So that wastage of power will be prevented. This in turns create an automatic power reduction. In the fig.1, the proposed architecture of DHLS is shown.

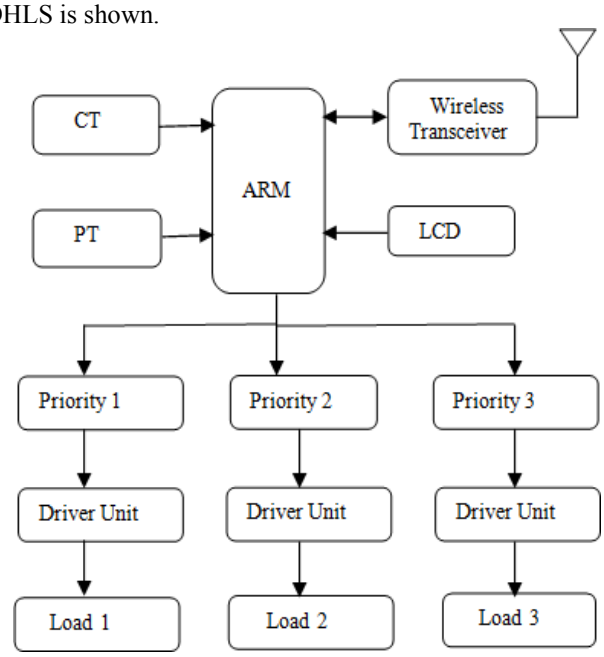

Fig.1. Proposed DHLS architecture.

II.DESIGN AND IMPLEMENTATION

The proposed architecture uses an ARM processor as a core. To the processor the power management priority settings will be programmed. Current transformer and the potential transformer will calculate the power factor and it will be given to the processor continuously. This information will be processed by the processor and it will calculate the amount for that consumed power. For easy understanding this information will be displayed on the device itself. This unit will also have a priority based load sharing in order to manage the power usage. This priority levels will be turned on or turned off according to the interrupts generated by the home server section. So that an automatically power consumption method will be implemented in the home section. The DHL system is

connected to the wireless communication section. Here, ZigBee is used as a network technology. ZigBee is a transceiver it can be attached to the processor section and to the home server section.

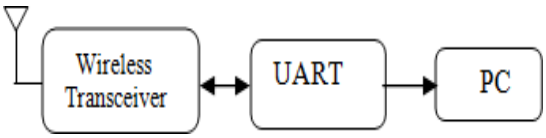

Fig.2. Home server section.

The home server section is shown on Fig.2. In this part, the ZigBee module is interfaced on a server which will collect the continuous data from the DHLS. The amount level will also be displayed on the server part. So that a user can give control signals according to those consumption. When a control signal is generated, this information will be send to the processor. Then the processor will check the interrupt and then according to the program the particular priority setup will be activated in the home section. This will avoid unwanted power usage in home section.

III. OVERVIEW OF THE DHLS SYSTEM

This system uses ARM processor as a core and wireless sensor network communication as a transmission medium for the data transfer. This DHLS consists of two important sections. One is DHL device section and the other one is Home server. These two devices will be interlinked with the help of ZigBee wireless communication. The processor will be connected to the CT and PT which in turns separate the voltage level and current level to the processor. According to the written program the processor will calculate the power factor and its corresponding amount will be displayed on the device. An interrupt based priority control is introduced in order to achieve the effective home lighting with power saving. Through the WSN, the consumption detail will be send to the home server section. In the home server section, every option will be available. So, according to the use selection, a unique will be send to the processor core via ZigBee communication. The processor receives that signal and check with the program and then automatically, the corresponding priority levels will come to activation which in turns controls the power consumption.

IV.SYSTEM HARDWARE

A. ARM Processor

The ARM7 family includes the ARM7TDMI, ARM7TDMI-S, ARM720T, and ARM7EJ-S processors. The ARM7TDMI core is the industry's most widely used 32-bit embedded RISC microprocessor solution. Optimized for cost and power-sensitive applications, the ARM7TDMI solution provides the low power consumption, small size, and high performance needed in portable, embedded applications. The ARM7TDMI core uses a three-stage pipeline to increase the flow of instructions to the processor. This allows multiple simultaneous operations to take place and continuous operation of the processing and memory systems.

Operating Modes: The ARM7TDMI core has seven modes of operation:

- User mode is the usual program execution state.
- Interrupt (IRQ) mode is used for general purpose interrupt handling.
- Supervisor mode is a protected mode for the operating system.
- Abort mode is entered after a data or instruction pre fetch abort.
- System mode is a privileged user mode for the operating system.
- Undefined mode is entered when an undefined instruction is executed.

The interrupt setting of ARM supports the DHLS to response to the interrupt coming from the server section.

Interrupt Controller: The Vectored Interrupt Controller (VIC) accepts all of the interrupt request inputs from the home server section and categorizes them as Fast Interrupt Request (FIQ), vectored Interrupt Request (IRQ), and non-vectored IRQ as defined by programmable settings. So DHLS system can able to separate the command signals and easily will select the priority. The programmable assignment scheme means that priorities of interrupts from the various peripherals can be dynamically assigned and adjusted. Fast interrupt request (FIQ) has the highest priority. If more than one request is assigned to FIQ, the VIC combines the requests to produce the FIQ signal to the ARM processor. The fastest possible FIQ latency is achieved when only one request is classified as FIQ, because then the FIQ service routine does not need to branch into the interrupt service routine but can run from the interrupt vector location. If more than one request is assigned to the FIQ class, the FIQ service routine will read a word from the VIC that identifies which FIQ source(s) is(are) requesting an interrupt.

Vectored IRQs have the middle priority. Sixteen of the interrupt requests can be assigned to this category. Any of the interrupt requests can be assigned to any of the 16 vectored IRQ slots, among which slot 0 has the highest priority and slot 15 has the lowest. Non-vectored IRQs have the lowest priority. The VIC combines the requests from all the vectored and non-vectored IRQs to produce the IRQ signal to the ARM processor. The IRQ service routine can start by reading a register from the VIC and jumping there. If any of the vectored IRQs are pending, the VIC provides the address of the highest-priority requesting IRQs service routine, otherwise it provides the address of a default routine that is shared by all the non-vectored IRQs. The default routine can read another VIC register to see what IRQs are active.

B. Current Transformer

A current transformer (CT) is a type of instrument transformer designed to provide a current in its secondary winding proportional to the alternating current flowing in its primary. They are commonly used in metering and protective relaying in the electrical power industry where they facilitate the safe measurement of large currents, often in the presence of high voltages. The current transformer safely isolates measurement and control circuitry from the high voltages typically present on the circuit being measured. After measuring this information will be send to the processor.

C. Potential Transformer

PTs or VTs are the most common devices used. These devices are conventional transformers with two or three windings (one primary with one or two secondary). They have an iron core and magnetically couple the primary and secondary. The high side winding is constructed with more copper turns than the secondary(ies), and any voltage impressed on the primary winding is reflected on the secondary windings in direct proportion to the turns ratio or PT ratio.

D. UART Communication

Serial data communication uses two methods, asynchronous and synchronous. The synchronous method transfers a block of data (characters) at a time while the asynchronous transfers a single byte at a time. It is possible to write software to use either of these methods, but the programs can be tedious and long. For this reason, there are special IC chips made by many manufacturers for serial data communications. These chips are commonly referred to as UART (Universal Asynchronous Receiver-Transmitter) and USART (Universal Synchronous-Asynchronous Receiver-Transmitter). The ARM chip has a built-in UART.

E. Data Transfer Rate

The rate of data transfer in serial data communication is stated in bps (bits per second). Another widely used terminology for bps is baud rate. The baud rate used in this DHLS for data transmission is 9600.

F. RS232 Standards

RS232 is the most widely used serial I/O interfacing standard. This standard is used in PCs and numerous types of equipment. However, since the standard was set long before the advent of the TTL logic family, its input and output voltage levels are not TTL compatible. In RS232, a 1 is represented by -3 to -25V, while a 0 bit is +3 to +25V, making -3 to +3 undefined. For this reason, to connect any RS232 to a microcontroller system we must use voltage converters such as MAX232 to convert the TTL logic levels to the RS232 voltage level, and vice versa. MAX232 IC chips are commonly referred to as line drivers.

G. Max3232

MAX3232 is compatible with RS-232 standard, have dual transceiver. Each receiver converts TIA/EIA-232-E levels into TTL/CMOS levels. Each driver converts TTL/CMOS levels into TIA/EIA-232-E levels. The MAX3232 is characterized for operation from -40°C to +85°C for all packages.MAX3232 is purposed for application in high-performance information processing systems and control devices of wide application.

H. Zigbee Module

The XBee/XBee-PRO RF Modules are designed to operate within the ZigBee protocol and support the unique needs of low-cost, low-power wireless sensor networks. The modules require minimal power and provide reliable delivery of data between remote devices. The modules operate within the ISM 2.4 GHz frequency band.

Key Features:

- **High Performance, Low Cost**
  - Indoor/Urban: up to 300' (100 m)
  - Outdoor line-of-sight: up to 1 mile (1.6 km)
  - Transmit Power Output: 100 mW (20 dBm) EIRP
  - Receiver Sensitivity
- **Low Power**
  - TX Current: 295 mA (@3.3 V)
  - RX Current: 45 mA (@3.3 V)
  - Power-down Current: < 1 µA @ 25oC

I. Mounting Considerations

The XBee modules were designed to mount into a receptacle (socket) and therefore do not require any soldering when mounting it to a board. The XBee-PRO Development Kits contain RS- 232 and USB interface boards which use two 20-pin receptacles to receive modules. Fig.3 XBee-PRO Module Mounting to an RS-232 InterfaceBoard.

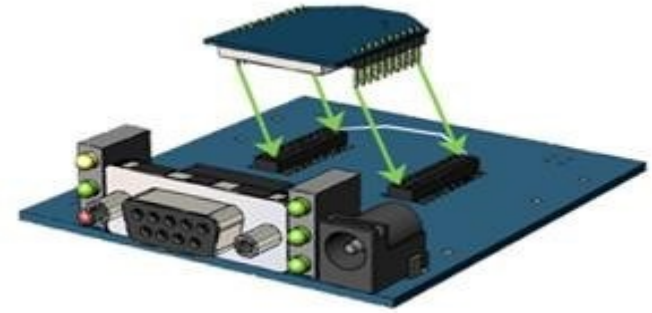

Fig.3. Mounting the Zigbee module.

J. UART Data Flow

Devices that have a UART interface can connect directly to the pins of the Zigbee module as shown in the fig.4 below.

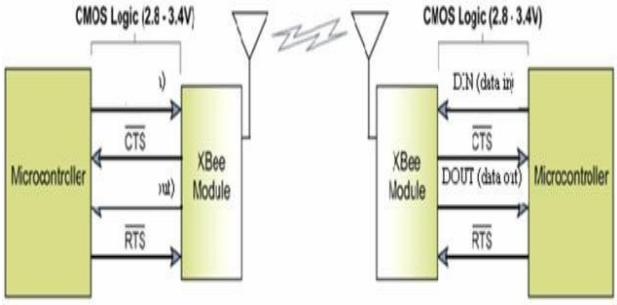

Fig.4. Zigbee UART Dataflow.

The XBee modules maintain small buffers to collect received serial data, which is illustrated in the figure below. The serial receive buffer collects incoming serial characters and holds them until they can be processed. The serial transmit buffer collects data that is received via the transceiver that will be transmitted out to the UART. So, the Zigbee can do the transceiver operation.

K. LCD Display Module

Liquid crystal displays (LCDs) have materials which combine the properties of both liquids and crystals. Rather than having a melting point, they have a temperature range

within which the molecules are almost as mobile as they would be in a liquid, but are grouped together in an ordered form similar to a crystal.

V. SYSTEM SOFTWARE

A. VB Platform

In this system we are using a home server section to monitor the power consumption to control the lighting system on the priority basis. This output will be displayed on the computer screen using visual basic software.

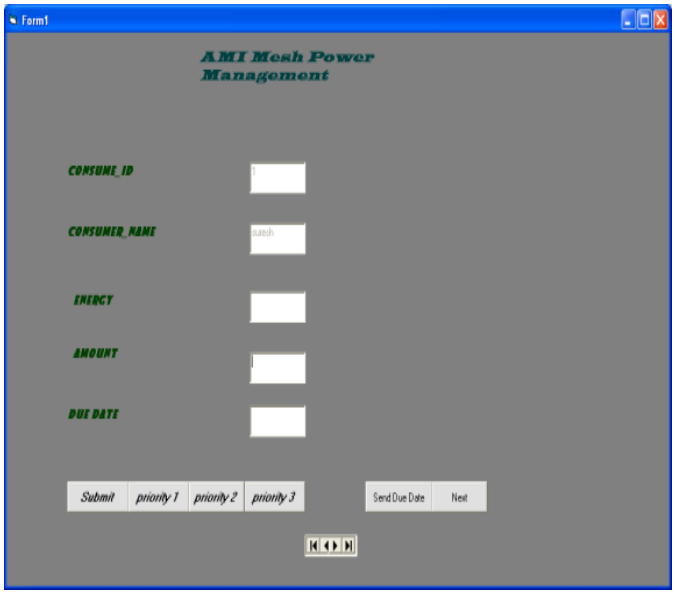

Fig.5.DHLS control screen.

The above fig.5 shows the DHLS monitor and control section. The controlling person can monitor the current power consumption at the same time according to the requirement we can control the lighting system.

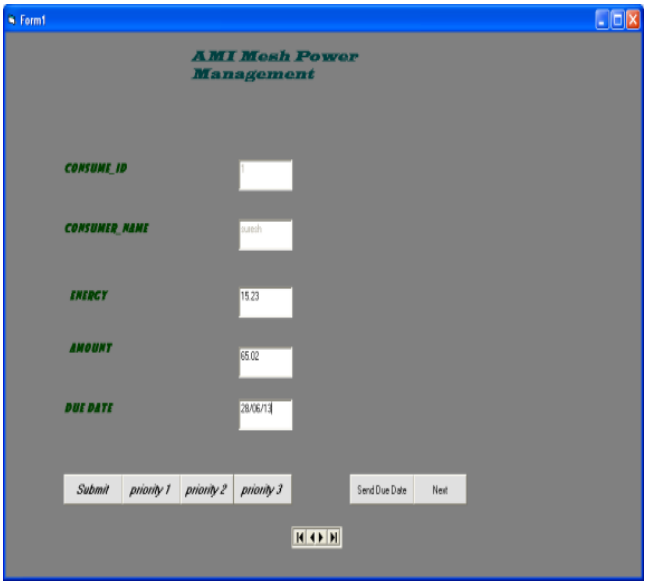

Fig.6. DHLS control screen data display.

The DHLS display window has the feasibility to show the amount and energy consumption as shown in Fig.6. The hardware system will calculate the power factor by values coming from CT and PT. Then according to the program the amount will be calculated. Through UART communication this data will transfer to PC. This type of data display will be useful for all class of users. In that screen itself different options will be available. According to the inputs different commands will be generated and it will be transferred to the ARM Processor through the UART communication. The processor will compare these interrupt commands with the program and it will do the pre defined operation.

Design Flow Chart: The flow chart of the DHLS is shown below Fig.7 with all the functional blocks. The step by step working of the hardware is given in the functional blocks.

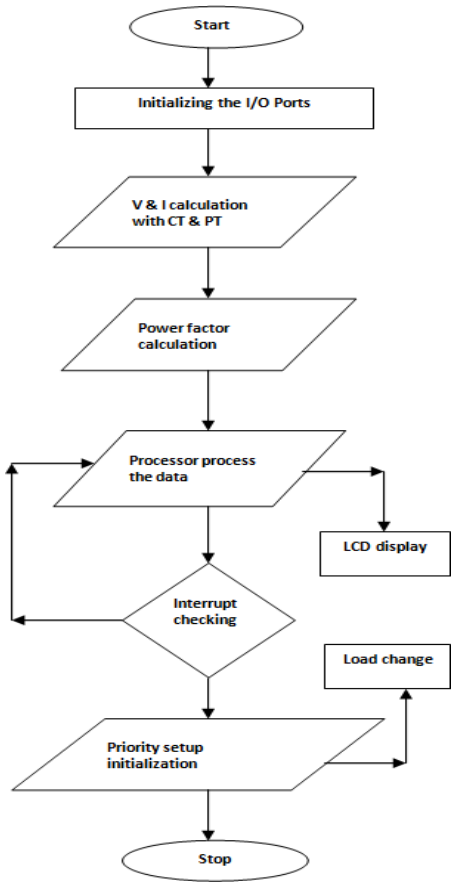

Fig.7. Flowchart of DHLS platform.

VI. CONCLUSION

Power consumption is an essential need in the day to day life. In order to make the power saving DHLS is playing an effective role to bring the power wastage factor in control. In this system, display section is kept in the device in a visible manner. At the same time the controlling person also can see the energy and amount value through the home server. Then according to the requirements the control commands will be passed to the DHLS device which will turn on or off the load with respect to the priority. Thus the power can be managed in an efficient way.

VII. REFERENCE

[1]José A. Gutierrez, Edgar H. Callaway, Raymond L. Barnett, "LowRate Wireless Personal Area Networks, Enabling Wireless Sensorswith IEEE 802.15.4," IEEE Press, Nov. 2003, ISBN 0-7381-3557-7,2004.

[2]General Electric Company, “Energy Efficiency Comparisons of Wireless Communication Technology Options for Smart Grid Enabled Devices,” Dec. 2010.
[3]Yuan-Jen Chang and Wen-Tzeng Huang, "A Novel Design ofData-Driven Architecture for Remote Monitoring and RemoteControl of Sensors over a Wireless Sensor Network and the Internet",Journal of Internet Technology, Vol. 12 No. 1, P.129-137, January2011.
[4]Megalingam, R.K.; Krishnan, A.; Ranjan, B.K.; Nair A.K.; , "Advanceddigital smart meter for dynamic billing, tamper detection and consumer awareness," Electronics Computer Technology (ICECT), 2011 3rdInternational Conference on , vol.4, no., pp.389-393, 8-10 April 2011
[5]Rahman, M.M.; Mto, A.; , "Technologies required for efficient operationof a smart meter network," Industrial Electronics and Applications(ICIEA), 2011 6th IEEE Conference on , vol., no., pp.809-814, 21-23June 2011 [3] Grütz, A.: Jahrbuch Elektrotechnik ’98,Berlin · Offenbach: VDE VERLAG, 1997.
[6]Depuru, S.S.S.R.; Lingfeng Wang; Devabhaktuni, V.; Gudi, N.; , "Smart meters for power grid —Challenges, issues, advantages and status," Power Systems Conference and Exposition (PSCE), 2011 IEEE/PES , vol., no., pp.1-7, 20-23March,2011K.
[7]Shang-Wen Luan; Jen-Hao Teng; Shun-Yu Chan; Lain-Chyr Hwang; ,"Development of a smart power meter for AMI based on ZigBee communication," Power Electronics and DriveSystems, 2009. PEDS 2009. International Conference on , vol., no., pp.661-665, 2-5 Nov. 2009
[8] Hyun Sang Cho; Yamazaki, T.; Minsoo Hahn; Determining location of appliances from multi-hop tree structures of power strip type smart meters," Consumer Electronics, IEEE Transactions on , vol.55, no.4, pp.2314-2322, November 2009
[9]Kamat, Vithal N.; , "Enabling an electrical revolution using smart apparent energy meters & tariffs," India Conference (INDICON), 2011Annual IEEE , vol., no., pp.1-4, 16-18 Dec. 2011
[10]Khalifa, T.; Naik, K.; Nayak, A.; , "A Survey of Communication Protocols for Automatic Meter Reading Applications," Communications Surveys & Tutorials, IEEE , vol.13, no.2, pp.168-182, Second Quarter 2011 Khalifa, T.; Naik, K.; Nayak, A.; , "A Survey of Communication Protocols for Automatic Meter Reading Applications," Communications Surveys & Tutorials, IEEE , vol.13, no.2, pp.168-182, Second Quarter 2011.
[11]National Energy Technology Laboratory (2007-08) (PDF). “NETL Modern Grid Initiative - Powering Our 21st-Century Economy,” United States Department of Energy Office of Electricity Delivery and Energy Reliability. p. 17. Retrieved 2008-12-06.

e-Book

e-ISBN: 978-81-952843-9-9

Proceedings of Online International Conference on

SWARDAM-2021

8-9 March, 2021

Sustainable Water Resources Development and Management

Sponsored by

Technical Education Quality Improvement Programme (TEQIP Phase-III)

In Association with

Indian Society for Hydraulics
(Aurangabad Local Centre)

Indian Water Resources Society
(Aurangabad Local Centre)

Ujjain Engineering College, Ujjain, (M.P.)
(Under TEQIP-III-Twinning Activity)

Editors

Dr. D.G. Regulwar
Dr. U.J. Kahalekar
Dr. R.V. Shetkar
Dr. G.K. Patil

ORGANIZED BY

Department of Civil Engineering
GOVERNMENT COLLEGE OF ENGINEERING
Aurangabad – 431 005, Maharashtra, India
(An Autonomous Institute of Government of Maharashtra)

13. **Green Roofs: A Review of Performance and Limitations**
S.G. Taji, P.R. Ikhar, A.P. Keskar and D.G. Regulwar 71

14. **Water Quality of Rain Water Collected on the Terrace of a Building of Mangaluru City, West Coast of India**
Jithin Jose, A. Naveen Kumar, B.R. Manjunatha, R. Rajesha, M. Gune, K. Balakrishna, K.N. Krishnakumar and Aarif Ahmed 79

15. **Deriving Annual Erosivity Equation for Manasbal Lake Catchment using Data Analysis in Python**
Syed Bakhtawar Bilal and Owais Nazir 86

16. **Evaluation of the Basin Characteristics of Galma and Kubanni Catchments**
Shehu Gambo, Abubakar Isma'il, Abdullahi Umar, Abdulrahman Shu'aibu and A.D. Bello 93

17. **Investigations of Ground Water Potential Zones using RS and GIS**
Shriman N. Jirapure and K.A. Patil 100

18. **Determination of Crop Water Requirement and Irrigation Scheduling using CROPWAT and GIS**
Priyanka S. Misal and D.G. Regulwar 108

19. **GIS Approach in Demarcating Groundwater Potential Zones—A Case Study in Visakhapatnam District, A.P.**
I. Siva Parvathi, Arunima Mahapatra and B. Chiranjeevi 116

20. **Preparations of Hydrological Parameters of HRU's by using ArcGIS with SWAT Interface**
Kapil K. Gitte and D.G. Regulwar 124

21. **Case Study on Change in Surface Water Dynamics of Chambal River Basin using GEE and ARCGIS**
Harsh Raj Singh Sisodiya and Sandeep Narulkar 125

22. **Application of Soil Water Assessment Tool (SWAT) for Hilly Region of Tons River Basin**
Aradhana Thakur, Anupma Sharma and L.N. Thakural 136

23. **Correlation Assessment of Water Balance Parameters using SWAT Model for Upper Girna Sub-Catchment in Tapi Basin, India**
Prabhat Dwivedi, Lalit Kumar Gehlot and P.L. Patel 137

24. **A Solution to the Groundwater In verse Problem, Considering a System of Wells**
Nikolaos Nagkoulis 144

25. **Runoff Simulation of a Basin using MIKE11 NAM and AWBM Model**
Ankit Balvanshi and H.L. Tiwari 145

26. **Understanding the Impact of Seawater Intrusion and Anthropogenic Activities on Groundwater Quality of Coastal Districts of South Gujarat, India**
Chandrashekhar Bhagat, Mukul Puri, Pranab Kumar Mohapatra and Manish Kumar 152

27. **Ground Water Quality Modeling using Visual Modflow: A Review**
P. Aravind, S. Selvakumar, G. Thiyagarajan, Balaji Kannan and K. Boomiraj 154

GIS Approach in Demarcating Groundwater Potential Zones—A Case Study in Visakhapatnam District, A.P.

Dr. I. Siva Parvathi[1], Er. Arunima Mahapatra[2] and Mr. B. Chiranjeevi[3]

[1]Associate Professor, Department of Civil Engineering, Andhra University College of Engineering (A), Viskhapatnam–530003, India

[2]Assistant Professor, Department of Civil Engineering, Dr. L. Bullayya College of Engineering, Viskhapatnam–530013, India

[3]PG Student, Department of Civil Engineering, Andhra University College of Engineering(A), Viskhapatnam–530003, India

E-mail: [1]isparvathi@gmail.com

Abstract—*An ever-growing demand for freshwater has been driven by an increasing global population, along with more intensive agriculture and increasing industrial use. It is also important not only for targeting but also as a valuable resource to monitor and protect potential groundwater areas. Groundwater potential zones are commonly delineated using GIS tools. To identify the groundwater potential zones, twelve mandals in the Visakhapatnam district are selected as a case study. Geospatial data are being used in this research to measure the groundwater state of the field of study. The extent of land use land cover (LULC) in the study area was represented using nine categories. Different landscape parameters, such as geomorphology, geology, lineament, slope, drainage, LULC using satellite imagery and GIS methods, have been interpreted. These thematic layers were overlaid and multiplied with allocated weightage values to obtain a final weight map. The final map was integrated using the index overlay method following the multi- class map technique. The map was categorized using the groundwater index value into four groundwater potential zones and their distributions are very good, good, moderate, and poor. Theresults were found to be useful in enhancing groundwater resource strategy and management.*

Keywords: *GIS, Remote Sensing, Groundwater, Geology, Geomorphology, Lineaments, Potential zones.*

INTRODUCTION

Groundwater is the greatest freshwater supply on earth accessible to mankind. The water sourcesavailable do not meet the numerous residential, agricultural, and industrial needs of human beings due to the exponential population growth. Groundwater is used for drinking by about half of the urban population and more than 80% of the rural population[1]. Precipitation and streamflow (influent filtration) are the fundamental principles of groundwater recharge [2].Although underground freshwater is the largest supply available, the control and preservation of this critical resource have become important. Aircraft or satellite remote sensing data has becomean increasingly useful instrument for understanding the state of subsurface water [3]. For the selection of potential artificial recharge sites, [4] provides delineated prospective groundwater zones with the help of the weighted overlay method along with the boolean logic process.Several authors used a hydro-geomorphic approach based on GIS to identify areas conducive to the implementation and development of site suitability techniques for artificial recharge of the groundwater ([5],[6],[7],[8],[9]). In groundwater studies, particularly in hard rocks, lineaments have been observed to be significant. Remote sensing in combination with GIS has proved to be very useful in evaluating groundwater capacity ([10],[11],[12],[13],[14]). In morphometric research, remote sensing techniques are presented and approaches to groundwater analysis using satellite imaging have proved to be an effective tool ([15],[16]). Over-exploration of groundwater to satisfy the ever-increasing population's domestic needs leads to degradation ofthe groundwater, particularly during

summer, alarmingly and dramatically decreasing the yields of wells in urban areas. When most of the rainfall in the urban area goes as surface runoff and does not settle into the land due to growing construction activities of buildings and highways, this issue is further aggravated. For the present analysis, twelve mandals in the Visakhapatnam district are chosen to identify groundwater potential zones. An attempt is made to analyze and assess the groundwater potential, as well as to map the location to find a suitable solution to the current problems.

STUDY AREA

The selected research area is present in the Visakhapatnam district, Andhra Pradesh, India. Twelve mandals such as Modugula, Ravikamatam, Buchayapeta, Rolugunta, Makavarapalem, Kasimkota, Munagapaka, Golugonda, Narsipatnam, Kotauratla, Yalamanchili, are chosen for theanalysis of groundwater potential zones in the Visakhapatnam district. The research area is located between 180-8' and 170-24'N latitude and 820-59' and 820-18'E longitude with an area of2049.7 km2 as shown in Fig. 1. It is bounded partly by the Orissa state and partly by the Vizianagaram district. The area of research consists of numerous forms of classification of built- up area, reserve forest, current fallow, slope, plantation, vegetation, water bodies, and others.

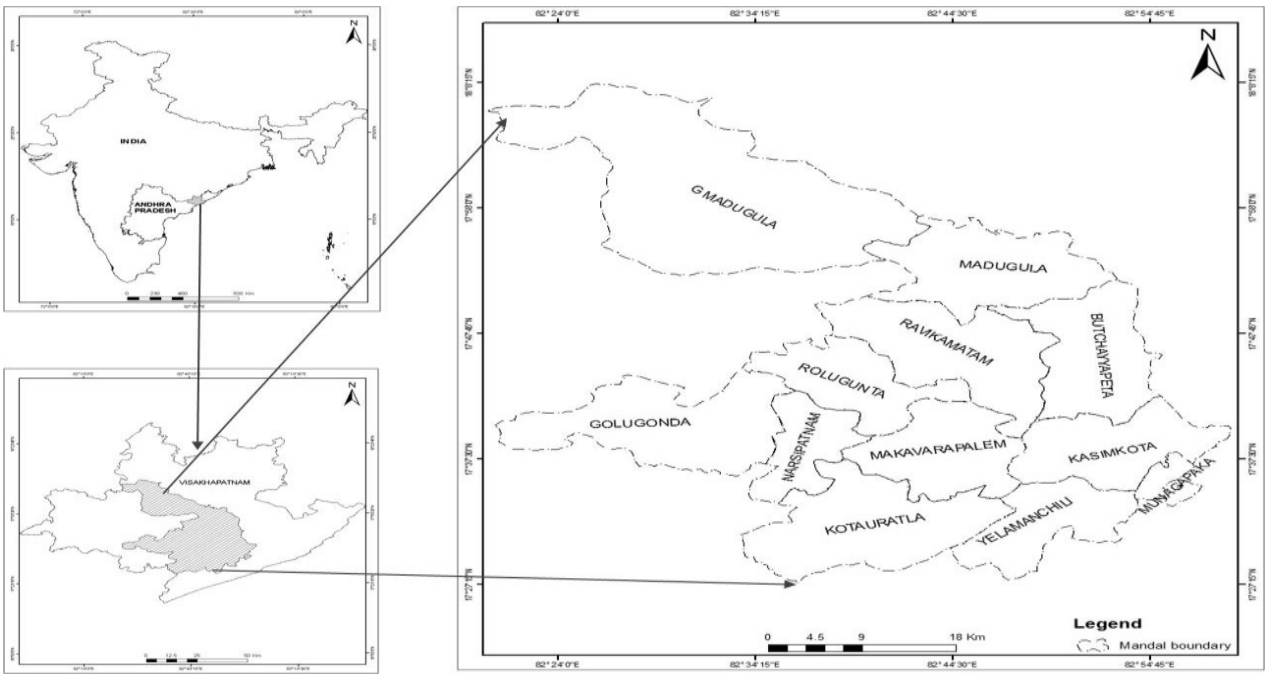

Fig. 1: Map Location of the Study Area [17]

METHODOLOGY

IRS-1D-LISS-III digital satellite imagery from December 2000 and IRS-P6-LISS III data from 2010 were used in this study[18]. Survey of India toposheets of 65j12, 65j8, 65k10, 65k11, 65k13, 65k14, 65k15, 65k5, 65k6, 65k9 on 1:50,000 scale are considered [19]. LULC of 2010 data has been prepared for the study area. Specific site investigations are also undertaken in the areas where the change is detected in parameters like LULC, geomorphology, geology, drainage pattern, road network. Fig. 2 represents the phases included in the GIS analysis of the current research.

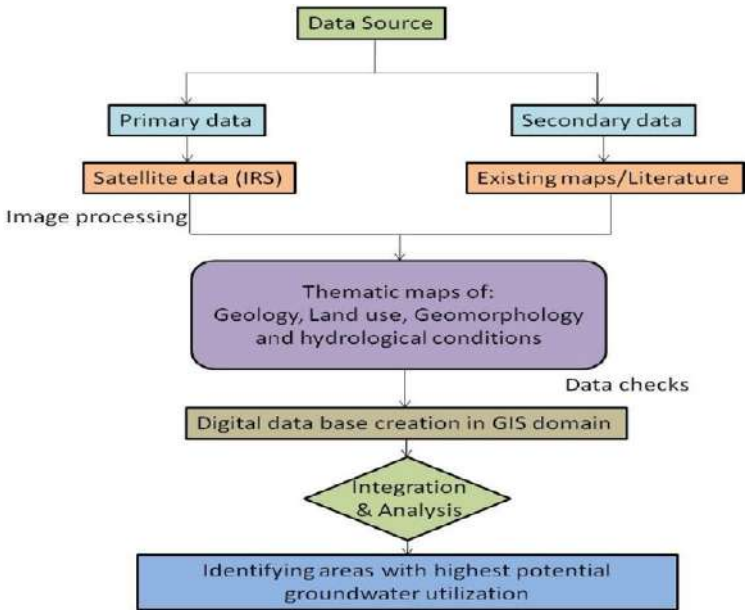

Fig. 2: Phases Included in GIS Analysis

RESULTS AND DISCUSSIONS

Advanced remote sensing and GIS techniques have been used to identify potential zones of groundwater in the selected twelve mandals of the Visakhapatnam district. For the presentstudy, thematic maps such as LULC, geology, lineaments, geomorphology, slope, and drainageare developed. The groundwater potential zones are obtained using the Arc GIS 9.3[20] by overlaying geology, geomorphology, lineaments, slope, and LULC maps as part of the Index Overlay System with a Multi-Class map.

DRAINAGE MAP

The stream ordering strategy is used to classify the specific stream segments into differentorders based on their importance and contribution to the drainage pattern[21]. The first-order stream is a single stream shown as 1, the second-order stream is formed by joining two first- order streams shown as 2, the third-order stream is formed by joining two second-order streams shown as 3, and the fourth-order stream is formed by joining two third-order streams as shownin Fig. 3. In the study area, the total length of the drainage network calculated using Arc GIS is 4714.8 km. The first order, second order, third order, fourth-order, and fifth-order drainage systems being 2917.3km, 1069.3km, 484.22 km, 189.92 km, 53.72 km long respectively. The bar chart of drainage pattern is depicted in Fig.4 which is represented in percentage.

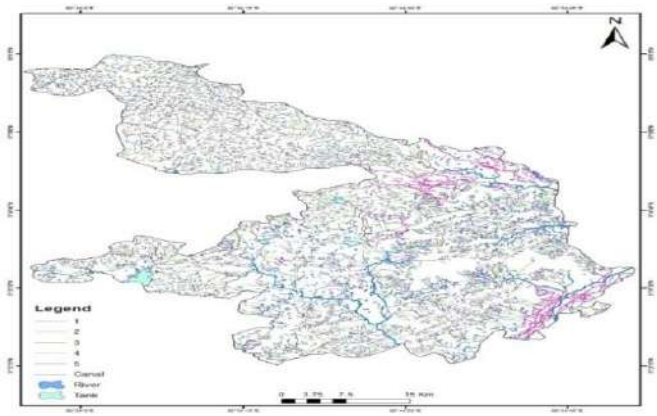

Fig. 3: Drainage Pattern of the Area

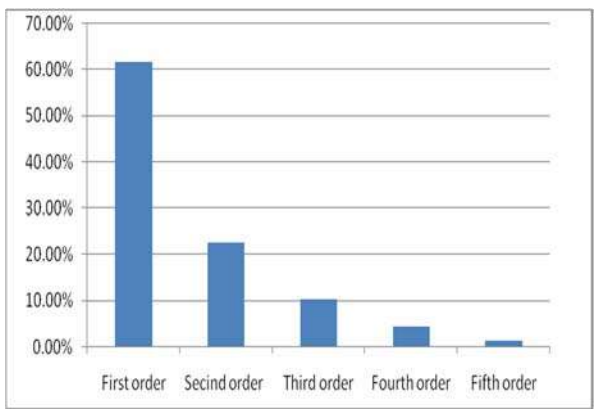

Fig. 4: Bar Chart of Drainage Pattern

GEOLOGICAL STUDIES

In groundwater occurrence, distribution and consistency, geological research is essential. The field of research consists of abundant high-grade metamorphic and igneous rocks. The geology map is shown in Fig.5, and the bar chart of geological characteristics from the present analysis is shown in Fig. 6. The proportion of Khondalite in the region is half that of the other geological features. The Khondalite spread in the study area is 1238.90 km2 with a coverage of 51.41%.The flood plain area is 26.90 km2 with a coverage of 1.11%. The Migmatite spread in the study area is 542.44 Km2 and its percentage is 22.51%.

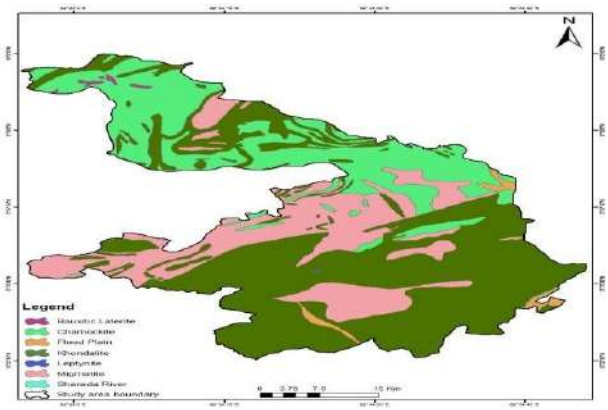

Fig. 5: Geology Map of the Study Area

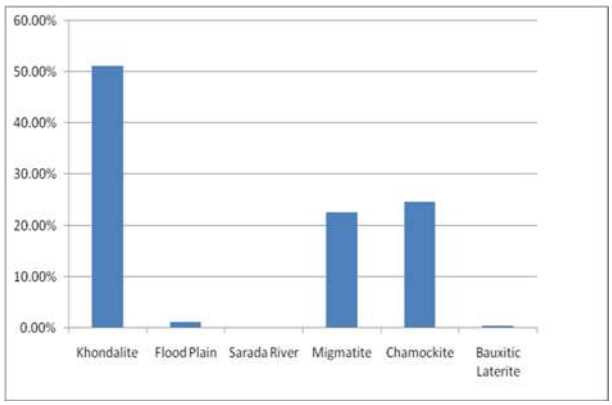

Fig. 6: Bar Chart of Geological Features

SOIL & LULC MAP STUDIES

Soil is a significant part of the soil structure and an essential aspect of the primary system of production. To consider their challenges, opportunities, and maintenance needs for their potentialuse, the soil map allows in understanding the nature and properties of soil in the research area. Advanced remote sensing and GIS methods were used in soil erosion assessment and watershed prioritization studies [22]. The study area contains red clayey soils, loamy soils, clayey soils withsandy and gravel. Fig. 7 shows the soil map of the research area. Built-up land, reserve forest, water bodies, vegetation, plantation, current fallow, others are the LULC classes delineated in the research area. The LULC occupies a total area of 2049.7 km^2 in the study region. The study area contains 126 canals. Area coming under built-up land is 89.92 km^2, forest reserve is 209.41 km^2, water bodies is 24.90 km^2, vegetation has coverage of 350.22 km^2, hilly terrain of 834.92 km^2, fallow lands coverage is 292.84 km^2 and other classes like wasteland has coverage of 349.73 km^2. Fig.8 shows the LULC classification for the research area.

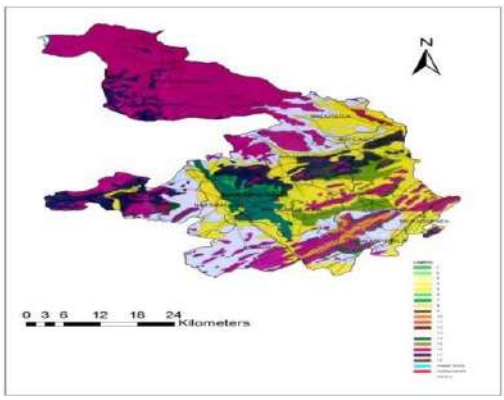

Fig. 7: Soil Classes of the Research Area

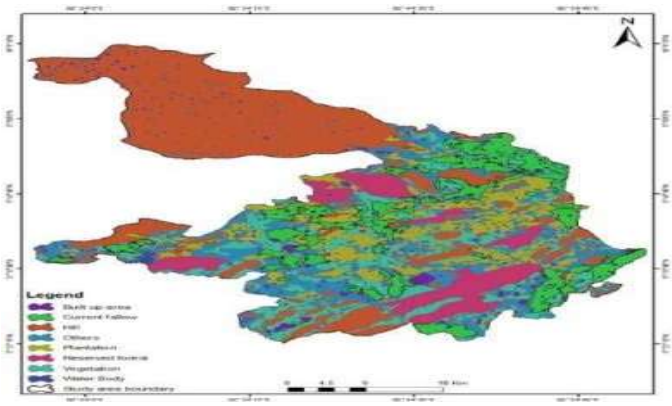

Fig. 8: LULC Classification for the Research Area

GEOMORPHOLOGICAL STUDIES

Geomorphological landform features found in the current research are weathered pediplain, alluvial fan, eroded pediplain, structural slope, complex bazada and pediment insulburg are represented in Fig. 9. Pediplains are categorized into three groups based on the weathering depth,namely shallow (PPS), moderate (PPM), and deep (PPD). The categories found in the present study are Pediplain weathered and Pediplain eroded. The degraded pediplain area present in our sample area is 79.123 km2 (3.28 % of the total area), weathered pediplain spread is 642.742 km2(26.67 % of the total area). One form of pediment soil is the pediment insulburg complex. The pediment insulburg complex has a spread area of 201.762 km2(8.39 % of the total area), the structural hill occupies an area of 826.315 km2(34.29 % of the total area). The percentages of thegeomorphological features of the research area are shown in Fig. 10.

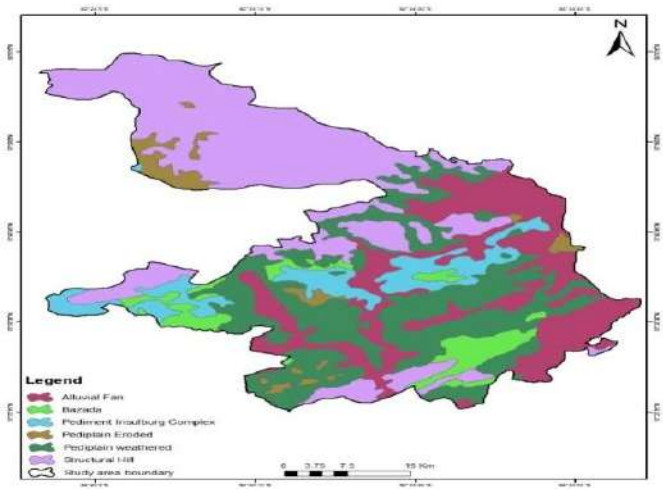

Fig. 9: Map of Geomorphology

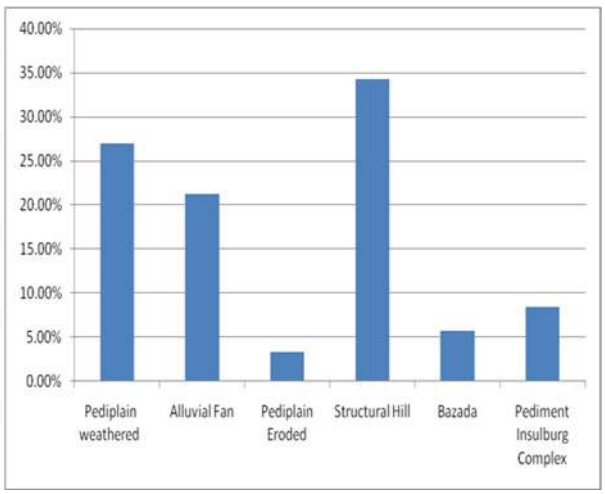

Fig. 10: Bar Chart of Geomorphology

LINEAMENTS MAP

Lineaments such as joints, fractures, and faults are very significant in hydro-geology, as they create pathways for groundwater movement. The existence of lineaments can serve as a conduit for the prospective zone of groundwater [6]. Extinction of large lineaments, reflecting a shear zone or a major fault, can extend the surface of hilly terrain to alluvial terrain. In the present study, several lineaments have been observed and each lineament has different trends and lengths. Fig.11shows the lineaments map of the research area. Abundant lineament density is identified in the hilly terrain, which is due to the structural control of the hilly landscape. Most of the lineaments are disrupted by numerous anthropogenic activities.

SLOPE STUDIES

The slope has a major part in predicting infiltration and surface runoff. Conversely, infiltrationis correlated to the slope, i.e. a milder slope, more infiltration and less runoff, and vice-versa. Using DEM, a degree slope map was developed. The degree of the slope affects flow velocity, run-off, infiltration rate, and other facets of soil transportation. The infiltration potential is poor when the flow velocity is high, and more soil erosion occurs when the slope is steep. In the gentle slope area, surface runoff is slow, allowing rainwater to percolate longer and thuspenetrate more effectively. The study region has been categorized into nearly level, gentle slope, moderate slope, steep slope, and very steep slope. The slope map of the research area is shown in Fig.12 and Table 1 represents the degree of slope category.

Table 1: Degree of Slope Associated with Slope Category

S. No	Percentage of Slope	Type of Slope Category
1	0-3%	Nearly level
2	3-5%	Gentle slope
3	5-10%	Moderate slope
4	10-15%	Steep slope
5	15-35%	Very steep slope

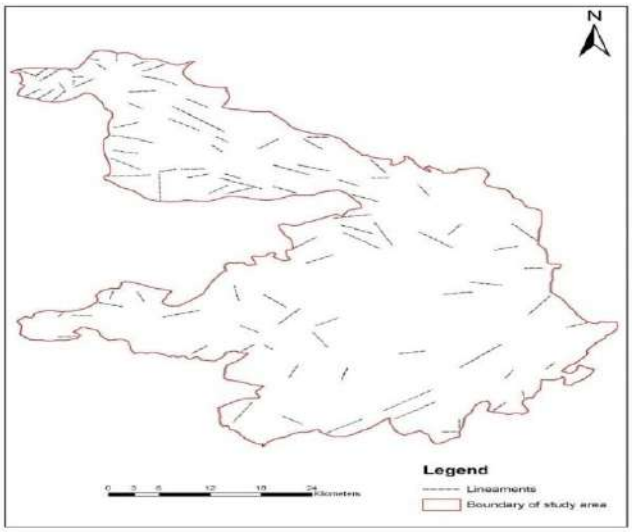

Fig. 11: Lineaments Map of Research Area

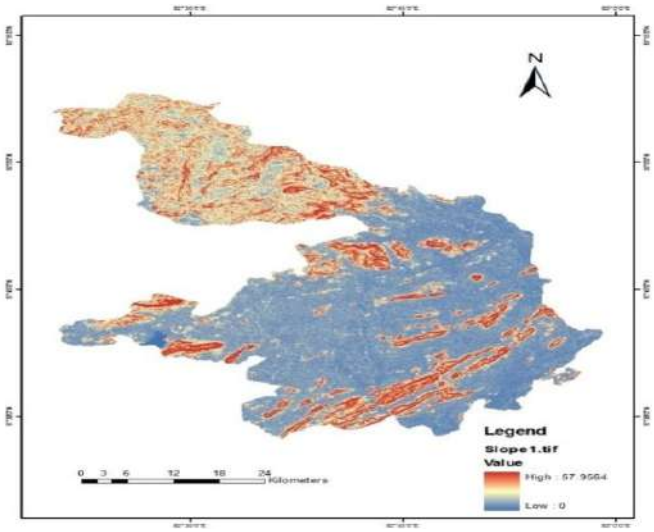

Fig. 12: Slope Map of Research Area

GROUNDWATER POTENTIAL ZONES

A spatial operation in which a thematic layer is superimposed over another to create a new layeris known as index overlay. Geology, geomorphology, lineaments, soils, slope, land use, land cover, and drainage pattern are some of the input layers used in the study of potential groundwater zones. The final phase of the GIS framework in this study is to analyze all data layers using the "Overlay" technique. To obtain a final vulnerability map, the score values forall individual classes for each map are allocated, along with the map weightages. Following are the list of weightages assigned to the classes:

M_1 = weightage × [class (Geology)],

M_2 = weightage × [class (Geomorphology)]

M_3 = weightage × [class (Lineaments)]

M_4 = weightage × [class (Slope)]

M_5 = weightage × [class (Soils)]

M_6 = weightage × [class (LULC)]

M_7 = weightage × [class (Drainage)]

The identified features of LULC, geomorphology, terrain features, and their groundwater prospects are shown in Table 2. The data from each grid cell is then calculated and shown as a map representing possible groundwater areas, as seen in Fig.13.It is identified that very good groundwater zones in the central region of the study area, good groundwater zones in the south- eastern part, moderate groundwater zones in the south-western part, and poor groundwaterzones are located in the north-western part of the study area.

Table 2: Features Listed in the Study Region

Groundwater Prospects	Land Use Land Cover Pattern	Geomorphological Features	Slope
Very good	Wetlands, Plantation, Water bodies	Valley fills, Pediplain	Plain and Gentle slope
Good	Water bodies, Agriculture land, Plantation, Vegetation, Fallow land	Pediplain, Bazada, Valley fills	Gentle slope
Moderate	Fallow land, Land with or without scrub, Built up area, Vegetation	Pediment zone, Bazada, Residual hills	Moderate slope
Poor	Reserve forest, Deciduous forest.	Structural hills, Denudational hills	Steep slope

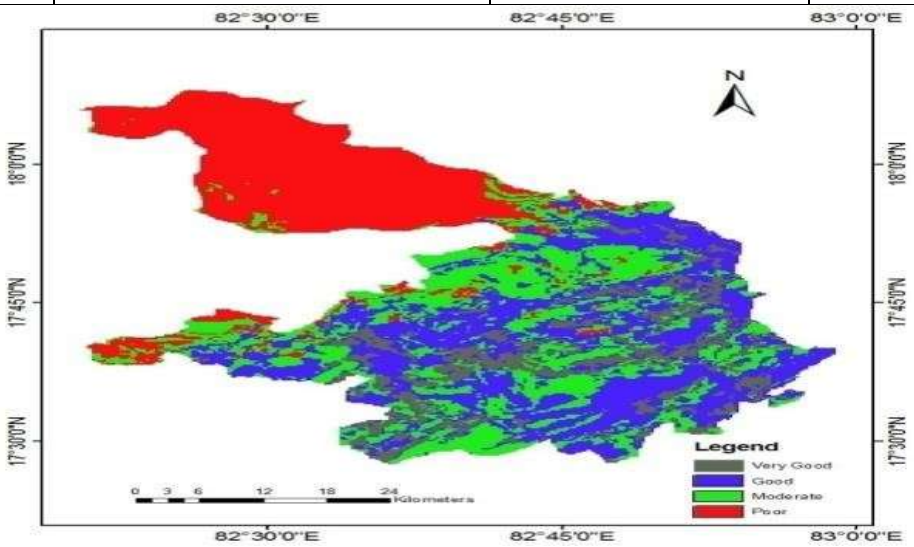

Fig. 13: Groundwater Potential Zones in the Study Area

CONCLUSIONS

Groundwater is a precious, restricted resource. Over the years, growing population, urbanization, and growth of agriculture have contributed to the development of a water stress condition through unscientific use of groundwater. A wide amount of data from differentsources is required for groundwater research. The index overlay method is incredibly useful in the categorization of groundwater potential zones. As effectively shown in the current study, advanced remote sensing and GIS will provide the required forum for convergent analysis of vast quantities of interdisciplinary information and decision-making for groundwater exploration. Four groundwater potential zones are identified in the integrated region. From the research study, wetlands in the near level zone slope were found to be especially good for groundwater exploration. Pediment zones of more than 10 degrees sloping scrubland are categorized as moderate potential groundwater areas. A slope greater than 20 degrees surrounded extensively by the structural hills was observed as poor potential areas. The present work also revealed the potential for using remote sensing and GIS methods for groundwater exploration analysis to enhance field monitoring.

REFERENCES

[1] Kumar G. Srinivasan D and Selva kumar R (2014). Journal of Innovative Science,Engineering and Technology 1-10.

[2] Gupta,Ravi.P, (1991).Remote Sensing Geology, New York: Spring-Verlag Berlin Heidelburg.

[3] Todd D.K, Mays L.W. (2005). *Groundwater Hydrology*, 3rd edn. Wiley, NJ, 636.

[4] Saraf, A.K. & Choudhury, P.R. (1998). Integrated remote sensing and GIS for groundwater exploration and identification of artificial recharge sites. Int. J. Remote Sens. 19(10), 2595–2616.doi: 10.1080/014311698215018.

[5] Ravi Shankar, M.N and Mohan G. (2005). GIS based hydro gemorphic approach for Identification of specific artificial-recharge techniques in the Deccan Volcanic Province. Journal of Earth System & Science 114(5); 505-14.

[6] Obi Reddy, GP, Chandra Mouli, K, Srivasav, SK., Srinivas, CV and Maji, A.K., (2000). Evaluation of groundwater potential zones using remote sensing data- A case study of Gaimukh watershed, Bhandara district, Maharashtra. J. Indian Soc. Remote sensing 28(1):19-32.

[7] Bahuguna, I.M., Nayak, S. Tamilarsan, V and Moses J (2003).Groundwater prospective zonesin basaltic terrain using remote sensing. J. of Indian Society of Remote Sensing 31(2):107 -118.

[8] Nag, S.K. (2005). Application of lineament density and hydro geomorphology to delineate groundwater potential zones of Baghmundi block in Prulia district, West Bengal. Jour. Indian Soc. Remote Sensing, v.33, pp.521-529.

[9] Sashikumar M.C. and Linora Metilda D. (2012). GIS approach for the demarcation of groundwater recharge potential zones in hard rock terrain, International Journal of Earth Sciences and Engineering ISSN 0974-5904, Vol. 05, No. 01, pp. 117–120.

[10] Murthy, K.S.R., (2000). Groundwater Potential in a Semi-arid Region of Andhra Pradesh: AGeographical Information System Approach, Int. J. of Remote Sensing, 21(10): 1867–1884.

[11] Pradeep Kumar G.N., P. Srinivas, K. Jaya Chandra and P. Sujatha, (2010). Delineation of Groundwater Potential Zones using Remote sensing and GIS Techniques: A Case Study of KumapalliVagu Basin in Andhra Pradesh, India. International Journal of Water Resource and Environmental Engineering, 2(3), pp 70-79.

[12] Ganesh Babu O, MC Sashikkumar, (2010). Demarcation of groundwater recharge potential zones for Tiruppur block using GIS. Journal of soil and water conservation, 9, pp 154-158.

[13] Preeja, K.R., Joseph, S., Thomas, J. And Vijith, H.(2011), Identification of groundwater potential zones of a tropical river basin (Kerala, India) using remote sensing and GIS techniques. Jour. Indian Soc. Remote Sensing, v.39, pp.83-94.

[14] Narendra. K, K. Nageswararao, P. Swarnalatha (2013). Integrating Remote Sensing and GISfor Identification of Groundwater Prospective Zones in the NaravaBasin, VisakhapatnamRegion, Andhra Pradesh. Journal Geological Society of India Vol.81, February, pp.248-260.

[15] Chakraborthy S, Sikdar P K, EnakshiAdhya and Paul P K. (2004). Land use land coverchanges and groundwater potential zoning in and around ranigang coal mining area, BardhamanDistrict, West Bengal- A GIS and Remote Sensing Approach, J. of Spatial Hydrology 4(2); 1-24.

[16] Jagadeeswara Rao, P., Harikrishna, P., and Suryaprakasa Rao, B. (2004). An integrated studyon groundwater resource of Peddagedda watershed. Journal of Indian Society of Remote Sensing32(3):307-311.

[17] https://www.google.com/search?q=google+map+india

[18] Bhuvan portal, https://bhuvan.nrsc.gov.in/bhuvan_links.php

[19] https://www.surveyofindia.gov.in/

[20] ArcGIS 9.3 https://arcgis-explorer.software.informer.com/9.3/

[21] Strahlers A. N. (1957).Quantitative Analysis of Watershed Geomorphology. American Geophysical Union Transactions, Volume 38, Pages 912-920.

[22] Amee K. Thakkar and S.D.D Himan (2007). Morphometric analysis and prioritization of mini watersheds in Mohar watershed Gujarat using remote sensing and GIS techniques. J. Indian Soc. Remote Sensing, Vol. 35: 313-321.

DATA COMMUNICATIONS AND COMPUTER NETWORKING

Dr. G. Vamsi Krishna
Dr. R. Shankar

CONTENTS

1. Introduction

1.1 Data Communication 1
1.2 Networks 2
1.3 Protocols and Standards 4
1.4 Line Configuration 6
1.5 Topology 8
1.6 Transmission Modes 14
1.7 Classification of Networks 16
1.8 OSI Reference Model 17
1.9 Functions of OSI Layers 18

2. Physical and Data Link Layer

2.1 Digital Data Transmission 24
2.2 Techniques of Data Communication 24
2.3 DTE/DCE 30
2.4 D-sub 9 Connector Pinout 34
2.5 EIA-449 35
2.6 EIA-530 37
2.7 X.21 Interface 39
2.8 Modems 39
2.9 Cable Modem 42
2.10 Transmission Media-Guided Media 43
2.11 Transmission Media-Unguided Media 55
2.12 Performance 63
2.13 Types of Errors 63
2.14 Error Detection 64

2.15 Checksum 66
2.16 Error Correction 67

3. LANs

3.1 Multiplexing 69
3.2 Types of Multiplexing 70
3.3 Multiplexing Application 74
3.4 Project 802 77
3.5 Ethernet 79
3.6 Token Bus 85
3.7 Token Ring 85
3.8 Abort frame 88
3.9 FDDI 89
3.10 IEEE 802.6 (DQDB Topology) 93
3.11 Switched Multi-megabit Data Service (SMDS) 96
3.12 Switching 99
3.13 Connectionless Service 111

4. Virtual-Circuit Networks

4.1 ISDN (Integrated Services Digital Network) 113
4.2 Access to ISDN 114
4.3 ISDN Layers 120
4.4 BISDN 124
4.5 X.25 Layers 125
4.6 ATM Definition 129
4.7 ATM Architecture 129
4.8 ATM Layers or ATM Protocol 134
4.9 LAN Emulation 142

DATA COMMUNICATIONS AND COMPUTER NETWORKING

This textbook brings the beginning student right to the forefront of the latest advances in the field, while presenting the fundamentals in a clear, straightforward manner. Students will find better coverage, improved figures and better explanations on cutting-edge material. The "bottom-up" approach allows instructors to cover the material in one course, rather than having separate courses on data communications and networking.

Price Rs 235.00
ISBN 978-1-63832-370-9

Chapter 10
Advance Machine Learning and Nature-Inspired Optimization in Heart Failure Clinical Records Dataset

Dukka Karun Kumar Reddy, H. S. Behera, and Weiping Ding

Abstract ML is a subset of computing procedures that aims to imitate human astuteness by swotting from its surroundings. It has become a challenging task to diagnose the ailment and provide the appropriate treatment at the right time because of the increasing population and disease. The recent technological advancements have propelled the adoption of innovative functional biomedical solutions in the public health sector. Procedures based on traditional ML have been applied effectively in computational biology to biomedical and medical applications. Biomedical solutions entail a complex series of procedures ranging from consultation to treatment and beyond to ensure that patients react optimally. These are considered the working horse in the new era of the so-called big data. The process's complexity can vary and encompass multiple phases of nuanced human–machine interplay with decision-making, which certainly derive the application of ML algorithms to enhance and systematize the automate processes. A population-based Natured inspired swarm algorithms is proposed to extract the relevant parameters of Tree-based ML algorithms by using hyperparameter tuning. The proposed framework attains the desired performance by using "Heart failure clinical records dataset" prediction from the UCI ML data repository.

Keywords Nature-Inspired optimization · Clinical data · Hyperparameter tuning · Clinical dataset · Heart failure

D. K. K. Reddy (✉)
Department of Computer Science Engineering, Dr. L. Bullayya College of Engineering, Visakhapatnam, Andhra Pradesh 530013, India
e-mail: karun.redy@gmail.com

H. S. Behera
Department of Information Technology, Veer Surendra Sai University of Technology, Burla 768018, India
e-mail: hsbehera_india@yahoo.com

W. Ding
School of Information Science and Technology, Nantong University, Nantong, China

J. Nayak et al. (eds.), *Nature-Inspired Optimization Methodologies in Biomedical and Healthcare*, Intelligent Systems Reference Library 233,
https://doi.org/10.1007/978-3-031-17544-2_10

11 Deep Neural Network–Based Security Model for IoT Device Network

Dukka Karun Kumar Reddy
Dr. L. Bullayya College of Engineering (for Women)

Janmenjoy Nayak
Aditya Institute of Technology and Management (AITAM)

Bighnaraj Naik
Veer Surendra Sai University of Technology

G. M. Sai Pratyusha
Dr. L. Bullayya College of Engineering (for Women)

CONTENTS

11.1 Introduction 224
11.2 Literature Review 226
11.3 Proposed Method 228
11.4 Dataset Description 231
11.4.1 IoT-Device-Network-Logs Dataset 231
11.4.2 OPCUA Dataset 232
11.4.2.1 Data Preprocessing 233
11.5 Experimental Configuration and Result Analysis 234
11.5.1 Performance Evaluation 234
11.5.2 Parameter Setting 235
11.5.3 Result Analysis 235
11.6 Conclusion 241
References 242

Laser applications for the optical exploration of the Dy^{3+} doped Li_2O-CaF_2-Al_2O_3-B_2O_3-SiO_2 glasses

Cite as: AIP Conference Proceedings **2269**, 030096 (2020); https://doi.org/10.1063/5.0019923
Published Online: 12 October 2020

D. Deenabandhu, K. Neeraja, K. Ephraim Babu, V. Venkata Kumar, K. Bueala Kumari, K. Samatha, and V. Veeraiah

Laser Applications for the Optical Exploration of the Dy^{3+} Doped Li_2O-CaF_2-Al_2O_3- B_2O_3- SiO_2 Glasses

D. Deenabandhu[1], K. Neeraja[2], K. Ephraim Babu[2,*], V. Venkata Kumar[3], K. Bueala Kumari[3], K. Samatha[4] and V. Veeraiah[4]

[1]*Department of Physics, Dr. L. B. College of Engineering for Women, Visakhapatnam, A.P, India.*
[2]*Department of Physics, Narasaraopeta Engineering College(A),Narasarao pet, Yellamanda (P.O) Guntur(D.T) Andhra Pradesh, 522601, India.*
[3]*Department of BS&H, St. Ann's College of Engineering & Technology, Nayunipalli village, ChallaReddyPalem Post, VetapalemMandal, Chirala, Prakasam District, AP - 523187, India*
[4]*Department of Physics, Andhra University, Visakhapatnam, Andhra Pradesh, 530003, India.*

*Corresponding author: ephraimbabu@gmail.com

Abstract. This paper provides details regarding the preparation, optical absorption, emission and FTIR spectral studies on $Dy3^+$ doped Li_2O-CaF_2-Al_2O_3- B_2O_3- SiO_2 glasses. Absorption spectrum reveals different bands and it analyzed by the use of JO-theory. Emission spectra of the samples display two transitions $^4F_{9/2}\rightarrow{}^6H_{15/2}$, $^4F_{9/2}\rightarrow{}^6H_{13/2}$, a clear enhancement is observed with increase the concentration of Dy_2O_3 ions. The CIE coordinates is measured for these glasses it demonstrates that the glasses produce bright white light, which are appropriate for the improvement of the laser materials and white light LED's.

INTRODUCTION

Within course of recent decades, rare-earth (RE) particles doped materials gained vast significance, because of their huge applications inside the discipline of photonics beside with solid state lasers, X-ray beam imaging, sensors, optical enhancers, optical and magnetic devices etc [1]. Therefore on layout of latest devices with high performance by choosing proper new host for trivalent RE ions. In seeking of new host, lithium calcium floroalumino borosilicate glasses are viewed as acceptable host for optically active ions as a result of their high transparency, low dissolving point and good suitableness for the physical and chemical properties of the RE ions [2]. In addition to this RE3+ based glasses have major importance due to exciting optical properties together with the sharp absorption and emission bands with high efficiencies of intense radiation from visible to IR regions below excitations conditions.

Normally in the current investigation glasses are the aggregate of glass former (SiO_2, B_2O_3, Al_2O_3), modifier (CaF_2) and spectra materials (Dy_2O_3). Silica, boric oxides are recognized as glass formers in sight of their technological and innovative applications. In these glasses, silicon occurs in four-fold coordination whereas boron will exist in three, four-fold coordination. The network property of these structural units is characterized by using Qn, where n (0–4) represents the number of bridging oxygen atoms per tetrahedron. Here the modifiers are distributed to the system; it'll increase the tendency to create the stable glasses. In case of boron, coordination conversion is found ($BO_3 \leftrightarrow BO_4$). Finally the spectra materials are responsible for optical analysis and the way they act intervals inside the structural change is enlightened in latter.

Altogether the RE particles, Dysprosium has varied applications in creating white LED's. Lanthanide (RE) based materials are used considerably in light materials that use nearly any kind of strength because of its excitation supply [3] that entirely suits with the spectrum of GaN-based LED's. This sort of glasses concerning the mid-infrared wavelength region provides a attainable as light sources for laser device applications [4]. The Dy^{3+} ions have dense

International Conference on Multifunctional Materials (ICMM-2019)
AIP Conf. Proc. 2269, 030096-1–030096-9; https://doi.org/10.1063/5.0019923
Published by AIP Publishing. 978-0-7354-2032-8/$30.00

electronic structure as a result of vast kind of vitality levels lying close to each other to form the crystal–discipline analysis and more [5]. In addition, the characteristics of lanthanide ions play a significant role in optical applications for example the emission attributes of a trivalent RE ions influence the host matrix throughout that the particles are assimilated. These ligand fields can have a control the optical absorption, emission and quantum proficiency of glass frame work. So, this glass matrix has wide emission cross-section area than crystals that are acceptable for the laser host.

The aim of the investigation is to incorporate the RE ions with numerous different modifier oxides that realize the glass composition changes on the optical properties of the Dy_2O_3 ions. The experimental results viz., XRD, Optical absorption, luminescence and FTIR spectral studies facilitate for this analysis.

EXPERIMENTAL WORK

The following Table-1shows the Dy^{3+} doped Li_2O-CaF_2-Al_2O_3 -B_2O_3-SiO_2 glasses that are developed for the current work. High quality of analytical reagents with 99.9% of purity of Li_2O, CaF_2, Al_2O_3, SiO_2, B_2O_3, and Dy_2O_3 are utilized for the prepared glass samples. Here dysprosium is employed as dopant inside the glasses community. The glass materials are synthesized with the support of melt quenching technique; through this the proposed portions of chemicals in mol% are taken in agate mortar and then powered to achieve consistent mixture, then it is taken in an silicon crucible and heated for around 1 hour in an temperature controlled furnace at range of 1350-1450°C. The melt was poured in a brass mould that is able to bring the desired form. The gained samples are now transferred into the annealing furnace of 450°C temp for annealing to stay away the thermal stress and to induce the structural balance for the optical applications.

TABLE 1: Glass compositions of investigating glasses

Glasses	Li_2O mol %	CaF_2 mol %	Al_2O_3 mol %	B_2O_3 mol %	SiO_2 mol %	Dy_2O_3 mol %
Pure	20	10	20	30	20	-
$Dy_{0.2}$	20	10	19.8	30	20	0.2
$Dy_{0.4}$	20	10	19.6	30	20	0.4
$Dy_{0.6}$	20	10	19.4	30	20	0.6
$Dy_{0.8}$	20	10	19.2	30	20	0.8
$Dy_{1.0}$	20	10	19.0	30	20	1.0

RESULTS

OPTICAL ABSORPTION, EXCITATION & EMISSION SPECTRA

The wavelength between 200-2000 nm absorption spectrum of Li_2O-CaF_2-Al_2O_3 -B_2O_3-SiO_2 glasses recorded at temperature which is shown in Fig 1 (a) & (b). The spectrum of undoped glasses doesn't display any bands. The spectra of investigated glasses exhibit a variety of bands; the found bands are allocated based on the defined energy levels [6] of Dy^{3+} ions of varied glass matrices. The bands are found approximately ~ 348, ~364, ~385, ~427, ~451, ~750, ~799, ~896, ~1087, ~1268, ~1674 nm. These bands are attributed to $^6H_{15/2} \rightarrow {}^4P^{3/2}$, $^6P^{7/2}$, $^4K_{17/2}$, $^4G11/2$, $^4I15/2$, $^6F3/2$, $^6F5/2$, $^6F7/2$ $^6F9/2$, $^6F_{11/2}$+$^6H_{9/2}$, $^6H_{11/2}$.

From the ascertained absorption edge, we've calculated the energy band gap (E_o) for indirect, direct transitions of the glasses respectively. The Tauc plots for direct transition in shown in Fig 2 (a) and indirect transition are shown in Fig 2 (b). The rate of ΔE are typically calculated the quantity of Dy_2O_3 increase that result in the rise in Urbach energy which is shown in Fig 3. The theoretical, evaluated cutoff wavelength, direct and indirect band gap are presented in Table 2.

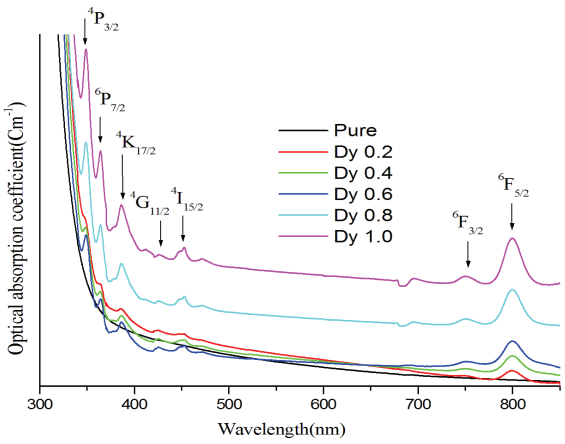

FIGURE.1 (a): UV-Vis absorption spectra of Li_2O-CaF_2-Al_2O_3- B_2O_3- SiO_2 doped with Dy_2O_3 glasses

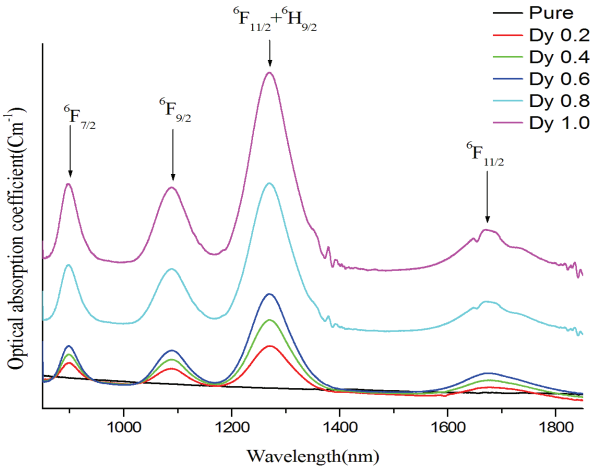

FIGURE.1 (b): NIR absorption spectra of Li_2O-CaF_2-Al_2O_3-B_2O_3- SiO_2doped with Dy_2O_3 glasses

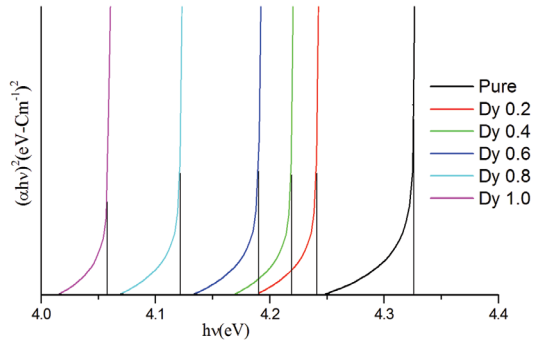

FIGURE.2 (a): Tauc plots to evaluate direct band gap of Li_2O-CaF_2-Al_2O_3- B_2O_3- SiO_2doped with Dy_2O_3 glasses

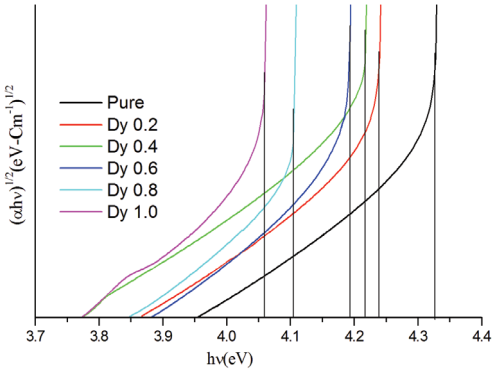

FIGURE.2 (B): Tauc plots to evaluate in-direct band gap of Li_2O-CaF_2-Al_2O_3- B_2O_3- SiO_2doped with Dy_2O_3 glasses

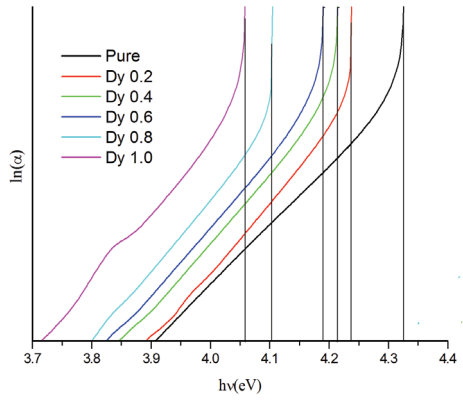

FIGURE.3:A plots of ln(a) and hm for of Li_2O-CaF_2-Al_2O_3- B_2O_3- SiO_2 doped with Dy_2O_3 glasses

TABLE.2: The cutoff wavelength, theoretical and evaluated values of direct and indirect band gap of Li_2O-CaF_2-Al_2O_3- B_2O_3- SiO_2 doped with Dy_2O_3 glasses

Glass Samples	Cutoff wavelength	Theoretical band gap	Direct band gap (eV)	Indirect band gap (eV)	Urbach energy (E) (eV)
Pure	287	4.32	4.32	4.32	0.2314
$Dy_{0.2}$	293	4.23	4.24	4.23	0.2369
$Dy_{0.4}$	295	4.21	4.21	4.21	0.2375
$Dy_{0.6}$	296	4.19	4.19	4.19	0.2386
$Dy_{0.8}$	302	4.11	4.12	4.10	0.2439
$Dy_{1.0}$	305	4.07	4.05	4.05	0.2469

Fig 4 shows the excitation spectrum of Li_2O-CaF_2-Al_2O_3 -B_2O_3-SiO_2 doped with Dy_2O_3 glasses with 0.2, 0.6 and 1.0 mol% are measured within the spectral range of 300-500 nm by monitoring at 573 nm that is associated to the transition of $^4F_{9/2} \rightarrow {}^6H_{13/2}$ transition. The spectrum displays seven bands focused at 322, 347, 362, 385,424,450 and 472 nm due to transition from $^6H_{15/2}$ ground state to $^4L_{19/2}$, $^4M_{15/2}+{}^4P_{7/2}$, $^4I_{11/2}$, $^4I_{13/2}+{}^4F_{7/2}$, $^4G_{11/2}$, $^4I1_{5/2}$, $^4F_{9/2}$ respectively [7]. The most intense peaks at 347 and 385 nm specify that the close to ultraviolet (UV) and blue LEDs are applicable for pumping to get efficient emission of Dy^{3+} ions.

The emission spectra of Li_2O-CaF_2-Al_2O_3 -B_2O_3-SiO_2 doped with Dy_2O_3 glasses are recorded at room temperature with excited wavelength 348 nm in region 400-600 nm. The emission spectra of those glasses exhibit two emission transitions that are prescribed to $^4F_{9/2} \rightarrow {}^6H_{15/2}$, $^4F_{9/2} \rightarrow {}^6H_{13/2}$[8]. The Fig 5 shows the emission spectra of Li_2O-CaF_2-Al_2O_3 -B_2O_3-SiO_2 with Dy_2O_3 glasses.

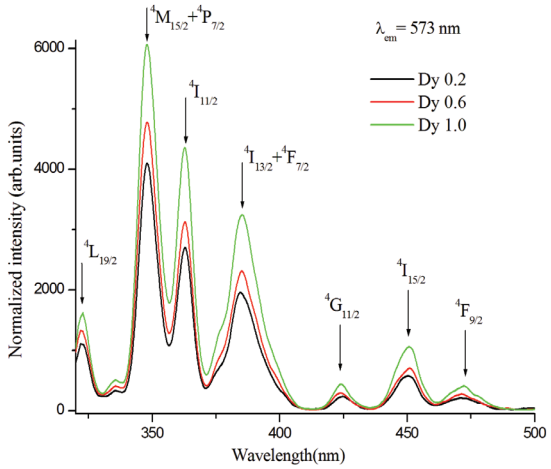

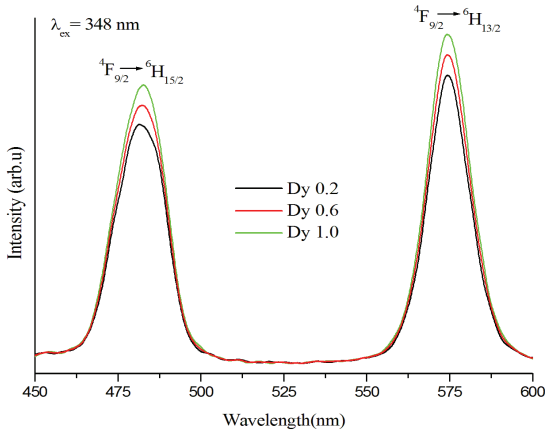

FIGURE.4: Excitation spectra of Li_2O-CaF_2-Al_2O_3- B_2O_3-SiO_2doped with Dy_2O_3 glasses

FIGURE.5: Emission spectra of Li_2O-CaF_2-Al_2O_3- B_2O_3- SiO_2 doped with Dy_2O_3 glasses

X-RAY DIFFRACTION SPECTRA

The XRD spectra of Li_2O-CaF_2-Al_2O_3 -B_2O_3-SiO_2 doped with Dy_2O_3 glasses are displayed in the Fig 6. The spectra comprise a broad bump at ~300(=2θ) and no intensive sharp lines are ascertained that the atoms inside the material are distributed in a random manner and broad bump might be present because of short rang order inside the glass materials. Within the X-ray diffraction spectra no sharp peaks were determined, that implies that the investigated glasses ensure the amorphous nature.

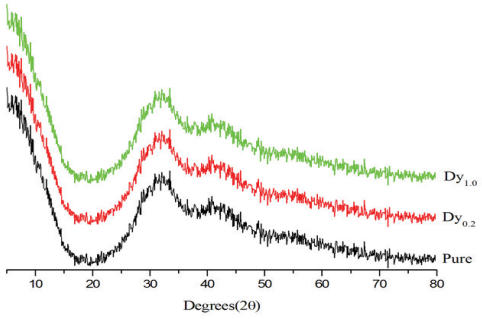

FIGURE.6: XRD spectra of Li_2O-CaF_2-Al_2O_3- B_2O_3- SiO_2doped with Dy_2O_3 glasses

INFRARED SPECTRA

The FT-IR spectroscopy is useful to look the character of surroundings of various cations inside the glass matrix. The examined glass samples are a mixture of glass formers (SiO_2 and B_2O_3) and intermediate compounds (Al_2O_3). The spectra of various vibrational groups with band positions and assignments of bands are conferred in Table 3 and are shown in Fig 7. A band associated to Si-O-Si/O-Si-O bending /rocking modes and AlO_6 units is placed concerning at 482 cm^{-1}[9]. The band detected at around 530 cm^{-1} and 580 cm^{-1} is known to the bending vibrations of B-O-Si linkage and vibrational modes of Si-O-Si linkage. Another vital band because of the vibrations of bridging oxygen's between B-O-B in BO_3 triangles is additionally observed at 635 cm^{-1}. The bands appeared within the region 900 cm^{-1} are attributed to characteristics vibrations of Q2 species of Si-O units, another band indicates the combined stretching vibrations vibrational modes of SiO_4 and BO_4 units at around 1050cm^{-1}[10]. The spectra displayed noticeable bands within the region 1200 cm^{-1} associated with stretching relaxation of B-O bond of trigonal BO_3 units with NBOs. The spectra additionally exhibited a band about at 1390-1405 cm^{-1} ascribed to B-O stretching relaxations of [BO_3] structural units [11], that are connected with the vibrational mode within the varied borate rings and therefore the nonbridging B-O bonds and Asymmetric B-O stretching relaxations of [BO_3] structural units are known in the region 1515 cm^{-1}[12].

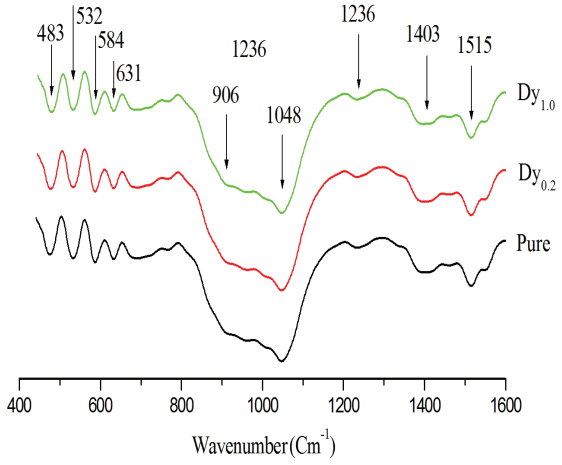

FIGURE.7:FTIR spectra of Li_2O-CaF_2-Al_2O_3-B_2O_3- SiO_2doped with Dy_2O_3 glasses

TABLE.3: The FT-IR band positions ofLi_2O-CaF_2-Al_2O_3- B_2O_3- SiO_2 doped with Dy_2O_3 glasses

Glass Samples			Band assignments
Pure	$DyM_{0.2}$	$DyM_{1.0}$	
482	483	482	Si-O-Si rocking vibrations /AlO_6 units
532	532	530	Bending vibration of B-O-Si linkages
584	584	586	Vibration modes of Si-O-Si linkage
631	631	631	Vibrations of bridging oxygen between B-O-B in BO_3 triangles
906	902	906	Characteristic vibrations of Q^2 species of Si-O units
1048	1048	1046	Combined stretching vibrations modes of SiO_4 and BO_4 units
1233	1233	1233	Stretching vibrations of B-O of the BO_3 units
1401	1399	1401	Stretching vibrations of B-O units from different borate groups
1511	1515	1515	Asymmetric B-O stretching relaxations of [BO_3] structural units

PHYSICAL PROPERTIES

To analyze the essential properties of the Li_2O-CaF_2-Al_2O_3-B_2O_3-SiO_2 doped with Dy_2O_3 glasses, the different values of density (d) and refractive index along with other physical parameters are evaluated and are presented in the Table 4[13]. From the varied physical properties, structural compactness of the materials will be understood by property of density. From the observations of the physical properties, it is noticed that each of the parameters are inversely proportional with increase in concentration of Dy_2O_3 ion. The polaraisability is also high at x=0.2 mol%, whereas, its ionic concentration is additionally will increases and eventual decrease is detected in interionic separation within the glass network region.

TABLE: 4. various physical properties of Li_2O-CaF_2-Al_2O_3- B_2O_3- SiO_2 doped with Dy_2O_3*glasses*

S.No	Physical Parameters	Pure	$Dy_{0.2}$	$Dy_{0.4}$	$Dy_{0.6}$	$Dy_{0.8}$	$Dy_{1.0}$
1	Density D (g/cm^3) (± 0.0001)	2.5383	2.5448	2.5454	2.5486	2.5893	2.6135
2	Average molecular weight (M)	67.074	67.615	68.158	68.700	69.242	69.784
3	ion concentration Ni (ions / cm^3) (±0.005)	-	0.4533	0.8997	0.1340	0.1818	0.2255
4	Interionic distance ri (A_0) (± 0.005)	-	28.04	22.31	19.53	17.70	16.42
5	Polaron radius r_p (A_0) (± 0.005)	-	11.30	8.992	7.872	7.133	6.619
6	Field strength (1015cm^{-2}) (± 0.005)	-	2.34	3.71	4.84	5.89	6.84
7	Electronic polarizability α_e (10-22 ions/cm^3)(± 0.005)	-	19.88	9.97	6.68	4.96	3.96
8	Refractive index n_d(± 0.0001)	1.683	1.679	1.675	1.674	1.673	1.672
9	Dielectric Constant (ε_0)	2.832	2.819	2.805	2.802	2.798	2.795
10	Reflection loss (R)	0.0343	0.0340	0.0337	0.0336	0.0335	0.0334
11	Molar reflectivity RM (cm^{-3})(± 0.005)	9.995	10.02	10.06	10.11	10.02	9.997

DISCUSSION

It Optical absorption spectra of Li_2O-CaF_2-Al_2O_3-B_2O_3-SiO_2 doped with Dy_2O_3 glasses measured within the spectral region 300-2000 nm. Totally, eleven transitions are observed for Dy_2O_3 based glasses within the 320-1800 nm spectral region. Among varied Dy_2O_3 doped glasses has higher spectral intensity for the transition $^6H_{15/2}\rightarrow$ $^6F_{11/2}$+$^6H_{9/2}$ and it's take into account as hypersensitive transition of Dy^{3+} ion. The environment of Dy^{3+} is of low symmetry, the field gradient imposed by substance and therefore the magnitude of induced f→ f transition is high, high yielding spectral intensity. Such transitions are termed as hypersensitive transitions [14]. The known hypersensitive transitions conform the selection rule in the case of Dy^{3+} ($4f^9$) ion, during this transition ($^6H_{11/2}$, $^6H_{9/2}$) is ascertained to be more hypersensitive compare to the opposite transitions. Due to the cause of non-bridging atoms the band gap of the samples are found to lower with increasing the Dy_2O_3 ions. The measurement for f-f transition of REs is provided by suggests that the Judd-Ofelt (JO) theory [15] for the oscillator strength of the intensity of the absorption bands. A least-square fitting approximation is employed to define Ω_λ parameters, which provide the most effective work between experimental and calculated oscillator strengths.

The lanthanide particles that possess distinctive coordination sites with non-centro symmetric potential build a contribution to considerably Ω_2. In spite of comparable coordination, the variations within the distortion at those particle sites might end in a distribution within the crystal field. By the approach of applying least square fitting procedure to see the J-O intensity parameters Ω_2, Ω_4 and Ω_6 exploitation through experimental measured oscillator strength, the obtained values are conferred in Table 5. The measured J-O intensity parameters determined within the present glass network are found to be in the order $\Omega_2 > \Omega_4 > \Omega_6$[16] that are shown in Table 6. In general, the JO parameters give data on the characteristics of bond among Ln ion and encompassing ligands in additionally to the symmetry of the surroundings of the Ln ions. The decreasing values of the magnitude of JO parameters ($\Omega_2 > \Omega_4 > \Omega_6$) for the studies glasses will be attributed to the presence of similar ion sites around the Dy^{3+} ions, that is associated to proof for the good quality of a glass host for optical and laser applications.

TABLE 5: Theoretical and experimental oscillator strength of Li_2O-CaF_2-Al_2O_3- B_2O_3- SiO_2 doped with Dy_2O_3 glasses

Transition $6H_{15/2}\rightarrow$	*Dy0.2*		*Dy0.4*		*Dy0.6*		*Dy0.8*		*Dy1.0*	
	$f_{cal,(x10-6)}$	$f_{exp,(x10-6)}$	$f_{cal,(x10-6)}$	$f_{exp,(x10-6)}$	$f_{cal,(x10-6)}$	$f_{exp,(x10-6)}$	$f_{cal,(x10-6)}$	$f_{exp,(x10-6)}$	$f_{cal,(x10-6)}$	$f_{exp,(x10-6)}$
$^4P_{3/2}$	2.16	1.39	2.16	1.38	2.18	1.39	2.17	1.42	2.19	1.48
$^4K_{17/2}$	2.21	0.94	2.19	0.95	2.23	0.95	2.24	0.96	2.26	0.98
$^4G_{11/2}$	0.17	0.13	0.17	0.13	0.19	0.12	0.18	0.13	0.18	0.14
$^4I_{15/2}$	0.94	0.54	0.94	0.55	0.96	0.55	0.97	0.57	0.99	0.58
$^6F_{3/2}$	0.178	0.20	0.178	0.19	0.181	0.20	0.179	0.21	0.182	0.21
$^6F_{5/2}$	1.69	0.93	1.69	0.92	1.72	0.94	1.74	0.96	1.78	0.96
$^6F_{7/2}$	1.93	2.04	1.95	2.04	1.95	2.05	1.94	2.05	1.96	2.06
$^6F_{9/2}$	2.79	2.76	2.79	2.80	2.81	2.82	2.81	2.84	2.82	2.84
$^6F_{11/2}+^6H_{19/2}$	10.67	10.70	10.73	10.72	10.73	10.73	10.75	10.74	10.78	10.76
$^6H_{11/2}$	1.38	1.53	1.41	1.53	1.42	1.54	1.42	1.56	1.42	1.58
Rms deviation	±0.704969		±0.697071		±0.715164		±0.70775		±0.709669	

TABLE 6:J-O intensity parameters of Li_2O-CaF_2-Al_2O_3- B_2O_3- SiO_2 doped with Dy_2O_3 glasses

GLASS SAMPLES	$\Omega_2 x10^{-20}$ (cm^{-2})	Ω_4 $x10^{-20}$ (cm^{-2})	Ω_6 $x10^{-20}$ (cm^{-2})
Dy0.2	6.18	3.26	2.62
Dy0.4	6.15	3.18	2.58
Dy0.6	6.11	3.15	2.53
Dy0.8	6.08	3.09	2.48
Dy1.0	6.02	3.02	2.47

The Photoluminescence spectra of Li_2O-CaF_2-Al_2O_3-B_2O_3-SiO_2 doped with Dy_2O_3 glasses displays intense blue and yellow emissions were seen at 484 and 574 nm corresponding to $^4F_{9/2}\rightarrow^6H_{15/2}$ (blue) and $^4F_{9/2}\rightarrow^6H_{13/2}$ (yellow) transitions of Dy^{3+} respectively. During which transition $^4F_{9/2}\rightarrow^6H_{13/2}$ has high intensity and contains a bright fluorescent yellow emission at 576 nm has been placed. The intensity magnitude relation dipole transition has been used to scope the symmetry of the local environment of the trivalent 4f ions. During this $^4F_{9/2}\rightarrow^6H_{13/2}$ transition of Dy^{3+} ion has additional intensity than $^6H_{11/2}$ conforms the asymmetric nature of the glass host. From the emission spectra emission peak positions, effective line widths and branching ratios are determined and are given in Table 7. Along with β_R values expected using the JO theory. The experimental β_R values are compared with those expected values using the JO theory for the glasses and located that their values are in close agreement with each other. The β_R values follow the trend as $^4F_{9/2}\rightarrow^6H_{13/2}>^4F_{9/2}\rightarrow^6H_{15/2}$ for the studied Li_2O-CaF_2-Al_2O_3-B_2O_3-SiO_2 doped with Dy_2O_3 glasses. The β_R is found to be maximum for the emission $^4F_{9/2}\rightarrow^6H_{13/2}$ band with the values 0.65 and 0.64 respectively. Fig 8 represents the energy level scheme for all the observed absorption, excitation and emission transitions of Dy^{3+} doped glasses.

TABLE 7: Various radiative properties of Li_2O-CaF_2-Al_2O_3- B_2O_3- SiO_2 doped with Dy_2O_3 glasses

Transitions from $^4F_{9/2}$	*Glass samples*									
	$Dy_{0.2}$		**$Dy_{0.4}$**		**$Dy_{0.6}$**		**$Dy_{0.8}$**		**$Dy_{1.0}$**	
	A(s^{-1})	**β%**	**A(s^{-1})**	**β%**	**A(s^{-1})**	**β%**	**A(s^{-1})**	**β%**	**A(s^{-1})**	**β%**
$^6H_{15/2}$	192.3	0.158	197.6	0.161	188.2	0.156	193.2	0.159	193.6	0.159
$^6H_{13/2}$	1023.7	0.841	1027.5	0.838	1017.2	0.843	1018.4	0.840	1019.6	0.840
	A_T=1216		A_T=1225.1		A_T=1205.4		A_T=1211.6		A_T=1213.2	
	τ_r=8.2		τ_r=8.16		τ_r=8.29		τ_r=8.25		τ_r=8.24	

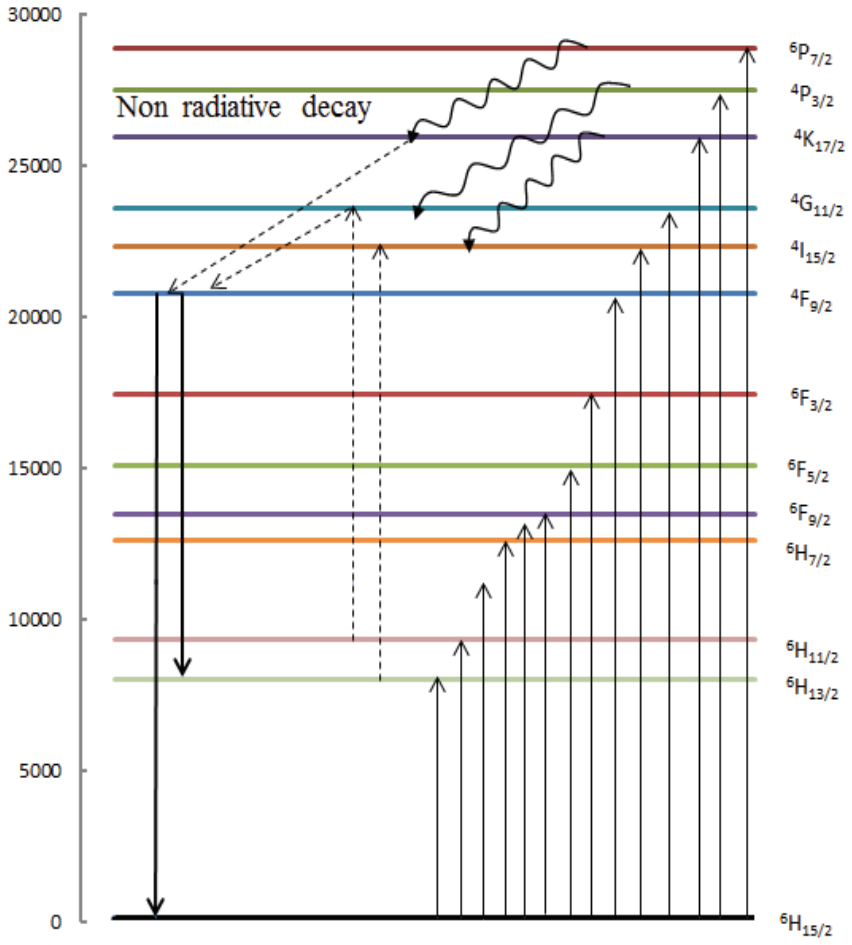

FIGURE.8: Energy level diagram of Li_2O-CaF_2-Al_2O_3- B_2O_3- SiO_2 doped with Dy_2O_3 glasses

The chromaticity coordinates (x,y) and color correlated temperature (CCT) of Li_2O-CaF_2-Al_2O_3-B_2O_3-SiO_2 doped with Dy_2O_3 glasses with varied doping concentration under excitation 348 nm were listed in Table 8 and chromaticity diagram and are displayed in Fig 9. As can see from Fig 9, based on the Dy^{3+} ions concentration the CIE coordinates are moves nearer to blue region and thus they diverged to yellow region. Further it is suggested that the coordinates are very near to the white light standard values. These outcomes make sure that these glasses are

promising materials for generating white light emission. The related color temperature (CCT) was also calculated. The CCT values gained for the current Dy^{3+} doped glasses are 3652-4912 K, from these it ascertained that each one the coordinated are originate to lie in white light region. This denotes that these materials are suited for optical and laser devices.

TABLE 8: The color coordinates of Li_2O-CaF_2-Al_2O_3- B_2O_3- SiO_2 doped with Dy_2O_3 glasses

Glass	The chromaticity coordinates		CCT(K)
	x	y	
$Dy_{0.2}$	0.345	0.325	4912.82
$Dy_{0.4}$	0.337	0.324	5277.93
$Dy_{0.6}$	0.368	0.328	4009.90
$Dy_{0.8}$	0.372	0.332	3906.73
$Dy_{1.0}$	0.381	0.336	3652.30

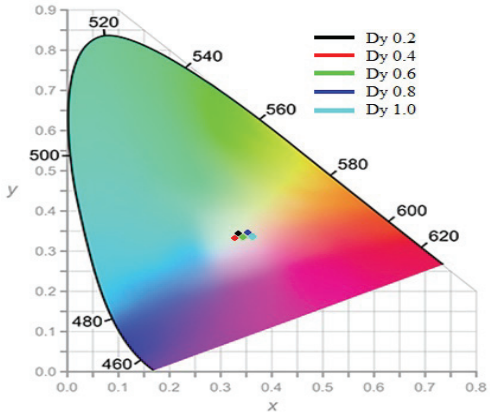

FIGURE.9: The color space chromaticity diagram of Li_2O-CaF_2-Al_2O_3- B_2O_3- SiO_2doped with Dy_2O_3 glasses

CONCLUSIONS

Dy^{3+} doped Li_2O-CaF_2-Al_2O_3- B_2O_3- SiO_2 glasses with virtuous optical stability was prepared. Optical absorption, luminescence, FTIR, XRD were recorded to study the prepared glasses. The optical absorption spectrum has measured by J-O theory and an affordable matching between experimental and theoretical oscillator strengths can be attained. The measured J-O parameters specify that these glasses have low covalency nature. Form the emission spectrum and CIE coordinates recommend that these glasses are appropriate for laser materials.

REFERENCES

[1]. Y.Dwivedi, S.B.Rai, Opt.Mater.31 (2009)1472–1477.
[2]. R. Praveena,C.K. Jayasankar, Spectrochim. Acta A 70 (2008) 577–586.
[3]. Florez, V.A. Jerez, J. Alloys Compd. 303–304 (2000) 355.
[4]. M. A. Marzouk • M. A. Ouis • Y. M. Hamdy, Silicon (2012) 4:221 227.
[5]. T.G.V.M. Rao, A. Rupesh Kumar, K. Neeraja, N. Veeraiah, M. Rami Reddy, SpectrochimicaActa Part A: Molecular and Biomolecular Spectroscopy 118 (2014) 744– 751.
[6]. T.Chengaiaha,K.Kiran Kumara, L.RamaMoorthy, Volume 5, Issue 10, Part 1, 2018, Pages 21232-21240.
[7]. G. Lakshminarayana, R. VidyaSagar, S. Buddhudu, Volume 403, Issue 1, p. 81-86.
[8]. Carnall W T, Fields P R and RajnakK ,ElecJ. Chem. Phys. 49, 4424 (1968).
[9]. P. Ramesh Babu, R. Vijay, D. Krishna Rao, J. Non-Cryst.Solids 370 (2013) 21–30.
[10]. A.M.B. Silva, C.M. Queiroz, S. Agathopoulos, R.N. Correia, M.H.V. Fernandes, J.M.Oliveira, J. Mol. Struct. 986 (2011) 16–21.
[11]. J. Santhan Kumar, J. Lakshmi Kumari, Opt. Mater. 35 (2013) 1320–1326.
[12]. Shaik Kareem Ahmmad, M.A. Samee, S.M. Taqiullah, Syed Rahman, Pages 329-339.
[13]. R.R.Reddy, Y.NazeerAhammed, P.AbdulAzeemaK.RamaGopalaT.V.R.Rao,S.BuddhudubN.SoorajHussain, Volume 77, Issue 2, 1 March 2003, Pages 149- 163.
[14]. R.Cases, M..AChamarro, R.Alcala, V.D.Rodriguez, Volumes 48–49, Part 2, 1991, Pages 509-514.
[15]. B.R. Judd, Optical Absorption Intensities of Rare-Earth Ions, Phys. Rev. 127 (1962)750.
[16]. S. Surendrababu, P. Babu, C.K. Jayasankar, Th. Troster, W. Sievers, G. Wortmann, Opt.Mater. 31 (2009) 642-631.

Journal of Physics: Conference Series

First-principles study of structural, elastic, electronic and optical properties of cubic perovskite $LiMgF_3$ for novel applications

First-principles study of structural, elastic, electronic and optical properties of cubic perovskite $LiMgF_3$ for novel applications

K. Ephraim Babu[1*], K. Neeraja[1], D. Deenabandhu[2], A. Mary Vijaya Ratna[3], V. Venkata Kumar[4], K. Bueala Kumari[4], Paulos Taddesse[5],G. Tewodros Aregai[6], MVK Mehar[7], B. Vikram Babu[8], K. Samatha[8] and V. Veeraiah[8]

[1]Department of Physics, Narasaraopeta Engineering College(A), Narasarao pet, Yellamanda (P.O) Guntur(D.T) Andhra Pradesh, 522601, India.
[2]Department of Physics, Dr. L. B. College of Engineering for Women,Visakhapatnam.
[3]Department of Physics, St. Joseph's College for Women(A), Visakhapatnam.
[4]Department of BS&H, St. Ann's College of Engineering & Technology, Nayunipalli village, ChallaReddyPalem Post, Vetapalem Mandal, Chirala, Prakasam District, AP.
[5]Department of Physics, College of Natural Sciences, Arba Minch University, Arba Minch, Ethiopia.
[6]Department of Physics, Aksum University, Ethiopia
[7]Department of Physics, P.R. Govt. College(A), Kakinada, E.G. Dist, A.P
[8]Department of Physics, Andhra University, Visakhapatnam, Andhra Pradesh, India.

*Corresponding author. E-mail: ephraimbabu@gmail.com

Abstract. Structural, elastic and optoelectronic properties of materials are important to identify their applications in technology. In the present paper $LiMgF_3$ is investigated to obtain these properties using the highly accurate full-potential linearized augmented plane wave (FP-LAPW) method. The exchange correlation effects are included through the generalized gradient approximation (GGA) and modified Becke-Johnson (mBJ) exchange potential. The structural optimization of $LiMgF_3$ is compared with previous results and is found to be in good agreement with those results. The predicted band structure shows an indirect (M-Γ) bandgap of 6.1 eV. The elastic properties such as elastic constants, anisotropy factor, shear modulus, Young's modulus, Poisson's ratio are calculated and based on these calculations it is found that this compound is elastically stable and brittle in nature. The contribution of different bands to the band structure is analyzed from the total and partial density of states curves. Optical properties like real and imaginary parts of dielectric function, refractive index, extinction coefficient, reflectivity, energy loss function, conductivity and absorption coefficient are presented. Based on the optical properties of the compound, it is predicted that $LiMgF_3$ is suitable for optoelectronic devices

1. Introduction

$LiMgF_3$ crystal is a candidate for vacuum-ultraviolet-transparent (VUV-transparent) material for lenses in optical lithography that are useful in the semiconductor industry [1,2]. Lithography technology requires to write more accurate circuit with many challenges like polarized light system, laser lens system, stronger light source, immersion technique, etc. Ternary compounds belonging to the group of fluoroperovskites have the general formula ABF_3, where A is alkali metal (A=Li, Na, K

and Rb) and B is alkaline-earth metal (B=Be, Mg, Ca, Sr and Ba). In this structure, ion A has large size than ion B. Moreover, the fluoroperovkite compounds can be used in the medical field to measure the dose during radiation therapy, and they may also be used in the manufacture of radiation imaging plates for X-rays, gamma-rays and thermal neutrons for medical and non-destructive testing applications.Perovskite-like fluorides generally have the wide bandgaps and are therefore preferable materials for lenses and transparent optical coatings. Thermoluminescence properties of $LiMgF_3$ doped with Ce, Er and Dy impurities are reported and suggested that this material is very attractive for many dosimetric applications [3]. Thermoluminescence characteristics of $LiMgF_3$ are activated by Dyions [4]. The thermoluminescence properties of $LiMgF_3$ doped with ErF_3 (1,2 and 4 mol%) are investigated by Munoz et al,[5]. From the literature it is found that $LiMgF_3$ doped with Ce,Er and Dy ions exhibit dosimetric applications. In the literature it is observed that $KMgF_3$ is also used for similar applications as reported in both experimental [6-9] and theoretical studies [10, 11]. It is well known that the materials with band gaps larger than 3.1 eV work well in the ultraviolet (UV) region of the spectrum [12-15]. Since $LiMgF_3$ is like the other fluoroperovskites and has a wide band gap larger than 6.1 eV, then it can be effectively used in UV based optoelectronic devices. However, its characteristics have not been investigated in detail till now [16]. In order to take full advantage of the properties of $LiMgF_3$ for more technological applications, it is necessary to investigate some of the physical properties. The aim of this work is to investigate the structural, elastic, electronic and optical properties of fluoro-perovskite $LiMgF_3$ by density functional theory (DFT) using the full potential linearized augmented plane wave (FP-LAPW) method, with LDA, GGA, and (mBJ) techniques.

2. Computational details

The crystal structure of the fluoroperovskite $LiMgF_3$ compound is cubic and it belongs to the space group Pm-3m (#221). The unit cell contains one molecule where the Li sits at the origin (0, 0, 0), the Mg at the body center (0.5, 0.5, 0.5) and the three fluorine atoms at the three face centers (0, 0.5, 0.5), (0.5, 0, 0.5) and (0.5, 0.5, 0). 'Figure 1' shows the crystal structure of $LiMgF_3$. In this paper, our calculations are performed using the full potential linearized augmented plane wave (FP-LAPW) method within density functional theory (DFT) [17,18] in the local density approximation (LDA)[19], generalized gradient approximation (GGA) of Wu-Cohen[20] and modified Becke-Johnson (mBJ) potentials[21] as utilized in the WIEN2K package [22]. A satisfactory degree of convergence was achieved by considering a number of FP-LAPW basis functions upto$R_{MT}Kmax$ = 8.0 (R_{MT} is the smallest muffin-tin radius). The muffin-tin sphere radii R_{MT} are taken to be 2.2, 1.8 and 1.6 atomic units (a.u.) for Li, Mg and F, respectively. The k-integration over the Brillouin zone is performed using a mesh of 35 k-points in the irreducible wedge of the Brillouin zone. The optical properties of the compound are calculated by using a denser mesh of 102 k-points. Within these spheres, the charge density and potential are expanded in terms of crystal harmonics upto angular momentum l_{max} = 10. The self-consistent calculations are considered to be converged when the total energy is stable within 0.01 mRy.

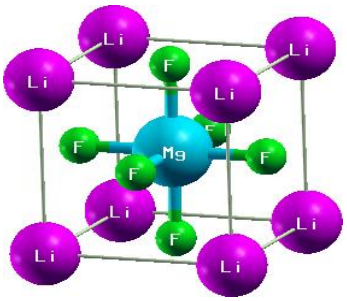

Figure 1. Crystal structure of $LiMgF_3$ obtained with XCrysDen

3. Results and discussion

3.1. Structural properties

In this subsection we calculated important structural parameters of $LiMgF_3$ using the volume optimization process. These parameters are the lattice constant, bulk modulus, pressure derivative of the bulk modulus and ground state total unit cell energy. The volume versus energy curve fits well by the Birch-Murnaghan equation of state [23]. From this fit, we can get the equilibrium lattice constant (a_0), bulk modlus (B_0) and pressure derivative of the bulk modulus (B'). These values are shown in Table 1.

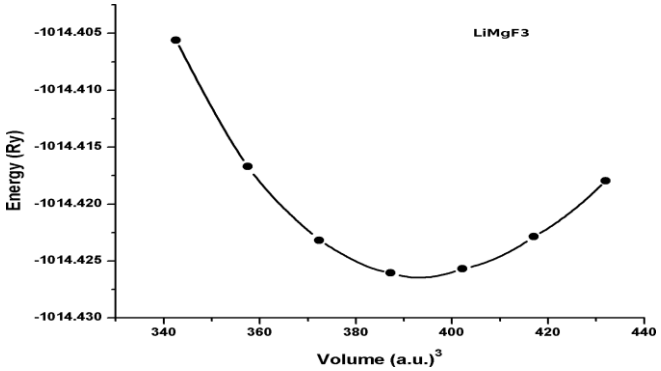

Figure 2. Dependence of total energy of cubic perovskite $LiMgF_3$ crystal on unit cell volume using GGA-WC.

We performed our calculations by using LDA[19], GGA-WC[20] approximations. The total energy per unit cell of $LiMgF_3$ in the cubic perovskite structure is shown in 'Figure 2'. Our calculated equilibrium lattice parameter (a_0) is in reasonable agreement with the experimental value. The bulk modulus (B_0) is a measure of the crystal rigidity, thus a large value of B_0 indicates high crystal rigidity. No previous experimental or theoretical result for this parameter is available for the $LiMgF_3$ compound for comparison with the present calculation.

Table 1. Calculated lattice constant a_0 (Å), bulk modulus B_0 (GPa) and pressure derivative (B'), ground state energy (E_0) of $LiMgF_3$

Method	Lattice Constant a_0 (Å)	B_0 (GPa)	B'	E_0 (Ry)
LDA	3.8057	85.7465	4.2453	-1010.6576
GGA-WC	3.8757	73.6252	4.3796	-1014.4261
Expt.	3.807[a]			

[a] Ref. [2], Experimental value

3.2. Elastic Properties

We further estimated the elastic constants C_{ij} of $LiMgF_3$ to characterize the elastic nature. The elastic constants C_{ij} are fundamental and indispensable for describing the mechanical properties of materials. The elastic constants of solids provide a link between the mechanical and dynamical behaviour of crystals, and define how a material undergoes stress deformations and then recovers and return to its original shape after stress ceases [24]. The elastic constants can provide valuable information about the structural stability, the bonding character between adjacent atomic planes, and anisotropic character. For cubic system, we have three independent elastic constants C_{11}, C_{12} and C_{44}. In order to determine them, the cubic unit cell is deformed using an appropriate strain tensor to yield an energy-strain relation. In this work, we have used the method developed by T. Charpin and implemented in the WIEN2K package [22]. The most interesting elastic constants such as the anisotropy factor (A), Young's modulus (E), Shear modulus (G) and Poisson's ratio υ are calculated by using the relations from references [25-27].In Table 2, we listed the calculated elastic constants, the bulk modulus (B_0),

anisotropy factor A, shear modulus G (in GPa), Young's modulus E (in GPa) and Poisson's ratio υ of the selected material.

Table 2. Calculated elastic constants, bulk modulus (B_0), anisotropy factor A, shear modulus G (in GPa), Young's modulus E (in GPa) and Poisson's ratio υ of the $LiMgF_3$

	C_{11}	C_{12}	C_{44}	B_0	A	G	E	υ	B/G
$LiMgF_3$	161.573	29.877	35.361	73.7756	0.5370	45.3981	84.3124	0.1825	1.6250

For calculating elastic constants of $LiMgF_3$ we followed the method of GGA-WC. The calculated elastic constants C_{ij} are positive and satisfy the mechanical stability criteria [28] in a cubic crystal: $(C_{11} - C_{12}) > 0$; $(C_{11}+2C_{12}) > 0$; $C_{11} > 0$; $C_{44} > 0$, and the bulk modulus B_0 also satisfies the criterion: $C_{12} < B < C_{11}$.

The bulk modulus calculated from the elastic constants using the formula $B_0 = (1/3)(C_{11}+2C_{12})$ within GGA-WC approximation is in good agreement with that obtained from the total energy minimization calculations (Table. 1). To the best of our knowledge no experimental or theoretical values for the elastic constants of this material have been published and hence our results can serve as a reference for future investigations. Similar work to calculate elastic properties of the other materials has been reported in the literature [10, 29]. The anisotropy factor (A) is equal to one for an isotropic material, while any value smaller or larger than one indicates anisotropy. The magnitude of the deviation from 1 is a measure of the degree of elastic anisotropy possessed by the crystal. We obtain the value of the anisotropy factor A as 0.5370 for this compound. This indicates that our compound is anisotropic.

Young's modulus (E) is a good indicator about the stiffness of the material. When it is higher for a given material, the material is stiffer. Poisson's ratio provides more information about the bonding forces than any other elastic property. The value of the Poisson's ratio (υ) for covalent materials is small ($\upsilon < 0.1$), whereas for ionic materials a typical value of υ is 0.25 [30]. In our calculations υ is 0.1825. Hence, a higher ionic contribution in an intra-atomic bonding for this compound is assumed. Mechanical properties such as ductility and brittleness of materials can be explained from the proposed relationship in Pugh's criteria. The shear modulus G represents the resistance to plastic deformation, while the bulk modulus B_0 represents the resistance to fracture. There exists a criterion for B_0/G ratio which separates the ductility and brittleness of materials. According to Pugh's criteria [31], the critical value is 1.75 i.e., if $B_0/G > 1.75$ the material is ductile, otherwise it is brittle. Thus according to Pugh's criteria, the material $LiMgF_3$ is brittle. Based on the experimental results, we find that $KMgF_3$ compound shows brittle nature [6]. Our theoretical results for $LiMgF_3$ also show similar nature.

3.3. Band Structure and Density of States (DOS)

Our theoretical results for $LiMgF_3$ also show similar nature. The calculated energy bands along the high symmetry lines in the Brillouin zone and total as well as partial density of states of LiMgF3 are shown in Figures. 3 and 4 respectively. We discuss our results for the electronic properties of LiMgF3 via the energy band, the total and partial density of states. The mBJ-GGA potential Vxc uses the mBJ exchange potential plus the GGA correlation potential and performs the calculations of bandgap precisely. This method provides the bandgaps almost equal to the experimental values [21]. The zero of energy is chosen to coincide with the valence band maximum (VBM), which occurs at M point, and the conduction band minimum (CBM) occurs at the Γ point resulting in an indirect band gap of 6.1 eV. On the basis of different bands; the total density of states (TDOS) could be grouped into four regions and the contribution of different states in these bands can be seen from the partial density of states (PDOS). In the first region around −4.5 eV to the Fermi energy level, the majority contribution is given by F *2p* states and minority contribution is given by Mg *3s*, Mg *2p* and Mg *3d* states, as seen in figure. 4.(d) and 4 (c). There is hybridization observed between F *2p* with Mg *3s* and Mg *2p* states. In the second region around 6 eV to 10 eV, an equal contribution is given by Li *2s* and

Li *2p* states as seen in Figure. 4 (b). In the region around 12 eV, a sharp peak is observed. The majority contribution due to Li *2p* states and minority contribution due to Li *2s* states are observed in this region. The contribution at 15 eV is mainly due to Mg *3s* states and partially due to Li *2p* states. In the region around 15 eV to 20 eV, majority contribution is by Mg *2p* states and minority contribution is given by Mg *3d* and F *2p* states. The first region within the range of −4.5 to 0 eV comprises the valence band. The second region above the Fermi level is the conduction band. In the conduction band from 6.0 eV to 12 eV majority contributions is from Li *2p* and Li *2s* states. From 12 to 20 eV the contribution is due to the Mg *3s*, Mg *2p*, Mg *3d* and Li *2p* states in the conduction band. The calculated band gap of $LiMgF_3$ is shown in Table 3. Our calculated indirect band gap is 6.11 eV, while the calculated value reported by others is 5.97 eV [2].

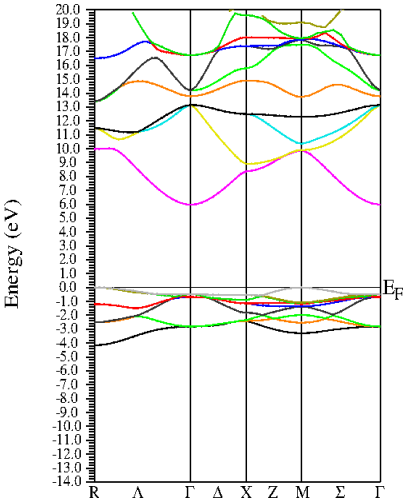

Figure 3.(a) Band structure of LiMgF3 along the high symmetry point

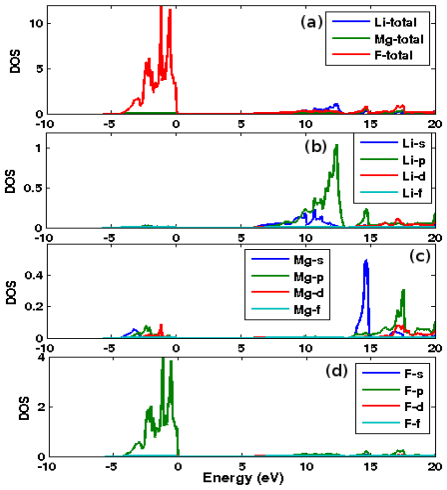

Figure 4. **(a)**Total and partial density of states **(b)** Li **(c)** Mg and **(d)** F in $LiMgF_3$

Table 3. Energy gap (eV) at high symmetry points for $LiMgF_3$

Method	M–Γ	Γ –Γ	R–X	R–M	M–M	R–R	R– Γ	X–X
mBJ-GGA	6.11	6.52	8.50	10.05	10.50	10.05	6.11	8.81

3.4. Charge Density

The charge density distributions are shown in Fig. 5. Charge density maps serve as a complementary tool for achieving a proper understanding of the electronic structure of the system being studied. The ionic character of any material can be related to the charge transfer between the cation and anion while covalent character is related to the sharing of the charge among the cation and anion. The covalent behaviour is due to hybridization of F *2p* with Mg *3s* and Mg *2p* states in the valence band near the Fermi Energy level. From the figures it is clear that the highest charge density occurs in the immediate vicinity of the nuclei. The near spherical charge distribution around Li indicates that the bond between Li and F is strong ionic, with no charge sharing among the contours of the respective atoms. It can be seen that most of the charge is populated in the Mg-F bond direction, while the maximum charge resides on the Mg and F sites. The corresponding contour maps of the charge density distributions are shown in Figure 5. (a) along (1 0 0) plane in 2D representation, Figure. 5.(b) along (1 0 0) plane in 3D representation and Fig. 5. (c) along (1 1 0) plane in 2D representation. Hence, we conclude that there exists a strong ionic bonding in Li-Mg and a mixture of ionic and weak covalent bonding in Mg-F.

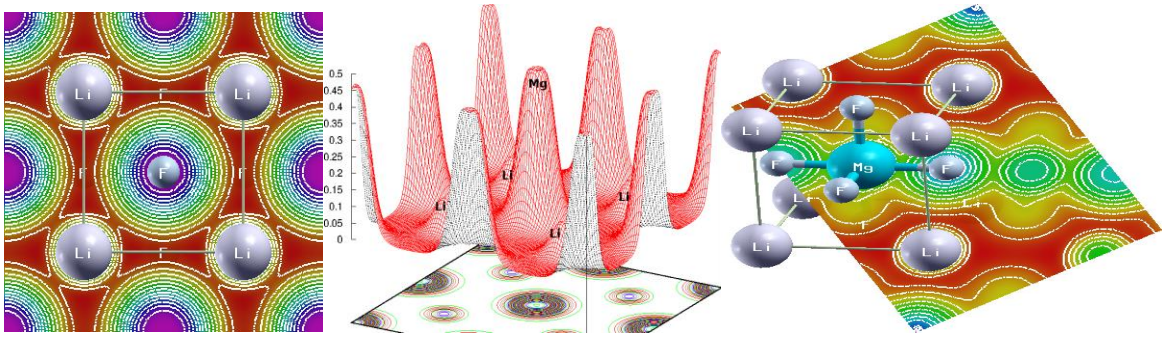

Fig. 5(a). Fig. 5. (b) Fig. 5. (c)

Figure 5. Charge density distribution of $LiMgF_3$ **(a)** along (1 0 0) plane in 2-D representation, **(b)** along (1 0 0) plane in 3-D representation **(c)** along (1 1 0) direction.

3.5. Dielectric and Optical Properties

The dielectric function $\varepsilon(\omega) = \varepsilon_1(\omega) + i\varepsilon_2(\omega)$ is known to describe the optical response of the medium at all photon energies. The imaginary part $\varepsilon_2(\omega)$ is directly related to the electronic band structure of a material and describes the absorptive behaviour. The imaginary part of the dielectric function $\varepsilon_2(\omega)$ is given [32,33] by

$$\varepsilon_2(\omega) = \left(\frac{4\pi^2 e^2}{m^2\omega^2}\right)\sum_{i,j}\int_k \langle i|M|j\rangle^2 \, f_i(1-f_i)\delta(E_{j,k}-E_{i,k}-\omega)d^3k \qquad (1)$$

where M is the dipole matrix, i and j are the initial and final states respectively, f_i is the Fermi distribution function for the i-th state, and E_i is the energy of electron in the i-th state with crystal wavevector k. The real part $\varepsilon_1(\omega)$ of the dielectric function can be extracted from the imaginary part using the Kramers-Kronig relation in the form [34-36]:

$$\varepsilon_1(\omega) = 1 + \frac{2}{\pi}P\int_0^{\infty}\frac{\omega'\varepsilon_2(\omega')d\omega'}{\omega'^2-\omega^2} \qquad (2)$$

where P implies the principal value of the integral.

The FP-LAPW is a good theoretical tool for the calculation of the optical properties of a compound. The optical properties give useful information about the internal structure of the $LiMgF_3$ compound. The GGA method is used to calculate the optical properties of this compound. The calculated optical properties of $LiMgF_3$ are shown in Figure 6. The imaginary part $\varepsilon_2(\omega)$ and the real part $\varepsilon_1(\omega)$ of the dielectric function, refractive index $n(\omega)$, extinction coefficient $k(\omega)$, Reflectivity $R(\omega)$, energy loss function $L(\omega)$, optical conductivity $\sigma(\omega)$ and absorption coefficient $\alpha(\omega)$ of $LiMgF_3$ are shown in Fig. 6, as functions of the photon energy in the range of 0-30 eV.

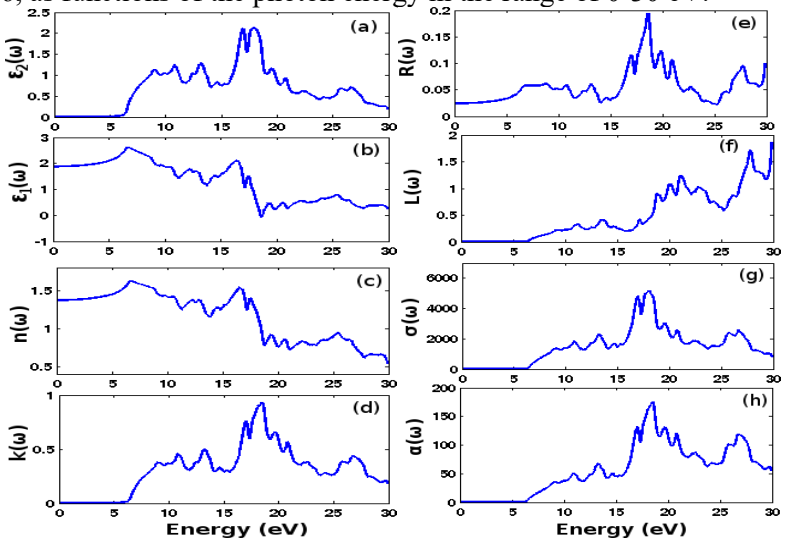

Figure 6. Optical spectra as a function of photon energy for cubic perovskite $LiMgF_3$

(a) Imaginary part $\varepsilon_2(\omega)$ and (b) real part $\varepsilon_1(\omega)$ of dielectric function (c) refractive index $n(\omega)$ (d) extinction coefficient $k(\omega)$, (e) reflectivity $R(\omega)$, (f) energy loss function $L(\omega)$, (g) optical conductivity $\sigma(\omega)$ and (h) absorption coefficient $\alpha(\omega)$ of $LiMgF_3$

The imaginary part $\varepsilon_2(\omega)$ gives the information of absorption behaviour of $LiMgF_3$. In the imaginary part $\varepsilon_2(\omega)$, the threshold energy of the dielectric function occurs at $E_0 = 6.14$ eV, which corresponds to the fundamental gap at equilibrium. The real part of the dielectric function $\varepsilon_1(\omega)$ is displayed in Figure 6 (b). This function $\varepsilon_1(\omega)$ gives us information about the electronic polarizability of a material. The static dielectric constant at zero is obtained as $\varepsilon_1(0) = 1.88$. From its zero frequency limit, it starts increasing and reaches the maximum value of 2.60 at 6.63 eV, and goes below 0 in negative scale for the range of 18.54 – 18.75 eV. The refractive index and extinction coefficient are displayed in Figures. 6 (c) and 6 (d).

When we look at the behaviour of imaginary part of dielectric function $\varepsilon_2(\omega)$ and extinction coefficient $k(\omega)$, a similar trend is observed from Figures 6 (a) and 6 (d). The extinction coefficient $k(\omega)$ reaches the maximum absorption in the medium at 18.48 eV. Frequency dependent refractive index $n(\omega)$, reflectivity $R(\omega)$, and optical conductivity $\sigma(\omega)$ are also calculated and the salient features of the spectra are presented in Table 4.

Table 4. Calculated zero frequency limits of refractive index n(0), reflectivity R(0), energy range for $n(\omega) < 1$, maximum values of refractive index $n(\omega)$, reflectivity $R(\omega)$ and optical conductivity $\sigma(\omega)$ of $LiMgF_3$

$LiMgF_3$	n (0)	Maximum n (ω)	Energy range (in eV) for n (ω) < 1	R (0) %	Maximum R (ω)	Maximum σ (ω) (in Ω-1 cm-1)
This work	1.37	1.61	18.54-30	2.43	18.59	5137.33

4. Conclusion

In summary, the structural, elastic, electronic and optical properties of the cubic perovskite $LiMgF_3$ are investigated using the full-potential linearized augmented plane wave method. The exchange correlation effects are included through the generalized gradient approximation and modified Becke-Johnson exchange potential. The lattice parameter at equilibrium is in reasonable agreement with previous calculations. Cubic perovskite $LiMgF_3$ is brittle and elastically anisotropic. The analysis of partial density of states revealed that the valence bonding region shows hybridization of F *2p* with Mg *3s*and Mg *2p* states. The energy band structure clearly demonstrates that $LiMgF_3$ is an indirect band gap (M- Γ) material. The optical properties such as dielectric function, reflectivity, absorption coefficient, optical conductivity, refractive index, extinction coefficient and electron energy loss function are studied in the energy range of 0-30 eV. The high absorption power of the compound in the visible and ultraviolet energy range predicts its usefulness in optical and optoelectronic devices in this range.

References

[1] T. Nishimatsu, N. Terakubo, H. Mizuseki, Y. Kawazoe, D.A. Pawlak, K. Shimamuri, T. Fukuda, *Jpn. J. Appl. Phys.,*2002, **41**, 365
[2] Riadh El Ouenzerfi, Shingo Ono, Alex Quema, Masahiro Goto, Masahiro Sakai, and Nobuhiko Sarukura, et al., *Journal of Applied Physics*, 2004, **96**, 7655-7659
[3] G. Kitis, C. Furetta and C. Sanipoli, *Radiation Protection Dosimetry*,2002,**100**, 247–250.
[4] R. Bernal , K. R. Alday-Samaniego , C. Furetta , E. Cruz-Zaragoza , G. Kitis , F. Brown & C. Cruz-Vázquez, *Radiation Effects and Defects in Solids: Incorporating Plasma Science and Plasma Technology,*2007, **162**:10-11, 699-708.
[5] I.C. Munoz , E.Cruz-Zaragoza, A.Favalli, C.Furetta, *Applied Radiation and Isotopes*, 2012, 70, 893–896.

[6] G. Vaitheeswaran, V. Kanchana, Ravhi S. Kumar, A. L. Cornelius, M. F. Nicol, A. Svane et.at., *Phys. Rev. B,* **76,** 014107.
[7] Furetta. C, Bacci. C, Rispoli. B, Sanipoli. C, Scacco. A., *Radiat. Prot.Dosim*.,1990,**33**, 107-110
[8] Gambarini. G, Marchese. P, Scacco. A, Sinha Roy. M, Marchesini. R., *Radiat. Prot. Dosim*. 1999, **84**, 211-214.
[9] Kitis. G, Furetta. C, Sanipoli. C, Scacco. A, *Radiat. Prot. Dosim,* 1999, **82(2)**, 151-152.
[10] M. Sahnoun, M. Zbiri, C. Daul, R. Khenata, H. Baltache, M. Driz, *Materials Chemistry and Physics,* 2005,**91**, 185-191.
[11] G. Pilania, Vinit Sharma, *J Mater Sci,* 2013, **48**, 7635–7641.
[12] Muhammad Maqbool, Martin E. Kordesch, A. Kayani, *J. Opt. Soc. Am. B***,** 2009**,26,** 998.
[13] K. Ephraim Babu, A. Veeraiah, D. Tirupati Swamy, V. Veeraiah, *Chin. Phys. Lett*.,2012,**29**, 117102.
[14] G. Murtaza, I. Ahmad, *J. Appl. Phys.,* 2012, 111, 123116.
[15] M. Maqbool, I. Ahmad, H.H. Richardson, M.E. Kordesch, *Appl. Phys. Lett*.,2007,**91**, 193511.
[16] Shingo Ono, Riadh El Ouenzerfi, Alex Quema, Hidetoshi Murakami, Nobuhiko Sarukura, et al., *Japanese Journal of Applied Physics,*2005,**44**, 7285–7290.
[17] Hohenberg P and Kohn W,*Phys. Rev. B*, 1964,**136**,864
[18] Kohn W and Sham L J, *Phys. Rev. A,* 1965, **140**, 1133
[19] J. P. Perdew, Y. Wang, *Phys. Rev. B*, 1992, **45,**13244.
[20] Z. Wu, R.E. Cohen, *Phys. Rev. B*, 2006, **73**, 235116.
[21] F. Tran, P. Blaha, *Phys. Rev. Lett*., 2009, **102**, 226401.
[22] P. Blaha, K. Schwarz, G. K. H. Madsen, D. Kvasnicka, and J. Luitz, in WIEN2K: An Augmented Plane Wave Plus Local Orbitals Program for Calculating Crystal Properties, Ed. by K. Schwarz (Vienna Technological University, Vienna, Austria, 2001).
[23] F. D. Murnaghan, Proc. Ntal. *Acad. Sci. USA*, 1944,**30**, 244.
[24] H. Reshak, M. Jamal, *J. Alloys Compd*., 2012, **543**, 147
[25] R. Hill, *Proc. Phys. Soc. Lond. A*, 1952, 65, 349.
[26] W. Voigt, Handbook of Crystal Physics, Teubner, Leipzig 1928.
[27] A. Russ, A. Angew, Mater. Phys., 1929, 9, 49.
[28] G. Grimvall, *Thermophysical properties of materials*, Elsevier, North-Holland Amsterdam, 1999, Enlarged and revised edition.
[29] M. Rajagopalan, R. Rajiv Gandhi, *Physica B*, 2012, **407**, 4731-4734.
[30] J. Haines, J. M. Leger, G. Bocquillon, *Annu. Rev. Mater. Res.,* 2001,**31**, 1
[31] S. F. Pugh, *Philos. Mag.,*1954, **45**, 823.
[32] N.V. Smith, *Phys. Rev. B*, 1971,**3**, 1862.
[33] C. Ambrosch-Draxl, J.O. Sofo,*Comput. Phys. Commun*.,2006,**175,** 1.
[34] M. Fox, Optical Properties of Solids, (Oxford University Press, New York, 2001).
[35] F. Wooten, Optical properties of Solids, (Acadmic Press, New York, 1972).
[36] M. Dressel, G. Gruner, Electrodynamics of Solids: Optical Properties of Electrons in Matter, Cambridge University Press, UK, 2002.

Chapter

Segmenting Images Using Hybridization of K-Means and Fuzzy C-Means Algorithms

Raja Kishor Duggirala

Abstract

Image segmentation is an essential technique of image processing for analyzing an image by partitioning it into non-overlapped regions each region referring to a set of pixels. Image segmentation approaches can be divided into four categories. They are thresholding, edge detection, region extraction and clustering. Clustering techniques can be used for partitioning datasets into groups according to the homogeneity of data points. The present research work proposes two algorithms involving hybridization of K-Means (*KM*) and Fuzzy C-Means (*FCM*) techniques as an attempt to achieve better clustering results. Along with the proposed hybrid algorithms, the present work also experiments with the standard K-Means and *FCM* algorithms. All the algorithms are experimented on four images. CPU Time, clustering fitness and sum of squared errors (SSE) are computed for measuring clustering performance of the algorithms. In all the experiments it is observed that the proposed hybrid algorithm *KMandFCM* is consistently producing better clustering results.

Keywords: image segmentation, clustering, K-Means, Fuzzy C-Means, hybridization, sum of squared error, clustering fitness

1. Introduction

Images are often the most important category among the available digital data. In the recent years, image data is increasing and will continue increase in the near future. Since it is difficult to deal with large amount of image data as the available data increases, it becomes crucial to use the automated tools for various purposes in connection to image data. The image processing provides wide range of techniques to deal with the images. By using the image processing techniques, we can make the work much easier not only for now, but also for the future when there will be more data and more work to do on the images.

Image segmentation is an essential image processing technique that analyzes an image by partitioning it into non-overlapped regions each region referring to a set of pixels. The pixels in a region are similar with respect to some characteristic such as color, intensity, or texture [1]. The pixels significantly differ with those in the other regions with respect to the same characteristic [2–4]. Image segmentation plays an important role in a variety of applications such as robot vision, object recognition, medical imaging and etc. [5–7]. Image segmentation approaches can be divided into four categories. They are thresholding, edge detection, region

extraction and clustering. Clustering techniques can be used for data segmenting image data as they are used for partitioning large datasets into groups according to the homogeneity of data points.

In clustering, a given population of data is partitioned into groups such that objects are similar to one another within the same group and are dissimilar to the objects in other groups [8, 9]. There are different categories of clustering techniques. These can be partitional (hierarchical and non-hierarchical), like K-means, PAM, CLARA, CLARANs [10, 11]; model-based, like Expectation Maximization, SOM, Mixture model clustering [12, 13]; or fuzzy-based like Fuzzy C-Means [14, 15].

Partitional clustering techniques attempt to break a population of data into some predefined number of clusters such that the partition optimizes a given criterion.

Formally, clusters can be seen as subsets of the given dataset. So, clustering methods can be classified according to whether the subsets are fuzzy or crisp (hard). In hard clustering, an object either does or does not belong to a cluster. These methods partition the data into a specified number of mutually exclusive subsets. However, in fuzzy-based clustering, the objects may belong to several clusters with different degrees of membership [16].

It is studied in the literature that many researchers experimented with the Fuzzy C-Means (*FCM*) algorithm in a wide variety of ways for achieving better image segmentation results [1, 17]. In [18], a penalized *FCM* (*PFCM*) algorithm is presented for image segmentation for handling noise by adjusting a penalty coefficient. The penalty term used here takes the spatial dependence of the objects into consideration, which is modified according to the *FCM* criterion. In [19], a fuzzy rule-based technique is proposed. It employs the rule-based neighborhood enhancement system to impose spatial continuity by post-processing on the clustering results obtained using *FCM* algorithm. In [20], a Geometrically Guided *FCM* (*GG-FCM*) algorithm is proposed, which is based on a semi-supervised *FCM* technique for multivariate image segmentation. In [21], a regularization term was introduced into the standard *FCM* to impose the neighborhood effect. In [22], this regularization term is incorporated into a kernel-based fuzzy clustering algorithm. In [23], this regularization) term is incorporated into the adaptive *FCM* (*AFCM*) algorithm [24] to overcome the noise sensitivity of *AFCM* algorithm.

However, it is found in the literature that a very less attention is paid towards the hybridization of clustering techniques for partitioning the datasets.

The present research work aims at developing hybrid clustering algorithms involving K-Means and Fuzzy C-Means (*FCM*) techniques for achieving better clustering results. As part of hybridization, two algorithms are developed, *KMFCM* and *KMandFCM*. The *KMFCM* algorithm first performs K-Means on the dataset and then performs *FCM* using the results of K-Means. The *KMandFCM* algorithm performs K-Means and *FCM* in the alternative iterations.

All the experiments are carried out using the datasets that are related to four images. For performance evaluation, CPU time, clustering fitness and sum of squared error (SSE) are taken into consideration.

The following sections provide a detailed discussion of K-Means (*KM*), Fuzzy C-Means (*FCM*), *KMFCM* and *KMandFCM* algorithms.

2. The K-Means (*KM*) algorithms

Partitional clustering methods are appropriate for the efficient representation of large datasets [11]. These methods determine *k* clusters such that the data objects in a cluster are more similar to each other than to the objects in other clusters.

The K-Means is a partitional clustering method, which partitions a given dataset into a pre-specified number, k, of clusters [25]. It is a simple iterative method. The algorithm is initialized by randomly choosing k points from a given dataset as the initial cluster centers, i.e., cluster means. The algorithm iterates through two steps till its convergence:

1. Data assignment: this step partitions the data by assigning each data object to its closest cluster center.

2. Updating the cluster centers: update the center of each cluster based on the objects assigned to that cluster.

The algorithm for K-Means is as follows [26]. Here, k represents the number of clusters, d represents the number of dimensions or attributes, X_i represents the ith data sample, μ_j (j = 1, 2, ..., k) represents the mean vector of cluster C_j, t is the iteration number. For termination condition the algorithm computes *percentage change*, Eq. (2). The algorithm terminates when *Percentage change* $< \alpha$. Here, α is assumed to be 3 since it is negligible.

***KM* algorithm**

1. Select k vectors randomly from the dataset as the initial cluster centers, μ_j (j = 1, 2, ..., k). Set the current iteration t = 0.

2. Assign each vector, X_i, to its closest cluster center using Euclidean distance, Eq. (1).

$$d\left(X_i, \mu_j\right) = \sqrt{\sum_{l=1}^{d}\left(x_{il} - \mu_{jl}\right)^2} \tag{1}$$

3. Update mean vectors μ_j (j = 1, ..., k).

4. Compute Percentage change as follows

$$\text{Percentage change} = \frac{|\Psi_t - \Psi_{t+1}|}{\Psi_t} \times 100 \tag{2}$$

where Ψ_t is the number of vectors assigned to new clusters in tth iteration and Ψ_{t+1} is the number of vectors assigned to new clusters in (t + 1)th iteration.

5. Stop the process if *Percentage change* $< \alpha$, otherwise set $t = t + 1$ and repeat the steps 2–4 with the updated parameter.

The K-Means uses Euclidean distance as a proximity measure for determining the closest cluster to which a data object is assigned [13]. The algorithm stops when the assignment of data points to the clusters no longer changes or some other criterion is satisfied. The K-Means is a widely used algorithm for clustering and it requires less CPU time. However, it mainly suffers from detecting the natural clusters that have non-spherical shapes or widely different sizes or densities [25].

3. The Fuzzy C-Means (*FCM*) algorithms

Fuzzy-based clustering techniques focus on modeling uncertain and vague information that is found in the real world situations. These techniques deal with the clusters whose boundaries cannot be defined sharply [14, 15]. By fuzzy-based clustering, one can know if data objects fully or partially belong to the clusters based

on their memberships in different clusters [27]. Among the fuzzy-based clustering methods, Fuzzy C-Means (*FCM*) is the most well-known algorithm as it has the advantage of robustness for obscure information about the clusters [1, 28].

In *FCM*, a dataset is grouped into k clusters, where every data object may relate to every cluster with some degree of membership to that cluster [16]. The membership of a data object towards a cluster can range between 0 and 1 [29]. The sum of memberships for each data point must be unity.

The *FCM* iterates through two phases for converging to a solution. First, each data object will be associated with a membership value for each cluster, and second, assigning the data object to the cluster with the highest membership value [2].

The algorithm for *FCM* is given below [30]. Here, U is the $k \times N$ membership matrix. While computing the cluster centers and updating the membership matrix at each iteration, the *FCM* uses membership weight, m. For most data $1.5 \leq m \leq 3.0$ gives good results [29]. In all our experiments, we take $m = 1.25$.

***FCM* algorithm**

1. Initialize parameters: select k vectors randomly as cluster means; set initial membership matrix $U^{(0)}_{k \text{ X } N}$, set the current iteration $t = 0$.

2. Assign each data object X_i to clusters using the membership matrix.

3. Compute jth cluster center as follows:

$$\mu_j^{t+1} = \frac{\sum_{i=1}^{N} (u_{ji})^m X_i}{\sum_{i=1}^{N} (u_{ji})^m} \tag{3}$$

4. Compute new membership matrix using

$$u_{ji}^{t+1} = \left[\sum_{l=1}^{k} \left(\frac{\left\| X_i - \mu_j^t \right\|^2}{\left\| X_i - \mu_l^t \right\|^2} \right)^{1/m - 1} \right]^{-1} \tag{4}$$

5. Assign each data object X_i to clusters using the membership matrix.

6. Compute *Percentage change* using Eq. (2).

7. Stop the process if the *Percentage change* is $< \alpha$. Otherwise, set $t = t + 1$ and repeat the steps 3–7 with the updated parameters.

FCM is widely studied and applied in geological shape analysis [31], medical diagnosis [32], automatic target recognition [33], meteorological data [28], pattern recognition, image analysis, image segmentation and image clustering [34–36], agricultural engineering, astronomy, chemistry [37], detection of polluted sites [38] and etc.

4. Hybridization involving K-Means and *FCM* techniques

The partitional [11] and fuzzy-based [16] methods are widely applied clustering techniques in several areas. The partitional clustering methods do hard clustering, where the dataset is partitioned into a specified number of mutually exclusive subsets. The K-Means, as a partitional clustering method is found in the research

literature as widely applied technique in a variety of experiments. While clustering the data, the K-Means aims at minimizing the local distortion [39, 40]. However, K-Means is ideal if the data objects are distributed in well-separated groups.

In fuzzy-based clustering, objects are not forced to fully belong to one cluster. Here, an object may belong to many clusters with varying degrees of membership. This membership can range between 0 and 1 indicating the partial belongingness of objects to the clusters [16]. Fuzzy clustering techniques help in understanding if the data objects fully or partially belong to clusters depending on their memberships [27]. In *FCM*, each data object belongs to each cluster with some degree of membership that ranges between 0 and 1 [29]. Here, clusters are treated as fuzzy sets. In general, introducing the fuzzy logic in K-Means is the Fuzzy C-Means algorithm [41].

The following sub-section discusses two algorithms that apply hybridization of K-Means (*KM*) and Fuzzy C-Means (*FCM*) clustering techniques [42]. These algorithms are *KMFCM* and *KMandFCM*. The *KMFCM* algorithm first performs K-Means on the given dataset and then performs the *FCM* using the results of K-Means. The *KMandFCM* algorithm performs K-Means and *FCM* in the alternative iterations on the given dataset. The detailed discussion of these hybrid algorithms is presented in the following subsections.

4.1 The *KMFCM* algorithm

The proposed hybrid clustering algorithm *KMFCM* first performs the K-Means (*KM*) technique completely on the given dataset. Using the resulted cluster centers of *KM* as cluster seeds, the *FCM* is performed on the given dataset till termination. Here, to run the first iteration of the *FCM*, the cluster centers and the membership matrix are calculated based on the results of *KM*. The remaining iterations continue as in the *FCM* algorithm.

The algorithm for the *KMFCM* is given below. Here, *KM*-Step is the K-Means step and *FCM*-Step is the Fuzzy C-Means step.

***KMFCM* algorithm**

1. ***KM*-Step**: select k vectors randomly from the dataset as the initial cluster centers μ_j ($j = 1, \ldots, k$). Set the current iteration $t = 0$.

2. Assign each data object X_i to its closest cluster center using Eq. (1).

3. Update cluster centers μ_j ($j = 1, \ldots, k$) and set $t = t + 1$.

4. Compute *Percentage change* using Eq. (2).

5. If *Percentage change* $\geq \alpha$, repeat steps 2–4.

6. ***FCM*-Step**: compute the membership matrix $U_{k \text{ X } N}^{(t)}$ using Eq. (4) based on the results of *KM*-Step.

7. Assign data objects to clusters using membership matrix.

8. For each cluster C_j, compute the center μ_j ($j = 1, \ldots, k$) using Eq. (3)

9. Compute *Percentage change* using Eq. (2).

10. Stop the process if *Percentage change* $< \alpha$. Otherwise, set $t = t + 1$ and repeat steps 6–9.

4.2 The *KMandFCM* algorithm

Clustering in *KMandFCM* is performed by executing K-Means and the *FCM* techniques in alternative iterations on the given dataset till termination. The first iteration is performed using K-Means assuming some randomly selected data points as cluster centers. The second iteration is performed using *FCM* technique. For this iteration the cluster means, covariance matrices and the membership matrix are calculated using the results of first iteration. Third iteration is performed using K-Means technique. This iteration computes cluster means using results obtained from the second iteration. In this way, clustering is performed using K-Means and *FCM* in the alternative iterations till termination.

The algorithm for the proposed *KMandFCM* algorithm is given below. Here, *KM*-Step is the K-Means step and *FCM*-Step is the Fuzzy C-Means step.

***KM and FCM* algorithm**

1.Select k vectors randomly from the dataset as initial cluster centers μ_j ($j = 1, \ldots, k$). Set the current iteration $t = 0$.

2.***KM*-Step**: assign each vector X_i to its closest cluster center using Eq. (1).

3.***FCM*-Step**: set $t = t + 1$.

4.For each cluster C_j, compute the center μ_j using Eq. (3)

5.Compute the new membership matrix $U^{(t)}_{k \text{ X } N}$ using Eq. (4)

6.Assign data objects to clusters using the membership matrix.

7.Compute *Percentage change* using Eq. (2).

8.Stop the process if *Percentage change* $< \alpha$. Otherwise, set $t = t + 1$.

9.***KM*-Step**: For each cluster C_j, compute new center μ_j using Eq. (3).

10.Assign each vector X_i to its closest cluster center using Eq. (1).

11.Compute *Percentage change* using Eq. (2).

12.Stop the process if *Percentage change* $< \alpha$. Otherwise, go to step 3.

For all the algorithms, i.e., *KM*, *FCM*, *KMFCM*, *KMandFCM*, the same termination condition, Eq. (2), is used.

5. Performance evaluation measures

For performance evaluation of algorithms, CPU time in seconds, sum of squared error [12] and clustering fitness [43] are taken into consideration and are calculated for all the algorithms.

5.1 Sum of squared errors

The objective of clustering is to minimize the within-cluster sum of squared error (SSE). The lesser the SSE, the better the goodness of fit is. The sum of squared error [12] for the results of each clustering algorithm is computed using the Eq. (5)

$$SSE = \sum_{j=1}^{k} \sum_{X_i \in C_j} \left(X_i - \mu_j\right)^2 \tag{5}$$

Here, X_i is the ith data object in the dataset, μ_j (j = 1, ..., k) is the center of the cluster C_j, and k is the number of clusters.

5.2 Clustering fitness

The main objective of any clustering algorithm is to generate clusters with higher intra-cluster similarity and lower inter-cluster similarity. So, it is also important to consider inter-cluster similarity while evaluating the clustering performance. In the present work, clustering fitness is also considered as a performance criterion, which requires the calculation of both intra-cluster similarity and inter-cluster similarity. The computation of clustering fitness also requires the experiential knowledge, λ. The computation of clustering fitness results in higher value when the inter-cluster similarity is low and results in lower value for when the inter-cluster similarity is high. Also that to make the computation of clustering fitness unbiased, the value of λ is taken as 0.5 [43].

(a) **Intra-cluster similarity for the cluster C_j:** it can be quantified via a function of the reciprocals of intra-cluster radii within each of the resulting clusters. The intra-cluster similarity [43] of a cluster C_j (1 = j = k), denoted as $S_{tra}(C_j)$, is defined in Eq. (6)

$$S_{tra}\left(C_j\right) = \frac{1+n}{1+\sum_1^n dist(I_l, Centroid)} \tag{6}$$

Here, n is the number of items in cluster C_j, I_j (1 = j = n) is the jth item in cluster C_j, and dist(I_j, *Centroid*) calculates the distance between I_j and the centroid of C_j, which is the intra-cluster radius of C_j. To smooth the value of $S_{tra}(C_j)$ and allow for possible singleton clusters, 1 is added to the denominator and numerator.

(b) **Intra-cluster similarity for one clustering result C**: it is denoted as $S_{tra}(C)$. It is defined in Eq. (7), [43]

$$S_{tra}(C) = \frac{\sum_1^k S_{tra}\left(C_j\right)}{k} \tag{7}$$

Here, k is the number of resulting clusters in C and $S_{tra}(C_j)$ is the intra-cluster similarity for the cluster C_j.

(c) **Inter-cluster similarity**: it can be quantified via a function of the reciprocals of inter-cluster radii of the clustering centroids. The inter-cluster similarity [43] for one of the possible clustering results C, denoted as $S_{ter}(C_j)$, is defined as Eq. (8)

$$S_{ter}(C) = \frac{1+k}{1+\sum_1^k dist\left(Centroid_j, Centroid^2\right)} \tag{8}$$

Here, k is the number of resulting clusters in C, 1 = j = k, $Centroid_j$ is the centroid of the jth cluster in C, $Centroid^2$ is the centroid of all centroids of clusters in C. We compute inter-cluster radius of $Centroid_j$ by calculating dist($Centroid_j$, $Centroid^2$), which is distance between $Centroid_j$, and $Centroid^2$. To smooth the value of $S_{ter}(C)$

and allow for possible all-inclusive clustering result, 1 is added to the denominator and the numerator.

(d) Clustering fitness: the clustering fitness [43] for one of the possible clustering results C, denoted as CF, is defined as Eq. (9)

$$CF = \lambda \times S_{tra}(C) + \frac{1-\lambda}{S_{ter}(C)} \tag{9}$$

Here, λ $(0 < \lambda < 1)$ is an experiential weight, $S_{tra}(C)$ is the intra-cluster similarity for the clustering result C and $S_{ter}(C)$ is the inter-cluster similarity for the clustering result C. To avoid biasedness in our experiments, λ is assumed to be 0.5.

6. Experiments and results

Experimental work has been carried out on the system with Intel(R) Core(TM) i3-5005U CPU@2.00GHz processor speed, 4GB RAM, Windows 7 OS (64-bit) and using JDK1.7.0_45. Separate modules are written for each of the above discussed methods to observe the CPU time for clustering any dataset by keeping the cluster seeds same for all methods. I/O operations are eliminated and the CPU time observed is strictly for clustering of the data.

Along with the newly developed hybrid algorithms, experiments are also conducted with the algorithms for standard K-Means (*KM*) and Fuzzy C-Means (*FCM*) for performance comparison. All the algorithms are executed using datasets that are related to four images. The details of these images are available in **Table 1**.

SNO	Image	Resolution	No. of points	No. of dimensions
1	Heart	341 × 367	125,147	3
2	Kidneys	473 × 355	167,915	3
3	Baboon	512 × 512	262,144	3
4	Lena	256 × 256	65,536	3

Table 1.
Medical Images.

The medical images used in the present experiment are heart image [44] and kidneys image [45] (**Figures 1** and **2**). The experiments are also carried out using two benchmark images. They are Baboon and Lena images [46] (**Figures 3** and **4**).

Below is the brief description of medical images.

The Heart is a medical image obtained from biology data repository [44]. It is in "jpeg" format. The 'Kidneys' is a colored MRI scan of a coronal section through a human abdomen, showing the front view of healthy kidneys and liver [45]. It is in 'jpeg' format. The Baboon and Lena are benchmark test images that are found frequently in the literature [46]. These are all in uncompressed "tif" format.

All the algorithms for standard K-Means (*KM*), standard Fuzzy C-Means (*FCM*), *KMFCM* and *KMandFCM* are executed on each image data with varying number of clusters (k = 10, 11, 12, 13, 14, 15). For all algorithms, same cluster seeds are used. Same termination condition Eq. (2) is used for all the experiments. The details of CPU time, clustering fitness and SSE of each algorithm for the all images are given in the following sub-sections (**Tables 2–13**). The results are also projected in their respective graphs (**Figures 5–16**).

6.1 Observations with Heart image

K	*KM*	*FCM*	*KMFCM*	*KM and FCM*
10	0.21	0.30	1.36	0.19
11	0.21	0.32	1.48	0.20
12	0.25	0.40	1.61	0.20
13	0.09	0.35	1.58	0.22
14	0.14	0.39	1.73	0.23
15	0.36	0.43	2.15	0.26

Table 2.
CPU time of each clustering technique (Heart image).

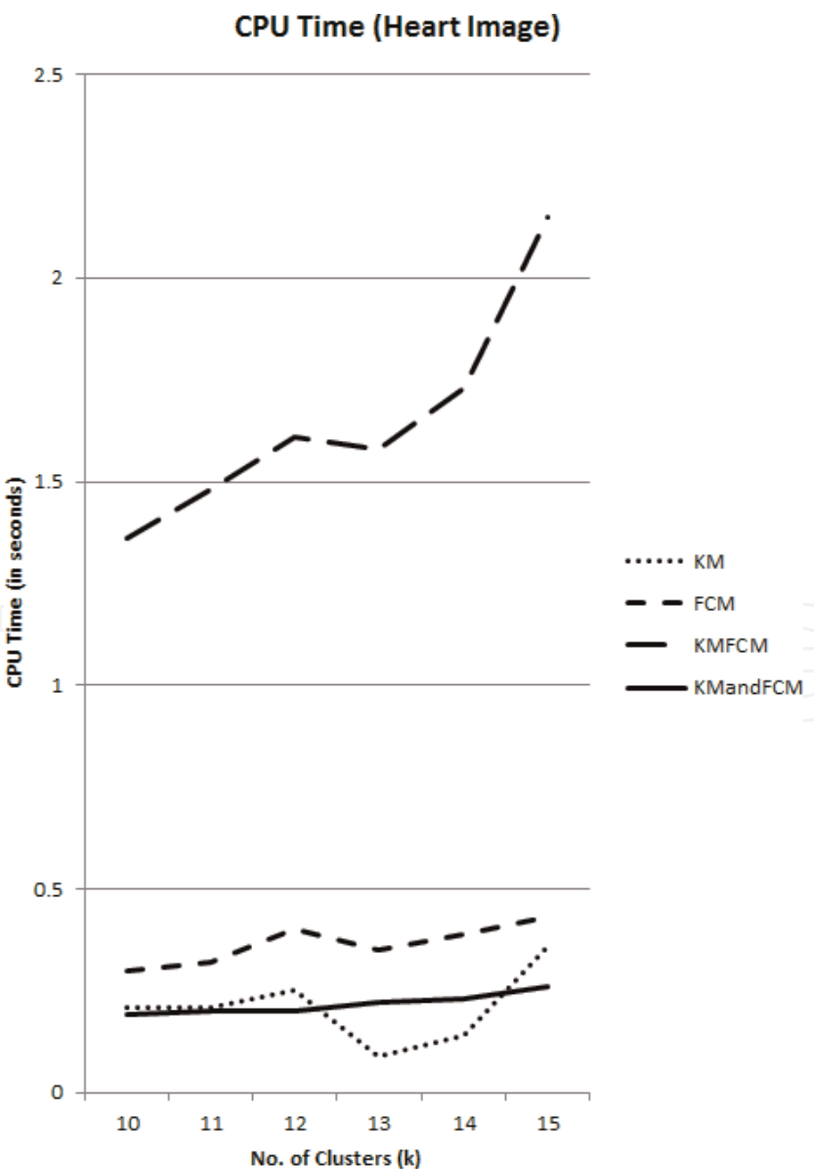

Figure 1.
CPU time (Heart image).

K	*KM*	*FCM*	*KMFCM*	*KM and FCM*
10	51.20	56.62	58.51	64.78
11	49.79	55.73	55.40	62.14
12	42.27	55.80	61.16	65.97
13	34.88	47.54	41.08	58.46
14	48.34	55.22	56.62	60.35
15	47.54	57.96	48.24	59.22

Table 3.
Clustering fitness of each clustering technique (Heart image).

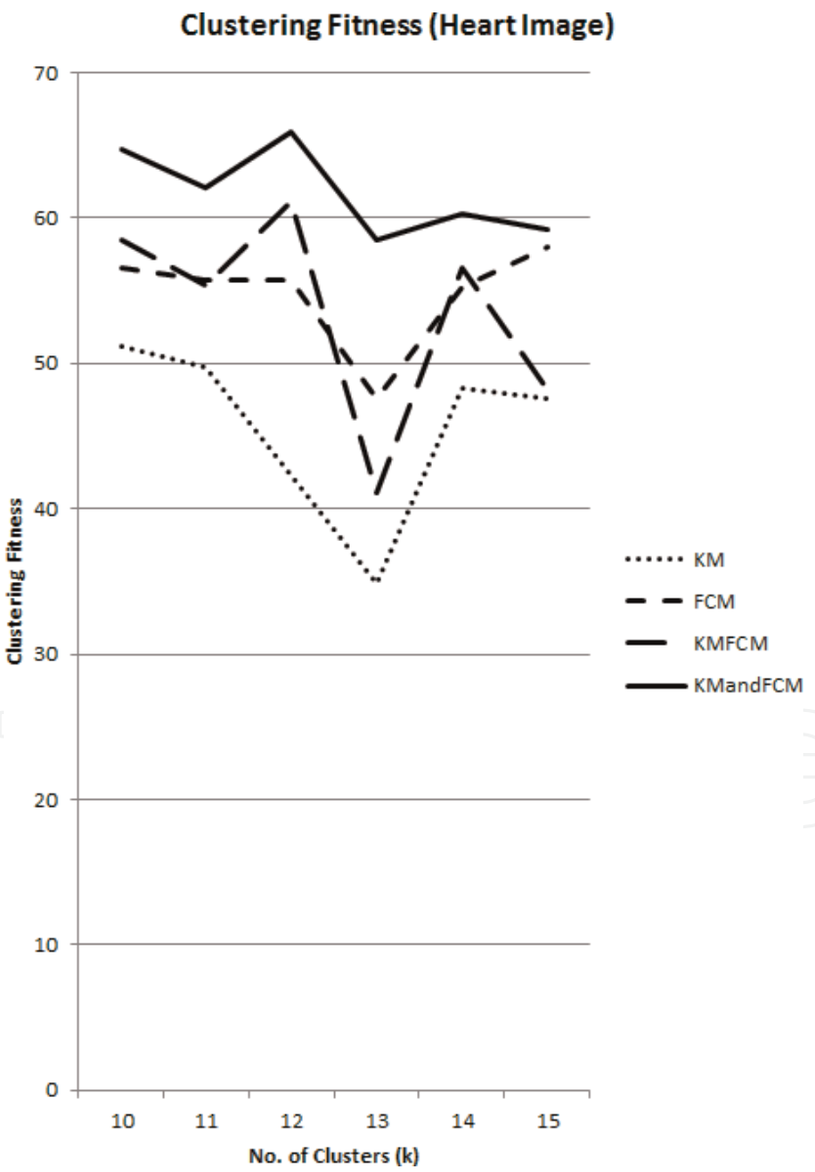

Figure 2.
Clustering Fitness (Heart image).

K	*KM*	*FCM*	*KMFCM*	*KM and FCM*
10	0.0163	0.0152	0.0148	0.0041
11	0.0150	0.0145	0.0074	0.0036
12	0.0173	0.0163	0.0059	0.0031
13	0.0185	0.0171	0.0285	0.0037
14	0.0142	0.0139	0.0113	0.0028
15	0.0138	0.0114	0.0241	0.0024

Table 4.
SSE of each clustering technique (Heart image).

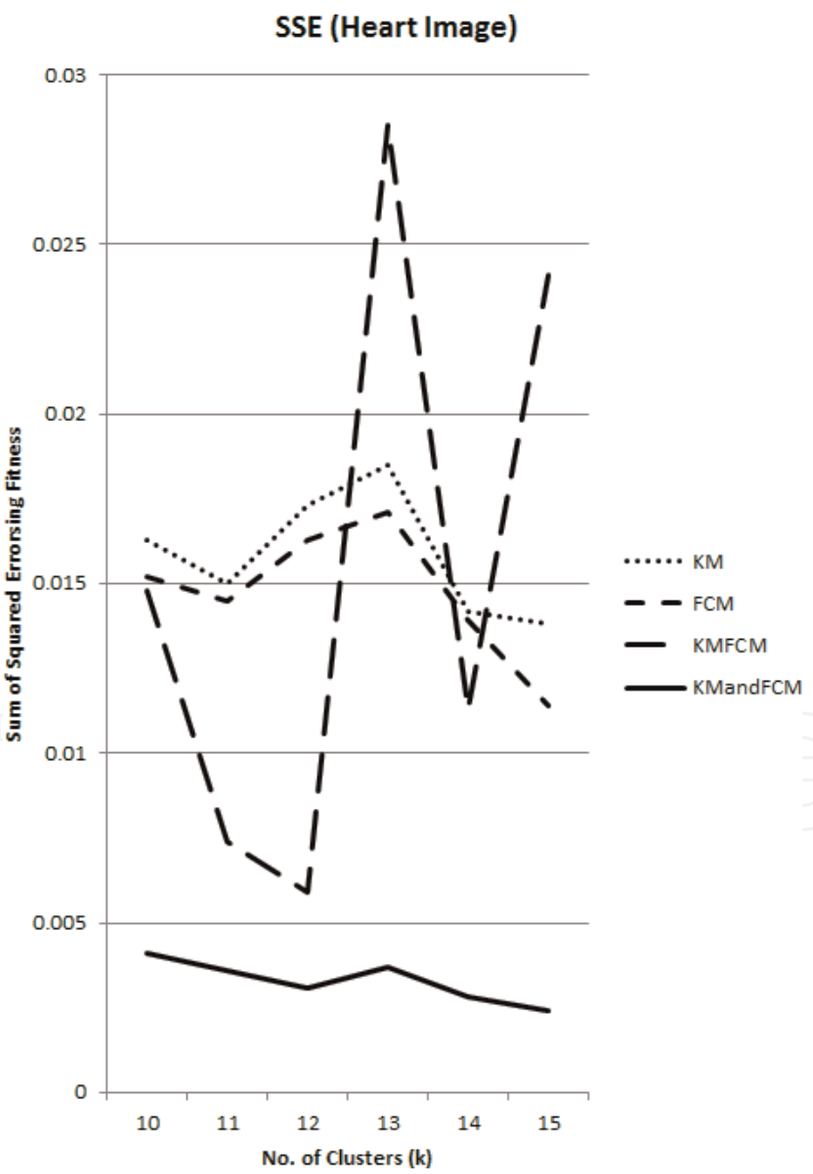

Figure 3.
Sum of squared errors (Heart image).

6.2 Observations with Kidneys image

K	*KM*	*FCM*	*KMFCM*	*KM and FCM*
10	0.09	0.68	1.58	0.55
11	0.13	0.41	1.83	0.26
12	0.81	0.58	2.64	0.46
13	0.08	0.47	2.07	0.30
14	0.24	0.60	2.40	0.31
15	0.65	1.78	2.22	1.06

Table 5.
CPU time of each clustering technique (Kidneys image).

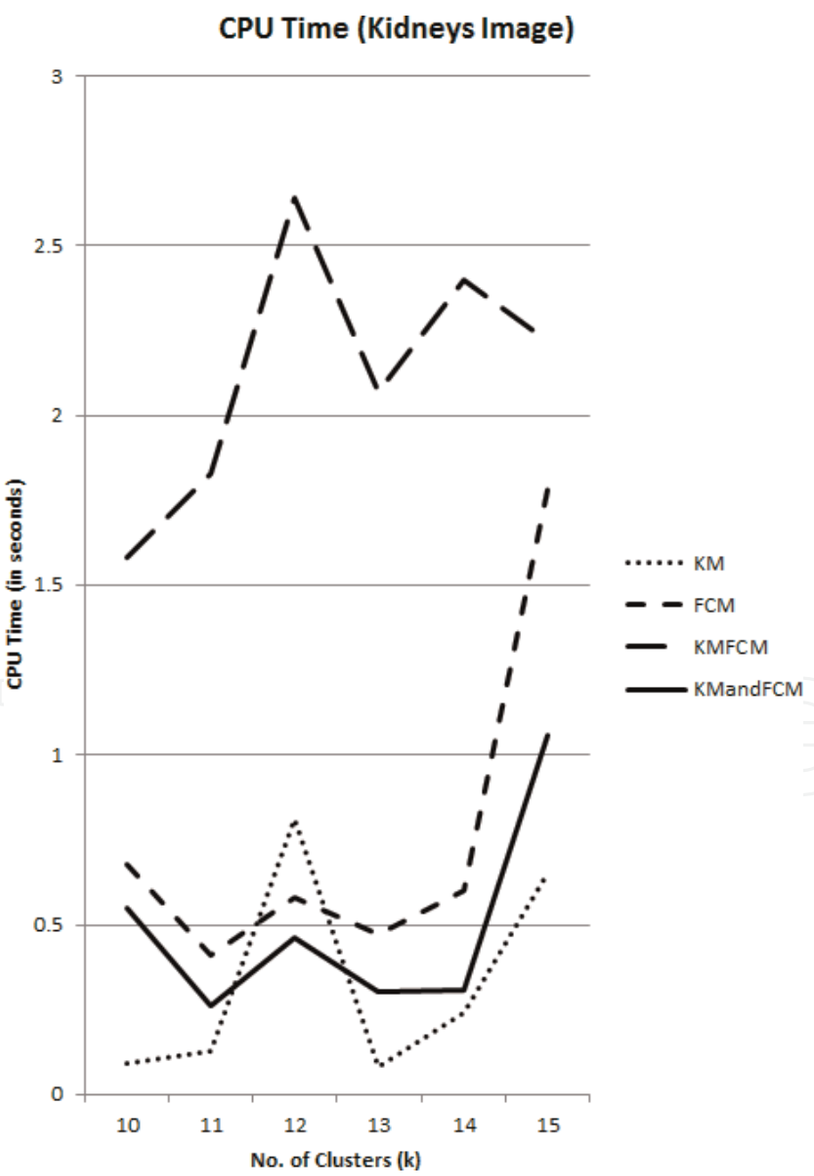

Figure 4.
CPU time (Kidneys image).

K	*KM*	*FCM*	*KMFCM*	*KM and FCM*
10	38.40	47.15	54.76	61.48
11	42.11	49.43	57.86	65.84
12	52.41	61.03	60.00	65.41
13	41.20	51.04	48.73	56.79
14	57.49	64.85	64.88	71.59
15	53.10	61.40	62.85	66.42

Table 6.
Clustering fitness of each clustering technique (Kidneys image).

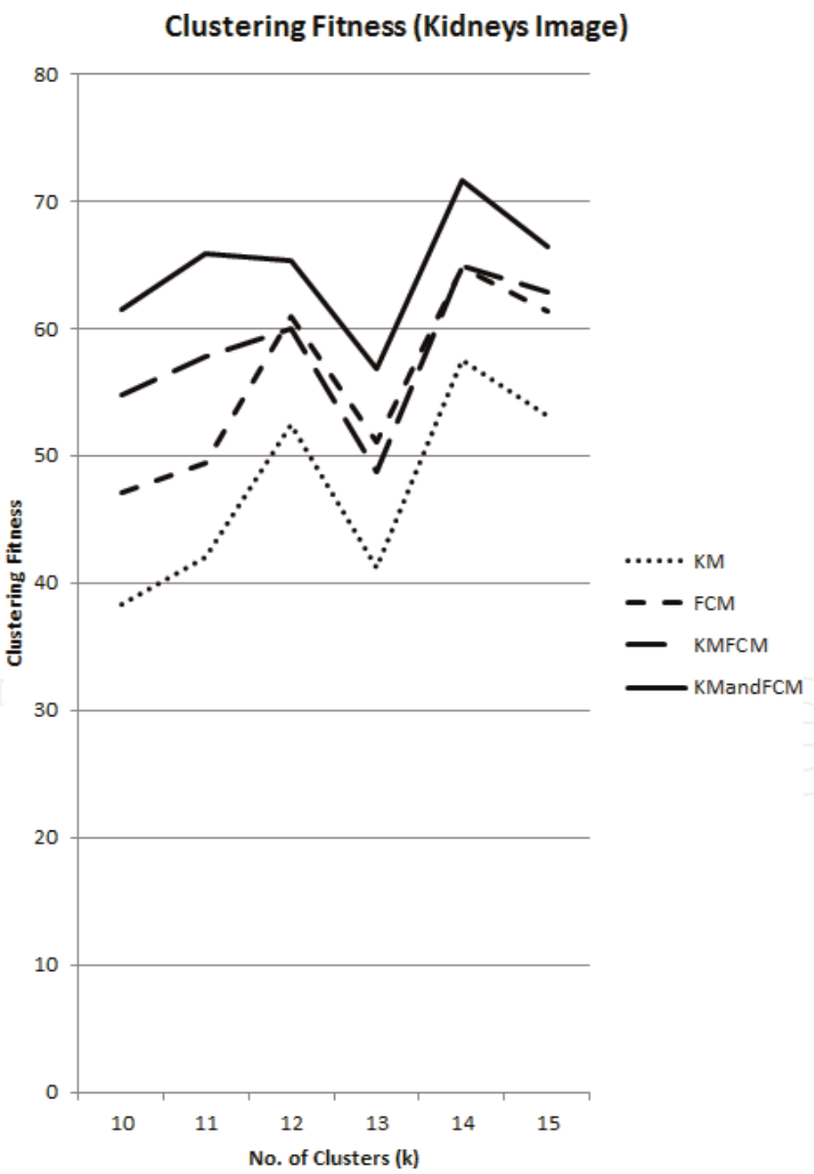

Figure 5.
Clustering Fitness (Kidneys image).

K	*KM*	*FCM*	*KMFCM*	*KM and FCM*
10	0.0281	0.0215	0.0129	0.0075
11	0.0265	0.0172	0.0114	0.0054
12	0.0249	0.0109	0.0140	0.0029
13	0.0123	0.0109	0.0191	0.0112
14	0.0144	0.0090	0.0067	0.0037
15	0.0115	0.0045	0.0028	0.0011

Table 7.
SSE of each clustering technique (Kidneys image).

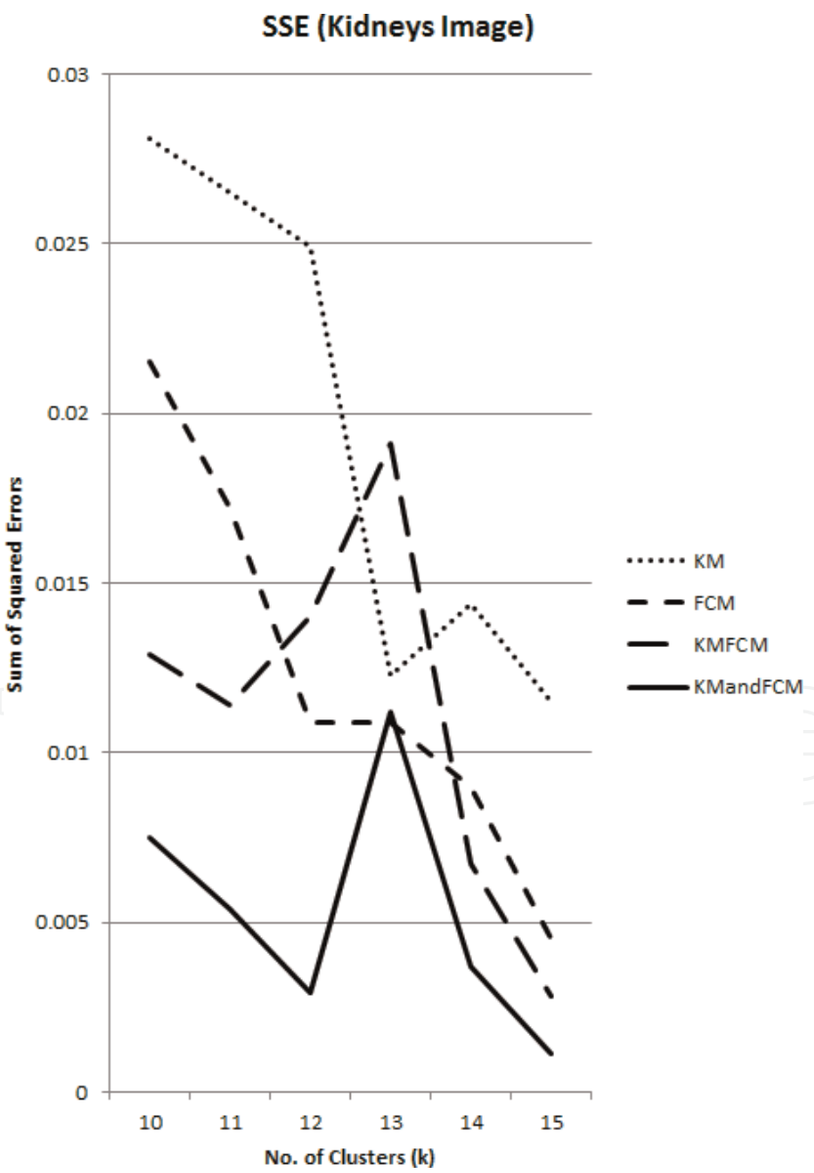

Figure 6.
Sum of squared errors (Kidneys image).

6.3 Observations with Baboon image

K	*KM*	*FCM*	*KMFCM*	*KM and FCM*
10	0.14	0.79	2.16	0.62
11	0.16	0.86	2.37	0.63
12	0.29	0.91	2.68	0.63
13	0.31	1.01	2.91	0.50
14	0.36	0.72	3.14	0.78
15	0.48	1.10	3.24	0.55

Table 8.
CPU time of each clustering method (Baboon image).

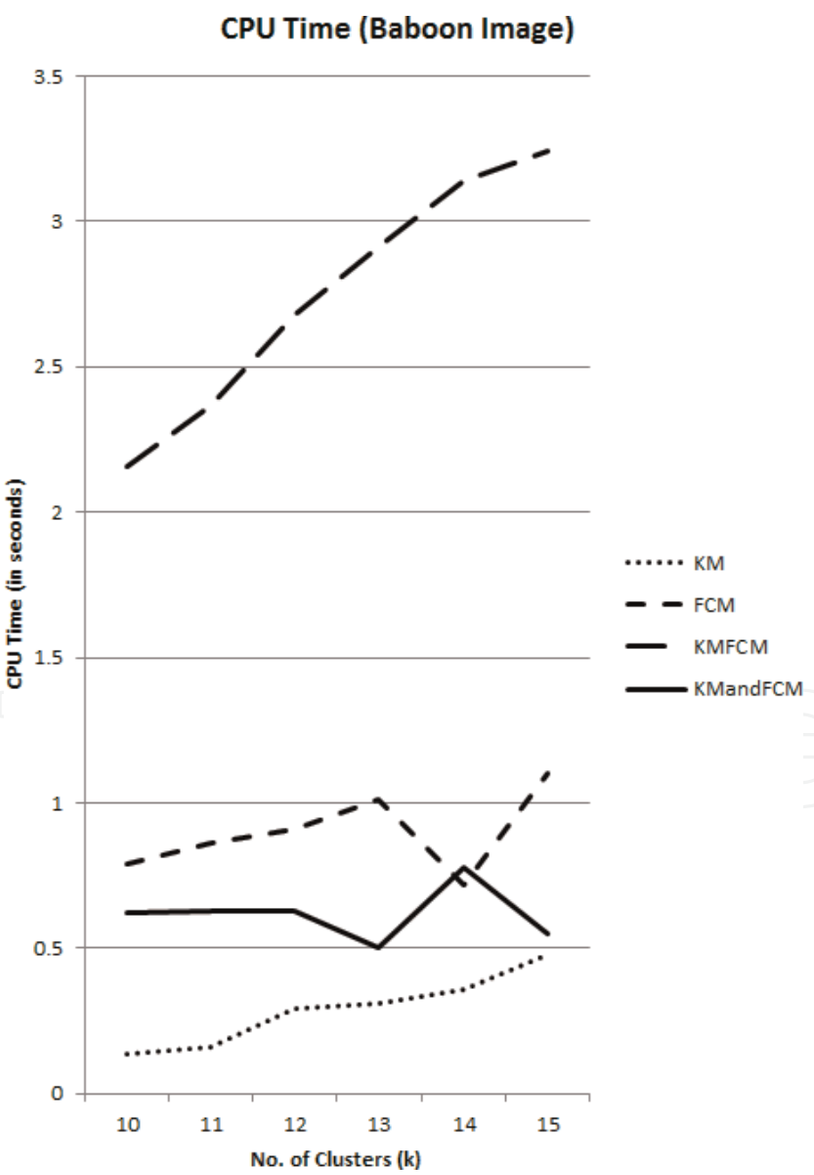

Figure 7.
CPU time (Baboon image).

K	*KM*	*FCM*	*KMFCM*	*KM and FCM*
10	30.22	32.17	36.02	39.07
11	22.28	29.71	37.36	39.49
12	28.70	32.63	35.13	39.57
13	31.28	33.47	40.39	42.28
14	25.92	29.49	37.77	39.81
15	36.48	38.16	34.43	39.98

Table 9.
Clustering fitness of each clustering method (Baboon image).

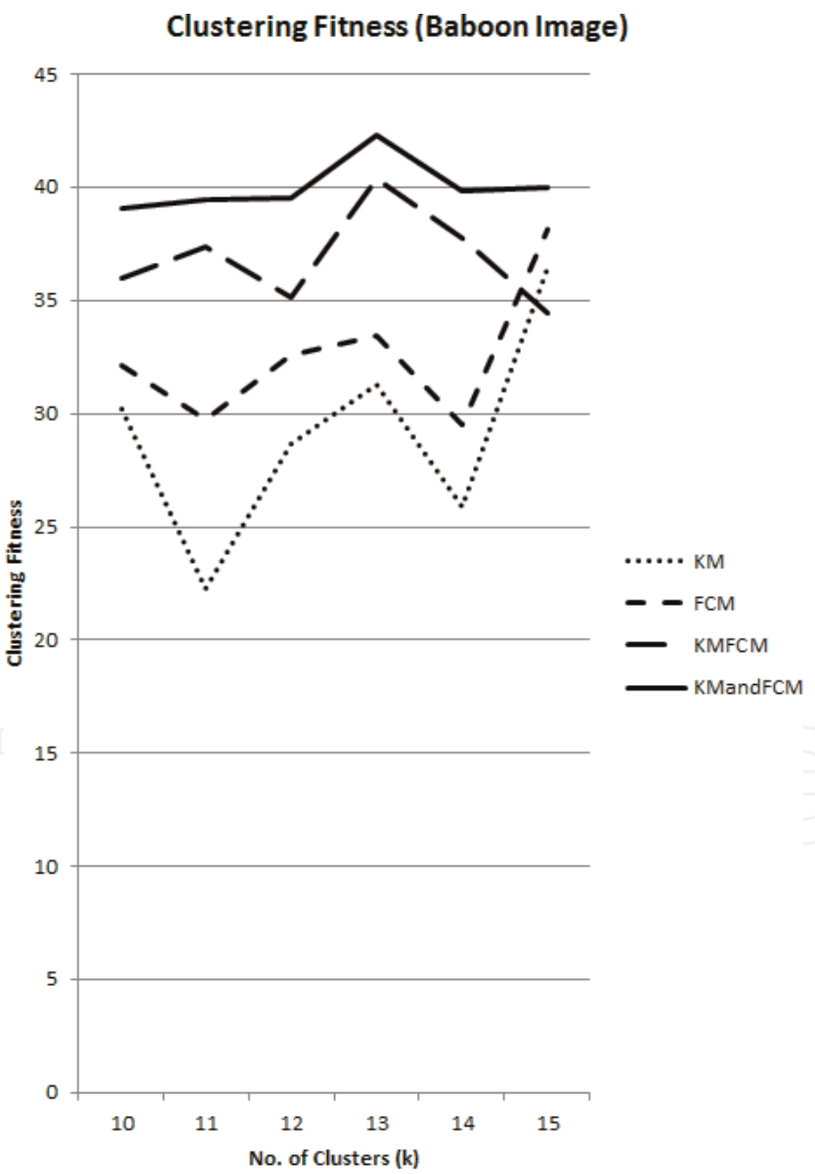

Figure 8.
Clustering fitness (Baboon image).

K	*KM*	*FCM*	*KMFCM*	*KM and FCM*
10	0.0080	0.0063	0.0059	0.0030
11	0.0073	0.0068	0.0037	0.0024
12	0.0099	0.0071	0.0053	0.0029
13	0.0065	0.0058	0.0070	0.0025
14	0.0087	0.0070	0.0041	0.0022
15	0.0069	0.0056	0.0027	0.0019

Table 10.
SSE of each clustering method (Baboon image).

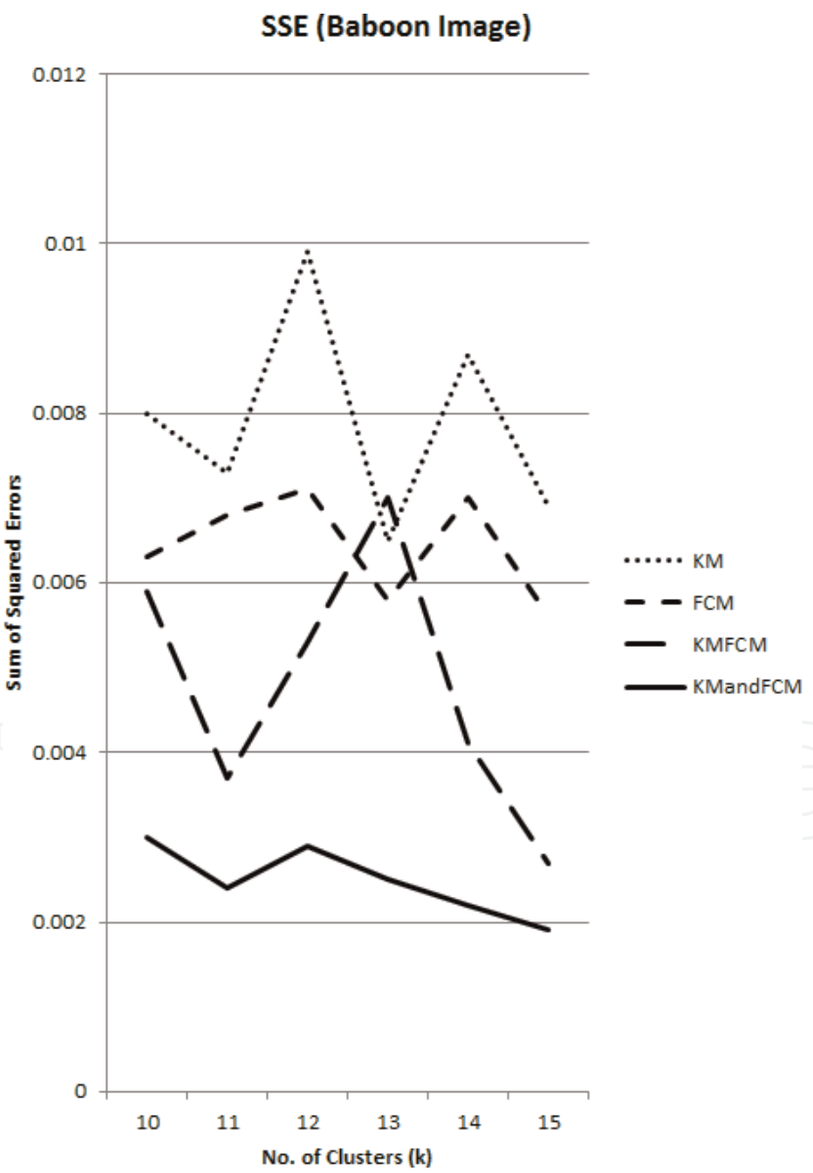

Figure 9.
Sum of squared errors (Baboon image).

6.4 Observations with Lena image

K	*KM*	*FCM*	*KMFCM*	*KMandFCM*
10	0.08	0.15	0.66	0.09
11	0.13	0.44	0.76	0.32
12	0.06	0.17	0.77	0.11
13	0.09	0.40	0.84	0.32
14	0.05	0.20	0.92	0.13
15	0.21	0.24	1.09	0.14

Table 11.
CPU time of each clustering method (Lena image).

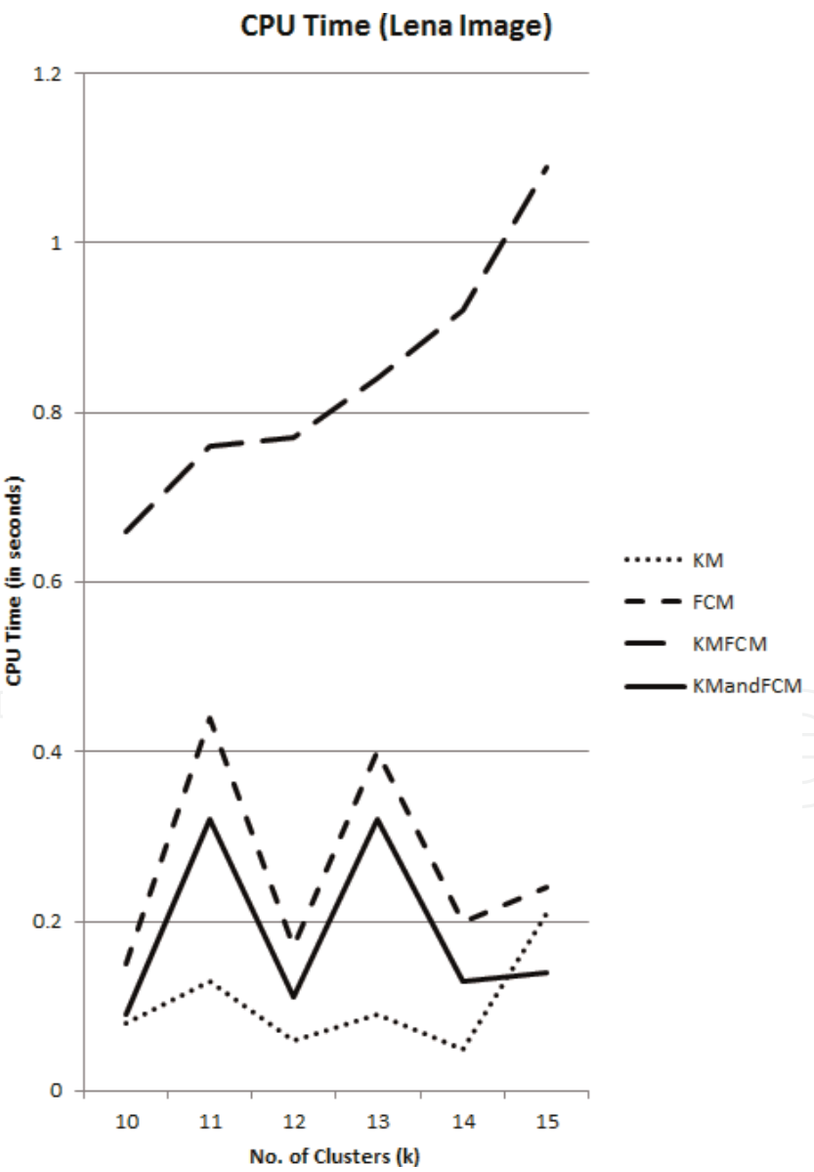

Figure 10.
CPU time (Lena image).

K	*KM*	*FCM*	*KMFCM*	*KM and FCM*
10	25.50	28.80	30.61	32.79
11	22.97	25.52	27.95	31.08
12	20.22	23.38	25.44	29.97
13	28.71	30.13	32.74	34.26
14	26.75	29.83	31.05	33.27
15	23.70	30.19	32.79	34.60

Table 12.
Clustering fitness of each clustering method (Lena image).

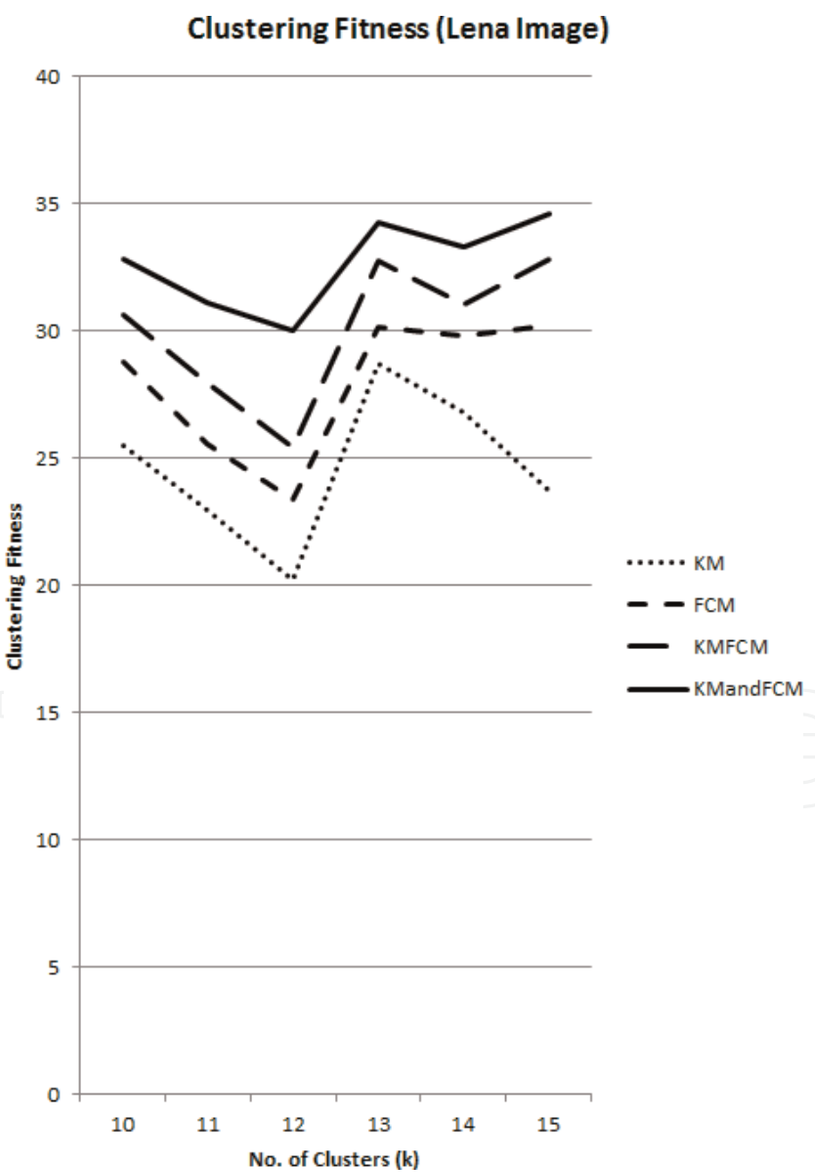

Figure 11.
Clustering fitness (Lena image).

K	*KM*	*FCM*	*KMFCM*	*KM and FCM*
10	0.0147	0.0127	0.0093	0.0034
11	0.0245	0.0218	0.0099	0.0041
12	0.0246	0.0178	0.0077	0.0034
13	0.0144	0.0106	0.0060	0.0027
14	0.0135	0.0110	0.0062	0.0024
15	0.0130	0.0100	0.0049	0.0022

Table 13.
SSE of each clustering method (Lena image).

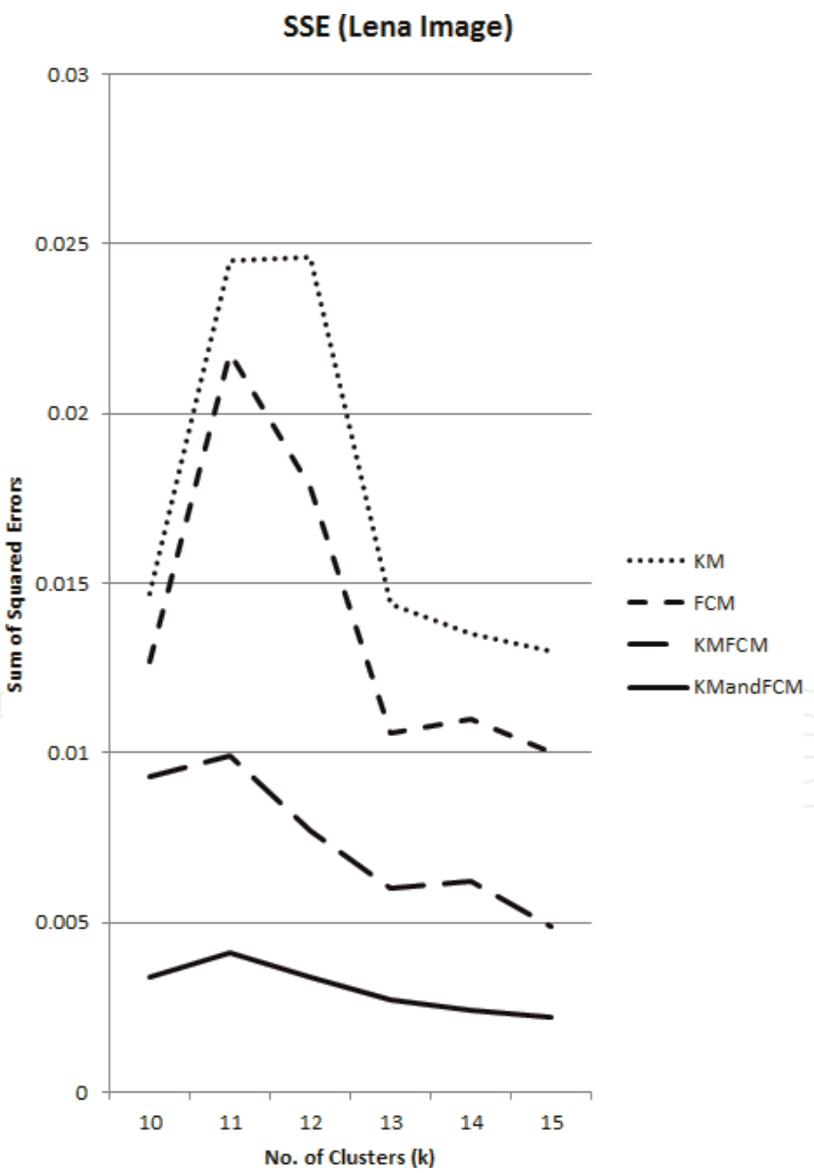

Figure 12.
Sum of squared errors (Lena image).

6.5 Original images used for present experimentation

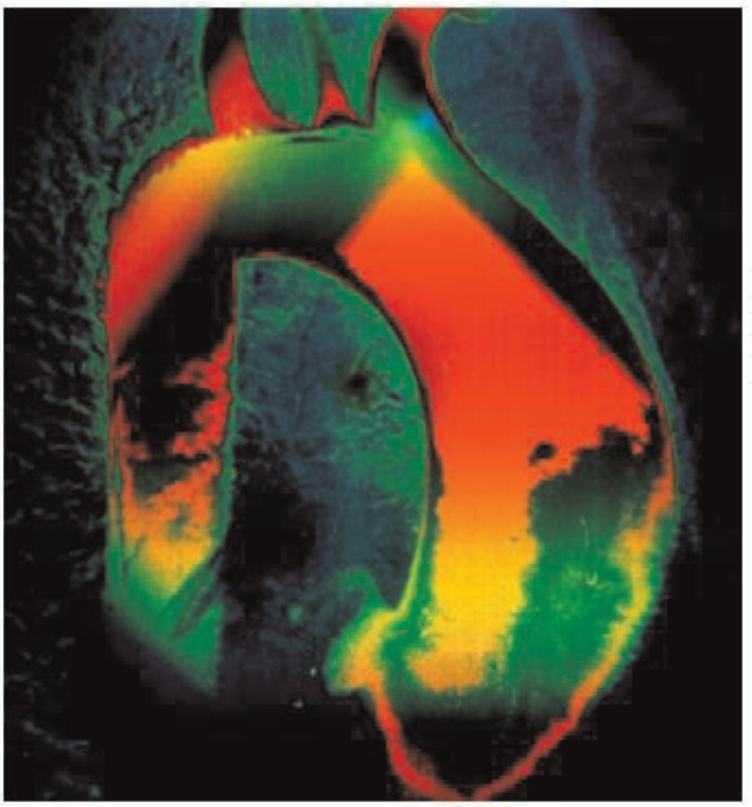

Figure 13.
Heart image.

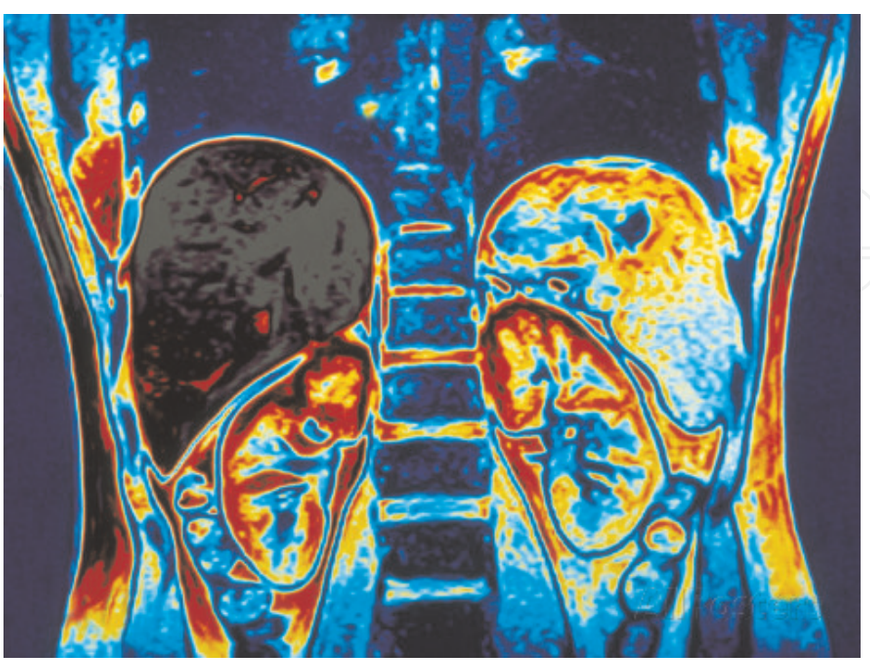

Figure 14.
Kidneys image.

Figure 15.
Baboon image.

Figure 16.
Lena image.

6.6 Comparison of segmentation results on Baboon image

As an example of the present experiments for image segmentation, segmentation results for Baboon image for 10 clusters are presented here. These results are generated by the above proposed hybrid clustering algorithms along with the standard K-Means and standard *FCM* algorithms.

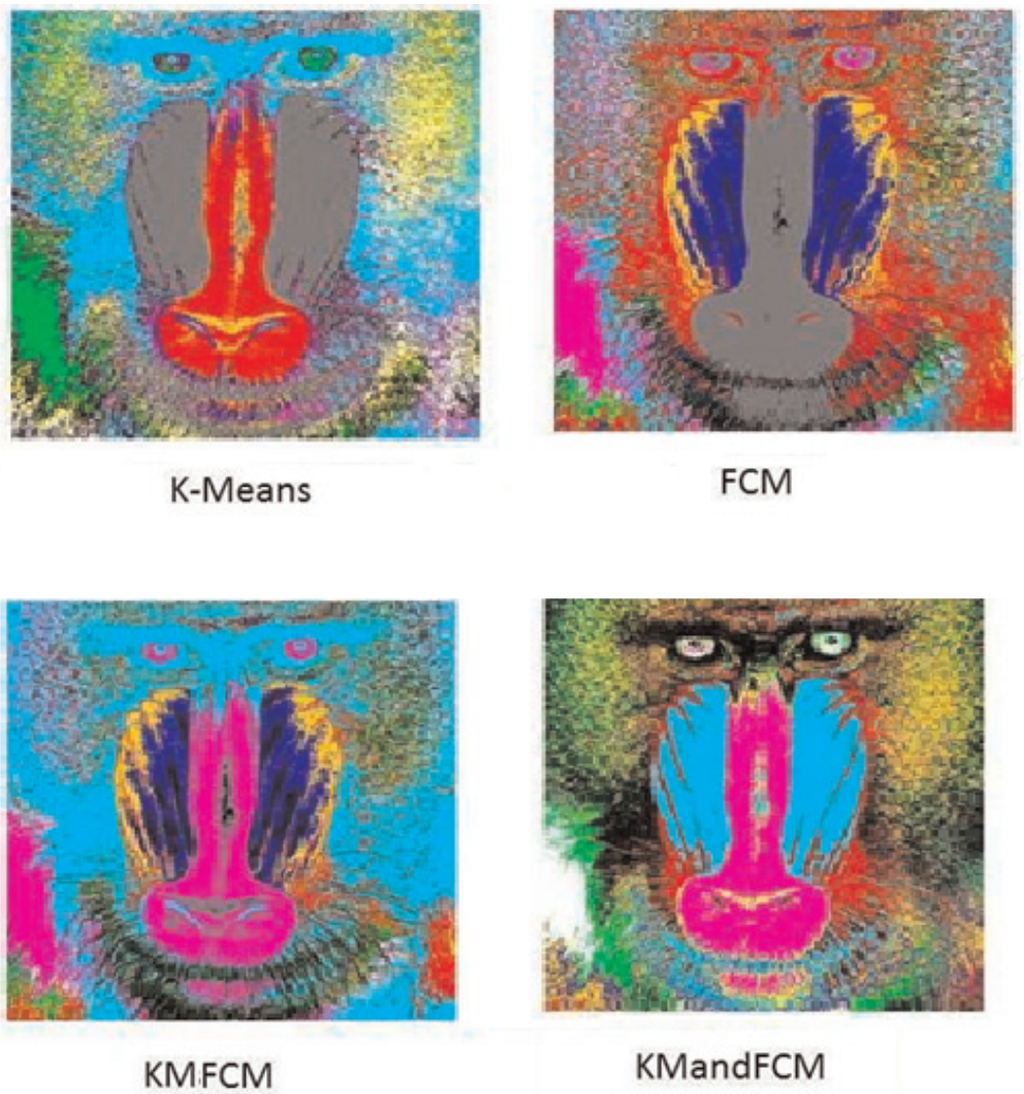

Figure 17.
Image segmentation results for Baboon image (for 10 Clusters).

For segmentation, here, each algorithm is executed using Baboon image data assuming that the number of clusters is 10, i.e., k = 10. Each segment is represented by each cluster. Separate color code is assigned to each cluster. The color codes are red, yellow, green, blue, orange, black, white, gray, cyan and magenta. The projections of all segmentation results generated by the algorithms are shown in **Figure 17**. The original Baboon image also shown in the figure.

In all the experiments, it is observed that hybrid clustering algorithm *KMandFCM* is showing better performance in terms of CPU, clustering fitness and SSE than the other algorithms.

7. Conclusion

The present chapter notably includes the study of hybridization of popular clustering algorithms, K-Means and *FCM*, and identifies the best hybridization strategy. All experiments are carried out for segmenting four images, which include two medical images also. For all the algorithms CPU time, clustering fitness and sum of squared error (SSE) are taken into consideration while carrying out their performance evaluation. In all the experiments that are conducted, the proposed

hybrid algorithm *KMandFCM* is exhibiting better performance in terms of CPU time, Clustering Fitness (CF) and SSE.

In all experiments, it is also observed that the proposed hybrid clustering algorithms are showing better performance than the standard K-Means and *FCM* algorithms. Especially the *KMandFCM* algorithm has good results when compared to all other algorithms. Thus, it could be concluded that the hybrid clustering algorithm *KMandFCM* will have good application in other fields too.

Author details

Raja Kishor Duggirala
Department of CSE, Dr. L. Bullayya College of Engineering (for Women), Visakhapatnam, A.P., India

*Address all correspondence to: rajakisgor@gmail.com

References

[1] Kaltri K, Mahjoub M. Image segmentation by gaussian mixture models and modified *FCM* algorithm. The International Arab Journal of Information Technology. 2014;**11**(1): 11-18

[2] Wang S, Geng Z, Zhang J, Chen Y, Wang J. A fuzzy C-means model based on the spatial structural information for brain MRI segmentation. International Journal of Signal Processing, Image Processing and Pattern Recognition. 2014;**7**(1):313-322

[3] Khan AM, Ravi S. Image segmentation methods: A comparative study. International Journal of Soft Computing and Engineering (IJSCE). 2013;**3**(4):84-92. ISSN: 2231-2307

[4] Fwu J-K, Djuric PM. EM algorithm for image segmentation initialized by a tree structure scheme. IEEE Transactions on Image Processing. 1997;**6**(2):349-352

[5] Bezdek JC, Hall LO, Clarke LP. Review of MR image segmentation techniques using pattern recognition. Medical Physics. 1993;**20**:1033-1048

[6] Pham DL, Xu CY, Prince JL. A survey of current methods in medical image segmentation. Annual Review of Biomedical Engineering. 2000;**2**:315-337

[7] Wells WM, LGrimson WE, Kikinis R, Arrdrige SR. Adative segmentation of MRI data. IEEE Transactions on Medical Imaging. 1996;**15**:429-442

[8] Fraley C, Raftery AE. Model-based clustering, discriminant analysis, and density estimation. Journal of the American Statistical Association. 2002; **97**(458):611, ABI/INFORM Global

[9] Hannah IH, Selva KS. Hybrid TRS-FA clustering approach for Web2.0 social tagging system. International Journal of Rough Sets and Data Analysis (IJRSDA). 2015;**2**(1):70-87. DOI: 10.4018/ijrsda.2015010105

[10] Nizar Banu PK, Andrews S. Performance analysis of hard and soft clustering approaches for gene expression data. International Journal of Rough Sets and Data Analysis (IJRSDA). 2015;**2**(1):58-69. DOI: 10.4018/ijrsda.2015010104

[11] Ayramo S, Karkkainen T. Introduction to partitioning-based clustering methods with a robust example (Tech. Rep. No. C. 1/2006). Agora, Finland: University of Jyvaskyla, Department of Mathematical Information Technology; 2006

[12] Han J, Kamber M. Data Mining Concepts and Techniques, 2/e. New Delhi, India: Elsevier Inc; 2007

[13] Tan P-N, Steinbach M, Kumar V. Introduction to Data Mining, 1/e. New Delhi, India: Pearson Education; 2007

[14] Zadeh LA. Fuzzy sets. Information and Control. 1965;**8**(3):338-353

[15] Lemiare J. Fuzzy insurance. Astin Bulletin. 1990;**20**(1):33-55

[16] Chen S, Zhang D. Robust image segmentation using *FCM* with spatial constraints based on new kernel-induced distance measure. IEEE Transactions on Systems, Man, and Cybernetics. 1998;**34**:1907-1916

[17] Tsai A, Zhang J, Willsky AS. Expectation-maximization algorithms for image processing using multiscale models and mean-field theory, with applications to laser radar range profiling and segmentation. Optical Engineering. 2001;**40**(7):1287-1301

[18] Yang Y. Image segmentation by fuzzy C-means clustering algorithm

with a novel penalty term. Computing and Informatics. 2007;**26**:17-31

[19] Tolias YA, Panas SM. On applying spatial constraints in fuzzy image clustering using a fuzzy rule-based system. IEEE Signal Processing Letters. 1998;**5**:245-247

[20] Noordam JC, Van Den Broek WHAM, Buydens LMC. Geometrically guided Fuzzy C-Means clustering for multivariate image segmentation. In: Proc. International Conference on Pattern Recognition. Vol. 1. 2000. pp. 462-465

[21] Ahmed MN, Yamany SM, Mohamed N, Farag AA, Moriarty T. A modified fuzzy C-means algorithm for Bias field estimation and segmentation of MRI data. IEEE Transactions on Medical Imaging. 2002;**21**:193-199

[22] Zhang DQ, Chen SC, Pan ZS, Tan KR. Kernel-based Fuzzy clustering incorporating spatial constraints for image segmentation. In: Proceedings of International Conference on Machine Learning and Cybernetics; Vol. 4. 2003. pp. 2189-2192

[23] Li X, Li L, Lu H, Chen D, Liang Z. Inhomogeneity correction for magnetic resonance images with Fuzzy C-Mean algorithm. In: Proc. SPIE Int. Soc. Opt. Eng. Vol. 5032. 2003. pp. 995-1005

[24] Pham DL, Prince JL. Adaptive fuzzy segmentation of magnetic resonance images. IEEE Transactions on Medical Imaging. 1999;**18**:737-752

[25] Wu X, Kumar V, Quinlan JR, Ghosh J, Yang Q, Motoda H, et al. Top 10 algorithms in data mining. Knowledge and Information Systems. 2007;**14**:1-37 (survey paper: DIO 10.1007/s10115-007-0114-2)

[26] Aggarwal N, Aggarwal K. A mid-point based k-mean clustering algorithm for data mining. International Journal on Computer Science and Engineering. 2012;**4**(6):1174-1180

[27] Das S. Pattern recognition using fuzzy c-means technique, international journal of energy. Information and Communications. 2013;**4**(1):1-14

[28] Lu Y, Ma T, Yin C, Xie X, Tian W, Zhong SM. Implementation of the fuzzy C-means clustering algorithm in meteorological data. International Journal of Database Theory and Application. 2013;**6**(6):1-18

[29] Bezdek JC, Ehrlich R, Full W. *FCM*: The fuzzy c-means clustering algorithm. Computers & Geosciences. 1984;**10** (2–3):191-203

[30] Klir GJ, Yuan B. Fuzzy Sets and Fuzzy Logic: Theory and Applications. Upper Saddle River, New Jersey: Prentice Hall of India Private Limited; 2005

[31] Bezdek JC, Ehrlich R, Full W. FCM: The Fuzzy c-Means Clustering Algorithm. Computers & Geosciences. 1984;**10**(2-3):191-203

[32] Bezdek JC. Feature selection for binary data-Medical diagnosis with fuzzy sets. In: Proc. Nat. Comput. Conf. AFIPS Press; 1972. pp. 1057-1068

[33] Cannon RL, Dave JV, Bezdek JC. Efficient implementation of fuzzy c-means clustering algorithm. IEEE Transactions on Pattern Analysis and Machine Intelligence. 1986;**8**(2):248-255

[34] Cannon RL, Jacobs C. Multispectral pixel classification with fuzzy objective functions. Cen. for Automation Res., Univ. Maryland, College Park, Tech. Rep. CAR-TR-51. 1984

[35] Gong M, Liang Y, Ma W, Ma J. Fuzzy C-means clustering with local information and kernel metric for image segmentation. 2013;**22**(2):573-584

[36] Krinidis S, Krinidis M, Chatzis V. Fast and robust fuzzy active contours. IEEE Transactions on Image Processing. 2010;**19**(5):1328-1337

[37] Yong Y, Chongxun Z, Pan L. A novel fuzzy C-means clustering algorithm for image thresholding. Measurement Science Review. 2004; **4**(1):11-19

[38] Hanesch M, Scholger R, Dekkers MJ. The application of fuzzy C-means cluster analysis and non-linear mapping to a soil data set for the detection of polluted sites. Physics and Chemistry of the Earth (Part A). 2001;**26**(11–12): 885-891. DOI: S1464-1895(01)00137-5

[39] Adebisi AA, Olusayo OE, Olatunde OS. An exploratory study of K-Means and expectation maximization algorithms. British Journal of Mathematics and Computer Science. 2012;**2**(2):62-71

[40] Kearns M, Mansour Y, Andrew YNg. An Information-theoretic analysis of hard and soft assignment methods for clustering. In: Uncertainty in Artificial Intelligence, 1997. pp. 282-293

[41] Ghosh S, Dubey SK. Comparative analysis of K-means and Fuzzy c-means algorithms. International Journal of Advanced Computer Science and Applications. 2013;**4**(4):35-39

[42] Raja Kishor D, Venkateswarlu NB. A Behavioral study of some widely employed partitional and model-based clustering algorithms and their hybridizations. In: Proceedings of the International Conference on Data Engineering and Communication Technology, Advances in Intelligent Systems and Computing 469; Springer Nature; 2017. DOI 10.1007/978-981-10-1678-3_56

[43] Han X, Zhao T. Auto-K dynamic clustering algorithm. Journal of Animal and Veterinary Advances. 2005;**4**(5): 535-539

[44] http://www.biologyreference.com/Bl-Ce/Cardiovascular-Diseases.html

[45] http://www.allposters.com/-sp/Colour-MRI-Scan-of-Abdomen-Showing-Kidneys-Liver-Posters_i10024816_.htm?UPI=AP10024816_PC14258389_FI0_SV6_IT1_VRV1

[46] http://www.imageprocessingplace.com/root_files_V3/image_databases.htm

Lecture Notes in Networks and Systems 210

Sanjoy Kumar Saha
Paul S. Pang
Debnath Bhattacharyya *Editors*

Smart Technologies in Data Science and Communication

Proceedings of SMART-DSC 2021

Springer

Contents

A Detailed Study on Optimal Traffic Flow in Tandem Communication Networks 1
N. Thirupathi Rao, K. Asish Vardhan, P. Srinivasa Rao, Debnath Bhattacharyya, and Hye-jin Kim

Detection of Brain Stroke Based on the Family History Using Machine Learning Techniques 17
Bandi Vamsi, Debnath Bhattacharyya, and Divya Midhunchakkaravarthy

Classification of Brain Tumors Using Deep Learning-Based Neural Networks 33
Jayavani Vankara, Muddada Murali Krishna, and Srikanth Dasari

Deep Learning for Lung Cancer Prediction: A Study on NSCLC Patients 41
Madhuri Thimmapuram, Sowjanya Pentakota, and H. Naga Chandrika

Lung Cancer Detection Using Improvised Grad-Cam++ With 3D CNN Class Activation 55
Eali Stephen Neal Joshua, Midhun Chakkravarthy, and Debnath Bhattacharyya

An Automatic Perception of Blood Sucker on Thin Blood Splotch Using Graphical Modeling Methods 71
D. Sushma, K. V. Satyanarayana, N. Thirupathi Rao, Debnath Bhattacharyya, and Tai-hoon Kim

Dual Detection Procedure to Secure Flying Ad Hoc Networks: A Trust-Based Framework 83
Shikha Gupta, Neetu Sharma, Rakesh Rathi, and Deepak Gupta

An E-Waste Collection System Based on IoT Using LoRa Open-Source Machine Learning Framework 97
Puppala Ramya, V. Ramya, and M. Babu Rao

Deep Learning Techniques for Air Pollution Prediction Using Remote Sensing Data 107
Bhimavarapu Usharani and M. Sreedevi

A Real and Accurate Diabetes Detection Using Voting-Based Machine Learning Approach 125
Udimudi Satish Varma, V. Dhiraj, B. Sekhar Babu, V. Dheeraj Varma, Gudipati Bharadwaja Sri Karthik, and V. Rajesh

Performance Analysis of a Simulation-Based Communication Network Model with NS2 Simulator 139
G. Rajendra Kumar, B. Dinesh Reddy, N. Thirupathi Rao, and Debnath Bhattacharyya

A Comparative Analysis on Resource Allocation in Load Balancing Optimization Algorithms 147
P. S. V. S. Sridhar, Sai Sameera Voleti, Manisha Miriyala, Nikitha Rajanedi, Srilalitha Kopparapu, and Venkata Naresh Mandhala

Artificial Intelligence-Based Vehicle Recognition Model to Control the Congestion Using Smart Traffic Signals 161
Aleemullakhan Pathan, Nakka Thirupathi Rao, Mummana Satyanarayana, and Debnath Bhattacharyya

A Literature Review on: Handwritten Character Recognition Using Machine Learning Algorithms 173
Sachin S. Shinde and Debnath Bhattacharyya

Tweet Data Analysis on COVID-19 Outbreak 183
V. Laxmi Narasamma, M. Sreedevi, and G. Vijay Kumar

An IoT Model-Based Traffic Lights Controlling System 195
B. Dinesh Reddy, Rajendra Kumar Ganiya, N. Thirupathi Rao, and Hye-jin Kim

A Comparative Study on Construction of 3D Objects from 2D Images 205
Mohan Mahanty, Panja Hemanth Kumar, Manjeti Sushma, Illapu Tarun Chand, Kombathula Abhishek, and Chilukuri Sai Revanth Chowdary

A Deep Learning-Based Object Detection System for Blind People 223
Kalam Swathi, Bandi Vamsi, and Nakka Thirupathi Rao

Pothole Detection Using Deep Learning 233
Pathipati Bhavya, Ch. Sharmila, Y. Sai Sadhvi, Ch. M. L. Prasanna, and Vithya Ganesan

Automatic Determination of Harassment in Social Network Using Machine Learning 245
Bhanu Prakash Doppala, S. NagaMallik Raj, Eali Stephen Neal Joshua, and N. Thirupathi Rao

Enhanced Performance of ssFFT-Based GPS Acquisition 255
Harshali Mane, Matcha Venu Gopala Rao, V. Rajesh Chowdhary, and S. M. M. Naidu

Optimized Deep Neural Model for Cancer Detection and Classification Over ResNet 267
Pavan Nageswar Reddy Bodavarapu, P. V. V. S. Srinivas, Pragnyaban Mishra, Venkata Naresh Mandhala, and Hye-jin Kim

A Steady-State Analysis of a Forked Communication Network Model 281
Sk. Meeravali, N. Thirupathi Rao, Debnath Bhattacharyya, and Tai-hoon Kim

A Comparative Analysis of With and Without Clustering to Prolonging the Life of Wireless Sensor Network 301
S. NagaMallik Raj, Debnath Bhattacharyya, and Divya Midhunchakkaravarthy

A Study on Techniques of Soft Computing for Handling Traditional Failure in Banks 309
T. Archana Acharya and P. Veda Upasan

Lesion Detection and Classification Using Sematic Deep Segmentation Network 321
Anil B. Gavade, Rajendra B. Nerli, and Shridhar Ghagane

Automatic Gland Segmentation for Detection of CRC Using Enhanced SegNet Neural Network 337
Mohan Mahanty, Debnath Bhattacharyya, and Divya Midhunchakkaravarthy

Smart Cyclones: Creating Artificial Cyclones with Specific Intensity in the Dearth Situations Using IoT 349
G. Subbarao, S. Hrushikesava Rao, Lakshmi Ramani Burra, Venkata Naresh Mandhala, and P. Seetha Rama Krishna

Machine Learning-Based Application to Detect Pepper Leaf Diseases Using HistGradientBoosting Classifier with Fused HOG and LBP Features 359
Matta Bharathi Devi and K. Amarendra

Tracking Missing Objects in a Video Using YOLO3 in Cloudlet Network 371
M. Srilatha, N. Srinivasu, and B. Karthik

Face Hallucination Methods—A Review 379
Venkata Naresh Mandhala, A. V. S. Pavan Kumar,
Debnath Bhattacharyya, and Hye-jin Kim

Image Encryption for Secure Internet Transfer 389
G. Dheeraj Chaitanya, P. Febin Koshy, D. Dinesh Kumar,
G. Himanshu, K. Amarendra, and Venkata Naresh Mandhala

Author Index 397

Classification of Brain Tumors Using Deep Learning-Based Neural Networks

Jayavani Vankara, Muddada Murali Krishna, and Srikanth Dasari

Abstract Deep neural networks have grown as the most interesting topic in past few years. This new machine learning technique has been applied in several real-world applications. It can be considered as a machine learning tool of high strength for solving the higher dimension problems. Deep neural network is used in this paper, for organizing the 66 brain MRI datasets into categories of four. We have considered four dissimilar classes; those are glioblastoma, sarcoma, metastatic bronchogenic carcinoma tumors and normal tumors. The classifier has been integrated with the discrete wavelength transform (DWT), which is used as a tool for extracting features, and the principal components analysis (PCA) for dimensionality reduction.

Keywords Brain tumor · Deep learning · Neural network · Classification

1 Introduction

The human brain is considered as most important and composite organ in a human body parts, which has billion of cells. A brain tumor is the resultant of an uncontrolled and unrestricted cell division. It leads to irregular and uncurbed group formation of cells inside and around the brain, which increases the change and cause of abnormal brain activity and destroys the healthy cells [1, 2]. Brain tumors have two classifications, i.e., benign or low-grade tumors called grade 1 and grade 2 and malignant or high-grade tumor which are called grade 3 and grade 4. Malignant tumors are more aggressive than benign tumor. The mass of abnormal cells does not contain cancer

J. Vankara · M. M. Krishna (✉) · S. Dasari
Department of CSE, Dr. Lankapalli Bullayya College of Engineering, Visakhapatnam, Andhra Pradesh, India
e-mail: muralimuddada@lbce.edu.in

J. Vankara
e-mail: vjayavani@lbce.edu.in

S. Dasari
e-mail: dsrikanth@lbce.edu.in

S. K. Saha et al. (eds.), *Smart Technologies in Data Science and Communication*,
Lecture Notes in Networks and Systems 210,
https://doi.org/10.1007/978-981-16-1773-7_3

cells. The rate of growth of benign brain tumors is moderate and does not escalate into other tissue. Malignant brain tumors contain cancer, a cell whose rate of growth is quite rapid and tends not to have clear frontier. Malignant tumors grow rapidly, so they are more menacing and can easily spread to other parts of the brain.

Based on the origination, the damaged tumors in the brain are classified into two types, namely primary tumors and secondary tumors. Primary tumors arise in brain by self and escalate to other parts of the brain, while secondary tumors arise elsewhere and escalate to the brain [3, 4]. Brain MRI (MRI scan), one of the current methods for brain tumors detection, is modeled for understanding the present status in together finding phase and treatment phase. MRI images have played a great impact in the automatic medical imaging technology as it provides transparent and complete information about the brain structure and the abnormalities within it [3, 5, 6]. There are various techniques presented by various researchers using MRI images as they have high resolution and can be scanned and loaded to computer. However, in the previous few decades, support vector machine (SVM) and neutral networks (NN) were extensively used [7]. The modern research has broadened its wings to deep learning and is one of the most functional techniques of machine learning. The deep learning architecture is proficient enough for solving an intricate and multifarious problem without using a large number of nodes, for example, SVM and K-nearest neighbor. This is why they are frequently used in innumerous areas of health informatics like medical analysis of image, bioinformatics and medical informatics [7–9].

The concept of classification of brain tumor is summarized in this paper by using deep learning and MRI images as the input. Finally, its performance is calculated based on various benchmarks. The aim of this technique is to distinguish between different categories of tumors such as sarcoma, glioblastoma, multiforme and metastatic bronchogenic carcinoma tumors by using the MRI images of brain. The set of features that are obtained via DWT are used in this technique. DWT is a routine used for extracting features from the sliced brain MRI images, which are helpful in training the DNN classifier for segregating the various brain tumors. The paper is planned as follows: Sect. 1 gives concise prologue, and Sect. 2 covers a preview on deep learning concept and as well as its architecture. In Sect. 3, the tactics has been described, and experimental results and discussion are fully explained and described.

2 Synopsis of Deep Learning

DL is a subdivision of machine learning (ML). It deals with superior and major datasets. It is based on multiple training levels of neural layers using a set of input features. In this, the higher-level neurons are defined from the neurons in the previous level, and the same lower-level neurons can be utilized as input by various neurons of the next level [10]. The DL framework enhances the conventional neutral network (NN) by attaching several intermediate layers, bounded by the input and the output

layers, in the traditional NN architecture for complex and nonlinear relationships [8–10]. CNN is a type of deep learning architecture which has gained recognition in few years because of its ability to solve the complex and stringent problems in relatively shorter period [8, 9]. A convolutional neural network model is a chain of feed forward layers. This type of network is implemented using max or average pooling layers in convolutional neural network. After the last pooling operation, CNN then uses the output of the pooling layer to feed into a fully connected feed forward neural network (FFNN) which converts the 2D outputs of the prior layers into 1D output for classification [10].

One significant feature of CNN models is that they can work without the procedure of extracting features before applying it. The greatest and major disadvantages of CNN architecture are that its processing is slow and hence it is quite time consuming. The next disadvantage considered is, as another significant point, the complexity in training. The training is difficult since it needs a large labeled dataset. The next disadvantage, which can be considered, is its hardware requirement. The hardware requirement is more for processing images with higher pixel counts, for example, 256 × 256 [11–13]. Deep neural network (DNN) is a type of DL architecture, which is importantly useful for classification or regression. It is basically a FNN in which the data passes from the input neural layer to the output classifier layer through number of hidden intermediate layers which are normally more than two [14, 15]. Figure 1 depicts the architectural structure of CNN where N1 represents the first neural layer containing neurons for input data, NO represents the classifying layer which consists of neurons for the various categories of the output, and Nh1 are the intermediate layers.

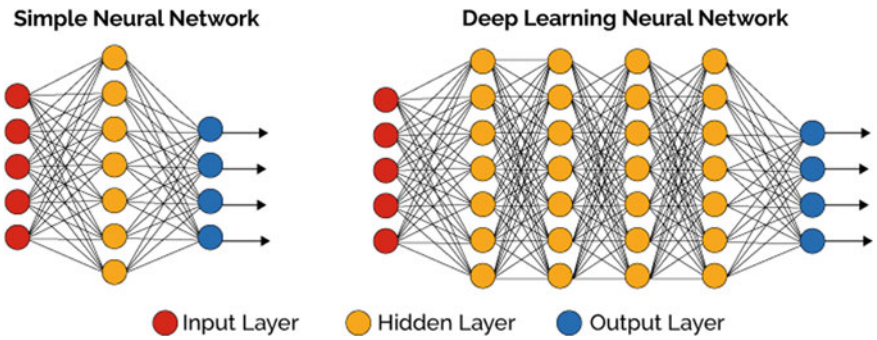

Fig. 1 DNN architecture [16]

3 Problem Statement

The MRI scan image of the brain is categorized into four different classes, which we have considered are glioblastoma, normal, sarcoma and metastatic bronchogenic carcinoma tumors using DNN classifier.

4 Proposed Model

The methodology suggested uses DNN architecture for classification. It basically acts as a classifier to recognize the tumors in MRI images. The complete steps of the tactic can be understood as the following steps:

a. Data acquisition that contains the MRI image of brain.
b. Fuzzy C-means for the segmentation of MRI image.
c. Extraction of the features using discrete wavelet transform (DWT) and dimensionality reduction using PCA.
d. Applying deep neural network (DNN) for classification.

The total modeling of the analyzer consists of three distinct steps, namely data analysis, data acquisition and data visualization. Data visualization is the output phase.

A. Data Acquisition

According to the WHO, a hundred types of brain tumors are known which might vary in source, location, size of the tissues and character. In this technique, the focus will be only on three types of carcinogenic tumors. They being: Glioblastoma: These are classified as grade 4 malignant brain tumors. These tumors are extremely dreadful in nature. These are crucial tumors. These develop from astrocytes, which are star shaped cells and supports the nerve cells. It mainly initiates in the cerebrum.

Sarcoma: It varies in grades from grade 1–grade 4 and starts from the connective tissues like blood vessels.

Metastatic Bronchogenic Carcinoma: This is a secondary malignant tumor in brain. This starts from bronchogenic carcinoma lung tumor and then slowly spreads in the brain. The dataset needed is collected from Website of Harvard Medical School (https://med.harvard.edu/AANLIB/). This set of data consists of 66 MRI images of real human brain, in which 44 are abnormal and 22 are normal. The brain MRIs were in T2 weighted axial plane and 256 * 256 pixels.

B. **Image Segmentation**

Image segmentation is basically non-trivial task and helps in differentiating the normal part of the brain tissues such as white matter (WM) and grey matter (GM)

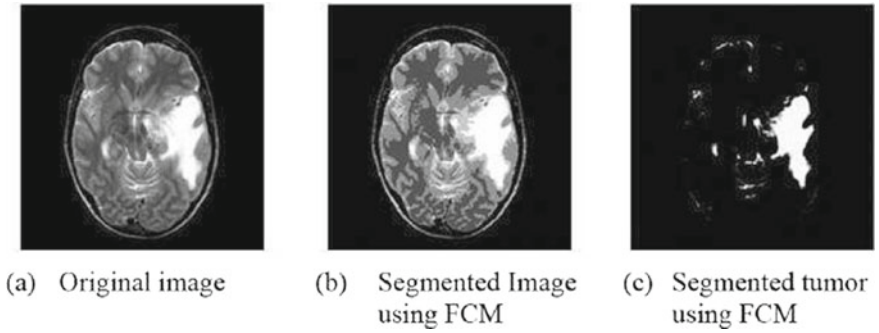

Fig. 2 Segmented image using C-means algorithm

tissue in MRI scans [12]. This procedure is of high eminence as it acts as the input for the next phase. We have used the technique of fuzzy C which means cumulating technique to subdivide the image since it had good result in the earlier works and good for correlation purpose [13]. Figure 2 shows the segmented image using fuzzy logic algorithm.

C. Feature Extraction and Dimensionality Reduction

Once we are done with the segmentation of the MRI image, the feature extraction followed by dimensionality reduction stage comes into the picture. The features are extracted using discrete wavelength transform (DWT) which extracts the most pertinent features at contrasting aspects and scales as they provide information of the signal by the help of cascaded filter bands or high pass and low pass filters in order to obtain the characteristics in a hierarchical manner [13]. Two levels Discrete Wavelength Transform disintegration of an image is verified in Fig. 3, where the coefficient of low pass and the high pass filters are represented by the functions h(n) and g(n), respectively. There are four sub-band images at each level as a result, i.e., (LL, LH, HH and HL). The estimate component of an image is LL sub-band, whereas LH, HL and HH sub-bands might be considered as the important constituent of the image. [13, 14]. In our approach, we have used three-phase decomposition of Haar

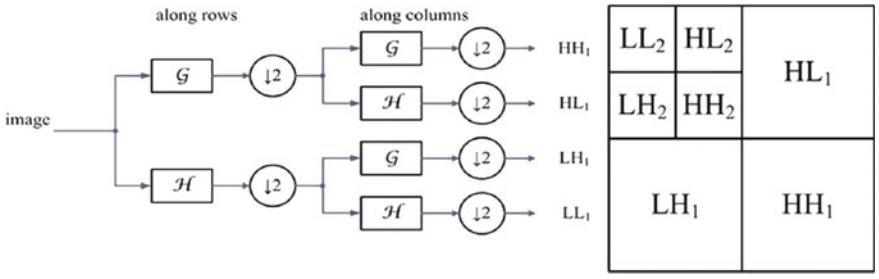

Fig. 3 Representation of level 1 and level 2 decomposition

wavelet that was adopted in our earlier endeavor [13] to extract 32 * 32 = 1024 features for every MRI scan [13].

D. Classification

After the selection and extraction of feature, the deep neural network is used for categorization and is executed on the feature vectors obtained. In order to build and train the deep neural network, having a seven layers of hidden model, the seven-gold cross validation procedure is used. We even used another ML classification algorithm from WEKA (https://www.cs:waikato:ac:nz/ml/weka/) for evaluating and calculating the performance of chosen classifier [13].

5 Experiment Results and Discussions

Two tools were used for the results and experiment.

(1) The brain MRI dataset was prepared, and MATLAB R2015a was used for first three steps.
(2) For the evaluation and classification of preferred classifier, WEKA 3.9 tool was used.

The efficiency of the proposed procedure was measured on the benchmark of average categorization rate, F-measure average recall and average area under ROC curve (AUC) of all the four classes, i.e., glioblastoma, normal, sarcoma and metastatic bronchogenic carcinoma tumors. As seen from Fig. 4 and Table 1, deep neural

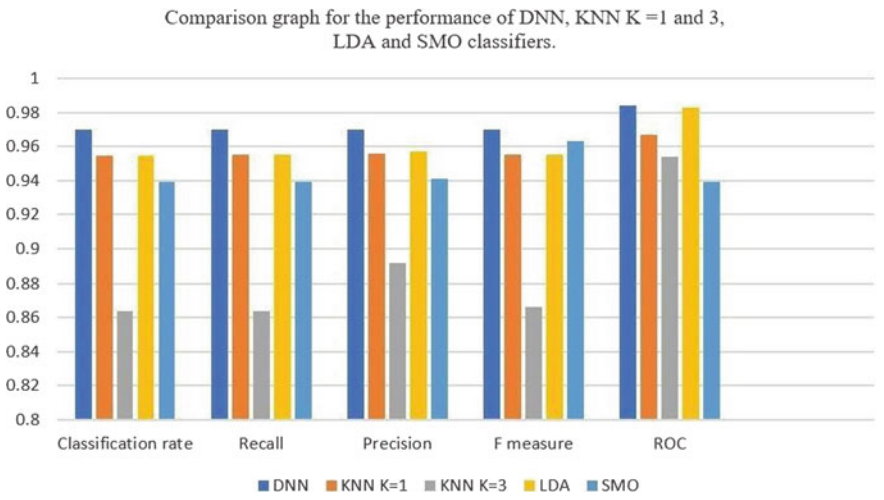

Fig. 4 Graphical comparison for DNN and KNN

Table 1 Performance of the different benchmark algorithms

Algorithm	Classification rate (%)	Recall	Precision	F-measure	AUC (ROC)
DNN	97.77	0.89	0.97	0.97	0.84
KNN K = 1	93.15	0.86	0.856	0.75	0.67
KNN K = 3	76.56	0.84	0.82	0.66	0.54
LDA	92.15	0.55	0.57	0.55	0.83
SMO	92.85	0.39	0.41	0.63	0.39

network classifier provided better and improved results when fused with DWT feature extraction tool when compared to other classifiers.

6 Conclusion and Forthcoming Efforts

This paper has presented a practiced procedure combining DWT and DNN, which classifies the MRI scanned images to three types of tumors of brain. The processing time and size of the images were quite good for implementing the process. It is also tested with large size of images for better understanding of the model developed. The currently considered DNN classifier is working well when compared with the other model considered in the current article.

References

1. A. Kavitha, L. Chitra, R. Kanaga, Brain tumor segmentation using genetic algorithm with svm classifier. Int. J. Adv. Res. Electr. Electron. Instrum. Eng. **5**(3), 10–16 (2016)
2. T. Logeswari, M. Karnan, An improved implementation of brain tumor detection using segmentation based on soft computing. J. Cancer Res. Exp. Oncol. **2**(1), 06–014 (2010)
3. K.G. Khambhata, S.R. Panchal, Multiclass classification of brain tumor in MRI images . Int. J. Innov. Res. Comput. Commun. Eng. **4**(5), 8982–8992 (2016)
4. V. Das, J. Rajan, Techniques for MRI brain tumor detection: a survey. Int. J. Res. Comput. Appl. Inform. Technol. **4**(3), 53–66 (2016)
5. E.I. Zacharaki, S. Wang, S. Chawla, D. Soo Yoo, R. Wolf, E. R. Melhem, C. Davatzikos, Classification of brain tumor type and grade using MRI texture and shape in a machine learning scheme. Magn. Reson. Med. Off. J. Int. Soc. Magn. Reson. Med. **62**(6), 1609–1618 (2009)
6. L. Singh, G. Chetty, D. Sharma, A novel machine learning approach for detecting the brain abnormalities from MRI structural images, in *IAPR International Conference on Pattern Recognition in Bioinformatics*. (Springer, Berlin (2012), pp. 94–105
7. Y. Pan, W. Huang, Z. Lin, W. Zhu, J. Zhou, J. Wong, Z. Ding, Brain tumor grading based on neural networks and convolutional neural networks, in *37th Annual International Conference of the IEEE Engineering in Medicine and Biology Society (EMBC)*. IEEE (2015), pp. 699–702.
8. G. Litjens, T. Kooi, B.E. Bejnordi, A.A.A. Setio, F. Ciompi, M. Ghafoorian, J. Van Der Laak, B. Van Ginneken, C.I. Sanchez, A survey on deep learning in medical image analysis. Med. Image Anal. **42**, 60–88 (2017)

9. D. Ravi, C. Wong, F. Deligianni, M. Berthelot, J. Andreu-Perez, B. Lo, G.-Z. Yang, Deep learning for health informatics. IEEE J. Biomed. Health Inform. **21**(1), 4–21 (2016)
10. S. Tharani, C. Yamini, Classification using convolutional neural network for heart and diabetics datasets. Int. J. Adv. Res. Comput. Commun. Eng. **5**(12), 417–422 (2016)
11. K.B. Ahmed, L.O. Hall, D.B. Goldgof, R. Liu, R.A. Gatenby, Fine-tuning convolutional deep features for MRI based brain tumor classification, in *Medical Imaging 2017: Computer-Aided Diagnosis* (International Society for Optics and Photonics, 2017), p. 101, no. 34, p. 101342E
12. N. Gordillo, E. Montseny, P. Sobrevilla, State of the art survey on MRI brain tumor segmentation. Magn. Reson. Imaging **31**(8), 1426–1438 (2013)
13. H. Mohsen, E. El-Dahshan, E. El-Horbaty, A. Salem, Brain tumor type classification based on support vector machine in magnetic resonance images. Ann. Dunarea De Jos University of Galati, Math. Phys. Theor. Mech. Fascicle II Year IX (XL) **1**, 10–21 (2017)
14. M. Ahmad, M. Hassan, I. Shafi, A. Osman, Classification of tumors in human brain MRI using wavelet and support vector machine. IOSR J. Comput. Eng. **8**(2), 25–31 (2012)
15. N. Asmita Ray, Thirupathi Rao and Debnath Bhattacharyya: Analysis of Breast Cancer Detection and Classification in Early Stage from Digital Mammogram. Asian Int. J. Life Sci. **20**(2), 1–15 (2019)
16. https://cdn-images-1.medium.com/max/800/1*5egrX--WuyrLA7gBEXdg5A.png. Accessed on 5 Jan 2021

Reduction of PAPR in OFDM Signals Using Grey Wolf Optimization Combined with SLM

Reddi Sridevi[1(✉)] and T. Madhavi[2]

[1] Assistant Professor, Department of ECE, Dr. L. B College of Engineering, Visakhapatnam, India
himasri_sss@yahoo.com
[2] Professor, Department of ECE, GITAM Deemed to be University, Visakhapatnam, India
madhavitatineni@gitam.edu

Abstract. The most widely used multiplexing technique in present wireless communication scenario is Orthogonal Frequency Division Multiplexing. PAPR is one of the most challenging observation and problem in the signals which are transmitted in the system. Different optimization techniques are been proposed to reduce PAPR. In this paper, SLM combined with grey wolf optimization technique is proposed and the results are been compared with other SLM based optimization techniques like SLM-GA, SLM-FA. The PAPR reduction accuracy and the level of complexity have been reduced using the proposed approach. The proposed model is simulated using Matlab software tool.

Keywords: OFDM · SLM · Genetic algorithm · Firefly algorithm · Grey wolf optimization

1 Introduction

Orthogonal Frequency Division multiplexing (OFDM) might be an adjustment subject go down for a few of the chief in vogue remote and broadcast communications standards. When contrasted with the standard recurrence division multiplexing amid which sub groups aren't any covering. The essential impression of OFDM is lifted piece rate is transmitted into a lesser piece rate of bearers. Each bearers are symmetrically kept up. OFDM flag create a tangled flag by multiplexing. OFDM learning is started by taking contribution to sequential to parallel convertor. The IFFT will get the compulsory range to time area and give the transporter which are symmetrical. The FFT is that the flip over technique for IFFT. It translates the time space flag to recurrence space and its job is to look out the particular transmission wave shape. High unearthly capability gives more data organizations (Figs. 1, 2, 3, 4, 5, 6 and 7).

Solidarity to RF delay incredible execution in unregulated and controlled repeat bunches bring down multi-way mutilation works in complex indoor circumstances and at speed in vehicles. It is utilized in high rate advanced broadband frameworks like advanced TV proliferation, computerized sound and video circulation. The essential favourable position of OFDM over single-transporter plans is its capacity to manage serious channel conditions (for instance, weakening of high frequencies in an

A. Kumar et al. (eds.), *ICDSMLA 2019*, Lecture Notes in Electrical Engineering 601,
https://doi.org/10.1007/978-981-15-1420-3_10

exceedingly long copper wire, narrowband impedance and frequency selective debilitating on account of multipath) while not convoluted exertion channels. Channel exertion is improved because of OFDM is likewise seen as abuse a few gradually adjusted narrowband motions of one immediately tweaked band flag. The low picture rate makes the work of a watch interim between images sensible, making it feasible to wipe out inter symbol interference (ISI) and use echoes and time-spreading on simple TV these square measure noticeable as ghosting and obscuring.

It is performed by exploitation of different reception apparatuses what's more, precoding the information, different learning streams can be sent over divergent ways. The strategy required by MIMO at prime paces would be generally advantageous exploitation OFDM balance, in light of OFDM changes over a quick learning channel into assortment of parallel, bring down speed channels. In OFDM framework representation, the info signals are unit tweaked basically exploitation of PSK or QAM and attempt IFFT activity at the transmitter wrap up. The symmetrical subcarriers are unit made at the transmitter wrap up. These signs have high pinnacle values in time area and these pinnacle esteems are unit alluded as high peak to average power ratio (PAPR) that might be a result of summation of sine waves and non steady envelope. High PAPR increment the intricacy of ADC and DAC. RF speakers work underneath awfully high direct locale anyway once we pass the flag with high PAPR it will include non-straight locale that outcomes in twisting.

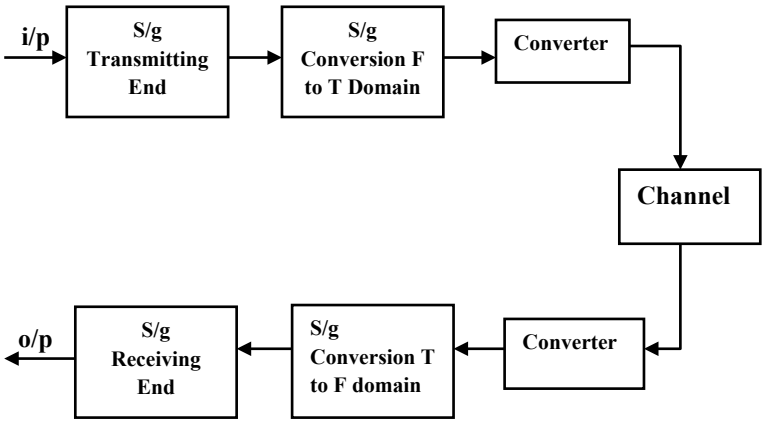

Fig. 1. General OFDM system

2 Related Work

OFDM in communications offers multi carrier transmission of signals which have high spectral efficiency, power efficiency, invulnerability to the frequency selective fading channels [1]. OFDM frameworks experience the ill effects of a vast peak to average power ratio (PAPR) of the transmitted signs, requiring control enhancers with an extensive direct range. In this way, the OFDM beneficiary's identification is exceptionally delicate to the nonlinear devices [2]. Some of the reduction techniques have

been proposed in previous versions such as partial transmit sequence (PTS) [3] in which phase shift operation is performed by the constant phase vectors. Selective mapping technique is further proposed to reduce PAPR, in this scheme multiple sequences with less PAPR is transmitted [4, 5]. Some of the eligible techniques to obtain better use of spectral is cognitive radio. To enhance the significance of the method some of the allocation method based on particle swarm optimization, genetic algorithm are proposed in [6]. Further fuzzy logic and ant colony optimization are been in considered at transmitting end and receiving end [7]. Different approaches have been performed and algorithms like cross entropy is proposed in [8]. Further optimization techniques like harmonic search optimization is proposed to reduce the PAPR in OFDM systems [9].

3 PAPR and Selective Mapping(SLM)

3.1 PAPR

The PAPR in OFDM is given by ratio of maximum power and its average power.

$$PAPR = \frac{max\left(|x(t)|^2\right)}{E\left\{|x(t)|^2\right\}} \tag{1}$$

Here E{.} is the expectation value. From the above equation it is clear that when the value of $max\left(|x(t)|^2\right)$ is decreased the PAPR will be reduced. When the value of PAPR is high the system complexity will also increase and hence this proposes a SLM-GWO to minimise the PAPR.

3.2 Selective Mapping Technique

The selective mapping technique introduced in the year 1996, which is designed to give positive features in performing distortion less operations in OFDM systems. The design of SLM composed using rotation of phases as required for the given input. The phase rotation is performed and the best selected signal gets transmitted with a reduced amount of PAPR. The working of SLM technique is termed as (2)

$$S^x = \left(S^1, S^2, S^3 \ldots\ldots\ldots\ldots S^x\right) \tag{2}$$

where x = [0, 1, 2, …….. X] which are required to create blocks in OFDM.

So the blocks B(x) can be given as (3):

$$\begin{aligned} B^{(x)} &= \left(B_0^{(x)}, B_1^{(x)}, B_2^{(x)}, \ldots B_{M-1}^{(x)}\right)^T \\ &= \left[S_0^{(x)} B_0, S_1^{(x)} B_1, \cdots S_{M-1}^{(x)} B_{M-1}\right]^T \end{aligned} \tag{3}$$

After rotation of the blocks the signal is kept separately as the original information which is given as input is converted into time domain as the IFFT operation which is present at input changes the signal frequency domain into time domain. The reduction or the value of PAPR depends on the volume of input sequences and the depth in the information of input sequences.

4 Grey Wolf Based SLM

The Grey Wolf Optimizer(GWO) algorithm mimics the leadership hierarchy and hunting mechanism of grey wolves in nature. Four types of grey wolves such as alpha, beta, delta, and omega are employed for simulating the leadership hierarchy.

The Gray Wolf Optimizer (GWO) calculation copies the administration order and chasing mechanism of wolves. Four different of grey wolves need to be considered that are alpha, beta, delta, and omega are utilized for simulating the authority chain of command. There are three important steps in hunting- searching for prey, encircling prey and attacking the prey. These three are implemented to perform optimization technique. The three best agents are denoted as $P(\alpha)$, $P(\beta)$ *and* $P(\delta)$. The velocities are termed as Eqs. (4), (5), (6).

The equations can be shown as:

$$V_\alpha = |C.P_\alpha(t) - P(t)| \tag{4}$$

$$V_\beta = \left|C.P_\beta(t) - P(t)\right| \tag{5}$$

$$V_\delta = |C.P_\delta(t) - P(t)| \tag{6}$$

The position are updated as Eqs. (7), (8) (9):

$$P_1 = P_\alpha - B.V \tag{7}$$

$$P_2 = P_\beta - B.V \tag{8}$$

$$P_3 = P_\delta - B.V \tag{9}$$

where B and C are the vector coefficients which are calculated as Eqs. 10 and 11

$$B = 2b.r_1 - b \tag{10}$$

$$C = 2.r_2 \tag{11}$$

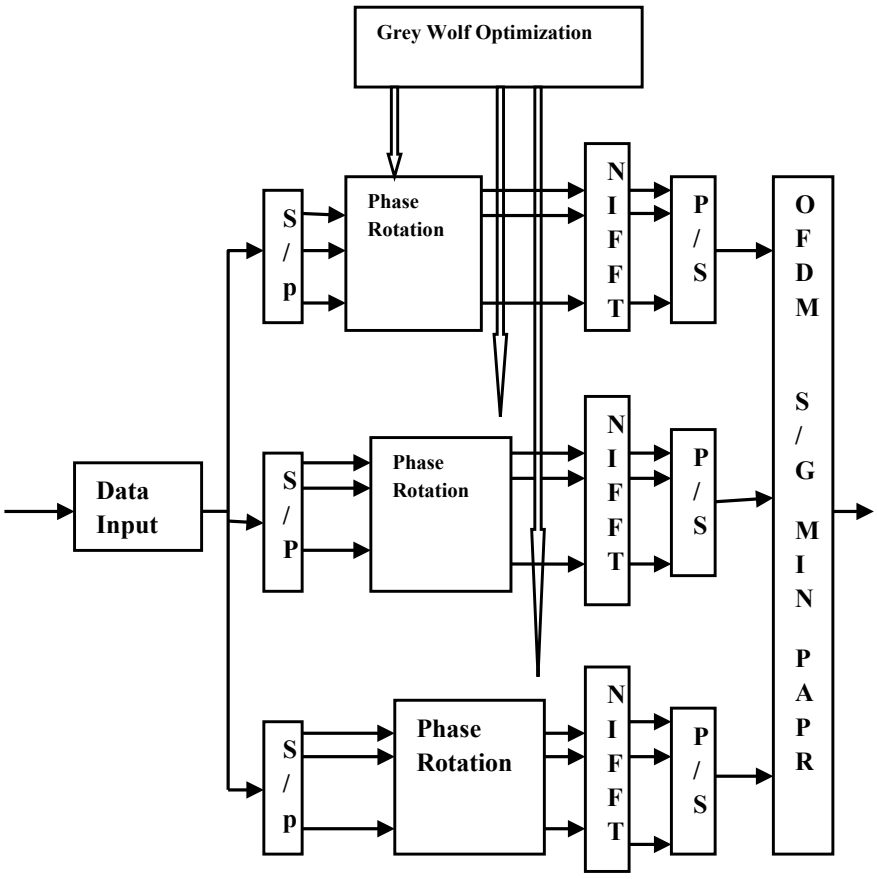

Fig. 2. Proposed GWO-SLM architecture

The grey wolf optimization based SLM algorithm is given as:

Step 1: Initialise input data $I_x = I_1 I_2 I_3 \ldots I_n$
Step 2: Serial bit of data converted to parallel bits
Step 3. Rotating the phase of bits and applying GWO for the bits
Step 4. Initialization of the search agents (wolfs) b, B, C
Step 5: Calculate the fitness function
Step 6: Find the best wolfs and is given as X_α, X_β *and* X_δ

Step 7: Update the position of b, B, C
Step 8: Calculate the fitness function
Step 9: update the position of X_α, X_β *and* X_δ
Step 10: Find the best and form a unique phases
Step 11: Obtain the Min PAPR signal.

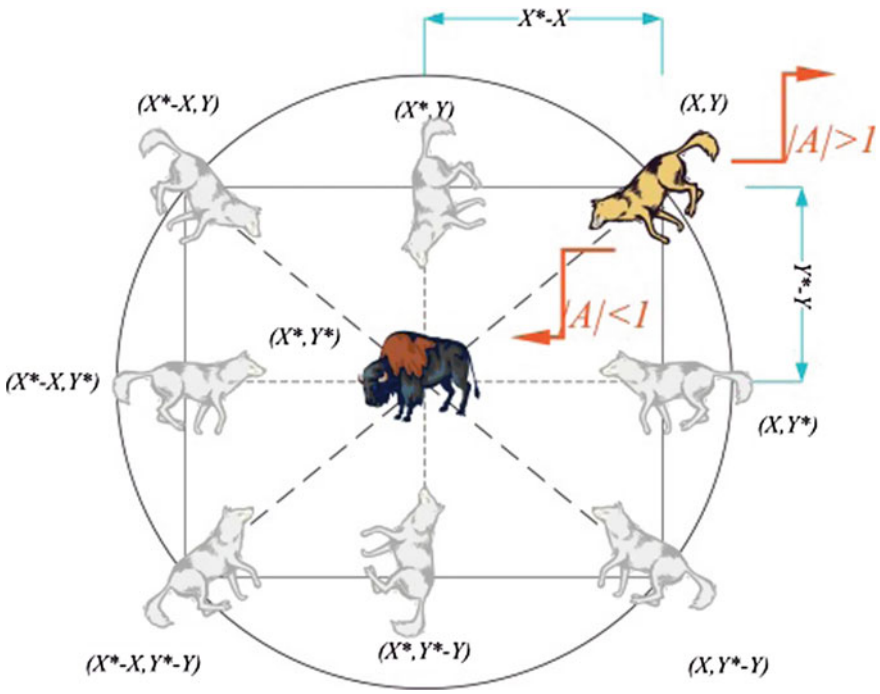

Fig. 3. Position vectors and their possible next locations.

5 Results and Discussion

For M = 4,

The best optimal value for PAPR found by SLM is: 8.9192
The best optimal value for PAPR found by GA is: 7.5908
The best optimal value for PAPR found by FA is: 6.739
The best optimal value for PAPR found by GWO is: 6.5102.

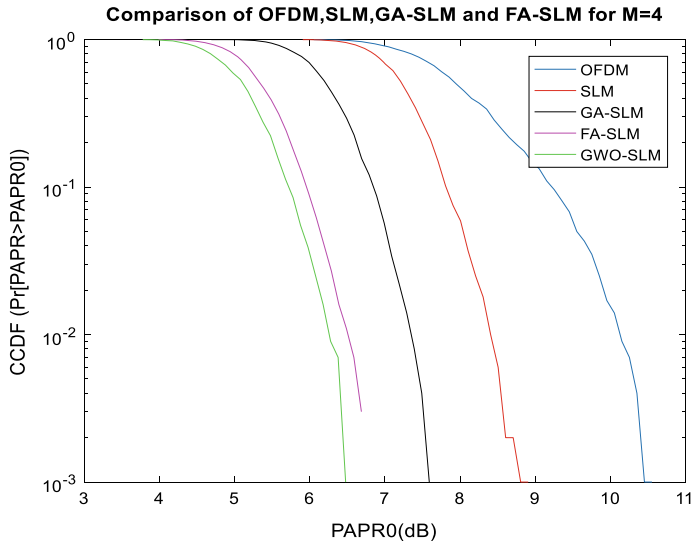

Fig. 4. CCDF versus PAPR for M = 4

For M = 8,

The best optimal value for PAPR found by SLM is: 8.042
The best optimal value for PAPR found by GA is: 7.092
The best optimal value for PAPR found by FA is: 6.239
The best optimal value for PAPR found by GWO is: 5.712.

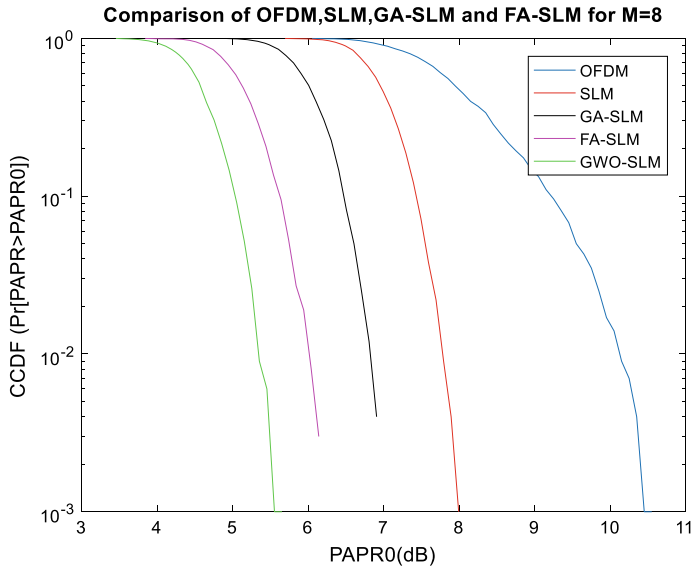

Fig. 5. CCDF versus PAPR for M = 8

For M = 16,

The best optimal value for PAPR found by SLM is: 7.891
The best optimal value for PAPR found by GA is: 6.634
The best optimal value for PAPR found by FA is: 5.842
The best optimal value for PAPR found by GWO is: 5.22.

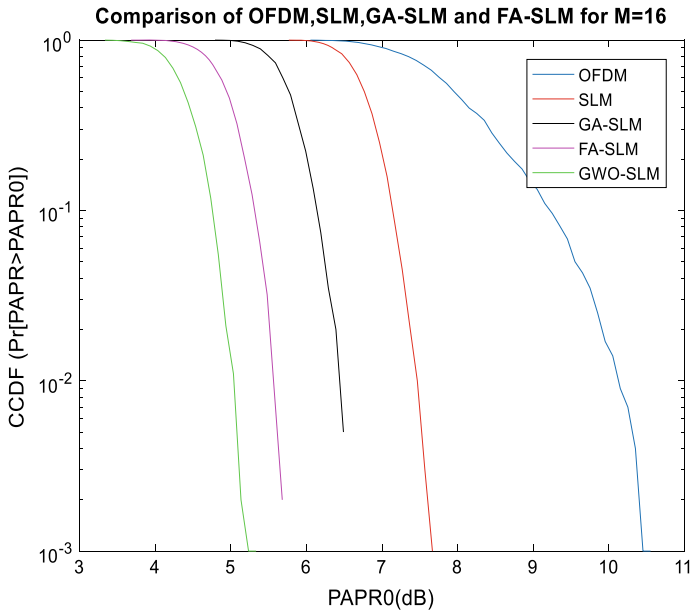

Fig. 6. CCDF versus PAPR for M = 16

For M = 32

The best optimal value for PAPR found by SLM is: 7.426
The best optimal value for PAPR found by GA is: 6.249
The best optimal value for PAPR found by FA is: 5.445
The best optimal value for PAPR found by GWO is: 4.82.

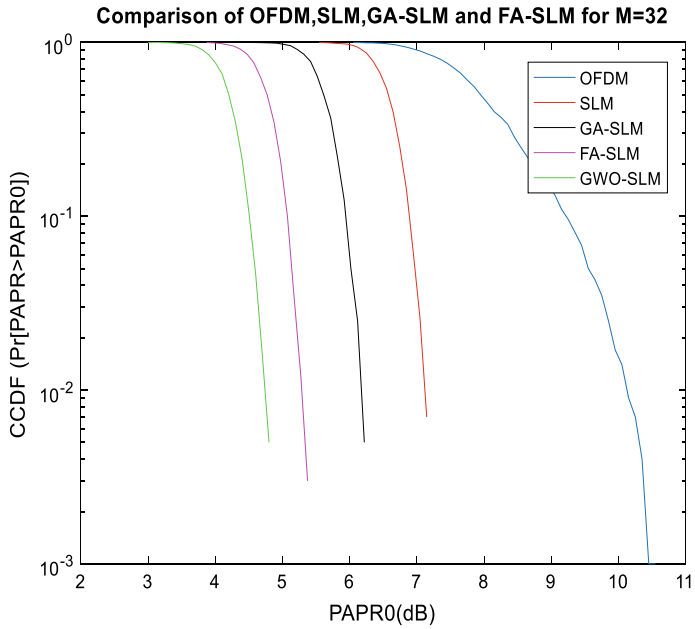

Fig. 7. CCDF versus PAPR for M = 32

As the number of phase sequences M increases the PPAR is gradually decreasing to some extent. The PAPR reduction performance of OFDM signal will not be considerably improved and it will also add more computational complexity. The comparison results proves that the PAPR is decreased using GWO-SLM when compared with GA-SLM and FA-SLM.

6 Conclusion

In this paper, an efficient SLM technique based on Grey wolf optimization technique is proposed to achieve PAPR reduction. The PAPR reduction performance of the proposed SLM-OFDM system using grey wolf for optimum phase rotation factors searching was compared with the original OFDM and conventional SLM-OFDM and Firefly Algorithm based SLM systems. According to the simulation results, the proposed grey wolf based SLM-OFDM output performs well compared with OFDM system and FA based SLM OFDM, and also Grey Wolf based OFDM achieves low computational complexity. The proposed technique shows satisfying results in reducing the PAPR. PAPR decrease in writing shows achievability and high execution of this strategy as a quick and well execution approach. The proposed GWO-SLM is very much useful for communication systems. The experimental results are proved using Matlab tool.

References

1. Wu Y, Zou WY (1995) Orthogonal frequency division multiplexing: a multi-carrier modulation scheme. IEEE Trans. Consum Electron 41(3):392–399
2. Jiang T, Wu Y (2008) An overview: peak-to-average power ratio reduction techniques for OFDM signals. IEEE Trans Broadcast 54(2):257–268
3. Tellado J (2000) Peak to average power reduction for multicarrier modulation. Ph.D. dissertation, Stanford University
4. Carson N, Gulliver TA (2002) Peak-to-average power ratio reduction of OFDM using repeat-accumulate codes and selective mapping. In: IEEE international symposium on information theory (ISIT 2002). p 244
5. Han SH, Lee JH (2004) PAPR reduction of OFDM signals using a reduced complexity PTS technique. IEEE Signal Process Lett 11(11):887–890
6. Zhao Z, Peng Z, Zheng S, Shang J (2009) Cognitive radio spectrum allocation using evolutionary algorithms. IEEE Trans Wireless Commun 8(9):4421–4425
7. Salehinejad H, Pouladi F, Talebi S (2010) A metaheuristic approach to spectrum assignment for opportunistic spectrum access. In: 17th IEEE international conference on telecommunications (IEEE ICT 2010). Doha, Qatar, pp 234–238
8. Wang LQ, Tellambura C (2008) Cross-entropy-based sign-selection algorithms for peak-to-average power ratio reduction of OFDM systems. IEEE Trans Signal Process 56(10):4990–4994
9. Wang Y, Chen W, Tellambura C (2010) A PAPR reduction method based on artificial bee colony algorithm for OFDM signals. IEEE Trans Wireless Commun 9(9):1–6
10. Han SH, Lee JH (2005) An overview of peak-to-average power ratio reduction techniques for multicarrier transmission. IEEE Wireless Commun Mag 12(2):56–65
11. Salehinejad H Talebi S (2010) Dynamic fuzzy logic-ant colony system-based route selection system. Appl Comput Intell Soft Comput 428270:2010. https://doi.org/10.1155/2010/428270
12. Zhang Y, Ni Q, Chen HH, Song Y (2008) An intelligent genetic algorithm for PAPR reduction in a multi-carrier CDMA wireless system. In: IEEE international conference on wireless communication and mobile computing (IWCMC). pp 1052–1057
13. Geem ZW (2009) Music-inspired harmony search algorithms: theory and applications. Springer, Berlin, Germany
14. Müller SH, Hubber JB (1997) OFDM with reduced peak-toaverage power ratio by optimum combination of partial transmit sequences. IEEE Electron Lett 33:368–369
15. Wen JH, Lee SH, Huang YF, Hung HL (2008) A suboptimal PTS algorithm based on particle swarm optimization for PAPR reduction in OFDM systems. EURASIP J Wireless Commun Netw 14

Chapter 8
A Computational Comparison of Swarm Optimization Techniques for Optimal Load Shedding Under the Presence of FACTS Devices to Avoid Voltage Instability

G. V. Nagesh Kumar
Vignan's Institute of Information Technology (Autonomous), India

B. Venkateswara Rao
V. R. Siddhartha Engineering College (Autonomous), India

D. Deepak Chowdary
Dr. L. Bullayya College of Engineering (for Women), India

Polamraju V. S. Sobhan
Vignan's Foundation for Science, India

ABSTRACT

Voltage instability has become a serious threat to the operation of modern power systems. Load shedding is one of the effective countermeasures for avoiding instability. Improper load shedding may result in huge technical and economic losses. So, an optimal load shedding is to be carried out for supplying more demand. This chapter implements bat and firefly algorithms for solving the optimal load shedding problem to identify the optimal amount of load to be shed. This is applied for a multi-objective function which contains minimization of amount of load to be shed, active power loss minimization, and voltage profile improvement. The presence of with and without static VAR compensator (SVC), thyristor-controlled series capacitor (TCSC), and unified power flow controller (UPFC) on load shedding for IEEE 57 bus system has been presented and analyzed. The results obtained with bat and firefly algorithms were compared with genetic algorithm (GA) and also the impact of flexible AC transmission system (FACTS) devices on load shedding problem has been analyzed.

DOI: 10.4018/978-1-5225-5134-8.ch008

INTRODUCTION

Nowadays, voltage instability has been considered as one of the reason for the blackouts all over the world. Blackouts occurs due to contingency, such as the outage of an important transmission line or the outage of a major generator, or insufficient reactive power support at important buses due to a high loading condition or a combination of both the aspects. The requirement for improved efficiency at the same time as maintaining system stability necessitates the development of improved system analysis approaches and the improvement of advanced technologies. The Load shedding is a type of emergency control that is designed to ensure system stability by curtailing system load to match generation. It is an effective corrective control action in which a part of the system loads are disconnected according to certain priority in order to protect the power system. Load shedding is considered as the last resort tool for use in that extreme situation and usually the less preferred action to be adopted, but in this kind of problem it is vital to prevent the system from collapsing (Kundur, 1993). Load shedding schemes are mainly classified into two types those are under frequency load shedding scheme and under voltage load shedding scheme. Under frequency load shedding scheme has been used, to protect the power system stability from major disturbances. However, the analysis of recent blackouts suggests that voltage collapse and voltage-related problems are also important concerns in maintaining system stability. For this reason, voltage also needs to be taken into account in load shedding schemes. This type of scheme is called under voltage load shedding scheme. The load shedding problem is formulated using optimization methods. These methods are used to find the amount of load to be shed based on Optimal Power Flow frame work. The purpose of an Optimal Power Flow (OPF) function is to schedule the power system control parameters which optimize a certain objective function while satisfying its equality and inequality constraints, power flow equations, system security and equivalent operating limits. The equality constraints are the nodal power balance equations, while the inequality constraints are the limits of all control or state variables. OPF has been widely used for both the operation and planning of a power system. Introduced by Tinney (1967) and discussed by Carpentier (1979), the control variables include generator active powers, generator bus voltages, transformer tap ratios and the reactive power generation of shunt compensators.

A wide variety of classical optimization techniques have been applied in solving the OPF problems considering a single objective function, such as nonlinear programming, quadratic programming, linear programming, Newton-based techniques sequential unconstrained minimization technique, interior point methods and the parametric method but unfortunately these methods are infeasible in practical systems because of non-linear characteristics like valve point effects. Hence, it becomes essential to develop optimization techniques which are capable of overcoming these drawbacks and handling such difficulties. Optimization problems have been solved by many population-based optimization techniques in the recent past. These techniques have been successfully applied to non-convex, non-smooth and non-differentiable optimization problems. Some of the population-based optimization methods are genetic algorithm, Cuckoo Search Algorithm (Dung A. Le &Dieu N. Vo, 2016), bat Search Algorithm (Rao & Kumar, 2015), Quasi-Oppositional Biogeography-Based Optimization, Hybridization of Biogeography Based Optimization (HBBO) (Prabhneetkaur and Taranjotkaur, 2014), Anticipatory Multi objective Cuckoo Search (AMOCS) algorithm (SamikshaGoel, Arpita Sharma and V. K. Panchal, 2014),Teaching Learning Based Optimization (Aparajita Mukherjee, Sourav Paul & Provas Kumar Roy, 2015)artificial bee colony optimization (Rahul Khandelwal, J. Senthilnath, S. N. Omkar and Narendra Shivanath, 2016).

Flexible AC Transmission System (FACTS) controllers could be a suitable alternative to provide reactive power support at the load centers locally and hence keep the voltages within their safe operating limits to minimize the load shedding (Hingorani & Gyugyi, 2000). The FACTS devices use reliable high-speed thyristor based controllable elements such as SVC, TCSC, and UPFC etc. are designed based on state of the art developments in power semiconductor devices. J. G. Singh et al. suggested a new sensitivity based approach to locate Thyristor Controlled Series Compensator (TCSC) and Unified Power Flow Controller (UPFC) to enhance power system loadability. The new sensitivity factors may be effectively used for placement of TCSC and UPFC for increasing the system's loadability. Voltage stability analysis of large power systems using the modal analysis technique has further been proposed by B Gao et al. Modal analysis through bus, branch and generation participation factors provide useful information, which can then be utilized for placement of FACTS devices. Bus participation factors have been taken into consideration for determining the most suitable sites by Y.Mansour et al. Various optimization techniques have also been used for determining suitable locations for FACTS device to improve voltage profile and damping of the system.

A. Ramasamy et al brought into view the correlation between FVSI index and UVLS scheme. Under Voltage Load Shedding (UVLS) is one of the various methods used to sustain voltage stability. Alternatively, Fast Voltage Stability Index (FVSI) index has proven to be a good indicator for voltage stability in a system. From the simulation, results clearly indicate that FVSI index can be used to identify location to be load shed and thus reduce probability of Voltage Instability.

In (H. Am briz-Perez, E.Acha, C.R. Fuerte-Esquivel & A.De la Torre, 1998), has been showed the issue of UPFC modeling within the context of OPF solutions. The nonlinear optimization problem is solved by newton's method leading to highly robust iterative solutions even for cases of large scale power networks, where hundreds of variables are to be optimized is presented in literature. (RR Aparna, 2016), explains the use of swarm intelligence techniques for different applications. In 2016 (Dung A. Le & Dieu N. Vo, 2016), uses a cuckoo search algorithm (CSA) to solve the optimal reactive power dispatch (ORPD) problem in power system operation considering the power loss and voltage deviation. The advantages of the CSA method are few control parameters and high optimal solution quality. The objective of the ORPD problem is to minimize real power losses or bus voltage deviation satisfying equality and inequality constraints of real and reactive power balance. In this the authors use the single objective function for solving ORPD problem. Static synchronous series compensator (SSSC) is one of the most effective flexible AC transmission systems (FACTS) devices used for enhancing power system security. Optimal location and sizing of SSSC are investigated for solving the optimal reactive power dispatch (ORPD) problem in order to minimize the active power loss in the transmission networks. Optimal reactive power dispatch (ORPD), a sub problem of OPF, has significant influence on the economic and secure operation of power systems. (SusantaDutta, Provas Kumar Roy **&** Debashis Nandi, 2016) use chemical reaction optimization (CRO) to solve the above problem with minimization of single objective function. Out of the several FACTS devices UPFC is one of the most important shunt-series connected FACTS devices to improve voltage stability and minimize the amount of load to be shed (Padiyar & Uma Rao, 1999; Lashkar Ara & Kazemi, 2012).

In this chapter, FACTS devices like SVC, TCSC and UPFC are considered to minimize the load curtailment. An optimal power flow problem is formulated with the objective to minimize the amount of load to be shed, the total real power losses and voltage deviation subjected to constraints along with FACTS devices limits. To deal with the above problem new metaheuristic optimization techniques called bat and firefly algorithms have been proposed. In this chapter the impact of SVC, TCSC and UPFC

on minimization of load shedding problem has been examined with bat and firefly algorithms. The effectiveness of the proposed algorithms has been tested on IEEE 57-bus system without and with SVC, TCSC and UPFC. The obtained results are compared with Genetic algorithm. To show the effectiveness of the algorithms, their population size and parameters are also varied. In this chapter voltage stability has been analyzed using line based voltage stability index called 'Fast Voltage Stability Index' (FVSI).

The remaining organization of the chapter is as follows. Section 2 presents the various FACTS devices like SVC, TCSC and UPFC; Section 3 presents multi objective OPF problem formulation. The implementation of Meta heuristic optimization algorithms to the problem is given in Section 4. Numerical results and discussion are followed in Section 5. Section 6 presents' future research directions finally, the conclusion is given in section 7.

FACTS DEVICES

Static VAR Compensator (SVC)

Static VAR Compensator is the simple and popular shunt connected FACTS device. The SVC is modeled as a variable susceptance device. The SVC device can either inject reactive power (capacitive) or absorb it (inductive) as per system requirements. The sizing of the SVC located at a bus is done until the voltage at the bus is 1.0 p.u. The variable susceptance model is shown in Figure 1.

Current drawn by the SVC is

$$I_{svc} = jB_{svc}V_k \tag{1}$$

SVC absorbed or injected reactive power at bus k is

$$Q_{svc} = -V_k^2 B_{SVC} \tag{2}$$

Figure 1. Variable Shunt Susceptance

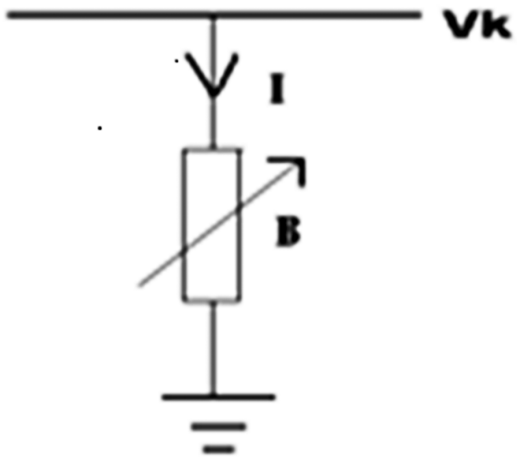

The real and reactive power variations at k^{th} bus related to the susceptance of the SVC are given in equation 3. The total susceptance B_{svc} is taken as the state variable.

$$\begin{bmatrix} \Delta P_k \\ \Delta Q_k \end{bmatrix}^i = \begin{bmatrix} 0 & 0 \\ 0 & Q_k \end{bmatrix}^i \begin{bmatrix} \Delta \theta_k \\ \Delta B_{svc} \,/\, B_{svc} \end{bmatrix}^i \tag{3}$$

After completion of iteration, susceptance value of the SVC is updated as per the optimization rules. Initial values of the SVC susceptance is consider to be B=0.02p.u, B_{min}= -1.0p.u, B_{max}=1.0p.u

Thyristor-Controlled Series Capacitor (TCSC)

Thyristor-controlled series capacitor scheme is developed by Vithaythil and others. TCSC also enhances a system's stability. The basic module of the TCSC is represented in Figure 2. It consists of a series compensating capacitor shunted by thyristor controlled reactor. Thyristor inclusion in the TCSC module enables it to have a smoother control of reactance against system parameter variations. This is modeled as a controllable reactance, is inserted in series with the transmission line to adjust the line impedance and thereby controls power flow.

In this study, reactance of the transmission line is adjusted by using TCSC directly. The TCSC is modeled as variable impedance and its rating depends on the reactance of the transmission line where the TCSC is located. The impedance equations are written as in equations 4 and 5.

$$\mathrm{Z_{line}} = \mathrm{R_{line}} + \mathrm{X_{line}} \tag{4}$$

$$\mathrm{X_{ij}} = \mathrm{X_{line}} + \mathrm{X_{TCSC}} \tag{5}$$

Figure 2. Basic TCSC model

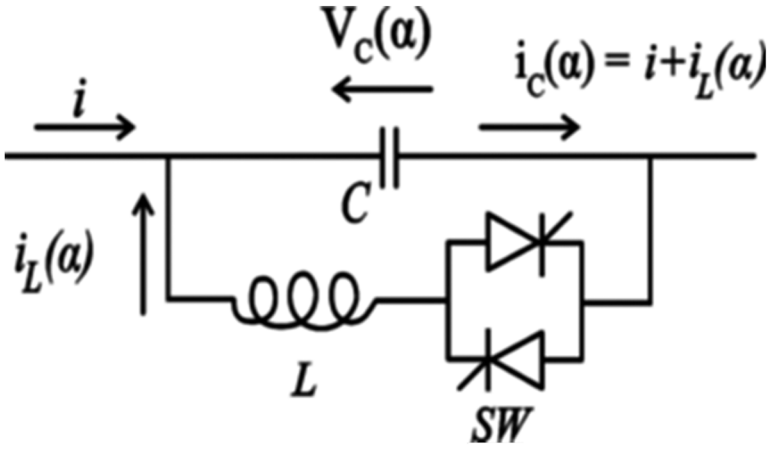

where XTCSC is reactance of TCSC, in order to avoid over compensation, the working range of the TCSC is selected between -0.8Xline and 0.6Xline.

The transfer admittance matrix of the TCSC is given by

$$\begin{bmatrix} I_i \\ I_j \end{bmatrix} = \begin{bmatrix} jB_{ii} & jB_{ij} \\ jB_{ji} & jB_{jj} \end{bmatrix} \begin{bmatrix} Vi \\ V_j \end{bmatrix} \tag{6}$$

For capacitive operation, equations are given in 7 and 8

$$\mathrm{B_{ii}} = \mathrm{B_{jj}} = \frac{1}{\mathrm{X_{TCSC}}} \tag{7}$$

$$\mathrm{B_{ij}} = \mathrm{B_{ji}} = -\frac{1}{\mathrm{X_{TCSC}}} \tag{8}$$

For inductive operation the signs are reversed

The active and reactive power equations at bus k are:

$$\mathrm{P_i} = \mathrm{V_i V_j B_{ij}} \sin(\theta_\mathrm{i} - \theta_\mathrm{j}) \tag{9}$$

$$\mathrm{Q_i} = -\mathrm{V_i^2 B_{ii}} - \mathrm{V_i V_j B_{ij}} \cos(\theta_\mathrm{i} - \theta_\mathrm{j}) \tag{10}$$

When the series reactance regulates the amount of active power flowing from bus i to bus j the change in reactance of TCSC is

$$\Delta \mathrm{X_{TCSC}} = \mathrm{X_{TCSC}^{i}} - \mathrm{X_{TCSC}^{(i-1)}} \tag{11}$$

Based on optimization rules, the state variable XTCSC of the series controller is updated.

Unified Power Flow Controller

Gyugyi proposed the UPFC concept is used for real time control and dynamic compensation of the ac transmission system (Tiwari & Sood, 2012; Ghahremani & Kamwa, 2013). UPFC provides multi-functional flexibility required to solve many of the problems in the power system. The UPFC is able to control simultaneously or selectively all the parameters affecting power flow in the transmission line (i.e. voltage magnitude, line impedance and phase angle). This capability signifies the term ‘unified’ in the UPFC (Radu, 2006; Padiyar & Kulakarni, 1998).

The UPFC consists of two voltage-source converters, one connected in shunt and one connected in a series. The series converter of the UPFC injects an AC voltage with the controllable magnitude and phase angle in a series with the transmission line via a series connected coupling transformer. The basic function of shunt converter is to supply or absorb the real power demanded by the series converter at the common DC link. It can also generate or absorb controllable reactive power and provide independent shunt reactive compensation for the line which is shown in Figure 3. Thereby, the UPFC can fulfil the functions of reactive shunt compensation, series compensation and phase shifting (Mihalie, Zunko & Povh, 1994). The device is an amalgamation of a shunt connected Static Synchronous Compensator (STATCOM) and a series connected Static Synchronous Series Compensator (SSSC). The combination of above two devices is UPFC. In UPFC exchange of real and reactive has been obtained through shared DC linkage. It is also capable of generation or absorption of controlled reactive power, thus providing autonomous shunt reactive compensation. The UPFC not only performs the functions of STATCOM, SSSC, and the phase angle regulator but also provides additional flexibility by combining some of the functions of these controllers (Tiwari, 2012; Gyugyi, 1995).

UPFC voltage sources are written in equations 12 and 13,

$$V_{vR}(\cos\delta_{vR} + j\sin\delta_{vR}) \tag{12}$$

$$V_{cR}(\cos\delta_{cR} + j\sin\delta_{cR}) \tag{13}$$

where V_{vR} and δ_{vR} are the controllable voltage magnitude and phase angle of the voltage source representing the shunt converter. Similarly, V_{cR} and δ_{cR} are the controllable voltage magnitude and phase angle of the voltage source representing the series converter. The source impedance is considered to be resistance less. (i.eR_{vR}=0, R_{cR}=0)

Figure 3. Schematic arrangement of the Unified Power Flow Controller

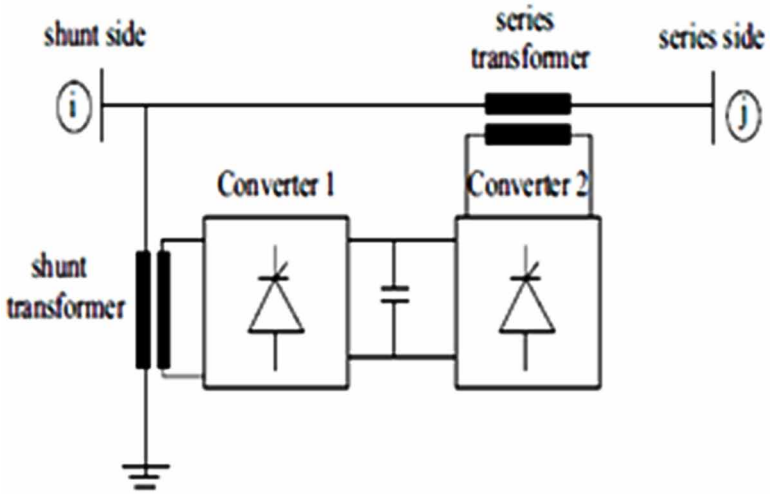

The UPFC using solid state controllers provides functional flexibility to handle practically all the power flow control and transmission line compensation problems which are generally not obtained by variable impedance type thyristor-controlled controllers. Installing UPFC in the system improves the voltage profile that will reduce the amount of load to be shed. The starting values of the UPFC voltage sources are taken to be V_{cr} =0.04 p.u, δ_{cr}=87.13^0, V_{vr} =1 p.u. and δ_{vr} = 0^0. The source reactances are taken as X_{cr}=X_{vr} = 0.1 p.u.

PROBLEM FORMULATION

In this chapter, the optimal amount of load to be shed is identified by new optimisation techniques namely bat and firefly algorithms to avoid voltage instability. Impact of SVC, TCSC and UPFC on load shedding problem has been analysed with optimization techniques. In this chapter multi objective function is formulated to improve the stability of the system which consists of three parameters. These three components are active power loss minimisation, minimization of voltage deviation and minimization of amount of load to be shed.

Objective Function

In multi objective optimization problem, each objective would be considered for the optimal solution. The multi objective index for the performance calculation of amount of load to be shed is considered along with the active power loss and voltage deviation is given in equation 14.

$$\text{Min } F = \text{Min}\left(W_1 * F_{\text{Ploss}} + W_2 * F_{\text{VD}} + W_3 * F_{\text{LS}}\right) \tag{14}$$

where W_1+W_2+W_3 =1 and

$W_1 = 0.3$, $W_2 = 0.3$, $W_3 = 0.4$

Select these values based on trial and error method.

- **Active Power Loss:** This objective consists of minimizing the active power losses in the transmission lines. It can be expressed as in equation 15,

$$F_{\text{PLoss}} = \min\left(P_{\text{Loss}}\right) = \min\left(\sum_{k=1}^{\text{ntl}} \text{real}(S_{ij}^{k} + S_{ji}^{k})\right) \tag{15}$$

where ntl=no. of transmission lines

S_{ij} is the total complex power flow of line i – j

- **Voltage Deviation:** To have a good voltage performance, the voltage deviation at each bus must be made as small as possible. The Voltage Deviation (VD) can be expressed in equation 16,

$$\mathrm{F_{VD}} = \min\left(\mathrm{VD}\right) = \min\left(\sum_{\mathrm{k=1}}^{\mathrm{Nbus}} \vdots \mathrm{V_k} - \mathrm{V_k^{ref}} \vdots^2\right) \tag{16}$$

V_k is the voltage magnitude at bus k

V_k^{ref} is the reference voltage magnitude at bus k

- **Amount of Load to be Shed:** This objective function is interruption load minimisation. Load interruption can be defined as the total load to be shed in order to maintain the voltage at appropriate level (Arief, 2010; Yasin, 2013; Cheraghi Valujerdi, 2012; Fernandes, 2008).

$$\mathrm{F_{LS}} = \min\left(\text{Amount of Load to be shed}\right) = \min\left(\Delta \mathrm{S_{shed\ i}}\right) \tag{17}$$

where $\Delta S_{shed\ i}$ is the total amount of load to be shed at bus i.

Equality constraints:

$$\sum_{\mathrm{i=1}}^{\mathrm{N}} \mathrm{P_{Gi}} = \sum_{\mathrm{i=1}}^{\mathrm{N}} \mathrm{P_{Di}} + \mathrm{P_L} \tag{18}$$

$$\sum_{\mathrm{i=1}}^{\mathrm{N}} \mathrm{Q_{Gi}} = \sum_{\mathrm{i=1}}^{\mathrm{N}} \mathrm{Q_{Di}} + \mathrm{Q_L} \tag{19}$$

where i=1,2,3,.....,N and N = no. of. Buses

P_L is total active power losses; Q_L is total reactive power losses

Inequality constraints:

$$V_{Gi}^{\min} \le V_{Gi} \le V_{Gi}^{\max} \tag{20}$$

$$P_{Gi}^{\min} \le P_{Gi} \le P_{Gi}^{\max} \tag{21}$$

$$Q_{Gi}^{\min} \leq Q_{Gi} \leq Q_{Gi}^{\max} \tag{22}$$

SVC Limits

$$\mathrm{B}_{\mathrm{svc}}^{\min} \leq \mathrm{B}_{\mathrm{svc}} \leq \mathrm{B}_{\mathrm{svc}}^{\max} \tag{23}$$

TCSC Limits

$$\mathrm{X}_{\mathrm{tcsc}}^{\min} \leq \mathrm{X}_{\mathrm{tcsc}} \leq \mathrm{X}_{\mathrm{tcsc}}^{\max} \tag{24}$$

UPFC device limits:

$$\mathrm{V}_{\mathrm{vr}}^{\min} \leq \mathrm{V}_{\mathrm{vr}} \leq \mathrm{V}_{\mathrm{vr}}^{\max} \tag{25}$$

Vvr is the shunt converter voltage magnitude (p.u)

$$\mathrm{V}_{\mathrm{cr}}^{\min} \leq \mathrm{V}_{\mathrm{cr}} \leq \mathrm{V}_{\mathrm{cr}}^{\max} \tag{26}$$

Vcr is the series converter voltage magnitude (p.u)where P_L is the active power loss in the system, P_{Gi} is the active power generation at bus i, P_{Di} is the real power demand at bus i, Q_{Gi} is the reactive power generation at bus i. Q_{Di} is the reactive power demand at bus i, N and ng are the number of buses and no of generators in the system respectively.

Load curtailment limits:

$0 \leq P_{\text{shed i}} \leq P_{\text{Di}}$

$0 \leq Q_{\text{shed i}} \leq Q_{\text{Di}}$

where $P_{shed,i}$ is the amount of load to be shed at bus i in MW

$Q_{shed,i}$ is the amount of load to be shed at bus i in MVAR

Fast Voltage Stability Index (FVSI)

The voltage stability indices referred to indicate the voltage collapse. In this chapter, line-based voltage stability index is implemented to evaluate the voltage stability analysis in a power system. This index is called as Fast Voltage Stability Index (FVSI). It is given in equation 27. The system becomes unstable if FVSI is equal to or greater than unity.

$$\mathrm{FVSI}_{ij} = \frac{4\ \mathrm{Z}^2\mathrm{Q}_j}{\mathrm{V}_i^2\ \mathrm{X}} \tag{27}$$

where

Z = Impedance of the line
X = Reactance of the line
Q_j = reactive power at bus j
(receiving end bus)
V_i = voltage magnitude at bus i
(sending end bus)
$FVSI_{ij}$ = FVSI for line connected between bus i and bus j.

Any line in the system that exhibits FVSI close to unity indicate that the line is may lead to system violation. So FVSI has to be maintained less than unity in order to maintain a stability of the system (Ratniyomcha & Kulworawa-nichpong, 2009).

OPTIMIZATION METHODS FOR OPTIMAL LOADSHEDDING

Overview of the Optimization techniques

Modern engineers are facing with problems like system design, construction and maintenance. In all these problems, the main goal is to obtain a better solution with less effort. The effort required for the desired output is usually formulated as a function with considered limitations. Optimization is also defined as the technique employed to get the maximum or minimum value of a function. It has been used widely in several technical fields. Some of these are design of aircraft and aerospace structures for minimum weight, calculating optimal trajectories of space vehicles, designing civil engineering structures like frames, foundations, towers, chimneys, bridges, and dams for minimum cost, designing water resource systems for maximum benefit, Optimal plastic design of structures, developing material handling equipment such as conveyors, trucks, and cranes at minimal costs, designing maximum efficiency pumps, turbines, and heat transfer equipment, Optimum electrical machinery design for motors, generators, and transformers, Optimum design of electrical networks, power systems, Optimal production planning, controlling, and scheduling, Selecting site for an industry, Planning of maintenance and replacement of equipment to reduce operating costs, Devising best strategies to obtain maximum profit in the presence of competition and Optimum design of control systems.

A multi-objective optimization problem is an optimization problem that involves multiple objective functions. In mathematical terms, a multi-objective optimization problem can be formulated as

$$\mathrm{Min\ f}\left(\mathrm{X}\right) = \min(f_1\left(x\right), f_2\left(x\right), f_3\left(x\right), \ldots . f_k\left(x\right) \tag{28}$$

S.t $x \in X$

Subjected to the constraints

$$g_i\left(X\right) \leq 0, \quad i = 1,2,3,\ldots,p$$

$$h_i\left(X\right) = 0, \quad i = 1,2,3,\ldots,q$$

where X is an m-dimensional vector called the design vector, f(X) is termed the objective function, and g_i (X) and h_i (X) are known as inequality and equality constraints, respectively. The number of variables m and the number of inequality constraints p and the number of equality constraints q. The problem stated in Eq. (28) is called a constrained multi objective optimization problem.

Genetic Algorithm

Genetic Algorithms (GAs) are one of various techniques amongst the Evolutionary Algorithms, which search for solutions to optimization problems through "evolving" better solutions. Genetic Algorithms have found application in science, engineering, business and social sciences. GAs has been developed by John Holland, his colleagues and students at the University of Michigan during the early 1970's. Also, they have gained popularity over the recent years in fields of science and engineering. GAs have been successfully applied to optimization problems like wire routing, scheduling, adaptive control, game playing, cognitive modelling, transportation issues, traveling salesman problems, optimal control problems, etc. GAs are general-purpose search techniques based on principles inspired from the genetic and evolution mechanisms observed in natural systems and populations of living beings.

In lieu to Optimal Power Flow, the major steps of the GA as applied can be summarized as under:

1. "Creation of an initial population through the random generation of a set of feasible solutions (chromosomes).
2. Evaluation of each chromosome by solving the objective function.
3. Determining fitness function for each chromosome in the population.
4. Application of GA operators to generate new populations.
5. Copying the optimal solution from the current into the new population.
6. Generating new members (typically 1-10% of the population size), as neighbors to solutions in the current population, and adding them to the new population.
7. Applying crossover operators to complete members of the new population.
8. Applying mutation operator to the new population".

Bat Algorithm

Bat algorithm (BA) is a metaheuristic method which uses population of points to search for a global minimum of a function over continuous search space. This bat algorithm is developed using the concept of echolocation behaviour of micro bats with varying pulse rates of emission and loudness. This

method is based upon the certain approximations that all bats use echolocation to sense distance, and distinguish between food and background barriers in some magical way. To search for prey, Bats usually fly haphazardly with velocity v at position x with a fixed frequency f_{min}, varying wavelength and loudness (Yang, 2008; Yang, X. S 2011). Depending on the proximity of their target, they can automatically adjust the frequency of their emitted pulses and adjust the rate of pulse emission assuming that the loudness varies from a large value A_O to a minimum constant value A_{min}. It is even assumed that frequency ranges from 0 to f_{max} because higher frequencies have short wavelengths and travel shorter distances, so that the rate of pulse can be 0 or 1, where 0 means no pulses and 1 means maximum rate of pulse emission. Search for prey is intensified by a local random walk and selection of the best continues until certain stop criteria are met. This essentially uses a frequency-tuning technique to control the dynamic behaviour of a swarm of bats, and the balance between exploration and exploitation can be controlled by tuning algorithm-dependent parameters in bat algorithm (Yang, X. S, 2010). The basic steps of the bat algorithm are summarized and are given bellow in the pseudo code.

"Objective function f(x), $x = (x_1, x_2, ..., x_d)^T$
Initialize the bat population x_{ii} (ii = 1, 2, ..., n) and v_{ii}
Define pulse frequency f_{ii} at x_{ii}
Initialize pulse rates r_{ii} and the loudness A_{ii}
while(t <Max number of iterations)
Generate a new solution by changing frequency,
And modifying velocities and solutions [equations (2) to (4)]
if(rand >r_{ii})
Select a best solution in the available solutions
Create a local solution around the selected best solution
end if
Create a new solution by flying randomly
if(rand <A_{ii} & $f(x_{ii}) < f(x_o)$)
Accept the new solutions
Increase r_{ii} and reduce A_{ii}
end if
Rank the bats and find the current best x_o
End while
Post process results and visualization"

The step by step implementation of bat algorithm can be described as follows:

Step 1: *Initialize the load flow data, and bat parameters such as the size of population (N), the maximum number of generations (N_gen), Loudness (L), Pulse rate (PR) and the number of variables to be optimized (D).*

Step 2: *Generate the initial population of N individuals randomly in the feasible area. Consider the optimized variables. Therefore, all the solutions are practicable solutions and the object is to find the best possible one.*

Step 3: *Evaluate the fitness for each individual in the population according to the objective function.*

Step 4: *Generate a new resident.*
Step 5: *Stop the process and print the best individual if the stopping criterion is satisfied, else go back to step 4.*

Firefly Algorithm

Firefly algorithm (FA) is a kind of stochastic search techniques based on the mechanism of natural behavior of fireflies. The firefly algorithm is a metaheuristic algorithm, enthused by the sporadic behavior of fireflies. The primary objective for a firefly's flash is to act as a signal system to entice other fireflies (X.S. Yang, 2009; Yang 2010). This algorithm is based upon the following assumptions those are all fireflies are unisexual, so that one firefly will be a focus for all other fireflies. Charismatic is proportional to their vividness, and for any two fireflies, the less bright one will catch the fancy of the brighter one. However, the vividness can decrease as their distance increases. If there are no fireflies dazzling than a given firefly, it will move haphazardly and the vividness should be associated with the objective function. Vividness is proportional to value of search-space function in case of maximization problem.

There are two important disputes in firefly algorithm, first is light intensity variation and other is vividness variation. It is assumed that vividness of firefly is ascertained by its vividness which in turn associated with search-space function. The vividness of the firefly is calculated objective value F(x) at a particular location x. Vividness is relative and it varies with distance between two fireflies. Light is also absorbed by the air and it also gets decreased with increasing distance so vividness is allowed to show a discrepancy with degree of absorption. The firefly algorithm function can be described as: initially consider an objective function F(x). Generate an initial population of n fireflies X_i, i=1, 2, 3…n. Calculate Light intensity at X_i which is determined by F (X). Delineate the light absorption coefficient. Now compare the light intensities of fireflies and move the firefly which is having lesser light intensity towards the brighter one. Then vary the vividness with distance. Now echelon the fireflies and discover the best solution. It may create as gbest. In optimization problem where number of fireflies are greater than number of local optima, the initial locations of the n fireflies should be distributed relatively uniformly throughout the entire search space. During the execution, the fireflies converge into all of these local optima, the global optima is determined. Firefly algorithm will approach the global optima when n tends to infinite and number of iterations is greater than 1 but in reality it has abrupt convergence. The basic steps of the Firefly algorithm can be summarized in the pseudo code given below (Lukasik & Zak, 2009).

$\boldsymbol{x}$), $\boldsymbol{x}$ = (x1,…,xd)T
Generate initial population of fireflies $\boldsymbol{x}_{ii}$(i=1, 2…, n)
Light intensity I_{ii} at x_{ii} is determined by f($\boldsymbol{x}_{ii}$)
Define light absorption coefficient γ
***while**(t <MaxGeneration)*
***for**ii = 1: n all n fireflies*
***for**jj = 1: ii all n fireflies*
if**(I_{jj}> I_{ii}), More firefly ii towards jj in d-dimension; **end if
Attractiveness varies with distance r
Evaluate new solutions and modify the light intensity
***end for** jj*

end for *ii*
Rank all the fireflies and find the current best firefly
end while
Post process results and visualization

The bat and firefly algorithms are implemented to find the optimal amount of load to be shed by considering without and with SVC, TCSC and UPFC. In this study, the real and reactive loads at buses, real power generation and voltages of the generator buses are considered as variables to optimize the multi objective function. For the considered IEEE-57 bus system, the Genetic algorithm, bat algorithm and firefly algorithm are applied. The simulation is carried out with an initial population having 20 individuals with a maximum generation number equal to 50.

RESULTS AND DISCUSSION

Load shedding is one of the effective solutions for avoiding instability. However, optimal load shedding needs to be carried out to meet more demand. This chapter implements the bat and firefly algorithms for solving the optimal load shedding problem. The objective function consists of minimizing the amount of load to be shed, active power loss minimization and voltage profile improvement. The load shedding problem is analyzed for the IEEE 57 bus system. Further, the effect of FACTS devices like SVC, TCSC and UPFC on load shedding problem is examined. IEEE 57 bus system is considered for case study. In this system, bus 1 is considered as slack bus and 2, 3, 6, 8, 9 & 12 are considered as generator buses. All other buses are considered as load buses. All these buses are interconnected by 80 transmission lines. Multi objective optimization for optimal load shedding is simulated using GA, BA & FA and results have been presented and analyzed. Table 1 and Table 2 represent the input parameters of the bat and firefly algorithms respectively. Table 3 represents the generator characteristics of IEEE 57 bus system.

Optimal Load Shedding With SVC Device Using Bat And Firefly Techniques

SVC is placed at bus number 31 because it is lowest voltage bus. Table 4 and Table 5 showcase the voltage profiles without and with the placement of SVC at 31-bus in IEEE57 bus system using bat algorithm and firefly algorithm respectively. There is an observable change in the voltage profile of the system with the installation of SVC. The firefly algorithm is established to be a better technique than bat algorithm in improving the voltage profile.

Table 1. Input parameters of bat algorithm

S.No	Parameters	Quantity
1	Population size	20
2	Number of generations	50
3	Loudness	0.5
4	Pulse rate	0.5

Table 2. Input parameters of Firefly Algorithm

S.No	Parameters	Quantity
1	Number of fireflies	20
2	Max Generation	50
3	Alpha	0.5
4	Beta	0.5
5	Gama	1

Table 3. Generator Characteristics of IEEE 57 Bus System

Generator Bus no	a ($/MW²/hr)	b ($/MW/hr)	c ($/hr)	P_G^{min} (MW)	P_G^{max} (MW)
1	0.0775	20	0	0	575
2	0.01	40	0	0	100
3	0.25	20	0	0	140
6	0.1	40	0	0	100
8	0.02222	20	0	0	550
9	0.01	40	0	0	200
12	0.32258	20	0	0	410

Table 4. Voltage Profiles Comparison before and after installing SVC in optimal load shedding using bat algorithm

	Load Shedding Without SVC		Load Shedding With SVC	
Bus No	Voltage (p.u)	Phase Angle	Voltage (p.u)	Phase Angle
1	1.04	0	1.04	0
2	1.0357	1.1509	1.01	1.3632
3	1.0183	1.5235	1	-0.8131
4	1.0066	0.888	0.9954	-1.5834
5	0.9986	0.682	0.9949	-2.0035
6	1	1.0228	1	-1.7632
7	0.9863	0.137	0.9917	-0.8225
8	1.005	1.7483	1.005	2.0214
9	1	0.9849	1	0.4627
10	0.987	-2.2244	0.9986	-2.376
11	0.9804	-0.9579	0.9943	-1.6717
12	1.015	-1.7333	1.015	-1.6877
13	0.9808	-1.687	1.0005	-2.4608
14	0.956	-2.5766	0.9933	-3.6137
15	1.0122	-0.3215	1.0177	-1.3241
16	1.0153	-2.5607	1.0187	-1.7305
17	1.0204	-2.1404	1.0204	-2.1235

continued on following page

Table 4. Continued

	Load Shedding Without SVC		Load Shedding With SVC	
Bus No	**Voltage (p.u)**	**Phase Angle**	**Voltage (p.u)**	**Phase Angle**
18	0.9686	-3.8159	0.9708	-6.0589
19	0.9117	-5.1436	0.9598	-7.9972
20	0.9094	-5.1921	0.9661	-8.4447
21	0.9009	-5.133	0.9882	-7.6203
22	0.9081	-5.0077	0.9929	-7.6212
23	0.9069	-5.0834	0.9898	-7.6393
24	0.9038	-5.3594	0.9536	-7.1524
25	0.9012	-12.3353	0.906	-12.5987
26	0.9069	-4.9091	0.952	-6.8645
27	0.9208	-3.7698	0.961	-5.0101
28	0.9471	-2.8134	0.9712	-3.802
29	0.9679	-2.1723	0.9818	-2.9656
30	0.9077	-13.2257	0.9478	-13.3322
31	**0.9043**	**-14.4136**	**1**	**-14.3372**
32	0.9097	-13.3153	0.9490	-13.6936
33	0.9069	-13.3758	0.9250	-13.7383
34	0.9197	-6.8281	0.9457	-8.7034
35	0.9289	-6.5386	0.9543	-8.4939
36	0.9408	-6.2075	0.9651	-8.2502
37	0.9487	-5.9002	0.9737	-8.0997
38	0.9698	-4.8285	0.9937	-7.5878
39	0.9481	-5.9684	0.9719	-8.106
40	0.9411	-6.3062	0.9635	-8.2415
41	0.9334	-6.0772	0.9744	-6.5012
42	0.9022	-7.5211	0.938	-8.37
43	0.9658	-2.4314	0.9871	-3.0908
44	0.9687	-4.4081	1.0032	-6.5556
45	0.9715	-2.7193	1.0213	-3.6266
46	0.9291	-4.251	0.9957	-5.1542
47	0.906	-5.3731	0.9902	-6.6341
48	0.9898	-5.1941	0.9929	-6.8905
49	0.9094	-5.3855	0.9901	-6.2493
50	0.9113	-5.5914	0.9717	-6.0461
51	0.9724	-3.8773	0.9945	-3.8155
52	0.9286	-3.0633	0.9399	-3.7593
53	0.9142	-3.3455	0.9241	-3.9934
54	0.9464	-2.1355	0.9521	-2.6997
55	0.9879	-0.596	0.9896	-1.0857
56	0.9037	-7.817	0.9326	-9.2341
57	0.9083	-8.4341	0.9272	-10.1059

Table 5. Voltage Profile Comparison before and after installing SVC in optimal load shedding using Firefly algorithm

	Load Shedding Without SVC		Load Shedding With SVC	
Bus No	**Voltage (p.u)**	**Phase Angle**	**Voltage (p.u)**	**Phase Angle**
1	1.04	0	1.04	0
2	1.0332	0.4692	1.01	0.2648
3	1.0126	-0.2266	1	-0.69
4	1.0027	-0.9924	0.9953	-1.3541
5	0.9973	-1.429	0.9949	-1.5885
6	1	-1.1993	1	-1.2585
7	0.9859	-1.0545	0.9922	-1.5323
8	1.005	1.2752	1.005	0.4903
9	0.9974	-0.4728	1	-0.9862
10	0.9859	-3.0882	0.9986	-3.1467
11	0.9786	-2.0752	0.9946	-2.6423
12	1.015	-2.1506	1.015	-2.0134
13	0.9795	-2.5101	1.0006	-3.0423
14	0.9547	-3.4093	0.9934	-4.1786
15	1.0104	-1.0342	1.0177	-1.4167
16	1.018	-2.2126	1.0198	-1.6988
17	1.0224	-1.8422	1.0246	-1.2846
18	0.9644	-5.644	0.971	-5.8956
19	0.9096	-6.6723	0.959	-8.0714
20	0.9086	-6.5097	0.9648	-8.6694
21	0.9088	-6.1049	0.9884	-8.0484
22	0.9065	-5.9188	0.993	-8.0869
23	0.9053	-6.0011	0.9899	-8.11
24	0.9124	-6.3838	0.9539	-7.7125
25	0.9001	-13.3715	0.9062	-13.1505
26	0.9178	-5.9451	0.9525	-7.4361
27	0.92	-4.9103	0.9616	-5.6786
28	0.9465	-3.9893	0.9719	-4.507
29	0.9673	-3.3697	0.9835	-3.6934
30	0.9076	-14.2577	0.9498	-13.8799
31	**0.9005**	**-15.4298**	**1**	**-14.8749**
32	0.9019	-14.293	0.9498	-14.2165
33	0.9051	-14.3538	0.9280	-14.2612
34	0.9178	-7.75	0.9455	-9.2171
35	0.927	-7.4568	0.9541	-9.0062
36	0.9389	-7.1225	0.9649	-8.7615

continued on following page

Table 5. Continued

	Load Shedding Without SVC		Load Shedding With SVC	
Bus No	**Voltage (p.u)**	**Phase Angle**	**Voltage (p.u)**	**Phase Angle**
37	0.9469	-6.8088	0.9735	-8.6024
38	0.9282	-5.7116	0.9674	-8.0531
39	0.9462	-6.8804	0.9717	-8.6147
40	0.9392	-7.2266	0.9632	-8.7625
41	0.9315	-7.1683	0.9744	-7.3676
42	0.9059	-8.5905	0.9384	-9.173
43	0.964	-3.5421	0.9873	-4.0334
44	0.9971	-5.2513	1.0033	-6.9393
45	0.97	-3.484	1.0218	-3.8415
46	0.9277	-5.1011	0.9956	-5.6937
47	0.9469	-6.2396	0.9901	-7.1472
48	0.9883	-6.0651	0.9929	-7.3928
49	0.908	-6.2498	0.99	-6.7949
50	0.9101	-6.459	0.9716	-6.6641
51	0.9713	-4.7449	0.9943	-4.5569
52	0.9274	-4.323	0.9403	-4.6469
53	0.9128	-4.6399	0.9244	-4.9709
54	0.9443	-3.5044	0.952	-3.8905
55	0.9853	-2.0285	0.989	-2.4661
56	0.9211	-8.8577	0.9335	-9.9703
57	0.9068	-9.4549	0.9282	-10.794

The maximum and minimum limits of bus voltage magnitude are considered as 1. 1p.u and 0.9p.u, respectively while B_{SVC} limits range from -1 to 1 p.u. The MATLAB program is simulated for optimal load shedding problem using Genetic, bat and firefly algorithms for both the cases i.e without SVC and with SVC. Results of the various parameters in the considered objective function are presented in Table 6.

The system load curtailment in the absence of SVC, with bat algorithm is 137.9777 MW, while it is reduced to 135.5223 MW with the Firefly algorithm. On placement of SVC, the load to be tripped is reduced measurably. The load to be shed is found to be the least with Firefly algorithm.

Fast Voltage Stability Index is employed in determining the stability of the system. The influence of load shedding on stability index along with the SVC is analysed. The results are presented in Table 7 for both bat and firefly algorithms. A remarkable change is observed in the FVSI values with the incorporation of SVC, which is further improved with Firefly algorithm. The results are plotted in Figure 4 and Figure 5.

The computational capabilities of the two techniques are analysed. Figure 6 and Figure 7 indicates the convergence of the objective function using bat and firefly algorithm without SVC. These figures show that the Firefly algorithm gives a better value as compared to the bat algorithm, but the bat algorithm takes lesser number of generations to get the final steady value. The same thing holds well without SVC also, and this can be seen from the Figure 8 and Figure 9.

Table 6. Objective function parameters without and with SVC using bat and firefly Algorithm in Load Shedding problem

	Without SVC	With SVC	Without SVC	With SVC	Without SVC	With SVC
	GA-OPF		BA-OPF		FA-OPF	
Real Power Losses (MW)	17.4023	14.5279	16.7969	14.0070	16.4094	11.6515
Voltage Deviation in all Buses (p.u)	5.1236	2.5682	4.9117	2.2587	4.9726	2.1763
Amount of Load Shed (MW)	138.638	125.342	137.977	123.921	135.522	121.653
Objective Function	3423.65	1867.25	3333.64	1806.64	3273.59	1776.45
FVSI value for all lines (p.u)	6.6794	4.1027	6.5773	3.9025	6.5396	3.7716
Size of SVC (p.u)	---	0.2135	---	0.2121	-----	0.1958

Table 7. Comparison of Maximum FVSI value using bat and firefly algorithms

Algorithm	Power System Status	Maximum FVSI value in single line
GA	Without SVC	0.2896
	With SVC	0.1904
BA	Without SVC	0.2863
	With SVC	0.1891
FA	Without SVC	0.2847
	With SVC	0.1883

Figure 4. Comparison of FVSI with and without SVC using bat Algorithm

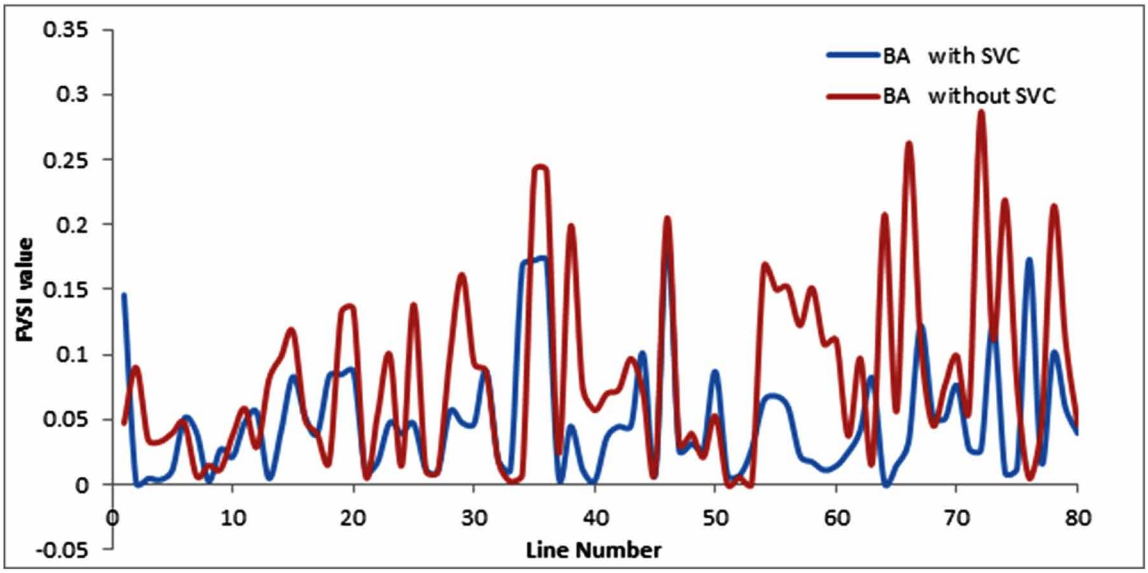

Figure 5. Comparison of FVSI with and without SVC using Firefly Algorithm

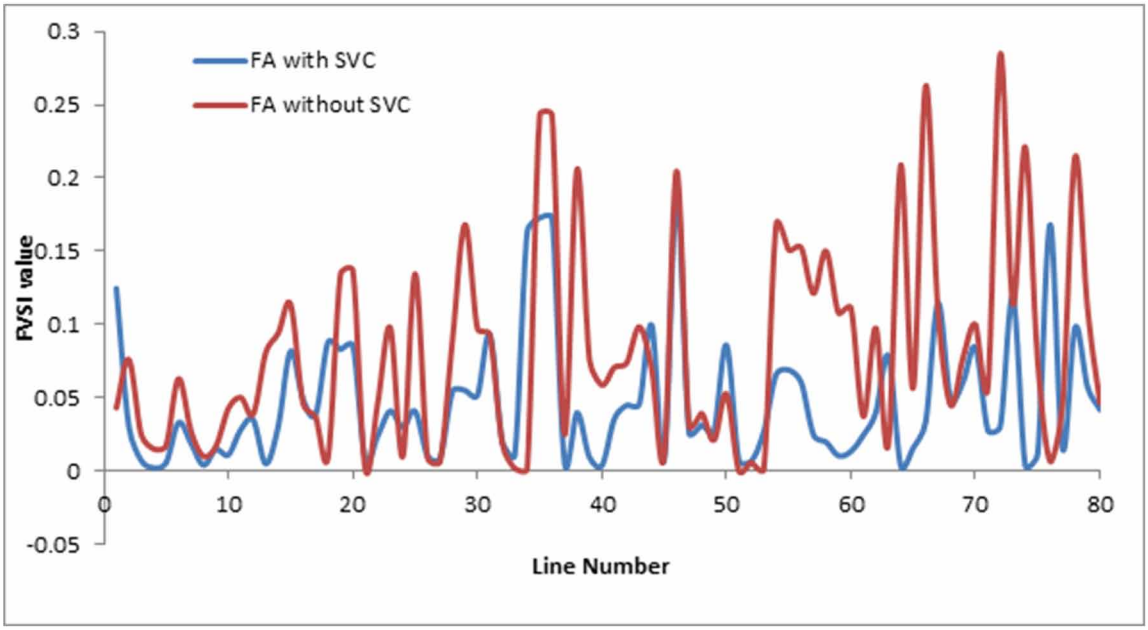

Figure 6. Convergence of the objective function using BA without SVC

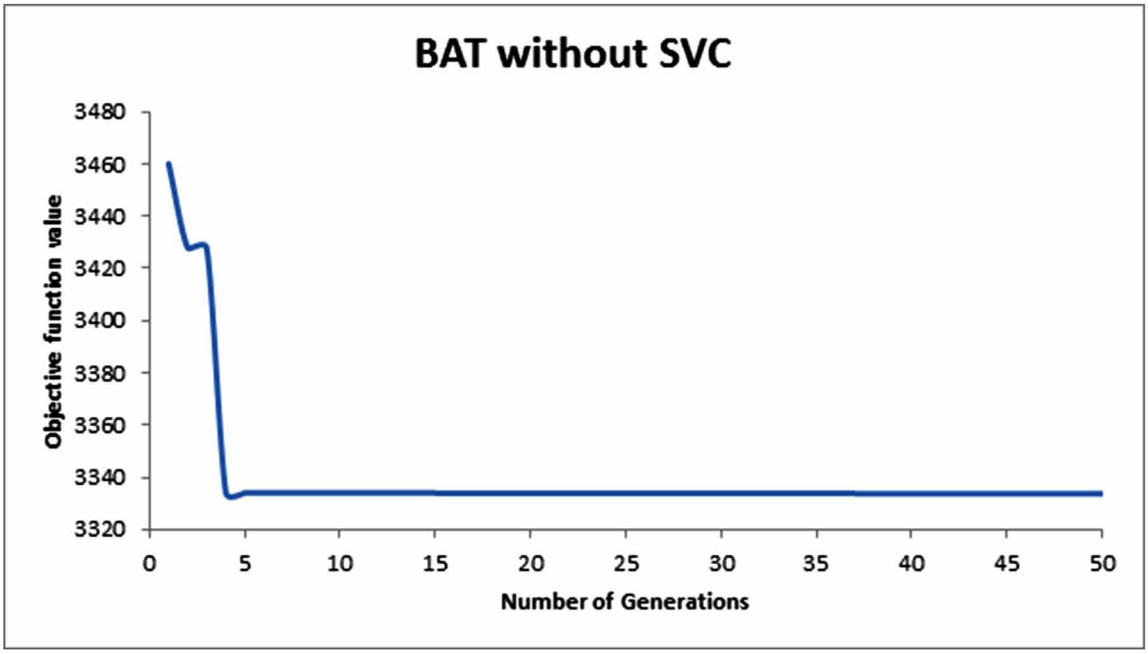

Figure 7. Convergence of the objective function using FA without SVC

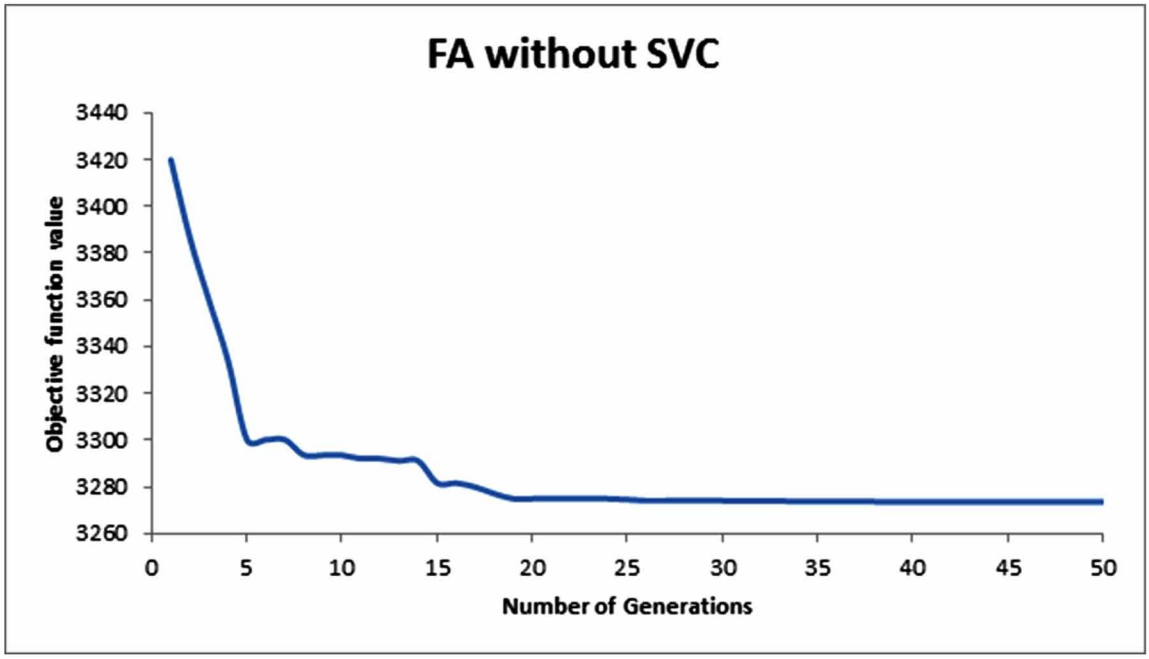

Figure 8. Convergence of the objective function using BA with SVC

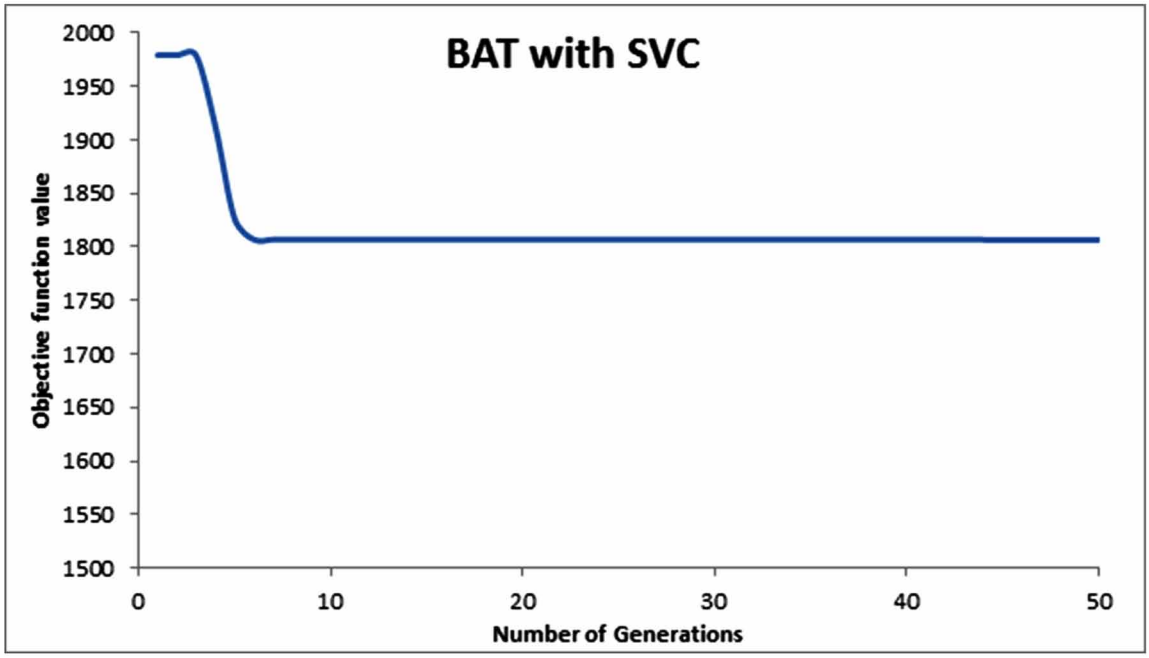

Figure 9. Convergence of the objective function using FA with SVC

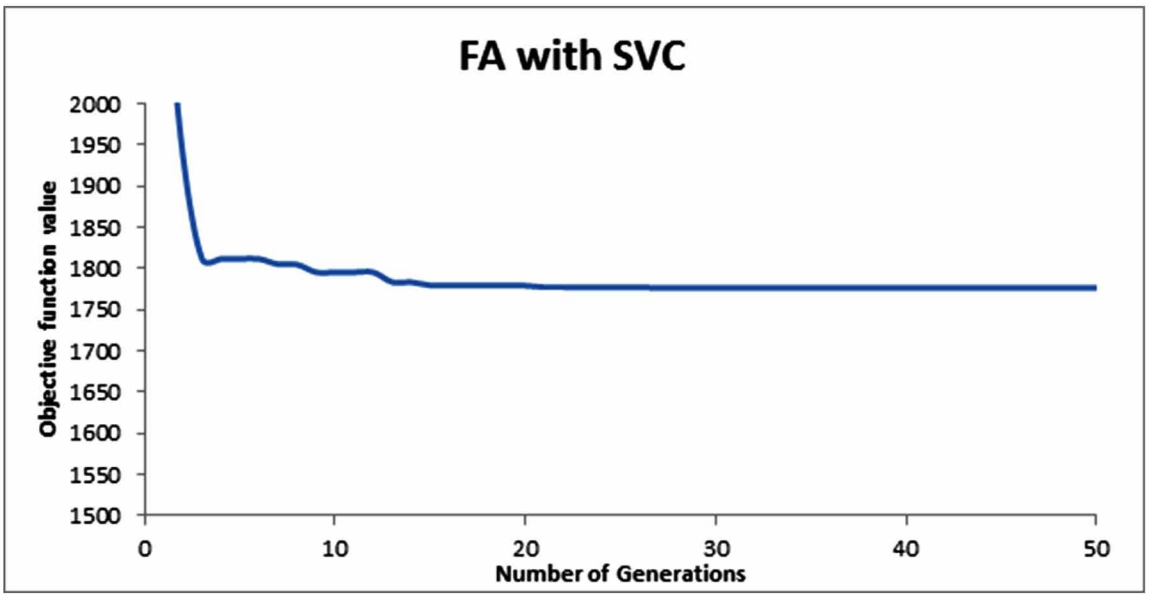

Optimal Load Shedding With TCSC Device Using Bat and Firefly Techniques

The optimal load shedding problem is analyzed with the placement of series FACTS controller TCSC. bat and Firefly algorithm are used in solving the optimal load shedding problem and the under voltage load shedding scheme is employed. The problem is solved for an IEEE 57 bus system and the impact of the TCSC on the system is analyzed. Simulated results are presented in Table 8.

From the results, it can be observed, that optimized load shedding is done with the Firefly algorithm along with the placement of TCSC.

Table 8. Comparison of objective function parameters without and with TCSC using bat and Firefly Algorithms in Load Shedding problem

Parameters of the System	GA Without TCSC	GA With TCSC	BA Without TCSC	BA With TCSC	FA Without TCSC	FA With TCSC
Real Power Losses (MW)	17.4023	15.5915	16.7969	15.1523	16.4094	15.0535
Voltage Deviation (p.u)	5.1236	3.3162	4.9117	3.2745	4.9726	3.2668
Amount of Load Shed (MW)	138.638	126.89	137.97	125.02	135.52	122.00
Objective Function	3423.65	1915.34	3333.64	1895.15	3273.59	1795.05
FVSI for all lines (p.u)	6.6794	4.6841	6.5773	4.3363	6.5396	4.3084
Reactance of TCSC (p.u)	---	0.23	-----	0.2	------	0.18

Optimal Load Shedding With UPFC Device Using Bat and Firefly Techniques

UPFC is a combination of shunt and series controllers and the load shedding problem is analyzed with a UPFC device. Power system problems can be effectively solved by using metaheuristic optimization methods because of their execution flexibility and controlling ability. With the same objective of minimizing the amount of load to be shed, analysis is carried out incorporating the UPFC device and optimal load shedding is done by two different Metaheuristic optimization techniques, bat and Firefly algorithm and it is compared with Genetic algorithm. On simulating the MATLAB program results are obtained for IEEE 57 bus system and are presented in Table 9. From this it is observed that the amount of load to be shed is 118.6538 MW in firefly algorithm incorporating with UPFC which is less as compared to bat and genetic algorithms.

Overall results obtained with the placement of SVC, TCSC and UPFC for optimal load shedding are presented in Table 10. The series cum shunt controller UPFC had a better edge over the other FACTS devices. Optimal load shedding through Firefly algorithm technique excelled over the bat algorithm.

Table 11 indicates the FVSI values. From this it is observed that by incorporating the UPFC in Firefly algorithm maximum FVSI value is 0.2045p.u obtained for line no 46 and without UPFC maximum

Table 9. Objective function parameters without and with UPFC using bat and firefly algorithms in Load Shedding problem

	GA-OPF		**BA-OPF**		**FA-OPF**	
	Before Installing UPFC	**Before Installing UPFC**	**Before Installing UPFC**	**After Installing UPFC**	**Before Installing UPFC**	**After Installing UPFC**
Real Power Losses (MW)	17.4023	13.9468	16.7969	12.8415	16.409	11.565
Voltage Deviation (p.u)	5.1236	2.1845	4.9117	1.9311	4.9726	1.9071
Amount of Load Shed (MW)	138.638	122.829	137.9777	120.9992	135.52	118.65
Objective Function	3423.65	1752.94	3333.64	1716.62	3273.59	1647.93
FVSI for all lines (p.u)	6.6794	4.0926	6.5773	3.8392	6.5396	3.6410

Table 10. Comparison of amount of load to shed with different FACTS controllers using bat and firefly algorithms

	BA-OPF			**FA-OPF**		
	Size of SVC 0.2121p.u	**Size of TCSC 0.2p.u**	**Size of UPFC Vcr =0.1205, Vvr = 1.1393**	**Size of SVC 0.1958p.u**	**Size of TCSC 0.18p.u**	**Size of UPFC Vcr =0.1131, Vvr =1.1392**
Amount of Load Shed (MW)	123.921	125.02	120.999	121.653	122.008	118.653

Table 11. Comparison of Maximum FVSI value using bat and firefly algorithms

	Power System Status	Minimum Bus Voltage (p.u) and Bus No	Maximum FVSI Value and Line Connected Between Bus No (Sending End – Receiving End)
GA	Without UPFC	0.8892 (31)	0.2896 (line no 72) (44-45)
	With UPFC	1 (31)	0.2125 (line no 46) (34-32)
BA	Without UPFC	0.9043 (31)	0.2863 (line no 72) (44-45)
	With UPFC	1 (31)	0.2091 (line no 46) (34-32)
FA	Without UPFC	0.9050 (31)	0.2847 (line no 72) (44-45)
	With UPFC	1 (31)	0.2045 (line no 46) (34-32)

FVSI value is 0.2847p.u obtained for line no 72. So by incorporating the UPFC, FVSI values are reduced which indicates the improvement of the voltage stability.

Figure 10 and Figure 11 indicates the convergence of the objective function using bat and firefly algorithm with UPFC, these figures shows that Firefly algorithmgives best value compared to bat algorithm but bat algorithms takes less number of generations to get the final steady value. Same thing is holds good for the convergence of the objective function using bat and firefly algorithms without UPFC, it can be observed from the Figure 12 and Figure 13, Figure 14 represents the Fast Voltage Stability Index for lines with and without UPFC using bat Algorithm. Figure 15 represents the Fast Voltage Stability Index for lines with and without UPFC using Firefly Algorithm. From these figures it has been observed that by incorporating the UPFC in the system FVSI values at lines are reduced which are near to the zero, indicates that voltage stability has been improved.

Figure 10. Convergence of the objective function using BA with UPFC

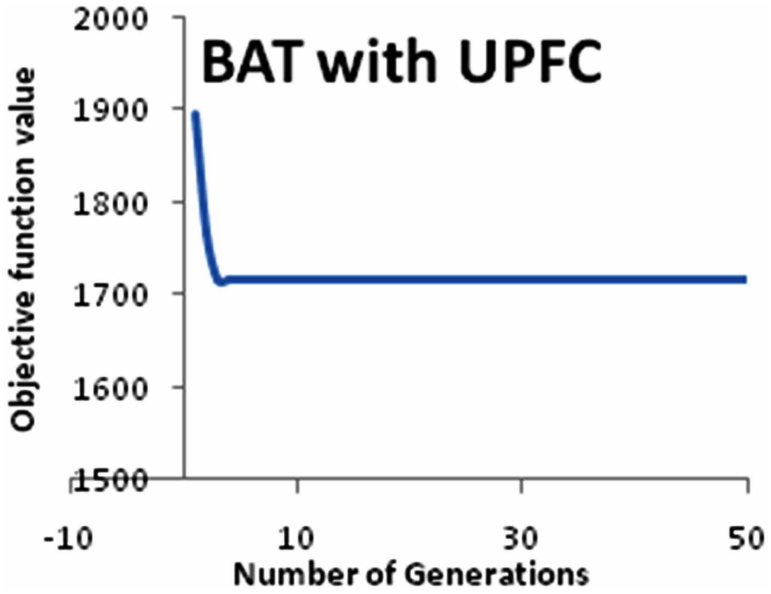

Figure 11. Convergence of the objective function using FA with UPFC

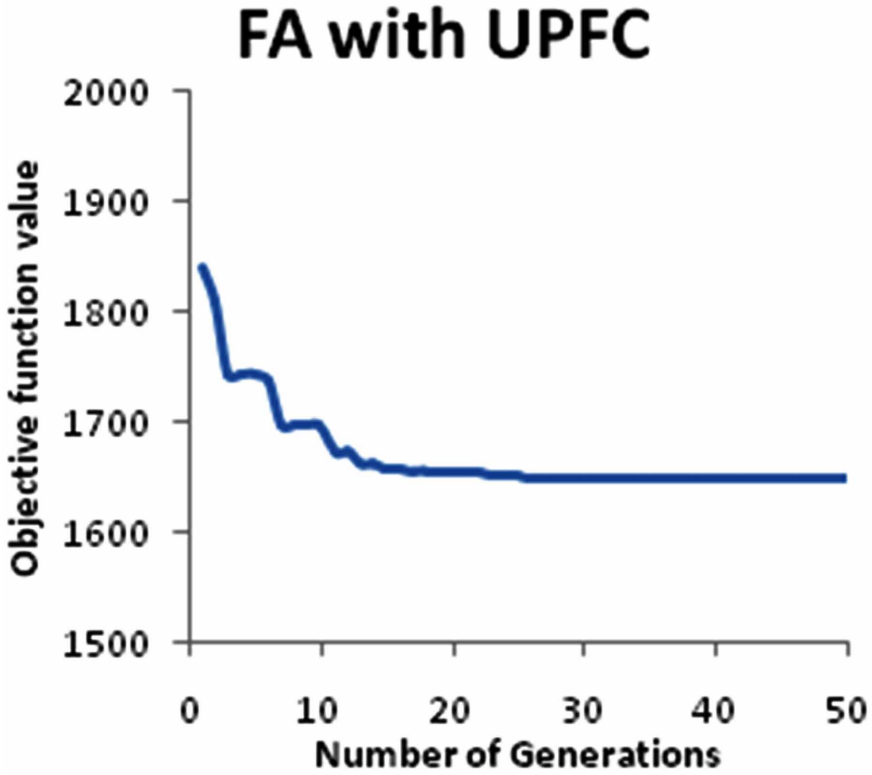

Figure 12. Convergence of the objective function using BA without UPFC

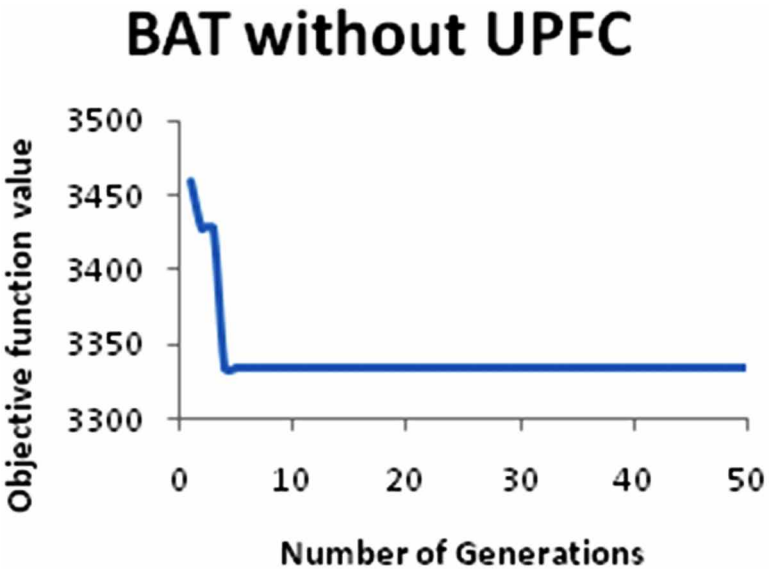

Figure 13. Convergence of the objective function using FA without UPFC

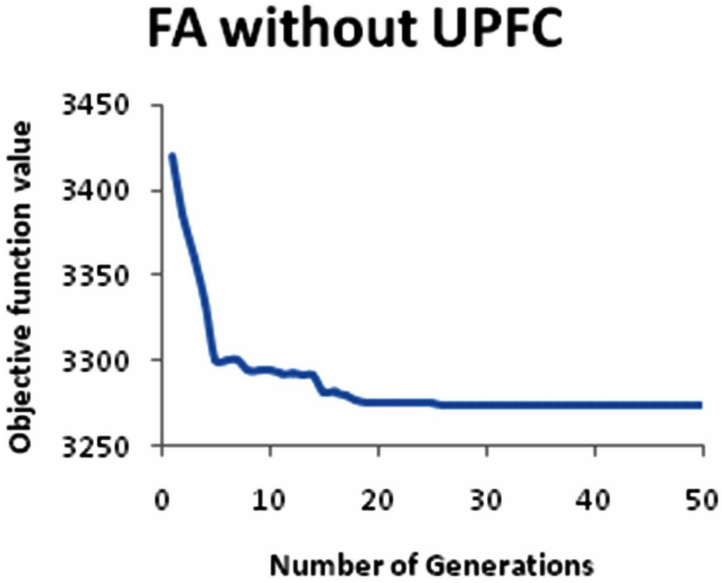

Figure 14. Comparison of FVSI with and without UPFC using bat Algorithm

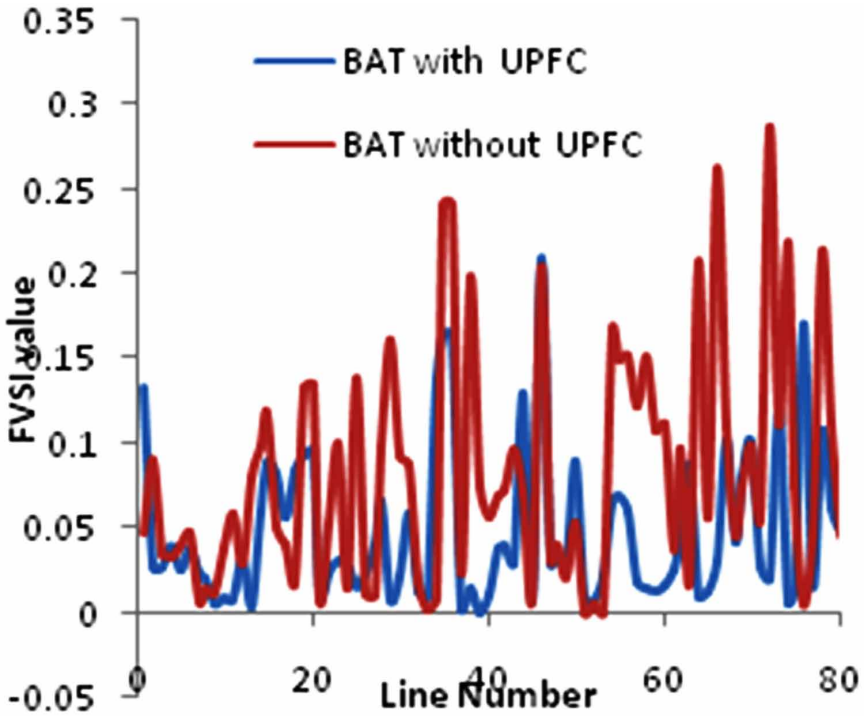

Figure 15. Comparison of FVSI with and without UPFC using Firefly Algorithm

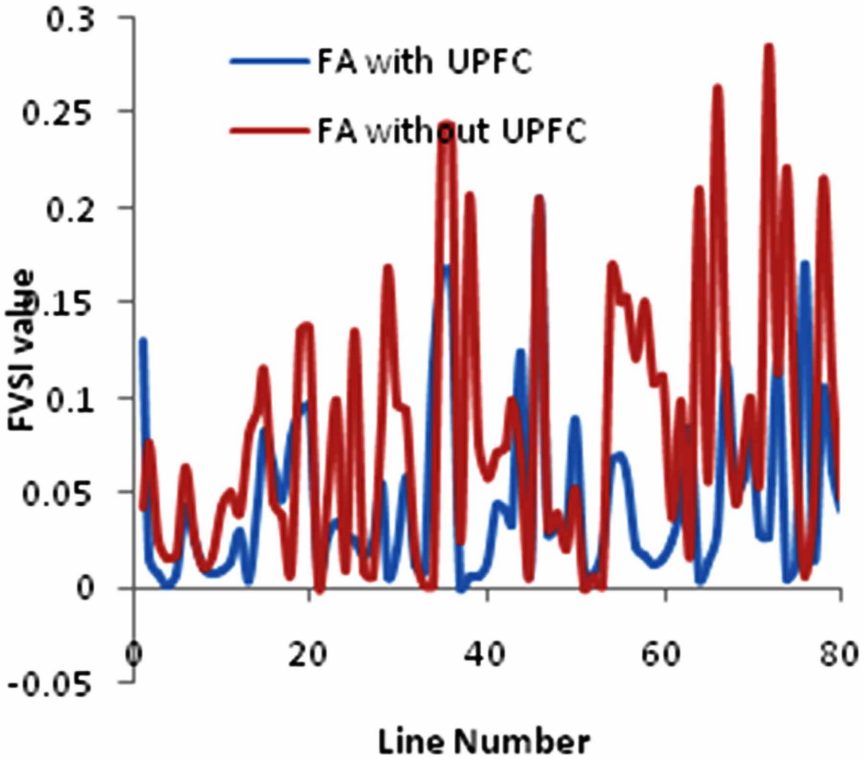

Table 12 and Table 13 indicate the objective function value and time for computation with variation of parameters of Firefly and bat algorithms. From these it has been observed that by taking loudness and pulse rate as 0.5 in bat algorithm gives better results similarly in firefly algorithm $\alpha=\beta=0.5,\gamma==1$ gives better results. Table 14 represents the objective function value, time for computation for different population size using bat and firefly algorithms. From this it is observed that by increasing the population size objective function value improved but time for computation increases so the population size 20 is the best value from the view point of objective function value and time of computation.

FUTURE RESEARCH DIRECTIONS

A combination of these optimization techniques as hybrid optimization techniques can be implemented for future work to get better results. In this chapter power system performance has been enhanced by using single FACTS device that is SVC, TCSC and UPFC individually only it can be implemented with multi type FACTS devices for future work and to achieve better performance. Here optimization planning is done for static environment. For future work this can be a challenging topic for planning for dynamic environment.

Table 12. Comparison of objective function value with variation of different parameters of Firefly algorithm

Firefly Parameters		FA-OPF	
		Without UPFC	With UPFC
α=β=0.5,γ=1	Time for computation (sec)	22.8490	26.859
	Objective function value	3273.5984	1647.9307
α=β=0.4,γ=1	Time for computation (sec)	24.5865	26.22001
	Objective function value	3274.288	1648.2474
α=β=0.3,γ=1	Time for computation (sec)	25.1336	27.03758
	Objective function value	3275.557	1648.9013
α=β=0.2,γ=1	Time for computation (sec)	24.4728	27.20770
	Objective function value	3276.150	1649.4731

Table 13. Comparison of objective function value with variation of different parameters of bat algorithm

Bat Parameters		BA-OPF	
		Without UPFC	With UPFC
Loudness=0.5 Pulse rate=0.5	time for computation (sec)	25.0641	29.59813
	Objective function value	3333.6494	1716.6244
Loudness=0.4 Pulse rate=0.4	Time for computation (sec)	24.7003	31.98822
	Objective function value	3334.405	1716.9387
Loudness=0.3 Pulse rate=0.3	Time for computation (sec)	25.3972	32.36781
	Objective function value	3334.9504	1717.6386
Loudness=0.2 Pulse rate=0.2	Time for computation (sec)	26.0541	34.37184
	Objective function value	3335.123	1718.0408

Table 14. Comparison of objective function value with different population sizes

*P- Size		FA-OPF		BA-OPF	
		Without UPFC	With UPFC	Without UPFC	With UPFC
10	Time for computation (sec)	12.649134	17.362509	13.220731	16.159404
	Objective function value	3275.3937	1649.2125	3334.9235	1717.0186
20	Time for computation (sec)	22.84907	26.32859	25.06411	29.59813
	Objective function value	3273.5984	1647.9307	3333.6494	1716.6244
30	Time for computation (sec)	38.542848	44.499639	40.897537	50.007029
	Objective function value	3273.5691	1647.2289	3333.1784	1715.8954
40	Time for computation (sec)	48.982572	54.908505	49.594485	71.198184
	Objective function value	3273.3010	1647.2073	3332.7003	1715.6118

*P-Size = Population size

CONCLUSION

This chapter presents bat and firefly algorithms for optimal load shedding problem to avoid voltage instability. The bat and Firefly algorithms were applied to solve the optimization problem formulated in the optimal power flow framework with the consideration of various network constraints. It is shown from the simulation results that the methods can effectively improve voltage stability of the power system. The Firefly algorithm processes at a fast speed compared to bat and genetic algorithms. Statistical studies based on multiple independent runs also reveal that Firefly algorithm is a quite robust tool compared to bat and genetic algorithms because of its ability to generate nearly identical results. The load-shedding system has undoubtedly benefited in terms of avoiding voltage instability and minimizing real power losses. This chapter also presents the impact of FACTS controllers like SVC, TCSC and UPFC on load shedding problem. Stability analysis is carried out by computing Fast Voltage Stability Index. The result shows that incorporating the FACTS devices like SVC, TCSC and UPFC in the IEEE 57 bus system reduces the real power loss, improves the voltage profile and enhances the system stability. However, optimal load shedding is attained with Firefly algorithm. Device-wise UPFC showed a better result than SVC and TCSC. Utilizing the FACTS controllers in load shedding problem improved the voltage stability.

REFERENCES

Am briz-Perez, Acha, Fuerte-Esquivel, & De la Torre. (1998). Incorporation of a UPFC model in an Optimal Power Flow Using Newton's method. *IEE Proceedings. Generation, Transmission and Distribution*, *145*(3).

Aparna, R. R. (2016). Swarm Intelligence for Automatic Video Image Contrast Adjustment. *International Journal of Rough Sets and Data Analysis*, *3*(3), 21–37. doi:10.4018/IJRSDA.2016070102

Ara, Kazemi, & NabaviNiaki. (2012). Multi objective Optimal Location of FACTS Shunt-Series Controllers for Power System Operation Planning. *IEEE Transactions on Power Delivery, 27*(2), 481-490.

Carpentier. (1979). Optimal Power Flows. *Electrical Power and Energy Systems, 1*, 959-972.

Dutta, S., Roy, P. K., & Nandi, D. (2016). Optimal Allocation of Static Synchronous Series Compensator Controllers using Chemical Reaction Optimization for Reactive Power Dispatch. *International Journal of Energy Optimization and Engineering*, *5*(3), 43–62. doi:10.4018/IJEOE.2016070103

Gao, Morison, & Kundur. (1992). Voltage Stability Evaluation using Modal Analysis. *IEEE Transactions on Power Systems*, *7*(4), 1529–1542.

Ghahremani, E., & Kamwa, I. (2013, May). Optimal Placement of Multiple-Type FACTS Devices to Maximize Power System Loadability Using a Generic Graphical User Interface. *IEEE Transactions on Power Systems, 28*(2), 764–778. doi:10.1109/TPWRS.2012.2210253

Goel, S., Sharma, A., & Panchal, V. K. (2014). Multiobjective Cuckoo Search for Anticipating the Enemy's Movements in the Battleground. *International Journal of Applied Metaheuristic Computing*, *5*(4), 26–46. doi:10.4018/ijamc.2014100102

Gyugyi, Schauder, Williams, Rictman, Torgerson, & Edris. (1995). The Unified Power Flow Controller; A New Approach to Power Transmission Control. *IEEE Trans on Power Delivery, 10*(2), 1085-1097.

Hingorani, N. G., & Gyugyi, L. (2000). *Understanding FACTS: Concepts and Technology of Flexible AC Transmission System*. IEEE Press.

Kundur, P. (1993). *Power System Stability and Control*. New York: McGraw-Hill, Inc.

Le, D. A., & Vo, D. N. (2016). Cuckoo Search Algorithm for Minimization of Power Loss and Voltage Deviation. *International Journal of Energy Optimization and Engineering*, *5*(1), 23–34. doi:10.4018/IJEOE.2016010102

Mansour, Xu, Alvarado, & Chhewangrinzin. (1994). SVC placement using Critical Modes of voltage stability. *IEEE Transactions on Power Systems*, *9*(2), 757–763.

Mihalie, Zunko, & Povh. (1994). Improvement of Transient using Unified Power Flow Controller. *IEEE Trans*.

Mukherjee, A., Paul, S., & Roy, P. K. (2015). Transient Stability Constrained Optimal Power Flow Using Teaching Learning Based Optimization. *International Journal of Energy Optimization and Engineering*, *4*(1), 18–35. doi:10.4018/ijeoe.2015010102

Padiyar, K. R., & Kulakarni, A. M. (1998). Control design and simulation of unified power flow controller. *IEEE Transactions on Power Delivery*, *13*(4), 1348–1354. doi:10.1109/61.714507

Padiyar, K.R., & Uma Rao, K. (1999). Modeling and Control of Unified Power Flow Controller For Transient Stability. *Electrical Power and Energy Systems, 21*.

Prabhneetkaur & Taranjotkaur. (2014). A Comparative Study of Various Metaheuristic Algorithms. *International Journal of Computer Science and Information Technologies*, *5*(5), 6701–6704.

Rahul Khandelwal, J. (2016). A Novel Multiobjective Optimization for Cement Stabilized Soft Soil based on Artificial Bee Colony. *International Journal of Applied Metaheuristic Computing*, *7*(4), 1–17. doi:10.4018/IJAMC.2016100101

Ramasamy, V. & ZainalAbidin. (2009). A study on FVSI index as an indicator for under voltage load shedding (UVLS). *Proceedings of ICEE 2009 3rd International Conference on Energy and Environment*, 84-88. doi:10.1109/POWERI.2006.1632526

Ratniyomcha, T., & Kulworawanichpong, T. (2009). Evaluation of voltage stability indices by using Monte Carlo simulation. *Proceedings of the 4th IASME / WSEAS International Conference on Energy & Environment (EE'09)*, 297-302.

Singh, J. G., Singh, S. N., & Srivastava, S. C. (2006). Placement of FACTS controllers for enhancing power system loadability. In *Power India Conference*. IEEE.

Tinney, W. F., & Hart, C. E. (1967, November). Power Flow- Solution by Newton's Method. *IEEE Transactions*, *86*, 1449.

Tiwari, P. K., & Sood, Y. R. (2012). Efficient and optimal approach for location and parameter setting of multiple unified power flow controllers for a deregulated power sector. *IET Generation, Transmission & Distribution*, *6*(10), 958–967. doi:10.1049/iet-gtd.2011.0722

VenkateswaraRao, B., & Nagesh Kumar, G. V. (2014). Optimal Location of Thyristor Controlled Series Capacitor for reduction of Transmission Line losses using bat Search Algorithm. *WSEAS Transactions on Power Systems, 9*, 459-470.

Yang, X. S. (2008). *Nature-Inspired Metaheuristic Algorithms*. Luniver Press.

Yang, X.-S. (2009). Firefly algorithms for multimodal optimization. *Stochastic Algorithms: Foundation and Applications SAGA*, *5792*, 169–178. doi:10.1007/978-3-642-04944-6_14

Yang, X. S. (2010). A New Metaheuristic bat Inspired Algorithm. Nature Inspired Cooperative Strategies for Optimization (NISCO 2010), Studies in Computational Intelligence. Springer. doi:10.1007/978-3-642-12538-6_6

Yang, X. S. (2010). *Firefly algorithm, Levy flights and global optimization. In Research and Development in Intelligent Systems XXVI* (pp. 209–218). London, UK: Springer. doi:10.1007/978-1-84882-983-1_15

Yang, X. S. (2011). Bat Algorithm for Multi objective Optimization. *International Journal of Bio-inspired Computation*, *3*(5), 267–274. doi:10.1504/IJBIC.2011.042259

KEY TERMS AND DEFINITIONS

Bat Algorithm: Bat algorithm was developed by X. S. Yang in 2010 and works based on echo location behavior of micro bats.

FA: Firefly algorithm was developed by X. S. Yang in 2008 and works based on flashing behavior of fire fly.

FACTS: Alternating current transmission systems incorporating power electronic-based and other static controllers to enhance controllability and increase power transfer capability.

FACTS Devices or FACTS Controllers: A power electronic-based system and other static equipment that provide control of one or more AC transmission system parameters.

Optimization: It is the action of making the best or most effective use of a situation or resource.

SVC: Static VAR compensator is the most popular shunt connected FACTS controller. The SVC is modeled as a variable susceptance device and its value is tuned in order to achieve a specified voltage magnitude that meets the constraints. The SVC device can either inject reactive power (capacitive) or absorb it (inductive) as per system requirements.

TCSC: The basic Thyristor-controlled series capacitor is a method of "rapid adjustment of network impedance". Apart from controlling line power transfer capability, TCSC also enhances a system's stability. It consists of a series compensating capacitor shunted by thyristor controlled reactor. Thyristor inclusion in the TCSC module enables it to have a smoother control of reactance against system parameter variations.

UPFC: A combination of static synchronous compensator (STATCOM) and a static series compensator (SSSC) which are coupled via a common dc link, to allow bidirectional flow of real power between the series output terminals of the SSSC and the shunt output terminals of the STATCOM, and are controlled to provide concurrent real and reactive series line compensation without an external electric energy source.

Theory of machines covered all topics for engineering students. Beginning with an introduction to Mechanisms and Machines, the authors goes on to cover Graphical and Analytical approaches to Velocity analysis, Mechanisms with Lower pairs, Cams, Gear Trains The book is inclusive of three appendices on Units, Mathematics and S.I. Units. The book is self-explanatory and the authors maintains a fine balance between practice problems and conceptual clarity. The book is also used for the candidates of competitive examinations like Indian Engineering Services(IES) and GATE.

1) Mrs. M.Amareswari Reddy did her B.E (Mechanical), M.E (Machine Design) and pursing Ph.D from Andhra University, Visakapatnam, INDIA.
2) Mrs.M.N.V.Krishna Veni did her B.E(MPIE), M.E (CAD/CAM) and pursing Ph.D from Andhra University, Visakapatnam, INDIA. Both are working as an Asst.Professors in ANITS Engg. College.

978-613-9-45537-9

TOM1

FOR AUTHOR USE

Reddy, Krishna Veni

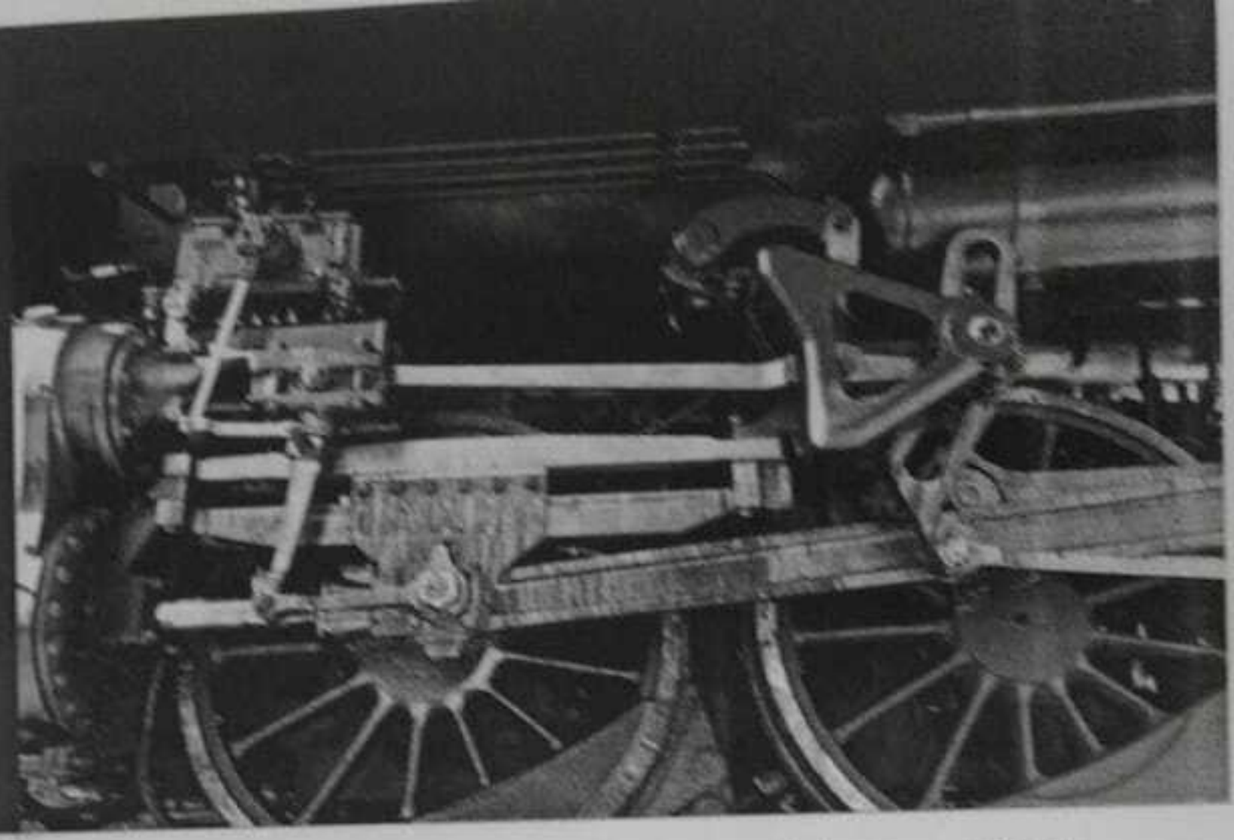

M. Amareswari Reddy
M.N.V Krishna Veni

Theory of machines-I

Kinematics of machinery

LAP LAMBERT Academic Publishing

XXIV HYDRO 2019 International Conference

(Hydraulics, Water Resources, Coastal Engineering)

December, 18-20, 2019

VOLUME - II

Editors

Prof. M. Gopal Naik

Prof. N. Suresh Kumar

Prof. M. Anjaneya Prasad

Prof. P. Raja Sekhar

Dr. K. Shashikanth

Dr. (Mrs). S.V.S.N.D.L. Prasanna

Dr. Harish Gupta

Organized by

Department of Civil Engineering,
University College of Engineering (A), Osmania University
Hyderabad - 500 085.

In Association with

Indian Society for Hydraulics, Pune

Supported by

TEQIP-III &VSSUT, Burla, Odisha

Contents

S.No.	Title	Page No.
	Volume – II	
	THEME-VI **CLIMATE CHANGE AND EXTREME EVENTS**	
1.	Impact of Climate Change on Future Reference Evapo-transpiration (ET) in Central Region of Madhya Pradesh *Ankit Balvanshi and H L Tiwari*	1735
2.	Trend Detection in Temperature using Mann-Kendall Test: A Case Study to Assess Climate Changes in Rajasthan State *Darshan Mehta and S. M. Yadav*	1739
3.	Entropy based Spatio Temporal Patterns of the Daily PrecipitationVariability over Central India *G. Ravi Kumar and R. Maheswaran*	1751
4.	Statistical Downscaling of Daily Mean Rainfall Series for Future Projection – A Case Study of Odisha *Monalisa Sahu, Raj Beer Padhee and Anil Kumar Kar*	1761
5.	Bivariate Drought Frequency Analysis using Copula Method *P. Mishra, R. Padhee and B. Naik*	1777
6.	Seasonal Correlation between Rainfall and Temperature of Patiala City *Sanjoy Gorai, Gurnoor Singh, Dwarikanath Ratha and Amit Dhir*	1786
7.	Spatio-Temporal Variation of Climate *Subhashree Soumya and A. K. Kar*	1794
8.	Spatio-Temporal Analysis of Trend and Non-Stationarity of Rainfall in Hemavathi Basin *B. Y. Chinmayi and H. Ramesh*	1802
9.	Projecting the Change in Rainfall Trends over Maharashtra using Extreme Value Distribution *S. S. Shah, S. N. Londhe and N. S. Gandhre*	1809
10.	Comparative Study on Drought in Marathwada using SPI and SPEI *Vishnu U. Krishnan, A.B Mirajkar and Saranya C. Nair*	1815
11.	Impact of Grid Resolution on the Prediction of Tropical Cyclone FANI using ARW Model *G. Venkata Rao, K. Venkata Reddy and Y. Navatha*	1822
12.	Impact of Climate Change on Manair River Basin *Suram Anil and Anand Raj P*	1829

24th HYDRO 2019, INTERNATIONAL CONFERENCE, OSMANIA UNIVERSITY, HYDERABAD, INDIA
18-20, December 2019

Real Time Flood Forecast for Vamsadhara River Basin through Unsteady Flow Simulation

Arunima Mahapatra[1], Venkatesh Kinthala[2] and Vazeer Mahammood[3]
[1,2&3]Department of Civil Engineering, Andhra University College of Engineering (A), Visakhapatnam, Andhra Pradesh, India.
arunimamohanty@yahoo.co.in, amarvenkatesh.karthik@gmail.com and vazir81c158@gmail.com

Abstract

Successful flood disaster management relies on the ability to predict floods and their corresponding flood inundation areas to minimize loss of life and property. The large catchment area that falls under the Vamsadhara river in Andhra Pradesh and Odisha states with the increased possibility of floods caused majorly due to the frequent cyclones that form along the coast are the major causative factors that necessitate the creation of a flood forecasting model that can be used for flood warning and disaster management. This is done by conducting hydrological and hydraulic studies to estimate peak discharges and flood inundation plains induced by these cyclones for current and future land use conditions. Hydrological modelling is a commonly used tool to estimate the basin's hydrological response due to precipitation. HEC-HMS model is used to simulate rainfall-runoff process by utilising both spatial and non-spatial data such as rainfall, gauge-discharge data, and topographic and hydraulic parameters. It is more realistic to consider unsteady flow when assessing the impact of flood moving down a river. In the present study a real-time flood inundation model for two dimensional unsteady flow conditions was developed using GIS. The extreme flood events that occurred in 2006 and 2013 in this area were used as input data to the model. The methodology involved DEM hydrologic processing using HEC-GeoHMS and HEC-HMS. The output is in the form of flood inundation maps generated using HEC-RAS, from which an efficient flood disaster management can be achieved and also a sustainable watershed management can be planned.

Keywords: Flood inundation modelling, River Vamsadhara, Unsteady flow, HEC-RAS.

1. INTRODUCTION

Water is said to be the source of life on earth. Since the existence of humankind, drought and floods have majorly influenced mankind in a manner so indescribable that on the one hand while drought set man on the search for the elixir of life, establishing civilizations on the boundaries of rivers and tributaries, while the same water in uncontrollable proportions in the form of heavy downpour and the resulting flood wiped off entire civilizations. India with its huge and ever growing population is the second most flood affected country world-wide after Bangladesh. The densely populated areas, along with the often erratic cyclonic activity along the coastal areas which become high risk areas for occurrence of flood and inundation create additional problems for flood management. Predicting the occurrence of and then containing the possible loss to life and property due to floods has always been a major area of concern.

A variety of mitigation measures can be identified and implemented to reduce or minimize the impact of flooding. Such mitigation measures include flood forecasting and warning, adopting proper land-use planning, flood-prone area zoning and management. The process of flood inundation mapping is an essential component of flood risk management because flood inundation maps do not only provide accurate geospatial information about the extent of floods, but also, when coupled with a geographical information system, can help decision makers extract other useful information to assess the risk related to floods such as human loss, financial damages, and environmental degradation. For these reasons, flood maps have been widely used in practice to assess the potential risk of floods.

Precipitation is the only source of runoff and flood in the one or other form but the transformation of the runoff from precipitation is governed by the parameters such as land use, soil type, evaporation, and storage. HEC-HMS [6] deals with the basic water balance equation taking into account major parameters that governs

runoff and is capable of modelling rainfall runoff event. While, HEC-RAS can simulate the runoff hydraulics through the channel based on the channel morphology and can generate the extent of the inundated region. Coupling these two models can assess the inundated region for a known storm event. Further, the calibrated coupled model can be used for future flood plain mapping with the future rainfall data and land use scenarios.

Knebl et al. (2005) [4] developed a flood model for regional scale using NEXRAD rainfall, GIS and hydrological model HEC-HMS/ RAS) for San Antonio River Basin. The results were revealed that the model found to be satisfactory. Villazonet al. (2009) [8] analyzed the flow dynamic process and the quantification of the peak discharge by using HEC-RAS. Flooding in Pirai river responds entirely to flash floods and therefore unsteady flow had to be simulated it was done using derived hydrographs from measured hourly water level as boundary conditions. Durga Rao et al. (2011) [3] developed a real time flood forecasting hydrological model for Godavari Basin using various spatial and non-spatial inputs like DEM, rainfall, topographic, hydrologic parameters, guage- discharge data etc. The modeling approach includes rainfall -runoff modeling, calibration and validation of model with observed historical discharge data. Accuracy was found to be good in estimating the peak flood discharge.

2. STUDY AREA

River Vamsadhara, lying between the Rushikulya river of Odisha and the river Godavari in Andhra Pradesh, is an important east flowing river prone to frequent floods with a total aerial extent of 10830.5sq.km.covering 8,015 sq.km in Odisha and the remaining 2,815 sq.km in Andhra Pradesh respectively. The river originates in the border of Thuamul Rampur in the Kalahandi district and Kalyansinghpur in Rayagada district of Odisha and runs for a distance of 254 Kilometers, while flowing through Rayagada and Gajapati districts of Odisha and into the Srikakulam district of Andhra Pradesh where it joins the Bay of Bengal at Kalingapatnam. It lies between 18°15'N and 19°57'N latitude and 83°25'E and 84°57'E longitude.

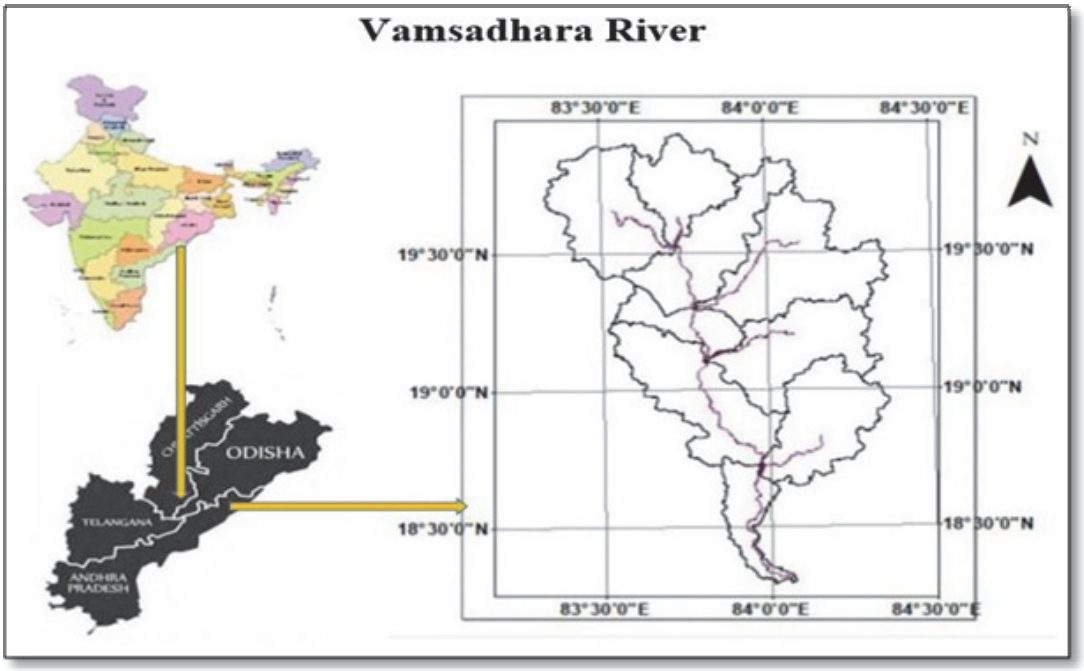

Figure 1 Location Map of the study area of Vamsadhara river basin

3. OBJECTIVES OF THE STUDY

The objectives of the present study are as follows:

- To analyze the DEM of study area using ArcGIS10.2 to attain a set of input files for hydrologic and hydraulic models.
- To derive flood hydrographs using real time data at the selected river gauge stations Gotta barrage and Gunupur.
- To generate the geometry (2D Flow Area) of the river basin using RAS MAPPERS tool in HEC-RAS.
- To conduct the unsteady flow analysis of the river using HEC-RAS.
- To delineate the flood inundation plains for the selected events in the years 2006 and 2013.

4. SOURCES OF DATA AND MATERIALS

Required data for simulation of runoff are daily precipitation data, observed streamflow data, digital elevation model (DEM), LULC data. These data sets were gathered and produced from various sources as shown in Table 1.

Table 1 Collection of Data from various sources

S.No	Data Type	Source
1	SRTM DEM (90m resolution)	Earth Explorer, http://eros.usgs.gov
2	Annual rainfall data grids from the year 2001 to 2013, Land use/Land cover map of study area	NRSC, Hyderabad
3	River gauge data at Gotta barrage	Chief engineer's office, Water Resources department, Visakhapatnam
4	River gauge data at Gunupur	CWC, Bhubaneswar [2]
5	Resourcesat-1, LISS III image of 03-02-13	Bhuvan website

In the present study, HEC-GeoHMS 10.2 in ARCGIS 10.2 is used for Hydrological processing of DEM. To determine the flood hydrographs HEC-HMS 4.2.1[5] is used. To generate the river geometry and flood inundation plains RAS MAPPERS is used and to run the unsteady flow Analysis HEC-RAS 5.0.4 is used as discussed in the following sections.

5. METHODOLOGY

In the present study, the SRTM DEM of 90m resolution is projected using UTM (Universal Transverse Mercator) zone 44, WGS 1984. The DEM is prepared for processing drainage extraction after filling sinks in HEC-GeoHMS [7]. Now this DEM as input, flow direction map is obtained. Further the flow direction map as input, flow accumulation map is obtained which in turn used for extracting drainage network of the area. Catchment grid delineation and drainage line processing are generated. The project setup for the study area is developed by giving the outlet point location as input. Then the slope map is prepared from the DEM which in turn used to generate basin slope. CN Grid is generated from Soil Land use polygon and classified Hydrological soil groups as inputs. Basin characteristics such as river length and river slope are generated from river and DEM. Hydrologic parameters such as River auto name, Basin Auto name and CN lag are generated. After mapping GeoHMS units to HMS units, background shape file and basin model file, meteorological model files are generated to export the file data from GeoHMS to HMS. The methods used in the model are the SCS Unit Hydrograph as the Transform Method, SCS-CN as the Loss Method and Muskingum parameters k and x values

in Flood RoutingMethod. K and x values are obtained by trial and error method, where x=0.2 and K=6 are taken for the model.

Using real time rainfall data, the inflow and outflow discharge in every reach of the river is determined for the selected flood events in the years 2006 and 2013 in HMS. These inflows are given as inputs in HEC-RAS and also with Manning's n value taken as n=0.04 for the basin .Comparison between computed and observed flows are determined at the gauge station Gotta and Gunupur. River geometry such 2D Flow area generated in RAS Mappers.Unsteady flow analysis for the river is generated for the selected flood events using HEC-RAS [1].HEC has added the ability to perform two-dimensional (2D) hydro- dynamic routing within the unsteady flow analysis portion of HEC- RAS 2D flow modeling is accomplished by adding 2D flow area elements into the model in the same manner as adding a storage area. A 2D flow area is added by drawing a 2D flow area polygon; developing the 2D computational mesh; then the 2D flow areas are directly connectedto boundary conditions to the 2D areas. Further the velocity, depth, water surface elevation profiles, obtained are imported in ArcGIS to generate flood inundation mapping.

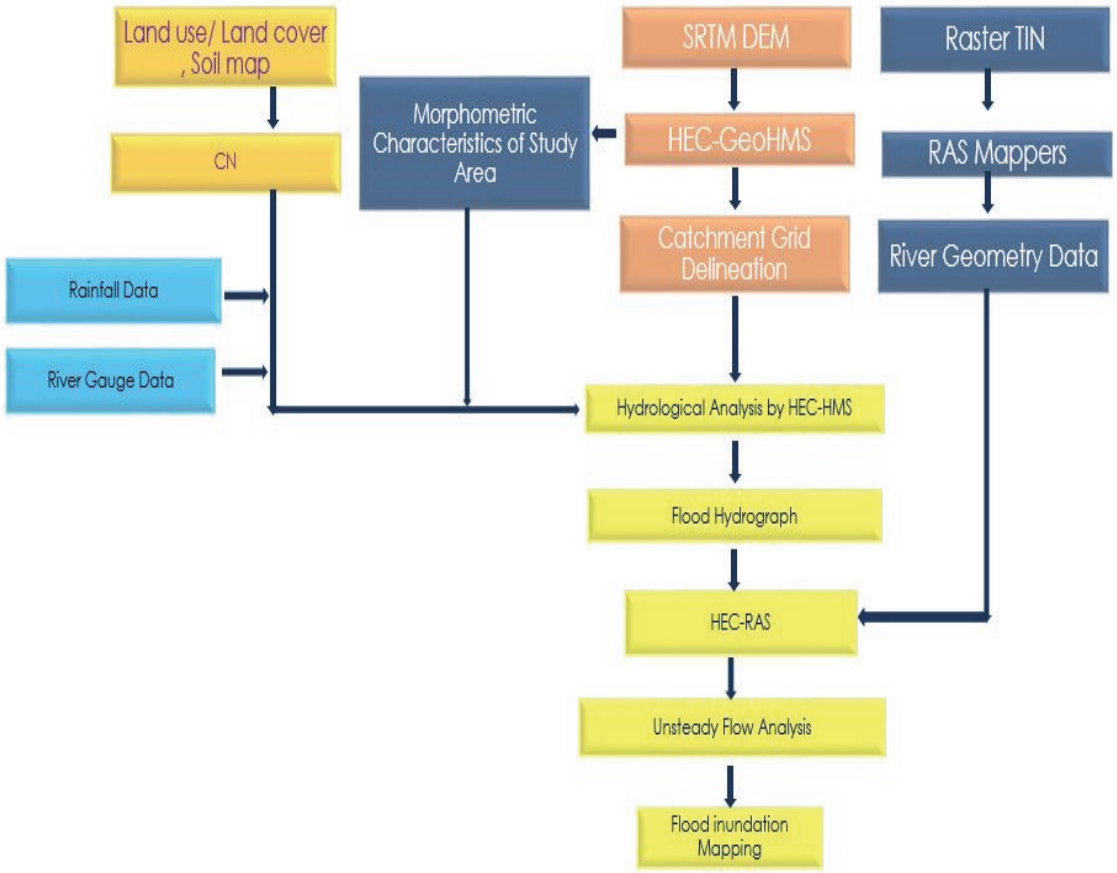

Figure 2 Overall Methodology

5.1 SCS-CN METHOD

The Soil Conservation Service (SCS) model developed by United States Department of Agriculture (USDA) computes direct runoff through an empirical equation that requires the rainfall and a watershed coefficient as inputs. The watershed coefficient is called as the curve number (CN), which represents the runoff potential of the

land cover soil complex. This model involves relationship between land cover, hydrologic soil class and curve number. The method is based on an assumption of proportionality between retention and runoff in the form. Normally the SCS model computes direct runoff with the help of following relationship:

$S = \frac{25400}{CN} - 254$ $Q = \frac{(P-0.2S)^2}{(P+0.8S)}$

Where, Q is Depth of runoff, P is Monthly Rainfall, S is Maximum potential retention and CN is Curve Number.

5.2 SCS-UNIT HYDROGRAPH THEORY

The Soil Conservation Service (SCS) proposed a parametric unit hydrograph (UH) model (SCS 1972). The model is based on averages of UH derived from gauged rainfall and runoff for a large number of watersheds. The model considers the dimensionless SCS hydrograph, topographic, and meteorological parameters in computing the unit hydrograph. The description of the model is as follows:

$Q_{peak} = \frac{(2.8R*A)}{T_{peak}}$, $T_{peak} = \frac{D}{2} + T_{lag}$, $T_{lag} = \frac{L^{0.8}\left(\frac{1000}{CN} - 9\right)^{0.7}}{7344.45\sqrt{S}}$ $L = 890\, A^{0.65}$, $T_c = 1.67 T_{lag}$

where, Q_{peak} is peak discharge, T_{peak} is time to peak, T_{lag} is time lag, S is slope of the watershed, CN is curve number, A is area of the watershed, and L is hydraulic length of the watershed.

5.3 MUSKINGUM FLOOD ROUTING METHOD

The Muskingum method uses the basic hydrologic continuity equation we've used before, and a storage term that depends both on the inflow and outflow: S=K(xI+(1-x)Q) , where x is a weighting factor between 0 and 0.5 that says something about how inflow and outflow vary within a given reach, and K is the travel time of the flood wave. For the case of a linear reservoir like we talked about, S depends only on outflow, so x=0 and S=KQ. In a perfectly smooth channel, x=0.5 and S=0.5 K(I+Q), which results in simple translation of the wave. Typical streams have values of x=0.2 to 0.3.

5.4 EQUATIONS OF 2D-UNSTEADY FLOW MODEL

HEC-RAS will combine continuity and the Diffusion-Wave form of the momentum equation to compute the water surface elevation at a point in time, i.e. WSEL. The unsteady differential form of the Mass Conservation(Continuity) equation is:

$$\frac{\partial H}{\partial t} + \frac{\partial (uh)}{\partial x} + \frac{\partial (vh)}{\partial x} + q = 0 \qquad \text{.....(1)}$$

where t is time, H is a water surface elevation, h is the water depth, q is a source or sink term, and u and v are the velocity components in the X and Y direction.

In vector form,

$$\frac{\partial H}{\partial t} + \nabla hV + \frac{\partial (vh)}{\partial x} + q = 0 \qquad \text{..... (2)}$$

where V= (u, v) is the velocity and (∇) is the vector of the partial derivative given by $\nabla = \left(\frac{\partial}{\partial x}, \frac{\partial}{\partial y}\right)$

The Diffusion Wave form of the Momentum Equation can jest regarded the barotropic pressure gradient and bottom friction.

$-g\nabla H = C_f V$ ..... (3)

where g is gravity acceleration and C_f is the bottom friction. HEC-RAS use Manning's formula, the Diffusion-Wave Equation results:

$$-g\nabla H = \frac{n^2 g|V|}{R^{\left(\frac{4}{3}\right)}} \quad \text{..... (4)}$$

where n is the Manning's Roughness Coefficient and R is Hydraulic Radius. The velocity will have determined by a balance between barotropic pressure gradient and bottom friction.

$$V = -\frac{(RH)^{2/3}}{n}\frac{\nabla H}{(\nabla H)^{1/2}} \quad \text{.....(5)}$$

$$\frac{\partial H}{\partial t} - \nabla\left(\frac{R(H)^{\frac{2}{3}}}{n(\nabla H)^{\frac{1}{2}}}\right)\nabla H + q = 0 \quad \text{.....(6)}$$

Now, the Diffusion Wave can be direct substitution in the Mass Conservation, [2].

6. RESULTS

1. The peak flood discharge obtained at Gotta and Gunupur from flood forecasting model for the flood event of 2006 are 2,064.44 cumecs and 1,883.16 cumecs and the corresponding observed discharges at Gotta and Gunupuris 2,094.90 cumecs and 1907.31 cumecs respectively.
2. The peak flood discharges found at Gotta and Gunupur for Phailin 2013 are 4,169.54 cumecs and 2169.84 cumecs and the corresponding observed discharges at Gotta and Gunupur are 2607.40 cumecs and 1603.20 cumecs.
3. 2D Unsteady flow analysis is done for the flood events of 2006 and 2013. The corresponding maximum water surface elevations are as 22.55m and 21.91m (M.S.L). The max velocity is found to be 5.11m/s and 4.11m/s respectively for 2006 and 2013.
4. The flood inundation maps are generated for the flood events during the cyclones, 2006 and the Phailin 2013.The areal extents of inundation caused by cyclone are 247.91 sq. km. and 246.303sq.km. for 2006 and 2013
5. The villages inundated in Srikakulam district have been identified for the flood events during the cyclones (2006) and the Phailin (2013). Following above results obtained are given in the following tables.

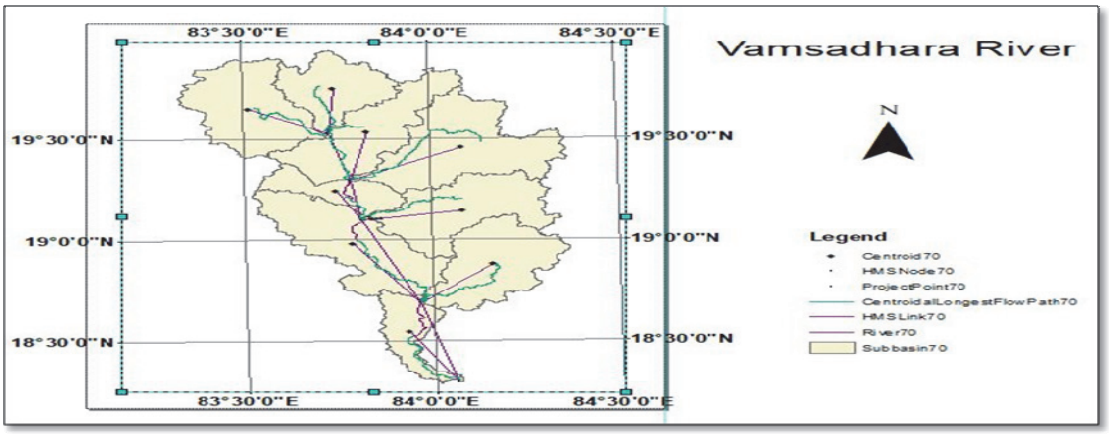

Figure 3 Basin Model

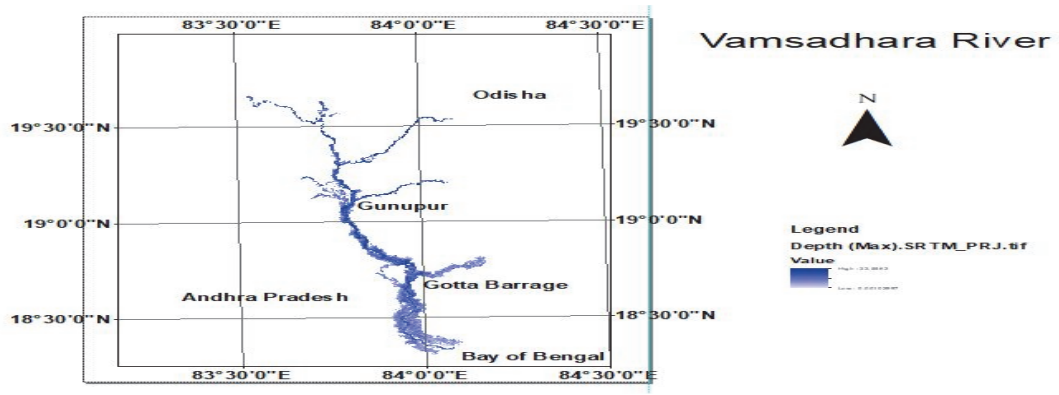

Figure 4 Flood Inundation Map for Depth (Max) generated using Ras-Mappers during cyclone 2006

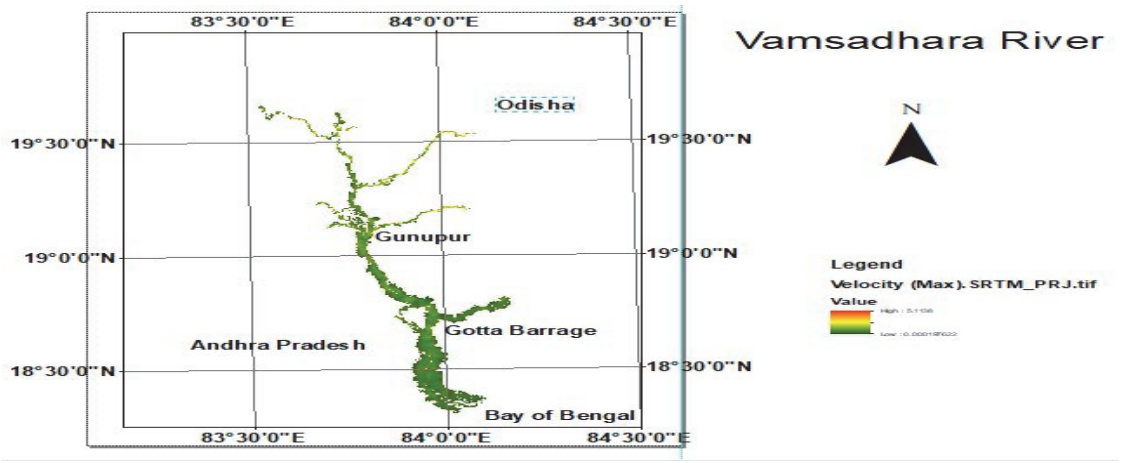

Figure 5 Flood inundation Map for Velocity(Max) using Ras-Mappers during cyclone 2006

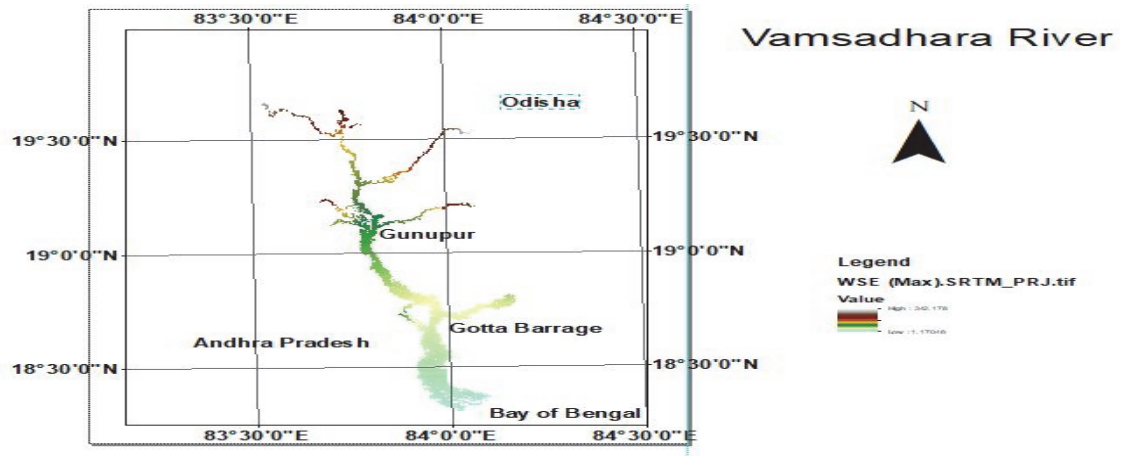

Figure 6 Flood inundation Map for WSE(Max) generated using Ras-Mappers during cyclone 2006

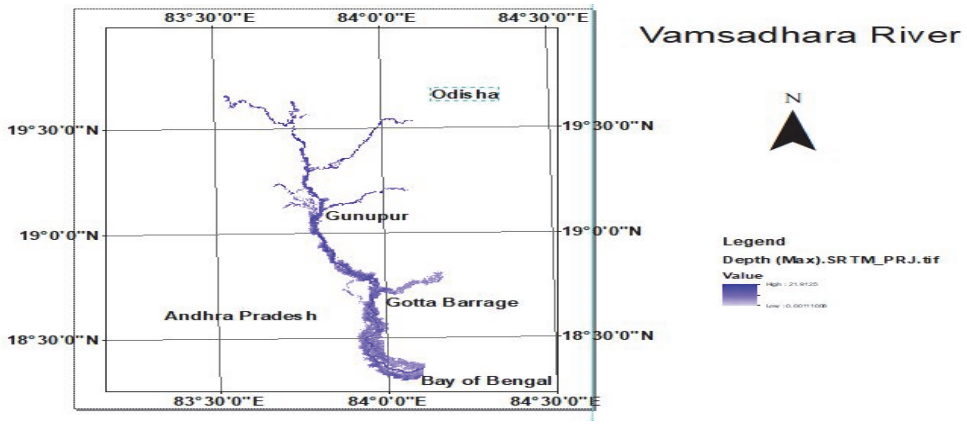

Figure 7 Flood inundation Map for Depth(Max) using Ras-Mappers during cyclone Phailin, 2013

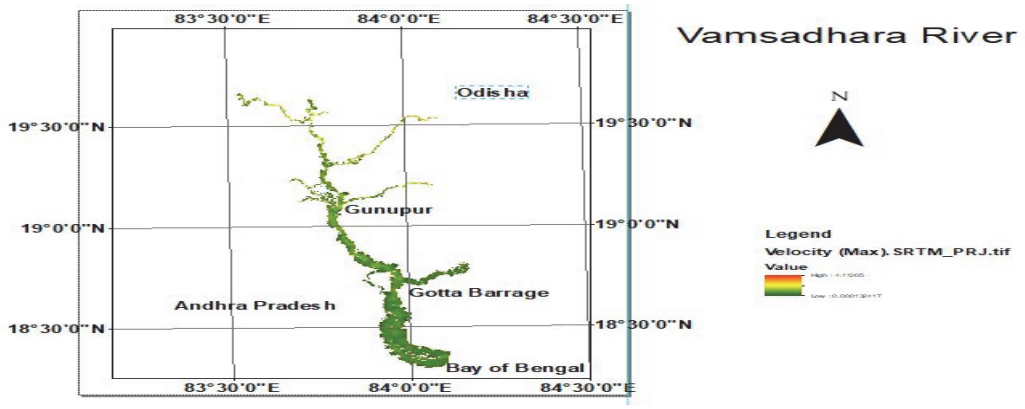

Figure 8 Flood inundation Map for Velocity(Max) generated using Ras-Mappers during cyclone Phailin, 2013.

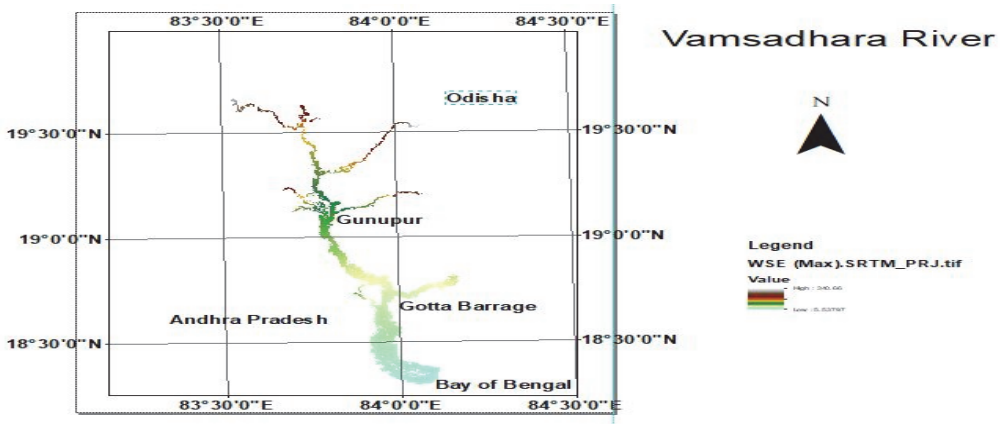

Figure 9 Flood inundation Map for WSE(Max) generated using Ras-Mappers during cyclone Phailin, 2013.

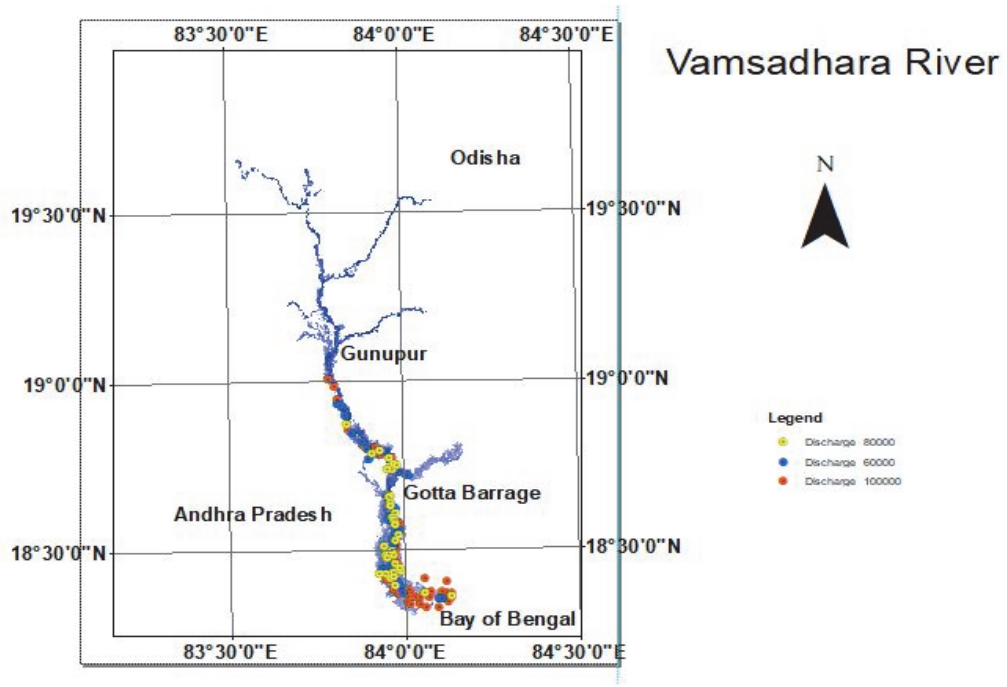

Figure 10 Point map representing villages inundated in Srikakulam district for various discharge levels (According to the district disaster management plan given by the Collectorate, Srikakulam).

Table 1 Villages inundated in Srikakulam district during the cyclone 2006.

Object ID	Village Name	Object ID	Village Name	Object ID	Village Name
1	Singidi	36	Anguru	71	Kuntibadra
2	Liviri	37	Rugada	72	Hamsa
3	Ghanasara	38	Bhagiradhapuram	73	Marrivalasa
4	Sirisivada	39	Mahalaxmipuram	74	Timadam
5	Mathala	40	Pindruvada	75	Syrigam
6	Pasakudu	41	Ambravalli	76	Allada
7	Kosali	42	Peddasavalapuram	77	Muddadapeta
8	Komanapalli	43	Karakavalasa	78	Kabagam
9	Rellivalasa	44	Srimukhalingam	79	Venkatapuram
10	Akkarapalli	45	Mettapeta	80	Ambajipeta
11	Wadavalasa	46	Nagarikatakam	81	Potayyavalasa
12	Dabbapadu	47	Atchutapuram	82	Gopalavalasa
13	Telikipenta	48	Suravaram	83	Makivalasa
14	Yeragam	49	Dompaka	84	Chennapuram
15	Kotrivanipeta	50	Ramakrishnapuram	85	Chodavaram
16	Komanapalli	51	Gollapeta	86	Sivarampuram
17	Lingannaidupeta	52	Andhavaram	87	Devadi
18	Parlam	53	Jogulapeta	88	Paraselli
19	Yathapeta	54	Ramadasupeta	89	Kothapalavalasa
20	Udakalapeta	55	Telagavalasa	90	Mabagam
21	Butchipeta	56	Kameswaripeta	91	Nandigam
22	Madapam	57	Kollavanipeta	92	Rajarampuram
23	Varahanarasimhapuram	58	Lukulam	93	Talasamudram
24	Geddavanipeta	59	Chennulavalasa	94	Urjam
25	Dola	60	Gadannapeta	95	Santhalaxmipuram
26	Pallipeta	61	Narasinganaidupeta	96	Ponnam
27	Anandapuram	62	Ampalam	97	Batteru
28	Ramachandrapuram	63	Ponnampeta	98	Ronanki
29	Chevakulapeta	64	Neradi	99	Karajada
30	Dimmidijola	65	Nulakajodu	100	Bhairi
31	Akulatampara	66	Battili	101	Buravalli
32	VN Puram	67	Solikiri	102	Ambalavalasa
33	Somarajapuram	68	Kaduma	103	Saliahundam
34	Penugottivada	69	Nivagam	104	Gara
35	Ponnuturu	70	Kuddigam	105	Kalingapatnam

Table 2 Villages inundated in Srikakulam district during the cyclone Phailin, 2013.

Object_ID	Village Name	Object_ID	Village Name	Object_ID	Village Name
1	Singidi	40	Bhagiradhapuram	79	Marrivalasa
2	Liviri	41	Mahalaxmipuram	80	Timadam
3	Ghanasara	42	Pindruvada	81	Syrigam
4	Sirisivada	43	Ambravalli	82	Allada
5	Mathala	44	Peddasavalapuram	83	Muddadapeta
6	Vaspa	45	Karakavalasa	84	Kabagam
7	Pasakudu	46	Srimukhalingam	85	Venkatapuram
8	Kosali	47	Mettapeta	86	Ambajipeta
9	Komanapalli	48	Nagarikatakam	87	Potavvavalasa
10	Jilledupeta	49	Atchutapuram	88	Gopalavalasa
11	Rellivalasa	50	Suravaram	89	Makivalasa
12	Akkarapalli	51	Dompaka	90	Chennapuram
13	Wadavalasa	52	Ramakrishnapuram	91	Chodavaram
14	Dabbapadu	53	Gollapeta	92	Sivarampuram
15	Telikipenta	54	Andhavaram	93	Devadi
16	Yeragam	55	Jogulapeta	94	Paraselli
17	Kotrivanipeta	56	Ramadasupeta	95	Kothapalavalasa
18	Komanapalli	57	Telagavalasa	96	Mabagam
19	Lingannaidupeta	58	Kameswaripeta	97	Nandigam
20	Parlam	59	Kollavanipeta	98	Rajarampuram
21	Yathapeta	60	Lukulam	99	Talasamudram
22	Udakalapeta	61	Chennulavalasa	100	Urjam
23	Butchipeta	62	Nagadam	101	Susaram
24	Madapam	63	Urlam	102	Santhalaxmipuram
25	Varahanarasimhapuram	64	Badam	103	Boringivalasa
26	Geddavanipeta	65	Gadannapeta	104	Gollavalasa
27	Dola	66	Narasinganaidupeta	105	Ponnam
28	Pallipeta	67	Ampalam	106	Batteru
29	Anandapuram	68	Edulavalasa	107	Ronanki
30	Ramachandrapuram	69	Ponnampeta	108	Karajada
31	Chevakulapeta	70	Neradi	109	Bhairi
32	Dimmidijola	71	Nulakajodu	110	Buravalli
33	Akulatampara	72	Battili	111	Ambalavalasa
34	VN Puram	73	Solikiri	112	Saliahundam
35	Somarajapuram	74	Kaduma	113	Gara
36	Penugottivada	75	Nivagam	114	Vommaravalli
37	Ponnuturu	76	Kuddigam	115	Kalingapatnam
38	Anguru	77	Kuntibadra		
39	Rugada	78	Hamsa		

7. CONCLUSIONS

The Two Dimensional unsteady flow model developed for the Vamsadhara river basin has given satisfactory results. There is no similar work done so far for this basin and hence comparison of the results obtained with historical data could not be made. Although the real-time flood inundation model was developed for the catchment regions surrounding the two guage stations of Gunpur in Odisha and Gotta barrage in Srikakulam district of Andhra Pradesh state, the calibration and validation of the model was done for the region downstream of Gotta barrage only due to availability of the corresponding data. Once the data for the catchment region surrounding the Gunpur region is available, then the 2D unsteady flow study for that region will be performed as further study. The results also showed that unsteady flow analysis where depth, velocity and water surface elevation maps generated in HEC-RAS are found to be satisfactory. Further these flood inundation maps are imported to GIS for validating with the records of Srikakulam district collectorate and the results found that the output maps are sufficiently accurate Real time flood inundation model developed for the part of the catchment downstream of Gotta barrage has also given satisfactory results. Routing parameters taken for evaluation of the flood model like travel time and runoff coefficient at Gotta and Gunupur guage discharge stations for the year 2006 indicates good performance as the percentage error in simulated peak for 2006 are 1.4 %and 1.2% which are acceptable. While for the year 2013 percentage error in simulated peak are 50% and 30%. This variation is due to travel time taken from all the reaches and mean rainfall in the sub basins.

As the calibrated model performed well in simulating stream flow, this model can be used as a reference model for real-time flood forecasting for watersheds in Vamsadhara river basin as well as other hydro-meteorologically

similar river basins. Work is being done for geo-referencing this model with Google Earth so that flooding can be highlighted on Google Maps.

ACKNOWLEDGEMENT

The authors express sincere thanks for kind assistance rendered in the form of data and related matter by officials and personnel of the India Meteorological Department, Survey of India (Bhubaneswar), Central Water Commission (Bhubaneswar), National Remote Sensing Center (Hyderabad), Srikakulam collectorate office (Disaster Management Plan), Water Resources Dept (Vizag).

REFERENCES

Brunner, Gary W. 2016. "HEC-RAS River Analysis System 2D Modeling User 'S Manual." US Army Corps of Engineers Hydrologic Engineering Center.

Central Water Commission of India, C. (1989). Manual on Flood Forecasting. New Delhi: Central Water Commission.

Korada Hari Venkata Durga Rao, V. V. (2011). A distributed model for real-time flood forecasting in the Godavari basin using space inputs. International Journal of Disaster Risk Science 2(3) , 31-40.

M R Knebl, Z. L. (2005). Regional scale flood modeling using NEXRAD rainfall, GIS and HEC- HMS/RAS: A case study for the San Antonio river basin summer 2002 storm event. Journal of Environmental Management (75), 325-336.

US Army Corps of Engineers, USACE (2000), Hydrological Modeling System HEC-HMS Technical Reference Manual. Hydrologic Engineering Centre, Davis, CA.

US Army Corps of Engineers, USACE (2001), Hydrological Modeling System HEC-HMS User's Manual. Hydrologic Engineering Centre, Davis, CA.

US Army Corps of Engineers, USACE (2003), Geospatial Hydrological Modeling Extension HEC-GeoHMS User's Manual. Hydrologic Engineering Centre, Davis, CA.

Villazon, M F.,Aranibar,C.,Willams,P.2009.Hydrodynamics unsteady flow model applied to river Pirai for flood events estimation in Santa Cruz-Bolivia. Proceedings at :1st International Congress of Hydro-climatology.CD-ROM PP.1-12. Publisher: SENAMHI. 24-28 August Cochabamba, Bolivia.

Medical Image Classification Through Deep Learning

Kaushik Raghupathruni and Madhavi Dabbiru

Abstract The authors investigate the problem of image classification. Earlier, the task of image classification is accomplished by traditional machine learning techniques and other shallower neural network models. Later with the evolution of deeper networks, convolutional neural networks have gained without importance due to its outstanding accuracy in various domains. Unlike in real-world datasets for performing the classification of various images under different categories, the job of biomedical image classification of chest X-rays is quite tedious due to overlapping characteristics of X-ray images. The objective of this paper is to classify the images of chest X-rays and predict the pneumonia traces in lungs. Inception V3 model, with transfer learning is applied on this medical dataset. The model is implemented in Keras as front-end library with tensor flow framework. The training on this dataset to generate a custom model file on GTX 1070 video card consumed 30 min yielding 98% training accuracy and 99% validation accuracy.

Keywords Image classification · Deep learning · Convolution neural networks · Transfer learning

1 Introduction

This Image classification techniques play a vital role in the arena of artificial intelligence as the features of every image is unique. Deep learning is subset of machine learning methods in contrast to task-specific algorithms. Deep learning uses a layered structure of algorithms called an artificial neural network (ANN). Deep learning is

K. Raghupathruni (✉)
Department of CSSE, Andhra University, Visakhapatnam, Andhra Pradesh, India
e-mail: kaushikraghupathruni@gmail.com

M. Dabbiru
Department of CSE, Dr. L. Bullayya College of Engineering for Women, Visakhapatnam, Andhra Pradesh, India
e-mail: drlbcse@gmail.com

H. S. Behera et al. (eds.), *Computational Intelligence in Data Mining*, Advances in Intelligent Systems and Computing 990,
https://doi.org/10.1007/978-981-13-8676-3_23

popular today due to the Convolution neural networks [1]. The crucial parts of a CNN are convolutional layers. They will identify and capture important features in the pixels of the image. Layers that are deep will learn to detect simple features whereas higher layers will combine basic features into more high-level features and showcase classification predictions [2].

The chest X-ray is one of the important tests performed by radiologists whose report is helpful in diagnosing many lung diseases. It is very tiresome process to make clinical diagnoses with chest X-rays than with CT scan images. With computerized diagnosis, radiologists can make chest X-ray diagnoses more quickly and accurately. Thus the problem is a binary classification where the input images are chest X-ray images and the output belongs to either of the two class labels: pneumonia or non-pneumonia. The authors investigate how to train a CNN that can perform binary classification of pneumonia X-rays with high accuracy. The authors used the Chest X-ray dataset [3]. The input data set is then trained and then it is tested and validated in order to find the prediction accuracy results. The paper is organized as follows: Sect. 2 discusses the related work, Sect. 3 narrates the terminology and methodology, Sect. 4 analyzes the experimentation results and Sect. 5 gives the results and then conclusions followed by references.

2 Related Work

The intimate relationship between the layers and spatial information in CNNs renders them well suited for image processing and understanding, and they generally perform well at autonomously extracting salient features from images. Samet Akcay et al. [4], implemented transfer learning on deep convolutional neural network for object classification in X-ray baggage imagery data for identifying hand guns. Aniruddha [5] explored the process of transfer learning on the computer vision problems in plant phenotyping database. Benjamin Antin et al. [6], worked on supervised learning techniques to perform binary classification on pneumonia detection using chest X-rays.

3 Procedure

Functionalities-

1. Data pre-processing: In this we collect the datasets of biomedical images and then we pre-process them for testing.
2. Train the model: The given datasets should be trained properly to test the datasets for validation.
3. Validate the model: Now the tested models should be validated through its prediction result.

InceptionV3

The power of transfer learning by adapting existing image classification architecture (Inception V3) to a custom task: categorizing biomedical images to help doctors, radiologists, and other hospital staff in organizing various biomedical images generated at medical labs is the proposed system.

Transfer learning

Retraining deep learning models for customized image classification [7]. When classifying images, model is built from initial stage for the best fit. Transfer learning may not be as efficient as a model built from blueprint which undergoes full training, but is surprisingly effective for many applications. It allows model creation with significantly reduced training data and time by modifying any of the standard deep learning models. Here Inception V3 is retrained with chest X-ray images (Fig. 1) [8].

The inception V3 architecture is made up of modules called inception modules, as described in Fig. 2, which contain a set of convolutional operations. Convolution layer performs this by using multiple filters where each filter moves around the input

Fig. 1 Architecture of inception v3

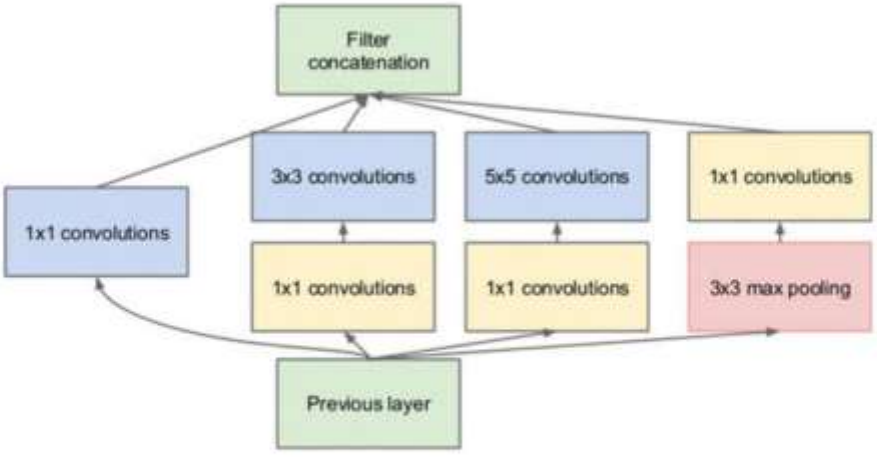

Fig. 2 Inception module

image and prepares activation map. Feature maps are built from the activation maps generated by different filters. Inception module consists of 1×1, 3×3 and 5×5 convolutions along with a 3×3 max pooling. Pooling layers performs subsampling of the input image and contributes to the reduction of input image size. The 1×1 convolution layer reduces the dimensionality of its feature map, by passing the feature map through the Rectified Linear Unit (ReLU). The aim of ReLU layer is to induce non linearity to the given system. ReLUs work with great accuracy and speed. With this dimensionality reduction happens which is less by a factor of 10, saving a lot of computations and time.

In this approach based on inception architecture, the last layer of Inception has been retrained using Softmax Regression where we generate probabilities based on our evidences extracted from the images. The evidences are computed based on a sum of weights detected by the intensity of pixels, with added bias.

The pneumonia identification from chest X-rays is a binary classification problem, where the input is a chest Xray image X and the output is a binary label $z \in \{0,1\}$indicating the absence or presence of pneumonia. We optimize the weighted binary cross entropy loss.

4 Experimentation

The experimentation is carried using i5 4500 rpm processor, 8 GB RAM, Nvidia GTX 1070 video card on windows 10 OS. The Programs are implemented using Tensorflow, Anaconda, Python.

4.1 Training

We used the Chest X ray images (anterior-posterior) selected from the retrospective cohorts of pediatric patients of one to five years old from Guangzhou Women and Children's Medical Center, Guangzhou which contains 5865 X-Ray images (JPEG) of two categories. The first set of X-Rays is contained with pneumonia and the second set containing healthy cases. For the pneumonia detection task we split the dataset into training (5,219), validation (19), test (627). The inputs were scaled to 229*229 size as it is the required size for the Inception V3 model. We augmented the training data with random horizontal flipping.

4.2 Hyper Parameters

The Incpetion V3 model pre-trained on Imagenet dataset is retrained on the dataset with total parameters of 21,802,784, out of which 21,768,352 are trainable parame-

5. Results

We investigate how to train a CNN that can classify medical images with high accuracy. We considered the biomedical database which consists of 2 classes. The dataset is split into training data set and test data set. The input dataset is then trained and is validated in order to find the prediction accuracy results. We implemented this medical image classifier by training inception v3 with a custom biomedical image dataset.

The dataset [4][9] is organized into 3 folders (train, test, val) and contains subfolders for each image category (Pneumonia/Normal). There are 5,863 X-Ray images (JPEG) and 2 categories (Pneumonia/Normal).

Figure 3: Illustrative Examples of Chest X-Rays in Patients with Pneumonia

We have trained our networks with a batch size 32 for 100 epochs. The training time for 100 epochs took around 30 minutes on the specified hardware. The values shown in table 1 can be inferred from figure 4. In Figure 4, the X-axis shows the number of epochs, ranging from 0 to 100. The Y-axis shows the training accuracy ranging from 0.550 to 1.00 when multiplied by 100 gives training accuracy at the epoch. This graph is obtained by tensor board visualization during the training of the model through 100 epochs.

Table 1: Accuracy of image classifier

No. of Epochs	Training Accuracy
30	75%
50	86%
100	99%

Evaluation metrics:

The training accuracy gives us the percentage of images used in the current training batch that were labeled correctly. The validation accuracy is the precision on a randomly selected group of images from a different set during training. The training accuracy is less reflective of the performance of the classifier during because it is based on images that have already been learned from and hence, the network is at risk of over-fitting. A better measure is the validation accuracy. If there is significant mismatch between the training accuracy and validation accuracy, then that is indicative that the network is memorizing potentially unhelpful features that don't generalize well. Inception splits the training data into 3 parts where 80% are used as the training set, 10% are used as validation set, and 10% are used as a testing set during the training. In that way over-fitting is avoided and bottlenecks are fine tuned. Then the validation set has been passed through for tuning and the test set has been sent through for classification. Figures 4 to 8 depict the evaluation metrics of Inception v3 model.

the validation accuracy from 0.820 to 100. When multiplied by 100 gives validation loss at the current epoch. This graph is obtained by tensor board visualization during the training of the model through 100 epochs. Figure 8 depicts line plot for the categorical accuracy for 100 epochs.

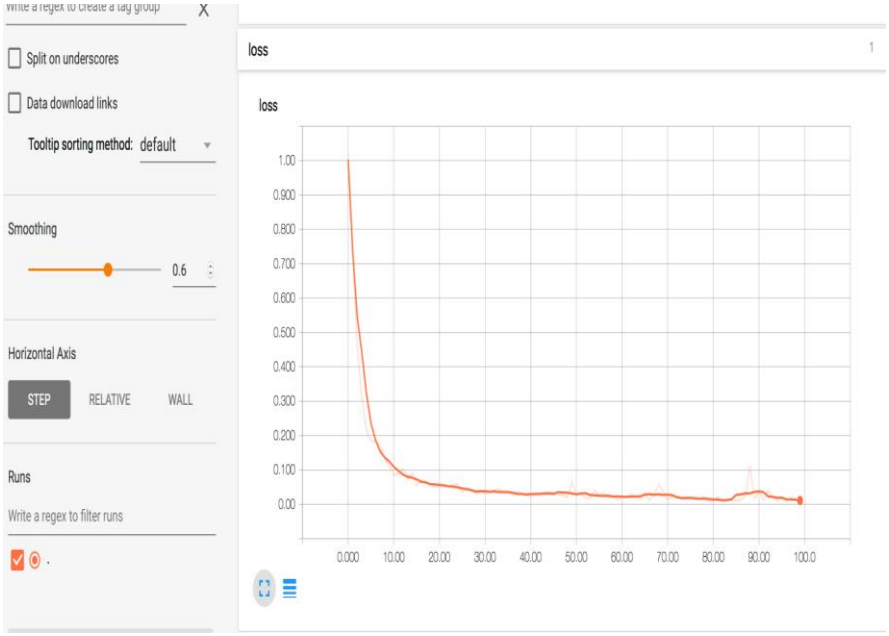

Figure 5: Training validation graph from tensor board visualization.

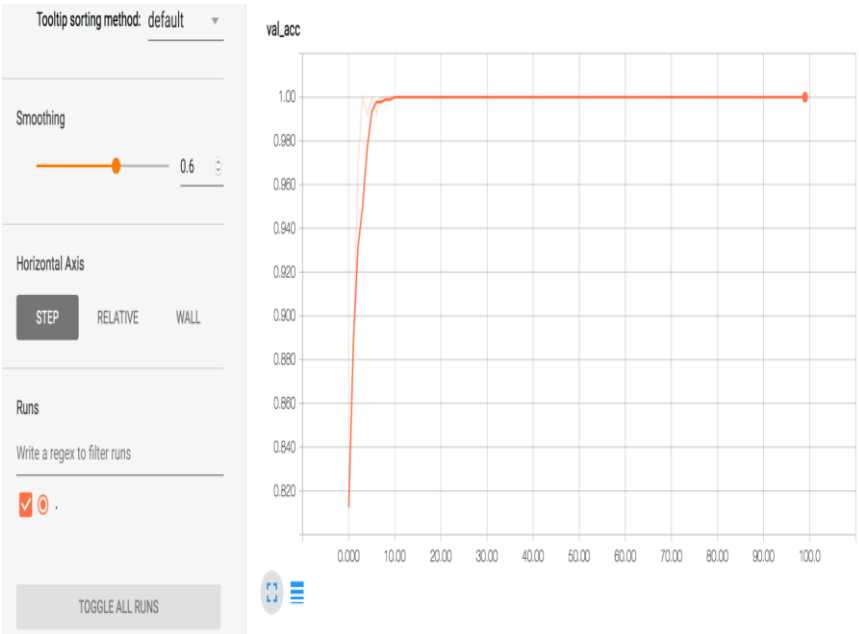

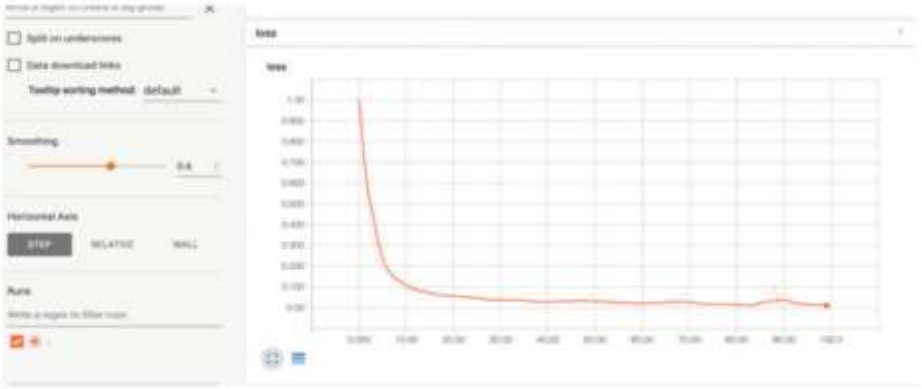

Fig. 5 Training validation graph from tensor board visualization

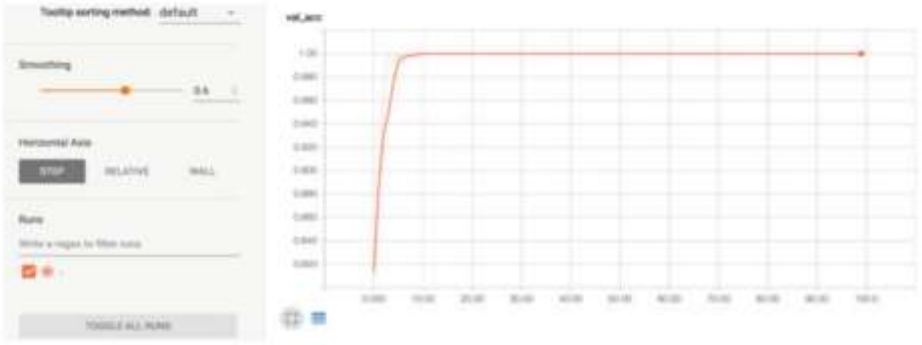

Fig. 6 Validation accuracy graph from tensor board visualization

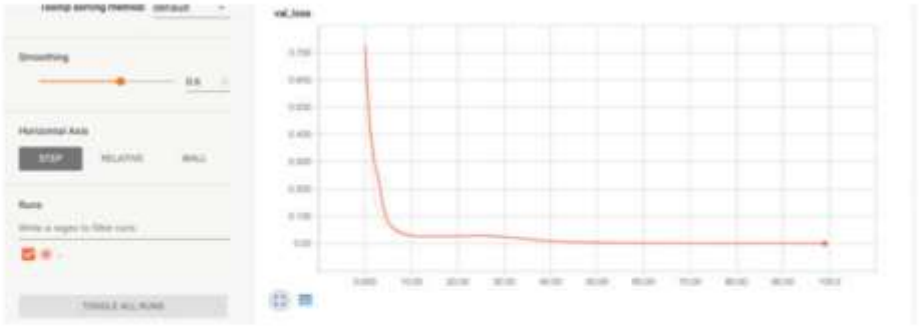

Fig. 7 Validation loss graph from tensor board visualization

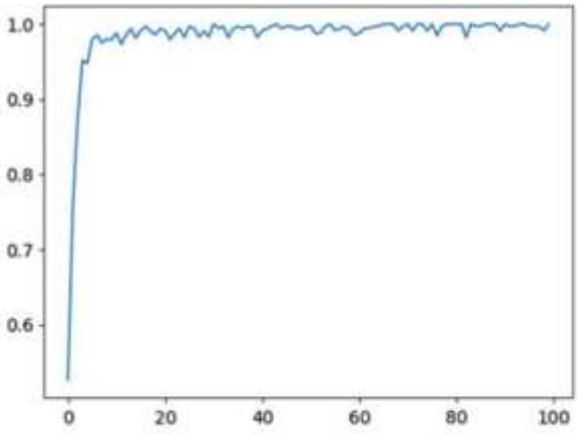

Fig. 8 Line Plot for the categorical accuracy for 100 epochs

Fig. 9 Confusion matrix for prediction accuracy

	Pred.Nor	Pred. Pneu
GT Nor	67.70%	32.20%
GT Pneu	21.40%	78.50%

Confusion Matrix

To evaluate the quality of our image classifier, we make use of a confusion matrix. Prediction accuracy is given in Fig. 9.

Pred.Nor indicates Predictive Normal, Pred. Pneu indicates Predictive Pneumonia, GT Nor indicates Ground Truth Normal image, GT Pneu indicates Ground Truth Pneumonia image. The tabulated values are average of 20 images.

6 Conclusion

In this paper, deep convolution neural network architecture is used to classify chest X-ray images in order to identify pneumonia diseased X-ray images. Inception v3 architecture is trained on the medical images such as chest X-ray using transfer learning for classification into 2 categories of images namely pneumonia disease images and healthy chest images. This model has delivered venerable results of 98% training and 99% validation accuracies. In the arena of clinical applications, Inception v3 model is proved to produce greater accuracy in performing classification provided decent training, sufficient dataset and adequate training time.

Very often it is quite difficult for the radiologists to understand images of tests due to their overlapping behavior and consumes a lot of time in reading them and end up with precise reports. With the advent of deep learning technology, it became easy for the radiologists to analyze the images and automatically generates reports with accuracy within a short span of time.

Acknowledgements The data that supports the findings of this study are available in National Institutes of Health [9]. These data are approved from the following resources available in the public domain at https://www.nih.gov/news-events/news-releases/nih-clinicalcenter-provides-one-largest-publicly-available-chest-x-ray-datasets-scientific-community. A standard ethical committee has approved this data set and the dataset has no conflict of interest/ethical issues with any other public source or domain.

References

1. Szegedy, C., Liu, W., Jia, Y., Sermanet, P., Reed, S.: Anguelov, D., Erhan, D., et.al.: Going deeper with convolutions (2014)
2. He, K., Zhang, X., Ren, S., Sun, J.: Deep residual learning for image recognition (2015)
3. http://www.cell.com/cell/fulltext/S0092–8674(18)30154-5
4. Akcay, S., Kundegorski, M.E, Devereux, M., Breckon, T.P.: Transfer learning using convolutional neural networks for object classification within X-Ray baggage security imagery. IEEE (2016)
5. Tapas, A.: Transfer learning for image classification and plant phenotyping. Int. J. Adv. Res. Comput. Eng. Technol. **5**(11) (2016)
6. Antin, B., Kravitz, J., Martayan, E.: Detecting pneumonia in chest X-Rays with supervised learning, http://cs229.stanford.edu/proj2017/final-reports/5231221.pdf (2017)
7. Nguyen, L.D.: Deep CNNs for microscopic image classification by exploiting transfer learning and feature concatenation. In: IEEE International Symposium on Circuits and Systems (ISCAS) (2018)
8. Szegedy, C., Vanhoucke, V., Ioffe, S., Shlens, J., et.al.: Rethinking the inception architecture for computer vision (2015)
9. Data set https://www.nih.gov/news-events/news-releases/nih-clinical-center-provides-one-largest-publicly-available-chest-x-ray-datasets-scientific-community

Advances in Intelligent Systems and Computing 999

Asit Kumar Das
Janmenjoy Nayak
Bighnaraj Naik
Soumen Kumar Pati
Danilo Pelusi *Editors*

Computational Intelligence in Pattern Recognition

Proceedings of CIPR 2019

Springer

A Q-Learning Approach for Sales Prediction in Heterogeneous Information Networks

Sadhana Kodali, Madhavi Dabbiru and B. Thirumala Rao

Abstract In today's world, recommenders have grabbed a major importance to improve the sales where this paper provides the use of machine learning approach which involves machine learning technique like Q-learning that has an evident prediction on improving the sales. The logical network that can be formed for the mobiles and sales can be treated as a heterogeneous information network and traversing this semantic network gives meaningful meta-paths. The reinforcement learning technique, Q-Learning, is applied to predict the sales of a product.

Keywords Machine learning · Meta-path · Q-learning · Heterogeneous information network

1 Introduction

With the evolution of machine learning and innovative algorithms, the approach to reach customer with a good prediction which can improve the sales is the main motto of many companies. With machine learning, we can identify different patterns which have evolved to identify many pattern recognition techniques. To learn from previous models and to predict reliable and better results from previous steps are the main aims of the learning algorithms. A network of objects which interact with each other logically is called heterogeneous information network [1]. These networks can be traversed from one object to the other forming what are called as meta-paths. The

S. Kodali (✉) · B. T. Rao
Department of CSE, Koneru Lakshmaiah Education Foundation, Guntur Dt, Vaddeswaram 522502, Andhra Pradesh, India
e-mail: sadhanalendicse@gmail.com

B. T. Rao
e-mail: drbtrao@kluniversity.in

M. Dabbiru
Department of CSE, Dr. L. Bullayya College of Engineering for Women, Visakhapatnam, Andhra Pradesh, India
e-mail: drlbcse@gmail.com

A. K. Das et al. (eds.), *Computational Intelligence in Pattern Recognition*, Advances in Intelligent Systems and Computing 999,
https://doi.org/10.1007/978-981-13-9042-5_72

main aim of this work is to traverse various meta-paths and iterate over these paths to predict the method to improve sales using the Q-Learning algorithm [2].

1.1 Heterogeneous Information Networks

Heterogeneous information networks are the object interaction networks. These objects of various types interact based on semantics and use different object relations to form links between the objects. As different objects are involved in the interaction with different links the network is called a heterogeneous information network. An example of heterogeneous information network can be user–actor–movie–director. In the other case, if the same objects are involved with same kind of relationship, it is called a homogeneous information network. The best example can be student–university–student.

A homogeneous information network is a subset of heterogeneous information network. The traversal of different objects with different links can lead to a variety of paths and these are called as meta-paths. User1–(watches)–Movie1–(directed by)–Director1 and so on. Traversing these meta-paths leads to very reasonable and valuable information. On this information, if machine learning strategies are applied they lead to pattern recognition, prediction, classification, and better recommendations also.

2 Related Work

Reinforcement learning (RL) [3] is a machine learning area that helps to decide some agents to take actions that involve better reward. The RL is based upon the environment in which the object acts and the agent which is nothing but the reinforcement learning algorithm. The agents present in RL need to have explicit goals, they should interact with the environment and make decision-making strategies on the environment. An agent upon interaction with the environment can make changes or affect the environment. Examples include making a move in chess, a robot performing an action, hitting the target in a game, etc. The effects of these actions may be unpredicted or unknown.

Reinforcement learning is a nature of learning by observing and interacting with the environment. The reinforcement learning deals with a set of problems that take the feedback from the previous solutions, which mean to say RL deals with closed loop problems. Reinforcement learning helps to learn some control strategies for autonomous agents. Reinforcement learning includes computational approach in order to understand and automate the decision-making. RL assumes to have training information that is available to compute the reward which leads to the next state.

Learning can be mainly categorized as two types [4] as shown in Fig. 1:

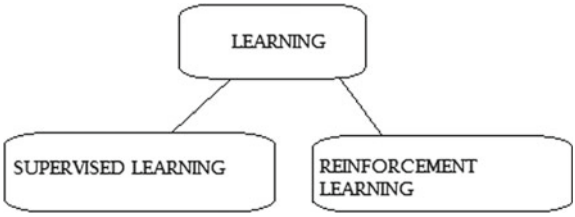

Fig. 1 Types of learning

1. Supervised learning: Learning can be done from the training samples of input.
2. Reinforcement learning: Learning can be done with an action that gives a reward which leads to a new state.

The reinforcement learning can further be classified into model-based and model-free approach. In model-based approach, optimal policy is derived by learning from the model. In model-free approach, optimal policy is derived without learning from the model [5]. Reinforcement learning is based upon behavioral pattern of making decision to decide and the kind of action so that the reward is increased. The agent learns the next states in an on-the-go approach without having a prior knowledge of the states. The important notations that are used in the reinforcement learning are the following [6]:

1. Policy: It is a function to calculate the next action for any given state. An optimal policy is a function which maximizes the optimal reward or reinforcement of a particular state.
2. Exploitation: It is used to learn the best action from the current state.
3. Exploration: All the states must be observed and explored to select an action which should be different from the existing best action.
4. Blame attribution problem: The problem which is used to define the occurrence of reward or punishment for a given action. Because an action may lead to a reward or an action can also cause a punishment. The occurrence of a reward can be delayed after a very long time a particular action has occurred or a set of sequence of actions put together can lead to desirable reward.
5. Identification of delayed rewards: The actions which may not seem to be effective now can later lead to great rewards. Later these actions which were ineffective in the beginning are now termed as good actions. The most important aspect of reinforcement learning is that the future rewards must be traced back to previous actions. The backpropagation of actions is simple if the state space is static but if the environment is dynamic the prediction and backpropagation of actions for good reward is very difficult. The complexity of the problem increases if the environment is dynamic.
6. Explore–Exploit dilemma: If a set of actions were identified as good actions from which better rewards were obtained, then the question is whether to choose from these set of actions or is there any probability to have a better action is called the explore exploitation problem. An agent must always try to explore better actions otherwise its policy cannot be improved.

The reason for exploration is to find an optimal policy that leads to an optimal solution. And if the agent keeps on exploring and does not learn from what it explored is not a good learning approach the reason for this is that the past actions must be learned to find a better reward.

7. Learning rate: This is the rate at which the agent is either forgetful or learns quickly to override the previous information. The learning rate is indicated as α.The value of α is either zero or one. The value of $\alpha = 0$ if the agent does not learn anything new. If $\alpha = 1$ the agent takes only the latest updated information. (8) Discounted reward: This is an approach to assign weight to the reward so that the previous experiences are relevant to the later ones. The discount factor is given as γ which decreases with time. The value of γ lies between zero and one. If $\gamma = 0$ it means the agent is opportunistic as it considers only current rewards. If γ value is closer to 1 it is an indication of the agent considering the long term rewards.
8. Reward signal: The reward signal is used to identify the good and bad events that affect the agent's rewards. The other special case of a reward signal is the value function which indicates the good events in the long run.

Reinforcement learning is goal-directed learning. Reinforcement learning can also be categorized as model based and model free [7]. Methods or approaches of reinforcement learning that include planning are called model-based methods. Methods which are trial and error based are model-free methods. Reinforcement learning is a good approach for finding structures and patterns from an unreliable environment. Also, the methods are further classified as weak methods and strong methods. A weak reinforcement learning method is based upon search and learning, whereas a strong reinforcement learning is based on specific knowledge.

Applying the reinforcement learning on a heterogeneous information network is a very good example for RL. It contributes to the agent environment interaction may be the environment is an author–paper–author network, a social network, etc. The decision-making goal-oriented steps can be studied with the help of reinforcement learning on the heterogeneous network. RL is an approach which combines the dynamic programming and the neural network when applied over a semantic heterogeneous network can lead to many desirable goals like identifying of the best papers in a paper–author–paper network. Identifying the best sales, finding out more relevant friends in a social network, etc.

3 Methodology

3.1 Q-Learning

Q-Learning is a reinforcement technique used in machine learning. An optimal policy is obtained by an agent by learning from the history of the past actions. The history of events is formed between the agent which is in a particular state upon an action

and reward goes to a next state. This can be indicated as a set of state action and reward.

$$st0 \rightarrow a0 \rightarrow rw1 \rightarrow st1 \rightarrow a1 \rightarrow rw2 \rightarrow st2 \rightarrow a2 \rightarrow rw3 \ldots \quad (1)$$

where st_0 represents an initial state upon an action, a_0 results in a reward rw_1 that leads to a new state st_1, and this sequence continues. Each sequence is called as an experience which is indicated as a tuple $\langle sti - ai - rwi + 1 - sti + 1 \rangle$.

The Q-Learning algorithm uses a table of Q[S, A] where S represents the set of states and A represents the set of actions. The recent educated guess of $Q[S, A]$ is represented as $Q^*[S, A]$ which is obtained after calculating a temporal difference which is a metric used in Q-Learning.

3.2 Temporal Difference

Temporal difference: In order to predict the next grade when a set of previous grades are given by taking an average of the previous grades. Let $g1, g2, g3 \ldots gm$ be the set of old grades then the average of these grades is given as the new estimate which can be obtained as $Am = \frac{(g1+g2+g3+g4+\cdots+gm)}{m}$. Am is now the average grade.

$$m^* Am = g1 + g2 + g3 + \cdots + gm = (m-1)(Am-1) + gm \quad (2)$$

Dividing Eq. 2 by m, we get

$$Am = (1 - 1/m)(Am - 1) + gm/m$$

Let $1/m = \alpha$

$$Am = Am - 1 + \alpha(gm - Am - 1) \quad (3)$$

The temporal difference is $gm - Am - 1$. The value of α lies between "0" and "1". An experience is a tuple which contains a state, action, reward, new state and is denoted as experience $\langle st - a - rw - st' \rangle$ provides a data point which is a reward plus an estimated future value $Val(s')$. This new data point generated is called a return. Q-learning uses a method called an off-policy method in which it follows an optimal policy in every action it carries out.

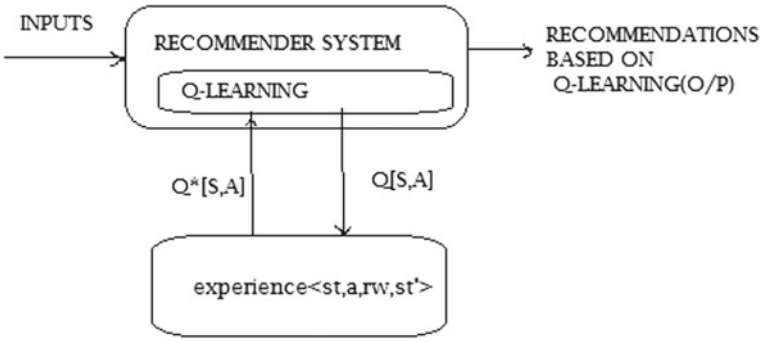

Fig. 2 Workflow in recommendations using Q-learning

Q-Learning algorithm

Input: State St, Action a.
Step 1: Initialize Q[S,A], where S is a set of states and A is a set of actions.
Step 2:for(: :)
{
An initial state st_i upon action a_i gives a reward rw_i which leads to a new state st'_{i+1}
Estimate the temporal difference using $Am = Am - 1 + \alpha(gm - Am - 1)$
$Q[S, A] = Q[S, A] + \alpha\left(rw + \gamma \max Q\left[S', A'\right] - Q[S, A]\right)$
Update $Q[S, A] to Q^*[S, A]$
}

The workflow diagram based on Q-learning for recommenders can be understood from Fig. 2. The inputs are given to the Q-learning-based recommender system and upon the set of model-free learning we get recommendations as required output.

4 Discussion

The Apple iPhone unit sales and revenue data are used to theoretically assess the Q-learning applied on meta-paths. The dataset is available at https://data.world/rflprr/iphone-sales [8]. There are three attributes in these sales data, the first attribute is named as category which gives the quarter number for every year. The first quarter is Q1(October–December), Q2(January–March), Q3(April–June), and Q4(July–September).

The unit sales of iPhone are given in decimal values which are in millions and the third attribute gives year-over-year (yoy) growth. From this dataset, three logical objects quarter-unit of sales-yoy growth form a meta-path and by traversing these meta-paths and applying the Q-learning algorithm, we calculate the new estimated

Table 1 Sample records in the dataset

Category	iPhone	YOY growth
Q2/07	0.141	0
Q3/07	0.489	0
Q4/07	1.036	0
Q1/08	0.817	0
Q2/08	0.483	242.55
Q3/08	4.406	801.02
Q4/08	2.94	183.78
Q1/09	2.427	197.06
Q2/09	3.06	533.54
Q3/09	4.606	4.54
Q4/09	5.578	89.73

points from the existing, from which we can build a best recommender system. The sample dataset values are shown in Table 1.

The first year 2007 is the initial year with initial year-over-year growth equal to zero. The next state that can be reached is Q1 of year 2008. The new estimate from the year 2007 Q4–Q1 in 2008 can be calculated using Eq. 4 with the value of $\alpha = 1/4 = 0.25$

$$A = \frac{(0.141 + 0.489 + 1.036 + 0.817)}{4} = 0.62075 \tag{4}$$

The same can be calculated using previous values given in (2) as follows:

$$A = \frac{(0.141 + 0.489 + 1.036)}{3} + 0.25\frac{0.817 - (0.141 + 0.489 + 1.036)}{3} = 0.62075 \tag{5}$$

The values predicted in Eqs. 4 and 5 give the same result. Equation 5 is computed with the Q-Learning strategy which helps in backtracking to the previous path, i.e., while computing the result of A_4 we can also obtain A_3 which serves as a learning step for A_4.

The yoy growth between Q2 (2007) and Q3 (2008) is 558.47 which is treated as the reward. Figure 3 shows an experience of previous state, action, reward, and the

Fig. 3 Experience $\langle st - a - rw - st' \rangle$ for the year 2007–2008

Fig. 4 Experience $\langle st - a - rw - st' \rangle$ for the year 2008

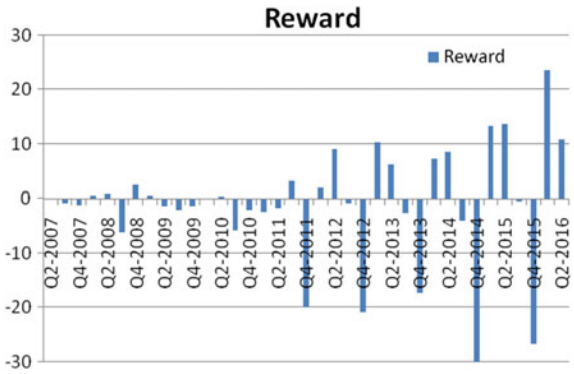

Fig. 5 Graph which depicts the reward for each quarter

next state. From Table 1, the Quarter 2 of year 2007 has made 0.141 million sales and Q3 of 2007 has made 0.489 sales. The reward can be calculated as the difference of 0.141 and 0.489 which is 0.348. With this reward, the old state Q2/7 and an action of sales are moved to Q3/7 and so on. Figure 4 also is a similar example for an experience in the year 2008 that took place between the four quarters.

The sales data reward is calculated and depicted as a graph in Fig. 5.

The other applications of Q-Learning can be in education, medicine, robotics, industrial automation, and finance. In [9], these applications were discussed and a scope for research is also proposed.

5 Conclusion

Machine learning has a wide application in many aspects of our life. This method of machine learning by identifying the various meta-paths in a heterogeneous information network is very useful for effective predictions. The above graph shows the prediction of sales for each year which is calculated as a reward and moving from one year to the other is a traversal of states and each action indicates the sales made in that year. The same methodology can be applied to observe the grades of students, sales of particular items, and so on. One of the main advantages of using Q-Learning which is an off-policy algorithm is that it is an optimal policy and converges to an optimal solution may it be a deterministic or nondeterministic Markov decision process (MDP). The important advantage of choosing reinforcement learning is that it

requires very less time to find a good solution. The basic reason is that for every situation that is encountered a solution is provided of what to do and not how to do.

References

1. Shi, C., Li, Y., Zhang, J., Sun, Y., Yu, P.S.: A survey of heterogeneous information network analysis. J. Latex Class Files **14**(8) (2017)
2. Christopher, J.C.H., Watkins, P. D.: Q-Learning. J. Mach. Learn. **8**(2–4), 279–292. Springer Link
3. Machine Learning for Humans part 5: Reinforcement Learning. https://medium.com/machine-learning-for-humans/
4. Ayodele, T.O.: Types of Machine Learning Algorithms. In: Zhang, Y. (ed.) New Advances in Machine Learning (2010). ISBN: 978-953-307-034-6
5. Quentin, J.M., Huys, A.C., Seriès, P.: Reward based learning, Model based, Model free. Encycl. Comput. Neurosci. (2014). https://doi.org/10.1007/978-1-4614-7320-6_674-1. Springer Science Business Media, New York
6. Volker Sorge: Introduction to AI. http://www.cs.bham.ac.uk/vxs/teaching/ai/slides/lecture12-slides.pdf
7. Sutton, R.S., Barto, A.G.: Reinforcement Learning: An Introduction, 2nd edn. (2014)
8. https://data.world/rflprr/iphone-sales
9. Lorica, B.: Practical Applications of reinforcement learning in industry (2017). Accessed 14 Dec 2017

Premier Reference Source

Critical Developments and Applications of Swarm Intelligence

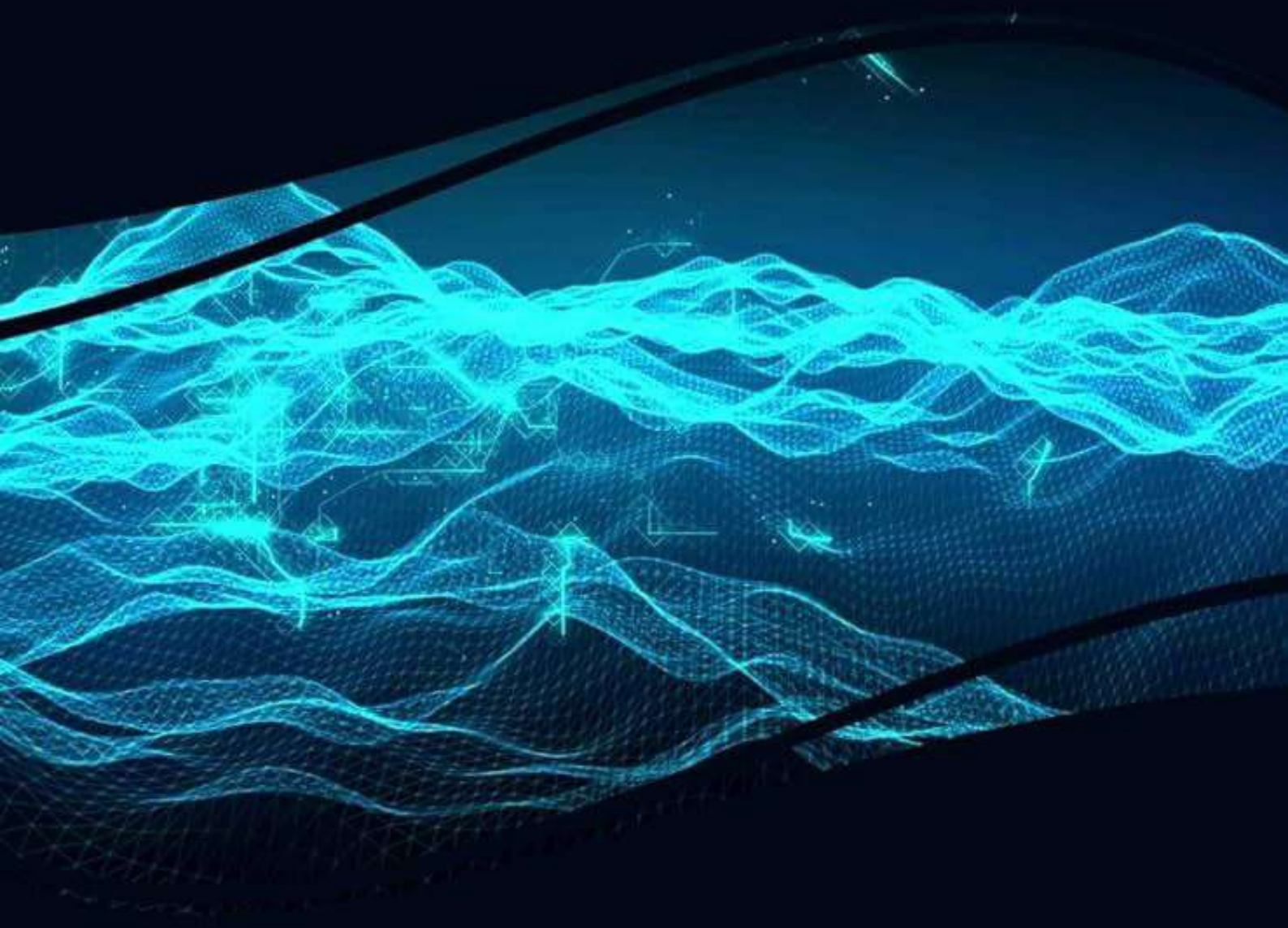

Yuhui Shi

IGI Global
DISSEMINATOR OF KNOWLEDGE

Published in the United States of America by
IGI Global
Engineering Science Reference (an imprint of IGI Global)
701 E. Chocolate Avenue
Hershey PA, USA 17033
Tel: 717-533-8845
Fax: 717-533-8661
E-mail: cust@igi-global.com
Web site: http://www.igi-global.com

Library of Congress Cataloging-in-Publication Data

Names: Shi, Yuhui, editor.
Title: Critical developments and applications of swarm intelligence / Yuhui Shi, editor.
Description: Hershey, PA : Engineering Science Reference, [2018] | Includes bibliographical references.
Identifiers: LCCN 2017035978| ISBN 9781522551348 (h/c) | ISBN 9781522551355 (eISBN)
Subjects: LCSH: Swarm intelligence.
Classification: LCC Q337.3 C75 2018 | DDC 006.3/824--dc23 LC record available at https://lccn.loc.gov/2017035978

This book is published in the IGI Global book series Advances in Computational Intelligence and Robotics (ACIR) (ISSN: 2327-0411; eISSN: 2327-042X)

British Cataloguing in Publication Data
A Cataloguing in Publication record for this book is available from the British Library.

Critical Developments and Applications of Swarm Intelligence

Yuhui Shi
Southern University of Science and Technology, China

A volume in the Advances in Computational Intelligence and Robotics (ACIR) Book Series

Advances in Computational Intelligence and Robotics (ACIR) Book Series

Ivan Giannoccaro
University of Salento, Italy

ISSN:2327-0411
EISSN:2327-042X

Mission

While intelligence is traditionally a term applied to humans and human cognition, technology has progressed in such a way to allow for the development of intelligent systems able to simulate many human traits. With this new era of simulated and artificial intelligence, much research is needed in order to continue to advance the field and also to evaluate the ethical and societal concerns of the existence of artificial life and machine learning.

The **Advances in Computational Intelligence and Robotics (ACIR) Book Series** encourages scholarly discourse on all topics pertaining to evolutionary computing, artificial life, computational intelligence, machine learning, and robotics. ACIR presents the latest research being conducted on diverse topics in intelligence technologies with the goal of advancing knowledge and applications in this rapidly evolving field.

Coverage

- Intelligent control
- Natural Language Processing
- Synthetic Emotions
- Computational Intelligence
- Computational Logic
- Computer Vision
- Adaptive and Complex Systems
- Machine Learning
- Artificial life
- Brain Simulation

The Advances in Computational Intelligence and Robotics (ACIR) Book Series (ISSN 2327-0411) is published by IGI Global, 701 E. Chocolate Avenue, Hershey, PA 17033-1240, USA, www.igi-global.com. This series is composed of titles available for purchase individually; each title is edited to be contextually exclusive from any other title within the series. For pricing and ordering information please visit http://www.igi-global.com/book-series/advances-computational-intelligence-robotics/73674. Postmaster: Send all address changes to above address.

Table of Contents

Preface xvi

Section 1
Swarm Intelligence Algorithms

Chapter 1
Unified Swarm Intelligence Algorithms 1
Yuhui Shi, Southern University of Science and Technology (SUSTech), China

Chapter 2
Local Best Particle Swarm Optimization Using Crown Jewel Defense Strategy 27
Jiarui Zhou, Harbin Institute of Technology, China
Junshan Yang, Shenzhen University, China
Ling Lin, Shenzhen University, China
Zexuan Zhu, Shenzhen University, China
Zhen Ji, Shenzhen University, China

Chapter 3
Multi-Objective Binary Fish School Search 53
Mariana Gomes da Motta Macedo, University of Pernambuco, Brazil
Carmelo J. A. Bastos-Filho, University of Pernambuco, Brazil
Susana M. Vieira, University of Lisboa, Portugal
João M. C. Sousa, University of Lisboa, Portugal

Chapter 4
City Group Optimization: An Optimizer for Continuous Problems 73
Yijun Yang, Southern University of Science and Technology, China

Chapter 5
Magnetotactic Bacteria Optimization Algorithm (MBOA) for Function Optimization: MBOA Based on Four Best-Rand Pairwise Schemes 97
Lili Liu, LiaoCheng University, China
Hongwei Mo, Harbin Engineering University, China

Chapter 6
An Analysis on Fireworks Algorithm Solving Problems With Shifts in the Decision Space and Objective Space 119
Shi Cheng, Shaanxi Normal University, China
Junfeng Chen, Hohai University, China
Quande Qin, Shenzhen University, China
Yuhui Shi, Southern University of Science and Technology, China

Section 2
Swarm Intelligence Applications

Chapter 7
Assessment of Gamma-Ray-Spectra Analysis Method Utilizing the Fireworks Algorithm for Various Error Measures 155
Miltiadis Alamaniotis, Purdue University, USA
Lefteri Tsoukalas, Purdue University, USA

Chapter 8
A Computational Comparison of Swarm Optimization Techniques for Optimal Load Shedding Under the Presence of FACTS Devices to Avoid Voltage Instability 182
G. V. Nagesh Kumar, Vignan's Institute of Information Technology (Autonomous), India
B. Venkateswara Rao, V. R. Siddhartha Engineering College (Autonomous), India
D. Deepak Chowdary, Dr. L. Bullayya College of Engineering (for Women), India
Polamraju V. S. Sobhan, Vignan's Foundation for Science, India

Chapter 9
Using Particle Swarm Optimization Algorithm as an Optimization Tool Within Developed Neural Networks 215
Goran Klepac, Raiffeisenbank Austria, Croatia

Chapter 10
Squeeze Casting Parameter Optimization Using Swarm Intelligence and Evolutionary Algorithms 245
Manjunath Patel G. C., Sahyadri College of Engineering and Management, India
Prasad Krishna, National Institute of Technology Karnataka, India
Mahesh B. Parappagoudar, Padre Conceicao College of Engineering, India
Pandu Ranga Vundavilli, Indian Institute of Technology Bhubaneswar, India
S. N. Bharath Bhushan, Sahyadri College of Engineering and Management, India

Chapter 11
Swarm-Intelligence-Based Communication Protocols for Wireless Sensor Networks 271
Lucia Keleadile Ketshabetswe, Botswana International University of Science and Technology, Botswana
Adamu Murtala Zungeru, Botswana International University of Science and Technology, Botswana
Joseph M. Chuma, Botswana International University of Science and Technology, Botswana
Mmoloki Mangwala, Botswana International University of Science and Technology, Botswana

Chapter 12
Image Reconstruction of Electrical Impedance Tomography Using Fish School Search and Differential Evolution 301
Valter Augusto de Freitas Barbosa, Universidade Federal de Pernambuco, Brazil
Wellington Pinheiro dos Santos, Universidade Federal de Pernambuco, Brazil
Ricardo Emmanuel de Souza, Universidade Federal de Pernambuco, Brazil
Reiga Ramalho Ribeiro, Universidade Federal de Pernambuco, Brazil
Allan Rivalles Souza Feitosa, Universidade Federal de Pernambuco, Brazil
Victor Luiz Bezerra Araújo da Silva, Escola Politécnica da Universidade de Pernambuco, Brazil
David Edson Ribeiro, Universidade Federal de Pernambuco, Brazil
Rafaela Covello Freitas, Escola Politécnica da Universidade de Pernambuco, Brazil
Manoela Paschoal, Universidade Federal de Pernambuco, Brazil
Natália Souza Soares, Universidade Federal de Pernambuco, Brazil
Rodrigo Beltrão Valença, Universidade Federal de Pernambuco, Brazil
Rodrigo Luiz Tomio Ogava, Universidade Federal de Pernambuco, Brazil
Ítalo José do Nascimento Silva Araújo Dias, Universidade Federal de Pernambuco, Brazil

Chapter 13
Multi-Thresholding of Histopathological Images Using Fuzzy Entropy and Parameterless Cuckoo Search 339
Krishna Gopal Gopal Dhal, Midnapore College (Autonomous), India
Mandira Sen, Tata Consultancy Services, India
Sanjoy Das, University of Kalyani, India

Chapter 14
Optimized Base Station Sleeping and Smart Grid Energy Procurement Scheme to Improve Energy Efficiency 357
Qiang Wang, Yulin Normal University, China
Hai-Lin Liu, Guangdong University of Technology, China

Chapter 15
Using Cuckoo Search Algorithm for Hybrid Flow Shop Scheduling Problems Under Makespan Criterion 379
M. K. Marichelvam, Mepco Schlenk Engineering College, India
Ömür Tosun, Akdeniz University, Turkey

Chapter 16
Particle Swarm Optimization for Model Predictive Control in Reinforcement Learning Environments 401
Daniel Hein, Technische Universität München, Germany
Alexander Hentschel, AxiomZen, Canada
Thomas A. Runkler, Siemens AG, Germany
Steffen Udluft, Siemens AG, Germany

Compilation of References 428

About the Contributors 467

Index 476

Detailed Table of Contents

Preface xvi

Section 1
Swarm Intelligence Algorithms

Chapter 1
Unified Swarm Intelligence Algorithms 1
Yuhui Shi, Southern University of Science and Technology (SUSTech), China

In this chapter, the necessity of having developmental learning embedded in a swarm intelligence algorithm is confirmed by briefly considering brain evolution, brain development, brainstorming process, etc. Several swarm intelligence algorithms are looked at from a developmental learning perspective. A framework of a developmental swarm intelligence algorithm, which contains capacity developing stage and capability learning stage, is further given to help understand developmental swarm intelligence (DSI) algorithms, and to guide to design and/or implement any new developmental swarm intelligence algorithm and/or any developmental evolutionary algorithm. Following DSI, innovation is discussed and an innovation-inspired optimization (IO) algorithm is designed and developed. Finally, by combing the DSI and IO algorithm together, a unified swarm intelligence algorithm is proposed, which contains capacity developing stage and capability learning stage and with three search operators in its capability learning stage to mimic the three levels of innovations.

Chapter 2
Local Best Particle Swarm Optimization Using Crown Jewel Defense Strategy 27
Jiarui Zhou, Harbin Institute of Technology, China
Junshan Yang, Shenzhen University, China
Ling Lin, Shenzhen University, China
Zexuan Zhu, Shenzhen University, China
Zhen Ji, Shenzhen University, China

Particle swarm optimization (PSO) is a swarm intelligence algorithm well known for its simplicity and high efficiency on various problems. Conventional PSO suffers from premature convergence due to the rapid convergence speed and lack of population diversity. It is easy to get trapped in local optima. For this reason, improvements are made to detect stagnation during the optimization and reactivate the swarm to search towards the global optimum. This chapter imposes the reflecting bound-handling scheme and von Neumann topology on PSO to increase the population diversity. A novel crown jewel defense (CJD) strategy is introduced to restart the swarm when it is trapped in a local optimum region. The resultant

algorithm named LCJDPSO-rfl is tested on a group of unimodal and multimodal benchmark functions with rotation and shifting. Experimental results suggest that the LCJDPSO-rfl outperforms state-of-the-art PSO variants on most of the functions.

Chapter 3
Multi-Objective Binary Fish School Search 53
Mariana Gomes da Motta Macedo, University of Pernambuco, Brazil
Carmelo J. A. Bastos-Filho, University of Pernambuco, Brazil
Susana M. Vieira, University of Lisboa, Portugal
João M. C. Sousa, University of Lisboa, Portugal

Fish school search (FSS) algorithm has inspired several adaptations for multi-objective problems or binary optimization. However, there is no particular proposition to solve both problems simultaneously. The proposed multi-objective approach binary fish school search (MOBFSS) aims to solve optimization problems with two or three conflicting objective functions with binary decision input variables. MOBFSS is based on the dominance concept used in the multi-objective fish school search (MOFSS) and the threshold technique deployed in the binary fish school search (BFSS). Additionally, the authors evaluate the proposal for feature selection for classification in well-known datasets. Moreover, the authors compare the performance of the proposal with a state-of-art algorithm called BMOPSO-CDR. MOBFSS presents better results than BMOPSO-CDR, especially for datasets with higher complexity.

Chapter 4
City Group Optimization: An Optimizer for Continuous Problems 73
Yijun Yang, Southern University of Science and Technology, China

City group refers to a collection of cities. Through the development and growth, these cities form a chain of metropolitan areas. In a city group, cities are divided into central cities and subordinate cities. Generally, central cities have greater chances to develop. However, subordinate cities may not have great chances to develop unless they are adjacent to central cities. Thus, a city is more likely to develop well if it is near a central city. In the process, the spatial distribution of cities changes all the time. Urbanologists call the above phenomena the evolution of city groups. In this chapter, the city group optimization algorithm is presented, which is based on urbanology and mimics the evolution of city groups. The robustness and evolutionary process of the proposed city group optimization algorithm are validated by testing it on 15 benchmark functions. The comparative results show that the proposed algorithm is effective for solving complexly continuous problems due to a stronger ability to escape from local optima.

Chapter 5
Magnetotactic Bacteria Optimization Algorithm (MBOA) for Function Optimization: MBOA Based on Four Best-Rand Pairwise Schemes 97
Lili Liu, LiaoCheng University, China
Hongwei Mo, Harbin Engineering University, China

Magnetotactic bacteria is a kind of prokaryotes with the characteristics of magnetotaxis. Magnetotactic bacteria optimization algorithm (MBOA) is an optimization algorithm based on the characteristics of magnetotaxis. It mimics the development process of magnetosomes (MTSs) in magnetotactic bacteria. In this chapter, four pairwise MTSs regulation schemes based on the best individual and randomly chosen one are proposed to study which scheme is more suitable for solving optimization problems. They are

tested on 14 functions and compared with many popular optimization algorithms, including PSO, DE, ABC, and their variants. Experimental results show that all the schemes of MBOA are effective for solving most of test functions but have different performance on a few test functions. The fourth MBOA scheme has superior performance to the compared methods on many test functions. In this scheme, the algorithm searches around the current best individual to enhance the convergence of MBOA and the individual can migrate to the current best individual to enhance the diversity of the MBOA.

Chapter 6
An Analysis on Fireworks Algorithm Solving Problems With Shifts in the Decision Space and Objective Space..... 119
Shi Cheng, Shaanxi Normal University, China
Junfeng Chen, Hohai University, China
Quande Qin, Shenzhen University, China
Yuhui Shi, Southern University of Science and Technology, China

Fireworks algorithms for solving problems with the optima shifts in decision space and/or objective space are analyzed. The standard benchmark problems have several weaknesses in the research of swarm intelligence algorithms for solving single objective problems. The optimum shift in decision space and/or objective space will increase the difficulty of problem solving. Modular arithmetic mapping is utilized in the original fireworks algorithm to handle solutions out of search range. The solutions are implicitly guided to the center of search range for problems with symmetrical search range via this strategy. The optimization performance of fireworks algorithm on shift functions may be affected by this strategy. Four kinds of mapping strategies are compared on problems with different dimensions and different optimum shift range. From experimental results, the fireworks algorithms with mapping to the boundary or mapping to limited stochastic region obtain good performance on problems with the optimum shift. This is probably because the search tendency is kept in these two strategies.

Section 2
Swarm Intelligence Applications

Chapter 7
Assessment of Gamma-Ray-Spectra Analysis Method Utilizing the Fireworks Algorithm for Various Error Measures 155
Miltiadis Alamaniotis, Purdue University, USA
Lefteri Tsoukalas, Purdue University, USA

The analysis of measured data plays a significant role in enhancing nuclear nonproliferation mainly by inferring the presence of patterns associated with special nuclear materials. Among various types of measurements, gamma-ray spectra is the widest utilized type of data in nonproliferation applications. In this chapter, a method that employs the fireworks algorithm (FWA) for analyzing gamma-ray spectra aiming at detecting gamma signatures is presented. In particular, FWA is utilized to fit a set of known signatures to a measured spectrum by optimizing an objective function, where non-zero coefficients express the detected signatures. FWA is tested on a set of experimentally obtained measurements optimizing various objective functions—MSE, RMSE, Theil-2, MAE, MAPE, MAP—with results exhibiting its potential in providing highly accurate and precise signature detection. Furthermore, FWA is benchmarked against genetic algorithms and multiple linear regression, showing its superiority over those algorithms regarding precision with respect to MAE, MAPE, and MAP measures.

Chapter 8
A Computational Comparison of Swarm Optimization Techniques for Optimal Load Shedding Under the Presence of FACTS Devices to Avoid Voltage Instability 182
G. V. Nagesh Kumar, Vignan's Institute of Information Technology (Autonomous), India
B. Venkateswara Rao, V. R. Siddhartha Engineering College (Autonomous), India
D. Deepak Chowdary, Dr. L. Bullayya College of Engineering (for Women), India
Polamraju V. S. Sobhan, Vignan's Foundation for Science, India

Voltage instability has become a serious threat to the operation of modern power systems. Load shedding is one of the effective countermeasures for avoiding instability. Improper load shedding may result in huge technical and economic losses. So, an optimal load shedding is to be carried out for supplying more demand. This chapter implements bat and firefly algorithms for solving the optimal load shedding problem to identify the optimal amount of load to be shed. This is applied for a multi-objective function which contains minimization of amount of load to be shed, active power loss minimization, and voltage profile improvement. The presence of with and without static VAR compensator (SVC), thyristor-controlled series capacitor (TCSC), and unified power flow controller (UPFC) on load shedding for IEEE 57 bus system has been presented and analyzed. The results obtained with bat and firefly algorithms were compared with genetic algorithm (GA) and also the impact of flexible AC transmission system (FACTS) devices on load shedding problem has been analyzed.

Chapter 9
Using Particle Swarm Optimization Algorithm as an Optimization Tool Within Developed Neural Networks 215
Goran Klepac, Raiffeisenbank Austria, Croatia

Developed neural networks as an output could have numerous potential outputs caused by numerous combinations of input values. When we are in position to find optimal combination of input values for achieving specific output value within neural network model it is not a trivial task. This request comes from profiling purposes if, for example, neural network gives information of specific profile regarding input or recommendation system realized by neural networks, etc. Utilizing evolutionary algorithms like particle swarm optimization algorithm, which will be illustrated in this chapter, can solve these problems.

Chapter 10
Squeeze Casting Parameter Optimization Using Swarm Intelligence and Evolutionary Algorithms 245
Manjunath Patel G. C., Sahyadri College of Engineering and Management, India
Prasad Krishna, National Institute of Technology Karnataka, India
Mahesh B. Parappagoudar, Padre Conceicao College of Engineering, India
Pandu Ranga Vundavilli, Indian Institute of Technology Bhubaneswar, India
S. N. Bharath Bhushan, Sahyadri College of Engineering and Management, India

This chapter is focused to locate the optimum squeeze casting conditions using evolutionary swarm intelligence and teaching learning-based algorithms. The evolutionary and swarm intelligent algorithms are used to determine the best set of process variables for the conflicting requirements in multiple objective functions. Four cases are considered with different sets of weight fractions to the objective function based on user requirements. Fitness values are determined for all different cases to evaluate the performance of evolutionary and swarm intelligent methods. Teaching learning-based optimization and multiple-objective particle swarm optimization based on crowing distance have yielded similar results.

Experiments have been conducted to test the results obtained. The performance of swarm intelligence is found to be comparable with that of evolutionary genetic algorithm in locating the optimal set of process variables. However, TLBO outperformed GA, PSO, and MOPSO-CD with regard to computation time.

Chapter 11

Swarm-Intelligence-Based Communication Protocols for Wireless Sensor Networks 271
Lucia Keleadile Ketshabetswe, Botswana International University of Science and Technology, Botswana
Adamu Murtala Zungeru, Botswana International University of Science and Technology, Botswana
Joseph M. Chuma, Botswana International University of Science and Technology, Botswana
Mmoloki Mangwala, Botswana International University of Science and Technology, Botswana

Social insect communities are formed from simple, autonomous, and cooperative organisms that are interdependent for their survival. These communities are able to effectively coordinate themselves to achieve global objectives despite a lack of centralized planning, and the behaviour is referred to as swarm intelligence. This chapter presents a study of communication protocols for wireless sensor networks utilizing nature-inspired systems: social insect-based communities and natural creatures. Three types of insects are used for discussion: ants, termites, and bees. In addition, a study of the social foraging behavior of spider monkeys is presented. The performances of these swarm-intelligence-based algorithms were tested on common routing scenarios. The results were compared with other routing algorithms with varying network density and showed that swarm-intelligence-based routing techniques improved on network energy consumption with a control over best-effort service. The results were strengthened with a model of termite-hill routing algorithm for WSN.

Chapter 12

Image Reconstruction of Electrical Impedance Tomography Using Fish School Search and Differential Evolution 301
Valter Augusto de Freitas Barbosa, Universidade Federal de Pernambuco, Brazil
Wellington Pinheiro dos Santos, Universidade Federal de Pernambuco, Brazil
Ricardo Emmanuel de Souza, Universidade Federal de Pernambuco, Brazil
Reiga Ramalho Ribeiro, Universidade Federal de Pernambuco, Brazil
Allan Rivalles Souza Feitosa, Universidade Federal de Pernambuco, Brazil
Victor Luiz Bezerra Araújo da Silva, Escola Politécnica da Universidade de Pernambuco, Brazil
David Edson Ribeiro, Universidade Federal de Pernambuco, Brazil
Rafaela Covello Freitas, Escola Politécnica da Universidade de Pernambuco, Brazil
Manoela Paschoal, Universidade Federal de Pernambuco, Brazil
Natália Souza Soares, Universidade Federal de Pernambuco, Brazil
Rodrigo Beltrão Valença, Universidade Federal de Pernambuco, Brazil
Rodrigo Luiz Tomio Ogava, Universidade Federal de Pernambuco, Brazil
Ítalo José do Nascimento Silva Araújo Dias, Universidade Federal de Pernambuco, Brazil

Electrical impedance tomography (EIT) is a noninvasive imaging technique that does not use ionizing radiation with application both in environmental sciences and in health. Image reconstruction is performed by solving an inverse problem and ill-posed. Evolutionary and bioinspired computation have become a

source of methods for solving inverse problems. In this chapter, the authors investigate the performance of fish school search (FSS) and differential evolution (DE) using non-blind search (NBS) considering meshes of 415, 3190, and 9990 finite elements. The methods were evaluated using numerical phantoms consisting of electrical conductivity images with objects in the center, between the center and the edge, and on the edge of a circular section. Twenty simulations were performed for each configuration. Results showed that both FSS and DE are able to perform EIT image reconstruction with large meshes and converge faster by using non-blind search.

Chapter 13
Multi-Thresholding of Histopathological Images Using Fuzzy Entropy and Parameterless Cuckoo Search 339
Krishna Gopal Gopal Dhal, Midnapore College (Autonomous), India
Mandira Sen, Tata Consultancy Services, India
Sanjoy Das, University of Kalyani, India

This chapter presents a multi-level histopathological image thresholding approach based on fuzzy entropy theory. This entropy measure is maximized to obtain the optimal thresholds of the image. In order to solve this problem, one self-adaptive and parameter-less cuckoo search (CS) algorithm has been employed, which leads to an accurate convergence towards the optima within less computational time. The performance of the proposed CS is also compared with traditional CS (TCS) algorithm and particle swarm optimization (PSO). The outcomes of the proposed fuzzy entropy-based model are compared with Shannon entropy-based model both visually and statistically in order to establish the perceptible difference in image.

Chapter 14
Optimized Base Station Sleeping and Smart Grid Energy Procurement Scheme to Improve Energy Efficiency 357
Qiang Wang, Yulin Normal University, China
Hai-Lin Liu, Guangdong University of Technology, China

In this chapter, the authors propose a joint BS sleeping strategy, resource allocation, and energy procurement scheme to maximize the profit of the network operators and minimize the carbon emission. Then, a joint optimization problem is formulated, which is a mixed-integer programming problem. To solve it, they adopt the bi-velocity discrete particle swarm optimization (BVDPSO) algorithm to optimize the BS sleeping strategy. When the BS sleeping strategy is fixed, the authors propose an optimal algorithm based on Lagrange dual domain method to optimize the power allocation, subcarrier assignment, and energy procurement. Numerical results illustrate the effectiveness of the proposed scheme and algorithm.

Chapter 15
Using Cuckoo Search Algorithm for Hybrid Flow Shop Scheduling Problems Under Makespan Criterion 379
M. K. Marichelvam, Mepco Schlenk Engineering College, India
Ömür Tosun, Akdeniz University, Turkey

In this chapter, cuckoo search algorithm (CSA) is used to solve the multistage hybrid flow shop (HFS) scheduling problems with parallel machines. The objective is the minimization of makespan. The HFS scheduling problems are proved to be strongly non-deterministic polynomial time-hard (NP-hard).

Proposed CSA algorithm has been tested on benchmark problems addressed in the literature against other well-known algorithms. The results are presented in terms of percentage deviation (PD) of the solution from the lower bound. The results indicate that the proposed CSA algorithm is quite effective in reducing makespan because average PD is observed as 1.531, whereas the next best algorithm has result of average PD of 2.295, which is, in general, nearly 50% worse, and other algorithms start from 2.645.

Chapter 16
Particle Swarm Optimization for Model Predictive Control in Reinforcement Learning Environments 401
Daniel Hein, Technische Universität München, Germany
Alexander Hentschel, AxiomZen, Canada
Thomas A. Runkler, Siemens AG, Germany
Steffen Udluft, Siemens AG, Germany

This chapter introduces a model-based reinforcement learning (RL) approach for continuous state and action spaces. While most RL methods try to find closed-form policies, the approach taken here employs numerical online optimization of control action sequences following the strategy of nonlinear model predictive control. First, a general method for reformulating RL problems as optimization tasks is provided. Subsequently, particle swarm optimization (PSO) is applied to search for optimal solutions. This PSO policy (PSO-P) is effective for high dimensional state spaces and does not require a priori assumptions about adequate policy representations. Furthermore, by translating RL problems into optimization tasks, the rich collection of real-world-inspired RL benchmarks is made available for benchmarking numerical optimization techniques. The effectiveness of PSO-P is demonstrated on two standard benchmarks mountain car and cart-pole swing-up and a new industry-inspired benchmark, the so-called industrial benchmark.

Compilation of References 428

About the Contributors 467

Index 476

Elemental Analysis of Indian Natural Chrysoberyl Gemstones by PIXE Technique

- Authors
- Authors and affiliations

- S. Siva Jyothi
- G. Padmaja Rani
- P. Venkateswarulu
- R. VenkateswaraRao
- T. R. Rautray

Conference paper
First Online: 07 August 2019

Part of the Lecture Notes on Multidisciplinary Industrial Engineering book series (LNMUINEN)

Abstract

A selected number of Indian Eastern Ghats' natural Chrysoberyl gemstones were studied with a powerful nuclear analytical proton-induced X-ray emission (PIXE) technique. Sixteen elements, including Al, Cr, Ti, V, Cu, Fe, Pb, Mo, La and Ce, were identified in these Chrysoberyl gemstones and may be helpful in interpreting the various geochemical circumstances and the probable cause of their origin in the Eastern Ghats. The PIXE technique is an attractive method for quickly determining the elemental concentration of a material. The PIXE measurements were performed at the Ion Beam Laboratory, Institute of Physics (IOP), Bhubaneswar, using 3 MV tandem accelerator. The well-collimated 3 meV proton beam of 2 mm diameter was employed to irradiate the gemstone samples. Moreover, preliminary XRD studies of different Chrysoberyl patterns were performed and major compositional elements were confirmed by XRD. The chemical constituents of Chrysoberyl gemstones from Visakhapatnam, Andhra Pradesh, India, were analysed, and gemological studies were performed. Thus, in the present study, the usefulness and versatility of the PIXE system for research in geo-scientific methodology particularly in gemology are established.

Keywords

Chrysoberyl gemstones PIXE XRD Eastern Ghats India and trace elements

Notes

Acknowledgements

The authors are thankful to the college administrators of ANITS, Dr L.B. College of Engineering for women and Lendi Institute of Engineering and Technology for granting necessary permissions and time to undertake this sophisticated work. The authors are also very much thankful to the chief and scientific staff of the Institute of Physics, Bhubaneswar, India, for giving necessary time slot, permission and access to operate PIXE. Further, the authors very much thankful to the Prof. Kasipathi, Department of Geology Andhra University.

References

1. 1.

Klein, C., Hurlbut, C.S., Jr.: Manual of Mineralogy, 20th edn. Willy, New York. ISBN 0-471-80580-7 (1985)Google Scholar

2. 2.

Johansson, T.B., Akselsson, R., Johansson, S.A.E.: X-ray analysis: Elemental trace analysis at the 10–12 g level. Nucl.Inst. Meth. Phys. Res. Sect. B. **84**(1), 141–143 (1970)CrossRefGoogle Scholar

3. 3.

Rogers, P.S.Z., Duffy, C.J.; Benjamin, T.M., Maggiore, C.J.: Geochemical applications of nuclear microprobes. Nucl. Instr. Meth. B **3**, 671–676 (1984)CrossRefGoogle Scholar

4. 4.

Benjamin, T.M., Duffy, C.J., Maggiore, C.J., Rogers, P.S.Z., Woolum, D.S., Burnett, D.S., Murrell, M.T.: Microprobe analyses of rare earth element fractionation in meteoritic minerals. Nucl. Instr. Meth. B **3**, 677–680 (1984)CrossRefGoogle Scholar

5. 5.

Johansson, S.A.E., Campbell, J.L.: PIXE—A Novel Technique for Elemental Analysis. Wiley, New York (1988)Google Scholar

6. 6.

Sie, S.H., Ryan, C.G., Cousens, D.R., Griffin, W.L.: Nucl. Instr. Meth. B **40**(41), 690–697 (1989)CrossRefGoogle Scholar

7. 7.

Tenorio, D., Almazán-Torres, M.G., Monroy-Guzmán, F., Rodríguez-García, N.L., Longoria, L.C.: Characterization of ceramics from the archaeological site of San Miguel Ixtapan, Mexico State, Mexico, using NAA, SEM, XRD and PIXE techniques. J. Radio. Anal.Nucl. Chem. **266**, 471–480 (2005)CrossRefGoogle Scholar

8. 8.

Ryan, S.R., Fischbeck, H.J., Chesnut, K.: Correlation of archaeological ceramics and clays using an external-beam PIXE analysis of the major elemental constituents. Nucl. Instr. Meth. B **10**(11), 645–649 (1985)CrossRefGoogle Scholar

9. 9.

Dias Da Cunha, K., Pereira, J.A.M., Barros Leite, C.V.: PIXE and PDMS methods applied to aerosols analysis. Aerosol Sci. Technol. **32**(5), 453–464 (2010)CrossRefGoogle Scholar

10. 10.

VenkateswaraRao, R., Mary Anupama, P., Guru Mahesh, D., Iqbal, A.W., Ramakrishna, Y., Venkateswarulu, P.: Estimation of trace elements in various parts of human teeth using external beam PIXE. Int. J. Phy. Appl. **2**, 123–134 (2010)Google Scholar

11. 11.

Uda, M., Tsunokami, T., Murai, R., Maeda, K., Harigai, I., Nakayama, Y., Yoshimura, S., Kikuchi, T., Sakurai, K., Sasa, Y.: Quantitative analysis of ancient Egyptian pigments by external PIXE. Nucl. Instr. Meth. B **75**, 476 (1993)CrossRefGoogle Scholar

12. 12.

Orlic, I., Tang, S.M.: Elemental depth profiles in marine sediments of Singapore coastal waters. Nucl. Instr. Meth. B **150**, 291–297 (1999)CrossRefGoogle Scholar

13. 13.

Neelmeijier, C., Brissaud, I., Caliigaro, T., Demortier, G., Hautojarvi, A., Mader, M., Martinot, L., Schreiner, M., Tuurnala, T., Weber, G.: Paintings—A challenge for XRF and PIXE analysis. X-ray Spectrom. **29**, 101–110 (2000)CrossRefGoogle Scholar

14. 14.

Mohapatra, A., Rautray, T.R., Patra, A.K., Vijayan, V., MohantyRajeeb, K.: Elemental composition in mud crab Scylla serrata from Mahanadhi estuary, India. In situ irradiation analysis by external PIXE.Food Chem. Toxicol. **47**, 119–123 (2008)CrossRefGoogle Scholar

15. 15.

Caliigaro, T., Poirot, J.P., Querre, G.: Trace element fingerprinting of jewellery rubies by external beam PIXE. Nucl. Instr. Meth. B **15**, 628–634 (1999)CrossRefGoogle Scholar

16.16.

Olabanji, S.O., Ige, O.A., Mazzoli, C., Ceccato, D., Akintunde, J.A., De Poli, M., Moschini, G.: Accelerator-based analytical technique in the evaluation of some Nigeria's natural minerals: fluorite, tourmaline and topaz. Nucl. Instr. Meth. B **240**, 350–355 (2005)CrossRefGoogle Scholar

17.17.

Chanda, S.C., Manna, A., Vijayan, V., Nayak, P.K., Ashok, M., Acharya, H.N.: PIXE & XRD analysis of nano crystals of Fe, Ni and Fe_2O_3. Mater.Lett. **61**, 5059–5062 (2007)Google Scholar

18.18.

Khandaker, N.I., Ahmed, M., Garwan, M.A.: Study of volcanic sediments by micro beam-PIXE technique. Nucl. Instr. Meth. B **109**/110, 587 (1996)CrossRefGoogle Scholar

19.19.

Mohanty, A.K., Das, S.K., Vijayan, V., Senagupta, D., Saha, S.K.: Geochemical studies of monazite sands of Chhatrapur beach deposit of Orissa, India by PIXE and EDXRF method. Nucl. Instr. Meth. B **211**, 145–154 (2003)CrossRefGoogle Scholar

20.20.

Nayak, P.K., Vijayan, V.: Complementory PIGE, PIXE, EDXRF and γ-ray spectroscopic investigation on natural chromites. Nucl. Instr. Meth. B **245**, 505–510 (2006)CrossRefGoogle Scholar

21.21.

SrinivasaRao, K., VenkateswaraRao, R., Kasipathi, C., SivaJyothi, S., Ramakrishna, Y., Venkateswarulu, P.: Advanced instrumental technique of analysis—PIXE: a best practice of mineral industry. In: Proceedings of the National Seminar cum Workshop on Environment and sustainable Development in Mineral Industry and Solid Waste Management (ESD-MISM), Visakhapatnam, India, 11–13 Mar 2011, pp. 170–174Google Scholar

22.22.

Kasipathi, C.: Mineral resources of Visakhapatnam District, A.P. Visakhapatnam Sci. J. (A.P. Akad. Sci Publ.) **1**, 39–42 (1997)Google Scholar

23.23.

Rosenblum, S.: Am. Mineral. **43**, 170 (1958)Google Scholar

24.24.

Vijayan, V., Behera, S.N., Ramamurthy, V.S., Puri, S., Shahi, J.S., Singh, N.: Elemental composition of fly ash from a coal-fires thermal power plant: A study using PIXE and EDXRF. X-ray Spectrum. **26**, 65 (1997)CrossRefGoogle Scholar

25.25.

Maxwell, J.A., Campbell, J.L., Teesdale, W.J.: The Guelph PIXE software package II. Nucl. Instr. Meth. B **95**, 407 (1995)CrossRefGoogle Scholar

26.26.

Elderd, R.A., Kusko, B.H., Cachill, T.A.: The external PIXE milliprobe at Davis: Laser alignment, PIXE calibration and quality assurance. Nucl. Instr. Meth. B **3**, 579–583 (1984)CrossRefGoogle Scholar

27.27.

Farell, E.F., Fang, J.H., Newnham, R.E.: Refinement of the chrysoberyl structure. Am. Mineral. **48**, 804–810 (1963)Google Scholar

28.28.

Newnham, R.E., Dehaan, Y.M.: Refinement of the alpha-Al_2O_3, Ti_2O_3, V_2O_3, and Cr_2O_3 structures. Zeit.Krist. **117**, 235–237 (1962)CrossRefGoogle Scholar

29.29.

Smith, D.K., Newkirk, H.W., Kohn, J.S.: The crystal structure and polarity of beryllium oxide. University of California Radiation Laboratory Report 7022 (1962)Google Scholar

Copyright information

About this paper

CrossMark

Cite this paper as:

Siva Jyothi S., Padmaja Rani G., Venkateswarulu P., VenkateswaraRao R., Rautray T.R. (2019) Elemental Analysis of Indian Natural Chrysoberyl Gemstones by PIXE Technique. In: Pujari S., Srikiran S., Subramonian S. (eds) Recent Advances in Material Sciences. Lecture Notes on Multidisciplinary Industrial Engineering. Springer, Singapore.
https://doi.org/10.1007/978-981-13-7643-6_24

- **First Online**07 August 2019
- **DOI**https://doi.org/10.1007/978-981-13-7643-6_24
- **Publisher Name**Springer, Singapore
- **Print ISBN**978-981-13-7642-9
- **Online ISBN**978-981-13-7643-6
- **eBook Packages**Chemistry and Materials ScienceChemistry and Material Science (R0)

A High Speed Two Step Flash ADC

K. Lokesh Krishna[1(✉)], Yahya Mohammed Ali Al-Naamani[2], and K. Anuradha[3]

[1] S.V.College of Engineering, Tirupati, Andhra Pradesh, India
[2] S.V.C.E.T., Chittoor, Andhra Pradesh, India
[3] L.B.C.E.W., Visakhapatnam, Andhra Pradesh, India
kayamlokesh78@gmail.com

Abstract. As wireless communication equipment's are demanding higher speed of operation, low power and into the digital domain, it becomes essential to design a high speed and low power ADC. This paper presents a novel power efficient, high-speed two step analog to digital converter (ADC) architecture combining two whole Flash ADCs with feed forward circuitry. The proposed circuit has been designed to overcome the drawbacks of the conventional flash ADC which draws more power due to the high speed comparator bank. Also the proposed two-step ADC employs a modified double tail comparator circuit which operates at high speed and consumes less power. The individual block of two step flash ADC is designed, simulated and implemented in CMOS 130 nm N-well technology operated at 1.8 V power supply voltage. The ADC consumes 2.32mW with a resolution of 6-bits for input signal frequencies upto 1 GHz and occupies a silicon area of 0.226 mm^2. The operating speed of the design is 10 GHz and the simulated static INL and DNL is found to remain within 0.15LSB and 0.42LSB respectively.

Keywords: Threshold inverter quantizer · Comparator · Register · Low power Time interleaving · Residue amplifier and CMOS

1 Introduction

Existing electronic systems such as Software Defined Radios, Aircraft communications, High performance Data Acquisition Systems, Broad band wireless communication systems, Medical Imaging and Diagnostic equipment's, High frequency oscilloscopes, Spectrum analyzers, 4G Long Term Evolution (LTE) systems, Signal generators, Communication test equipment's and High frequency oscilloscopes demand high data rates with low power consumption. The signals that we experience in our daily lives are analog. These signals are non-quantized, low amplitude or high amplitude and continuously vary with time. Nowadays due to the advances in digital processing techniques, utmost processing is carried out in digital domain only. The advantages of digital signal processing techniques are easier to design since exact values of voltages and currents are not required, accurate and highly precise, data storage is easier, logic can be reprogrammed, and less prone to noise. Hence it becomes essential that the received signal must be transformed to digital at some instance of processing.

I. Zelinka et al. (Eds.): ICSCS 2018, CCIS 837, pp. 826–836, 2018.
https://doi.org/10.1007/978-981-13-1936-5_84

A data converter is a microelectronic circuit that is used to translate the given analog input voltage signal to output digital voltage signal or a digital input signal to an analog output signal. Hence data converter circuits are extensively used as interface between analog and digital circuits and vice-versa. Broadly there are two various types of data converter circuits such as (i) ADC and (ii) Digital to Analog Converter (DAC). ADC transforms an analog signal (which is continuous time and continuous magnitude) into corresponding digital signals (discrete time and discrete magnitude). Generally there are different ADC architectures available to be used for different emerging applications. Identification of an ADC for a given applications is determined by its design specifications. However no single ADC architecture is found to be appropriate for all these applications. Selection of the correct ADC necessitates tradeoffs between conversion time, silicon area, resolution, static performance, channel count, cost and dynamic performance. Irrespective of the applications, the three key parameters to be considered in the design of ADC circuit are dynamic linearity over large operating bandwidth, die area and power consumption.

Various ADC architectures such as Flash type, Two-step flash type, Dual Slope type, Sigma-Delta, Pipeline and Interleaving are available for various applications. The performance of an ADC is frequently affected by the type of the input signal they process. Because the given input analog signal is continuous in nature, ADCs suffer numerous problems such as clock jitter, nonlinear input impedance, number of bits, signal and clock skew, number of components, chip size, power dissipation etc. These problems limit the use of ADC architectures for various applications. In all the available ADC architectures, Flash analog to digital converter circuits are very fast converters and are well appropriate for large bandwidth applications. Flash ADCs are realized by connecting high speed comparator circuits in series. The number of high speed comparators required to realize a flash ADC is (2^N-1), where N denotes resolution of the converter. But the disadvantage is that they draw a lot of power as the resolution of the converter circuit increases which in turn reflects in the increase in the silicon area. Due to this flash ADCs are restricted to a resolution of (4–6) bits. Also as the chip size increases, more problems associated with signal and clock routing becomes noticeable. Pipelined analog to digital converter architecture are mostly used for sampling signals from hundreds of kilo samples per second (KS/s) upto 800 MS/s with resolutions varying from (6-16) bits. Sigma-Delta ($\sum$-Δ) ADC architectures are used principally in applications requiring lower speed while requiring a trade-off of sampling speed for resolution by oversampling, followed by filtering techniques to decrease quantization noise.

Sigma-Delta ($\sum$-Δ) ADC architecture are used in low speed applications with resolution ranging from (12–24) bits. Dual slope type ADCs deliver high resolution and offer good in-line frequency and noise rejection. Time interleaved ADCs uses few identical analog to digital converters to process regular sampled data series at a faster rate than the operating rate of each individual ADC. Due to the Time inter leaving technique, the operating bandwidth of the converter is increased which allows for easier frequency planning and reduction in circuit complexity and price of the anti-aliasing filter that is typically used at the front stage of analog to digital converter. Successive Approximation Register (SAR) analog to digital converter architectures are used in applications requiring medium to very high resolution and with sample rate of the order of 10MS/s

to 100MS/s. Recent improvements in architectural design and scaling of transistors allowed for decrease in power consumption and high speed operation.

Two step analog to digital converter architecture also known as subranging converters offers the best tradeoff between sampling speed, power consumption and latency. The two-step flash ADC generates the digital output in multiple stages using multiple clock cycles. The principal component in the design of two-step flash architecture is the high speed comparator. The number of required high speed comparators reduces which in turn reflects in the reduction of power consumption and silicon area.

Nasri et al. presents the implementation of a low-power 4-bit high sample rate folding-flash ADC which uses a novel unbalanced double-tail dynamic comparator and results in major reduction of the kick-back noise [1]. Wang et al. propose an column-level two-step ADC [2]. A four way time interleaved ADC driving four sets of track and hold switches that suits the requirements of NRZ 10G Ethernet (10GE) standard is proposed [3]. Ferragina et al. describes the design of low-power and high resolution flash architecture which utilizes interpolation technique and V-I converters operated as preamplifier stage [4]. Ritter et al. present a flash ADC that doesn't use a track and hold circuit or time interleaving technique which reflects in reduction of circuit complexity and operates at high speed [5]. A wide input bandwidth and low power ADC operating at 1 GHz appropriate for ultra-wide band system is proposed [6]. Tretter et al. presents the design and characterization of single-core flash ADC, which is capable of reaching high sampling rate without using time interleaving technique [7]. In this proposed work a high speed two step flash architecture is designed, simulated and implemented using CMOS 130 nm technology.

The summary of this work is as follows. Section 2 explains the background of two step flash ADC architecture and various parameters associated with the proposed work. Section 3 presents the design and implementation of the proposed two-step architecture. Section 4 shows the obtained simulation results. Lastly the conclusions are drawn in Sect. 5.

2 Two Step Flash ADC Architecture

Two-step flash architecture also called as the parallel, feed forward architecture is separated into two whole flash ADCs with feed-forward circuitry [9]. Figure 1, shows the diagram of two step flash architecture. The first part of the converter performs a rough evaluation of the value of the input voltage signal, and the second converter performs a fine conversion. The main benefit of this architecture is that the number of high speed comparators are greatly reduced from (2^N-1) to $2*(2^{N/2}-1)$, where N denotes the number of bits of the converter. In the proposed two-step flash ADC 6-bits are considered. So in a conventional flash ADC 63 comparators are essential, whereas the two-step flash ADC requires only 14 comparators. The given input signal voltage is first sampled by the Sample and Hold (S/H) circuit, and then the most significant bits (MSBs) are converted by the first 3-bit flash ADC. This output is then transformed back to an analog signal voltage with the 3-bit (DAC). The end result of this calculation, called as residue is now multiplied by an amplifier by $2^{N/2}$ times and given as input to the second 3-bit

flash ADC. This second 3-bit ADC yields the least significant bits (LSB) through another flash conversion.

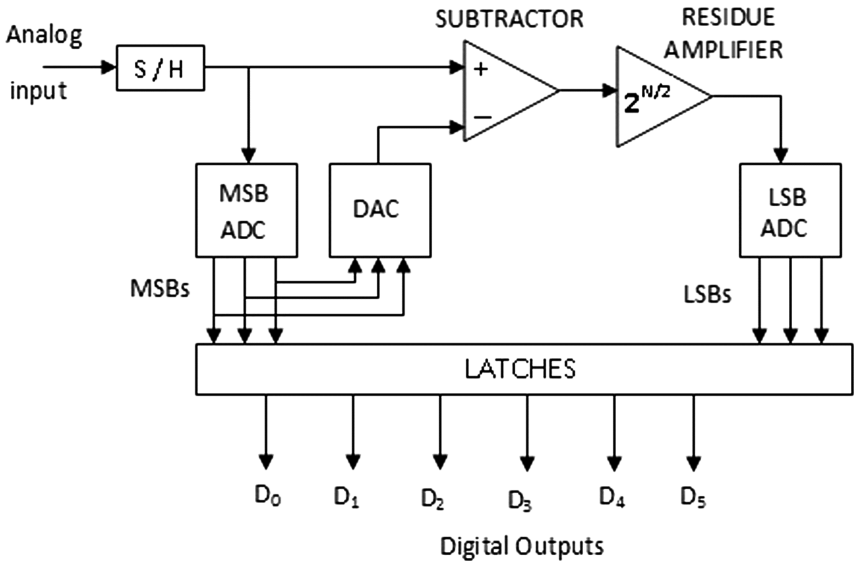

Fig. 1. Proposed diagram of two step Flash ADC

The inner blocks of two step flash ADC are explained below:

2.1 Comparator Circuit

Comparators implemented using CMOS technologies are the most vital basic building blocks in analog and mixed-mode circuit designs. The diagram of comparator circuit is presented in Fig. 2.

A CMOS comparator circuit is used to equate the given analog input signal with a reference signal (V_{ref}) and generates a binary signal output. In this proposed work the design of comparator plays a major role in high speed conversion. There are different kinds of comparator architectures such as clock based dynamic comparator, clock based double tail comparator, continuous time comparator, threshold inverted quantization (TIQ) based comparator and standard cell based comparator.

Clock built dynamic comparators are used in ultra-high speed applications due to the strong regenerative feedback used in the regenerative latch. The main advantage of these circuits are very less static power consumption, high input impedance and complete rail-to-rail output voltage swing is available. But the disadvantages are more delay due to the stacking of several transistors. The double tail comparator circuit offers less delay and operates at lower VDD. Finally standard cell comparators also work at lower supply voltages and gives better stability. In the proposed two step flash ADC, a modified double tail comparator circuit is used.

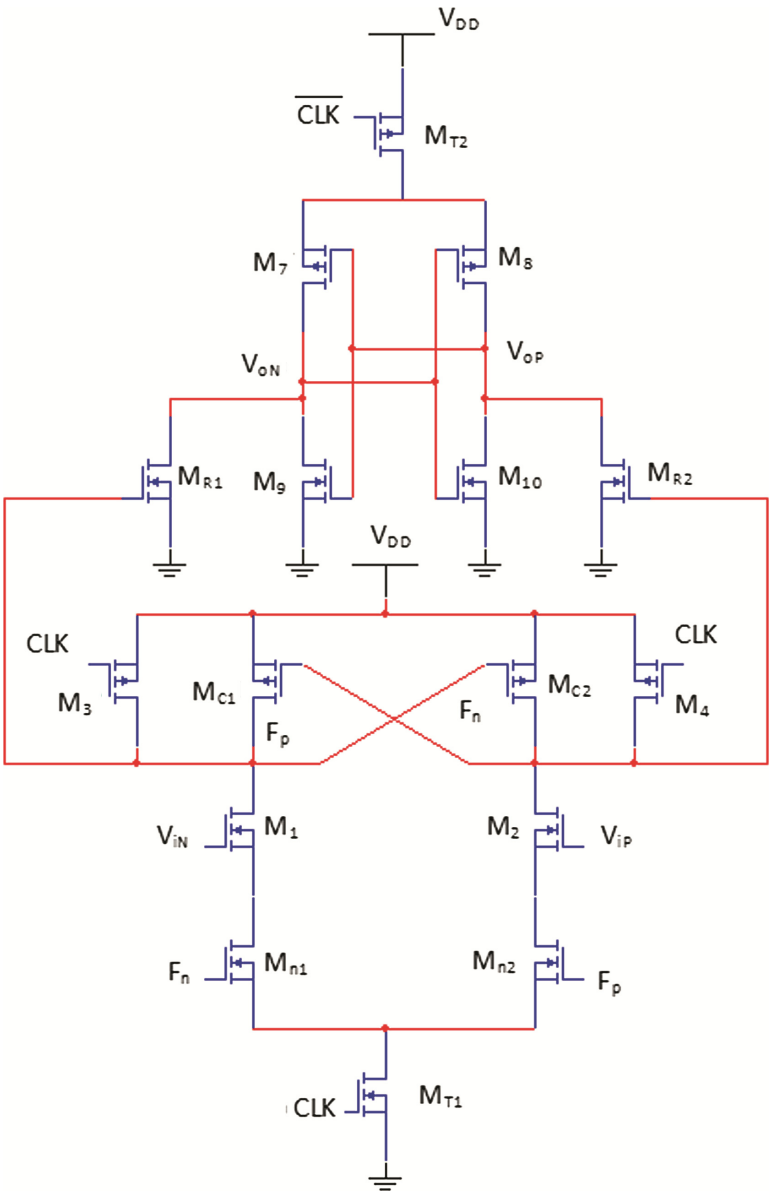

Fig. 2. Schematic of comparator circuit

During the reset stage of operation i.e. when CLK = 0, both M_{T1} and M_{T2} are off. So M_4 and M_3 pulls both F_p and F_n nodes to V_{DD}. Hence M_{C2} and M_{C1} are switched off. The intermediate stage consisting of transistors M_{R1} and M_{R2} resets both latch outputs to ground. Similarly during decision making phase i.e. when CLK = V_{DD}, both M_{T1} and M_{T2} are switched on. At the commencement of this decision making phase, both the

transistors are still cut off. Thus F_n and F_p jump to fall with changed rates according to the input signal voltages.

2.2 3-Bit Flash ADC

It contains a resistive divider network with 8 resistors, which offers the reference voltage to each input terminal of comparator. The reference voltage for each comparator is one LSB greater than the reference voltage for the comparator proximately below it. The output of a comparator circuit produces logic high output when its analog input signal voltage exceeds the voltage at another input terminal applied to it. Else, the output voltage of the comparator becomes logic low. A thermometric code is then translated to get the suitable 3-bit digital code [8]. Figure 3, shows the diagram of 3-bit flash ADC.

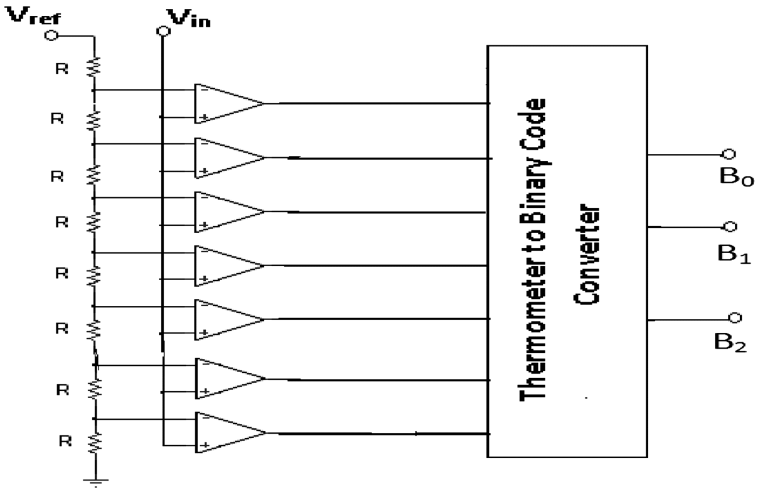

Fig. 3. Block diagram of 3-bit flash architecture

2.3 3-Bit Resistive DAC Circuit

Figure 4, shows a resistor string 3-bit DAC implemented with switches. In this implementation, transmission gates are used rather than n-channel switches. A transmission gate approach has extra source and drain capacitance to ground, but this extra capacitance is offset by the reduced series switch resistance, which is due to the inherent circuit configuration i.e. due to the parallel combination of n-channel and p-channel. Resistive type DACs does not suffer from the charge injection problems as noticed in the capacitive type DACs. Also a resistive type DAC has very small systematic error voltage and is inherently monotonic and compatible with purely digital technologies. Moreover the resistive type DAC occupies less silicon area than the capacitive type DAC.

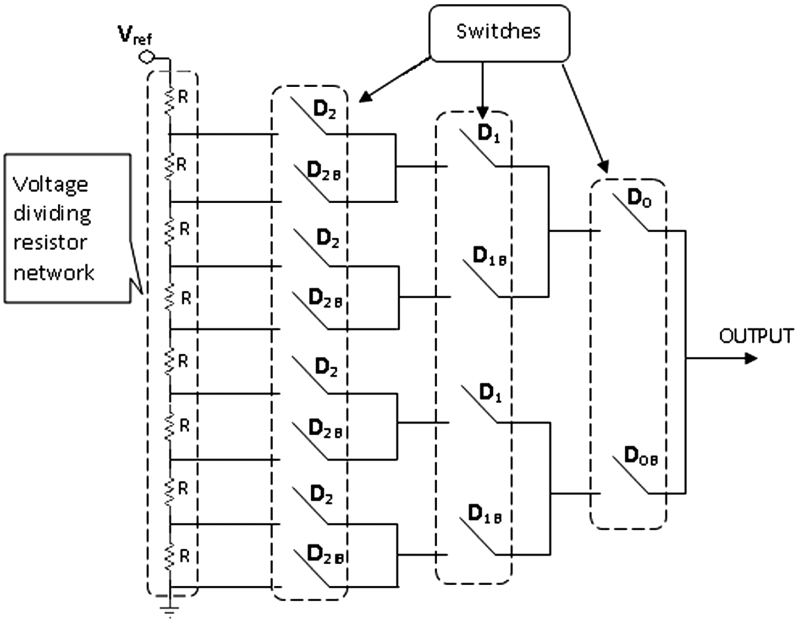

Fig. 4. 3-bit resistive string DAC

3 System Implementation

The two step flash ADC is realized by interconnecting all the individual circuits such as sample and hold circuit, 3-bit flash architecture, subtractor circuit, 3-bit resistive DAC, and residue amplifier. All these individual circuits are implemented on the HSPICE and Cadence schematic editor. The entire schematic of 6-bit two step flash architecture is shown in Fig. 5.

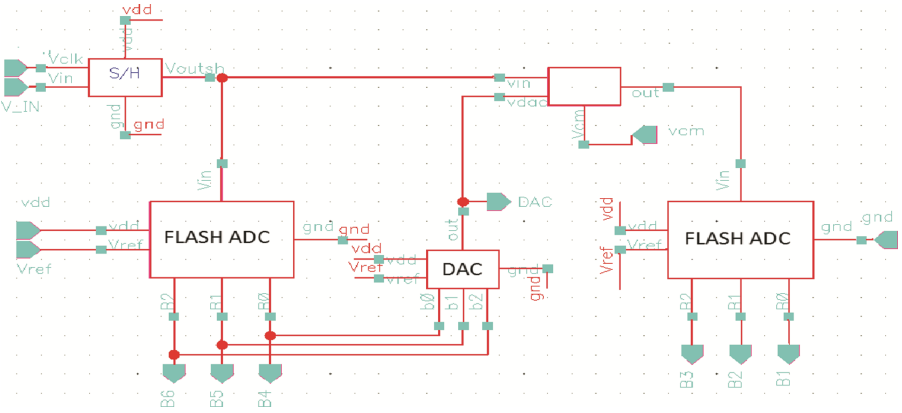

Fig. 5. Schematic diagram of 6-bit two-step flash ADC

4 Simulation

The summary of the proposed 6-bit two-step flash ADC was simulated using Cadence spectre in 130 nm CMOS technology. The simulated results of the double-tail comparator circuit are shown in Fig. 6.

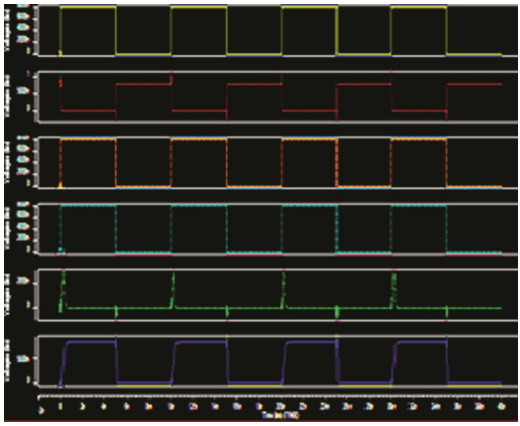

Fig. 6. Simulation results of double tail comparator

Figures 7 and 8 presents the simulated results of 3 bit flash ADC and 6 bit two-step flash architecture

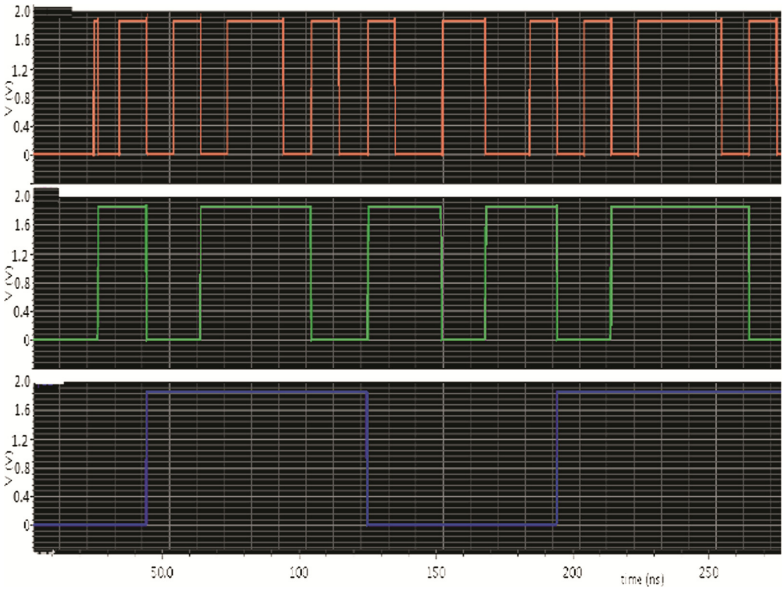

Fig. 7. Simulation results of 3-bit flash architecture

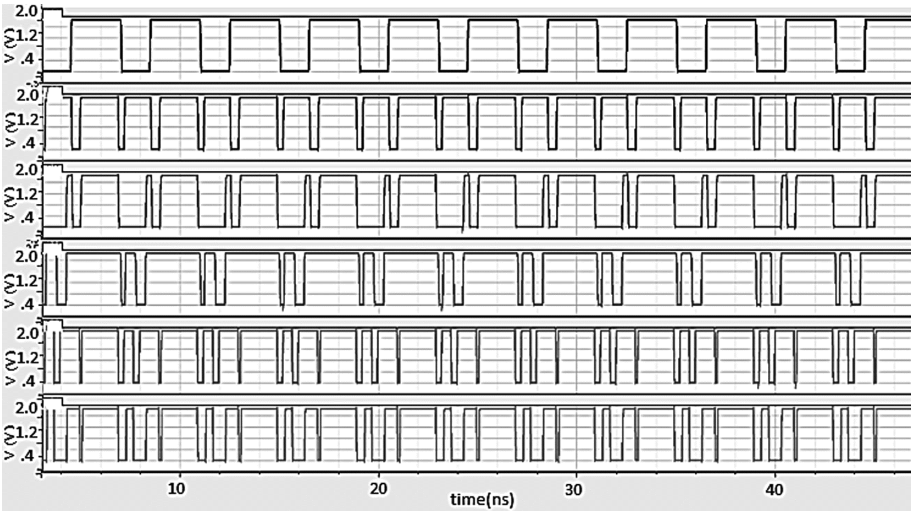

Fig. 8. Simulated results of 6-bit two-step flash architecture

The simulated static integral non-linearity (INL) error of the proposed two-step flash architecture is shown in Fig. 9. The simulated static DNL error of the proposed two-step flash architecture is presented in Fig. 10. Because INL and DNL are less than 0.4LSB, this proposed two step flash ADC exhibits higher linearity.

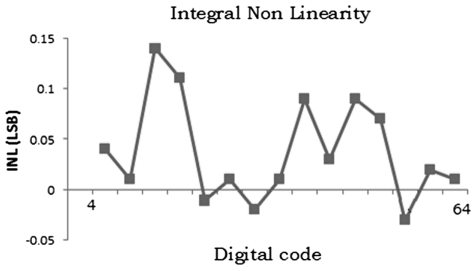

Fig. 9. Simulated INL

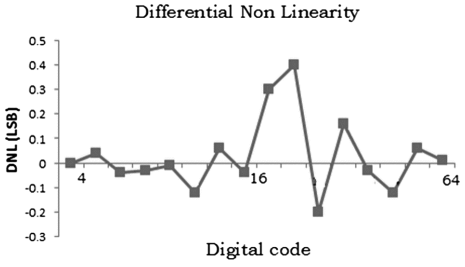

Fig. 10. Simulated DNL

The performance summary of the proposed 6 bit two step flash architecture is given in Table 1.

Table 1. Summary of two–step flash ADC

Technology	CMOS 130 nm
Resolution	6 bits
Input voltage range	1.0 $V_{P\text{-}P}$
Power Supply	1.8 V
Sampling frequency	10 GHz
Input Signal Frequency	upto 1 GHz
Area	0.226 mm^2
Power dissipation	2.32 mW
DNL	$-0.18LSB \leq DNL \geq 0.42LSB$
INL	$-0.02LSB \leq INL \geq 0.15LSB$
SNDR	68 dB

5 Conclusion

This work highlights the design, simulation and implementation of a high speed and low powered 6 bit two step flash ADC operating at a clock frequency of 10 GHz. As the sampling frequency of two-step flash ADCs increases, the design of comparators play a key role as it contribute to both low power and high speed. A modified double tail comparator circuit is used in the proposed system to attain the high operating speed and consumes low power. The proposed two-step flash architecture is operated at a power supply of 1.8 V and the obtained power consumption is only 2.32 mW. Operating speed of the proposed ADC is 10 GHz. The simulated static DNL and INL are measured to be between 0.15/−0.02LSB and 0.42/−0.18LSB respectively. The ADC occupies a silicon die area of 0.226 mm^2 shows a high signal to noise distortion ratio (SNDR) of 68 dB. These attractive specifications of the proposed two step flash architecture make it favorable for evolving applications such as in wireless USB system, where low power and high speed is of utmost importance.

References

1. Nasri, B., Sebastian, S.P., You,K.D., RanjithKumar, R., Shahrjerdi, D.: A 700 µW 1GS/s 4-bit folding-flash ADC in 65 nm CMOS for wideband wireless communications. In: 2017 International Symposium on Circuits and Systems (ISCAS), Baltimore, MD, pp. 1–4. IEEE (2017)
2. Wang, G., Lu, W., Zhang, L., Zhang, Y., Chen, Z.: 14-bit 20 µW column level two step ADC for 640 × 512 IRFPA. Electron. Lett. **51**(14), 1054–1056 (2013)
3. Varzaghani, A., et al.: 10.3GS/s, 6-Bit Flash ADC for 10G ethernet applications. IEEE J. Solid-State Circ. **48**(12), 3038–3048 (2013)

4. Ferragina, V., Ghittori, N., Maloberti, F.: Low-power 6-bit flash ADC for high-speed data converters architectures. In: 2006 International Symposium on Circuits and Systems, Island of Kos. IEEE (2006)
5. Ritter, P., Le Tual, S., Allard, B., Möller, M.: Design considerations for a 6 Bit 20 GS/s SiGe BiCMOS Flash ADC without track-and-hold. IEEE J. Solid-State Circ. **49**(9), 1886–1894 (2014)
6. Lien, Y.-C., Lin, Y.-Z., Chang, S.-J.: A 6-bit 1GS/s low-power flash ADC. In: 2009 International Symposium on VLSI Design, Automation and Test, Hsinchu, pp. 211–214 (2009)
7. Tretter, G., Khafaji, M.M., Fritsche, D., Carta, C., Ellinger, F.: Design and characterization of a 3-bit 24-GS/s flash ADC in 28-nm low-power digital CMOS. IEEE Trans. Microw. Theory Technol. **64**(4), 1143–1152 (2016)
8. Krishna, K.L., Srihari, D., Reena, D., Ramashri, T.: A 4b 40 Gbps 140 mW 2.2 mm^2 0.13 μm pipelined ADC for I-UWB receiver. In: 2013 International Conference on Computing, Communications and Networking Technologies (ICCCNT), pp. 1–6. IEEE (2013)
9. Baker, R.J.: CMOS Circuit Design, Layout and Simulation. IEEE Press Series on Microelectronic systems, vol. 2. Wiley-Interscience, Hoboken (2013)

Proceedings of the Second International Conference on Inventive Systems and Control (ICISC 2018)
IEEE Xplore Compliant - Part Number:CFP18J06-ART, ISBN:978-1-5386-0807-4; DVD Part Number:CFP18J06DVD, ISBN:978-1-5386-0806-7

A 10-bit High Speed Pipelined ADC

Alfakhri M.Murshed
B.Tech student,
Department of ECE
S.V.C.E.T. (Autonomous)
Chittoor, Andhra Pradesh
mzamhb@gmail.com

K. Lokesh Krishna
Associate Professor,
Department of ECE,
S.V.C.E.T. (Autonomous),
Chittoor, Andhra Pradesh
kayamlokesh78@gmail.com

M.Abdullah Saif
Sana Community Center
Sana'a, Yemen

K. Anuradha
Associate Professor,
Department of CSE
L.B.C.E.W, Visakhapatnam

***Abstract*— The design of a 10-bit, 200MS/s Pipelined Analog to Digital Converter (ADC) is presented in this paper. The implemented pipelined ADC employs techniques such as pipeline stage scaling algorithm, to lower power, capacitor ratio independent conversion scheme, a nested gain boosting technique and thin oxide transistors with clock bootstrapping. The fully realized is measured under different input frequencies with a sampling rate of 200MS/s and it consumes 46.8mW from a 1.8V power supply. The pipelined ADC implemented in 130nm CMOS technology exhibits signal-to-noise plus distortion ration SNDR of 54.7dB and occupies a die area of 0.31mm^2.**

Keywords*— low power, data converter, op-amp, time-interleaving, high linearity, comparator, and amplifier.

I. INTRODUCTION

In the real world, most data is described by analog signals. In order to control the data using a processor or controller, a data converter circuit is very much essential. A data converter is an electronic circuit that is used to convert analog signal to digital signal or digital signal to analog signal. Currently, there has been rapid progress in the design of electronic systems for various applications. The prominence of data converter circuits in the implementation of digital computers and signal processing in communications, image processing, instrumentation and industrial control systems is increasing by leaps and bounds. Hence data converter circuits are widely used as interface between analog and digital circuits. In general there are two different types of data converter circuits. They are (i) Analog to Digital Converter (ADC) and (ii) Digital to Analog Converter (DAC). Analog to Digital Converter converts an analog signal (continuous time and continuous magnitude) into digital signals (discrete time and discrete magnitude).

ADCs are used in various applications such as Medical Imaging, Wireless Telecommunications, Audio and Video Processing Systems, Software radio and Instrumentation. Broadly there are numerous ADC architectures available to be used for these applications. But selection of an ADC is determined by the application and its specifications. However no single ADC architecture is found to be appropriate for all these applications. At present the major advances in consumer electronics are reflected in smart phones, notebook computers, camcorders, tablets and portable storage devices. All these devices employ various wireless technologies. Also wireless infrastructural systems such as satellite communication systems, cellular base stations, and various electronic warfare systems require the direct digitization of analog signal in the giga-hertz range. High-speed, low power consumption and high resolution are the important requirements in many wireless portable applications.

Different ADC architectures such as Two-step flash type, Sigma-Delta, Flash type, Integrating type, Pipeline and Interleaving are being used to deliver these requirements for various applications. The performance of an ADC is affected by the nature of the input signal they process. Because the input analog signal is continuous in nature, ADCs suffer numerous problems such as clock jitter, nonlinear input impedance, number of bits, signal and clock skew, number of components, chip size, power dissipation etc. These problems limit the use of ADC architectures for various applications. Flash ADCs are very fastest converters and are well suitable for large bandwidth applications. But the main problem is that they consume lot of power as the resolution of the converter increases which in turn reflects in the increase in the size of the chip. Also as the chip size increases, more problems associated with signal and clock routing becomes noticeable.

Two step ADCs also well known as subranging converters is a cross between a flash ADC and pipeline ADC can be used to realize higher resolution and small power. Pipelined ADC architecture is a more specialized application of the two-step architecture and has been developed to be the most popular architecture for sampling rates from a few mega samples per second (MS/s) to 500 MS/s, with resolutions ranging from 8 bits to 20 bits. Successive Approximation Register (SAR) ADCs are used for applications requiring medium to high resolution (8-16) bits and with sample rates fewer than 20MS/s. The advantage using this architecture is that they provide low power consumption as well as a small form factor. Sigma-Delta ($\sum$-Δ) ADC architecture are used in low speed applications with resolution ranging from (12-24) bits. Integrating ADCs provide high resolution and can offer good line frequency and noise rejection. Time interleaved ADCs uses multiple identical analog to digital converters to process regular sample data series at a faster rate than the operating rate of each individual ADC. Time inter leaving technique will relax the power-speed tradeoffs of ADC and minimizes metastability error rate while

increasing the input capacitance. Sampling rate in excess of 500 MHz and bit resolution of more than 8 bits are increasingly required to accommodate the very high bandwidth required in many high speed communication applications. Siddharth Devarajan et al. describe a 12-bit 10GS/s interleaved (IL) pipeline ADC implemented in 28nm CMOS technology. It uses eight pipeline sub-ADCs which are interleaved to achieve 10GS/s sample rate, and mismatches between sub- ADCs are calibrated in the background [1]. D. G. Muratore et al. presents a novel pipeline configuration which is designed and simulated in a 65nm CMOS technology and achieves 2.66 GS/s with 8-bit resolution [2]. Long Yang et al. presents the design of a low power 16-bit 100MS/s pipelined ADC implemented in 180nm CMOS technology [3]. X. Zheng et al. presents a 14-bit 250 MS/s ADC fabricated in a 180nm CMOS process, which targets at optimizing linearity, operating speed, and power efficiency [4].

Currently pipelined ADCs are the best choice for use in high speed communication systems, charge coupled device-based imaging systems, data acquisition systems, ultrasonic medical imaging, base station, digital video, cable modem and fast Ethernet [5]-[8]. Finally pipelined ADCs are appropriate alternatives to time interleaved ADCs. The outline of the work is as follows. Section II discusses the theoretical background of pipelined ADC architecture and various parameters associated with the proposed work. Section III describes the implementation of the proposed pipelined ADC. The simulation results are presented in Section IV. Finally conclusions are provided in Section V.

II. PIPELINED ADC ARCHITECTURE

The Pipelined ADC has turn out to be the best standard architecture for sampling rates from 10 MS/s upto 500 MS/s. When compared to the two-step flash ADC which has just two stages, pipelined ADCs can have multiple cascaded stages. Each stage of the pipelined ADC consists of a sample-and-hold circuit, a sub-ADC, a DAC, a subtractor circuit and an inter-stage gain amplifier [9]. The block diagram of a pipelined ADC architecture is shown in figure 1.

The input analog signal Vin is first sampled and held steady by a sample and hold (S/H) circuit and is given to a flash ADC [12]. The flash ADC in stage one quantizes it into required number of bits. This digital output bits is then fed to DAC, and the analog output is subtracted from the original input signal. The difference called as “residue” is then amplified and fed to the next stage. This gained-up residue continues through the pipeline stages, providing bits per stage until it reaches the final flash ADC, which resolves the last LSB bits. Because the bits from each stage are determined at different points in time, all the bits corresponding to the same sample are time-aligned with shift registers before being fed to the digital error correction logic circuit. It is important to note that when a stage finishes processing a sample, determining the bits, and passing the residue to the next stage, it can then start processing the next sample received from the sample and hold circuit embedded within each stage.

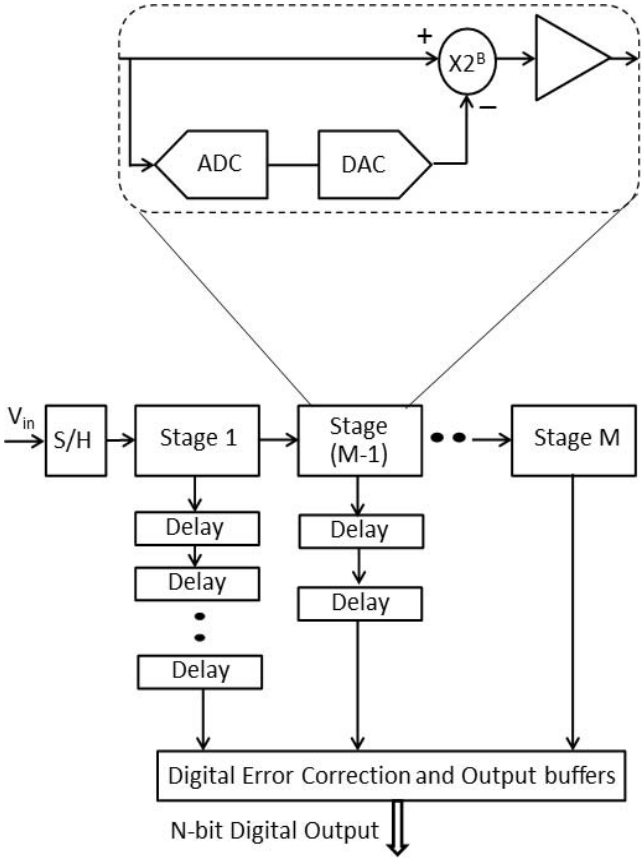

Fig.1 Pipelined ADC Architecture

Due to this pipelining operation, high throughput rate is obtained. Recently pipeline ADCs have improved significantly in terms of speed, power, resolution, signal to noise ratio and dynamic performance. The important specifications considered in this design are resolution=10bits, power supply voltage=1.8V, input bandwidth=upto 1GHz, sampling speed=200MS/s, power dissipation less than 50mW and fabricated in 130nm CMOS technology.

III. SYSTEM IMPLEMENTATION

This section discusses the design of the individual building blocks of the pipelined ADC. The performance of these blocks will determine the performance of each pipelined stage and the final performance of the 10-bit converter. The pipelined ADC architecture shown in figure 1 has 10 stages, each stage having one sub-ADC, one sub-DAC and one gain stage. All these blocks are implemented on the HSPICE and Cadence schematic editor.

A. Sample and Hold (S/H)circuit:

S/H circuit is a key analog building block in many applications. The purpose of the sample and hold circuit is to sample an input analog signal and hold this value over a certain length of time for sub sequent processing. Here input signal is sampled based on the clock frequency. Figure 2 shows the schematic diagram of sample and hold circuit. The input to the sample and hold circuit is a sine wave having amplitude of 1.2Vp-p, power supply is ±1.8V, and clock frequency is 200MS/s. To avoid loading effect, a Voltage follower circuit is connected at the output side.

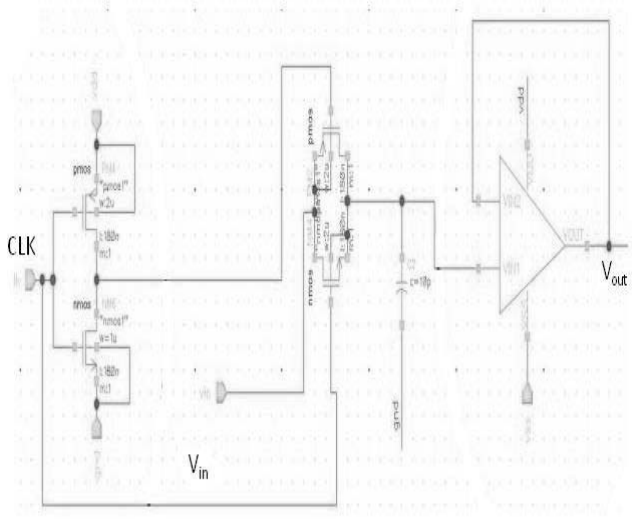

Fig.2 Sample and Hold schematic circuit

B. Comparator circuit:

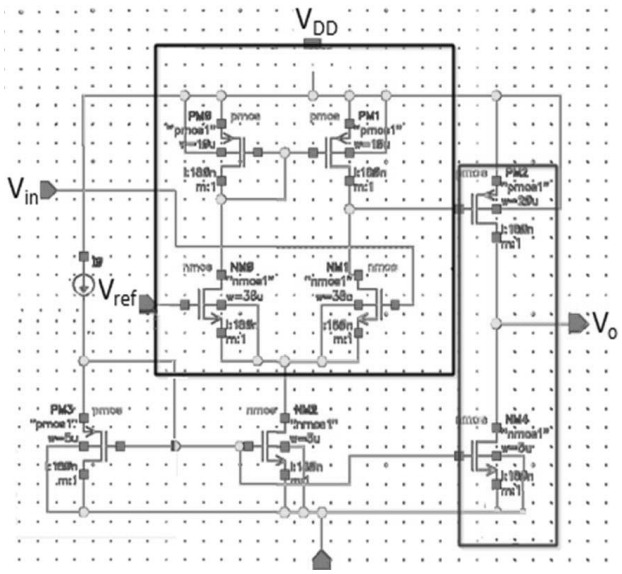

Fig.3 Comparator schematic circuit

A CMOS Comparator circuit is used for comparing the input voltage with a known reference voltage. If the input voltage is greater than reference voltage the comparator output is one, else if the input voltage is less than reference voltage the comparator output is zero. Figure 3 shows the schematic diagram of sample and hold circuit. Here transistors M_1 and M_2 act as a differential pair. Table 1 shows the transistor sizes used in the comparator circuit. The source of transistors M_1 and M_2 are connected with the current sink for biasing. The transistors M_3 and M_4 are PMOS based current mirror, used to realize the load. The transistor M_8 is connected in common source configuration which helps to improve the gain of the complete stage.

Table 1 Transistor sizes

Transistor	Width(m)
M_1	2.6µ
M_2	2.6µ
M_3	0.6µ
M_4	0.6µ
M_5	0.5µ
M_6	0.55µ
M_7	20µ
M_8	22µ

C. 1.5 bit Flash ADC conversion circuit:

The 1.5 bit flash ADC conversion in each pipeline stage consists of two comparators. Figure 4 shows the schematic circuit diagram of 1.5 bit Flash ADC conversion.

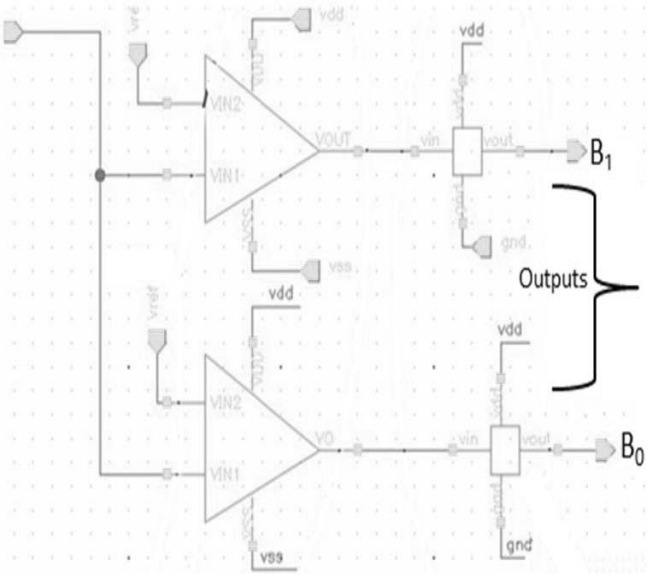

Fig.4 Schematic of 1.5 bit conversion flash ADC

This architecture used here is 1.5 bit per stage. The 1.5 bit sub ADC threshold voltages are $+V_{ref}/4$ and $-V_{ref}/4$. The ADC input range is $+V_{ref}/2$ and $-V_{ref}/2$. The operation of this

circuit is when input signal V_{in} is greater than $-V_{ref}/4$ the output digital bits are 00 and input signal Vin is in between the $+V_{ref}/4$ and $-V_{ref}/4$ the output digital bits are 01, and V_{in} is greater than $+V_{ref}/4$ the output digital bits of this design is 10. Table 2 shows the outputs of the sub-ADC.

Table 2 Sub-ADC output values

V_{in}	Range	output bit values	
		B_1	B_0
$V_{in} > (V_{ref}/4)$	U	1	0
$-\left(\frac{V_{ref}}{4}\right) \le V_{in} \le +(V_{ref}/4)$	M	0	1
$V_{in} \le -(V_{ref}/4)$	L	0	0

D. DAC:

The function of DAC unit is used to reconvert the output produced by the flash ADC into a quantized analog signal. Table 3 shows the outputs of the DAC.

Table 3 Sub-ADC output values

V_{in}	Range	ADC		DAC output
		B_1	B_0	
$V_{in} > (V_{ref}/4)$	U	1	0	$+\left(\frac{V_{ref}}{4}\right)$
$-\left(\frac{V_{ref}}{4}\right) \le V_{in} \le +(V_{ref}/4)$	M	0	1	0
$V_{in} \le -(V_{ref}/4)$	L	0	0	$-\left(\frac{V_{ref}}{4}\right)$

E. First stage of Pipelined ADC:

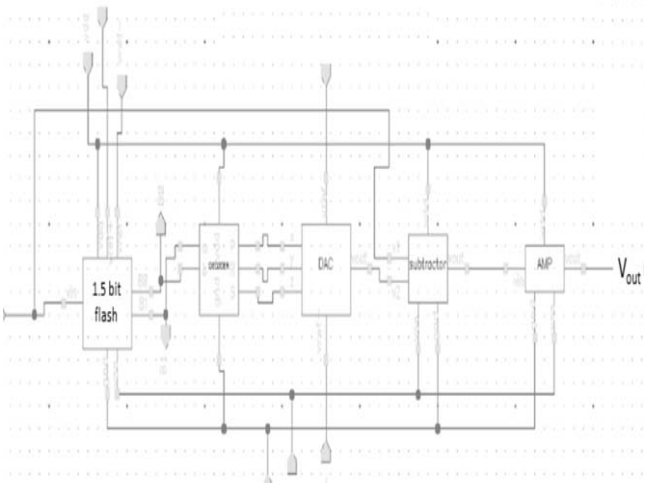

Fig.5 Schematic of first stage of Pipelined ADC

The first stage of pipelined ADC is a sample and hold circuit, 2-bit flash, MDAC (DAC, Subtractor and operational Amplifier). The schematic diagram of first stage of pipelined ADC is shown in the figure 5.

F. Digital Error Correction logic circuit:

Digital error correction logic circuit is mainly used for eliminating the offset error from sub sequent stages in a pipeline ADC. If sub sequent stages detect an error, this error is digitally eliminated by adding or subtracting the bits from the digital bits. Figure 6 shows the schematic diagram of digital error correction logic circuit. Half adder and Full adders are used in realizing the Digital Error Correction logic circuit.

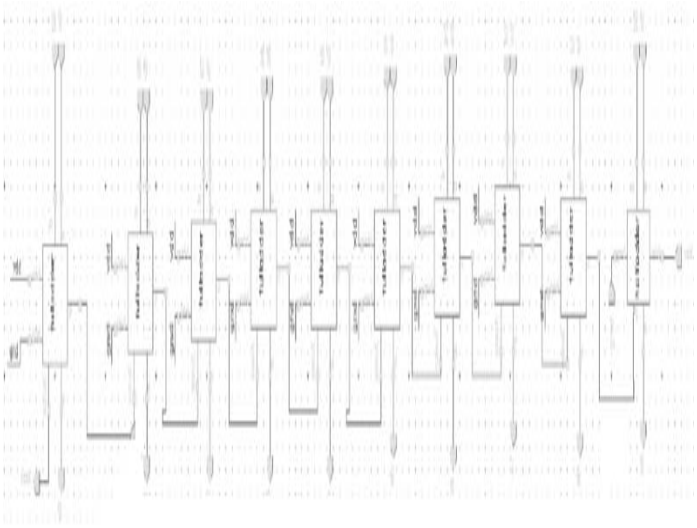

Fig.6 Digital error correction logic schematic circuit

IV. SIMULATION RESULTS

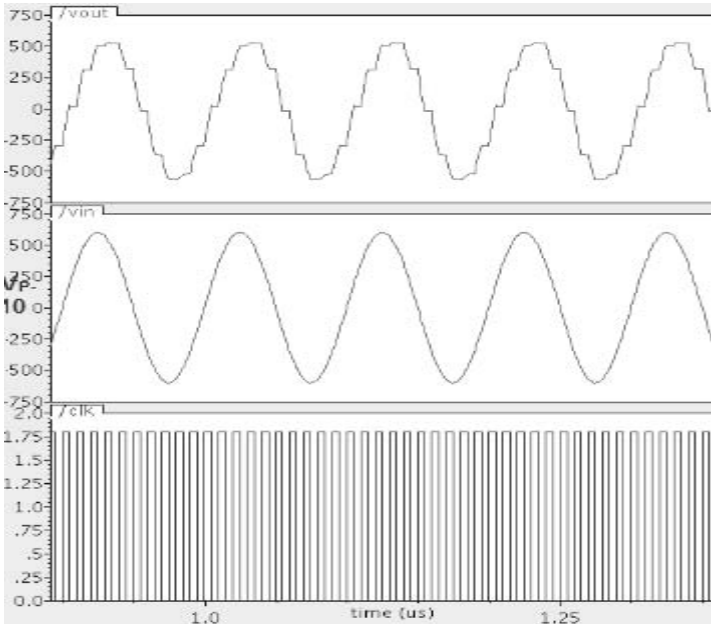

Fig.7 Simulation results of S/H circuit

The performance of the proposed 10-bit pipelined ADC was simulated using Cadence spectre. The entire pipelined ADC

circuit is designed in 130nm CMOS technology. The simulation results of sample and hold circuit is shown in figure 7. The input to the sample and hold circuit is a sine wave having amplitude of 1.0Vp-p, power supply is ±1.2V, and clock frequency is 5GHz. The input signal is sampled based on the clock signal frequency. The simulation results of 1.5 bit ADC are shown in figure 8.

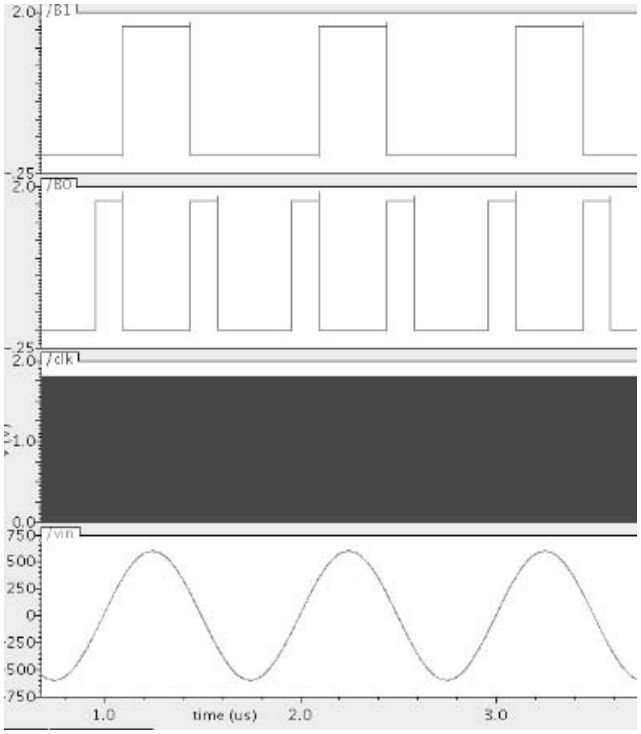

Fig.8 Simulation results of 1.5 bit ADC

The entire design of the pipelined ADC is carried out using 130nm CMOS technology and the results obtained are summarized in table 4.

Table 4 Summary of Pipelined ADC

Resolution	10 bits
Technology	CMOS 130nm
Power Supply	+ 1.8V
Sampling frequency	10GHz
Input Signal Frequency	upto 1GHz
Input voltage range	$1.0V_{P-P}$
Power dissipation	46.8mW
Area	$0.31mm^2$
SNDR	54.7dB

The layout of the 10-bit pipelined ADC is shown in the figure 9.

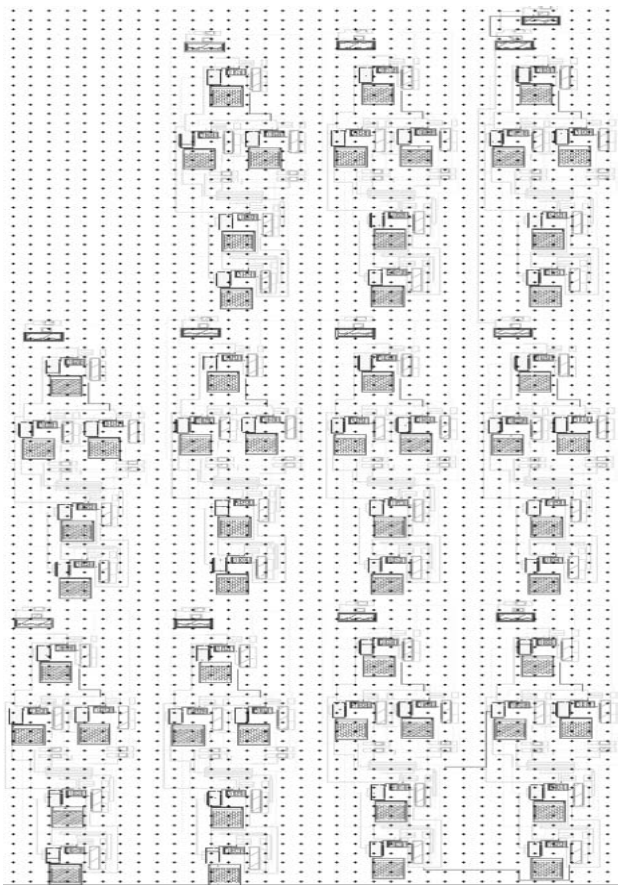

Fig.9 Layout of Pipelined ADC

V. CONCLUSIONS

In this paper, a 10-bit 200Ms/s pipelined ADC is designed and implemented in a 130nm CMOS process technology. The ADC is operated at a power supply of 1.8V and the simulated power consumption is only 46.8mW. The sampling frequency of the proposed ADC is 10GHz. The ADC with an active die area of $0.31mm^2$ shows a maximum signal to noise distortion ratio (SNDR) of 54.7dB. The designed pipeline ADC can be used in applications such as data acquisition systems, ultrasonic medical imaging, base station, digital video, cable modem and fast Ethernet.

REFERENCES

[1] S. Devarajan et al., "A 12-b 10-GS/s Interleaved Pipeline ADC in 28-nm CMOS Technology," in IEEE Journal of Solid-State Circuits, vol. 52, no. 12, pp. 3204-3218, Dec. 2017.

[2] D. G. Muratore, E. Bonizzoni and F. Maloberti, "A pipeline ADC for very high conversion rates," 2016 IEEE International Symposium on Circuits and Systems (ISCAS), Montreal, QC, 2016, pp. 1446-1449.

[3] L. Yang, Z. Wang, L. Zhou and W. Feng, "A low power pipelined ADC with improved MDAC," 2016 International Conference on Control,

Decision and Information Technologies (CoDIT), St. Julian's, 2016, pp. 624-627.

[4] X. Zheng et al., "A 14-bit 250 MS/s IF Sampling Pipelined ADC in 180 nm CMOS Process," in IEEE Transactions on Circuits and Systems I: Regular Papers, vol. 63, no. 9, pp. 1381-1392, Sept. 2016.

[5] L. Kull et al., "CMOS ADCs towards 100 GS/s and Beyond," 2016 IEEE Compound Semiconductor Integrated Circuit Symposium (CSICS), Austin, TX, 2016, pp. 1-4.

[6] Wu Hai-jun, Chen Zhen-hai, Yu Zong-guang and Wang Wei-xing, "A 12-bit 250MSPS Pipeline ADC with 4Gbps serial output interface," 2016 13th IEEE International Conference on Solid-State and Integrated Circuit Technology (ICSICT), Hangzhou, 2016, pp. 1464-1466.

[7] K. C. Kuo, "A 1.2V 10 bits 100-MS/s analog-to-digital converter with a 8-stage pipeline and a 2 bits flash ADC," 2017 International Conference on Applied System Innovation (ICASI), Sapporo, 2017, pp. 1638-1641.

[8] S. Choi et al., "A Self-Biased Current-Mode Amplifier With an Application to 10-bit Pipeline ADC," in IEEE Transactions on Circuits and Systems I: Regular Papers, vol. 64, no. 7, pp. 1706-1717, July 2017.

[9] K. L. Krishna, et al, "A 4b 40 Gbps 140 mW 2.2 mm2 0.13 μm pipelined ADC for I-UWB receiver," 2013 Fourth International Conference on Computing, Communications and Networking Technologies (ICCCNT), Tiruchengode, 2013, pp. 1-6.

[10] C. J. Tseng, C. F. Lai and H. S. Chen, "A 6-Bit 1 GS/s Pipeline ADC Using Incomplete Settling With Background Sampling-Point Calibration," in IEEE Transactions on Circuits and Systems I: Regular Papers, vol. 61, no. 10, pp. 2805-2815, Oct. 2014.

[11] Jie Sun and Jianhui Wu, "A high speed pipeline ADC with 78-dB SFDR in 0.18 um BiCMOS," 2016 International Symposium on Integrated Circuits (ISIC), Singapore, 2016, pp. 1-4.

[12] R.Jacob Baker. “CMOS Mixed Signal Circuit Design”. IEEE Press Series on Microelectronic systems, NJ (2008).

A 6-Bit Low Power SAR ADC

K. Lokesh Krishna[1(✉)], K. Anuradha[2], and Alfakhri M. Murshed[3]

[1] S.V. College of Engineering, Tirupati, Andhra Pradesh, India
kayamlokesh78@gmail.com
[2] L.B.C.E.W., Visakhapatnam, Andhra Pradesh, India
[3] S.V.C.E.T., Chittoor, Andhra Pradesh, India

Abstract. The design of a 6-bit, 100 MHz successive approximation register (SAR) analog to digital converter (ADC) is presented in this paper. The implemented SAR ADC is realized by using SAR logic, a 6-bit DAC, a sample and hold circuit and a comparator circuit. The fully realized system is measured under different input frequencies with a sampling rate of 100 MHz and it consumes 36.7 μW from a 1.8 V power supply. The ADC implemented in 130 nm CMOS technology exhibits signal-to-noise plus distortion ration SNDR of 64.2 dB and occupies a die area of 0.14 mm^2.

Keywords: Data converter · High linearity · Low power · Time-interleaving Comparator · Amplifier

1 Introduction

Physically most data in the real world is described by analog signals. In order to control/process the data using a microprocessor or microcontroller, a data converter circuit is very much indispensable. A data converter is a microelectronic circuit that is used to transform analog signal to digital signal or a digital signal to analog signal. Currently, there has been rapid progress in the design of electronic systems for various applications. The prominence of data converter circuits in the implementation of digital computers and signal processing in communications, image processing, instrumentation and industrial control systems is increasing by leaps and bounds. Hence data converter circuits are extensively used as interface between analog and digital circuits. In general there are two different types of data converter circuits. They are (i) Analog to Digital Converter (ADC) and (ii) Digital to Analog Converter (DAC). Analog to Digital Converter converts an analog signal (continuous time and continuous magnitude) into digital signals (discrete time and discrete magnitude).

ADCs are used in various applications such as Wireless Telecommunication circuits, Medical Imaging technologies, Audio and Video Processing Systems, Software radio and Instrumentation. Broadly there are numerous ADC architectures available to be used for these applications. But selection of an ADC is determined by the application and its specifications. However no single ADC architecture is found to be appropriate for all these applications. At present the major advances in consumer electronics are reflected in smart phones, notebook computers, camcorders, tablets and portable storage devices. All these devices employ various wireless technologies. Also

S. Verma et al. (Eds.): CNC 2018, CCIS 839, pp. 642–652, 2019.
https://doi.org/10.1007/978-981-13-2372-0_57

wireless infrastructural systems such as satellite communication systems, cellular base stations, and various electronic warfare systems require the direct digitization of analog signal in the giga-hertz range. High resolution, High speed and low power consumption are the essential requirements in many wireless portable applications.

Different ADC architectures such as Flash type, Two-step flash type, Integrating type, Sigma-Delta, Pipeline and Interleaving are being used to deliver these requirements for various applications. The performance of an ADC is often affected by the nature of the input signal they process. Because the input analog signal is continuous in nature, ADCs suffer numerous problems such as clock jitter, nonlinear input impedance, number of bits, signal and clock skew, number of components, chip size, power dissipation etc. These problems limit the use of ADC architectures for various applications. Flash ADCs are very fastest converters and are well suitable for large bandwidth applications. But the main problem is that they consume lot of power as the resolution of the converter increases which in turn reflects in the increase in the size of the chip. Also as the chip size increases, more problems associated with signal and clock routing becomes noticeable.

Two step ADCs also well known as subranging converters is a cross between a flash ADC and pipeline ADC can be used to realize higher resolution and small power. Pipelined ADC architecture is a more specialized application of the two-step architecture and has been developed to be the most popular architecture for sampling rates from a few mega samples per second (MS/s) to 500 MS/s, with resolutions ranging from 8 bits to 12 bits.

Sigma-Delta ($\sum$-Δ) ADC architecture are used in low speed applications with resolution ranging from (12–24) bits. Integrating ADCs provide increased resolution and can offer good line frequency and noise rejection. Time interleaved ADCs uses several identical analog to digital converters to process regular sampled data series at a faster rate than the operating rate of each individual ADC. Time inter leaving technique will relax the power-speed tradeoffs of ADC and minimizes metastability error rate while increasing the input capacitance.

Presently Successive Approximation Register (SAR) ADCs are being used in many applications, due to the innovations in architectural design and process scaling techniques of the transistors, which in turn lead to the improvements in low power consumption and high speed operation. SAR analog to digital converters are highly power efficient. Also in recent years, time interleaving of SAR ADCs have led to operate in the giga hertz range. One of the reasons SAR ADCs are doing better is because they use simple logic circuitry (both analog and digital) that tend to scale well and benefit from the evolving newer technologies day by day.

Lai *et al.* [1] presented a SAR analog-to-digital converter implemented in TSMC 0.18-um CMOS process which can be used as a part of the biological signal acquisition system. It employs single-sided switching method that reduces DAC switching energy, thereby achieves low power consumption. Yan *et al.* [2] proposes a two channel interleaved 6-bit 2GS/s SAR ADC design, that employs different comparators using small sized capacitor for each stage, which eliminates digital control delay. Zhu *et al.* [3] presents a high-speed and low-power SAR ADC, that uses a common-mode based charge recovery switching method. Kull *et al.* [4] presents a single-channel SAR ADC which operates at high-speed by converting each sample with two alternate

comparators clocked asynchronously and a redundant capacitive DAC with constant common mode to improve the accuracy of the comparator. Kuo *et al.* [5] propose a new structure namely the charge redistribution DAC to reduce the area cost and power consumption and to enhance the bandwidth. Yang *et al.* [6] proposed an asynchronous ADC realized by time interleaving two ADCs based on the binary successive approximation (SA) algorithm using a series capacitive ladder circuit. Lee *et al.* [7] implemented an ultra-low power SAR ADC for biosignal acquisition systems which utilized a passive sample-and-hold circuit, and an op-amp free, capacitor-based DAC. Compared to the previous related works, a 6-bit low power and medium resolution successive approximation register ADC is designed and simulated in this work.

The outline of the work is as follows. Section 2 discusses the theoretical background of successive approximation register ADC architecture and various parameters associated with the proposed work. Section 3 describes the implementation of the proposed SAR ADC. The simulation results are presented in Sect. 4. Finally conclusions are provided in Sect. 5.

2 Successive Approximation Register ADC Architecture

An SAR analog to digital converter works on the principle of binary search algorithm. This algorithm requires exactly N steps for converting the analog input voltage to an N-bit digital output. Figure 1 shows the block diagram of 6-bit SAR analog to digital converter. It includes a SAR control logic block which is realized using D-flip flop with set and reset controls, a sample and hold circuit, 6-bit digital to analog converter and a comparator circuit [8]. Initially the most significant bit of 6-bit control logic block has been set to 100000. The output of the SAR logic block is connected to 6-bit DAC. This in turn produces equivalent analog output voltage. The output of the 6-bit DAC is compared with the output of the Sample and Hold (S/H) circuit. If the DAC output is higher than the sample and hold output, then the comparator produces a logic zero output, else the comparator produces logic high.

Based on the output of comparator circuit, the SAR control logic will remains the same or reset the control logic block [9]. Recently the design of SAR ADCs has been enhanced considerably in terms of speed, power, resolution, signal to noise ratio and dynamic performance. The important specifications considered in this design are resolution = 6 bits, power supply voltage = 1.8 V, input bandwidth = upto 1 GHz, sampling rate = 100 MHz, power dissipation less than 2 mW and fabricated in 130 nm CMOS technology.

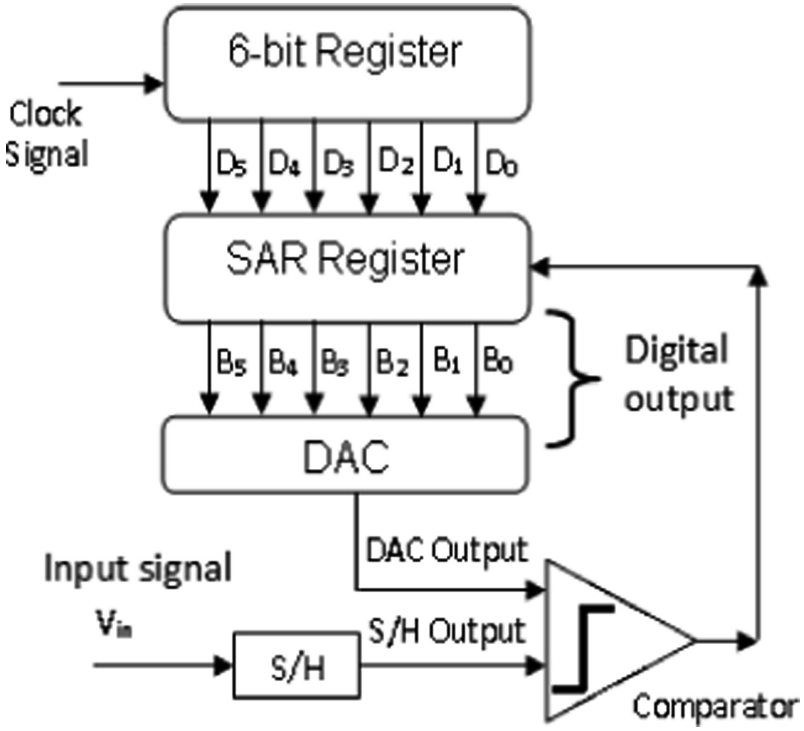

Fig. 1. Block diagram of 6-bit SAR analog to digital converter

3 System Implementation

This section discusses the design of the individual building blocks of the SAR ADC. The performance of these blocks will govern the performance of each stage and then finally the performance of the 6-bit converter. All these blocks are implemented on the HSPICE and Cadence schematic editor.

3.1 Sample and Hold Circuit

The S/H circuit is a key analog building block in many applications. The purpose of the sample and hold circuit is to sample an input analog signal and hold the analog input value over a certain interval of time for sub sequent processing. Here input signal is sampled based on the clock frequency. Figure 2 shows the schematic diagram of sample and hold circuit. It consists of a transmission gate circuit and a sampling capacitor. As long as the clock signal is high i.e. V_{DD} output voltage is same as the input voltage. When the clock signal becomes low, the input signal is sampled and the output voltage is same as the voltage across the sampling capacitor. The input to the sample and hold circuit is a sine wave having amplitude of 1.2 $V_{p\text{-}p}$, power supply is ± 1.8 V, and clock frequency is 100 MS/s. A voltage follower circuit is connected at the output side, in order to avoid the loading effect.

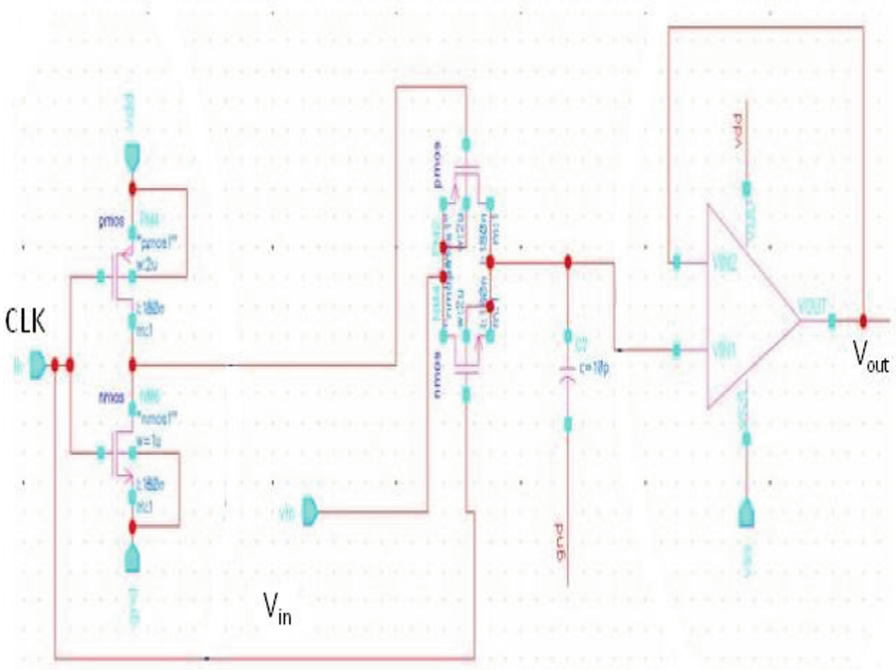

Fig. 2. Sample and hold circuit schematic diagram

3.2 Comparator Circuit

A CMOS Comparator circuit is used for comparing the input voltage with a known reference voltage. If the input voltage is greater than reference voltage the comparator output is one, else if the input voltage is less than reference voltage the comparator output is zero. Here transistors M_1 and M_2 act as a differential pair. The source of transistors M_1 and M_2 are connected with the current sink for biasing. The transistors M_3 and M_4 are PMOS based current mirror, used to realize the load. The transistor M_8 is connected in common source configuration which helps to improve the gain of the complete stage. The comparator schematic is shown in Fig. 3.

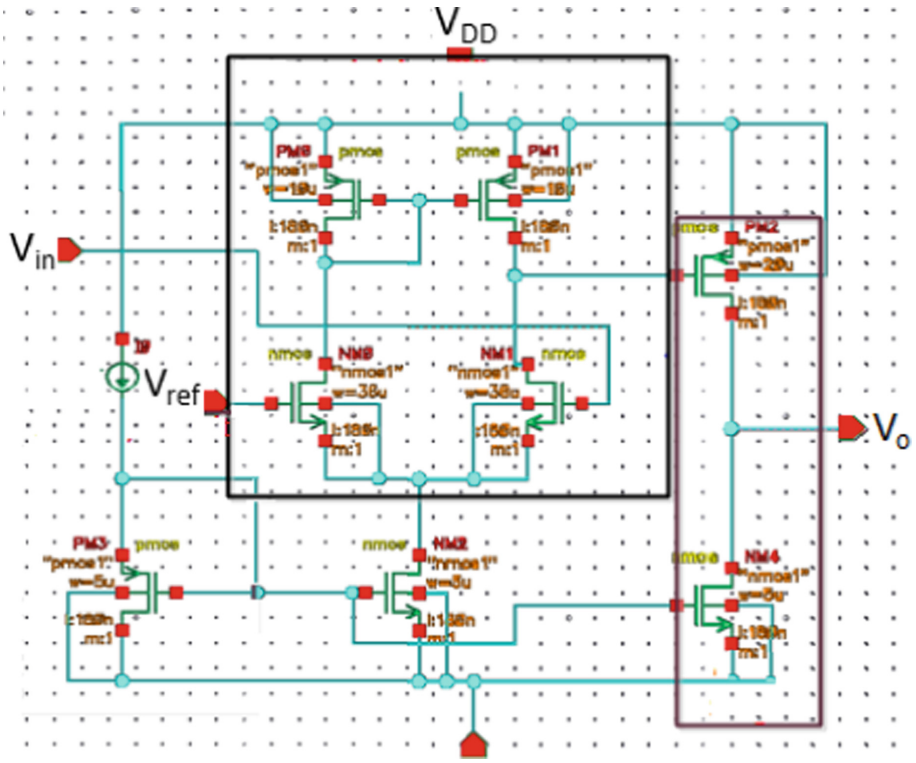

Fig. 3. Comparator schematic

3.3 6-Bit Digital to Analog Converter Circuit Using Transmission Gates

The Fig. 4 shows the 6-bit DAC circuit implemented using resistive ladder network and transmission gates. The resistive ladder network consists of 64 resistors. Based on the values of SAR registers, the distributed voltage is compared with the sample and hold circuit output by comparator.

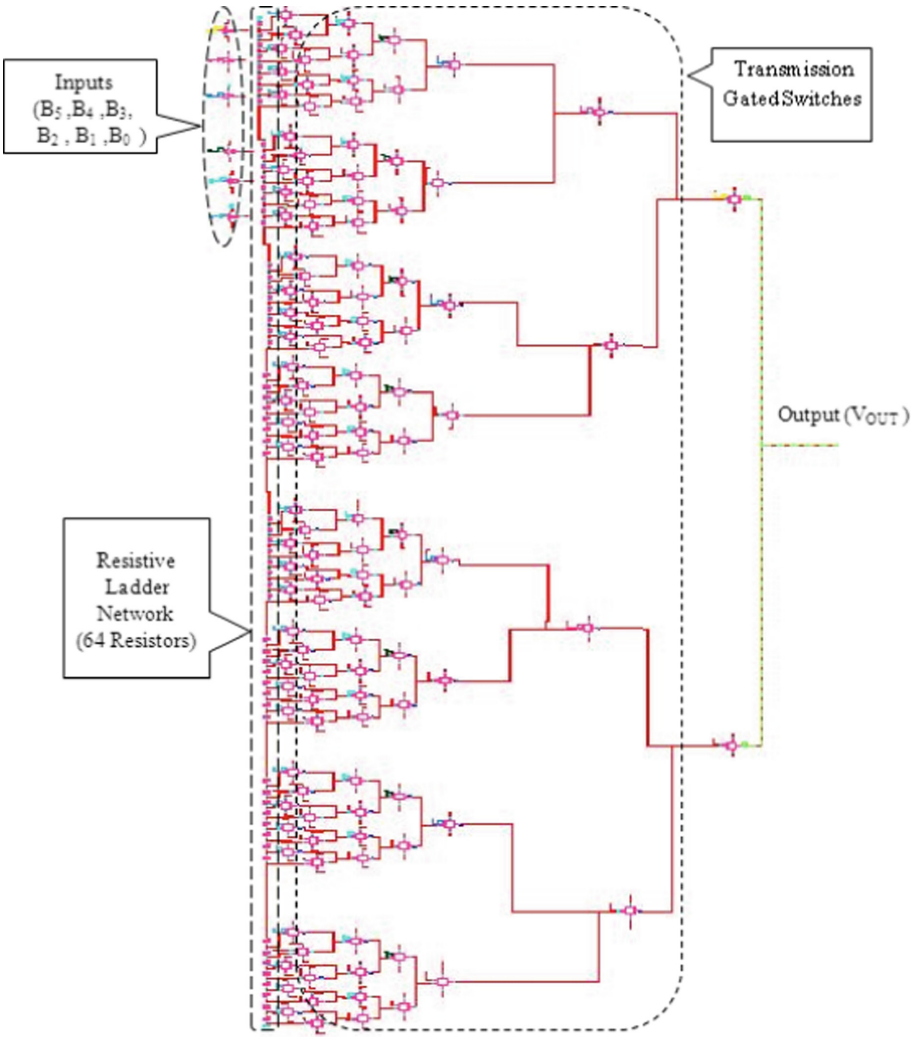

Fig. 4. Schematic of 6-bit DAC

4 Simulation Results

The performance of the proposed 6-bit SAR ADC was simulated using Cadence spectre. The entire SAR ADC is designed in 130 nm CMOS technology. The simulation results of sample and hold circuit is shown in Fig. 5. The input to the sample and hold circuit is a sine wave having amplitude of 1.0 Vp-p, power supply is ±1.8 V, and clock frequency is 800 MHz. The input signal is sampled based on the clock signal frequency.

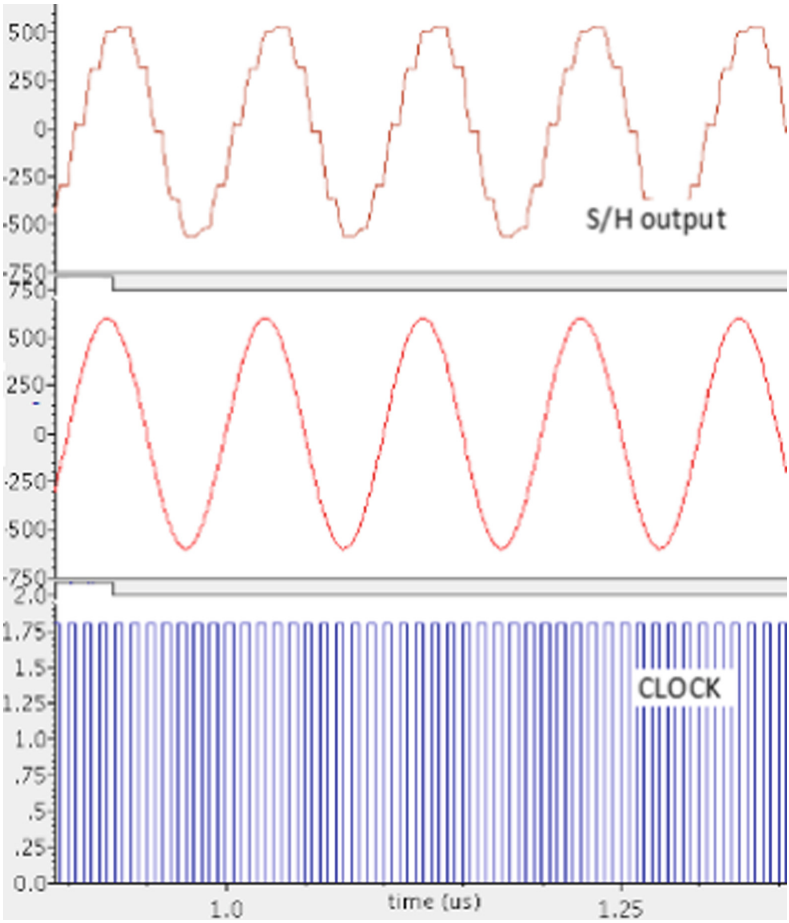

Fig. 5. Simulation results of sample and hold circuit

The final simulation results of 6-bit SAR ADC are shown in Fig. 6. The entire design of the SAR ADC is carried out using 130 nm CMOS technology.

The results obtained are summarized in Table 1.

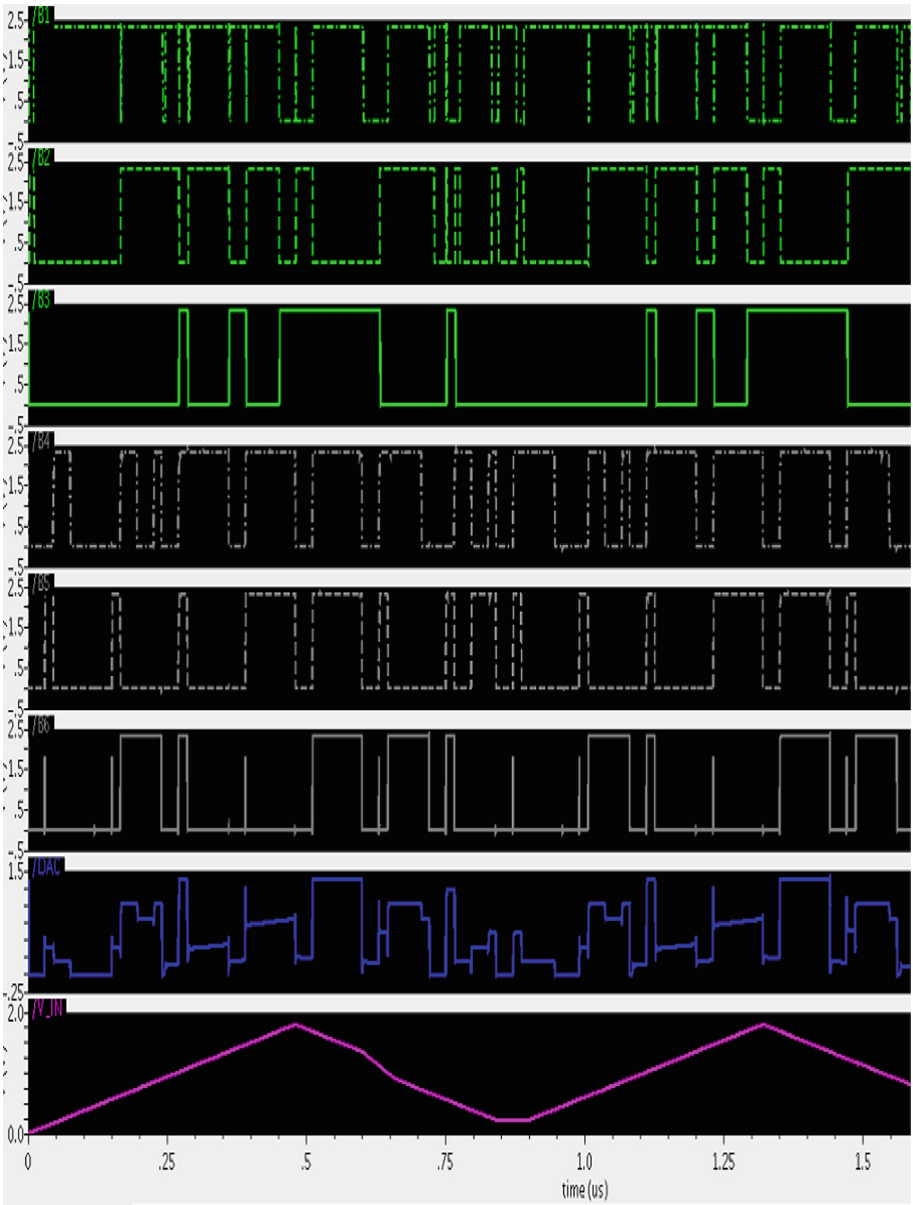

Fig. 6. Simulation results of 6-bit SAR ADC

Table 1. Summary of the 6-bit SAR ADC

Resolution	6 bits
Technology	CMOS 130 nm
Power supply	+1.8 V
Sampling rate	100 MHz
Input signal frequency	upto 1 GHz
Input voltage range	1.0 V_{P-P}
Power dissipation	36.7 μW
Area	0.14 mm^2
SNDR	64.2 dB

5 Conclusion

In this paper, a 6-bit 100 MHz successive approximation register ADC is designed and implemented in a 130 nm CMOS process technology. The ADC is operated at a power supply of 1.8 V and the simulated power consumption is only 36.7 μW. The sampling rate of the proposed ADC is 100 MHz. The ADC with an active die area of 0.14 mm^2 shows a maximum signal to noise distortion ratio (SNDR) of 64.2 dB. The designed SAR ADC can be used in applications requiring lower power dissipation, resolution requirement is medium and speed required is also not high which is MHz to KHz range such as in ultrasonic medical imaging and wireless transmission sensor networks.

References

1. Lai, W.C., Huang, J.F., Hsieh, C.G., Kao, F.T.: An 8-bit 2 MS/s successive approximation register analog-to-digital converter for bioinformatics and computational biology application. In: 2015 IEEE 12th International Conference on Networking, Sensing and Control, Taipei, pp. 576–579 (2015)
2. Yan, F., Libing, Z., Liyuan, L., Dongmei, L.: A 2GSPS 6-bit two-channel-interleaved successive approximation ADC design in 65 nm CMOS. In: 2013 International Conference on Computational and Information Sciences, Shiyang, pp. 1640–1643 (2013)
3. Zhu, Y., et al.: A 10-bit 100-MS/s reference-free SAR ADC in 90 nm CMOS. IEEE J. Solid-State Circ. **45**(6), 1111–1121 (2010)
4. Kull, L., et al.: A 3.1 mW 8b 1.2 GS/s single-channel asynchronous SAR ADC with alternate comparators for enhanced speed in 32 nm digital SOI CMOS. IEEE J. Solid-State Circ. **48** (12), 3049–3058 (2013)
5. Kuo, H.L., Lu, C.W., Lin, S.G., Chang, D.C.: A 10-bit 10 MS/s SAR ADC with the reduced capacitance DAC. In: 2016 5th International Symposium on Next-Generation Electronics (ISNE), Hsinchu, pp. 1–2 (2016)
6. Yang, J., Naing, T.L., Brodersen, R.W.: A 1 GS/s 6 bit 6.7 mW successive approximation ADC using asynchronous processing. IEEE J. Solid-State Circ. **45**(8), 1469–1478 (2010)
7. Lee, S.Y., Cheng, C.J., Wang, C.P., Lee, S.C.: A 1-V 8-bit 0.95 mW successive approximation ADC for biosignal acquisition systems. In: 2009 IEEE International Symposium on Circuits and Systems, Taipei, pp. 649–652 (2009)

8. Krishna, K.L., Ramashri, T.: VLSI design of 12-Bit ADC with 1 GSPS in 180 nm CMOS integrating with SAR and two-step flash ADC. J. Theor. Appl. Inf. Technol. **68**(1), 27–35 (2014)
9. Baker, R.J.: CMOS Circuit Design, Layout and Simulation, 3rd edn. Wiley-IEEE Press, Hoboken (2010)

A k-NN-Based Approach Using MapReduce for Meta-path Classification in Heterogeneous Information Networks

Sadhana Kodali, Madhavi Dabbiru, B. Thirumala Rao and U. Kartheek Chandra Patnaik

Abstract Classification of the nodes along with the interconnected semantic edges in a Heterogeneous Information Network (HIN) has a lot of significance in identifying the class labels which involves the application of knowledge and dissemination of knowledge from one node to the other. In this paper, the authors applied PathSim similarity measure for finding k-nearest neighbors along with the use of the well-known MapReduce paradigm to classify the meta-paths in a Heterogeneous Information Network. Applying MapReduce simplified the classification approach which deals with huge data present in the Heterogeneous Information Networks. Experiments were carried out on movie theater dataset, and the results are accurate and successful.

Keywords Classification · k-NN · MapReduce-based classification Meta-path

Sadhana Kodali (✉) · B. Thirumala Rao
Department of CSE, Koneru Lakshmaiah Education Foundation, Vaddeswaram 522502, India
e-mail: sadhanaphd@gmail.com; sadhanalendicse@gmail.com

B. Thirumala Rao
e-mail: drbtrao@kluniversity.in

Madhavi Dabbiru
Department of CSE, Dr. L. Bullayya College of Engineering for Women, Visakhapatnam 530016, Andhra Pradesh, India
e-mail: drlbcse@gmail.com

U. Kartheek Chandra Patnaik
Department of CSE, Lendi Institute of Engineering & Technology, Jonnada, Vizianagaram 535005, India
e-mail: ukcp.lendi@gmail.com

J. Nayak et al. (eds.), *Soft Computing in Data Analytics*,
Advances in Intelligent Systems and Computing 758,
https://doi.org/10.1007/978-981-13-0514-6_28

1 Introduction

In today's world of interconnectivity between objects, a semantic network is formed which is called the Heterogeneous Information Network [1]. The autonomous objects present in the information network are treated as nodes which may be distributed, and the semantic relationships between these nodes are treated as edges. A social network is a best example of a heterogeneous network [2]. Observing and traversing the semantic paths connected between the nodes of a heterogeneous network can evolve many new and interesting things like the drug discovery, finding new friends, prediction of links, movie recommendations, item recommendations which are the major applications of the Heterogeneous Information Networks. To classify these nodes which are labeled is a challenging task. The existing algorithms like RankClass, HnetMine were based on path-based classification. The k-NN algorithm is one of the best approaches for classifying the data which is distributed. In this paper, the k-NN algorithm is applied to classify the meta-path which is formed by the traversal of the path between the objects using a similarity measure proposed in PathSim [3]. In this paper, the authors propose the approach to classify the nodes in the meta-path using k-NN with PathSim similarity measure, and later, they applied the MapReduce [4] to identify the nodes which are similarly close to each other.

1.1 Example of Heterogeneous Information Network

A Heterogeneous Information Network (HIN) is the semantic connectivity between the autonomous objects. The traversal of the semantic paths over a heterogeneous network gives a meta-path. Using a meta-path as an input, the commuting matrix is computed. The commuting matrix is calculated between two different kinds of attributes as in [5]. Attributes of category 1 are treated as row and attributes of category 2 are treated as columns. If there is a mapping present between the two attributes, then the matrix will have a value one; otherwise, the value is zero. Using this commuting matrix, the k-NN measure is applied with PathSim similarity calculation given as Eq. 1.

$$S(x:y) = 2\left(P_{x\to y:}\, P_{x\to y}\varepsilon P\right)/\left|\left(P_{x\to x:}\, P_{x\to x}\varepsilon P\right) + \left|\left(P_{y\to y:}\, P_{y\to y}\varepsilon P\right)\right|\right. \quad (1)$$

After which the input is given to the map task followed by the reduce task to observe the relevance between the classified entities. The rest of the paper is organized as follows: Sect. 2 narrates related work, Sect. 3 details the proposed approach, Sect. 4 discusses experimentation, and Sect. 5 concludes the paper followed by references.

2 Related Work

Heterogeneous Information Networks are formed by the interaction between different kind of objects and the semantic relationship between them. A number of classification algorithms are proposed for classification of HIN like the HetPathMine, Graffiti, and RankClass. But the well-known supervised learning-based classification using k-NN is more popular, and the use of this k-NN with the application of MapReduce is an excellent solution to classify huge networks which involve interaction among heterogeneous objects with semantic relationships.

2.1 Similarity Calculation

The network can be considered as a graph where the objects are the nodes and the connecting relationship between these objects is the edge. When these objects are traversed via a meaningful relationship, a meta-path is formed. The meta-paths can be more in number. The k-NN algorithm is applied to these meta-paths which is a graph-based k-NN, the similarity between the nodes is computed by using the PathSim similarity measure, and the weight factor is replaced with the similarity measure computed. To compute this similarity measure between nodes, the commuting matrix is formulated. The values presented in the commuting matrix are the weights between these nodes. The following example can be considered: if a person watches a movie in a theater, the meta-paths can be obtained in this manner: person —movie—theater. The commuting matrix can be formed between the person and theaters based on the number of times he visits the theater. This is shown in Fig. 1a.

The similarity between P1 and P2 are computed as $2 * (2 * 2 + 3 * 4)/(2 * 2 + 3 * 3) + (2 * 2 + 4 * 4) = 0.9696$. The similarity scores in the same way are calculated between each person which measures how similar they visit the theaters as shown in Fig. 1b.

Fig. 1 **a** Commuting matrix, **b** similarity scores

Person\Theatre	T1	T2	T3
P1	2	3	0
P2	2	4	1
P3	1	2	3

(a) Commuting Matrix

Person\Similarity Score	PathSim Similarity
P1,P2	0.969
P1,P3	0.888
P2,P3	0.742

(b) Similarity scores

The network can be considered as a graph where the objects are the nodes and the connecting relationship between these objects is the edge. When these objects are traversed via a meaningful relationship a meta-path occurs. The meta-paths can be any in number. The k-NN algorithm is applied to these meta-paths which is a graph based k-NN and the similarity between the nodes is computed by using the PathSim similarity measure and the weight factor is replaced with the similarity measure computed. To compute this similarity measure between nodes, the commuting matrix is formulated. The values presented in the commuting matrix are the weights between these nodes. The following example can be considered if a person watches a movie in a theatre, the meta-paths can be obtained in this manner: person -movie - theatre. The commuting matrix can be formed between the person and theatres based on the number of times he visits the theatre. This is shown in figure 1(a).

The similarity between P1 and P2 are computed as 2* (2*2+3*4)/ (2*2+3*3) + (2*2+4*4) =0.9696.The similarity scores in the same way are calculated between each person which measures how similar they visit the theatres are shown in figure 1(b).

3 Approach

The heterogeneous information network is traversed to find out all the possible meta- paths in it. After all the meta-paths are obtained the k-NN algorithm is computed with PathSim similarity calculation.

Table 1: Algorithm for graph based k-NN using PathSim similarity construct

k-NN algorithm to classify nodes in HIN
Step 1:Input $X=X_l \cup X_{ul}$ Step 2: Construct the commuting matrix. Step 3: Apply the PathSim similarity measure using equation 1. $S(x:y)=2(P_{x->y} : P_{x->y} \in P) / \mid (P_{x->x} : P_{x->x} \in P)+ \mid (P_{y->y} : P_{y->y} \in P) \mid$ Step 4: Write the similarity measures to a file which should serve as an input to MapReduce.

Table 2: Algorithm using MapReduce to obtain classification

k-NN algorithm to classify nodes in HIN
Step 1:Input file containing names of the nodes and corresponding similarities Step 2:Use the Map task to get the corresponding <key,Value> pairs Step 3: specify the similarity ranges to make partitions. Step 4: The last reducer receives the unlabelled nodes and their similarities.

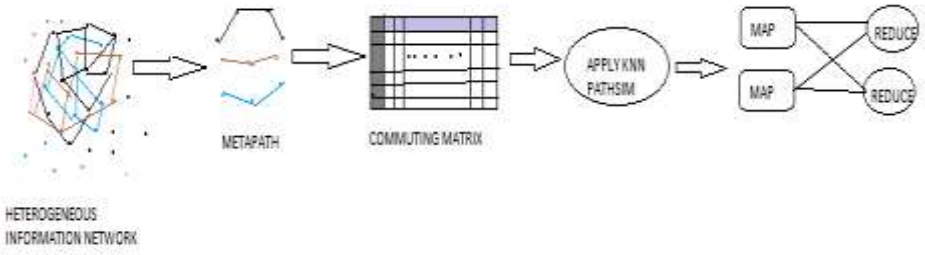

Figure 2: Approach for k-NN classification using MapReduce.

The Table 1 represents the algorithm which takes the graph which contains the labeled and unlabeled nodes from which the meta-paths are identified and a commuting matrix is computed using the Pathsim similarity measure. The calculated similarities are given as an input to the Map Reduce task. The Table 2 shows the working of the MapReduce task in which we also identified the k Nearest Neighbors and the output is written to a part-r-00000 file.

The input to the Mapper is a file which contains the Manhattan distance of the similarity scores between two objects. The similarity score is computed using the PathSim similarity measure. The Manhattan distance is used to compute the distance between two similar points which is given by $dist\ (x_i: xj) = \Sigma|x_i\text{-}x_j|$. The Mapper writes a set of <*Key, Value*> pairs where *Key* contains the names of the attributes and *Value* is the List of similarity scores which are computed using the distance metric. The Reducer compares a test value with every other value in the List and with the specified *k* value the Nearest Neighbors are identified. The k-NN classifies the given similarity scores which is obtained as an output in the part-r00000 file which is stored onto HDFS.

4 Experimentation

The experimental results are tested on a single node Hadoop machine with 8GB RAM. The training data sets are stored onto the HDFS. The experiment is initially preceded with 30 records then increased it to 120,191 then slowly to 781 records. For all the above mentioned the map and reduce tasks were completed 100% and generated the k neighbors with the specified *k* value. The below figure shows an example of the result obtained after generating the hadoop jar file and using the dataset stored on HDFS. We took the training data of the theatre data set and classified three labels.

Figure 3: MapReduce execution Results.

The figure 3 shows the final execution after the MapReduce which is run on a pseudo distributed environment. The runtimes for different dataset sizes are represented in a graph as shown in figure 4.

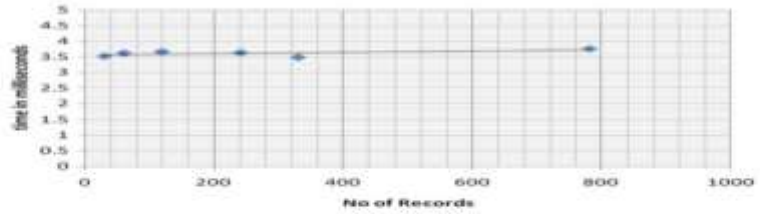

Fig. 4 Graph showing the runtime analysis

Fig. 5 Final output obtained on benchmark data

Synthetic data consists of 780 records generated by the authors. In the training dataset, we have considered person versus number of times the movie watched in nearby theaters. In the benchmark data, the person versus the movie ratings is considered. The ratings are given as inputs to the MapReduce task where the k-NN classifier is applied to identify the first five ratings of every movie present in the dataset. The final output is represented in Fig. 5. The execution times are shown in a graph, and the entire tuples in the dataset took just 4.55 ms to execute on a stand-alone machine where Hadoop is installed. The accuracy of the classification results is then computed in the subsection below.

4.1 Classification Accuracy

The classification accuracy is given as the number of correct predictions made divided by the number of predictions. The percentage of classification accuracy for our datasets has turned to be 100% for all the data records. The classification accuracy for the synthetic data is depicted in Table 3.

Table 4 represents the classification accuracy of benchmark data. All the jobs submitted to the MapReduce are done and the top five neighbors for every unique movie id present in the data are generated. Figure 6 represents the execution times plotted for the various sizes of datasets.

Table 3 Classification accuracy

Dataset size	Accuracy (%)
30	100
60	100
120	100
240	100
480	100
781	100

Table 4 Accuracy for benchmark datasets

Dataset size	Accuracy (%)
5000	90
10,000	94
20,000	92
30,000	95
40,000	92
65,536	98

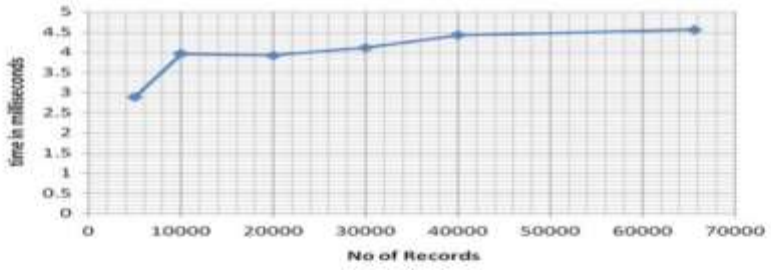

Fig. 6 Execution times for 65,536 records

5 Conclusions

In this paper, the authors suggested the approach of k-NN-based classification using meta-path similarity and the use of MapReduce to classify the Heterogeneous Information Networks. As the object heterogeneity increases, it is difficult to classify the labeled and unlabeled entities, but with this proposed approach, any kind of HIN input can be given and applied the basic classification approach with the support of MapReduce to handle big graphs which are nothing but the big data obtained from the HIN. The experiments are conducted on a stand-alone machine on which Hadoop is installed in pseudo-distributed mode. Our future work is to observe the distributed data as most of the HINs have the nodes scattered in a distributed manner by running the MapReduce task on parallel machines.

References

1. Shi, C., Li, Y., Zhang, J., Sun, Y., Philip, S.Y.: A survey of heterogeneous information network analysis. J. Latex Class Files **14**(8) (2015)
2. Han, J., Sun, Y.: Mining heterogeneous networks principles and methodologies (2012)
3. Sun, Y., Han, J., Yan, X., Yu, P.S., Wu, T.: PathSim: meta path based TopK similarity search in heterogeneous information networks. Proc. VLDB Endow. **4**(11) (2011)
4. Dean, J., Ghemawat, S.: MapReduce: simplified data processing on large clusters. OSDI 11 Mar 2004
5. Kodali, S., Dabbiru, M., Meduri, K.: Constraint based approach for minging heterogeneous information networks. In: Proceedings of 6th IEEE IACC 2016, 27–28 Feb 2016
6. https://grouplens.org/datasets/movielens/